UNIVERSITY OF SOUTHAMPTON

Faculty of Engineering and Physical Sciences
School of Engineering

Computational Aeroelasticity for Next–generation Aircraft

by

Daniel Kharlamov
Master of Science

A thesis for the degree of
Doctor of Philosophy

January 2021

University of Southampton

Abstract

Faculty of Engineering and Physical Sciences
School of Engineering

Doctor of Philosophy

Computational Aeroelasticity for Next–generation Aircraft

by Daniel Kharlamov

During the conceptual stage of an aeroplane design project, the use of high–fidelity computational methods as a routine engineering design tool for the estimation of aerodynamic loads on wings is prohibitive due to the high computational costs for design exploration studies. This difficulty can be overcome by a novel methodology for rapid, physics–based predictions of aerodynamic loads and can be deployed as a unified approach for subsonic and transonic flow analysis in steady–state and unsteady flow regimes. The approach, which is presented in this thesis, is based on three components: 1) a cost–effective flow solver of the infinite–swept wing problem that captures sectional viscous phenomena, 2) a steady–state and unsteady Vortex–Lattice method (VLM) that captures three–dimensional inviscid flow effects around a finite wing, and 3) an appropriate coupling algorithm that corrects low–fidelity three–dimensional inviscid flow with high–fidelity sectional nonlinear viscous aerodynamic data. In this thesis the formulation of all three components of this approach are described in detail followed by test cases, where the capabilities and performance of the novel efficient nonlinear aerodynamic model are demonstrated in steady–state and unsteady flow regimes. Finally, in this work the application of this mixed–fidelity and low–cost aerodynamic model is demonstrated in the field of computational aeroelasticity, where the aerodynamic algorithm is coupled with a nonlinear geometrically–exact beam model with the purpose of obtaining aerodynamic loads on highly deflected and twisted aeroplane wings. The computational aeroelasticity framework, which incorporates the nonlinear FE–beam model and the aerodynamic coupling code, provides the ability to obtain rapid aeroelastic results, which are in the same order of magnitude of the accuracy as results obtained by high–fidelity computationally intensive aeroelasticity frameworks.

Contents

Nomenclature

Acronyms

CO_2	Carbon Dioxide
ACARE	Advisory Council of Aviation Research in Europe[2]
CAD	Computer Aided Design
CFD	Computational Fluid Dynamics
DLR	Deutsches Zentrum für Luft– und Raumfahrt
EDF	Electric–Ducted Fan
FALCon	Fast Aerodynamic Loads Calculations
FSI	Fluid–Structure–Interaction
GEBT	Geometrically–Exact Beam Theory
HALE	High–Altitude Long–Endurance
HALE UAV	High–Altitude Long–Endurance Unmanned Aerial Vehicle
HAPS	High–Altitude Pseudo–Satellites
HAR	High Aspect Ratio
HARW	High Aspect Ratio Wing
MDO	Multidisciplinary Design Optimisation
MG	Design Maturity Gate
NOx	Nitrogen Oxides, a mixture of binary compounds of oxygen and nitrogen
ONERA	Office National d'Études et de Recherches Aérospatiales
q3D	Quasi–3D aerodynamic approach
RANS	Reynolds–Averaged Navier–Stokes equations
UVLM	Unsteady Vortex–Lattice method
VABS	Variational Beam Sectional Analysis
VAM	Variational–Asymptotic method
VLM	Vortex–Lattice method

Greek Symbols

α	Angle of attack	[*rad*]

α_0	Zero lift angle of attack	$[rad]$
α_e	Effective angle of attack	$[rad]$
α_{ind}	Induced angle of attack	$[rad]$
$\Delta\alpha$	Angle of attack correction increment	$[rad]$
$\Delta\alpha$	Pitching angle of attack increment, only in Section 3.4.2	$[rad]$
$\Delta\beta$	Side–slip correction increment	$[rad]$
$\Delta\dot{\Gamma}_{i,j}$	Time derivative of the leading edge vortex intensity of a VLM panel	$[m^2/s^2]$
Γ	Vortex–ring intensity	$[m^2/s]$
γ	Taper ratio of a wing, $\gamma = c_{Tip}/c_{Root}$	$[-]$
Λ	Geometrical sweep of a wing section or a wing	$[rad]$
ν	Relaxation factor	$[''\text{-}'']$
ω	Frequency	$[1/s]$
Φ	Velocity potential, see Section 2.1	$[m^2/s]$
ρ	Density of the fluid	$[kg/m^3]$
τ	Reduced time, $\tau = tV/c_{ref}$	$[-]$
$\theta_{x,j}$	Current aeroelastic deflection angle	$[rad]$
ε	Prescribed convergence tolerance error	$[''\text{-}'']$
θ_1^b	1st Wiener–Milenković rotation parameter	$[-]$
θ_2^b	2nd Wiener–Milenković rotation parameter	$[-]$
θ_3^b	3rd Wiener–Milenković rotation parameter	$[-]$

Roman Symbols

$\Delta\dot{\mathbf{x}}_{c,n}$	Velocity of the collocation point of a VLM panel	$[m/s]$
$\delta\mathbf{F}_j$	Spanwise aerodynamic force	$[N]$
$\delta\mathbf{F}_{i,j}$	Steady–state aerodynamic force on a wing bounded VLM panel	$[N]$
$\delta\mathbf{F}_{i,j}^u$	Unsteady aerodynamic force contribution of a VLM panel in unsteady flow regime	$[N]$
Δh	Vertical displacement increment, only in Section 3.4.2	$[m]$
Δx^b	Translational displacement of a FEM beam node in x–direction	$[m]$
Δy^b	Translational displacement of a FEM beam node in y–direction	$[m]$
Δz^b	Translational displacement of a FEM beam node in z–direction	$[m]$
$\dot{h}$	Vertical plunge velocity, only in Section 3.4.2	$[m/s]$
$\mathbf{\Gamma}$	Vector of vortex–ring intensities of all wing bounded VLM panels	$[''m^2/s'']$
$\mathbf{A}$	Aerodynamic influence matrix in VLM	$[''-'']$
$\mathbf{f}^b$	Displacement vector of a FEM node, see Equation 3.87	$[\,]$
$\mathbf{n}$	Normal vector	$[m]$
$\mathbf{q}_{nm}$	Normalised velocity contribution of the vortex–ring of the	

	m–th VLM panel on the collocation point of the n–th VLM panel	$[s]$
$\mathbf{R}$	Right–hand–side vector containing in VLM non–circulatory velocity contribution	$[''m^2/s'']$
$\mathbf{R}_z$	Rotation matrix about the z axis	$[-]$
$\mathbf{S}$	FEM stiffness matrix	$[\,]$
$\widetilde{C}_{L,inv}$	Quasi–steady lift force coefficient in UVLM	$[-]$
a_{nm}	Aerodynamic influence coefficient, $a_{nm} = \mathbf{n}_n \cdot \mathbf{q}_{nm}$	$[-]$
AR	Aspect ratio of the wing, $AR = b^2/S$	$[-]$
b	Wing span of the wing	$[m]$
c	Chord length of a wing	$[m]$
C_D	Aerodynamic drag force coefficient	$[-]$
c_f	Non–dimensional friction coefficient, $c_f = \tau/q_\infty$	$[-]$
C_L	Aerodynamic lift force coefficient	$[-]$
C_L^α	Lift slope, $C_L^\alpha = dC_L/d\alpha$	$[1/rad]$
C_M	Aerodynamic moment coefficient	$[-]$
c_p	Non–dimensional pressure coefficient, $c_p = (p - p_{ref})/q_\infty$	$[-]$
$C_{D,ind}$	Induced drag force coefficient	$[-]$
$C^u_{L,inv,n}$	Unsteady lift force coefficient contribution in UVLM	$[-]$
$C_{L,max}$	Maximal lift force coefficient at stall	$[-]$
$C_{M,0.25}$	Aerodynamic moment coefficient of an aerofoil with respect to quarter chord	$[-]$
E	Young modulus	$[N/m^2]$
G	Shear modulus	$[N/m^2]$
I_2	Area moment of inertia in direction x_2 of the local GEBT beam frame of reference, see Figure 3.11	$[m^3]$
I_3	Area moment of inertia in direction x_3 of the local GEBT beam frame of reference, see Figure 3.11	$[m^3]$
J	Torsional constant	$[m^3]$
k	Reduced frequency, $k = \omega c_{ref}/V$	$[-]$
K_2	Shear coefficients in direction x_2 of the local GEBT beam frame of reference, see Figure 3.11	$[m^2]$
K_3	Shear coefficients in direction x_3 of the local GEBT beam frame of reference, see Figure 3.11	$[m^2]$
m_{MTOW}	Maximal take–off weight	$[kg]$
m_{OEW}	Operating empty weight	$[kg]$
N	Total number of wing bounded VLM panels on a VLM lattice, $N = N_i \times N_j$	$[-]$
N_b	Total number of beam nodes in a FEM beam mesh	$[-]$
N_i	Total number of wing bounded chordwise VLM panels on a VLM lattice	$[-]$

N_j	Total number of wing bounded spanwise VLM panels on a VLM lattice	$[-]$
p	Pressure	$[N/m^2]$
q	Angular pitch velocity, only in Section 3.4.2	$[rad/s]$
q_∞	Dynamic pressure at the farfield, $q_\infty = 0.5\rho_\infty V_\infty^2$	$[N/m^2]$
R	Range (only in Section 1.2)	$[m]$
r	Distance between two positions	$[m]$
Re	Reynolds–number	$[-]$
S	Cross–section area of the beam (only in Section 3.5.1)	$[m^2]$
S	Reference wing area	$[m^2]$
u	Cartesian aerodynamic flow velocity in x–direction	$[m/s]$
V	Velocity magnitude	$[m/s]$
v	Cartesian aerodynamic flow velocity in y–direction	$[m/s]$
w	Cartesian aerodynamic flow velocity in z–direction	$[m/s]$
w	Induced downwash velocity, only in Section 3.2.1.2 and Section 3.2.2.2	$[m/s]$
y^+	Dimensionless wall distance	["-"]
(C_L/C_D)	Aerodynamic efficiency	$[-]$
Δx_p	Centre of aerodynamic sectional pressure	$[m]$

Subscripts

∞	Quantity at the freestream farfield of the flow field
i	Chordwise index of the collocation point on a VLM lattice
j	Spanwise index of the collocation point on a VLM lattice
inv	Flow quantity obtained with an inviscid computational method, here VLM or UVLM
visc	Nonlinear viscous quantity, for example $C_{L,visc}$ or $C_{D,visc}$, obtained by 2D or 2.5D+ ISW– or 3D (U)RANS CFD solver

List of Figures

List of Tables

Acknowledgements

I can state with no hesitation that I was very lucky being a doctoral student at the University of Southampton. I have gained a lot of additional experience in the field of computational modelling of aerodynamics and aeroelasticity during this time, extended my skills in programming and management. While being completely responsible for this PhD candidacy I have developed also a lot of additional skills outside of the technical field. Therefore, I would like to thank my both supervisors, Dr Andrea Da Ronch and Dr Scott Walker, who were guiding me very professionally during this time and brought me back on track when it was required. Further, I would also like to thank my colleges and good old friends from my office, especially Dr Jacob Turner, Antonio Reyes, Manuel Buitrago and Riccardo Rubini, with who I have spend great time and with who I have discussed many interesting topics and ideas in science and technology. This inspired and motivated me constantly during the entire project. I also would like to acknowledge my discussions with Dr Angelo Niko Grubišić about the aerodynamics of wingsuites and the application of the presented computational methodology in this field. Dr Angelo Niko Grubišić was a highly enthusiastic aeronautical engineer and wingsuite pilot. He passed away in 2019. I will always miss him. At the University of Southampton I have visited from time to time the *University of Southampton Russian speaking society*. I have met there many friends and had a great and funny time with them.

I would like to thank my good old friends in Germany Ilya, Dima, Sonja and Ivan, who always supported and gave me motivation remotely from Germany during my time in UK.

I would also like to mention my current two colleges, Dr Marie Albisser and Dr Cédric Decrocq, from ISL (*Institut franco–allemand* de recherches de Saint–Louis) in France, which gave me in the final stage of my PhD very useful and important feedback on two journal papers on which this thesis is mostly based on.

Finally, I would like to acknowledge the support of my family, which constantly motivated me during good and tough times of this doctoral candidacy. They always believed in me, even when I did not. There are no words, which describes how thankful I am to all of you!

Declaration of Authorship

I declare that this thesis and the work presented in it is my own and has been generated by me as the result of my own original research.

I confirm that:

1. This work was done wholly or mainly while in candidature for a research degree at this University;
2. Where any part of this thesis has previously been submitted for a degree or any other qualification at this University or any other institution, this has been clearly stated;
3. Where I have consulted the published work of others, this is always clearly attributed;
4. Where I have quoted from the work of others, the source is always given. With the exception of such quotations, this thesis is entirely my own work;
5. I have acknowledged all main sources of help;
6. Where the thesis is based on work done by myself jointly with others, I have made clear exactly what was done by others and what I have contributed myself;
7. Parts of this work have been published as:
   see Ref. [108], [48], [47]

Signed:..... Date:.....

Chapter 1

Introduction

In the modern daily life aviation, and primarily commercial air transportation, takes an inevitable role providing the ability to maintain social contacts and business developments around the world. During the last half century, besides advances in aerodynamics and materials, a significant breakthrough in this area has been made by introducing the jet–propulsion to commercial aviation followed by a complete redesign of the overall aeroplane configuration. By the introduction of legendary airliners like the De Havilland Comet, Tupolev Tu–104 or the Boeing B707, air transportation has become available to a significant part of the worldwide population. In the last decades, after the introduction of jet–powered civil aviation huge progress in jet–propulsion, configurational aerodynamics and aviation materials has been made leading to economically more efficient aeroplanes. In recent years, significant progress has been made by introducing novel composite materials, which have led to more lightweight and fuel–efficient aeroplanes like the Boeing 787 Dreamliner or the Airbus A350. Those aeroplanes are fitted with extra–large turbofan–engines with a high bypass–ratio, and their structure consists significantly of lightweight composite materials. As commonly known, the commercial aviation market is highly competitive. Thus, for the future, there is a high demand for commercial air–vehicles which are even more efficient and, therefore, even more economical[6][11]. Additionally, future aviation technology needs to become more friendly to the environment by reducing noise and emissions. The European ACARE[1] released emission reduction targets which have to be met by the future aeroplanes within the next 20 to 40 years. However, as stated in Ref. [36], these targets are too optimistic if the design procedure for future commercial aeroplanes continues to be conventional, for example, employing empirical knowledge–based handbook methods during the early conceptual design stage or linear computational methods corrected with knowledge–based semi–empirical corrections preserving today's dogmas of commercial aeroplane design. By relying on such methods, for which computational cost is indeed the lowest compared to other alternatives, it is expected that the design

[1] Advisory Council of Aviation Research in Europe

of future aeroplanes is not going to make revolutionary progress and meet the design targets set, for example, by ACARE. Therefore, the aviation industry is currently facing on the one side the challenge to break away from semi–empirical computational design methods based on knowledge collected over the last decades in design of commercial aviation, and on the other side manage the additional project risks due to the uncertainty which is related to novel advanced designs. Thus, a significant rethinking of the design of commercial aviation and its design methodologies has to take place by introducing novel approaches on the one side, while keeping the overall design risks and design uncertainties as low as possible on the other side. This could allow establishing alternative aviation fuel, non–conventional technology and advanced aerodynamic design in the field of commercial aviation. Especially, novel reliable rapid numerical physics–based design methods have to be introduced, which could completely or partly replace old knowledge–based and semi–empirical design approaches in the future conceptual design stage of projects and introducing low computational cost methods based on real physics modelling. This could allow investigating design concepts which are located outside of today's knowledge–based design envelope and lead to highly advanced aviation technology, which will satisfy even more the future needs of commercial air transportation.

1.1 Review of major future trends in aviation technology

In this section, a short overview of the most recent alternative configurations and design studies is given starting with a review of future design concepts of aeroplane configurations, which are currently trending in the aviation research community. In Section 1.1.1 the employment of alternative aviation fuel systems based on hydrogen or bio–fuel from renewable sources is discussed. Further, in Section 1.1.2 hybrid–electric powertrain and its perspective of employment in general and commercial aviation are briefly reviewed. Finally, in Section 1.1.3 alternative approaches of the overall aerodynamic configuration design of future commercial air vehicles is presented.

1.1.1 Alternative fuel systems

The modern aviation propulsion systems are playing the central role in the negative impact of commercial aviation on the environment due to the emission of nitrogen oxide particles (NOx), carbon dioxide (CO_2) and noise. Over the last decades, turbojet, turbofan and turboprop engines were introduced into commercial aviation with great success. The environmental impact of those engines in the form of emissions and noise

were significantly reduced during the last decades. However, the further radical reduction of emissions and noise of aviation propulsion systems running on petroleum–based fuel is nearly impossible, as the technology is already converged against the most optimal solution of its class by employing today's state–of–the–art technology. Thus, the principal alternative in this area could be the replacement of the petroleum–based fuel by alternative propulsion fuel. One of the approach to tackle this challenge is the employment of aviation bio–fuel from renewable biomass resources. In Ref. [44], a general review and an assessment of this approach are presented. Another direction is given by the idea to replace the conventional fuel with hydrogen[105][46]. Hydrogen opens the perspective to employ fuel with the highest possible energy–density which exists in nature. The emission of such an aeroplane would contain only water–vapour and nitrogen oxide particles (NOx). Carbon–based emissions would not exist. This fuel was already successfully applied in aeroplanes like the Hes1 and Tupolev Tu–155[46]. However, today, this technology has still not matured to the stage where it can be used in daily life powering commercial aviation and remains still to be more a subject of basic scientific aviation research.

FIGURE 1.1: Hydrogen powered aeroplane with non–integral tank (source: [105])

1.1.2 Hybrid–electric powered air vehicles

Another attempt to reduce the demand for aviation gasoline is the introduction of hybrid–electric powered aeroplanes. In Ref. [12], an overview is given of electrical components, and electric propulsion architectures are presented. Further, existing commercial products, prototypes, demonstrators, and conceptual studies are discussed. However, the author concludes that a high–fidelity multidisciplinary design analysis and optimisation of an electric aeroplane which also includes safety and economic aspects remains today an open challenge. Another study is made by choosing an Airbus A320 class aeroplane as a baseline design with a range of about 2400 km, which is then equipped with an electric–ducted fan (EDF)[100]. Here, the sizing study of an electric engine powering a ducted fan on a discrete parallel hybrid–electric medium–range aeroplane is conducted. The author concludes, however, that with respect of the chosen baseline design derived from an Airbus A320, the strategy to replace the

conventional propulsion by a hybrid–electrical engine is not offering today the best solution according to the overall efficiency of the vehicle. The author concludes that the design study of a hybrid–electrical aeroplane must be carried out from scratch and should include more aspects than only the redesign of the powertrain. Further, Pornet and Isikveren[72] analysed a quad–fan narrow–body configuration which has two most advanced and geared turbofans and two electrical fans installed under the main wing. Here, conventional mechanical power is used to recharge the batteries and is also partly used for the propulsion. The study shows that the maximisation of the hybridisation of the powertrain leads to a significant reduction of required conventional fuel. However, the increase of the hybridisation will also affect the optimal flight speed and altitude negatively. Thus, such concepts could be successfully applied in the short–range/regional market segment or even general aviation. In this segment, the hybrid–electrical technology offers at the moment the greatest perspective. An example study is also made by Ref. [75] of a light hybrid–electrical motor–glider, where it is concluded that an introduction of the hybrid–electrical propulsion in this niche area would lower the noise and the environmental pollution while keeping the flight performance of such a powered glider at the same level as conventional engine powered gliders running on aviation gasoline. However, regarding the design process, the introduction of such a hybrid–electric powertrain would, as for commercial aviation, expand the design landscape by additional design variables describing the powertrain. It can be seen that the introduction of hybrid–electrical technology offers a significant reduction of the acoustic noise and the atmospheric pollution. However, using today's state–of–the art technology this approach can be only implemented successfully in the lightweight general or short–range/regional market segment.

FIGURE 1.2: Boeing SUGAR Volt concept (source: NASA/Boeing image)

1.1.3 Alternative aerodynamic design of commercial aeroplanes

It is known that the efficiency of a traditional turbofan engine depends on two main parameters: the fan pressure ratio and bypass ratio of the engine. To increase the overall engine efficiency, the bypass–ratio has to be maximised, and the fan pressure ratio minimised. However, for traditional configurations, where the engine is installed under the main wing, the limit of the fan diameter is almost reached. Thus, the integration of larger engines create today a nearly unsolvable challenge. In Ref. [106], ONERA[2] presents a conceptual aerodynamic study of possible future aerodynamic configurations, where four alternative designs of a future mid–range airliner with super large turbofan engines are analysed, and preliminary and detailed aerodynamic design work carried out. The result of this study are the presented four alternative configurations called NOVA (Nextgen ONERA Versatile Aircraft), which basic aerodynamic shape can be seen in Figure 1.3. The BLI configuration could be a real alternative configuration, where the bypass–ratio of the engines would be even higher and therefore the engine more efficient. Also, the BLI configuration has a clean wing providing a much higher aerodynamic efficiency, (C_L/C_D). Here, C_L is the total aerodynamic lift and C_D the total aerodynamic drag force coefficient in the cruise condition. However, due to the present boundary layer on the fuselage, the lifetime of the engine might be reduced as the turbulent boundary layer might cause vibrations on the engine as non–uniform and turbulent air enters the engine.

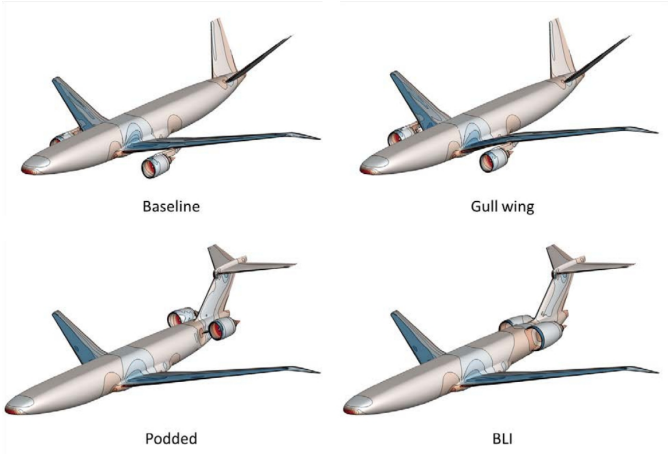

FIGURE 1.3: General view of the NOVA configurations (source: [106])

In Ref. [99], a preliminary design study of a so–called Joined–Wing configuration transport aeroplane for transonic Mach–numbers is presented, see Figure 1.4. The Joined–Wing approach is a collective name for Diamond Wings, Strut– and Truss–Braced Wings and Box Wings. Joined–Wing configurations offer the advantage to reduced significantly the induced aerodynamic drag force coefficient, $C_{D,i}$, of the configuration as no

[2]Office National d'Études et de Recherches Aérospatiales

finite wing tip is present on the main wing and tail in such design. This is automatically leading to higher aerodynamic efficiency, i.e. increased Lift–to–Drag ratio, (C_L/C_D).

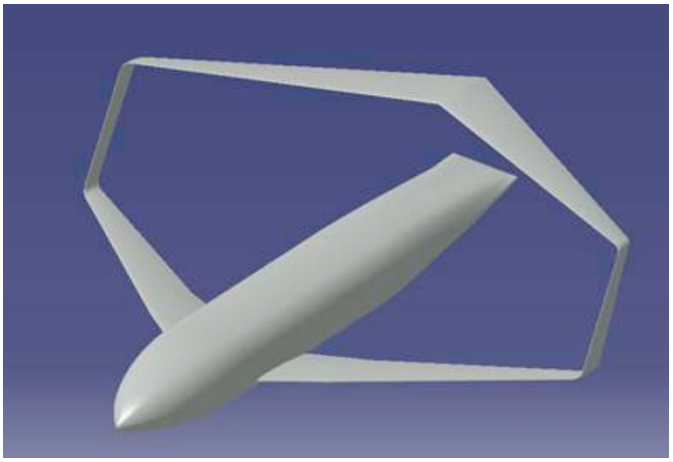

FIGURE 1.4: Joined–wing configuration (source: [99])

In Ref. [16], an overview of recent advances regarding such joined–wing configurations is given, and a detailed discussion of aerodynamics and structural integration is presented. Also, a parameter study of major macroscopic parameters, e.g. wing loading or cruise Mach number, is carried out with the aim to explore the design landscape of the presented *PrandtlPlane* configuration. This review paper is also covering important technological innovations and achievements made worldwide by various research groups in the related field. However, these configurations are structurally overconstrained and differ enormously from classical monoplane wings in their structural nature. The overconstrained nature of the wing results leads to additional parameters and mostly yet unknown design aspects which have to be managed during the design process. On the other side, this approach also offers great opportunities to design future highly efficient aeroplane configurations as a much larger design space is available. Unfortunately, a detailed exploration of the design envelope of joined–wing configurations is today still a very complicated challenge as it requires an enhanced interaction between different disciplines in aeronautical engineering. Here, a multidisciplinary optimisation (MDO) approach is inevitable, which includes the disciplines like aerodynamics, flight mechanics, control and aeroelasticity. This framework needs to build a strong link between them during an iterative search for an overall optimal design. Today, the author also notes that the quantification and exploitation of the real advantages of the joined–wing configuration approach is still unknown as the modern MDO frameworks, traditionally employed during conceptual design stages, are not providing enough fidelity to capture the design landscape of such an advanced approach carefully. On the other side, the employment of modern high–fidelity Computational Fluid Dynamics methods (CFD) within an MDO framework during a sizing study is too expensive due to its high computational cost. However, these high–fidelity tools are

necessary to explore all advantages and disadvantages of such joined–wing configurations by capturing all essential nonlinearities in aerodynamics and the overconstrained structure. For instance, the aeroelastic response of such a complex wing configuration could show extremely complex deformations and unsteady phenomena, which have to be extensively studied in the near future. Therefore, computational methods are required which demands low computational cost and can capture the required detail level necessary for the investigation of such an advanced conceptual configuration.

1.2 The rise of high–aspect ratio composite wings in commercial aviation

Aeroplane configurations based on the joined–wing approach are not expected to appear on the aviation market in the next several decades as this approach is too advanced and for now not feasible to be realised. Also, aeroplanes powered by hybrid–electrical or hydrogen powertrain seems to be subject of research and need to be further investigated. However, advances in aviation propulsion technology and materials can still lead to more economical and environmental friendly configurations. In Equation 1.1, Breguet range equation[73] is shown for a jet–powered aeroplane:

$$R = \left(\frac{C_L}{C_D}\right) \cdot \frac{V}{c_T g} \ln\left(\frac{m_0}{m_0 - m_f}\right) \tag{1.1}$$

Here, R is the range of an aeroplane with the aerodynamic efficiency, (C_L/C_D), in cruise conditions, thrust specific fuel consumption, c_T, cruise velocity, V, the mass of the aeroplane at departure, m_0, and the consumed fuel mass, m_f. Thus, the mass $m_0 - m_f$ is the total mass of the aeroplane on arrival. It can be clearly seen that the aerodynamic efficiency of the aeroplane configuration, (C_L/C_D), plays a significant role as it is directly proportional to the range of the aeroplane. The range of an aeroplane is usually a fixed design target. Thus, by following this observation, it can be stated that besides the introduction of more efficient aero–engines with a lower fuel specific consumption, c_T, and required fuel mass, m_f, for a specific design range, the efficiency can be furher maximised by increasing the aerodynamic efficiency, (C_L/C_D), of the overall configuration. This work deals with advanced design methodologies for the overall wing design of future aeroplanes. Therefore, the aerodynamic efficiency, (C_L/C_D), plays the central role in the presented and further discussed work.

Type of the aeroplane	(C_L/C_D)
Gliders	25 – 60
Commercial aviation	12 – 20
Military trainer	9 – 16
Fighters ($M < 1$)	10 – 13
Fighters ($M > 1$)	4 – 9

TABLE 1.1: Typical aerodynamic efficiency of different types of aeroplanes

In Table 1.1 the typical (C_L/C_D) values for different types of aeroplanes are shown. This parameter is highly influenced by the aspect ratio, AR, of the wing which is defined as:

$$AR = \frac{b^2}{S} \tag{1.2}$$

Here, b is the total span and S the projected area of the wing. The aerodynamics of high aspect ratio (HAR) wings is less impacted by the present wing tip vortex as less surface area is affected by this 3D aerodynamic phenomena, resulting in a decreased induced drag, $C_{D,i}$, and increased overall aerodynamic efficiency, (C_L/C_D). In the area of glider aviation, for example, the aspect ratio of wings can reach $AR \approx 20$ resulting in the highest aerodynamic efficiency ever reached in aviation. Gliders have the highest aerodynamic efficiency as the high–aspect ratio wing is a "clean" wing design without engine nacelles or other components on the wings which create the so called additional "parasite" drag while not contributing to the lift force of the wing. This high aerodynamic efficiency is required as gliders are not powered by an engine and have to stay airborne as long as possible. The employment of composite materials in this field of gliders and design of high–aspect ratio wings was introduced already several decades ago as the wing load, (m_{MTOW}/S), is significantly lower compared to commercial or even general aviation. Here, m_{MTOW} is the maximal take–off weight of the air vehicle. The additional project risks and design uncertainties related to the employment of the more advanced composite materials in wing design of less loaded glider wings (compared to general or commercial aviation) was manageable already in the past. However, over the last decades, also the wings of commercial aviation aeroplanes have undergone a significant stretching. In Figure 1.5 the aspect ratio of the main wing of commercial jet–powered air vehicles from 1947 is shown for narrow– and wide–body aeroplanes over the year of introduction.

One can further identify in Figure 1.6 the "Pareto–front" for long–haul wide–body aeroplanes, which relates the aspect ratio, AR, to number of passengers (PAX). The reason for this "Pareto–front" lies in the increased Root–Bending–Moment (RBM) of the wing, which the configuration has to maintain[3]. For narrow–body configurations in the

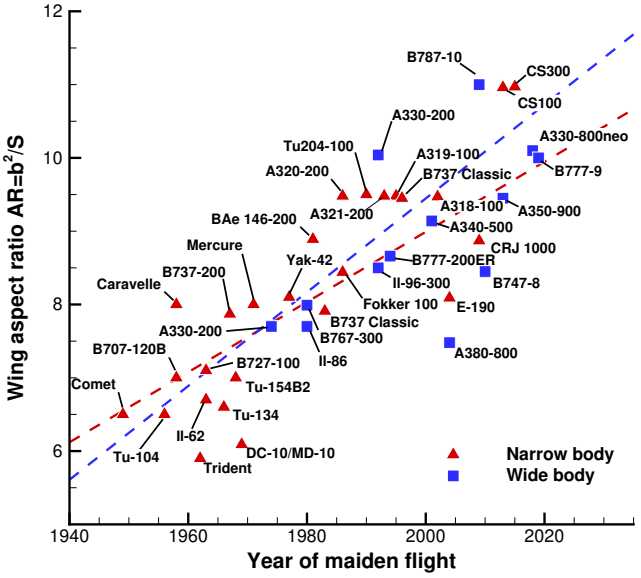

FIGURE 1.5: Wing aspect ratio AR of narrow– and wide–body commercial aeroplanes over the year of introduction[3]

regional–jet or middle–haul market segment no such "Pareto–front" is observed to this current date. Thus, in this market segment there is still optimisation potential for the next–generation composite wing for a regional– and a middle–haul configuration regarding the aspect ratio.

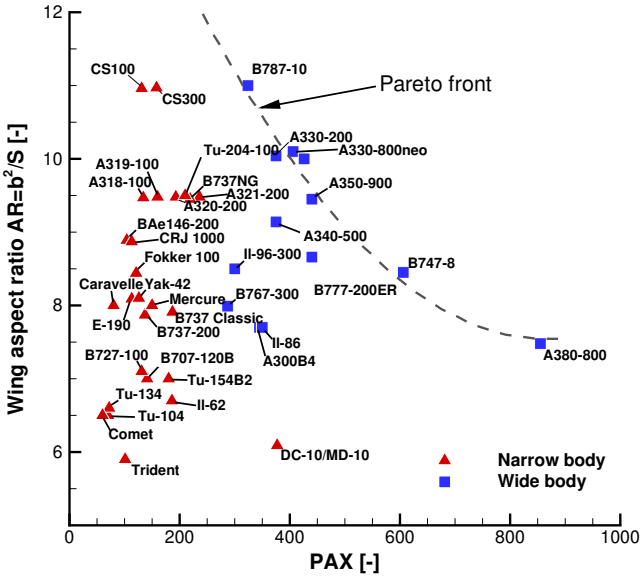

FIGURE 1.6: Wing aspect ratio AR of narrow– and wide–body commercial aeroplanes over the number of passengers (PAX)[3]

For the long–haul configurations, up to date, the highest aspect ratio has the Boeing B–787 Dreamliner with $AR = 11$. In Figure 1.7 the deflection for the wing on the ground, cruise condition in 12000 m altitude and at maximal load state is shown. While

providing high aerodynamic efficiency, it has to be noted that additional aeroelastic effects are not neglectable of such a flexible configuration.

FIGURE 1.7: Wing deflection under the ultimate load of the Boeing 787 Dreamliner (source: newfoxy.com)

1.3 Design methodology of future commercial aeroplanes and multidisciplinary optimisation

As an example, in Figure 1.8, a sequential diagram of the overall aeroplane design project at Bombardier Aerospace is shown. Generally, the whole project is subdivided into six major segments: Market analysis, conceptual design, preliminary design, detailed design and the final flight testing. The second, third and fourth part of the project stages involves design activities of engineers at three major detail levels.

Thus, during an aeroplane design project, the design goes through a series of maturity gates (MG), as shown in Figure 1.8. At the early conceptual design stage, the design landscape is investigated by employing empirical and linear methods[76], which are used to explore the large design landscape by only optimising general macroscopic design parameters with respect to the current and future requirements of potential customers. The employed methodology must provide low computational cost to be able to perform a parametric search on such a wide design landscape in a limited time frame. Throughout this stage, a down–selection of the design subspace is performed, and parameters are tightened and addressed in constantly increasing detail[71]. At a specific point of the overall project, the design is frozen, when the aerodynamic shape and structural layout is converged. Here, the aeroplane design target loads are set, which are the maximal limit loads the particular design has to maintain. Further, these loads are also used as certification load level. This design step, where the aerodynamic

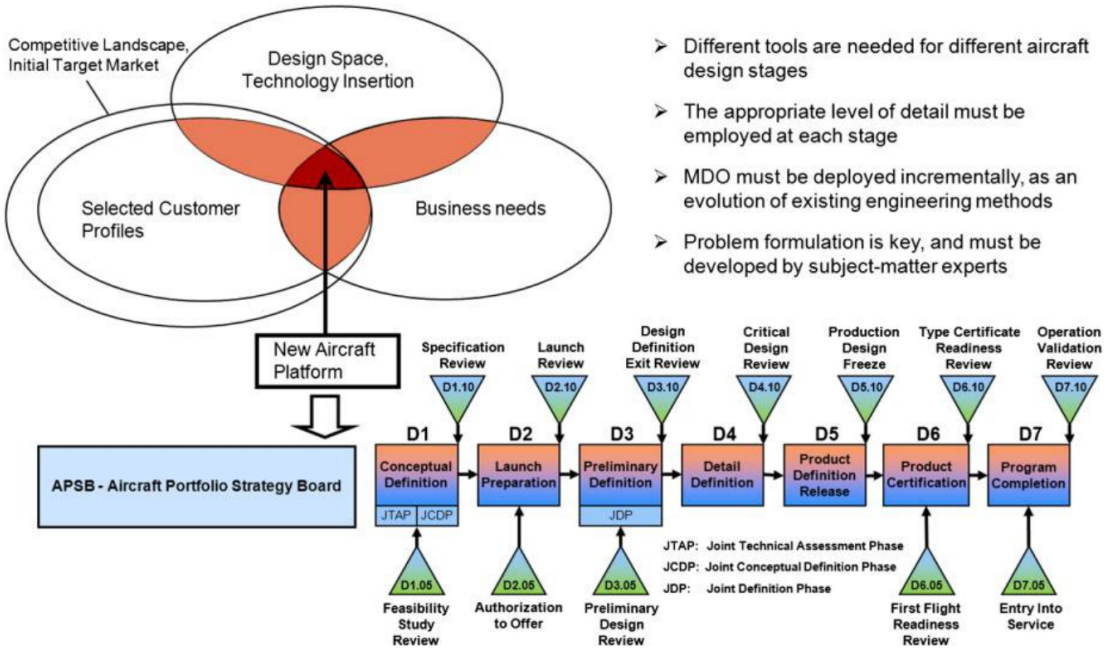

FIGURE 1.8: Deploying MDO in the Bombardier Aerospace Engineering System (BES) (source: [71])

shape and structural layout is finally defined, is a very critical stage in the context in the overall project, as an underestimation of the limiting loads can lead to a later expensive redesign of the configuration followed by additional penalties due to the program delay. On the other hand, an overestimation can lead to a heavier air vehicle and a degraded performance[31].

Nowadays, advanced unusual aeroplane configuration sizing studies can be addressed using the MDO (Multidisciplinary Design Optimisation) technique, where multiple aviation engineering disciplines like aerodynamics, control, structure and propulsion are coupled together in a single or distributed optimisation architecture and are considered during the optimisation procedure in the context of the overall design and its performance[37][14]. In Ref. [57] the different architectures of modern MDO algorithms are presented and compared against each other. Further, in Ref. [39] an adjoint–based optimisation solver DAFoam is presented which is implemented into the computational framework OpenFOAM and is integrated into a gradient–based optimisation framework MACH. Here, CFD technology based on Finite–Volume method (FVM) is used to solve the aerodynamic aspect of the MDO problem coupled together with structure, heat transfer and radiation. Another example is presented in Ref. [81] where the an MDO optimisation is preformed on a highly advanced hybrid–electrical aeroplane configuration. Here, FAST[3], an ONERA / ISAESUPAERO aeroplane sizing code, and

[3]Fixed–wing Aircraft Sizing Tool

OpenMDAO[37] are coupled together. However, as stated by the author, the application of MDO in a full overall aeroplane design procedure remains an open challenge.

In Figure 1.9, a typical traditional iterative design procedure during the early conceptual design stage is shown, where a wing is iteratively optimised with the aim of meeting the target loads and design parameters. At the beginning of the design study major design targets, like the centre of lift, lift force coefficient in cruise conditions, $C_{L,cruise}$, maximal lift force coefficient, $C_{L,max}$, and total drag force coefficient, C_D, are set. Then, the planform of the wing is defined including parameters like the sweep, taper ratio and dihedral of the wing. In the next step, numerical load estimations are performed employing a conceptual aerodynamic solver of mixed fidelity, which is often denoted in the literature as a quasi–3D aerodynamic coupling approach. This method relies on an iterative coupling of 3D linear methods, like the Lifting–line theory (LLT) or Vortex–Lattice method (VLM), and nonlinear sectional 2D and 2.5D infinite–swept–wing aerodynamic data obtained from experiments or CFD calculations[71]. Here, lift curves of the particular sectional aerofoils are picked from the precomputed database and are placed along the span at several positions on the thin VLM lattice, representing volumetric wing sections. By correcting the linear 3D flow results based on potential flow theory with nonlinear sectional aerodynamic data, a nonlinear 3D solution can be obtained at a highly reduced computational cost. The designer uses at this stage of the iterative loop the quasi–3D aerodynamic method until preliminary aerodynamic results are achieved, which are meeting the initial target goals. Once those target goals are met, a 3D CAD[4] model of the wing and a corresponding 3D CFD[5] grid is created using the planform parameters of the wing and geometrical shapes of the aerofoils placed optimally along the span. As a next step, 3D CFD computations are carried out on an HPC[6]–cluster and high–fidelity aerodynamic results are obtained based on 3D formulation of RANS[7]–equations. These results are then used to asses in the final stage of the loop again the design of the wing with respect to the initial design targets. Finally, a decision is made to repeat the loop and improve the design or to proceed to the next design step. One iteration can take up to nine months as here several departments of the design bureau are involved.

Such a design methodology is commonly established in the aviation industry[13]. However, the aeroelasticity, as earlier pointed out, becomes more and more important during the conceptual and preliminary design of a wing due to the increased employment of lighter, and therefore more flexible, materials on highly stretched wings. In the state–of–the–art design methodology shown in Figure 1.9 the high–fidelity results are

[4]Computer Aided Design
[5]Computational Fluid Dynamics
[6]High–Performance Computing
[7]Reynolds–Averaged Navier–Stokes equations

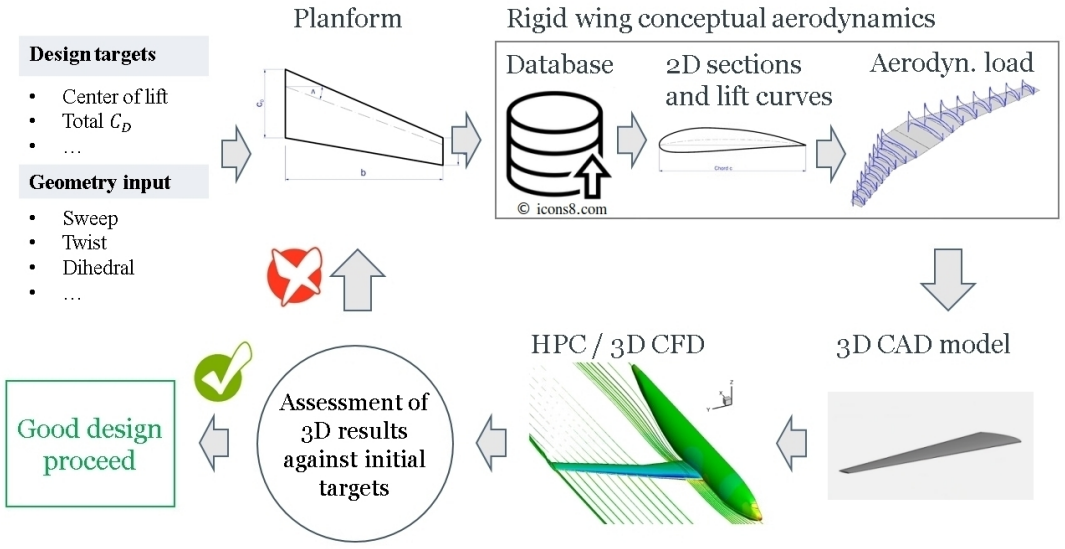

FIGURE 1.9: Traditional design loop of modern wings for commercial aviation

obtained according to the 3D undeformed wing geometry. Nowadays, computational aeroelastic assessment of the wing design is usually carried out by a separate department as a separate step outside the presented design loop. However, on HAR[8]–wings the aerodynamic load estimations obtained by the final step of the iterative loop using high–fidelity CFD computations can vary significantly due to the high structural deflection and twist of the wing in cruise conditions. Therefore, the aeroelastic aspect of the sizing study needs to be integrated directly into the design loop at the early stages of the project. In Figure 1.10 the steady–state aeroelasticity is considered in a proposed iterative design loop. Here, the quasi–3D conceptual aerodynamic solver of mixed fidelity estimates the aerodynamic forces on a flexible wing and is embedded into a rapid computational Fluid–Structure–Interaction (FSI) framework, coupled with a usually beam–based FEM solver which obtains the structural deformation of the wing. Here, on the structural part of the rapid computational FSI–framework, a geometrically exact nonlinear beam model (GEBT) can be employed to capture nonlinear geometric effects due to the large deflection of the composite wing[107][40][110]. Now, a deformed 3D CAD model of the wing for the particular cruise condition can be created by considering, besides the basic geometric parameters, also the aeroelastic twist and deflection of the wing obtained by preliminary FSI computation results. The high–fidelity aerodynamic results, which are required for the final assessment of the overall wing design, are obtained by computing 3D CFD simulation using the deformed geometry of the wing at cruise conditions.

This approach offers an efficient design procedure for HAR–wings where the computational cost is still manageable and the project uncertainties are highly reduced.

[8]High Aspect Ratio Wing

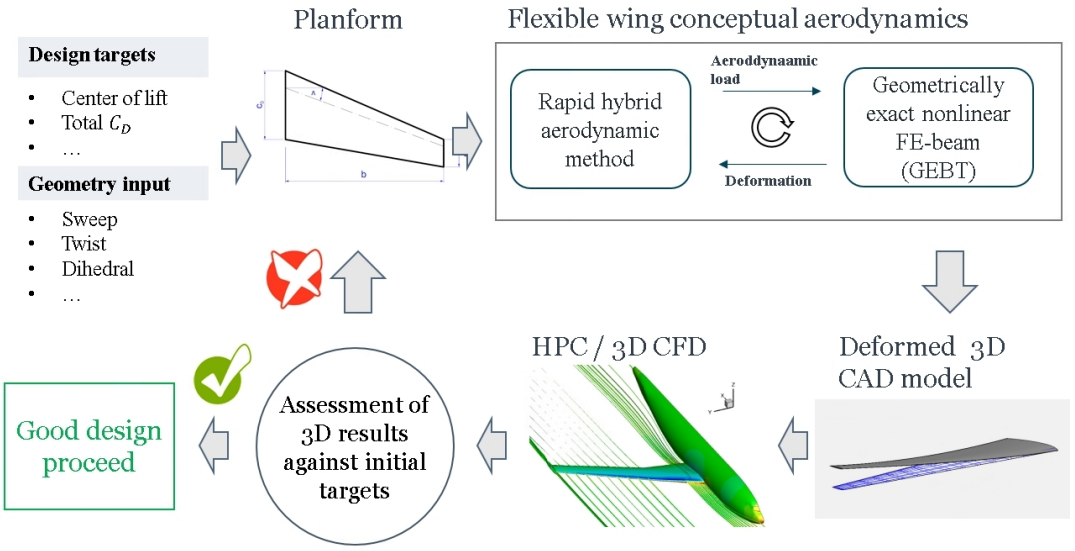

FIGURE 1.10: Proposed design loop of future HAR–wings

Furthermore, GEBT–based FEM methodologies are available, which can compute exact nonlinear deformation of a slender structure with variable cross–section properties at a fraction of the computational cost compared to high–fidelity (nonlinear) FEM methods[40][110]. By employing a geometrically–exact nonlinear FEM–beam solver, the overall project risks can be further reduced, and the design of highly flexible wings can be efficiently assessed.

1.4 Summary

In this chapter, a general overview of the most popular design directions of the future commercial aviation is briefly presented. It is also shown that in the near future concepts powered by alternative fuel–systems or air vehicles with advanced unconventional designs of the configuration are not going to be realised as profound engineering knowledge is missing in some disciplines, and the predictive capabilities of existing MDO–frameworks applied in the industrial field on the daily basis for practical conceptual aeroplane sizing studies are still partly or fully based on handbook and knowledge–based computational methods, preserving the conventional design dogma. Thus, to perform an aeroplane sizing study during an early project stage while using modern high–fidelity MDO techniques remain today still an open challenge[81].

For the wing aerodynamics, the overall efficiency of the conventional commercial aeroplane configurations can be increased by increasing the aspect ratio of the wing, AR. This challenging design goal is realisable in the near future. However, the aeroelasticity

will play a significant role already at the conceptual stage of the project as aeroelastic effects of such HAR–wings need to be considered already at early stages of the overall design program due to the increased flexibility of the wing structure[3][69]. By facing the challenge of a more flexible commercial aviation wing, a computational aeroelasticity framework is required, which can provide efficiently accurate high–fidelity results at a lowest possible computational cost. This FSI–framework need to be embedded directly as a standard engineering tool into the design procedure of a wing at the conceptual stage of a sizing study. The structural domain of the problem can be reduced to a beam–based structural model of a slender wing. Here, it is important to deploy a geometrically–exact formulated beam model (GEBT), as geometrical nonlinearities are not negligible on highly flexible structures[69]. Classical linear beam theories are linearised around the undeformed state of the geometry and assume therefore small geometric deformations of the structure. Thus, this methodology can not be used to estimate high wing tip deflections accurately[107]. Moreover, it can be assumed that the wing sections are rigid and are not changing their shapes. They can only be displaced and twisted in space. Thus, the complex structural nonlinear problem of a slender structure (i.e. a high–aspect ratio wing) can be reduced in its dimension to a geometrically–exact nonlinear beam problem by applying the variational–asymptotic method (VAM), while coupling it with variational beam sectional analysis (VABS) to estimate sectional stiffness and mass properties[110][103]. Due to this reduction of the dimension the trade–off between the physical detail level and computational cost is further increased while maintaining the physical fidelity of the structural domain of the aeroelastic problem. Also, this approach still offers possibilities to optimise the design, for example, by employing the approach of aeroelastic tailoring[49][64][56].

Chapter 2

Background

In this chapter literature review and background of different areas, which are involved in this research of a future efficient computational design methodology for estimation of aerodynamic loads on HAR–wings, is presented and discussed. In the area of the three–dimensional (3D) numerical aerodynamic methodology, the employed Vortex–Lattice method (VLM) code is based on the formulation of the potential flow model. Therefore, in Section 2.1 potential flow model is briefly discussed, and in Section 2.1.1 computational flow models based on the thin–lifting surface formulation and potential flow singularities are briefly reviewed. Next, in Section 2.2 literature review of the quasi–3D aerodynamic hybrid coupling algorithms is presented, and the historical background which dates back to the 1930s is discussed. The literature survey continues with the review of recent progress in the unsteady formulation of such an aerodynamic q3D–coupling approach. Following this section, in Section 2.3 the background of the novel 2.5D+ ISW–CFD URANS solver is presented, which is employed in the steady–state and unsteady aerodynamic q3D–coupling method for the estimation of the nonlinear viscous sectional flow at the particular span position of the wing. Here, the importance of the consideration of the crossflow phenomena on swept wings in high–speed flow regimes is discussed, and explained how this aerodynamic phenomena is included in the 2.5D+ ISW CFD formulation. Finally, recent advances in rapid aeroelasticity modelling of HAR–wings are reviewed in Section 2.4, including the nonlinear efficient beam–based structural model employing the Geometrically–Exact Beam Theory (GEBT).

2.1 Potential flow

The aerodynamic model based on the potential flow theory is the most simplified aerodynamic flow formulation. The potential flow is inviscid, incompressible and irrotational and is governed as follows:

$$\nabla \cdot \mathbf{V} = \nabla^2 \Phi = 0 \tag{2.1}$$

Here, $\mathbf{V} = [u, v, w]^T$ is the velocity vector at an arbitrary location. This is a linear and elliptic partial differential equation of the type of a Laplace equation for the velocity potential Φ, which results directly from the continuity equation of the incompressible potential flow. The three–dimensional flow velocities can be expressed as follows by knowing Φ:

$$u = \frac{\partial \Phi}{\partial x}, v = \frac{\partial \Phi}{\partial y}, w = \frac{\partial \Phi}{\partial z} \tag{2.2}$$

The solution of this flow formulation must be subject to an applied kinematic boundary condition on every point of the contour of the aerodynamic body and a boundary condition at the farfield. In the applications where the potential flow is solved, flow tangency condition on the surface of the aerodynamic body is enforced by:

$$\mathbf{n} \cdot \mathbf{V} = 0 \tag{2.3}$$

Here, $\mathbf{n}$ is the local normal vector and $\mathbf{V}$ is the velocity disturbance due to the moving aerodynamic body through a fluid according to space–fixed frame of reference. This expression means that the flow can not propagate through the solid surface, thus the normal flow velocity at a location on the surface of the body must be zero. Further, the flow needs to be subject to the farfield boundary condition:

$$\lim_{r \to \infty} \mathbf{V} = 0 \tag{2.4}$$

Here, r is the distance between an arbitrary point on the surface of the aerodynamic body and current point in space. Thus, at infinite range the velocity disturbance $\mathbf{V}$ decays to zero[45].

In modern aerodynamics, the common procedure to solve the potential flow on the boundary of an object moving through an incompressible and irrotational fluid is the approximate numerical estimation of the velocity potential, Φ, and velocity disturbance, $\mathbf{V}$, by applying the boundary–element methods, i.e. Green's function theory. This approach can be applied to both, 2D and 3D problems by identifying elementary solutions, i.e. singularities, on the boundary of the moving object. Those singularities

are algebraic functions with strengths which are a–priori unknown. By applying the superposition principle on this linear formulation of the flow problem the strength of all singularities placed on the boundary of the object can be estimated so that Equation 2.1 and Equation 2.3 are satisfied. From the point of view of solving the potential flow based on the singularity methodology the appropriate estimation of the strengths of the singularities, which are placed on the boundary, is performed by solving a set of algebraic equations. This enables to solve the potential flow problems around aerodynamics in an efficient and fast way. Further, methodologies which are based on singularity formulation are satisfying the farfield condition automatically as the disturbance velocity field, which they are inducing, decay with distance. The strength of the placed singularities is estimated this way that the flow tangency condition (Equation 2.3) is also fulfilled at any discrete location on the solid surface where the singularities are placed. However, the system of linear equations is still undetermined regarding the circulation around the aerodynamic body. Here, the Kutta–Joukowski flow condition needs to be imposed at the edge of the aerodynamic body where the flow separates from it and propagates towards the farfield. On a wing geometry, this would be typically the trailing edge of the wing. By imposing the Kutta–Joukowski condition, the flow becomes unique.

2.1.1 Thin–wing lifting surface methods

Classification of existing 2D and 3D methods based on the singularity approach can be categorised by the type of employed singularities: volumetric sources, doublets and vortexes. However, there are also codes existing which are employing a combination of those three types of singularities. In lifting surface methods, the wing is represented by a thin–surface on which the singularities are placed, and the strength of those singularities is estimated this way that the flow tangency condition on a set of discrete locations on the surface is fulfilled. In this type of linear aerodynamic formulations where the potential flow is solved the thickness of the aerodynamic body is neglected. Therefore, the volumetric source singularities are not playing a significant role in these models. A volumetric wing consisting of an asymmetric cambered aerofoil can be represented by a corresponding cambered thin–wing lifting surface. In subsonic flow regimes the additional effect of the sectional thickness of the wing has only a notable influence on the aerodynamic pressure drag force coefficient, C_D, but not on the aerodynamic lift force coefficient, C_L, as long as the local aerofoil thickness stays moderate under $t/c = 20\%$ with respect to the local chord length, c.

The order of the lifting surface methods can be increased by assuming that the singularity distribution is not constant on a single panel of the thin–wing lattice. High–order

methods provide the ability to use fewer panels. However, in practical application, this trade–off between accuracy and the size of the lattice is often not beneficial as finer lattices are often required to resolve geometrical details of the thin wing. Therefore, in the scientific and industrial environment low–order methods are mostly employed, which are faster and cheaper, while the necessary accuracy is achieved through a finer lattice. Further, nonplanar formulation can also increase the order of the model compared to conventional planar formulations of thin–wing singularity methods.

The Laplace equation is time–independent. However, the lifting surface methods can be extended to unsteady flows by introducing temporal dependence of the solution through the boundary conditions[60]. In the unsteady flow regimes, wake modelling is an important part of the formulation of lifting surface methods as the wake behind the surface is responsible for the unsteady temporal delay of the development of aerodynamic forces, also known as "aerodynamic lags". In unsteady flow regimes, the wake is shed from the lifting surface at the trailing edge of the wing and is, therefore, force–free. Thus, it moves with the flow away from the lifting surface following the local flow velocity in the wake area of the flow domain. When free–wake modelling is applied, the temporal shape of the wake becomes part of the flow solution. However, this approach is computationally expensive as at every vertex of the wake panels the local flow velocity needs to be estimated. Hence, simplification is often made by assuming a "flat" dynamic formulation of the wake. Here, the shape of the wake is prescribed and moves only according to prescribed freestream velocity. This flat wake simplification leads in most cases to acceptable results. However, when the wing undergoes highly unsteady motions in time and space involving complex kinematics or is heavily deflected, this assumption can lead to inaccuracies in the numerical results.

	Thin–strip	**DLM**	**UVLM**
Domain	Both	Frequency	Time
Dimension	2D	3D	3D
Singularity	Vortex	Doublet	Vortex
Higher order	No	Possible	Possible
Wake	Flat	Flat	Flat/Free

TABLE 2.1: Classification of inviscid and incompressible linear methods based on potential flow and thin–wing approximation[60]

In Table 2.1 three most popular computational thin–wing surface methods based on the singularity approach are presented: Thin–strip theory, Doublet–Lattice method (DLM) and the Vortex–Lattice method (VLM). The first method is the Thin–strip theory, which is also often referred to as the blade–element theory. It is based on Peter's finite–state model[70] or the state–space representation of unsteady aerofoil behaviour introduced

by Leisham[53]. This aerodynamic approach is often used to model HALE UAVs[1] due to their quasi–2D unswept ultra–high aspect ratio wings[82][68][89]. On such wings, the effect of the finite wing on the spanwise lift distribution is often neglected or corrected by a semi–empirical algebraic approach. The two–dimensional strip theory can be formulated in the time and frequency domain. The potential flow is obtained by placing vortex–singularities. Here, the formulation of the wake is flat as no induced wing tip vortexes are present on a two–dimensional geometry. This formulation can be extended by semi–empirical stall modelling as presented in Ref. [54]. However, this theory is not suitable for the quasi–3D approach which is presented in this work as the constructed computational framework also needs to be applicable on wings with a moderate aspect ratio of around $AR = 10$ or less. On such wing geometries, the wing tip vortex plays a significant role in the estimation of the local aerodynamic loads, and the effect of the finite wing needs to be taken into account by the employed aerodynamic method.

A singularity method which also resolves the spanwise aerodynamics on a finite wing is the so–called Doublet–Lattice method (DLM). It is formulated in the frequency domain in the three–dimensional space and employs doublets as singularities on its thin–wing lattice configurations. The DLM provides the solution to the Laplace's potential flow equation by employing the so–called acceleration–potential doublet[10]. Here, the lifting surface is subdivided into spanwise and chordwise panels. Due to the formulation of this method in the frequency domain, the solution is assumed as out–of–the–plane harmonic motions of the thin–wing and the flat wake. Even if this method is widely used, it is not applicable on wings with large deflections as the boundary conditions are linearised and flat wake is assumed. Also, DLM provides inaccurate results when in–plane kinematics like T–tail flutter occurs[61][62][97][15]. However, for flutter and gust response analysis it is the first–choice aerodynamic method providing beside the efficiency and low computational cost also robustness. However, its main disadvantage is the linearised boundary condition, which assumes only out–of–the–plane harmonic motions.

The presented steady–state and unsteady quasi–3D aerodynamic methodology is based in this research on the Vortex–Lattice method, which is formulated in the time domain by employing three–dimensional vortex–ring panels placed on the thin–wing lattice. The wake can be modelled as flat and free–wake. However, in most practical applications, flat formulation of the wake is sufficient and provide low computational cost. The vortex–rings are quadrilateral ring elements which consist of four discrete vortex segments in a closed loop. Also, the wake panels are consisting of vortex–rings composed of four discrete vortexes, and are convected in unsteady flow regimes into the farfield.

[1] High–Altitude Long–Endurance Unmanned Aerial Vehicles

In steady–state flow regimes an in–time frozen wake carpet is prescribed. VLM can be seen as an extension of Prandtl's lifting–line model (LLT)[92], where the only one horseshoe vortex per wing is replaced by a network of horseshoe vortexes resolving this way the chordwise and spanwise lift distribution of the thin–wing geometry at a higher detail level. The name Vortex–Lattice method (VLM) goes back to Falkner in 1946[30] and is since then improved and refined by many researchers. A detailed formulation of the steady–state and the unsteady variant of VLM can be found in Ref. [45]. The advantages of this approach compared to DLM are the not necessarily linearised boundary conditions, providing the ability to estimate aerodynamic loads also on highly flexible lifting–surfaces under a huge deflected and twisted state. VLM allows to assume general kinematics of the lattice, while not being restricted only to small out–of–the–plane harmonic motions like in DLM. Thus, VLM in steady–state and unsteady flows can also be applied on wings which are undergoing highly unsteady complex motions by employing nonplanar force formulation, non– linearised boundary conditions and free wake.

2.2 Quasi–3D hybrid aerodynamic coupling algorithm

In this section an introduction to the quasi–3D methodology of coupling two aerodynamic solvers of mixed–fidelity is given. Therefore, in Section 2.2.1 the background of the steady–state formulation of this approach is discussed and in Section 2.2.2 recent research activity in the field of the unsteady counterpart is presented.

2.2.1 Steady–state formulation

Nowadays, the application of Navier–Stokes (NS) equations is recognised by the scientific and industrial environment as a prerequisite for realistic flow applications. However, due to its enormous computational cost required to solve a single three–dimensional case the CFD technology became limiting for application in parameter searches and exploration of the design space. Therefore, besides surrogate modelling techniques[77] or adaptive design of experiments[19] a so–called quasi–3D approach is used for aerodynamic load estimations during early design stages. This approach employs Prandtl's linear lifting–line model (LLT) or linear Vortex–Lattice method (VLM), which are resolving the three–dimensional linear flow around a finite wing based on potential flow theory. In the quasi–3D approach, the nonlinear flow solution is obtained by correction of the linear sectional three–dimensional flow with nonlinear viscous 2D or 2.5D flow data obtained from experiments or 2D/2.5D CFD methods. The actual required computational cost for the quasi–3D approach is in steady–state flow conditions at the

same order of magnitude as Prandtl's lifting–line model (LLT) or the linear Vortex–Lattice method (VLM) once the sectional aerodynamic database is available.

MDO Level	Fidelity	Aerodynamics	Structures	Propulsion
CMDO	L0	Knowledge-based aerodynamics	Knowledge-based weight prediction	Fixed architecture, scaled engine model
	L1	Quasi-3D methods (3D VLM / Panel method + 2D High-Fidelity CFD)	Beam or thin-shell models	Variable architecture, generic rubber engine
	L1.5	Disciplinary L2 Surrogate Models		Surrogate model(s) from Engine supplier(s)
PMDO	L2	Mid-to-High Fidelity CFD (3D TSD to RANS)	Global FEM	Real engine model (fixed)
	L2.5	Disciplinary L3 Surrogate Models		
DMDO	L3	RANS	Detail FEM	

FIGURE 2.1: Deploying MDO in the Bombardier Aerospace Engineering System (BES) (source: [71])

In Figure 2.1 an overview is given of employed numerical methodologies at Bombardier Aerospace during the conceptual, preliminary and detailed design stages[71]. The quasi–3D methods in aerodynamics are employed at Bombardier Aerospace at the late conceptual design stage (L1) in combination with beam or thin–shell models representing the structure of the wing. The popularity of the quasi–3D aerodynamic approach in the industrial aerodynamic design of wings lies in the straightforward setup of the wing geometry, as no 3D geometry information is needed, requiring only information of the planform of the wing parametrised by a hand of geometrical parameters and sectional nonlinear aerodynamic aerofoil data from the database and its position along the span. This provides great flexibility during the conceptual design of the wing. Further, as already mentioned, the computational cost of quasi–3D methods are comparable with linear LLT or VLM methods once the nonlinear sectional aerodynamic data is available. The computation of the sectional aerodynamic database is performed usually with 2D/2.5D RANS ISW–CFD methods, whose computational cost is also manageable and the output reusable for other design studies. Moreover, quasi–3D methods can be easily extended with multidisciplinary considerations like icing effects and control sizing.

The first nonlinear coupling between linear lifting–line models and nonlinear viscous lift slopes of sectional wing aerofoils was proposed by Tani [90] in 1934 and Multhopp [58] in 1938. The approach corrects the circulation intensity of the vortex–ring elements within the linear lifting–line model, using sectional viscous lift curves of the aerofoils. This approach ensures a better match of the nonlinear lift slope of the entire finite wing

at higher angles of attack and improves the overall wing load estimation at high speeds. In 1947, a VLM based on the same approach was formulated, which iteratively corrects the numerical results obtained by the lifting–line model using nonlinear sectional lift curve data [85]. In 1951, Sivells et al. [86] extended the coupling algorithm to unswept wings in subsonic flow regimes, including flaps and ailerons. All these coupling algorithms are based on the so–called Γ–correction method. Those methods correct the vortex intensity, Γ, of the panels regarding the nonlinear sectional database and manipulate this way the aerodynamic load distribution on the lifting surface. Their results are in good agreement with 3D reference data before stall angle of attack, α_{stall}. However, the application range of Γ–based coupling algorithms is limited to the maximum lift coefficient of the entire wing, $C_{L,max}$. Beyond stall, the slope of the lift curve, C_L^{α}, becomes negative and the solution not unique. The non–uniqueness of Prandtl's lifting–line equation during the coupling procedure at post–stall flow conditions with negative nonlinear lift slopes was demonstrated by Sears[80] in 1956.

To overcome this problem, Tseng and Lan [94] proposed the α–based correction method in 1988. Their method couples the linear lifting–line model with sectional data by adjusting the freestream angle of attack on every spanwise panel independently. In the 2000s, Van Dam et al. [95, 96] further improved the coupling method and used it to predict the lift on swept wings at high angles of attack beyond the maximal lift force coefficient, $C_{L,max}$. The α–based correction method provides unique solutions at high angles of attacks where the sectional lift slope of the aerofoils is negative. Thus, this approach can be therefore also applied in the post–stall regions. Most recently, Gallay and Laurendeau extended the coupling algorithm to general wings in steady–state subsonic and transonic flight regimes and improved the aerodynamic load predictions at high angles of attack even further [33] [34] .

A profound overview of the application of the quasi–3D methodology within today's aeroplane design procedure is given by Piperni[71]. Nowadays, in the industrial environment the aerodynamic design of an aeroplane wing is built from early stages of the design procedure using quasi–3D method with the aim to obtain a pre–optimised shape. A typical application of the quasi–3D approach is shown in Ref. [93] where this method is exercised during optimisation of a flexible high–lift wing configuration. This approach is also often used for drag minimisation of an aeroplane wing. For example, in Ref. [29] this approach is utilised during an aerodynamic optimisation procedure with the goal to minimise the drag of a wing. Here, the required sectional two–dimensional aerodynamic data for the lift correction of the three–dimensional flow was obtained by the MSES aerofoil prediction tool introduced by Mark Drela in 1987, which itself is based upon the numerical solution of the Euler–equations coupled with

an integral formulation of the boundary layer model, and includes a build–in transition model[25]. However, this approach is only limited to low Reynolds–number flow regimes due to the formulation of the MSES solver. Another, very important application of the quasi–3D approach is the utilisation of it inside a wing twist optimiser with the overall aim to reduce the total aerodynamic drag[108]. At the late conceptual stage of the design procedure, the engineers are relying on a database of already existing aerofoil geometries and its aerodynamic characteristics. Thus, the optimisation of the aerofoil geometry itself at this stage is usually not an option anymore. Therefore, it is demonstrated in this publication how the computational aerodynamic q3D–coupling framework `FALCon`[2], which is presented in this thesis, can be utilised to minimise the overall drag of a wing by optimising the spanwise wing twist[108].

2.2.2 Unsteady hybrid coupling algorithms

The unsteady extension of the steady–state quasi–3D approach combining solvers of different fidelity is a relatively new field, where the research activity is currently ongoing. In 2017, Parenteau et al. presented another unsteady α–based coupling algorithm [66]. Here, two coupling algorithms are presented. The first algorithm is designed for quasi–steady aerodynamics. Here, the three–dimensional flow is represented by the linear three–dimensional UVLM solver and the nonlinear sectional flow effects are taken into account by precomputed sectional lift curve database of an aerofoil using an URANS CFD solver. This algorithm is intended for quasi–steady flow regimes at low reduced frequencies. The second algorithm utilises Theodorsen's unsteady aerodynamic model for a two–dimensional aerofoil[91] which undergoes unsteady forced harmonic pitch and/or plunge oscillations. This approach extends the validity of the second model to higher reduced frequencies by including this algebraic unsteady thin–aerofoil lift model into the formulation. However, it limits this model only to forced harmonic oscillations in pitch and plunge. Also for the second coupling algorithm Parenteau's approach utilises a precomputed sectional unsteady CFD–RANS database. Therefore, the presented aerodynamic unsteady model is suitable to be applied for a rigid wing to estimate unsteady aerodynamic loads while the wing undergoes a prescribed harmonic oscillation in pitch or plunge at a fixed frequency. Thus, this model can not be used to estimate, for instance, the aerodynamic loads on wings encountering unsteady aeroelastic flutter instability or aeroelastic buffeting, as here the involved sectional frequencies of the wing torsion and bending motions are a–priori unknown and are varying along the span of the wing.

[2]Fast Aerodynamic Load Calculation

2.3 Infinite–swept wing solver

The quasi–3D methodologies rely on a sophisticated 2D and 2.5D sectional estimation of aerodynamic data. Therefore, in this work a 2.5D+ ISW–CFD solver introduced at the University of Southampton is used, which is discussed in Ref. [31]. On swept wings, especially in transonic flow regimes, quasi–3D methods in combination with 2D sectional aerodynamic data are not providing reliable results. In these flow regimes, the sectional flow is affected by local crossflow phenomena in the boundary layer[42]. Those crossflow effects influence, in particular, the boundary layer separations and the position of the shock waves on swept wing sections. In the past, these unmodelled effects were corrected with knowledge–based and semi–empirical corrections and introduced this way additional inaccuracies and uncertainty of the conceptual aerodynamic results. Thus, over the last decades, the conceptual design of aerodynamic wings was limited to a well–known envelope and unconventional designs were prohibited due to the additional project risks and flow physics uncertainties.

In this work the novel 2.5D+ ISW–CFD solver is employed, which addresses a well defined industrial challenge, which is a (U)RANS–CFD solver specialised to solve flows around infinite–swept–wing (ISW) geometries at the computational cost of a 2D (U)RANS simulation. The new flow solution, which correctly reproduces the physics responsible for crossflow effects, is obtained using a truly 2D CFD grid, whereas the existing state–of–the–art methods rely on a 3D mesh of the aerofoil with a thickness of one cell along the span, which introduces additional computational cost to obtain a numerical solution. The computational cost of the employed ISW–CFD solver is reduced by at least 75% compared to that of the existing state–of–the–art 2.5D methods. With a limited effort required to enhance an existing computational fluid dynamics solver (either 2D or 3D), the ISW method was implemented in an industrial–grade package `DLR-tau` used across Europe for rapid engineering analysis. The solver, denoted as 2.5D+, is available in the `DLR-tau` flow solver from version 2016.1.0 for production [28] [79].

The `DLR-tau` flow solver is a finite–volume based CFD computational framework. It uses an edge–based vortex–centred scheme, where the convective terms may be computed via several first– and second–order schemes, including central and upwind scheme. The viscous terms are computed with a second–order central scheme. Time integration is performed either with various explicit Runge–Kutta schemes or the Lower–Upper Symmetric Gauss–Seidel (LU–SGS) implicit approximate factorisation scheme. For time–accurate computations, the dual time stepping approach of Jameson [43] is employed. The convergence rate is improved with a multigrid acceleration technique based on agglomerated coarse grids generated by a preprocessing tool. Several models

for turbulence closure are available including, for example, the one–equation Spalart–Allmaras (SA)[88] and more complex two–equation models of the k–ω family.

2.4 Fluid–Structure Interaction

The traditional FSI–frameworks based on CFD/CSD–coupling are used in the field of computational aeroelasticity in a very limited scope[16][21]. In most cases, high fidelity CFD codes are applied within a computational aeroelastic framework in a narrow subspace of the design landscape to analyse a specific configuration or highly limited set of designs[87][35][78]. Therefore, computational aeroelastic methods based on linear aerodynamic assumptions (i.e. LLT, DLM, VLM or classical 2D strip–theory) are still dominating the field of computational aeroelasticity since the 1960s [8] due to a) the straightforward set–up of the problem, using simplified description of the lifting surfaces; b) the low computational effort of the analysis, allowing envelope searches and parametric studies for aeroplane representative structural models; and c) its applicability, as the method has been calibrated on a number of existing aeroplane configurations to account for unmodelled nonlinear flow phenomena.

For the (computational) aeroelasticity of HAR–wing geometries a comprehensive review is given in Ref. [3] summarising the so far carried out work in this field. The lightweight composite HAR–wing is currently studied especially in the field of the so–called High–Altitude Long–Endurance (HALE) Unmanned Aerial Vehicles (UAV). One of the applications are the High–Altitude Pseudo–Satellites (HAPS), which are powered by solar or hydrogen powertrain and should stay airborne for several months or virtually forever at cruise altitudes around 20 km. This way, an alternative to satellites can be created for tasks, where an orbiting satellite would be too expensive. Here, an ultra–light composite high aspect ratio wing is required. However, such a wing is vulnerable to destructive fluid/structure interactions like torsional divergence and flutter. The employment of a rapid aeroelasticity framework integrated into the overall design loop is inevitable during the design procedure of such an air vehicle. Currently, there are several aeroelasticity frameworks combining low–fidelity aerodynamics and linear beam–based FEM or nonlinear geometrically exact formulations of a beam (GEBT). For instance, Wang presented the code NANSI (Nonlinear–Aerodynamics/Nonlinear–Structure Interaction)[104] which couples unsteady Vortex–Lattice method (UVLM) and the nonlinear geometrically exact formulated beam (GEBT). The formulation of GEBT assumes a beam which is geometrically exact defined in space and time and could be a subject of large structural deformations, while the internal structural strain is assumed as low. Here, the UVLM could be useful for low–aspect ratio wings or even Delta–wing as this thin–wing panel method is able to predict three–dimensional flow

effects in potential flow. An equivalent framework is the SHARP code (Simulation of High Aspect Ratio Planes) which is presented by Murua and also combines UVLM with a displacement–based geometrically exact beam theory model[61].

Some computational aeroelasticity tools are defined for high–aspect ratio wings only. For example, Mark Drela's conceptual tool ASWING combines unsteady lifting–line model with nonlinear isotropic beam formulation[24]. The fidelity of a lifting–line model is lower compared to (U)VLM and restricts the wing geometry to unswept high–aspect ratio wings only. Recently, a Matlab toolbox called UM/NAST (University of Michigan/Nonlinear Aeroelastic Simulation Toolbox) is presented by Shearer and Cesnik[83], where a strain–based geometrically nonlinear beam formulation is coupled with a finite state two–dimensional incompressible flow aerodynamic theory[70]. Furthermore, in the recent years the aeroelastic tailoring is also gaining more attention as it is the most cost–effective way to optimise composite airframe structures by modifying the layups of the composite material. This approach exploits the anisotropy of composite materials. For example, a detected adverse aeroelastic response of a wing during the late detailed stage of a project can be corrected quickly by changing the layup configuration of the composite material while avoiding a cost–intensive redesign of the wing shape. For instance, the computational framework NATASHA (Nonlinear Aeroelastic Trim and Stability of HALE Aircraft)[18], presented by Chang, Hodges and Patil, is able optimise high–aspect ratio wings by employing the method of aeroelastic tailoring. This code couples an intrinsic beam formulation with Peters' two–dimensional incompressible aerodynamic flow theory.

The three–dimensional structure of a wing can be dimensionally reduced and represented by a simplified one–dimensional structural beam model defined in three–dimensional space[109]. Normally, slender structures like a wing can be represented by one–dimensional (1D) beam elements when the cross–sectional dimension is much smaller compared to the total length of the object. Even if this approach is widely used since 1985, the research community continued to focus on a formulation allowing to define a beam with arbitrary cross–section properties[41]. A breakthrough happened in the 1990s when Hodges and his research team defined an efficient high–fidelity approach by proposing a mixed variational formulation based on exact intrinsic equations for dynamics of moving beams[40]. This approach is geometrically exact and nonlinear as it is able to resolve high deflections of the structure exactly[69]. However, the internal material strain inside the beam is assumed as small and only elastic. This approach found in the scientific and industrial environment since then a wide acceptance.

2.5 Summary

The foundation of the research, which is presented in this thesis, was discussed in this chapter. From the point of view of linear aerodynamic methods based on singularity approach three nowadays mainly employed methods are reviewed: 2D strip–theory, Doublet–Lattice method (DLM) and the Vortex–Lattice method (VLM). For the purpose of this research the 2D strip–theory is not adequate as it is not taking spanwise flow phenomena due to the finiteness of the wing into account which is present on typical wings of commercial air vehicles. Further, the DLM approach provides great advantages, especially during a computational analysis of gust response or flutter phenomena due to its formulation in the frequency domain. However, on the other side, it assumes only small out–of–the–plane harmonic motions of the geometry. For highly deflected wings or unsteady in–plane kinematics of the structure, for example, T–tail flutter, this method is not able to provide an accurate aerodynamic solution. Therefore, for further research, VLM is chosen as the basic inviscid three–dimensional flow solver solving efficiently three–dimensional potential flow around wings which are not only restricted to high aspect ratios, AR. This model is formulated in time–domain and provides the highest generality compared to the other two methods due to the non–linearised boundary conditions like in the DLM approach.

The quasi–3D approaches are very popular in the academic and industrial environment as they are able to provide nonlinear aerodynamic results by significantly improving the classical linear inviscid panel solution with two–dimensional nonlinear sectional aerofoil data, while keeping on the other side the computational cost comparable to linear aerodynamic panel methods. The steady–state formulation of the aerodynamic q3D–coupling methods was extensively studied over the last century. However, in recent decades the CFD technology made huge advances, and the sectional aerodynamic data usually obtained from wind tunnel experiments is now often replaced by data precomputed by 2D/2.5D ISW–CFD solvers. Therefore, in combination with the 2.5D+ ISW–CFD solver implemented in the `DLR-tau` computational framework an aerodynamic q3D–coupling method can be researched for steady–state flow regimes, which would also be applicable automatically as a unified engineering tool for low– and high–speed flow analysis and would be able to resolve the present crossflow effects in the boundary layer on swept wings accurately.

Further, parallel to this work research on unsteady extension of the aerodynamic q3D–coupling method is carried out also by other research groups. Especially, the work of Parenteau has to be mentioned here[66].

However, a formulation of an unsteady aerodynamic q3D–coupling method which is not only restricted to a specific type of the unsteady motion of the wing at a fixed pitching or plunging frequency remains still an open challenge.

In the field of computational aeroelasticity the computational FSI–frameworks based on the coupling of full–fidelity three–dimensional CFD and FEM codes are used today in a highly limited scope mostly to research the multiphysics of a particular design or to collect validation data for less computational intensive methods based on some flow assumption like the aerodynamic q3D–coupling method or other simplifications. Rapid, computationally less intensive, FSI–frameworks are discussed today mostly in the context of the design of low–speed ultralight HALE UAV aeroplanes where the compressibility of the fluid and sweep of the wing are not present. However, the advances which are made in this research field by employing the high–fidelity and cost–efficient nonlinear beam–based FEM–codes (for example GEBT) can also be applied in the design of wings for commercial air vehicles, which are usually operating in transonic flow regimes and are swept. Thus, an integration of the aerodynamic q3D–coupling algorithm in such an FSI–loop in combination with a GEBT formulation of the structural model and the application of such a robust aeroelasticity framework as a standard engineering tool for daily design procedures of transonic HAR–wings in the industrial environment remains still challenging and it is intended.

2.6 Aim and Objectives

With the introduction and motivation of the overall topic described in Chapter 1 and the literature survey of the current state–of–the–art discussed in this chapter, the aim of this thesis reads as:

> Develop a novel computational aerodynamic tool that combines models of different fidelity and cost, managing in such a way to provide rapid, yet accurate, predictions for low and high speed, steady and unsteady flow problems

In order achieve this aim, the following set of objectives are defined:

1. Implement a linear aerodynamic panel code based on the Vortex–Lattice method (VLM) formulation for steady–state and unsteady flow conditions which is suitable for computational aerodynamic analyses of low–speed aeroplane in an inviscid flow without flow separations, captures three–dimensional flow effects and models unsteady wake dynamics in unsteady mode and nonplanar aerodynamic

forces. The solver has to be conceived in such a way to facilitate exchange of relevant information with other aerodynamic solvers.

2. Formulate, implement and validate an aerodynamic q3D–coupling algorithm for steady–state flow regimes between nonlinear 2D/2.5D sectional aerodynamic data and three–dimensional linear and inviscid VLM panel code to capture local sectional flow nonlinearities, i.e. sectional flow separations, viscosity due to the boundary layer and compressibility. By coupling the three–dimensional VLM panel code with two–dimensional sectional aerodynamic data the fidelity of the model is increased to the order of a 3D RANS solution while keeping the computational cost at the same order of magnitude as the computational cost of the linear model. It must be a unified computational framework for low– and high–speed subsonic flow analysis suitable for swept and unswept wing geometries.

3. Extend this quasi–3D (q3D) aerodynamic coupling approach to unsteady flow regimes by adding an outer time–marching loop and embed directly a set of 2D CFD solvers, which delivers the required nonlinear transient sectional aerodynamic data for the coupling–procedure on–demand throughout the entire unsteady simulation.

4. Demonstrate the ability of the steady–state coupling algorithm to be deployed in a steady–state computational aeroelasticity framework to obtain high–fidelity aerodynamic loads on flexible wing geometries at highly reduced computational cost.

5. Perform extensive numerical studies on test cases of increasing complexity that demonstrate the advantages of the full computational framework over existing techniques.

2.7 Structure of this thesis

The thesis is subdivided into three major parts: In Chapter 3 the formulation of the employed linear steady–state and unsteady Vortex–Lattice method (VLM) is discussed, followed by the formulation of the 2.5D+ ISW–CFD (U)RANS CFD solver. Then, the formulation of the steady–state quasi–3D hybrid aerodynamic coupling algorithm is presented, and the unsteady extension of it is explained. Finally, in the last part of this chapter the methodologies related to the aeroelasticity are examined: the employed anisotropic beam–based FEM solver is presented, which is used to obtain the structural response of the wing during FSI–coupling activity, and the nonplanar extension of the aerodynamic q3D–coupling algorithm is discussed, making the aerodynamic solver suitable to estimate aerodynamic loads on highly deflected wings.

The mapping procedure of aerodynamic and structural data between the aerodynamic and structural domain of the FSI–problem is presented in the last part of this chapter.

The results of the validation studies of all parts of this research are presented in Chapter 4. Here, at first results of the validation study of the linear steady–state and unsteady Vortex–Lattice method (VLM) are presented, followed by an extensive validation of the steady–state nonlinear quasi–3D aerodynamic approach. The chapter is continued by the discussion of the validation results of the unsteady aerodynamic q3D–coupling method and accomplished by presenting results of the validation study of the steady–state computational aeroelasticity framework `FlexiFALCon`.

Finally, in Chapter 5 the conclusions to all three major parts of this research are given, followed by Section 5.4 where the future effort and possible future objectives of this research are outlined.

Chapter 3

Computational methodology

In this chapter, the methodology of all involved areas of this research is explained. The formulation of the employed linear Vortex–Lattice method (VLM) for steady–state and unsteady flows is presented in Section 3.2. Further, the formulation of the 2.5D+ ISW–(U)RANS–CFD solver, which is applied in this research to obtain the nonlinear sectional flow on a wing, is briefly discussed in Section 3.3, followed by a detailed description of the quasi–3D hybrid aerodynamic coupling algorithm for steady–state flow and its unsteady extension, see Section 3.4. Finally, in Section 3.5, the methodology of the aeroelasticity related aspects of this work are presented. Here, the employed structural model based on the nonlinear anisotropic beam–formulation is briefly discussed. Further, the extension of the quasi–3D aerodynamic method to nonplanar coupling procedure on deflected wings is revealed and, finally, the transfer of the aerodynamic and structural data between the two aerodynamic and structural domains of the computational FSI–framework `FlexiFALCon` is revealed.

3.1 Outline of the computational methodology

Analysing the external aerodynamics of a wing configuration to a suitable physical resolution is computationally expensive. To address this challenge, a methodology was developed that computes rapidly aerodynamic loads for steady and unsteady flows. The methodology is compatible with generally available aerodynamic models, using information and data shared during the aeroplane conceptual design, favouring a seamless integration within an existing environment.

The approach, which has been followed is to divide the overall problem of the complex flow into two simpler problems. The first part is to solve rapidly a *global* solution, which gives an overview of the impact of the wing planform design variables onto the three–dimensional aerodynamic wing loads. Those design variables, which play an important role during the late conceptual stage of a sizing activity of a future configuration, are the aspect ratio, taper ratio and sweep and dihedral angles of the wing. To account this part of the problem a linear VLM model is implemented for steady–state and unsteady flow regimes, see Section 3.2. This method is computationally cheap and is well optimised for fast computations of a simplified inviscid solution of the flow around a 3D wing. The second, *local*, problem deals with the more detailed flow physics to a desired accuracy around one or few 2D sections of the wing and includes viscous and compressible flow effects, as well as thickness effects, otherwise neglected in standard linear VLM. The sweep angle unites the two separate problems. Therefore, the sectional flow problem, which involves high–fidelity flow physics, is solved by the infinite–swept wing Navier–Stokes solver (ISW) which is implemented in `DLR-tau` CFD–framework, see Section 3.3, and is applied in this project. This solver can obtain a numerical solution around a 2D or a 2.5D wing section. The latter account also the crossflow effects due to the geometrical sweep angle of the section.

The two independent computational methods of different fidelities for the 3D flow (linear steady–state and unsteady VLM) and for the more detailed sectional 2D/2.5D flow problem are brought together by a q3D–coupling algorithm and unified under one computational framework, referred to as `FALCon`[1]. The coupling methodology of the 3D linear inviscid and the 2D/2.5D nonlinear viscous and compressible methods is described in Section 3.4, where also the novel extension of such a coupling approach to unsteady flows is examined, see Section 3.4.2. The rapid computational aerodynamic framework `FALCon` allows to obtain rapidly a more detailed numerical solution of medium till high aspect ratio wings, suitable for the deployment as a engineering design tool during early stages of an aeroplane sizing study. At this design stages usually a much more expensive high–fidelity 3D solution of the flow around a novel wing configurations is too expensive and, therefore, not yet available.

As an additional step of this work the computational aerodynamic tool `FALCon` is coupled with a geometrically exact formulated beam model (GEBT) in a steady–state computational aeroelasticity framework, referred to as `FlexiFALCon`. The aim of this project step is the demonstration of a seamless integration of `FALCon` into a multi–disciplinary analysis tool, which take also the structural aspects of the wing parameters into account and extend the modelling of the physics by the flexibility of the wing structure. This

[1] Fast Aerodynamic Load Calculation

step of the work is described in Section 3.5, where an overview of the employed structural GEBT model is given and the aeroelastic coupling procedure is explained.

3.2 Linear Vortex–Lattice Method

The VLM follows the classic implementation of Katz and Plotkin [45] and Murray [60]. However, there are certain necessary expedients to transform the classic implementation into one suitable to exchange information with an external, viscous solver.

3.2.1 Steady–state formulation

A typical VLM vortex–ring is shown in Figure 3.1. It is described by four quadrilateral edges. The four vortexes, composed to one single VLM vortex–ring, are placed shifted by the quarter chord, $c_k/4$, of the VLM panel into the farfield. The collocation point is the point where the kinematic boundary condition of the potential flow is fulfilled by imposing that the normal velocity component at this point is zero. It is placed at $3/4\ c_k$ of the local chord of the panel.

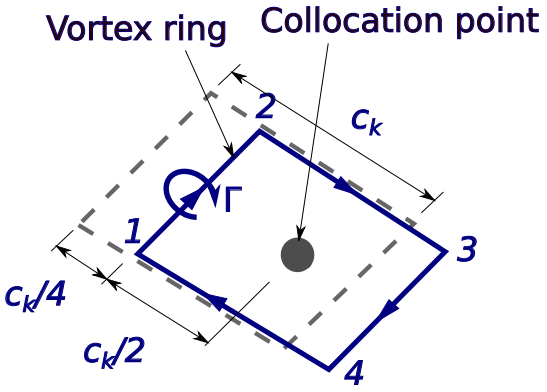

FIGURE 3.1: A single Vortex–Lattice VLM panel

In Figure 3.2 the two types of wing bounded VLM panel index are presented, which are employed in the following formulation. On the one side, the local chord– and spanwise indexing, (i, j), are used, where j is the spanwise and i the chordwise index of the VLM panels on a lattice. A VLM lattice is subdivided into N_i VLM panels along the chord and N_j VLM panels along the span. On the other side, for every algebraic equation of the steady–state (and later unsteady) VLM problem a global index, n, of the VLM panel is employed which also corresponds to the index of the algebraic equation for the particular wing bounded VLM panel in the set of all equations, which have to be solved for the unknown vortex–ring intensities, Γ_n.

In total, $N = N_i \times N_j$ wing bounded VLM panels are placed on a thin–wing lifting surface.

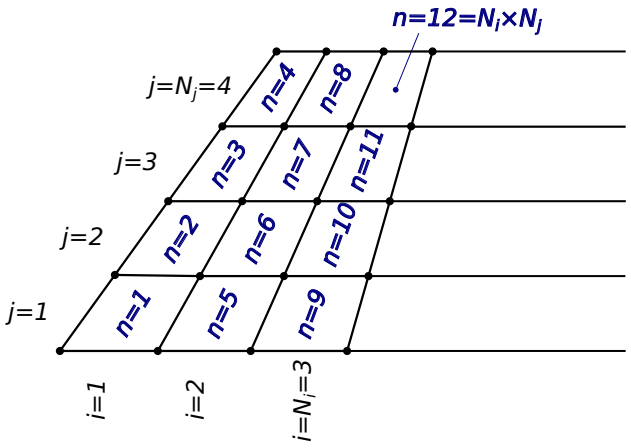

FIGURE 3.2: Local (i, j) and global n index of wing bounded VLM panels

Further, in Figure 3.3 one single spanwise section of a VLM lattice is shown. All VLM vortex–ring panels are shifted by the quarter–chord of the local geometric lattice panels, followed by a single wake panel going into the farfield behind the lifting surface. Every VLM panel has its own vortex–ring intensity, $\Gamma_{(i,j)}$. For the wake panel the vortex–ring intensity is the same as the corresponding vortex–ring intensity of the trailing edge wing bounded VLM panel to ensure that the Kutta–Joukowski flow tangency condition is fulfilled at the trailing edge of the wing, as described later.

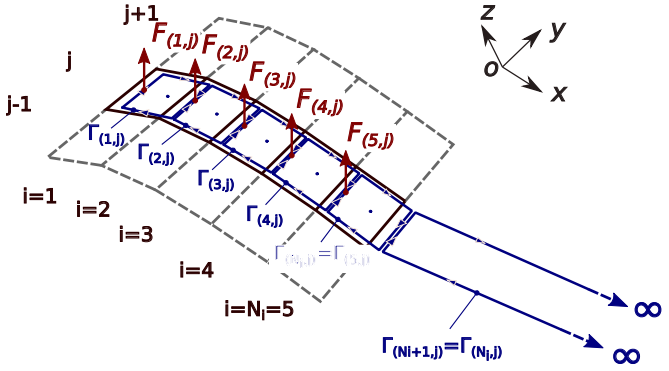

FIGURE 3.3: Steady–state VLM lattice of one spanwise row, j

As already described in the introduction, α–based coupling algorithms correct the local freestream angle of attack, α, acting on the collocation point of every VLM panel at the particular j–th span position:

$$\alpha_j = \alpha_{1,j} = \alpha_{2,j} = \cdots = \alpha_{N_i,j} = \alpha_\infty + \Delta\alpha_j \tag{3.1}$$

Here, α_∞ is the uniformly prescribed freestream angle of attack for all lift generating wing bounded panels. Finally, $\Delta\alpha_j$ is the actual correction increment of the freestream angle of attack prescribed for the row of all wing bounded VLM panels at the particular span position j, and is estimated by the hybrid q3D–coupling algorithm. By knowing the total freestream angle of attack, α_j, of all wing bounded vortex–rings at the particular j–th span position, the current freestream non–circulatory velocity vector at the collocation point of these VLM panels can be expressed as follows:

$$\mathbf{V}_{\infty,j} = \mathbf{V}_{\infty,1,j} = \mathbf{V}_{\infty,2,j} = \cdots = \mathbf{V}_{\infty,N_i,j} = V_\infty \begin{pmatrix} \cos\alpha_j \\ 0 \\ \sin\alpha_j \end{pmatrix} \tag{3.2}$$

For the linear steady–state VLM model the freestream angle of attack correction increment, $\Delta\alpha_j$, is permanently neglected at the entire lattice, i.e. $\Delta\alpha_j = 0$. This parameter is essential to estimate the nonlinear lift and acts as an interface between the quasi–3D aerodynamic hybrid coupling code and the linear VLM. The detailed role of $\Delta\alpha_j$ is described in Section 3.4.1.

Further, Biot–Savart law is applied in the present linear VLM module of `FALCon` to estimate a single induced circulatory velocity contribution, $\mathbf{V}_{nm}$, of the vortex–ring of the m–th VLM panel onto the collocation point of the n–th VLM panel[60]:

$$\mathbf{V}_{nm} = \Gamma_m \oint \frac{d\mathbf{s}_m \times \mathbf{r}_{nm}}{4\pi|\mathbf{r}_{nm}|^3} = \Gamma_m \mathbf{q}_{nm} \tag{3.3}$$

Here, Γ_m is the yet unknown intensity and $\mathbf{s}_m$ the geometrical contour line of the vortex–ring of the m–th VLM panel. Further, $\mathbf{r}_{nm}$ is the distance vector between the current position on the vortex–ring contour on the m–th panel and the collocation point of the n–th panel. The integral is evaluated clockwise. It needs to be noted that in this description of the linear VLM the global index n and m are the indices corresponding to the global matrix–vector index of the overall steady–state VLM problem, which formulation is derived later. For better clarity, the global index notation is used to formulate the linear set of algebraic equations.

A single vortex, which is shown in Figure 3.4, defined between X_1 and X_2 induces the velocity ΔV_{12} on an arbitrary point X in space as follows:

$$\Delta\mathbf{V}_{12} = \frac{\Gamma}{4\pi} \frac{\mathbf{r}_1 \times \mathbf{r}_2}{|\mathbf{r}_1 \times \mathbf{r}_2|^2} \mathbf{r}_0 \left(\frac{\mathbf{r}_1}{|\mathbf{r}_1|} - \frac{\mathbf{r}_2}{|\mathbf{r}_2|} \right) = \Gamma \cdot \mathbf{q}_{12} \tag{3.4}$$

Here, Γ is the vortex intensity, $\mathbf{r}_1$ is the directional vector between X_1 and X, $\mathbf{r}_2$ is the directional vector between X_2 and X and $\mathbf{r}_0$ is the directional vector between X_1 and X_2.

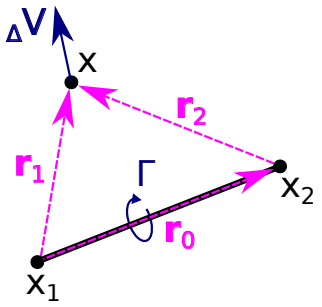

FIGURE 3.4: A vortex defined between X_1 and X_2 inducing velocity ΔV at arbitrary point X

Thus, Equation 3.3 can be also expressed as a discrete VLM formulation:

$$\mathbf{V}_{nm} = \Gamma_m \mathbf{q}_{nm} = \Gamma_m \left(\mathbf{q}_{nm,12} + \mathbf{q}_{nm,24} + \mathbf{q}_{nm,43} + \mathbf{q}_{nm,31} \right) \tag{3.5}$$

Here, $\mathbf{q}_{nm,12}$ is the normalised spanwise velocity contribution of the upper vortex, $\mathbf{q}_{nm,24}$ is the normalised chordwise velocity contribution of the right vortex, $\mathbf{q}_{nm,43}$ is the normalised spanwise velocity contribution of the bottom vortex and $\mathbf{q}_{nm,31}$ is the normalised chordwise velocity contribution of the left vortex of the m–th VLM panel. Further, Γ_m is the vortex ring intensity of the entire VLM panel. The four velocity contributions of the four vortexes of a one single VLM panel can be added to the normalised velocity contribution, $\mathbf{q}_{nm}$, of the m–th vortex ring onto the collocation point of the n–th VLM panel.

Therefore, the total local velocity, $\mathbf{V}_n$, acting on the collocation point of the n–th wing bounded vortex–ring panel can be stated as:

$$\mathbf{V}_n = \sum_{m=1}^{N} \Gamma_m \mathbf{q}_{nm} + \mathbf{V}_{\infty,n}(\Delta\alpha_n) \tag{3.6}$$

It contains the summation of all induced velocity contributions from all wing bounded vortex–rings, $\Gamma_m \mathbf{q}_{nm}$, onto the collocation point of the particular n–th VLM panel and the non–circulatory freestream velocity contribution, $\mathbf{V}_{\infty,n}$, which also acts at the collocation point of the n–th VLM panel. Here, it needs to be noted that the non–circulatory velocity contribution, $\mathbf{V}_{\infty,n}$, at the particular panel might be rotated by the angle of attack correction increment, $\Delta\alpha_n$, in the nonlinear aerodynamic q3D–coupling method to obtaining local nonlinear VLM panel lift. Thus, as it can be seen in Equation 3.2,

only in linear VLM $\mathbf{V}_{\infty,n}$ corresponds to the global freestream velocity vector, $\mathbf{V}_\infty$, i.e. $\mathbf{V}_{\infty,n} = \mathbf{V}_\infty$.

Further, the VLM kinematic boundary condition is applied by enforcing

$$\mathbf{n}_n \cdot \mathbf{V}_n = \mathbf{n}_n \cdot \left(\sum_{m=1}^{N} \Gamma_m \mathbf{q}_{nm} + \mathbf{V}_{\infty,n} \right) = 0 \tag{3.7}$$

on all wing bounded VLM panels of the lattice. Here, $\mathbf{n}_n$ is the normal vector of the n–th wing bounded VLM panel and enforces that the normal flow velocity at this collocation point is zero, see Equation 2.3.

At the trailing edge of the VLM lattice Kutta–Joukowski flow tangency condition is imposed to make the solution unique. This condition is imposed by setting the vortex–ring intensity, $\Gamma_{N_i+1,j}$, of the "frozen" wake panel at the j–th span position the same as the vortex–ring intensity of the corresponding wing bounded trailing edge VLM panel, $\Gamma_{N_i,j}$:

$$\Gamma_{N_i+1,j} = \Gamma_{N_i,j} \tag{3.8}$$

The vortex, which connects the wing bounded panel and the corresponding wake panel at the particular span position, j, is cancelled out due to the Kutta–Joukowski flow tangency condition (Equation 3.8) leading to one single vortex–ring placed at the trailing edge of the wing reaching into the farfield and consisting of six vertices, see Figure 3.3. That way the contribution of the wake panels are considered in Equation 3.7 and Equation 3.6 making the flow solution unique[45].

Finally, Equation 3.7 leads directly to a set of linear algebraic equations, which can be expressed for every wing bounded vortex–ring in matrix–vector form:

$$\begin{bmatrix} a_{11} & a_{21} & a_{31} & \cdots & a_{N1} \\ a_{12} & a_{22} & a_{32} & \cdots & a_{N2} \\ a_{13} & a_{23} & a_{33} & \cdots & a_{N3} \\ \vdots & \vdots & \vdots & \ddots & \vdots \\ a_{1N} & a_{2N} & a_{3N} & \cdots & a_{NN} \end{bmatrix} \begin{bmatrix} \Gamma_1 \\ \Gamma_2 \\ \Gamma_3 \\ \vdots \\ \Gamma_N \end{bmatrix} = \begin{bmatrix} -\mathbf{n}_1 \cdot \mathbf{V}_{\infty,1} \\ -\mathbf{n}_2 \cdot \mathbf{V}_{\infty,2} \\ -\mathbf{n}_3 \cdot \mathbf{V}_{\infty,3} \\ \vdots \\ -\mathbf{n}_N \cdot \mathbf{V}_{\infty,N} \end{bmatrix} \tag{3.9}$$

Here, $a_{nm} = \mathbf{n}_n \cdot \mathbf{q}_{nm}$ is a single aerodynamic influence coefficient between the collocation point of the n–th panel and the vortex–ring of the m–th VLM panel. Further, $\mathbf{\Gamma}$ is the unknown vortex–ring intensity vector of all wing bounded VLM panels, which has

to be solved by the linear algebra solver. On the right side of this system of linear equations the non–circulatory velocity contribution coming from the freestream conditions is located and will be modified by the freestream angle of attack correction increment, $\Delta\alpha$, by the later described q3D–coupling method. The system of equations can be expressed in the compact matrix–vector notation as follows:

$$\mathbf{A} \cdot \mathbf{\Gamma} = \mathbf{R}(\Delta\alpha) \tag{3.10}$$

Here, $\mathbf{A}$ is the aerodynamic influence matrix with the overall matrix dimension of $(N \times N)$ and $\mathbf{R}(\Delta\alpha)$ is the right–hand–side vector of the problem with the length N, which depends on the freestream angle of attack correction increment, $\Delta\alpha$, of all wing bounded VLM panels estimated by the nonlinear aerodynamic q3D–coupling method by incorporating Equation 3.2. Finally, $\mathbf{\Gamma}$ is the global vector of the unknown circulation intensities of all wing bounded VLM panels ordered by the global index n. For a deeper study of the linear Vortex–Lattice method (VLM), the reader is referred to Ref. [45].

During the iterative steady–state coupling procedure of the α–based aerodynamic q3D–coupling algorithm, this aerodynamic influence matrix, $\mathbf{A}$, is constant and need to be estimated only once at the beginning of the procedure. Thus, in `FALCon` the aerodynamic influence matrix $\mathbf{A}$ is then inverted once at the beginning of the iteration and reused to obtain the unknown $\mathbf{\Gamma}$ vector in respect to the right–hand–side vector, $\mathbf{R}(\Delta\alpha)$, which varies during the iterative coupling procedure of the aerodynamic q3D–coupling method:

$$\mathbf{\Gamma} = \mathbf{A}^{-1} \cdot \mathbf{R}(\Delta\alpha) \tag{3.11}$$

As long as the geometry of the VLM lattice is not changing in space (or in unsteady version also in time), $\mathbf{A}$, and therefore $\mathbf{A}^{-1}$, stays constant.

3.2.1.1 Steady–state aerodynamic force formulation

As the final step the linear aerodynamic forces are obtained as a post–processing step when the circulation intensities, $\mathbf{\Gamma}$, of all wing bounded panels are known. A modern vectorised nonplanar formulation is used here to obtain the aerodynamic forces of the wing bounded VLM panels by applying the Kutta–Joukowski theorem in vector form [84]:

$$\delta\mathbf{F}_{i,j} = \rho\mathbf{V}_{i,j} \times \mathbf{\Delta\Gamma}_{i,j} = \rho\Delta\Gamma_{i,j}\left(\mathbf{V}_{i,j} \times \Delta\mathbf{l}_{i,j}\right) \tag{3.12}$$

For the simplicity, here, the local discrete indexing (i, j) of the wing bounded VLM panels is again used. Further, ρ is the density of the fluid uniformly prescribed for the entire VLM lattice configuration and $\mathbf{V}_{i,j}$ is the local freestream velocity vector acting at the collocation point of the (i, j)–th vortex–ring element. Moreover, $\mathbf{\Gamma}_{i,j} = \Delta\Gamma_{i,j}\Delta\mathbf{l}_{i,j}$ is the total vortex strength placed at the quarter–chord line of the (i, j)–th wing bounded VLM panel, see Figure 3.3. Here, $\mathbf{l}_n$ is the geometric directional quarter–chord line vector of the particular VLM vortex–ring panel in vector form. The local vortex strength intensity, $\Delta\Gamma_{i,j}$, of the quarter–chord line of the panel is obtained from the global vector $\mathbf{\Gamma}$ as follows:

$$\Delta\Gamma_{i,j} = \begin{cases} \Gamma_{i,j} - \Gamma_{i-1,j} & \text{if } i > 1 \\ \Gamma_{i,j} & \text{if } i = 1 \end{cases} \tag{3.13}$$

Here, it needs to be distinguished whether the panel is located at the leading edge of the lattice ($i = 1$) or not ($i > 1$). The aerodynamic forces in the present VLM solver are evaluated at the midpoint of the panel's quarter–chord line. Equation 3.12 is an algebraic equation. The nonplanar formulation of the aerodynamic forces ensures that the nonplanar aerodynamic loads are resolved accurately on complex nonplanar wings.

The local lift force coefficient, $C_{L,inv,i,j}$, of the (i, j)–th panel can be estimated as follows:

$$C_{L,inv,i,j} = \frac{\delta F_{i,j,z}}{q_\infty S_{i,j} n_{z,i,j}} \tag{3.14}$$

Here, $\delta F_{i,j,z}$ is the vector component in z direction of the steady–state aerodynamic force vector, $\delta\mathbf{F}_{i,j}$. Further, $q_\infty = \frac{1}{2}\rho_\infty V_\infty^2$ is the dynamic pressure at the farfield and $S_{i,j}n_{z,i,j}$ is the reference surface area of the VLM panel projected on the xy–layer of the inertial frame of reference. Finally, the total inviscid lift at the particular span position, j, which is important for the later coupling procedure in the aerodynamic q3D–coupling method, can be obtained as by:

$$C_{L,inv,j} = \frac{\sum_{i=1}^{N_i} C_{L,inv,i,j} S_{i,j} n_{z,i,j}}{\sum_{i=1}^{N_i} S_{i,j} n_{z,i,j}} \tag{3.15}$$

3.2.1.2 Evaluation of the steady–state induced drag and the local spanwise induced angle of attack using the Treffz–plane method

In the steady–state formulation of VLM the Treffz–plane approach is used to estimate the induced drag, $C_{D,ind}$[45]:

$$C_{D,ind} = -\frac{1}{V_\infty^2 S_{j,z}} \sum_{j=1}^{N_w} \Gamma_{w,j} w_{ind,w,j} \Delta y_j \tag{3.16}$$

Here, N_w is the total number of wake panels and $\Gamma_{w,j}$ is the particular vortex intensity of the wake panel at the j–th span position. Further, Δy_j is the width of the wake panel at the j–th span position and $S_{j,z}$ is the projected reference surface area of the wing section at j–th span position. Finally, $w_{ind,w,j}$ is the induced downwash at the farfield behind the wing at the Treffz–plane induced by the wing geometry at the j–th span position. On the particular spanwise position, j, the local induced drag can be stated as:

$$C_{D,ind,j} = -\frac{\Gamma_{w,j} w_{ind,w,j} \Delta y_j}{V_\infty^2 S_{j,z}} \tag{3.17}$$

The central key of this formulation plays the induced downwash, $w_{ind,w,j}$ at the geometrical mid–point of the wake panel of the j–th spanwise lattice section. This value can be estimated as follows:

$$w_{ind,w,j} = \mathbf{n}_{w,j} \sum_{k=1}^{N_w} \Gamma_{w,k} \tilde{\mathbf{q}}_{j,k} \tag{3.18}$$

Here, $\mathbf{n}_{w,j}$ is the normal vector of the particular wake panel, $\Gamma_{w,k}$ is the vortex intensity of the k–th wake panel and $\tilde{\mathbf{q}}_{j,k}$ is the normalised velocity contribution of the k–th wake panel onto the mid–point of the j–th wake panel, where only streamwise vortexes of the panel are considered and spanwise panels are neglected:

$$\tilde{\mathbf{q}}_{j,k} = \mathbf{q}_{j,k,23} + \mathbf{q}_{j,k,41} \tag{3.19}$$

Thus, $\tilde{\mathbf{q}}_{j,k}$ is the summation of the non–dimensional velocity contribution of the vortex between vertices 2 and 3 and vortex between vertices 4 and 1 of the k–th wake panel onto the mid–point of the j–th wake panel, see Figure 3.1.

In Figure 3.5 a typical distribution of $w_{ind,w}$ along the span at the Treffz–plane of a rectangular wing is shown. At the wing tips of the wing w_w is maximal due to the wing tip vortex. It needs to be noted, that in Equation 3.18 only wake panels are considered as

the wing bounded panels are far away from the Treffz–plane and, therefore, only the wake panels have influence on the downwash w_w. This method is described in detail in Ref. [45].
Finally, the local spanwise distributed induced angle of attack, $\alpha_{ind,j}$, can be estimated as follows in steady–state flow:

$$\tan \alpha_{ind,j} = -\frac{w_{ind,w,j}}{V_\infty} \tag{3.20}$$

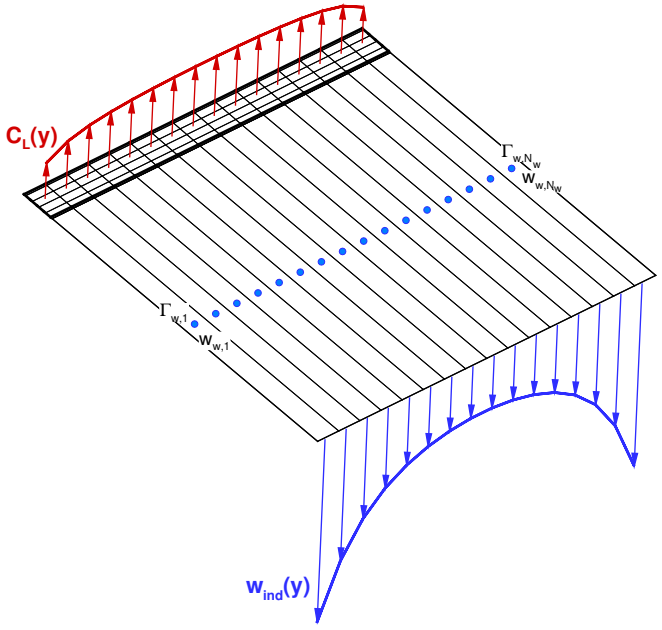

FIGURE 3.5: Induced downwash
on the Treffz–plane of a VLM lattice wake

3.2.2 Unsteady extension

In Figure 3.6 the arrangement of a typical unsteady VLM lattice segment is shown. It consists of wing bounded panels and free wake panels which are shed at every discrete time step, $t_i = t_0 + i\Delta t$, into the farfield. Thus, at t_0 only wing bounded VLM panels are present. Then, when the time marches on, at the trailing edge of the lattice, a new row of unsteady wake panels is shed. Their wake intensities, $\Gamma_{N_{i+1},j}$, are the same as the corresponding intensity of the wing bounded VLM panels at the trailing edge, $\Gamma_{N_i,j}$, at the moment they were shed at time step t_k:

$$\Gamma^{(t_k)}_{N_{i+1},j} = \Gamma^{(t_k)}_{N_i,j} \tag{3.21}$$

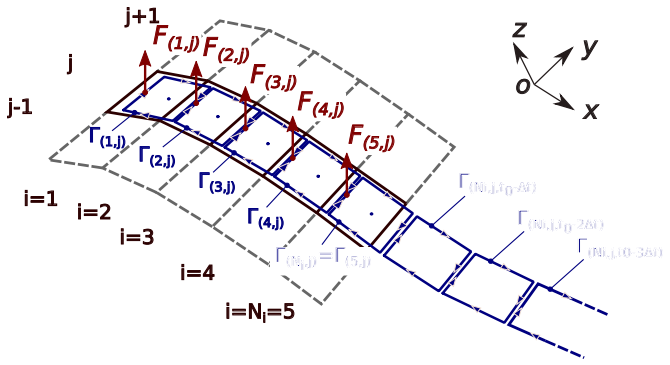

FIGURE 3.6: Unsteady Vortex–Lattice method

After the new wake panels are shed, they propagate with the local (free wake) or freestream velocity (flat formulation of the wake) into the farfield. The vortex–ring intensity estimated by Equation 3.21 on the newly created wake panel at the particular physical time, t_k, stays constant for the rest of the entire simulation. Here, the Kutta–Joukowski flow condition is automatically satisfied and makes the unsteady solution at every time step unique. Therefore, in the unsteady formulation of VLM the local flow velocity at the n–th collocation point of a wing bounded VLM panel can be stated as:

$$\mathbf{V}_n = \mathbf{V}_{n,aa} + \mathbf{V}_{n,ba} + \mathbf{V}_{\infty,n} + \Delta\dot{\mathbf{x}}_{c,n} \tag{3.22}$$

Here, $\mathbf{V}_{n,aa}$ is the circulatory velocity contribution induced by all wing bounded VLM lattice panels onto the collocation point of the n–th wing bounded panel at the particular time step, t_k. Further, $\mathbf{V}_{n,ba}$ is the circulatory velocity contribution of all wake panels onto the collocation point of the n–th wing bounded panel and $\mathbf{V}_{\infty,n}$ is the non–circulatory local freestream velocity contribution, see Equation 3.2. When the wing undergoes a relative motion in space, additional unsteady aerodynamic effects appear on the surface of the thin–wing lattice. Especially when the wing undergoes periodic motions, hysteresis effects will be notable in the aerodynamic forces. Therefore, here, $\Delta\dot{\mathbf{x}}_{c,n}$ is the additional velocity contribution of the n–th wing bounded VLM panel onto itself due to the unsteady motion of the entire VLM panel and is estimated by deriving the position of the collocation point over time using finite–difference approximation:

$$\Delta\dot{\mathbf{x}}_{c,n} \approx \frac{\Delta\mathbf{x}_{c,n}^{(k)} - \Delta\mathbf{x}_{c,n}^{(k-1)}}{\Delta t} \tag{3.23}$$

This quantity is evaluated at the collocation point of the n–th wing bounded vortex–ring only.

As in the steady–state formulation of VLM, in an unsteady counterpart the kinematic boundary condition is enforced at all collocation points of the lattice also by using Equation 3.7. Thus, by using Equation 3.22 in combination with Equation 3.7 one single algebraic equation for the n–th wing bounded VLM panel at the particular time step, t_k, can be expressed as follows:

$$\mathbf{n}_n \cdot \sum_{m=1}^{N} \Gamma_m^{(k+1)} \mathbf{q}_{nm} = -\mathbf{n}_n \left(\mathbf{V}_{\infty,n}^{(k)} + \sum_{m=1}^{N_w} \Gamma_{wake,m} \mathbf{q}_m + \Delta \dot{\mathbf{x}}_{c,n}^{(k)} \right) \tag{3.24}$$

Here, $N = N_i \cdot N_j$ is the total number of wing bounded vortex–ring elements and N_w is the total number of all wake panels which are present at the current physical time, t_k. The circulatory wing bounded vortex–ring intensities, $\Gamma_m^{(k+1)}$, for the next physical time step, t_{k+1}, are yet unknown and have to be estimated through solving the system of linear equations. The vortex–ring intensities of the wake panels, $\Gamma_{wake,m}^{(t_{k-1})}$, are known and therefore on the right side of the equation. Thus, the known unsteady right–hand–side velocity contribution, $\mathbf{V}_{R,n}$, on the n–th collocation point can be expressed as:

$$V_{R,n}^{(k)} = \mathbf{V}_{\infty,n}^{(k)} + \sum_{m=1}^{N_w} \Gamma_{wake,m} \mathbf{q}_{nm_w} + \Delta \dot{\mathbf{x}}_{c,n}^{(k)} \tag{3.25}$$

Now, the overall unsteady VLM problem for the particular time step, t_k, in unsteady flows can be expressed by a set of algebraic equations (Equation 3.24) in a matrix–vector state–space formulation as follows:

$$\begin{bmatrix} a_{11} & a_{21} & a_{31} & \cdots & a_{N1} \\ a_{12} & a_{22} & a_{32} & \cdots & a_{N2} \\ a_{13} & a_{23} & a_{33} & \cdots & a_{N3} \\ \vdots & \vdots & \vdots & \ddots & \vdots \\ a_{1N} & a_{2N} & a_{3N} & \cdots & a_{NN} \end{bmatrix} \begin{pmatrix} \Gamma_1 \\ \Gamma_2 \\ \Gamma_3 \\ \vdots \\ \Gamma_N \end{pmatrix} = \begin{pmatrix} -\mathbf{n}_1 \cdot \mathbf{V}_{R,1} \\ -\mathbf{n}_2 \cdot \mathbf{V}_{R,2} \\ -\mathbf{n}_3 \cdot \mathbf{V}_{R,3} \\ \vdots \\ -\mathbf{n}_N \cdot \mathbf{V}_{R,N} \end{pmatrix} \tag{3.26}$$

The same as for the steady–state counterpart of VLM, here, $a_{nm} = \mathbf{n}_n \cdot \mathbf{q}_{nm}$ is a single aerodynamic influence coefficient describing the influence of the m–th wing bounded vortex–ring element onto the collocation point of the n–th wing bounded VLM panel. The unknown vortex–ring intensities, $\mathbf{\Gamma}$, for all wing bounded VLM panels are obtained for the particular time step by solving Equation 3.26. These vortex–ring intensities are only valid for the particular time step, t_k.

$$\mathbf{A} \cdot \mathbf{\Gamma} = \mathbf{R}(\Delta\alpha) \tag{3.27}$$

3.2.2.1 Unsteady aerodynamic forces

The aerodynamic forces are estimated as a post–processing step after $\mathbf{\Gamma}$ is obtained for the particular time step, t_k. A nonplanar formulation is used to estimate aerodynamic forces on the wing bounded lattice by applying the vectorised Kutta–Joukowski theorem[84]. The quasi–steady contribution of the aerodynamic force vector on a VLM panel is estimated here the same as in the steady–state formulation of VLM by equation Equation 3.12. However, in unsteady flow regimes, additional unsteady force contribution depending on unsteady time depended flow quantities is present. Therefore, the additional contribution of the aerodynamic force vector is formulated as follows[84]:

$$\delta \mathbf{F}^{u}_{i,j} = \rho \Delta \dot{\Gamma}_{i,j} S_{i,j} \mathbf{n}_{i,j} \tag{3.28}$$

Here, ρ is the uniformly prescribed density of the fluid and $\Delta \dot{\Gamma}_{i,j}$ is the time derivative of the vortex–ring intensity at the quarter chord of the n–th wing bounded VLM panel at the particular physical time step, t_k. Further, $S_{i,j}$ is the surface area of the particular panel and $\mathbf{n}_{i,j}$ is the normal vector of the VLM panel. In UVLM this aerodynamic force contribution is added on top of the quasi–steady aerodynamic force described by Equation 3.12.

The time derivative of the vortex–ring intensity, $\Delta \dot{\Gamma}_{i,j}$, at the quarter chord line of the (i,j)–th panel is evaluated by applying a numerical first–order derivation scheme between the current time step, t_k, and the previous time step, t_{k-1}:

$$\Delta \dot{\Gamma}_{i,j} \approx \frac{\Delta \Gamma^{(t_k)}_{i,j} - \Delta \Gamma^{(t_{k-1})}_{i,j}}{\Delta t} \tag{3.29}$$

At t_0 the vortex intensity $\Delta \Gamma^{(t_{k-1})}_{i,j}$ is unknown and therefore assumed as zero for all VLM panels. Finally, the linear unsteady local lift force coefficient can be stated on a single n–th wing bounded VLM as:

$$C_{L,inv,i,j} = \widetilde{C}_{L,inv,i,j} + C^{u}_{L,inv,i,j} = \frac{\delta F_{z,i,j}}{q_\infty S_{i,j} n_{z,i,j}} + \frac{\delta F^{u}_{z,i,j}}{q_\infty S_{i,j} n_{z,i,j}} \tag{3.30}$$

Here, $\widetilde{C}_{L,inv,i,j}$ is the quasi steady and $C^{u}_{L,inv,i,j}$ is the unsteady contribution of the local lift force coefficient, $C_{L,inv,i,j}$, of one single wing bounded VLM panel. Further, $S_{i,j} n_{z,i,j}$ is the by the z–component of the normal vector of the VLM panel, $\mathbf{n}_{i,j}$, projected reference area of the vortex–ring onto the xy–layer. The total spanwise unsteady lift force coefficient, $C_{L,inv,j}$ at the particular span position, j, can be estimated the same way as in the steady–state formulation of the VLM using Equation 3.15.

3.2.2.2 Estimation of the unsteady induced angle of attack and induced drag

Finally, for the unsteady q3D–coupling algorithm accurate estimation of the induced angle of attack, α_i, plays an important role, as it allows to couple the inviscid 3D solution estimated by UVLM and the actual sectional transient viscous data, which is provided by URANS solvers. In the unsteady model of VLM the wake mesh is part of the solution and propagates at every time step into the farfield behind the wing bounded VLM lattice. Thus, the Treffz–plane method for the evaluation of the induced downwash, w_{ind}, and the induced angle of attack, α_{ind}, is not applicable here. Therefore, those quantities must be evaluated in the alternative way directly on the wing bounded VLM lattice panels.

The b_{nm} is the aerodynamic influence coefficient of the m–th vortex–ring onto the collocation point of the n–th VLM panel, where only both right stream– and left anti streamwise vortexes of a panel are considered (only spanwise contribution of the flow), see Figure 3.1:

$$b_{nm} = \mathbf{n}_n \cdot \tilde{\mathbf{q}}_{nm} \tag{3.31}$$

Here, $\tilde{\mathbf{q}}_{nm}$ is the normalised velocity contribution (see Equation 3.19) of the m–th vortex–ring, where only the two stream– and anti–streamwise vortexes of the panel, see Figure 3.1, are taken into account. The induced downwash coefficients, w_{ind}, and induced angle of attack, α_{ind}, are estimated in the presented unsteady VLM at the collocation points of all wing bounded vortex–ring elements at the particular physical time step, t_k, using the following vector–matrix multiplication:

$$\begin{pmatrix} w_{ind,1} \\ w_{ind,2} \\ w_{ind,3} \\ \vdots \\ w_{ind,N} \end{pmatrix} = \begin{bmatrix} b_{11} & b_{21} & b_{31} & \cdots & b_{N1} \\ b_{12} & b_{22} & b_{32} & \cdots & b_{N2} \\ b_{13} & b_{23} & b_{33} & \cdots & b_{N3} \\ \vdots & \vdots & \vdots & \ddots & \vdots \\ b_{1N} & b_{2N} & b_{3N} & \cdots & b_{NN} \end{bmatrix} \begin{pmatrix} \Gamma_1 \\ \Gamma_2 \\ \Gamma_3 \\ \vdots \\ \Gamma_N \end{pmatrix} \tag{3.32}$$

Hence, the matrix has a dimension of $(N \times N)$. This operation is carried out as a post–processing step for the current time, t_k, after the $\mathbf{\Gamma}$–vector is previously estimated using Equation 3.26. Finally, the local induced angle of attack, $\alpha_{ind,i,j}$, is estimated on every wing bounded vortex–ring panels at their collocation points by using Equation 3.20. The spanwise distribution of $\alpha_{ind,j}$, which is required for further unsteady coupling procedure, is then estimated by interpolating the appropriate induced angle of attack values of the particular spanwise lattice section, j, at the quarter chord where also the sectional inviscid lift, $C_{L,inv,j}$, is located, as described later in Section 3.4.2. The local

unsteady induced drag at the collocation point of a (i, j)–th single–wing bounded panel can then be estimated using:

$$\delta D_{ind,i,j} = \rho_\infty w_{ind,i,j} \Delta\Gamma_{i,j} \Delta y_{i,j} \tag{3.33}$$

The total span distributed induced drag, $\delta D_{ind,j}$, at the particular span position, j, can be estimated similarly as $C_{L,inv,j}$ by using summation of every chordwise induced drag force coefficient at the particular span position, j, see Equation 3.15. Finally, for the spanwise induced drag coefficient, $C_{D,ind,j}$, in can be stated:

$$C_{D,ind,j} = \frac{1}{q_\infty S_{j,z}} \sum_{i=1}^{N_i} \delta D_{ind,i,j} \tag{3.34}$$

3.3 Infinite–swept wing solver

The formulation of a high–level presentation of the infinite–swept wing Navier–Stokes solver is described here. However, the reader may also consult Ref. [31] for further details.

For a 2D analysis the flow solution does not depend on the third direction. Practically, when it comes to the analysis of swept wing cross–sections this approach becomes restrictive, as it does not take the crossflow effects into account which are present due to the geometrical sweep, Λ, of the section from the in–flight direction (or the direction of the in–coming flow). Especially at higher flow velocities on swept wing cross–sections the crossflow effects are becoming dominant, and greatly affect the flow development around the wing cross–section. With the purpose to take those effects also into account, the infinite–swept wing Navier–Stokes solver is developed for these cases in mind. In the ISW–RANS solver the flow component along the third direction is calculated as part of the solution process, rather than being prescribed. The solver allows to investigate a greater generality of flow conditions around unswept and swept wings, employing the same 2D grid traditionally used in a classical, 2D analysis.

The presented ISW model is implemented in the `DLR-tau` flow solver and is applied in this work to obtain the sectional flow physics around a 2D and a swept 2.5D wing cross–section. Due to its computational efficiency compared to existing state–of–the–art options, the implementation was denoted as `2.5D+`. The steady and unsteady `2.5D+` flow solver was demonstrated on single and multi–element wing sections in low– and high–speed flow regimes, using laminar and various turbulence models[31].

The flow solver was also applied to study transonic buffet for a family of wing configurations [27] and in aerodynamic shape optimisation using solvers of different fidelity [108].

The infinite–swept wing model (ISW) assumes a wing of an infinite span, which is swept at a moderate sweep angle, Λ. The chord length, c, is assumed as constant or slightly variant along the span. Such a solver is employed in this work to model local sectional aerodynamic nonlinear flow effects, which are not accounted by the linear Vortex–Lattice method based on potential three–dimensional flow theory.

In Figure 3.7a the arrangement of the global and local frame of reference is presented. The steady–state and unsteady Vortex–Lattice method is formulated in the global frame of reference (A–A cut). However, to take the crossflow effects efficiently into account, a more suitable frame of reference is defined for the ISW problem (A'–A' cut). The local frame of reference, (x', y', z') is rotated along the z–axis by the local sweep angle, Λ, this way that the y'–axis is aligned with the quarter–chord sweep of the wing.

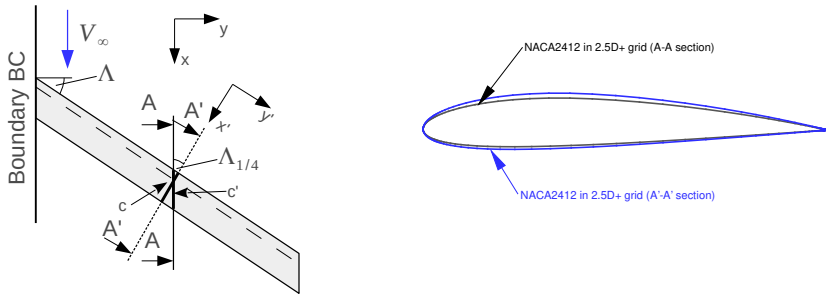

(A) Planform of a swept wing and arrangement of the frame of reference

(B) NACA2412 airfoil in global and local frame of reference, here $\Lambda_{1/4} = 30°$

FIGURE 3.7: Arrangement of global and local frame of reference of the employed 2.5D+ ISW-CFD solver

Traditional ISW–CFD solvers are performing their calculations on a one–cell width 3D stencil. There are two widely used approaches: "Sheared" and "beta" approach. The "sheared" approach uses a two–dimensional grid in the global frame of reference, where the grid layer is extruded "sheared" by the sweep angle, Λ, and on the two stencils of the grid periodic boundary conditions are imposed. The freestream boundary conditions at the farfield are formulated in the global frame of reference:

$$\mathbf{V}_\infty = V_\infty \begin{pmatrix} \cos\alpha_\infty \\ 0 \\ \sin\alpha_\infty \end{pmatrix} \tag{3.35}$$

The second approach, often denoted as the "beta" approach, is formulated in the local frame of reference, i.e. in (x', y', z'). Here, the two–dimensional aerofoil CFD mesh is extruded normal, and the freestream boundary conditions are transformed by the local sweep angle, Λ, where $\mathbf{R}_z(\Lambda)$ is the rotation matrix around the z–axis:

$$\mathbf{V}'_\infty = \mathbf{R}_z(\Lambda) \cdot \mathbf{V}_\infty = V_\infty \begin{pmatrix} \cos\alpha_\infty \cos\Lambda \\ \cos\alpha_\infty \sin\Lambda \\ \sin\alpha_\infty \end{pmatrix} \tag{3.36}$$

Besides the freestream velocity vector, $\mathbf{V}'_\infty$, in local frame of reference, the freestream angle of attack, α'_∞ and side–slip angle, β'_∞, are also transferred into the local frame of reference as follows[31]:

$$\tan\alpha'_\infty = \frac{w'}{u'} = \frac{\tan\alpha_\infty}{\cos\Lambda} \tag{3.37}$$

$$\sin\beta'_\infty = \frac{u'}{\sqrt{u'^2 + v'^2 + w'^2}} = \cos\alpha_\infty \sin\Lambda \tag{3.38}$$

For small freestream angles of attack, $\alpha_\infty < 15°$, a simplification can be made by assuming that $\beta'_\infty \approx \Lambda$. Also, due to the reduced absolute freestream velocity magnitude, $|\mathbf{V}'_\infty|$, in the body–attached local frame of reference the local Reynolds–number is also scaled down as follows:

$$Re'_\infty = Re_\infty \cos\Lambda_{1/4} \tag{3.39}$$

However, in practical applications, the impact due to the reduced Reynolds–number at moderate sweep angles, Λ, is nearly not notable and can be neglected by using Re in the "beta"–approach and the following 2.5D+ ISW–(U)RANS CFD solver.

As described in Ref. [31] the "sheared" and "beta" approaches employ a three–dimensional one–cell thick CFD mesh, which demands a higher computational cost to solve the NS[2]–equations. In this work, a so–called 2.5D+ approach is used, which solves the

[2]Navier–Stokes

ISW–RANS equations on a truly 2D stencil at a computational cost of a conventional two–dimensional CFD calculation. The key idea of this approach is to reformulate the NS–equations formulated usually with respect to the global frame of reference in the more suitable body–attached local frame of reference, (x', y', z'). In this frame of reference, it is assumed that the flow has a statistical homogeneity in the y'–direction along the swept span. This leads to the assumption that the flow is locally fully developed in the y'–direction. Thus, all terms in the NS–equation, which are transformed into the local frame of reference, containing $\partial(\cdot)/\partial y' = 0$ can be neglected simplifying that way the reformulated NS–formulation for the particular ISW problem. In Eqs. 3.40–3.44 the modified system of equations are presented.

$$\frac{\partial \rho}{\partial t} + \frac{\partial (\rho u')}{\partial x'} + \frac{\partial (\rho w')}{\partial z'} = 0 \tag{3.40}$$

$$\frac{\partial \rho u'}{\partial t} + \frac{\partial (\rho u' u')}{\partial x'} + \frac{\partial (\rho u' w')}{\partial z'} = -\frac{\partial p}{\partial x'} + \frac{\partial \tau'_{xx}}{\partial x'} + \frac{\partial \tau'_{xz}}{\partial z'} \tag{3.41}$$

$$\frac{\partial \rho v'}{\partial t} + \frac{\partial (\rho u' v')}{\partial x'} + \frac{\partial (\rho v' w')}{\partial z'} = \frac{\partial \tau'_{yx}}{\partial x'} + \frac{\partial \tau'_{yz}}{\partial z'} \tag{3.42}$$

$$\frac{\partial \rho w'}{\partial t} + \frac{\partial (\rho u' w')}{\partial x'} + \frac{\partial (\rho w' w')}{\partial z'} = -\frac{\partial p}{\partial z'} + \frac{\partial \tau'_{zx}}{\partial x'} + \frac{\partial \tau'_{zz}}{\partial z'} \tag{3.43}$$

$$\begin{aligned} \frac{\partial \rho e_0}{\partial t} + \frac{\partial (\rho h_0 u')}{\partial x'} + \frac{\partial (\rho h_0 w')}{\partial z'} &= \frac{\partial}{\partial x'} \left(u' \tau'_{xx} + v' \tau'_{xy} + w' \tau'_{xz} \right) \\ &+ \frac{\partial}{\partial z'} \left(u' \tau'_{zx} + v' \tau'_{zy} + w' \tau'_{zz} \right) - \frac{\partial \dot{q}'_x}{\partial x'} - \frac{\partial \dot{q}'_z}{\partial z'} \end{aligned} \tag{3.44}$$

Here, e_0 is the total energy and h_0 is the total enthalpy of the fluid[31]. It can be seen that the mass conservation equation, Equation 3.40, the momentum conservation equation along the x'–axis, Equation 3.41, and the momentum conservation equation along the z–axis, Equation 3.43, are itself decoupled from the momentum conservation equation along the y'–axis, Equation 3.42, which describes the crossflow momentum, $\rho v'$, of the ISW flow problem. The coupling between the crossflow momentum equation, Equation 3.42, and the rest of the momentum and the mass conservation equations is performed over the energy equation, Equation 3.44, through the shear forces τ'_{yx} and τ'_{yz} in the boundary layer. So, it can be followed that at low subsonic Mach–numbers, M, the crossflow is independent from the rest of the flow. However, with increasing Mach–number the crossflow starts to affect the overall aerodynamic load on the swept wing section as Equation 3.44 starts more and more influence the solution. This means that at low speeds Equation 3.42 is an independent additional transport equation, which has no impact on the overall sectional load[31]. Following this observation, it can be stated that at low–speed analysis on a swept wing, a conventional 2D solver is sufficient for the q3D–solver. However, in this work, the constructed aerodynamic q3D–coupling methodology, which employs this ISW–CFD solver, is applicable as one unified tool

for low speed and compressible high–speed transonic flow analyses, where the crossflow effects are playing an essential role at high–speed flow analysis. The crossflow at higher Mach–numbers modifies the transport equation, Equation 3.42, through the energy equation (Equation 3.44) over the viscous terms in the boundary layer of the flow. The formulation of the 2.5D+ ISW–RANS equations based on this modified Navier–Stokes system of equations is presented in Ref. [31] in detail. For a detailed study, the reader is referred to this source.

In this work the nonlinear sectional lift curves of the swept–wing sections for the steady–state solver are precomputed using the 2.5D+ ISW–RANS solver implemented in `DLR-tau` CFD framework with respect to the local frame of reference (x', y', z), which is rotated by the local quarter–chord sweep angle of the wing, $\Lambda_{1/4}$, around the z–axis ($A' - A'$ cut). In the unsteady aerodynamic q3D–coupling method this solver is integrated directly into the computational aerodynamic framework `FALCon` to obtain the viscous lift on–demand during the unsteady computations. In the local body–attached frame of reference the local chord length, c', becomes shorter compared to the global chord length, c, by a factor of $\cos \Lambda_{1/4}$. However, for the simplification of the geometry and the simulation setup it is decided to keep the local geometrical chord length same as the global chord length of the section, i.e. $c' = c$, in the employed 2D CFD grid. Therefore, the thickness of the aerofoil in the local frame of reference ($A' - A'$ cut), needs to be modified as follows:

$$\frac{z'}{z} = \frac{1}{\cos \Lambda_{1/4}} \tag{3.45}$$

Here, (z'/z) is the scaling factor of the thickness of the aerofoil geometry. A modified NACA2412 aerofoil shape in local frame of reference, suitable for 2.5D+ ISW–CFD computations, can be seen in Figure 3.7b. It needs to be noted, that the 2D mesh can be only geometrically stretch as long as the initial wall spacing of the CFD grid at the contour of the aerofoil is small enough and the condition of the initial non–dimensional wall distance, $y+ < 1$, is satisfied. As an alternative, one can also create a 2D aerofoil mesh, where the aerofoil contour is already in the local frame of reference.

The results obtained by the ISW solver are also with respect to the local frame of reference, (x', y', z). Thus, as the hybrid q3D–solver and the Vortex–Lattice method (VLM) are formulated in the global frame of reference, the precomputed aerodynamic data for the steady–state aerodynamic q3D–coupling method or the on–demand computed aerodynamic data for the unsteady aerodynamic q3D–coupling method needs to be transformed back to the global frame of reference, (x, y, z). The freestream angle of attack, α, can be transformed between the two different frames of references using Equation 3.37. Further, also the aerodynamic force and moment coefficients, i.e. C_L',

C'_D and $C'_{M,y'}$, needs to be transformed back to global frame of reference as they are estimated by the 2.5D+ ISW solver according to the local chord length, c':

$$C_x = C'_x \frac{c}{c'} = \frac{C'_x}{\cos\Lambda} \tag{3.46}$$

Here, C_x stands for the aerodynamic force and moment coefficients. Additionally, the viscous drag is formulated in the local frame of reference, (x', y', z'), according to the x'–axis, which is also rotated by Λ. Therefore, C_D is transformed by applying the trigonometric cosine additionally, as $D' = D\cos\Lambda$. For the aerodynamic moment coefficient, $C_{M,y}$, in the global frame of reference it needs to be remarked that there the reference length, c_{ref}, is in the global and local reference frame of reference the same. However, also here, the reference area, $S' \neq S$, and therefore this coefficient also needs to be scaled up by the factor $1/\cos\Lambda$.

The equations for the three aerodynamic force and moment coefficients are shown in Eqs. 3.47–3.49:

$$C_L = \frac{C'_L}{\cos\Lambda_{1/4}} \tag{3.47}$$

$$C_D = \frac{C'_D}{\cos^2\Lambda_{1/4}} \tag{3.48}$$

$$C_{M,y} = \frac{C'_{M,y'}}{\cos\Lambda_{1/4}} \tag{3.49}$$

Finally, it needs to be noted that in the `DLR-tau` 2.5D+ ISW–(U)RANS solver the reference freestream velocity in the local frame of reference, V'_∞, and the corresponding velocity in the global frame of reference, V_∞, are the same, i.e. $V'_\infty = V_\infty$.

3.4 Hybrid aerodynamic coupling algorithm

In this section the methodology is presented which describes the quasi–3D hybrid aerodynamic coupling algorithm between the three–dimensional inviscid Vortex–Lattice method (VLM) and two–dimensional nonlinear sectional aerodynamic data in steady–state and unsteady flow regimes. In Section 3.4.1 the steady–state formulation is presented, followed by the unsteady extension in Section 3.4.2.

3.4.1 Steady–state hybrid coupling procedure

The steady–state hybrid aerodynamic q3D–solver, depicted in Figure 3.8, builds on the α–based coupling algorithm introduced by Tseng and Lan [94] and Van Dam et al. [95, 96]. The key idea of this approach is to adjust the local freestream angle of attack along the span of the wing until the local lift on every section of the VLM lattice matches the corresponding two–dimensional nonlinear lift, $C_{L,visc}$, of the aerofoil wing sections obtained from precomputed nonlinear CFD–database. This way, viscous and compressible nonlinear three–dimensional aerodynamic loads can be estimated on VLM lattices at highly reduced computational cost. It has to be noted that in this approach the aerodynamic nonlinearity comes from the precomputed aerodynamic database, which contains the sectional aerodynamic lift and drag force coefficients, $C_{L,visc}$ and $C_{D,visc}$, impacted by the viscosity and compressibility of the flow physics. The three–dimensional flow effects, like the wing tip vortex, are represented here by the three–dimensional inviscid and linear Vortex–Lattice method.

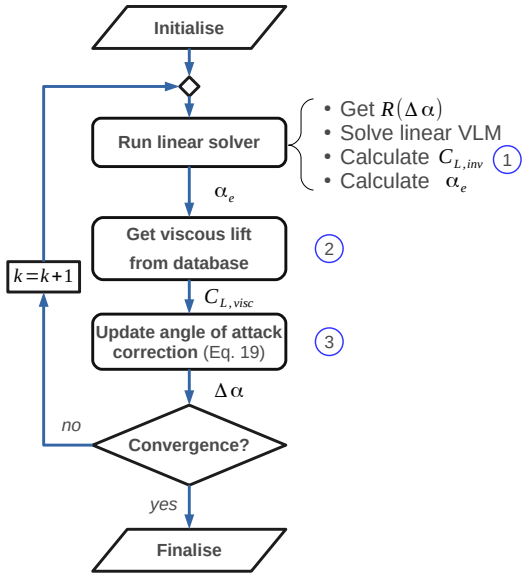

(A) Sequence diagram of the algorithm

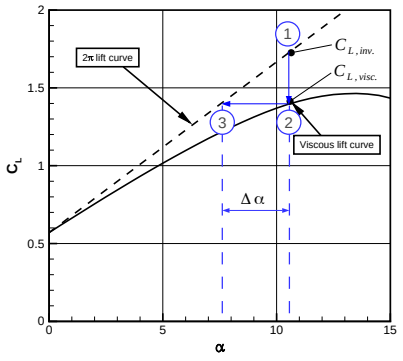

(B) Coupling inviscid and viscous lift curve

FIGURE 3.8: Steady–state hybrid coupling procedure

At the beginning of the procedure, the computation needs to be initialised. The initialisation includes the estimation of the inverted constant aerodynamic influence matrix, $\mathbf{A}^{-1}$. Therefore, $\mathbf{A}^{-1}$ needs to be estimated only once before the main iterative loop starts, see Equation 3.11. After this step, the iterative coupling procedure begins. Inside the loop, the global non–circulatory velocity contribution vector, $\mathbf{R}(\Delta\alpha)$, is re–estimated according to the actual angle of attack correction increment, $\Delta\alpha$, of all wing bounded VLM vortex–rings, see Equation 3.9.

Then, the linear system of equations is solved using Equation 3.11 to obtain the global vector $\mathbf{\Gamma}$ containing local vortex circulation intensities of the wing bounded VLM vortex–rings. The inviscid lift force, $C_{L,inv,j}$, at the particular span position, j, is obtained using Equation 3.15.

The corresponding spanwise effective angle of attack, α_e, in the global frame of reference at the particular iteration, k, can be stated as follows:

$$\alpha_{e,j}^{(k)} = \alpha_\infty - \alpha_{ind,j}^{(k)} = \frac{C_{L,inv,j}^{(k)}}{2\pi} - \Delta\alpha_j^{(k-1)} \tag{3.50}$$

Here, α_∞ is the uniformly prescribed global freestream angle of attack and $\alpha_{ind,j}^{(k)}$ is the spanwise induced angle of attack at the particular iteration, k. Further, $C_{L,inv,j}^{(k)}$ is the current inviscid spanwise lift force coefficient obtained by the linear VLM code, see Equation 3.15, at the spanwise VLM lattice section, j, and $\Delta\alpha_j^{(k-1)}$ is the actual total angle of attack correction increment estimated in the previous iteration, $(k-1)$, at the same spanwise position of the lattice. It has to be noted that the induced angle of attack, $\alpha_{ind,j}^{(k)}$, contains already the effect of the locally increased freestream angle of attack, $\Delta\alpha_j^{(k-1)}$, as this quantity is estimated by the linear Vortex–Lattice method at an locally increased sectional lift, $C_{L,inv,j}$, due to $\Delta\alpha_j^{(k-1)}$.

Along the chord at the particular spanwise position, j, the local freestream angle of attack correction step, $\Delta\alpha_j$, is prescribed uniformly:

$$\Delta\alpha_j = \Delta\alpha_{1,j} = \Delta\alpha_{2,j} = \cdots = \Delta\alpha_{N_i,j} \tag{3.51}$$

Historically, Equation 3.50 was proposed by Van Dam for the linear Lifting–Line method as follows[95, 96]:

$$\alpha_{e,j}^{(k)} = \frac{C_{L,inv,j}^{(k)}}{C_{L,visc}^{\alpha}} - \Delta\alpha_j^{(k-1)} + \alpha_{0,visc} \tag{3.52}$$

Here, $\alpha_{0,visc}$ is the zero lift angle of attack of the nonlinear sectional lift curve and $C_{L,visc}^{\alpha}$ is the particular lift slope of the sectional nonlinear lift curve at the current effective angle of attack, $\alpha_{e,j}^{(k-1)}$. However, this approach encounters numerical instability at the stall as here the viscous lift slope, $C_{L,visc}^{\alpha}$, becomes zero. Therefore, the lift slope has been assumed by Gallay as $C_{L,visc}^{\alpha} = 2\pi$ and constant throughout the entire iterative

procedure[33] [34]. In his work he proved that this assumption provides accurate results and stability also at stall.

The two–dimensional viscous sectional lift–force coefficient, $C_{L,visc,j}$, at the j–th span position is interpolated at the corresponding effective angle of attack, $\alpha_{e,j}$, from the tabulated and already precomputed or experimental viscous 2D or 2.5D aerodynamic database using standard interpolation techniques. In `FALCon` standard piecewise linear interpolation methodology is employed to obtain $C_{L,visc,j}$ at the particular span position, j, and the corresponding effective angle of attack, $\alpha_{e,j}$, estimated by Equation 3.50.

Once both the linear and the equivalent nonlinear viscous lift force coefficients are obtained the angle of attack correction increment, $\Delta\alpha_j$, is updated for the next iteration, $(k+1)$, at every span position, j, on the VLM lattice as follows:

$$\Delta\alpha_j^{(k)} = \Delta\alpha_j^{(k-1)} + \nu \frac{C_{L,visc,j}^{(k)} - C_{L,inv,j}^{(k)}}{2\pi} \tag{3.53}$$

Here, ν is the prescribed relaxation factor. A relaxation factor ν is required to make the iterative procedure more stable, especially at higher freestream angles of attack. This final step, described in Equation 3.53, completes one iteration of the steady–state hybrid coupling loop. The iterative loop continues until convergence of the inviscid lift coefficient distribution, $C_{L,inv}$, is achieved along the span within a prescribed convergence tolerance error, ε, on every spanwise section, j, of the VLM lattice:

$$\left| C_{L,visc,j} - C_{L,inv,j} \right| < \varepsilon \tag{3.54}$$

3.4.2 Unsteady extension of the hybrid coupling procedure

This section describes the formulation of the novel unsteady hybrid mixed–fidelity α–based q3D–coupling algorithm, which combines two solvers of different fidelities: a linear unsteady low–fidelity UVLM solver and a 2D or 2.5D high–fidelity URANS CFD solver. In this section the main novelty of this work is described. This section builds on the previous section, where the steady–state version of the α–based algorithm is presented.

The proposed unsteady hybrid q3D–coupling approach is presented in Figure 3.9 and is based on the steady–state α–based coupling procedure[94, 95, 96, 33, 34] extended

by an outer time–marching loop for the unsteady VLM and URANS solvers. The main differences regarding the equivalent steady–state approach are:

- the presence of an additional outer time loop, which time–marches the linear UVLM and URANS solvers
- the computation of unsteady viscous sectional aerodynamic data, i.e. $C_{L,visc}$, are performed by several independent `DLR-tau` URANS–solvers on–demand during the simulation, which are marching synchronously over time with the linear unsteady VLM
- the UVLM wake carpet which is shed dynamically from the trailing edge of the lattice at every new physical time step

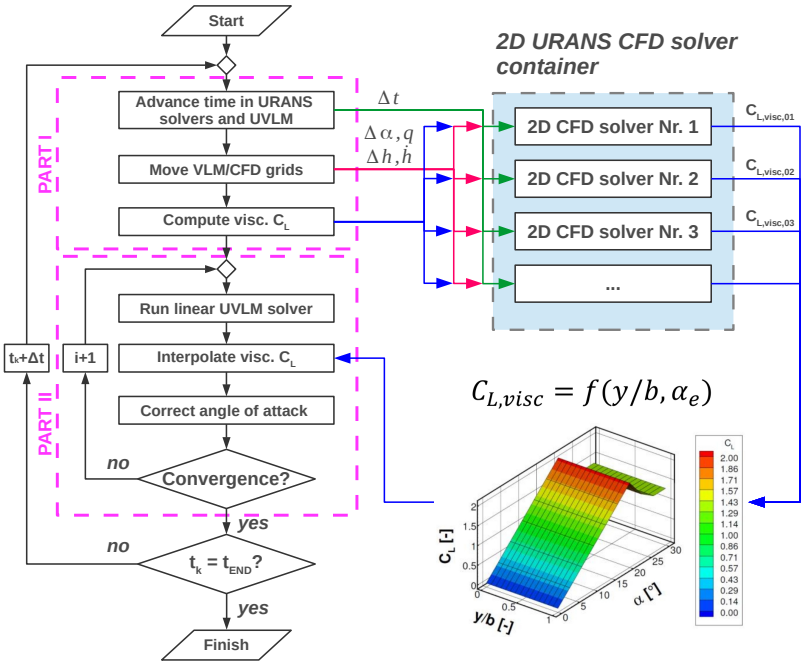

FIGURE 3.9: Unsteady hybrid coupling procedure for simultaneous time-marching of the unsteady VLM and URANS equations

For a specific time step, t_k, the unsteady version of the hybrid aerodynamic coupling algorithm between the sectional aerodynamic database and linear UVLM can be subdivided into Part I and Part II. In the first part the actual transient unsteady aerodynamic database is precomputed on–demand by synchronised 2D `DLR-tau` CFD solvers and parameterised along the span of the wing, y/b, and two–dimensional freestream angle of attack, α_{2D}. The result of the first part of this algorithm is a surface function of the viscous nonlinear lift, $C_{L,visc}(t_k, y/b, \alpha)$, which depends on the span, y/b, two–dimensional freestream angle of attack, α_{2D}, and is only valid for the particular time

step, t_k. This surface function is based on the tabulated data which is obtained by the synchronised CFD solvers, and is then used in the second part of the algorithm to obtain the actual unsteady three–dimensional nonlinear aerodynamic wing load on the VLM lattice for the particular time–step, t_k. The second part the algorithm performs iterative quasi–steady sub–iterations with the aim to obtain the actual nonlinear aerodynamic load on a finite–span VLM lattice by employing the on–demand precomputed nonlinear unsteady aerodynamic database for the particular time step, t_k. The second part of the algorithm is similar to the steady–state version of the α–based hybrid aerodynamic coupling approach described in Section 3.4.1.

3.4.2.1 Part I: Synchronous management of aerodynamic models

The overarching goal of *Part I* is to manage sectional aerodynamic data generation from the aerodynamic 2D or 2.5D+ ISW–CFD solver model. The different aspects of coordinating the time integration of the models are seen as elements of an interdependent process, managing them in a manner to optimise the performance of data generation for any arbitrary geometry motion.

Part I supervises critical aspects, such as, advancing the UVLM and URANS solutions in the time domain, adopting the same time step size. For cases with geometry motion, the position and rotation of the planar VLM lattice is trivially updated. Moving the 2D grid of the URANS solver is done by a rigid translation and rotation. This method is preferred over alternatives because in all cases, it avoids warping the mesh or re–meshing the grid, operations that would otherwise become necessary and add computational cost when performing an aeroelastic analysis with a 3D grid and 3D CFD. It is worth noting that a translation, i.e. in–plane or out–of–plane bending, and a rotation, i.e. torsion, are fundamental components to reconstruct any general type of motion. Motion rates have an impact on flow unsteadiness and shall be included. In the UVLM, the velocity of the collocation point of every wing bounded panel, $\Delta\dot{\mathbf{x}}_{c,n}$, contributes to Equation 3.22 and is calculated with finite difference from the actual position of the collocation point, see Equation 3.23. In the URANS solver, motion rates are imposed through additional unsteady whirl–flux velocities calculated once the motion at the current time step is known. As a result, `FALCon` offers the capability to analyse any arbitrary motion, whether prescribed or unknown a–priori. The current formulation of the unsteady coupling procedure supports the heave and pitch motion, parametrised as follows:

- $\Delta\alpha$: angle of attack increment in $[rad]$
- q : angular pitch velocity along the y–axis in $[rad/s]$
- Δh : vertical displacement increment in $[m]$
- $\dot{h}$: vertical plunge velocity in $[m/s]$

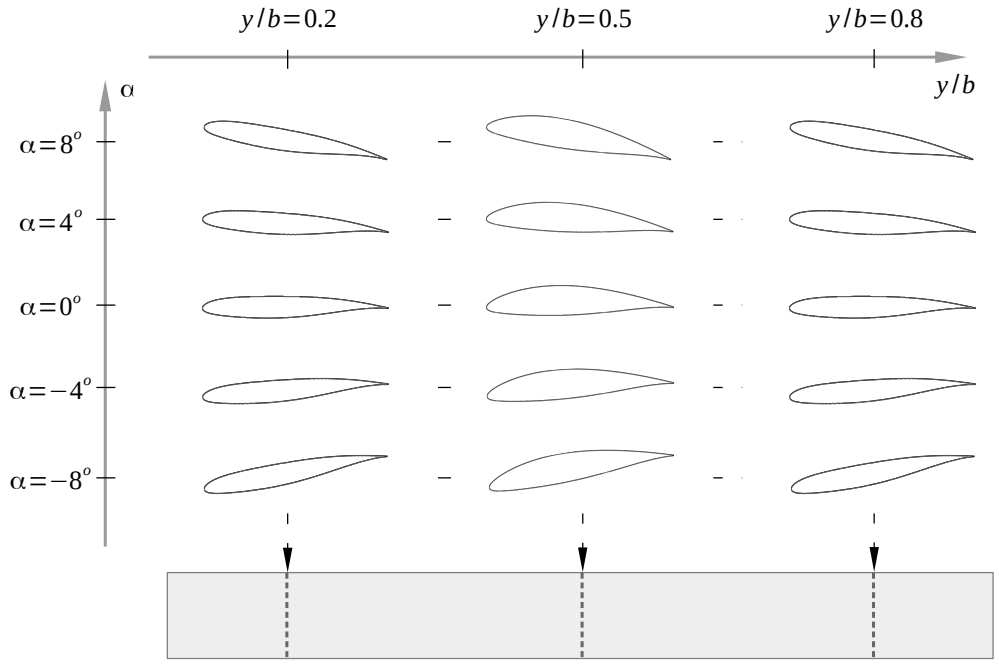

FIGURE 3.10: Schematic illustration of CFD–airfoil instances arranged in a $(N_{y/b} \times N_\alpha)$ tabulated data structure

Managing data generation is the most challenging aspect of the coupling algorithm. The view is to have a database, or container, of unsteady, viscous aerodynamic data which is interrogated on–demand during the iterative process coordinated by *Part II* (further details follow in Section 3.4.2.2). Confronted with existing alternatives already discussed in the Introduction, the implementation follows the most general approach which comes with a number of implementation challenges. With support of Figure 3.10, consider a wing with a cross section that varies along the span. As an example, three sections (20, 50 and 80% of the span) are considered where sectional aerodynamic characteristics are sought after. At the core of *Part I* is the ability to compute the dependence of the unsteady, sectional lift coefficient on the instantaneous angle of attack and on relevant motion rates, at each particular wing section. The dependence on the angle of attack is not unexpected because the approach builds upon the steady–state, α–based coupling algorithm. Referring back to Figure 3.10, *Part I* spawns for this

example 15 URANS analyses, grouped into three spanwise sections. Initially, the viscous database stores data from 15 RANS analyses which are initialised from different freestream values of the angle of attack. Figure 3.10 shows an exemplary range chosen between -8 and 8°. The initial database is steady–state and does not include unsteady effects. To overcome this limitation, at each time step iteration, t_k, the instantaneous motion and rates are known. Then, *Part I* spoons this information to all URANS analyses (which are marched in time using dual–time stepping [43]) and a new unsteady database valid at t_k is generated. Data are stored in a tabular form that visually takes the form of a carpet plot (see insert in Figure 3.9) representing the sectional, viscous $C_L(t_k)$ versus $\alpha_e(t_k)$ and y/b. In the figure, the dependence on motion rates is omitted for brevity. As explained in the next Section, *Part II* will access this database to extract at each wing section, y/b, the viscous lift coefficient necessary for the actual coupling procedure at the current time step, t_k, which is interpolated at a specified value of the effective angle of attack:

$$C_{L,visc}(t_k) = f(\alpha_e(t_k), y/b) \tag{3.55}$$

Two final considerations are worth giving. The first is for the initial angle of attack range, see Figure 3.10. *Part II* accesses the viscous aerodynamic database with a value of $\alpha_e(t_k)$ calculated from Equation 3.57. The iterative nature of data fusion, exemplified by Equation 3.59, proceeds through variations or corrections of the angle of attack. It is therefore critical to have a sufficiently wide range to avoid hampering the convergence of the algorithm (i.e. interpolation rather than extrapolation of the data). The second consideration relates to the motion. There are cases when the motion is unknown a–priori, e.g. in flight dynamics or aeroelastic studies. An external, dedicated model will then be responsible to calculate the motion and rates for a set of aerodynamic loads calculated at t_k. The motion information is then spooned to *Part I* that continues the above–mentioned process.

This parameterised function is valid only for the particular physical time step, t_k, and has to be re–estimated in the next physical time step again by advancing the physical time, $t_k + \Delta t$, in all CFD solvers, perform motion of the CFD grids and run dual–time stepping sub–iterations in all CFD solvers again. For the particular time step, t_k, this parameterised surface function is then used in the next part, *Part II*, of the algorithm to estimate the nonlinear aerodynamic wing load on the VLM lattice and obtain the time depended nonlinear UVLM solution for the particular physical time step, t_k.

Finally, it has to be remarked that if the wing consists of only one aerofoil shape geometry, is undergoing a prescribed motion and is rigid, only one set of CFD solvers at a single span position of the wing can be spawned using the same aerofoil CFD mesh at

various freestream angles of attack, α. In this case the surface function of $C_{L,visc}$ would not have a gradient along the span, (y/b), as it can be seen in Figure 3.9, as the gradient of the function along the span is only depending on the aerofoil shape geometry and varying unsteady motion rates along the span.

3.4.2.2 Part II: Data fusion

The following description is based on Van Dam's α–based coupling algorithm for steady–state flow regimes[95]. By having this as a reference, a mathematical formulation is presented here, which is adopted to unsteady flow regimes.

A possible approach is to resort to the calculation of the sectional, effective angle of attack, $\alpha_{e,j}$, using the formulation [52]

$$\alpha_{e,j} = \frac{C_n}{2\pi} \tag{3.56}$$

where C_n is the unsteady, sectional normal force coefficient from the inviscid solver. The caveat of this simple relationship is that C_n shall relate to the circulatory contribution only, but the UVLM does not separate the circulatory contribution from the non–circulatory one [51]. As a result, an overestimation of $\alpha_{e,j}$ has been observed which leads to a significant over–prediction of the unsteady, sectional, viscous lift coefficient, $C_{L,visc}$. Thus, an alternative suggestion to estimate the effective angle of attack, $\alpha_{e,j}$, at the particular span position, j, is denoted as

$$\alpha_{e,j} = \alpha_\infty - \alpha_{ind,j}|_{(c/4)} \tag{3.57}$$

where α_∞ is the nominal freestream angle of attack. The second term on the right hand side is the induced angle of attack directly at the quarter chord of the wing section calculated using the inviscid UVLM solver. Generally, the VLM formulation calculates the induced angle of attack at the collocation point of wing bounded panels. To obviate this conflict, $\alpha_{ind,j}|_{(c/4)}$ at the wing sectional quarter chord is based on chordwise interpolation of the values of α_i located at the collocation points of two or more chordwise panels, $N_i > 1$.

At the j–th wing section, the instantaneous, viscous lift coefficient $C_{L,visc}$ is extracted from the viscous database created at the actual time step, t_k. The database is interrogated with the value of $\alpha_{e,j}$ obtained from Equation 3.57. Then, the angle of attack

correction at the j–th wing section is estimated for the next time–frozen subiteration, $(i+1)$, for the particular time step, t_k

$$\Delta\alpha_j^{(k,i+1)} = \Delta\alpha_j^{(k,i)} + \nu \frac{C_{L,visc,j}^{(k,i)} - C_{L,inv,j}^{(k,i)}}{2\pi} \tag{3.58}$$

where ν is the relaxation factor used to control the update of the variable at each inner iteration. As depicted in Figure 3.9, *Part II* supervises the convergence behaviour of the pseudo–iterations. Convergence at each time step is achieved when the lift coefficient from the two aerodynamic sources, at all spanwise wing stations, meets the following condition:

$$\| C_{L,visc,j} - C_{L,inv,j} \| < \varepsilon \tag{3.59}$$

The parameter ε is a user–defined tolerance regulating solution accuracy. If this condition is met on every spanwise section of the VLM lattice, the iterative time–frozen loop stops and the calculation continues for the next time step, t_{k+1}.

3.4.3 Estimation of nonlinear viscous drag

The hybrid coupling algorithm of `FALCon` can also estimate the nonlinear total drag force coefficient, C_D, of the wing. The calculation of the total drag is performed as a post–processing step. The total drag of the wing configuration consists of the viscous sectional drag, $C_{D,visc}$, and the induced drag, $C_{D,ind}$:

$$C_{D,j} = C_{D,visc,j} + C_{D,ind,j} \tag{3.60}$$

For the total sectional drag force coefficient, $C_{D,j}$, the induced drag force coefficient, $C_{D,ind,j}$, is estimated by VLM in steady–state flow condition, see Section 3.2.1.2, and by UVLM in unsteady flow regimes, see Section 3.2.2.2. Further, the local sectional viscous drag, $C_{D,visc,j}$, at the j–th span position is obtained by interpolating the drag from the precomputed sectional aerodynamic database using the actual spanwise effective angle of attack, $\alpha_{e,j}$, at the particular j–th span position:

$$C_{D,visc,j} \Leftarrow f_{db}\left((y/b)_j, \alpha_{e,j}\right) \tag{3.61}$$

3.5 Fluid–Structure interaction

In this section, the methodology related to the steady–state aeroelasticity is discussed. At first, the anisotropic nonlinear beam–based FEM model is presented in Section 3.5.1. Then, in Section 3.5.2 it is discussed how to extend `FALCon` solver to cases with a flexible wing structure, and finally, in Section 3.5.3 the aeroelastic system including the mapping procedure of the data between the two aerodynamic and structural domains is explained.

3.5.1 Anisotropic beam theory

In order to account large structural deformation of the wing, a geometrically nonlinear FEM–beam model is required, which aim is to estimate the static deformation of the wing geometrically–exact deformed by the aerodynamic loads. Therefore, it was decided to employ an open–source tool named GEBT (Geometrically–Exact Beam Theory) developed by Yu and Blair[110][111][103][102]. This tool is designed to capture the physics of slender composite structures under large deflections and rotations and can consider exactly geometrical nonlinearities of the beam geometry. Plasticity of the material is neglected as the internal structural strains are considered as small and only elastic. The mathematical formulation of this tool is the mixed variational formulation based on exact intrinsic equations for dynamics of moving beams, which is developed by Hodges[40]. The exact intrinsic equations of this model are derived from Hamilton's weak principle, which is asymptotically formulated along the beam axis:

$$\int_{t_1}^{t_2} \int_0^L \left[\delta(K - U) + \delta\bar{W}\right] dx_1 dt = \delta\bar{A} \tag{3.62}$$

Here, t_1 and t_2 are the arbitrary fixed times, K is the kinetic and U is the internal strain energy of the beam. Respectively, $\delta\bar{W}$ is the virtual work of applied external loads and $\delta\bar{A}$ is the virtual action in the same temporal period, where δ is the usual Lagrangian variation for a fixed time. It needs to be noted that dx_1 is the local coordinate oriented coincidentally with the local beam axis, see Figure 3.11. The detailed formulation of this approach is given in Ref. [40].

This computational framework allows to define an initially curved and twisted network of beams and is able to perform different types of simulation on isotropic or composite slender structures with various section properties along the local beam axis:

- nonlinear static simulation
- nonlinear steady–state dynamic simulation
- nonlinear transient dynamic simulation
- eigenvalue analysis of small motions about the steady–state deformed state of the beam using a linearisation approach

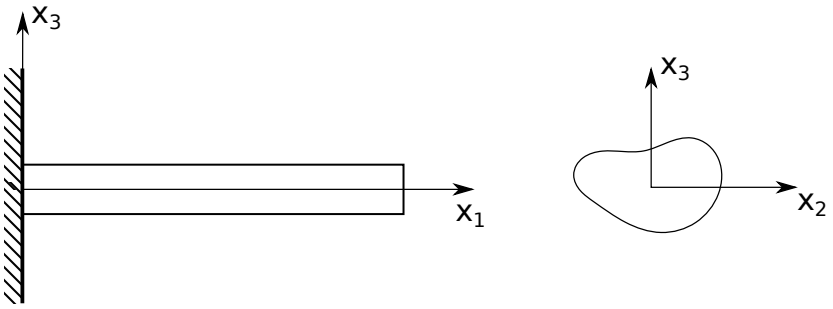

FIGURE 3.11: Local GEBT beam coordinate system

In `FlexiFALCon`, besides single–wing geometries, a full aeroplane configuration can be modelled using several VLM lifting–surface lattices representing the main wing, fin and tail of the aeroplane, connected by a single FEM beam mesh representing the structure of the vehicle with various cross–sectional structural properties. However, in this thesis, only single wings are modelled, and the results are discussed. Also, in this work, the second type of the GEBT model is used where all time derivatives of the formulation are neglected. All simulations can be performed by the tool GEBT using a linear and nonlinear formulation of the beam. This tool is implemented in `FORTRAN` and employs well–optimised libraries.

In GEBT it is required to provide the symmetric flexibility matrices of the particular cross–sections in the input file to link internal beam loads and internal structural strains:

$$\begin{Bmatrix} \gamma_{11} \\ 2\gamma_{12} \\ 2\gamma_{13} \\ \kappa_1 \\ \kappa_2 \\ \kappa_3 \end{Bmatrix} = \underbrace{\begin{bmatrix} S_{11} & S_{12} & S_{13} & \cdots & S_{16} \\ S_{21} & S_{22} & S_{23} & \cdots & S_{26} \\ S_{31} & S_{32} & S_{33} & \cdots & S_{36} \\ \vdots & \vdots & \vdots & \ddots & \vdots \\ S_{61} & S_{62} & S_{63} & \cdots & S_{66} \end{bmatrix}}_{=\mathbf{S}^{-1}} \begin{Bmatrix} F_1 \\ F_2 \\ F_3 \\ M_1 \\ M_2 \\ M_3 \end{Bmatrix} \tag{3.63}$$

Here, γ_{11} is the beam axial stretching strain, $2\gamma_{12}$ and $2\gamma_{13}$ are the engineering transverse shear strains, κ_1 is the twist measure, and finally κ_2 and κ_3 is the curvature about the local beam axis x_2 and x_3, see Figure 3.11. By providing an explicit inverted stiffness matrix, $\mathbf{S}^{-1}$, in the input file, the potential coupling between the different beam solicitations can be enabled or disabled through coefficients of the matrix. For instance, to enable the twisting of the wing, coefficient S_{44}, and for bending S_{55} needs to be non–zero. Complex cross–sectional modelling of composite or isotropic wing sections can be performed by applying the VABS (Variational Beam Sectional Analysis) approach presented in Ref. [17]. This code is able to take cross–sectional geometries into account which consists of anisotropic, non–homogeneous materials and estimate cost–efficiently the appropriate stiff– and mass–matrix of the cross section suitable for the GEBT input.

Hence, the flexibility matrix for an isotropic cross–section at its shear centre is defined as follows:

$$\mathbf{S}^{-1} = \begin{bmatrix} \frac{1}{ES} & 0 & 0 & 0 & 0 & 0 \\ 0 & \frac{1}{GK_2} & 0 & 0 & 0 & 0 \\ 0 & 0 & \frac{1}{GK_3} & 0 & 0 & 0 \\ 0 & 0 & 0 & \frac{1}{GJ} & 0 & 0 \\ 0 & 0 & 0 & 0 & \frac{1}{EI_2} & 0 \\ 0 & 0 & 0 & 0 & 0 & \frac{1}{EI_3} \end{bmatrix} \tag{3.64}$$

Here, E is the Young modulus, S is the area of the cross–section, G is the Coulomb modulus, K_2 and K_3 are the shear coefficients in direction 2 and 3 of the local beam frame of reference and, finally, I_2 and I_3 are the area moment of inertia also in direction 2 and 3 of the local beam frame of reference, see Figure 3.11. Further, for a simple Euler–Bernoulli beam this matrix can be even further simplified by neglecting shear strains γ_{12} and γ_{13} and setting in Equation 3.64 the second and third lines and columns to zero as demonstrated in Ref. [50].

3.5.2 Extension to nonplanar q3D–coupling algorithm

For non–planar coupling procedure the VLM solver is extended also by a side–slip correction angle, $\Delta\beta$. This correction increment corrects the non–circulatory freestream velocity vector, $\mathbf{V}_{\infty,j}$, on the VLM vortex–ring at the particular span position, j, by rotating it around the z–axis. Therefore, Equation 3.2 needs to be modified as follows:

$$\mathbf{V}_{\infty,i,j} = V_\infty \cdot \mathbf{R}_y(\alpha_{i,j}) \cdot \mathbf{R}_z(\Delta\beta_{i,j}) \cdot \mathbf{e}_{x_a} = V_\infty \begin{pmatrix} \cos\alpha_{i,j}\cos\Delta\beta_{i,j} \\ \sin\Delta\beta_{i,j} \\ \sin\alpha_{i,j}\cos\Delta\beta_{i,j} \end{pmatrix} \tag{3.65}$$

By correcting the orientation of the non–circulatory freestream velocity also with $\Delta\beta$ the linear VLM is now able to reproduce also nonlinear aerodynamic loads on highly deflected wing geometries. The employed linear VLM is formulated in the undeformed aerodynamic frame of reference, $< x_a, y_a, z_a >$, while the steady–state q3D–coupling procedure couples the nonlinear aerodynamic loads in deflected aerodynamic frame of reference, $< \hat{x_a}, \hat{y_a}, \hat{z_a} >$, which is rotated by the current aeroelastic deflection angle $\theta_{x,j}$ around the x_a–axis, as it can be seen in Figure 3.12.

In the steady–state q3D–coupling algorithm the spanwise aerodynamic force coefficient vector, $\hat{\mathbf{C}}_{inv,j} = [\hat{C}_{inv,D,j}, \hat{C}_{inv,S,j}, \hat{C}_{inv,L,j}]^T$, can be estimated by rotating the total spanwise aerodynamic forces by the current Eulerian aeroelastic deflection angle, $\theta_{x,j}$:

$$\begin{Bmatrix} \hat{C}_{D,j} \\ \hat{C}_{S,j} \\ \hat{C}_{L,j} \end{Bmatrix} = \mathbf{R}_x(\theta_{x,j}) \cdot \begin{Bmatrix} C_{D,j} \\ C_{S,j} \\ C_{L,j} \end{Bmatrix} \tag{3.66}$$

For the first aeroelastic coupling iteration in the computational FSI–framework the aeroelastic deflection angle, $\theta_{x,j}$, is zero on all spanwise segments of the VLM lattice. Here, $\mathbf{R}_x$ is the rotation matrix around the global x–axis. If the wing contains a natural dihedral in an unloaded state, this can be considered by a geometric deflection of the VLM lattice provided by the user. By following Equation 3.66 the aerodynamic lift coefficient, $\hat{C}_{L,inv,j}$, at a particular span position, j, in the deflected state of the wing can be stated as:

$$\hat{C}_{L,j} = C_{S,j}\sin\theta_{x,j} + C_{L,j}\cos\theta_{x,j} \tag{3.67}$$

Further, in the steady–state q3D–coupling algorithm the effective angle of attack, $\hat{\alpha}_{e,j}$, (Equation 3.50) is estimate here in the deflected aerodynamic frame of reference, $< \hat{x_a}, \hat{y_a}, \hat{z_a} >$:

$$\hat{\alpha}_{e,j}^{(k)} = \frac{\hat{C}_{L,inv,j}^{(k)}}{2\pi} - \Delta\hat{\alpha}_j^{(k-1)} \tag{3.68}$$

The angle of attack correction, $\hat{\alpha}_{ind,j}$, of the aerodynamic frame of reference can be obtained by:

$$\tan\Delta\hat{\alpha}_j = \tan\Delta\beta_j \cdot \sin\theta_{x,j} + \tan\Delta\alpha_j \cos\theta_{x,j} \tag{3.69}$$

This equation is derived from the general contemplation of a velocity vector, $\hat{V} = [\hat{u}, \hat{v}, \hat{w}]^T$, in the deflected aerodynamic frame of reference:

$$\begin{Bmatrix} \hat{u} \\ \hat{v} \\ \hat{w} \end{Bmatrix} = \mathbf{R}_x(\theta_{x,j}) \cdot \begin{Bmatrix} u \\ v \\ w \end{Bmatrix} \tag{3.70}$$

Thus, by normalising all velocity components by $\hat{u} = u$ the relation between $\tan\Delta\hat{\alpha}$ and $\tan\Delta\alpha$ and $\tan\Delta\beta$ can be seen:

$$\begin{Bmatrix} 1 \\ \hat{v}/\hat{u} \\ \hat{w}/\hat{u} \end{Bmatrix} = \begin{Bmatrix} 1 \\ \tan\Delta\hat{\beta} \\ \tan\Delta\hat{\alpha} \end{Bmatrix} = \begin{bmatrix} 1 & 0 & 0 \\ 0 & \cos\theta_{x,j} & -\sin\theta_{x,j} \\ 0 & \sin\theta_{x,j} & \cos\theta_{x,j} \end{bmatrix} \cdot \begin{Bmatrix} 1 \\ \tan\Delta\beta \\ \tan\Delta\alpha \end{Bmatrix} \tag{3.71}$$

Further, the aerodynamic freestream angle of attack correction increment in the deflected frame of reference, $\Delta\hat{\alpha}_j$, updates for the next iteration as follows:

$$\Delta\hat{\alpha}_j^{(k)} = \Delta\hat{\alpha}_j^{(k-1)} + \nu\frac{\hat{C}_{L,visc,j}^{(k)} - \hat{C}_{L,inv,j}^{(k)}}{2\pi} \tag{3.72}$$

The viscous sectional aerodynamic lift force coefficient, $\hat{C}_{L,visc}$, in deflected aerodynamic frame of reference is obtained directly from the viscous database and is already formulated with respect to the local deflected aerodynamic frame of reference. Finally, by applying Equation 3.71 in the inverted form

$$\begin{Bmatrix} 1 \\ \tan\Delta\beta \\ \tan\Delta\alpha \end{Bmatrix} = \mathbf{R}_x(\theta_{x,j})^{-1} \cdot \begin{Bmatrix} 1 \\ \tan\Delta\hat{\beta} \\ \tan\Delta\hat{\alpha} \end{Bmatrix} \tag{3.73}$$

the freestream angle of attack correction increment, $\Delta\alpha$, and side–slip correction increment, $\Delta\beta$, can be recovered form $\Delta\hat{\alpha}_j$ in the undeflected aerodynamic frame of reference, $< x_a, y_a, z_a >$, suitable for the linear VLM:

$$\tan\Delta\alpha = \tan\Delta\hat{\alpha}\cdot\cos\theta_{x,j} \tag{3.74}$$

$$\tan\Delta\beta = \tan\Delta\hat{\alpha}\cdot\sin\theta_{x,j} \tag{3.75}$$

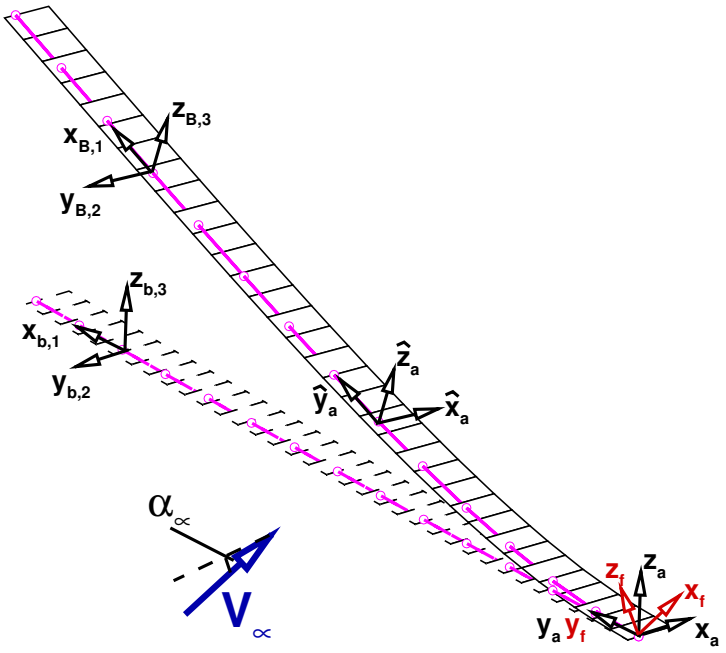

FIGURE 3.12: Frame of reference arrangement of GEBT

3.5.3 Aeroelastic coupling procedure of aerodynamic and structural models

In Figure 3.12 the arrangement of all defined frame of references for the structural and aerodynamic domains are shown: the aerodynamic undeformed body–fixed frame of reference is defined as $< x_a, y_a, z_a >$ by pointing the x–axis to the farfield behind the wing and y–axis along the wing. The linear VLM model is formulated in this frame of reference even if the lattice is highly deflected and twisted. The corresponding non-planar fixed aerodynamic frame of reference, $< \hat{x}_a, \hat{y}_a, \hat{z}_a >$, is defined locally along the deformed elastic axis of the wing. The coupling code is formulated according to this frame of reference. Further, the local undeformed frame of reference of the beam, $< x_b, y_b, z_b >$, is defined by orienting the x–axis along the local axis of the beam element and the z–axis upwards. The corresponding deformed local frame of reference of

the beam is defined by $< x_B, y_B, z_B >$. The last frame of reference axis is defined by $< x_f, y_f, z_f >$, which is the aerodynamic frame of reference of the employed Vortex–Lattice method (VLM), where the x_f–axis is aligned along the local flow direction.

The sequential diagram of the employed FSI–coupling interface between GEBT and `FALCon` can be seen in Figure 3.13. Here, within one inner loop of the coupling procedure at first, the linear VLM or the hybrid q3D–solver are executed, which estimates the aerodynamic loads on the currently deformed VLM lattice. Then, the aerodynamic forces, δF_j, located at every VLM section, j, are transferred to the nodes of the GEBT beam. Here, the aerodynamic loads, δF_j, are obtained from the spanwise distributed aerodynamic force coefficients, i.e. $C_{L,j}$, $C_{S,j}$ and $C_{D,j}$, in body attached frame of reference.

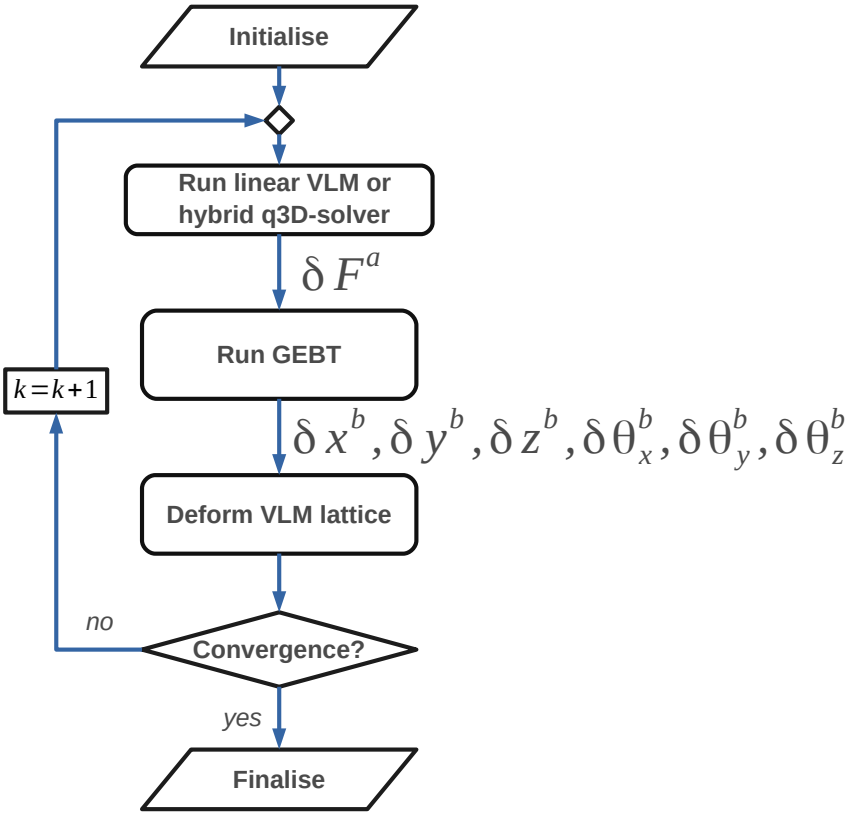

FIGURE 3.13: Schematics of the employed FSI–loop in FlexiFALCon

After the aerodynamic forces are mapped onto the beam nodes, the structural solver GEBT[110] estimates the deflection and twist of the beam nodes and the inner strains and forces of the beam are computed. The VLM lattice is deformed as the last step of the inner loop by estimating the total displacement of every geometrical VLM lattice vertices according to the beam deflection and twist. After that, the VLM vortex–ring lattice, which is shifted by a quarter–chord from the geometrical VLM lattice, is updated,

i.e. position of collocation point, four vortex–ring vertices and the normal vector of the vortex–ring. The FSI loop continues until an equilibrium between the aerodynamic and structural domain is reached.

3.5.3.1 Mapping of aerodynamic forces onto the structural FEM beam

The most complex and central aspect of a computational FSI–framework is the mapping of aerodynamic forces from the aerodynamic domain onto the structural domain and then the deformation of the VLM lattice geometry with respect of the beam deformation. In `FlexiFALCon`, the mapping procedure is shown in Figure 3.14 schematically.

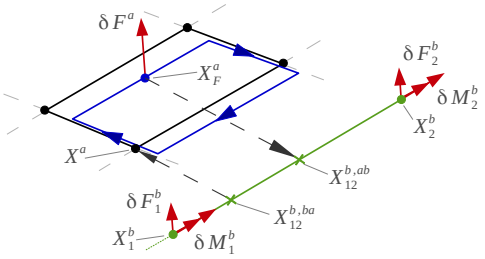

FIGURE 3.14: Mapping of aerodynamic forces and deformation of VLM lattice verices in FlexiFALCon

The sectional aerodynamic force, $\delta\mathbf{F}_j$ (here: $\delta\mathbf{F}^a$), at an arbitrary span position, j, of the VLM lattice is obtained by either summing up all aerodynamic forces along i–th direction at the section j (in linear mode) or obtaining them from the viscous sectional database at the particular converged effective angle of attack, $\hat{\alpha}_{e,j}$, computed by the aerodynamic q3D–coupling algorithm. In linear VLM the total sectional aerodynamic force is always located at the quarter–chord of the current local wing section, i.e. $\Delta x_p/c = 0.25$. However, in hybrid nonlinear aerodynamic q3D–solver the sectional aerodynamic force, $\delta\mathbf{F}_j$, can be shifted along the local chord of the wing section according to the actual sectional aerodynamic centre of pressure. The exact position of the aerodynamic centre of pressure on a VLM section can be estimated as follows:

$$\frac{\Delta x_p}{c} = 0.25 + \frac{dC_{M,0.25}}{dC_L} \tag{3.76}$$

Here, $C_{m,0.25}$ is the nonlinear viscous moment of the section with respect to the quarter–chord position of the local chord and is obtained from the viscous sectional database in the same way as the viscous lift force coefficient, $C_{L,visc}$, through interpolation of the aerodynamic database at the particular span position, (y/b), and at current effective

angle of attack, $\hat{\alpha}_e$. The absolute position, $\mathbf{X}_F^a$, of the sectional aerodynamic force, $\delta\mathbf{F}_j$, in undeformed aerodynamic frame of reference, $< x_a, y_a, z_a >$, is estimated as follows:

$$\mathbf{X}_{F_j} = \left(1 - \frac{\Delta x_p}{c}\right)\mathbf{X}_{LE,j} + \frac{\Delta x_p}{c}\mathbf{X}_{TE,j} \tag{3.77}$$

Here, $\mathbf{X}_{LE,j}$ is the position of the geometrical leading edge and $\mathbf{X}_{TE,j}$ is the position of the geometrical trailing edge of the j–th VLM lattice mesh section. For the mapping of the aerodynamic force, $\delta\mathbf{F}_j$, onto the beam, the corresponding position on the beam, $\mathbf{X}_{12}^{b,ab}$, needs to be estimated, see Figure 3.14. Here, ab means that $\mathbf{X}_{12}^{b,ab}$ is the corresponding position on the beam used for the mapping of the aerodynamic force onto the beam structure. For the correct interpolation, the distance between $\mathbf{X}_{F_j}$ and $\mathbf{X}_{12}^{b,ab}$ needs to be minimal. The minimal distance is given, when the vector $< \mathbf{X}_{F_j}, \mathbf{X}_{12}^{b,ab} >$ and $\mathbf{r}_{12} = \mathbf{X}_2^b - \mathbf{X}_1^b$ are orthogonal:

$$\mathbf{r}_{12} \cdot \left(\mathbf{X}_{12}^{b,ab} - \mathbf{X}_{F_j}\right) = 0 \tag{3.78}$$

Any point on a beam element segment can be represented in a parametrised way. The point located on a beam section can be described as:

$$\mathbf{X}^b = (1 - \lambda)\mathbf{X}_1^b + \lambda\mathbf{X}_2^b \tag{3.79}$$

with the parameter λ defined in the interval $\{\lambda \in \mathbb{R} |\, 0 \leq \lambda < 1\}$. Thus, for the mapping procedure of the aerodynamic force, $\delta\mathbf{F}_j$, at an arbitrary span position j of the VLM lattice the beam element segment is selected, where λ is in the required interval, and the length of the vector $< \mathbf{X}_{F_j}, \mathbf{X}_{12}^{b,ab} >$ is minimal compared to all other beam section. The parameter $\lambda_{12}^{b,ab}$ for the mapping of the aerodynamic force onto the FE–beam element can be estimated as follows:

$$\lambda_{12}^{b,ab} = \frac{\left(\mathbf{X}_{F_j} - \mathbf{X}_1^b\right) \cdot \mathbf{r}_{12}}{\mathbf{r}_{12} \cdot \mathbf{r}_{12}} \tag{3.80}$$

Thus, the corresponding mapping position on the beam is:

$$\mathbf{X}_{12}^{b,ab} = (1 - \lambda_{12}^{b,ab})\mathbf{X}_1^b + \lambda_{12}^{b,ab}\mathbf{X}_2^b \tag{3.81}$$

The linear interpolation of the aerodynamic force, $\delta\mathbf{F}^a$, onto both nodes of the beam section is preformed as follows:

$$\delta \mathbf{F}_1^b = \left(1 - \lambda_{12}^{b,ab}\right) \delta \mathbf{F}_j \tag{3.82}$$

$$\delta \mathbf{F}_2^b = \lambda_{12}^{b,ab} \delta \mathbf{F}_j \tag{3.83}$$

This both force contributions are only the contribution of the aerodynamic force vector, $\delta \mathbf{F}_j$, onto the corresponding two structural nodes of the particular FEM element segment. They have to be added on top of the contribution of other spanwise aerodynamic forces. Further, in the same manner the aerodynamic moments, $\delta \mathbf{M}_1^b$, and $\delta \mathbf{M}_2^b$, are estimated at $\mathbf{X}_1^b$ and $\mathbf{X}_2^b$:

$$\delta \mathbf{M}_1^b = \left(1 - \lambda_{12}^{b,ab}\right) \left(\mathbf{X}_F^a - \mathbf{X}_{12}^{b,ab}\right) \times \delta \mathbf{F}_j \tag{3.84}$$

$$\delta \mathbf{M}_2^b = \lambda_{12}^{b,ab} \left(\mathbf{X}_F^a - \mathbf{X}_{12}^{b,ab}\right) \times \delta \mathbf{F}_j \tag{3.85}$$

This is a mapping methodology based on linear interpolation techniques. In such a mapping method the total force and moment in both, the aerodynamic and structural domain after the mapping procedure are the same and no force and moment contribution can vanish or additional created.

3.5.3.2 Deformation of the VLM lattice

The deformation of the VLM lattice employs the same methodology. However, in VLM, the positions of the aerodynamic force and the geometrical vertices of the lattice are located at different places. Therefore, for the deformation of a vortex–ring vertex on the VLM lattice the estimated location of the corresponding point on the beam, $\mathbf{X}_{12}^{b,ab}$, is not valid. The estimation of the reference point on the FEM beam segment with respect to the position of a single VLM vortex–ring vertex, $\mathbf{X}^a$, is performed as follows:

$$\lambda_{12}^{b,ba} = \frac{\left(\mathbf{X}^a - \mathbf{X}_1^b\right) \cdot \mathbf{r}_{12}}{\mathbf{r}_{12} \cdot \mathbf{r}_{12}} \tag{3.86}$$

Here, *ba* means the direction of the mapping from the beam to the VLM lattice. For every *k*–th node on the beam FEM mesh the resulting vector is described as follows:

$$\mathbf{f}_k^b = \begin{Bmatrix} \Delta x_k^b \\ \Delta y_k^b \\ \Delta z_k^b \\ \theta_{k,1}^b \\ \theta_{k,2}^b \\ \theta_{k,3}^b \end{Bmatrix} \tag{3.87}$$

Here, the first three items are the translational displacements of the beam node and the last three items are the Wiener–Milenković rotational parameters[103][102], which are defined as follows:

$$\begin{pmatrix} \theta_1^b \\ \theta_2^b \\ \theta_3^b \end{pmatrix} = \bar{\mathbf{n}} \cdot 4 \tan \frac{\phi}{4} \tag{3.88}$$

Here, $\bar{\mathbf{n}} = [n_1, n_2, n_3]^T$ is the rotation axis and has the length of $|\bar{\mathbf{n}}| = 1$, and ϕ is the actual Eulerian rotation angle around that axis. From θ_1^b, θ_2^b and θ_3^b the axis, $\bar{\mathbf{n}}$, and the rotation angle, ϕ, are recovered and are used in the (3×3) rotation matrix:

$$\mathbf{R}(\bar{\mathbf{n}}, \phi) = \begin{bmatrix} n_1^2(1-\cos\phi) + \cos\phi & n_1 n_2(1-\cos\phi) - n_3 \sin\phi & n_1 n_3(1-\cos\phi) + n_2 \sin\phi \\ n_2 n_1(1-\cos\phi) + n_3 \sin\phi & n_2^2(1-\cos\phi) + \cos\phi & n_2 n_3(1-\cos\phi) - n_1 \sin\phi \\ n_3 n_1(1-\cos\phi) - n_2 \sin\phi & n_3 n_2(1-\cos\phi) + n_1 \sin\phi & n_3^2(1-\cos\phi) + \cos\phi \end{bmatrix} \tag{3.89}$$

By using $\lambda_{12}^{b,ba}$ the corresponding position on the beam, $\mathbf{X}_{12}^{b,ba}$, and the structural solution vector, $\mathbf{f}_{12}^{b,ba}$, can be obtained through linear interpolation:

$$\mathbf{X}_{12}^{b,ba} = (1 - \lambda_{12}^{b,ba})\mathbf{X}_1^b + \lambda_{12}^{b,ba}\mathbf{X}_2^b \tag{3.90}$$

$$\mathbf{f}_{12}^{b,ba} = (1 - \lambda_{12}^{b,ba})\mathbf{f}_1^b + \lambda_{12}^{b,ba}\mathbf{f}_2^b \tag{3.91}$$

Finally, the aerodynamic vertex position, $\mathbf{X}_{i+1}^a$, of the VLM lattice is updated for the next aeroelastic iteration, $(i+1)$, as follows:

$$\mathbf{X}_{i+1}^a = \mathbf{X}_{12}^{b,ba} + \mathbf{R}(\bar{\mathbf{n}}_{\mathbf{12}}^{\mathbf{b,ba}}, \phi_{12}^{b,ba}) \cdot \left(\mathbf{X}^a - \mathbf{X}_{12}^{b,ba}\right) + \begin{pmatrix} \Delta x_{12}^{b,ba} \\ \Delta y_{12}^{b,ba} \\ \Delta z_{12}^{b,ba} \end{pmatrix} \tag{3.92}$$

3.6 Summary

In this chapter the methodology of all related areas of this research has been discussed. For the linear steady–state and unsteady VLM the formulation closely follows Katz and Plotkin[45]. However, a nonplanar vectorised formulation of the aerodynamic forces is applied here[84] allowing also to estimate aerodynamic loads on highly deformed and nonplanar lattices accurately. Further, the formulation of the steady–state aerodynamic q3D–coupling algorithm is discussed and an extension to unsteady aerodynamics is presented, which is the main novelty and scientific contribution of this thesis. The unsteady aerodynamic q3D–coupling algorithm is not restricted to any type of unsteady motion of the lattice geometry, for example only for harmonic oscillations in pitch or plunge, and can be applied to any arbitrary wing kinematics as the unsteady nonlinear aerodynamic viscous reference loads are estimated here on demand by the URANS solvers embedded in the aerodynamic computational framework `FALCon` and can respond to any type of unsteady motion of the lattice.

In the last section, aeroelasticity related topics are discussed: The open source FEM code GEBT[110] representing the structural aspect of the wing as a nonlinear FE–beam is briefly introduced. As the development of that structural model is not part of this research, the reader is referred here to all related literature dealing with an anisotropic nonlinear beam formulation. Further, the adoption of the steady–state aerodynamic q3D–coupling algorithm to nonplanar aerodynamic coupling of deflected wings, which is required during the aeroelastic analysis, is described and, finally, the computational FSI–framework `FlexiFALCon` and its mapping procedures of the data between the structural and aerodynamic domain is presented. Here, the author extended the steady–state α–based coupling algorithm by a side–slip correction angle to account also aerodynamic loads on non–planar deflected wing geometries. In the following chapter the results of validation campaigns for all major fields of this research are presented.

Chapter 4

Results

In this chapter, the results of the validation campaigns are presented and the computational framework is demonstrated by several test cases. The chapter starts with Section 4.1 where the verification and validation results of the linear VLM in steady–state and unsteady flow regimes are presented. During this research, the linear Vortex–Lattice method (VLM) is implemented from scratch and is part of the computational aerodynamic framework `FALCon`. Therefore, the implementation was followed by an extensive validation campaign of the linear aerodynamic solver. Further, in Section 4.2 the validation results of the aerodynamic steady–state quasi–3D approach are presented, followed by Section 4.3 where the results of the validation campaign of the unsteady aerodynamic hybrid coupling algorithm are shown and discussed.

In the last section of this chapter, Section 4.4, the results of the validation campaign of `FlexiFALCon` are shown. `FlexiFALCon` is the computational FSI–wrapper of `FALCon` and couples the linear or q3D aerodynamic solver with a nonlinear geometrically–exact beam model. It performs, at the current state of the development, steady–state aeroelastic analysis of highly flexible wings. Therefore, in Section 4.4.1 results are presented of a high–aspect ratio wing in inviscid flow by running linear steady–state VLM of `FALCon` in combination with the nonlinear beam model. Finally, in Section 4.4.2 the validation campaign of `FlexiFALCon` is continued by validating this FSI–wrapper using a NACA2412 high aspect ratio wing in viscous and compressible flow at several Mach–numbers, where the presented hybrid aerodynamic coupling algorithm is used in the numerical fluid–structure interaction analysis.

4.1 Validation of the linear Vortex–Lattice Method

In this section the steady–state and unsteady VLM solvers are validated using simple test cases. In Section 4.1.1 the steady–state linear VLM solver is validated by comparing the obtained lift slope, C_L^α, of swept and unswept thin–wing geometries to a reference VLM code, and in Section 4.1.2 the linear UVLM model of `FALCon` is validated by using two test cases: A suddenly accelerated flat plate and a 2D aerofoil (VLM lattice of $AR = 100$), which undergoes a forced harmonic oscillation in pitch and plunge. Here, the results are compared to the algebraic model of Theodorsen describing a thin aerofoil in unsteady flow regimes[91]. The purpose of this section is to demonstrate the accuracy of the steady–state and unsteady linear VLM solver implemented in the computational aerodynamic framework `FALCon`, which serves later on in the q3D–coupling solver as the low–fidelity solver computing the 3D flow physics around a wing geometry.

4.1.1 Steady–state VLM model

In this section the results of the validation campaign of the steady–state linear Vortex–Lattice method (VLM) solver are presented. The purpose of this validation test case is the demonstration of the accuracy of the implemented linear VLM solver in `FALCon`. Therefore, a series of thin–wing geometries are examined and the resulting linear lift slope, C_L^α, is compared with reference results obtained by Mark Drela's VLM code `AVL`[26] at various aspect ratios, AR, and sweep angles, Λ, of the wing geometry.

In Figure 4.1 the lift slope of a single flat plate, swept by $\Lambda = 30^\circ$, is shown at various aspect ratios, AR, where results of a coarse, middle and fine lattice of the same geometry computed by the linear VLM of `FALCon` are compared. For the further validation study the middle sized lattice is chosen, which is discretised along the chord with $N_i = 8$ and along the half–span of the wing with $N_j = 26$ vortex–rings. The vertices of the wing bounded lattice are equidistant distributed across the lattice and are forming this way a uniform VLM vortex–ring mesh, see Figure 4.2b.

In Figure 4.2a the linear lift slope, C_L^α, of the thin–wing geometries of various sweep angles, Λ, are plotted versus the aspect ratio, $AR = b/c$. All lattices have a uniform taper ratio of $\gamma = 1.0$. Thus, the chord length along the span of the wing is uniform, $c = 1\ m$. All calculations for this study were carried out at a freestream angle of attack of $\alpha_\infty = 1.0^\circ$. The lift slope, C_L^α, is estimated from the obtained total linear lift, C_L, of the wing.

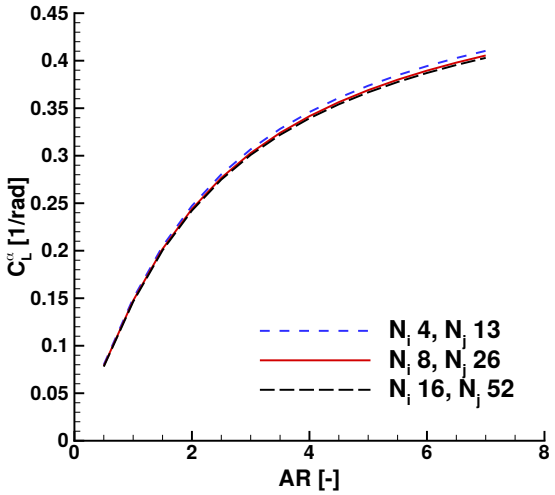

FIGURE 4.1: Lift slope of a flat and swept plate ($\Lambda = 30°$) of various aspect ratios, AR, obtained by linear VLM solver using three different mesh sizes of the lattice (coarse, 52 vertices, middle, 208 vertices, and fine, 832 vertices)

It can be seen that the linear steady–state VLM solver of FALCon matches the reference results with good agreement. This validation study shows that the linear VLM solver of FALCon is able to estimate aerodynamic loads on swept and unswept thin–wing geometries in inviscid flow at small angles of attack. Thus, the linear steady–state VLM solver is suitable for further application within the iterative hybrid aerodynamic q3D–coupling algorithm.

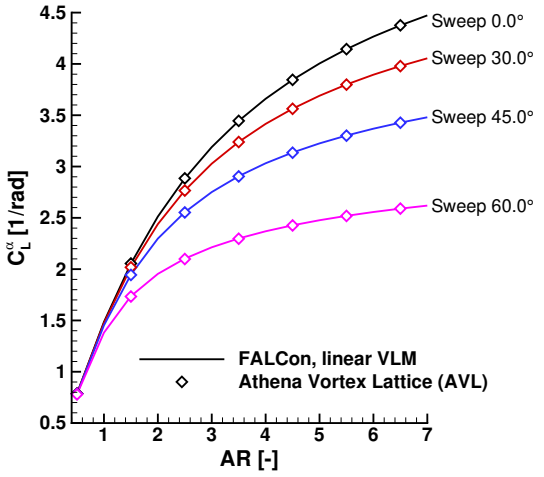

(A) Lift slope of rectangular wings at various sweep angles

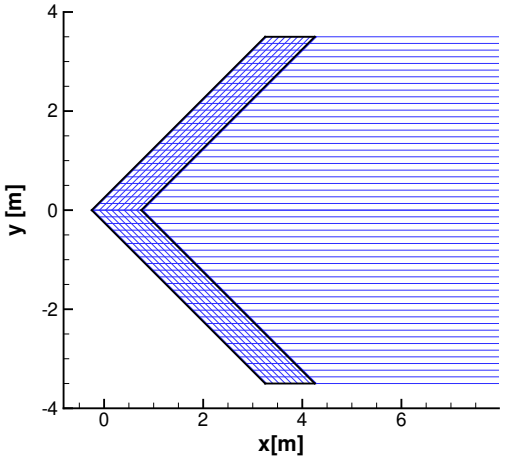

(B) VLM–lattice, Sweep 45.0°, AR 7.0

FIGURE 4.2: Validation of the steady–state linear VLM model by comparing the results to reference VLM model[26]

4.1.2 Unsteady VLM model

This section concerns the validation of the UVLM for a set of canonical problems: a suddenly accelerated flat plate of different aspect ratios, and a thin aerofoil undergoing forced motion in two degrees of freedom.

4.1.2.1 Suddenly accelerated flat plate

The lift coefficient build–up for a suddenly accelerated flat plate is reported in Figure 4.3 for values of the aspect ratio (AR) from 4 to infinity. The VLM lattice is subdivided into $N_i = 4$ chordwise and $N_j = 26$ spanwise vortex–ring elements, which vertices have an equidistant distribution long the chord and span. For the special case of $AR = \infty$, the flow is fully 2D. Practically, the UVLM uses for this special case a sufficiently large aspect ratio ($AR = 100$) combined with one spanwise panel, $N_j = 1$, to neglect modelling 3D effects. A nondimensional time step $\Delta\tau = 1/16$ is used for all unsteady analyses, where the reduced time, τ, is defined as follows:

$$\tau = \frac{tV_\infty}{c_{ref}} \tag{4.1}$$

Here, t is the physical time, c_{ref} is the reference chord length of the aerofoil and V_∞ is the freestream velocity. The initial impulsive part and the trend to steady–state for increasing times are well captured. Reference data are from Ref. [45].

As it can be seen in Figure 4.3, the results of the employed linear UVLM are matching the reference data from Katz and Plotkin[45] with a good agreement. This validation test case demonstrates that the unsteady linear VLM is implemented correctly and is able to estimate the unsteady time depended aerodynamic loads on a flat unswept plate of various aspect ratios, AR, while accelerated suddenly to constant velocity.

4.1.2.2 Forced motion of a thin aerofoil in pitch and plunge

The second validation test case is for a thin aerofoil undergoing a prescribed motion. The test case introduces the dependence on two degrees of freedom that are independently excited with the reduced frequency of oscillations:

$$k = \frac{\omega\, c_{ref}}{V_\infty} \tag{4.2}$$

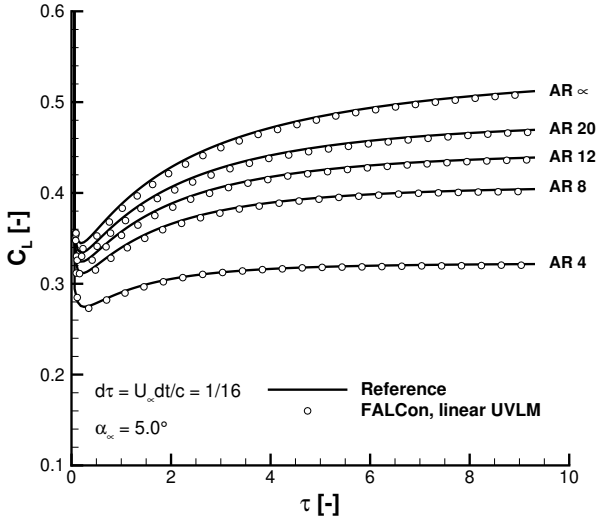

FIGURE 4.3: Sudden acceleration of a flat plate (N_i 8, N_j 26) of different aspect ratios AR at freestream angle of attack $\alpha = 5.0^\circ$ performed with linear unsteady Vortex-Lattice Method and compared to Katz and Plotkin (Ref [45])

Here, ω is the angular velocity, c_{ref} is the reference chord length and V_∞ is the freestream velocity. For an harmonic motion, the time history of the pitch degree of freedom is defined by

$$\alpha(\tau) = \alpha_0 + \alpha_A \sin(2k\tau) \tag{4.3}$$

where α_0 is the mean value and α_A the amplitude of oscillations. Similarly, for plunge

$$\xi(\tau) = \xi_0 + \xi_A \sin(2k\tau) \tag{4.4}$$

where $\xi = h/c$ represents the nondimensional plunge or heave. Two types of motion are here considered: 1) a pure pitch, defined by parameters $\alpha_0 = 0^\circ$ and $\alpha_A = 2.5^\circ$; and 2) a pure plunge, $\xi_0 = 0$ and $\xi_A = 0.1$. For both types of motion, three values of the reduced frequency are used: $k = 0.5$, 1.0 and 1.5.

In the UVLM, the 2D aerodynamics around the thin aerofoil is obtained using one panel in the spanwise direction, as in the previous Section for $AR = \infty$. The number of chordwise panels was determined by a convergence study, similarly to Ref. [59], and this is summarised in Table 4.1. It is worth noting that the nondimensional time step satisfies the relation $\Delta\tau = 1/N_i$.

This ensures that the chord length of new wake panels shed into the wake is equal to the chord length of wing bounded panels. The freestream velocity is in all cases constant: $V_\infty = 100.0\ m/s$.

k	N_i	N_j	$\Delta\tau[-]$
0.5	25	1	0.0400
1.0	28	1	0.0357
1.5	42	1	0.0238

TABLE 4.1: Lattice discretisation and physical time step sizes used for the test cases

Hysteresis loops are shown in Figure 4.4. Here, the third cycle of the unsteady results is presented where the initial transients are not present and only the periodic nature of the lift coefficient is highlighted. Reference data are obtained using Theodorsen's analytical model [91]. Good match between the analytical curves and the results obtained by the linear UVLM of `FALCon` can be observed for all cases, ranging from low to high values of the reduced frequency.

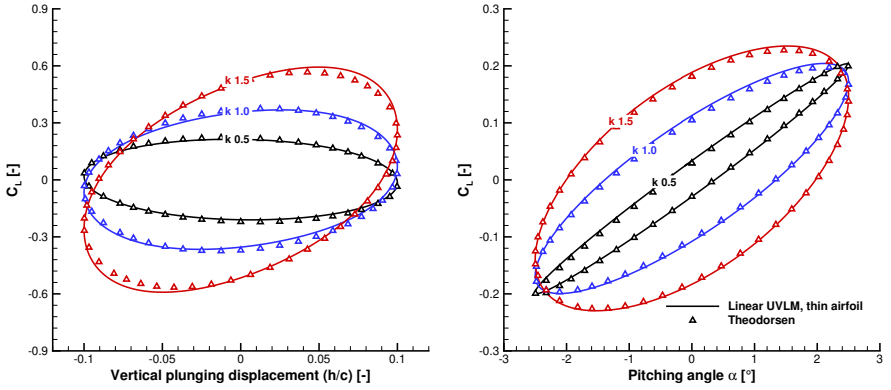

(A) Airfoil at harmonic plunge oscillations, amplitude $\Delta(h/c) = 0.2$

(B) Airfoil at harmonic pitch oscillations, amplitude $\Delta\alpha = 5.0°$

FIGURE 4.4: UVLM versus Theodorsen at various reduced frequencies $k = 0.5$, $k = 1.0$ and $k = 1.5$

4.2 Steady–state aerodynamic model

In this section results of the validation campaign of the steady–state aerodynamic hybrid q3D–coupling approach are presented. In the first part, a NACA2412–wing geometry is used with various geometrical parameters. The purpose of this test campaign is to validate the steady–state nonlinear aerodynamic solver in combination with aerodynamic sectional data computed by the 2.5D+ ISW–RANS CFD solver on swept and unswept wing geometries at several flow velocities. The first part of this NACA2412–test case contains also flow regimes at high freestream angles of attack, where the flow

is usually affected by flow separation, see Section 4.2.1. The systematic validation campaign using the NACA2412–wing continues further by analysing the accuracy of the steady–state aerodynamic q3D–coupling solver on the wing geometry with various geometrical sweep angles, Λ, and taper ratios, γ.

In Section 4.2.2 the second test case is presented. Here, the validation campaign continues by using the DLR–F4 wing/body configuration in transonic flow regimes. This test case uses a much closer geometry to modern commercial airliners containing a wing with complex geometrical parameters and a fuselage.

4.2.1 Systematic study around a NACA2412–wing in steady–state flow conditions

The first test case is for a NACA2412 aerofoil–wing of an aspect ratio of $AR = 10$ with various geometrical parameters, i.e. sweep angles, Λ, and taper ratios, γ. This section is subdivided into three main subsections: In Section 4.2.1.1 a validation study is conducted, where the aerodynamic loads, obtained by the hybrid q3D–coupling code at various freestream angles of attack, α_∞, are compared to reference data obtained by three–dimensional `DLR-tau` CFD code. For this study two wings, an unswept, $\Lambda = 0^\circ$, and a swept wing, $\Lambda = 30^\circ$, of a constant taper ratio of $\gamma = 1.0$ are used. The freestream angles of attack are also covering stall– and near post–stall flow conditions. Further, the calculations are performed at three Mach–numbers, $M = 0.3$, $M = 0.5$ and $M = 0.7$, to demonstrate the unified capabilities of this novel solver regarding the aerodynamic load estimation at low– and high–speed flow regimes. Furthermore, in Section 4.2.1.2 a sweep variation study of the same wing is conducted. Here, during this study, the freestream angle of attack is kept constant at $\alpha_\infty = 3^\circ$ and the aerodynamic load estimations are compared on the NACA2412–wing with various geometrical sweep angles. This study is carried out also at the same three Mach–numbers, $M = 0.3$, $M = 0.5$ and $M = 0.7$, and investigates the dependence of the accuracy of the novel aerodynamic q3D–coupling solver with respect to the geometrical sweep of the wing, Λ. Finally, in the last Section 4.2.1.3 the results of a validation study are discussed where the taper ratio, γ, of the $\Lambda = 30^\circ$ swept NACA2412–wing is varied. The validation is carried out also at constant freestream angle of attack of $\alpha = 3.0^\circ$. The aim of this study is the analysis of the accuracy of this novel hybrid coupling algorithm with respect to the geometrical taper ratio of the wing.

The results obtained by `FALCon` are compared to equivalent three–dimensional numerical data obtained by full–fidelity three–dimensional CFD code `DLR-tau`. Therefore, a structured volumetric CFD mesh of the NACA2412–wing with $2 \cdot 10^6$ grid nodes

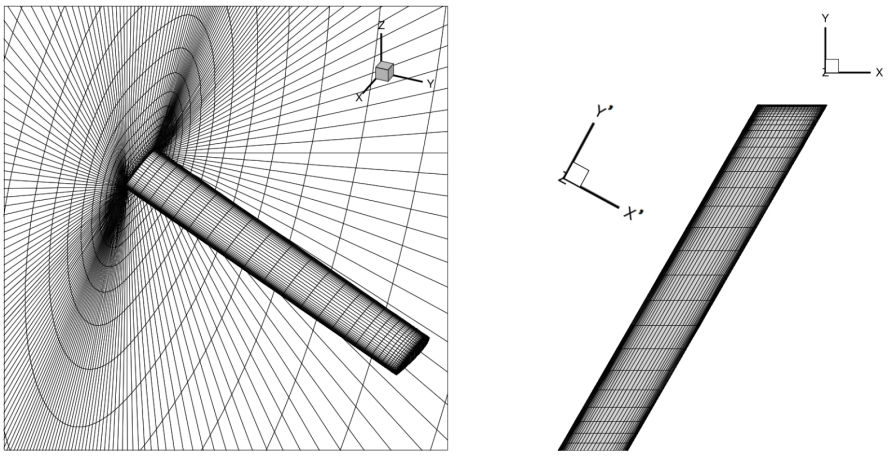

FIGURE 4.5: Three–dimensional volumetric CFD mesh of the swept NACA2412–wing ($\Lambda = 30°$) employed for three–dimensional CFD simulations

around the NACA2412–wing is created. The tip of this wing is kept flat. The two–dimensional CFD aerofoil mesh, used for the computation of the nonlinear sectional lift curves, is extracted directly from the symmetry layer of the three–dimensional mesh and contains $25.7 \cdot 10^3$ grid points. For the computation of the lift curves for swept wing sections this 2D mesh is then stretched vertically by the factor obtained from Equation 3.45. The employed 3D and 2D CFD meshes are of the structured O–grid mesh type. The farfield is located 100 chord lengths away from the wing geometry. The chord length of the wing is constant along the span, $c = 1\ m$. The three–dimensional mesh used for calculations of swept wings, $\Lambda > 0°$, or tapered wing geometries, $\gamma = c_1/c_0 < 1.0$, are modified by skewing and transforming the mesh point locations of the original unswept wing CFD mesh. In Figure 4.5 the three–dimensional swept and non–tapered CFD mesh is presented, and in Figure 4.6 the two–dimensional CFD mesh, which is also the symmetry layer of the three–dimensional grid, is shown.

The initial wall spacing of the 2D and 3D CFD–grids at the wall boundary is set to $\Delta y_0 = 1.3 \cdot 10^{-6}\ m$ to ensure that the dimensionless wall distance condition, $y^+ < 1.0$, is satisfied. Due to vertical stretching of the two–dimensional meshes necessary for the 2.5D+ computations of the sectional database at a particular sweep angle, Λ, the initial wall distance, Δy_0, is also stretched. Thus, the maximal initial wall distance is $\Delta y_0 = 1.7 \cdot 10^{-6}$ for the 2D CFD grid, employed during the computation of sectional aerodynamic database at a maximal geometrical sweep of this validation study of $\Lambda > 40°$. However, the non–dimensional wall distance condition is kept in all simulations under $y^+ < 1.0$ with the purpose to resolve the viscous boundary layer accurately.

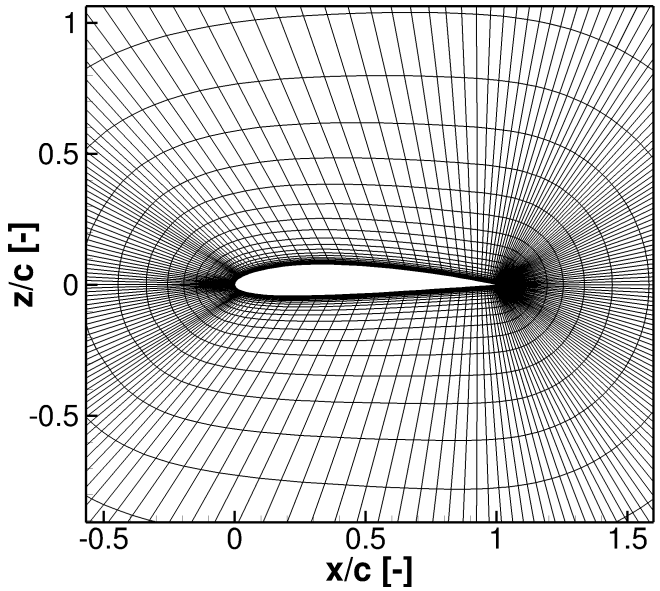

FIGURE 4.6: Two–dimensional CFD grid of the NACA2412 airfoil (25704 grid points) extracted from the three–dimensional mesh

As the temporal relaxation solver an implicit backward Euler–scheme in combination with a local steady–state time–stepping approach is employed. Further, the second–order central scheme is used to discretise the convective RANS flux. All computations are carried out at a constant Reynolds–number of $Re = 5.5 \cdot 10^6$. The one equation Spalart–Almaras turbulence model in its original formulation is used to model the turbulent flow[88]. The gas constant is set to $\kappa = 1.4$ and the Prandtl–number to $Pr = 0.72$. The described parameters are identical for 3D and corresponding sectional 2D CFD computations to ensure that the sectional two–dimensional flow corresponds to the three–dimensional flow.

4.2.1.1 Dependence on angle of attack

In this subsection results of the NACA2412–wing study are presented where the freestream angle of attack α_∞ is varied. This validation campaign is conducted separately on a swept wing, $\Lambda = 30^\circ$, and an unswept wing, $\Lambda = 0^\circ$, with the purpose to asses the accuracy of the hybrid q3D–coupling code at various Mach–numbers, M, and freestream angles of attack, α_∞, including also near post–stall flow regimes, i.e. $\alpha > \alpha_{Stall}$.

The results of the corresponding variation of the employed unswept VLM lattice discretisation is presented in Figure 4.7 for Mach $M = 0.7$. Three lattices are used with different vortex–ring resolutions. It can be seen that the numerical solution is already here independent from the lattice resolution.

Therefore, for the further results, presented in the following sections, the lattice is used, which is discretised in $N_i = 5$ chordwise and $N_j = 25$ spanwise vortex–rings on the half–wing.

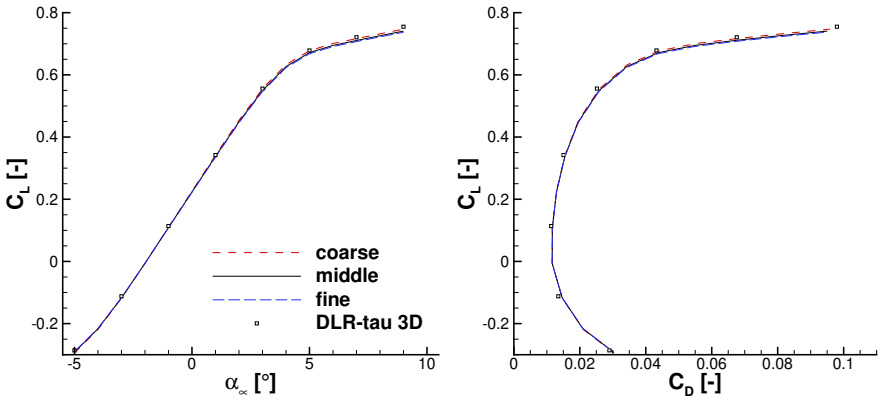

(A) Lift curve (B) Polar diagram

FIGURE 4.7: Variation of the VLM lattice size of the unswept NACA2412 wing at $M = 0.7$ (coarse: $N_i = 3$, $N_j = 13$, middle: $N_i = 5$, $N_j = 25$, fine: $N_i = 10$, $N_j = 50$)

Further, in Figure 4.8 the variation of the 2D angle of attack interval, $\Delta\alpha$, of the employed precomputed viscous 2D database of NACA2412 is presented and compared between 3D results estimated on the q3D–coupling alpgorithm while employing the middle sized VLM lattice. Also here, it can be seen that a resolution of the precomputed viscous database with an interval of $\Delta\alpha = 1.0^\circ$ is sufficient for the further investigation. As a general rule of thumb it has to be noted that the viscous sectional aerodynamic aerofoil database should be resolved by α in stall regions with a smaller $\Delta\alpha$ interval, whereas at linear part of lift curve (at small freestream angles of attack) two or three data points are sufficient.

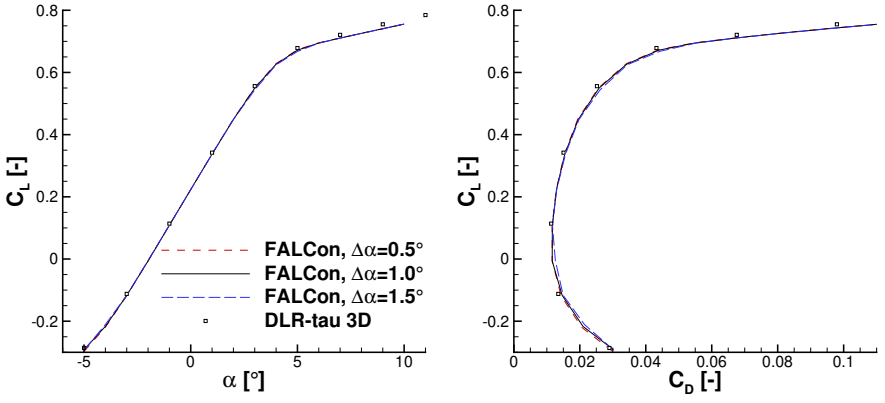

(A) Lift curve (B) Polar diagram

FIGURE 4.8: Variation of the angle of attack interval in the viscous NACA2412 2D airfoil database using the unswept wing geometry at $M = 0.7$

Unswept wing

For the unswept wing the required NACA2412 aerofoil lift and drag curve for the hybrid coupling procedure is computed only by the 2D `DLR-tau` CFD solver as no geometrical sweep of the wing is present. In Figure 4.9 the overall lift and drag force coefficients, C_L and C_D, are presented of the unswept wing of an aspect ratio of $AR = 10$ for all three Mach–numbers in steady–state flow condition. The data is obtained by the presented steady–state hybrid q3D–coupling code and is compared to three–dimensional CFD reference data and classical linear VLM.

At low–speed flow regimes, $M = 0.3$, the total lift force coefficient, C_L, matches at low freestream angles of attack, α_∞, the reference data obtained by linear VLM. However, at higher freestream angles of attack the overall lift slope, C_L^α, is decreased due to flow separations on the wing, which the linear VLM can not capture. At higher Mach–numbers it can be seen that the overall pre–stall lift slope, C_L^α, at moderate freestream angles of attack is slightly higher compared to the subsonic incompressible reference lift slope obtained by classical linear VLM, see Figure 4.9c and Figure 4.9e. This happens due to the additional compressibility effects, which are impacting the flow especially at $M = 0.7$. Further, it can be observed, that the total drag force coefficient, C_D, see Equation 3.60, estimated by the hybrid q3D–coupling code matches perfectly three–dimensional reference data. Also, it can be seen, that the classical linear VLM is only resolving the induced component of the drag force coefficient, C_D, of the thin–wing lattice which is lower compared to the three–dimensional reference drag obtained by 3D CFD.

At high angles of attack the flow is affected by local flow separations. Thus, in Figure 4.10 the pressure coefficient, c_p, of three–dimensional numerical CFD results is shown on the upper–surface of the wing. Further, in the same figures the friction coefficients, $c_{f,x}$, $c_{f,y}$ and $c_{f,z}$, are used to plot the stream lines. In Figure 4.10a for $M = 0.3$ it can be clearly seen that the separation is first time present at a freestream angle of attack of $\alpha_\infty = 13^\circ$ and progresses from the trailing edge towards the leading edge uniformly along the span of the wing. At high flow velocities, $M = 0.7$, the separation is first time present between $\alpha_\infty = 1^\circ$ and $\alpha_\infty = 5^\circ$ and progresses in the same way as in subsonic flow regimes towards the leading edge of the wing, see Figure 4.10c.

The spanwise local lift distribution, C_L, can be seen in Figure 4.11 for this unswept wing for the Mach–number $M = 0.3$, $M = 0.5$ and $M = 0.7$. At pre–stall conditions the hybrid q3D solver can obtain accurate load distributions on unswept wing geometries. However, at higher freestream angles of attack, α_∞, at stall and post–stall flow regimes the estimation of local spanwise lift is affected by discrepancies, as it can be seen for example for $M = 0.5$ and $M = 0.7$. The reason for the discrepancies which are present at

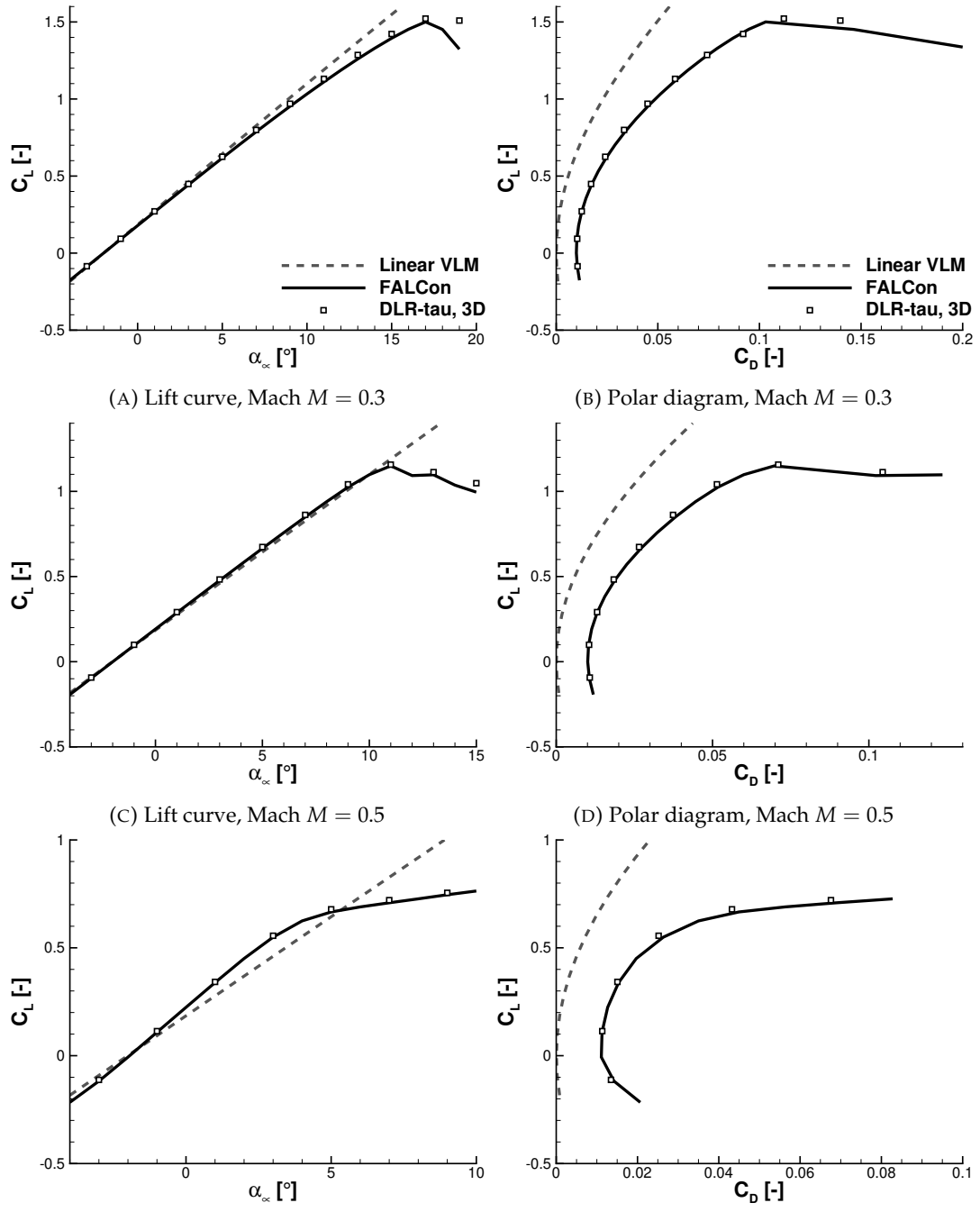

(A) Lift curve, Mach $M = 0.3$

(B) Polar diagram, Mach $M = 0.3$

(C) Lift curve, Mach $M = 0.5$

(D) Polar diagram, Mach $M = 0.5$

(E) Lift curve, Mach $M = 0.7$

(F) Polar diagram, Mach $M = 0.7$

FIGURE 4.9: Aerodynamic force coefficients of the unswept NACA2412 wing, $\Lambda = 0.0°$, with a taper ratio of $\gamma = 1.0$ and aspect ratio of $AR = 10$

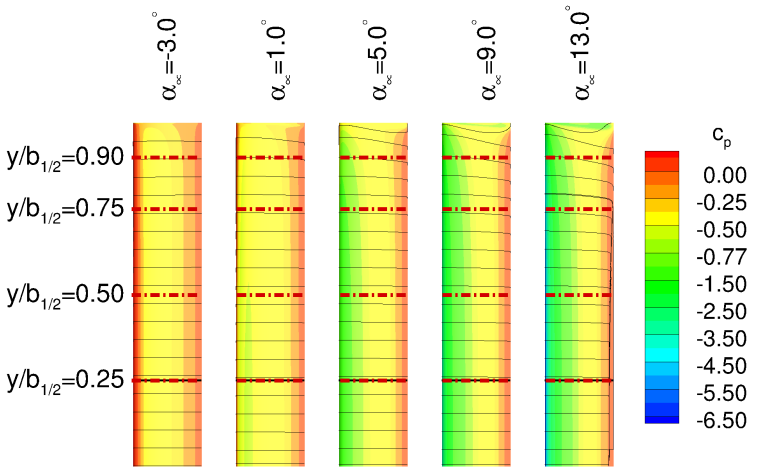

(A) Mach $M = 0.3$

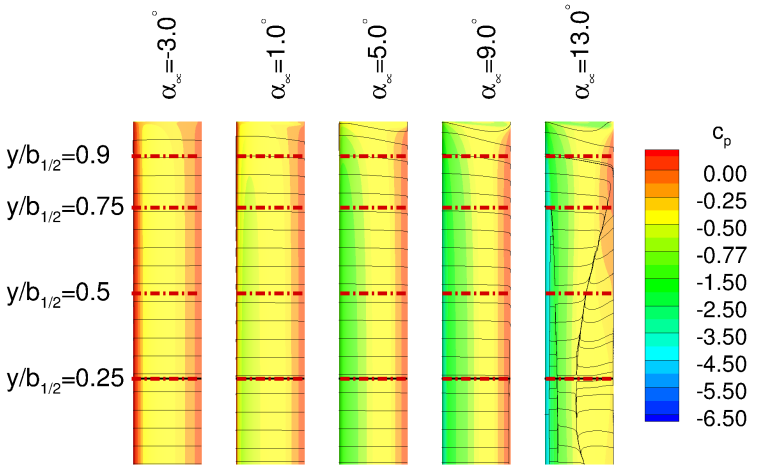

(B) Mach $M = 0.5$

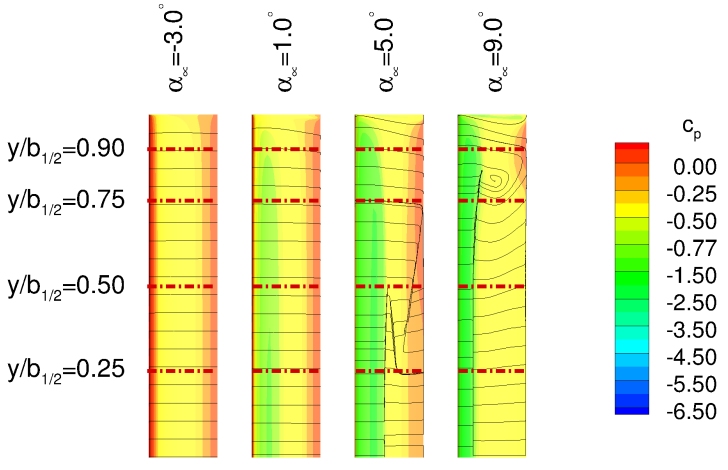

(C) Mach $M = 0.7$

FIGURE 4.10: Nondimensional pressure coefficient, c_p of unswept NACA2412 wing obtained with three–dimensional CFD (DLR-tau, 3D), $\Lambda = 0.0°$, Taper ratio $\gamma = 1.0$

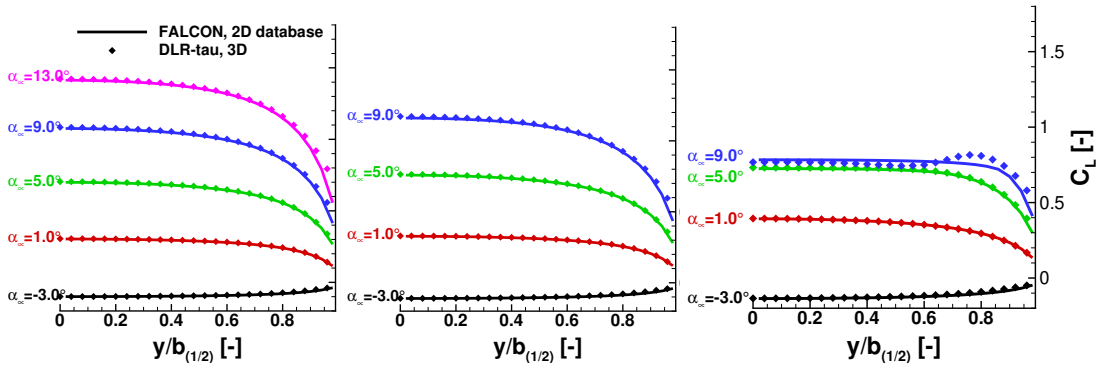

(A) Mach $M = 0.3$ (B) Mach $M = 0.5$ (C) Mach $M = 0.7$

FIGURE 4.11: Lift distribution along wing span of unswept NACA2412 wing, Sweep $\Lambda = 0.0°$, Taper ratio $\gamma = 1.0$

high freestream angles of attack, α_∞, is the violation of the assumption that the flow is locally fully developed along the span of the wing, i.e. $\partial(\cdot)/\partial y' = 0$[31], and therefore along the spanwise axis of the wing independent. Here, y' is the spanwise axis along the quarter–chord line of the wing and is only identical to y–axis in case of an unswept wing. For example, in Figure 4.10c it can be seen for $\alpha = 9.0°$ that a separation vortex is present at nearly 75% of the half–span of the wing. This is a three–dimensional local aerodynamic effect on the surface which leads to a not fully developed local flow in this region of the wing. The hybrid q3D–coupling code, based on this assumption, is not able to resolve accurately the flow in this region leading to the discrepancies of the local spanwise lift force coefficient, C_L. At moderate and higher freestream angles of attack, α_∞, the spanwise flow along the span (excluding the near wing tip region due to the wing tip vortex) is fully developed leading to correct estimation of the overall aerodynamic force coefficients and spanwise distributed wing loads.

The local flow physics for compressible Mach–number $M = 0.7$ can be seen for $\alpha = 1.0°$ in Figure 4.12, for for $\alpha = 5.0°$ in Figure 4.13 and for $\alpha = 9.0°$ in Figure 4.14. The sectional c_p– and c_f–distribution is obtained by computing the aerodynamic flow in 2D CFD at the particular effective angle of attack, α_e, of the converged `FALCon` solution at several span positions. It can be seen, that the sectional c_p– and c_f–distributions are matching the reference three–dimensional CFD results with a good agreement on most span positions of the wing and at most freestream angles of attack, α. However, it can be also noted that the accuracy of the estimations is in general decreased at the wing tip area compared to the corresponding three–dimensional CFD solution. The position of the suction peak is slightly mismatched at 90% of the half–span due to the present wing tip vortex, which is a local three–dimensional flow phenomena.

Thus, at the wing tip region of the wing the flow is not along the span fully developed and therefore not in the spanwise direction independent. Therefore, the validity of the hybrid coupling algorithm is in this region of the flow not given as the q3D coupling algorithm assumes always a spanwise independent sectional flow.

On the other side, it has to be noted that the presented q3D–approach is well capturing the sectional separation of the unswept wing at high angles of attack. In the region, where the flow is separated the pressure coefficient, c_p, stays constant and the friction coefficient, c_f, become negative along the chord due to reversed flow. This can be observed in Figure 4.13 and Figure 4.14.

Finally, in Table 4.2 the local relative error of the sectional aerodynamic lift force coefficient, C_L, is presented. This error is evaluated as follows:

$$\Delta e = \left| \frac{C_{L,hVLM} - C_{L,3D}}{C_{L,3D}} \right| \tag{4.5}$$

It can be seen, that the error at several span positions is below 1%. However, at transonic flow regimes ($M = 0.7$) and high angles of attack ($\alpha_\infty = 9°$) the error rises nearly to 6% of the local aerodynamic lift force coefficient, C_L, compared to three–dimensional reference CFD results.

		Spanwise location			
M	α_∞	25%	50%	75%	90%
0.3	1.0°	0.70	0.75	1.20	0.76
0.5	1.0°	0.71	0.70	1.00	0.40
0.7	1.0°	0.43	0.20	0.00	0.75
0.3	5.0°	0.67	0.58	0.60	0.43
0.5	5.0°	0.66	0.49	0.34	0.15
0.7	5.0°	0.90	1.24	0.82	1.09
0.3	9.0°	0.74	0.61	0.72	2.04
0.5	9.0°	0.86	0.58	0.60	2.13
0.7	9.0°	2.18	4.43	6.85	5.75

TABLE 4.2: Relative error, Δe, of the local spanwise lift between aerodynamic q3D–coupling algorithm and 3D `DLR-tau` on unswept NACA2412–wing in percent

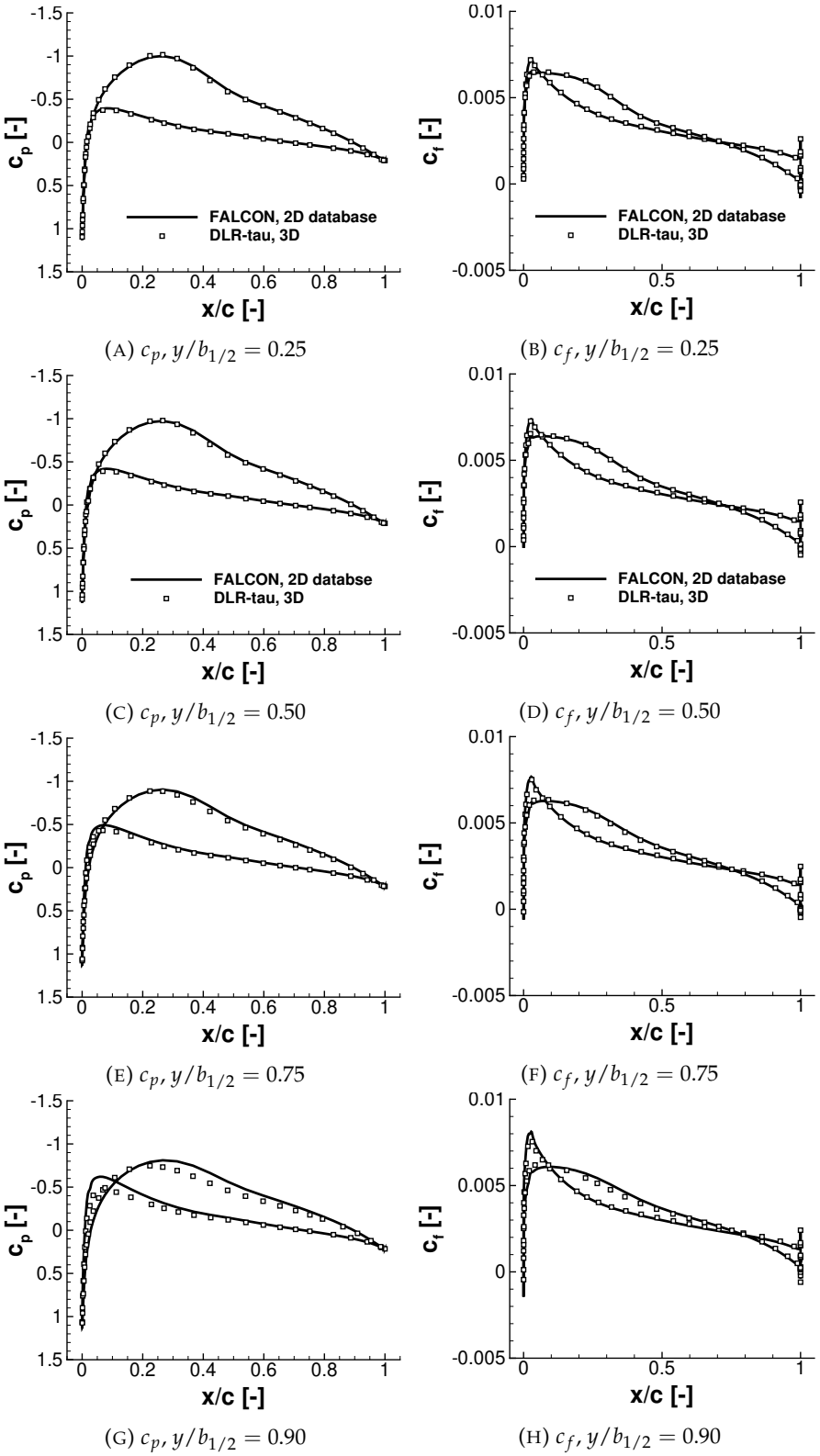

(A) $c_p, y/b_{1/2} = 0.25$ (B) $c_f, y/b_{1/2} = 0.25$

(C) $c_p, y/b_{1/2} = 0.50$ (D) $c_f, y/b_{1/2} = 0.50$

(E) $c_p, y/b_{1/2} = 0.75$ (F) $c_f, y/b_{1/2} = 0.75$

(G) $c_p, y/b_{1/2} = 0.90$ (H) $c_f, y/b_{1/2} = 0.90$

FIGURE 4.12: Sectional data of unswept NACA2412 wing, $M = 0.7$, $\alpha_\infty = 1.0°$, $\Lambda = 0.0°$

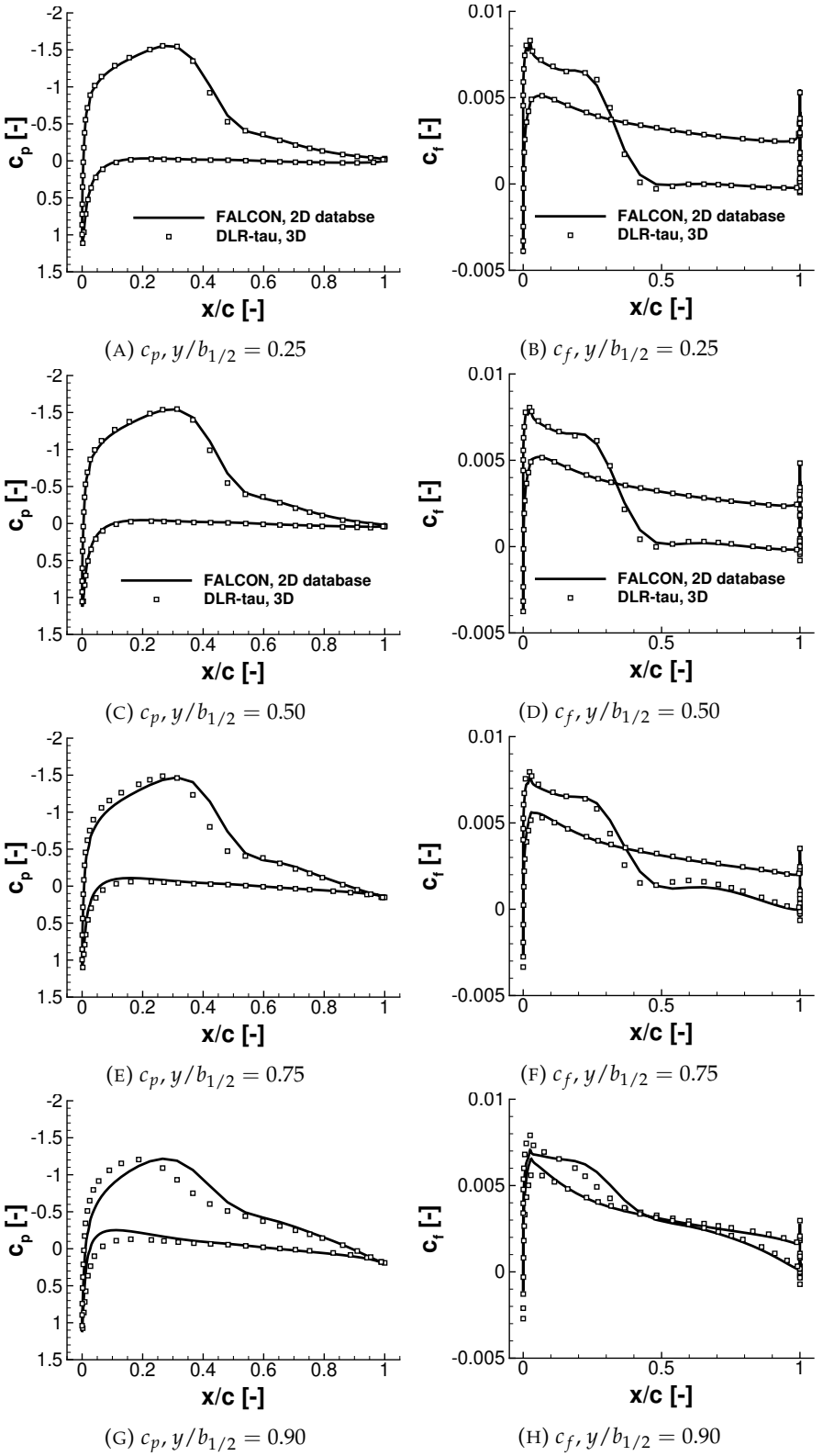

(A) $c_p, y/b_{1/2} = 0.25$

(B) $c_f, y/b_{1/2} = 0.25$

(C) $c_p, y/b_{1/2} = 0.50$

(D) $c_f, y/b_{1/2} = 0.50$

(E) $c_p, y/b_{1/2} = 0.75$

(F) $c_f, y/b_{1/2} = 0.75$

(G) $c_p, y/b_{1/2} = 0.90$

(H) $c_f, y/b_{1/2} = 0.90$

FIGURE 4.13: Sectional data of unswept NACA2412 wing, $M = 0.7$, $\alpha_\infty = 5.0°$, $\Lambda = 0.0°$

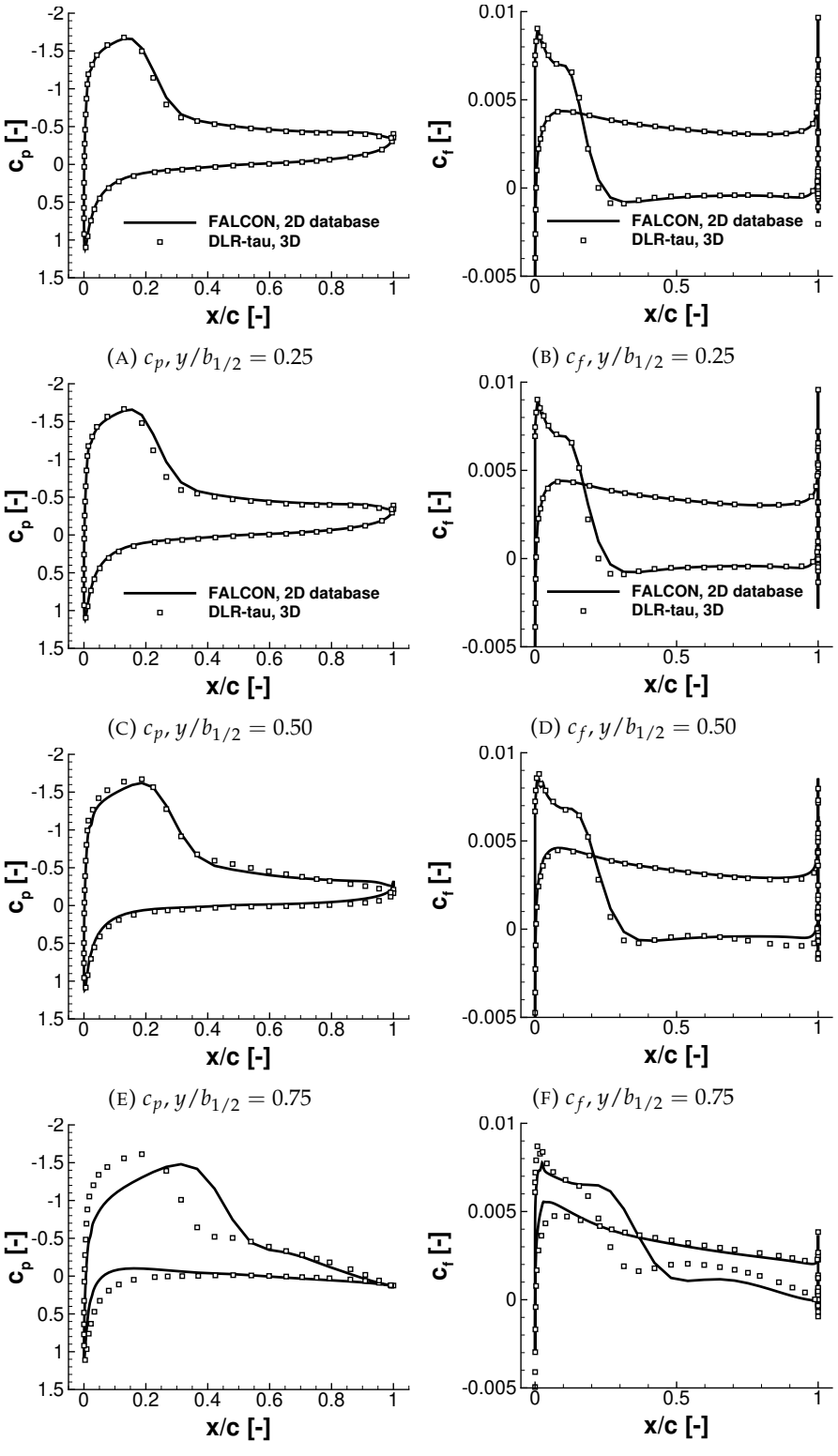

(A) $c_p, y/b_{1/2} = 0.25$ (B) $c_f, y/b_{1/2} = 0.25$

(C) $c_p, y/b_{1/2} = 0.50$ (D) $c_f, y/b_{1/2} = 0.50$

(E) $c_p, y/b_{1/2} = 0.75$ (F) $c_f, y/b_{1/2} = 0.75$

(G) $c_p, y/b_{1/2} = 0.90$ (H) $c_f, y/b_{1/2} = 0.90$

FIGURE 4.14: Sectional data of unswept NACA2412 wing, $M = 0.7$, $\alpha_\infty = 9.0°$, $\Lambda = 0.0°$

Swept wing

For the swept wing the computation of the aerodynamic sectional data is preformed in local frame of reference, which is shown in Figure 3.7a as the $(A' - A')$ cut. Therefore, the contour of the employed two–dimensional NACA2412 CFD grid stencil is stretched by factor $(1/\cos\Lambda) = 1.1547$ along the z–axis as shown in Figure 3.7b. The swept wing has a uniform sweep angle of $\Lambda = 30^\circ$ and is not tapered, i.e. $\gamma = 1.0$. The planform of the half–wing can be seen in Figure 4.17 at different freestream angles of attack, α_∞, and three Mach–numbers, $M = 0.3$, $M = 0.5$ and $M = 0.7$. Here, the non–dimensional pressure coefficient, c_p, is shown on the upper wing surface. The friction coefficients, $c_{f,x}$, $c_{f,y}$ and $c_{f,z}$, are used to plot the stream lines on the contour of the three–dimensional wing.

In Figure 4.15, the overall lift and drag force coefficients, C_L and C_D, of the entire swept wing are shown at several freestream flow conditions. The data computed by `FALCon` is also here compared with three–dimensional CFD results and classical linear VLM. Two datasets of the aerodynamic data obtained by the hybrid q3D–coupling code are presented, where the first one is obtained in combination with classical two–dimensional sectional aerofoil dataset, where crossflow effects are neglected, and the second one with the sectional dataset computed by the 2.5D+ ISW–RANS solver. In this figure it can be seen that with the increase of the Mach–number the lift slope, C_L^α, is also increased at moderate angles of attack. For the linear VLM, the lift slop is not affected by the compressibility of the fluid (and therefore independent from the Mach–number) due to the assumption that the potential flow is incompressible. However, in viscous nonlinear flow the lift slope, C_L^α, is affected by the Mach–number M. Therefore, in Figure 4.15e it can be seen that the hybrid aerodynamic q3D–coupling code in combination with sectional aerodynamic data obtained by the 2.5D+ ISW–CFD solver is able to predict the correct lift slope at $M = 0.7$ until $\alpha_\infty = 5.0^\circ$. However, the employment of classical 2D sectional aerodynamic data with neglected crossflow effects in the aerodynamic coupling code leads to a slightly overestimated lift slope, C_L^α, compared to three–dimensional CFD reference data.

In this example case, where the lift and drag prediction of a swept wing configuration with a sweep of $\Lambda = 30^\circ$ is studied, it is notable that the maximal lift force coefficient, $C_{L,max}$, is estimated less accurate compared to predictions in the previous example of the unswept geometry of the NACA2412–wing. As it can be seen in Figure 4.17 at $M = 0.7$ and $\alpha_\infty = 9.0^\circ$ the flow is highly separated and therefore along the quarter–chord line, y', see Section 3.3, not locally developed. Therefore, at this flow condition the validity of the 2.5D+ ISW–CFD model in combination with the coupling code is

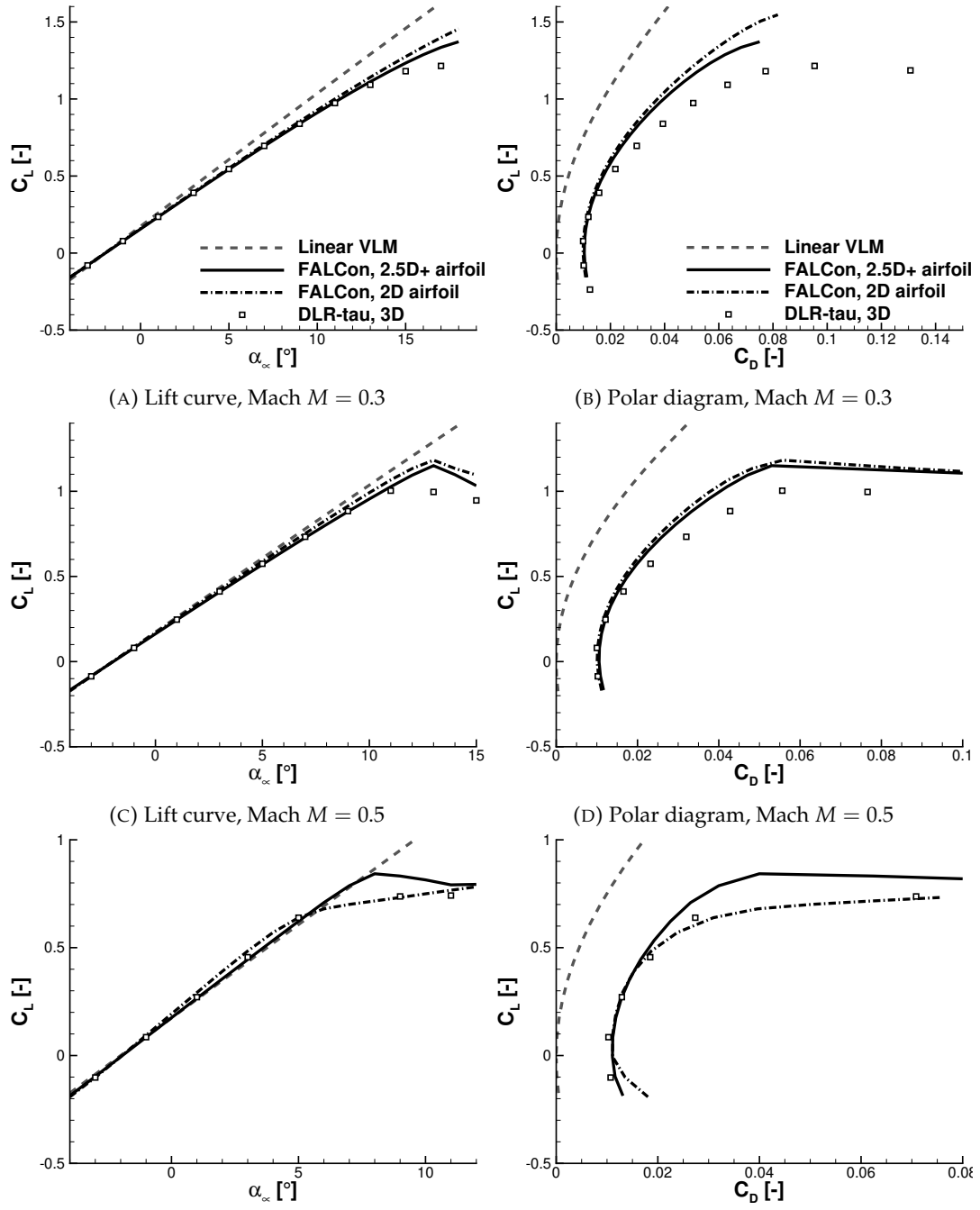

(A) Lift curve, Mach $M = 0.3$

(B) Polar diagram, Mach $M = 0.3$

(C) Lift curve, Mach $M = 0.5$

(D) Polar diagram, Mach $M = 0.5$

(E) Lift curve, Mach $M = 0.7$

(F) Polar diagram, Mach $M = 0.7$

FIGURE 4.15: Aerodynamic force coefficients of the swept NACA2412 wing, $\Lambda = 30.0°$, with a taper ratio of $\gamma = 1.0$ and aspect ratio of $AR = 10$

not given and therefore the maximal lift force coefficient, $C_{L,max}$, is overestimated compared to three–dimensional reference CFD data.

The local lift distribution of the swept half–wing is shown in Figure 4.16 for Mach–numbers $M = 0.3$, $M = 0.5$ and $M = 0.7$. Here, it needs to be noted that the coupling code is able to estimate the characteristic shape of the lift distribution of a swept wing, where the maximal local lift of the wing is shifted away from the symmetry layer towards the mid–span area of the half–wing. Also, it can be seen that the local lift is estimated much more accurately by the coupling code in combination with 2.5D+ sectional aerodynamic data compared to numerical results of the coupling code where crossflow is neglected (sectional 2D aerofoil dataset). Especially at high–speed flow regimes, crossflow effects have to be considered during the coupling procedure, as this comparison demonstrates. At $M = 0.7$ and $\alpha_\infty = 9.0°$ the coupling code fails to estimate the load distributions partly as here the upper surface of the wing is nearly completely covered by a complex three–dimensional separated flow, see Figure 4.17c, and therefore the validity of the aerodynamic q3D–coupling model in combination with 2D and 2.5D sectional aerodynamics is not given as no homogeneous flow along the span direction of the wing is present.

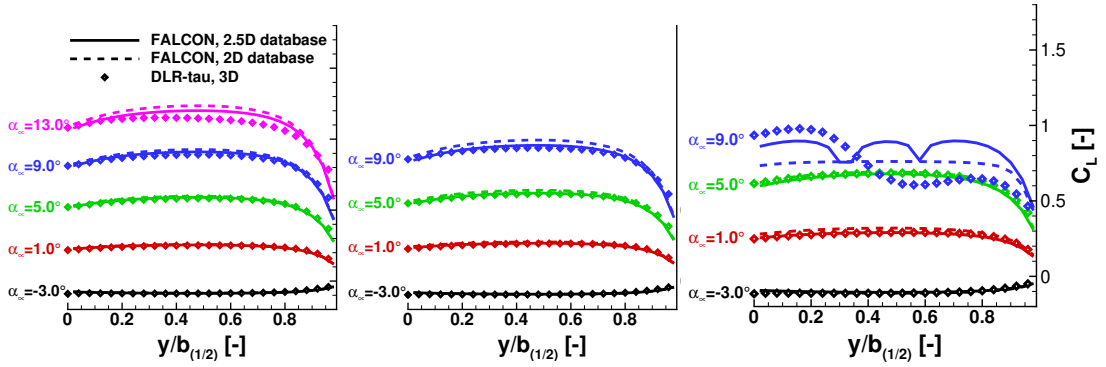

(A) Mach $M = 0.3$ (B) Mach $M = 0.5$ (C) Mach $M = 0.7$

FIGURE 4.16: Lift distribution along wing span of swept NACA2412 wing, Sweep $\Lambda = 30.0°$, Taper ratio $\gamma = 1.0$

The sectional aerodynamic flow data at $M = 0.7$ is presented in Figure 4.18 for $\alpha_\infty = 1.0°$, in Figure 4.19 for $\alpha_\infty = 5.0°$ and in Figure 4.20 for $\alpha_\infty = 9.0°$. Here, c_p and c_f plots are shown for 25%, 50%, 75% and for 90% of the half–wing. Sectional data obtained with the coupling code including and excluding crossflow effects are compared against numerical sectional results of the reference three–dimensional CFD data obtained by 3D `DLR-tau` CFD code. The difference of sectional c_p and c_f plots between the results obtained with the steady–state aerodynamic q3D–coupling method incorporating 2D and 2.5D+ sectional aerodynamic database is clearly visible, especially for high–speed flow regimes. For example, by neglecting the local crossflow at transonic flow velocities (2D

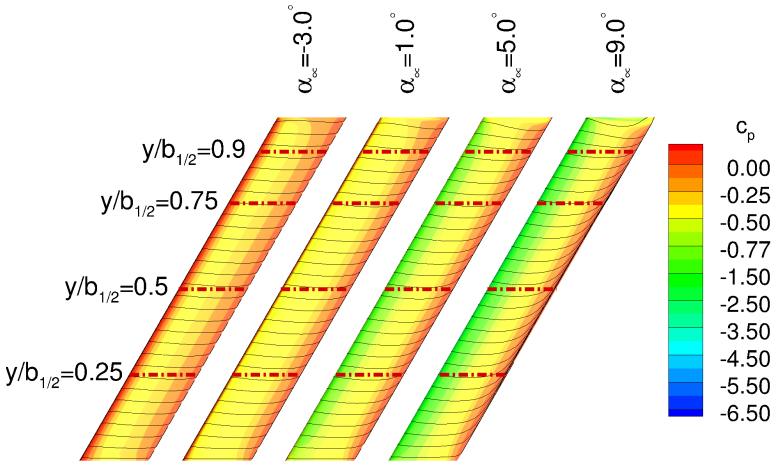

(A) Mach $M = 0.3$

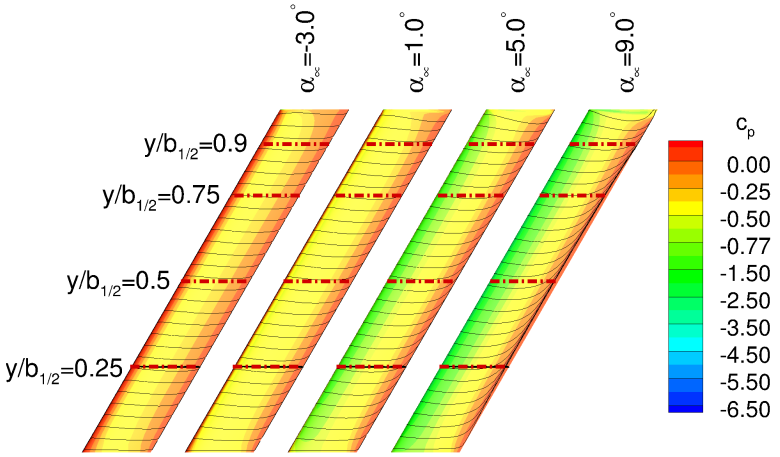

(B) Mach $M = 0.5$

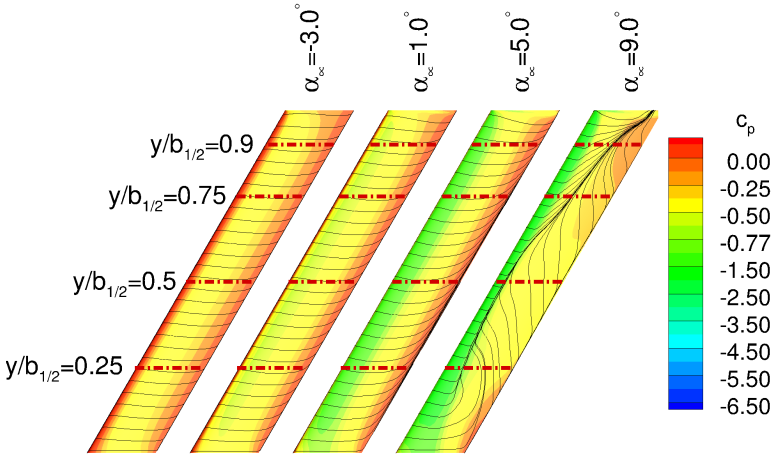

(C) Mach $M = 0.7$

FIGURE 4.17: Nondimensional pressure coefficient, c_p of swept NACA2412 wing obtained with three–dimensional CFD (DLR-tau, 3D), $\Lambda = 30.0°$, Taper ratio $\gamma = 1.0$

sectional dataset) the coupling code overestimates slightly the non–dimensional pressure coefficient, c_p, at $\alpha_\infty = 1.0°$. Further, at $\alpha_\infty = 5.0°$ the position and magnitude of the suction peak of the sectional non–dimensional pressure distribution, c_p, is not estimated correctly when classical 2D sectional aerodynamic data is employed during the coupling procedure. This leads to the slightly overestimated lift slope, C_L^α, shown in Figure 4.15e. Thus, here, it is demonstrated that on swept–wing geometries, especially at transonic Mach–numbers, the employment of sectional aerodynamic data, which includes the crossflow effects, is necessary to estimate correctly the local compressible aerodynamic load.

Finally, in Figure 4.20 the sectional aerodynamic flow comparison is presented at $M = 0.7$ and $\alpha_\infty = 9.0°$. As already mentioned, at this flow condition the validity of the aerodynamic q3D–coupling method is not given as here the upper surface of the wing section is mostly covered by separated flow, which is not locally fully developed and, therefore, is not independent with respect to the quarter–chord line of the wing. The aerodynamic q3D–coupling methodology assumes always an independent flow along the local quarter–chord line, as described in Section 3.3. Therefore, it fails to predict at this flow condition the aerodynamic wing load accurately. Compared to the three–dimensional reference CFD data it can be seen that the presented aerodynamic q3D–coupling method in combination with the 2.5D sectional aerodynamic data overestimates the local lift at the upper–front part of the four wing sections and is not estimating here separated flow, as the corresponding non–dimensional friction coefficient, c_f, is positive (thus, no reverse flow is present). This leads to an overestimated overall lift force coefficient, C_L, and an underestimated drag force coefficient, C_D, compared to three–dimensional reference CFD data. This can be clearly observed in Figure 4.15e and Figure 4.15f.

		Spanwise location							
		2D aerofoil				**2.5D aerofoil**			
M	α_∞	25%	50%	75%	90%	25%	50%	75%	90%
0.3	1.0°	3.39	2.65	0.75	2.72	1.81	1.08	0.75	4.10
0.5	1.0°	5.23	4.29	1.94	1.85	1.75	0.80	1.36	4.77
0.7	1.0°	10.95	9.80	6.37	1.94	0.73	0.48	3.19	6.36
0.3	5.0°	2.65	2.52	1.23	1.30	1.27	1.12	0.09	2.44
0.5	5.0°	4.26	4.11	2.52	0.21	0.95	0.74	0.64	2.96
0.7	5.0°	1.23	0.93	0.87	0.33	1.10	0.80	1.94	3.85
0.3	9.0°	3.52	4.03	2.99	0.12	1.71	2.14	1.26	1.52
0.5	9.0°	5.03	5.91	4.85	1.57	1.18	1.92	1.15	1.53
0.7	9.0°	19.79	22.15	16.52	20.02	8.65	42.72	38.03	30.69

TABLE 4.3: Relative error, Δe, of the local lift between aerodynamic q3D–coupling algorithm and 3D `DLR-tau` on swept wing ($\Lambda = 30°$) in percent

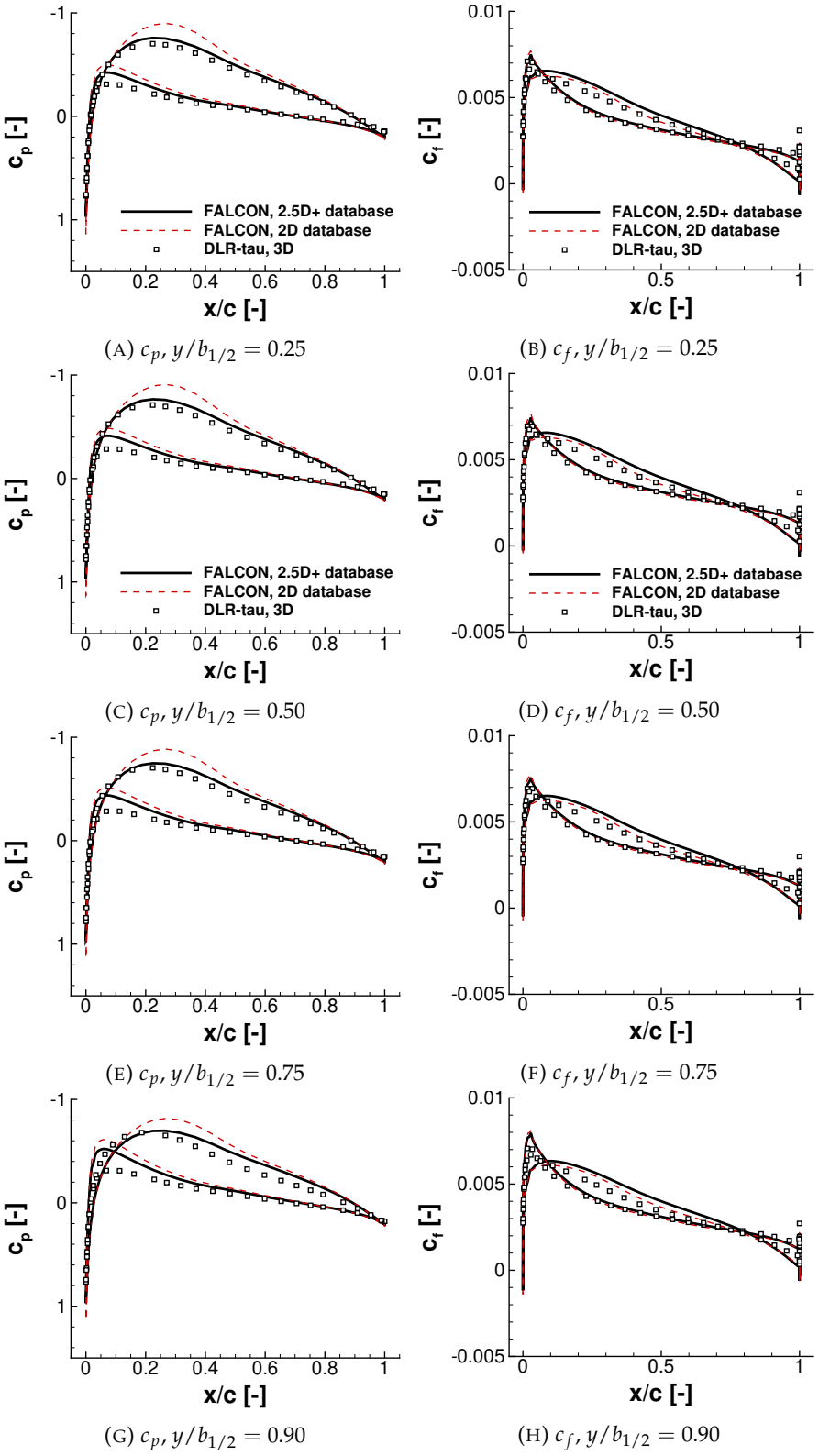

(A) $c_p, y/b_{1/2} = 0.25$ (B) $c_f, y/b_{1/2} = 0.25$

(C) $c_p, y/b_{1/2} = 0.50$ (D) $c_f, y/b_{1/2} = 0.50$

(E) $c_p, y/b_{1/2} = 0.75$ (F) $c_f, y/b_{1/2} = 0.75$

(G) $c_p, y/b_{1/2} = 0.90$ (H) $c_f, y/b_{1/2} = 0.90$

FIGURE 4.18: Sectional data of unswept NACA2412 wing, $M = 0.7$, $\alpha_\infty = 1.0°$, $\Lambda = 30.0°$

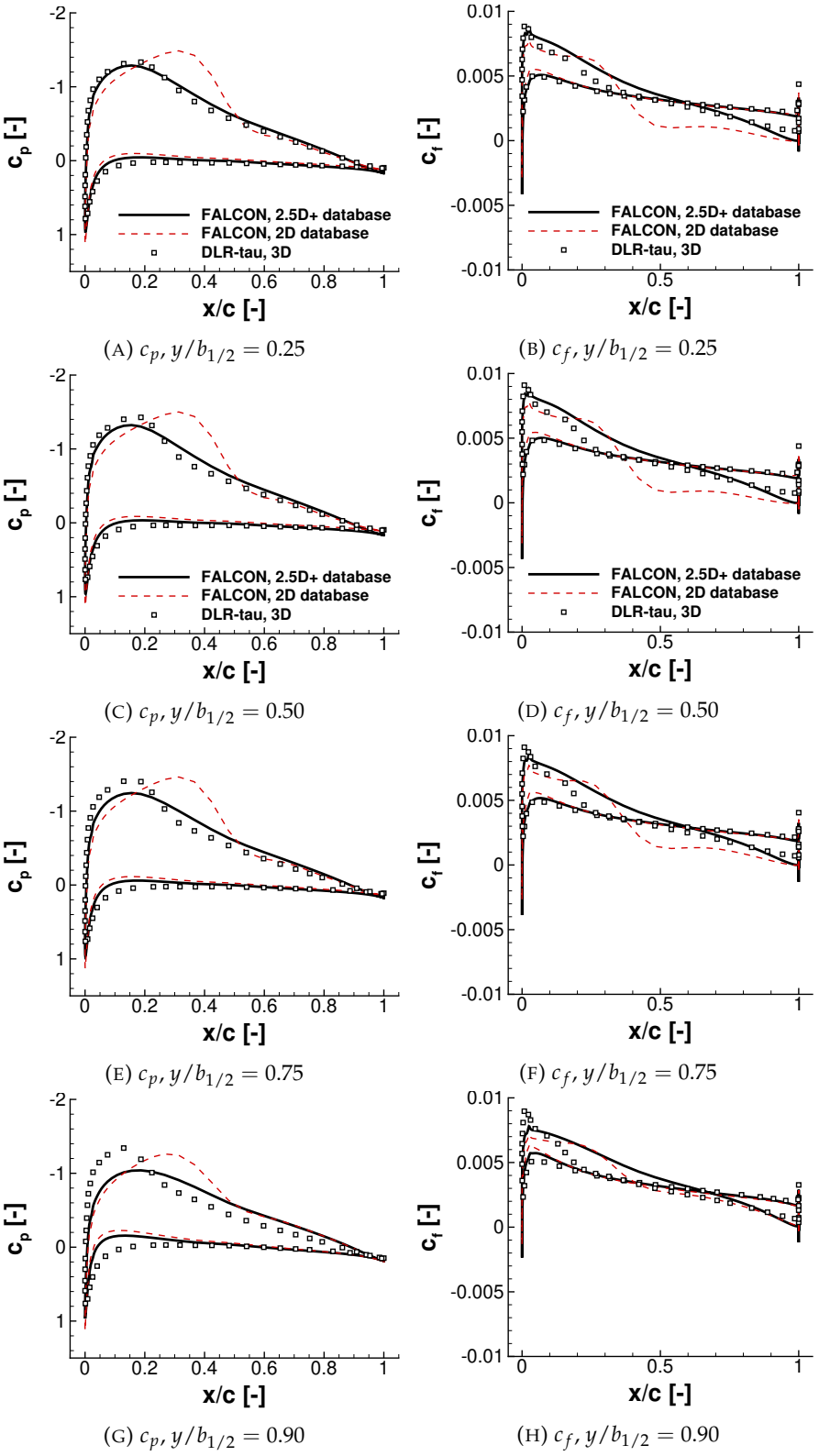

(A) $c_p, y/b_{1/2} = 0.25$ (B) $c_f, y/b_{1/2} = 0.25$

(C) $c_p, y/b_{1/2} = 0.50$ (D) $c_f, y/b_{1/2} = 0.50$

(E) $c_p, y/b_{1/2} = 0.75$ (F) $c_f, y/b_{1/2} = 0.75$

(G) $c_p, y/b_{1/2} = 0.90$ (H) $c_f, y/b_{1/2} = 0.90$

FIGURE 4.19: Sectional data of unswept NACA2412 wing, $M = 0.7$, $\alpha_\infty = 5.0°$, $\Lambda = 30.0°$

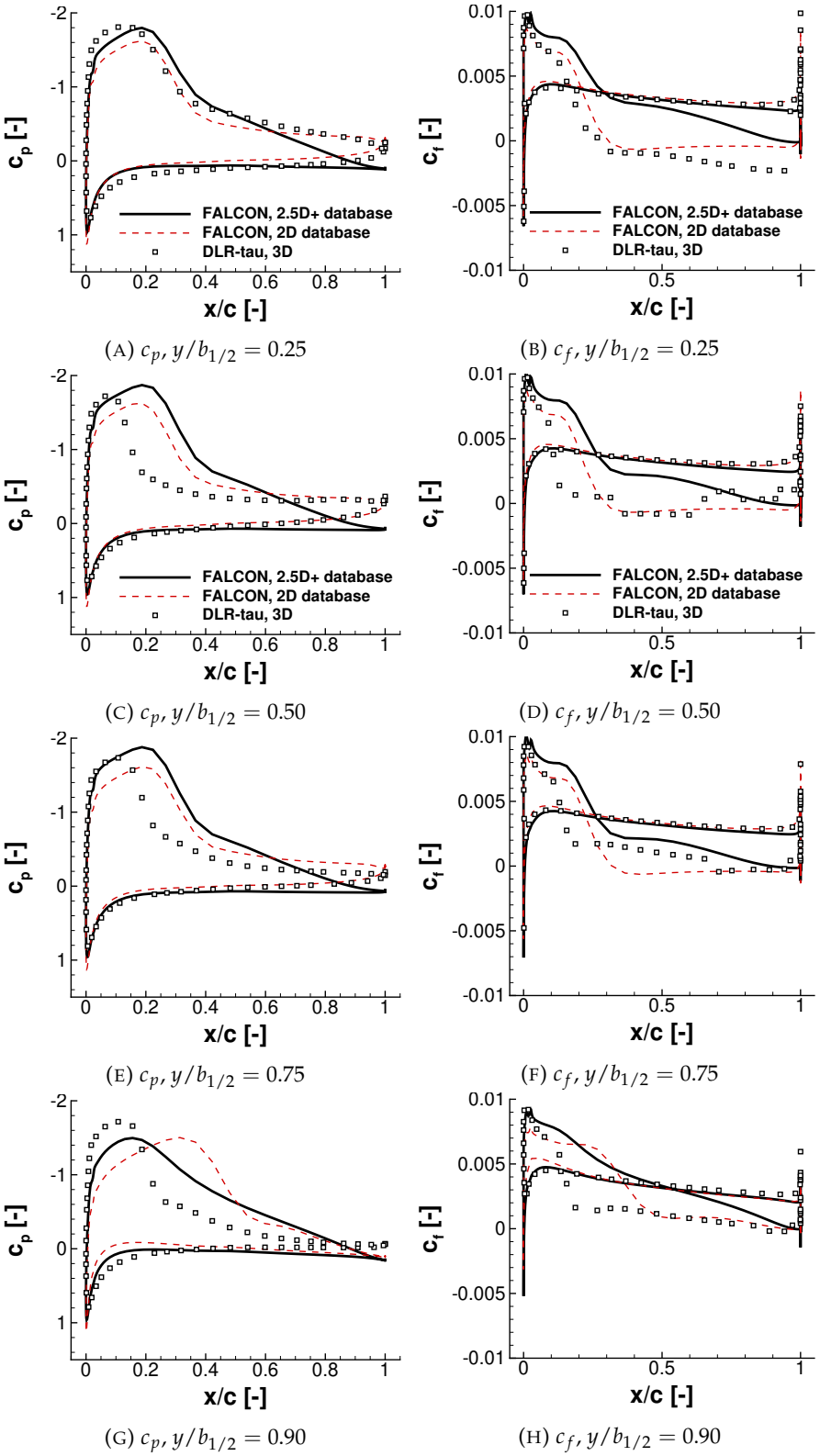

(A) $c_p, y/b_{1/2} = 0.25$

(B) $c_f, y/b_{1/2} = 0.25$

(C) $c_p, y/b_{1/2} = 0.50$

(D) $c_f, y/b_{1/2} = 0.50$

(E) $c_p, y/b_{1/2} = 0.75$

(F) $c_f, y/b_{1/2} = 0.75$

(G) $c_p, y/b_{1/2} = 0.90$

(H) $c_f, y/b_{1/2} = 0.90$

FIGURE 4.20: Sectional data of unswept NACA2412 wing, $M = 0.7$, $\alpha_\infty = 9.0°$, $\Lambda = 30.0°$

4.2.1.2 Dependence on sweep angle

In this section the validation campaign is continued, where the sweep of the NACA2412–wing at a constant freestream angle of attack of $\alpha_\infty = 3^\circ$ is varied. The purpose of this validation study is to analyse the accuracy of the coupling algorithm estimating aerodynamic loads on swept wings. The study is carried out at subsonic and transonic flow regimes, i.e. $M = 0.3$, $M = 0.5$ and $M = 0.7$. The wing geometries have a constant taper ratio of $\gamma = 1.0$. The employed wing geometry can be seen in Figure 4.21 for $\Lambda = 0^\circ$ and $\Lambda = 40^\circ$. Here, the non–dimensional pressure coefficient, c_p, is shown, which is obtained by the three–dimensional `DLR-tau` solver at $M = 0.7$ at a freestream angle of attack of $\alpha_\infty = 3^\circ$. The corresponding 3D CFD meshes are obtained by displacing the mesh points of the unswept 3D CFD mesh along the x–axis according to the corresponding sweep angle, Λ. The spatial distribution of the grid points and the size of the mesh are not changed.

In Figure 4.22 the aerodynamic lift force distributions are presented for the NACA2412–wing with four different sweep angles between $\Lambda = 0^\circ$ and $\Lambda = 40^\circ$. As it can be seen, the steady–state aerodynamic q3D–coupling algorithm is able to reproduce reliable aerodynamic results when it is used with sectional aerodynamic data of the NACA2412 aerofoil precomputed with the 2.5D+ ISW–RANS CFD solver. However, when sectional aerodynamic data of the NACA2412 aerofoil precomputed with conventional 2D CFD

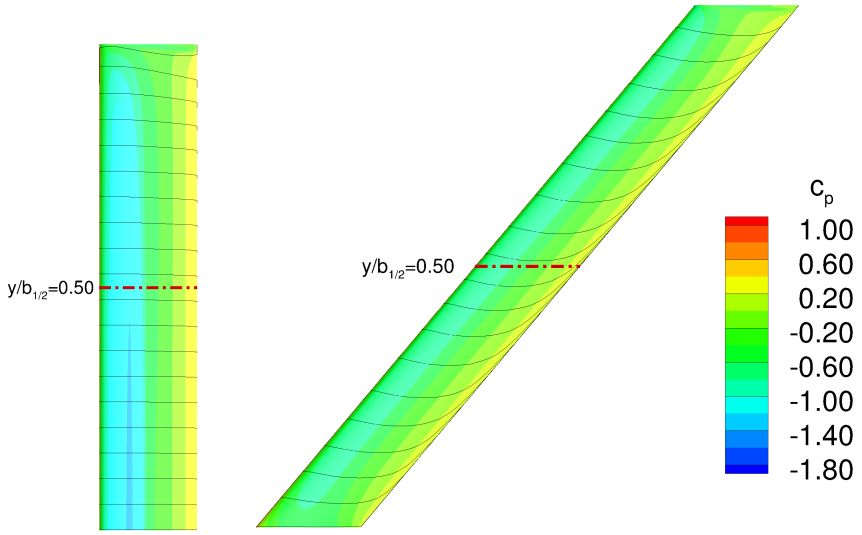

(A) Sweep $\Lambda = 0^\circ$ (B) Sweep $\Lambda = 40^\circ$

FIGURE 4.21: Nondimensional pressure coefficient, c_p of NACA2412 wing of different sweep angles at $M = 0.7$ and $\alpha_\infty = 3.0^\circ$ obtained with three–dimensional CFD (DLR-tau, 3D)

solver is used, the aerodynamic q3D–coupling algorithm overestimates the local sectional lift. This happens especially at high Mach–numbers, M, and sweep angles, Λ, as it can be seen in Figure 4.23 for a wing section at 50% of the half–span.

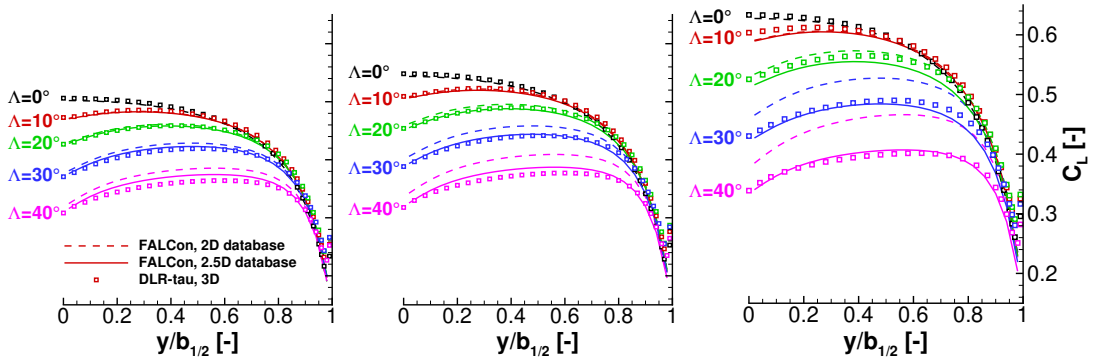

(A) Mach $M = 0.3$ (B) Mach $M = 0.5$ (C) Mach $M = 0.7$

FIGURE 4.22: Lift distribution along wing span, Taper ratio $\gamma = 1.0$, $\alpha = 3°$

The reason for the overestimated local lift, C_L, which is obtained with the aerodynamic q3D–coupling method in combination with nonlinear 2D aerodynamic data, can be seen in Figure 4.23. Here, the c_p plot is showed for the particular swept wing at the mid–span of the half–wing, $y/b_{1/2} = 0.5$, at various Mach–numbers, M. Especially at $M = 0.7$, it can be seen that the position of the local pressure suction peak of the section is not estimated correctly when 2D sectional aerodynamic data of the NACA2412–aerofoil on swept wing geometries is employed, as the crossflow component of the velocities is not considered in the boundary layer. Thus, for a successful application of the aerodynamic q3D–coupling method during high–speed or transonic aeroplane wing design procedures it is necessary to apply the novel efficient 2.5D+ ISW–RANS CFD solver to take accurately also crossflow phenomena into account.

Finally, in Table 4.4 the relative error of the local lift force coefficient, C_L, is shown between the steady–state aerodynamic q3D–coupling approach and the three–dimensional reference lift. The error is obtained using Equation 4.5. It can be seen that especially at $\Lambda = 40°$ relatively huge discrepancies are present at $M = 0.7$ when the aerodynamic q3D–coupling approach is used with a 2D sectional aerodynamic dataset.

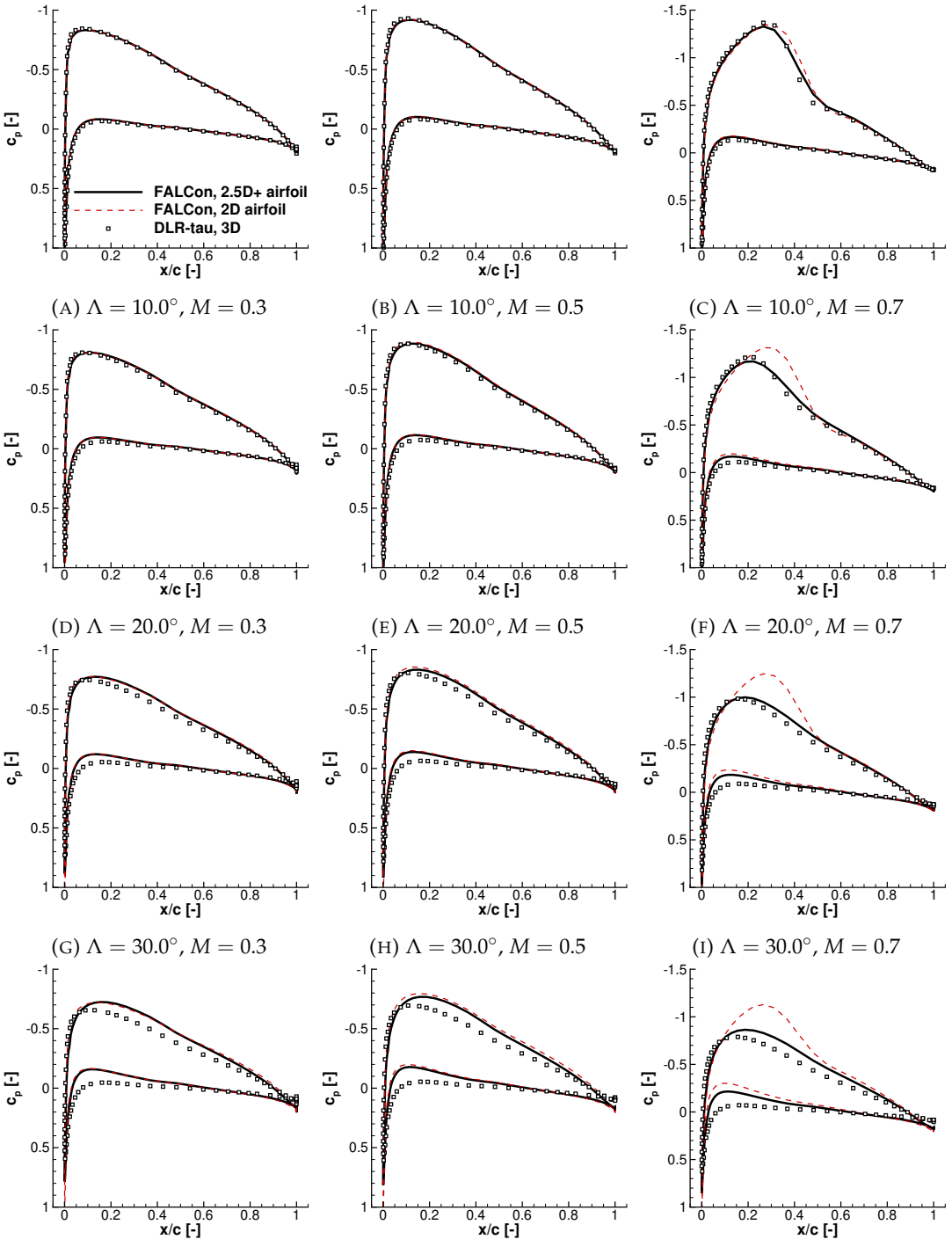

(A) $\Lambda = 10.0°$, $M = 0.3$ (B) $\Lambda = 10.0°$, $M = 0.5$ (C) $\Lambda = 10.0°$, $M = 0.7$

(D) $\Lambda = 20.0°$, $M = 0.3$ (E) $\Lambda = 20.0°$, $M = 0.5$ (F) $\Lambda = 20.0°$, $M = 0.7$

(G) $\Lambda = 30.0°$, $M = 0.3$ (H) $\Lambda = 30.0°$, $M = 0.5$ (I) $\Lambda = 30.0°$, $M = 0.7$

(J) $\Lambda = 40.0°$, $M = 0.3$ (K) $\Lambda = 40.0°$, $M = 0.5$ (L) $\Lambda = 40.0°$, $M = 0.7$

FIGURE 4.23: Non–dimensional pressure coefficient, c_p, at various sweep angles and Mach numbers, $\alpha_\infty = 3.0°$, $y/b_{1/2} = 0.5$

	2D aerodynamic dataset			**2.5D** aerodynamic dataset		
Sweep	**M 0.3**	**M 0.5**	**M 0.7**	**M 0.3**	**M 0.5**	**M 0.7**
0.0°	0.71	0.66	0.54	0.71	0.66	0.54
10.0°	0.65	0.50	0.74	0.79	0.90	1.01
20.0°	0.25	0.90	1.24	0.31	0.62	1.99
30.0°	2.21	3.76	7.61	0.83	0.47	1.21
40.0°	5.98	8.69	16.39	2.97	2.85	1.66

TABLE 4.4: Relative error, Δe, of the local lift at the mid–span section of the half–wing ($y/b_{1/2} = 0.5$) during the sweep variation

4.2.1.3 Dependence on taper ratio

In this final subsection results of the NACA2412 test case are presented where the taper ratio, γ, of the NACA2412 swept wing geometry with a constant geometrical sweep of $\Lambda = 30^\circ$ is varied at a constant freestream angle of attack of $\alpha = 3^\circ$. This validation study is also performed at three different Mach–numbers reaching from $M = 0.3$ till $M = 0.7$. The purpose of this validation test case is to capture flow physics on tapered wing geometries using the implemented q3D–approach.

For this variation, the taper ratio of the three–dimensional CFD mesh of the swept wing is modified by skewing the grid points of the 3D CFD grid to meet the geometrical taper ratio of the respective wing. The sweep, $\Lambda = 30^\circ$, of the employed wing geometries is defined with respect to the quarter–chord line of the wing and is constant along the span. For the predictions with the hybrid q3D–coupling algorithm the VLM lattice is also modelled as tapered wing geometry. The employed 2.5D aerodynamic sectional database along the span of the wing is precomputed for a constant sweep angle of $\Lambda = 30^\circ$.

In Figure 4.24 the planform of the two tapered variants of the swept NACA2412–wing are presented. Here, the geometry of the considered tapered wings is shown and pressure coefficient, c_p, is plotted on the upper surface of the wing, which is obtained by the three–dimensional `DLR-tau` CFD code at $M = 0.7$.

The numerical results are presented as spanwise lift distribution in Figure 4.25. Here, it can be seen that due to the sweep of the wing and the additional taper ratio, i.e. $\gamma < 1$, the outboard spanwise distributed lift is more pronounced with increasing Mach–number, M, and decreasing taper ratio, γ, than the inboard aerodynamic lift. It can be seen that the steady–state q3D–algorithm of `FALCon` is able to reproduce the same spanwise lift distribution as the equivalent 3D CFD–RANS method. However, a notable overall discrepancy of the spanwise local lift force coefficient, C_L, is visible on the wing geometry with the taper ratio of $\gamma = 0.5$ at high–speed flow regimes, $M = 0.7$. Here, the discrepancy between results is maximal at nearly $y/b_{1/2} = 0.75$ of the half–span of the wing. The corresponding non–dimensional pressure coefficient, c_p, of this wing at the same flow condition is presented in Figure 4.26, where in Figure 4.26c the pressure coefficient, c_p, is shown at 75% of the half–span of the wing for $M = 0.7$. It can be seen, that `FALCon` is slightly underestimating this section. Also, it can be seen that due to the tapered wing geometry the suction peak is located closer to the leading edge in the 3D results.

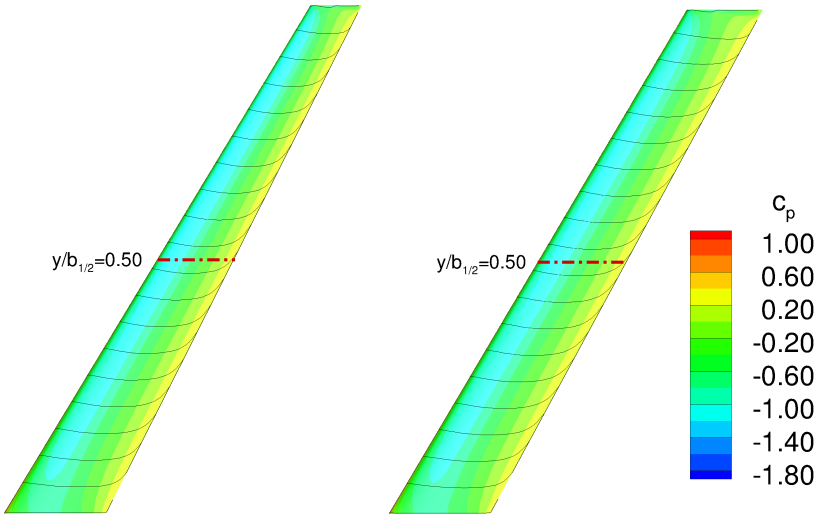

(A) Taper ratio $\gamma = 0.50$ (B) Taper ratio $\gamma = 0.75$

FIGURE 4.24: Nondimensional pressure coefficient, c_p of NACA2412 wing of different taper ratios and swept by $\Lambda = 30°$ around quarter–chord line at $M = 0.7$ and $\alpha_\infty = 3.0°$ obtained with three–dimensional CFD (DLR-tau, 3D)

The local error of the sectional lift force coefficient, C_L, can be seen in Table 4.5. The error is estimated using Equation 4.5. It is notable that at high Mach–number, $M = 0.7$, and at the low taper ratio of $\gamma = 0.5$ the error can reach up to 4.5% of the local lift.

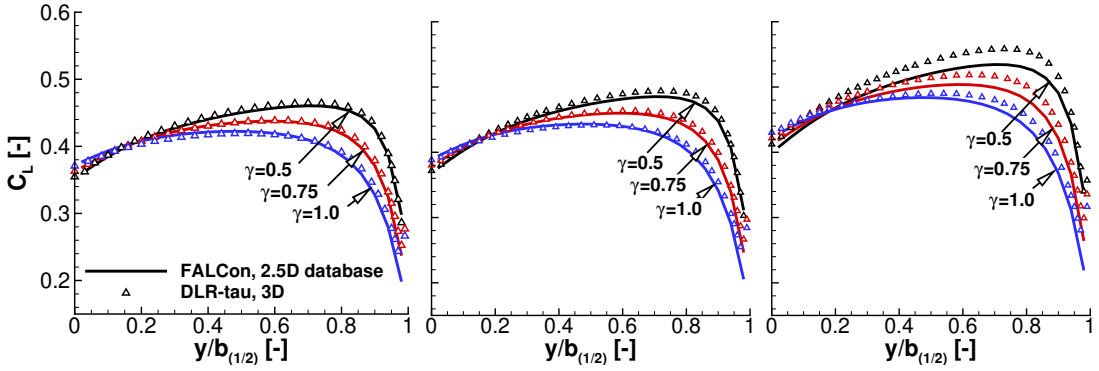

(A) Mach $M = 0.3$ (B) Mach $M = 0.5$ (C) Mach $M = 0.7$

FIGURE 4.25: Lift distribution along wing span, Sweep 30.0°, $\alpha = 3°$

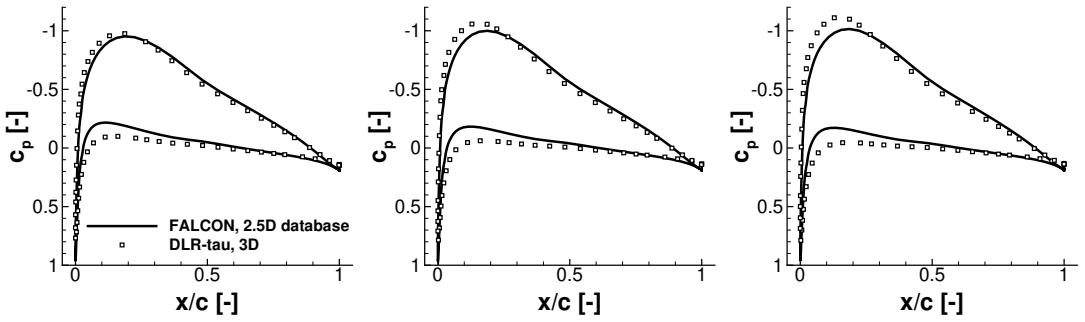

(A) $y/b_{1/2} = 0.25$, $\Delta e = 3.03\%$ (B) $y/b_{1/2} = 0.50$, $\Delta e = 3.60\%$ (C) $y/b_{1/2} = 0.75$, $\Delta e = 4.46\%$

FIGURE 4.26: Sectional data of tapered and swept NACA2412 wing, $M = 0.7$, $\alpha_\infty = 3.0^\circ$, $\Lambda = 30.0^\circ$, $\gamma = 0.5$

	$y/b_{1/2} = 0.5$			$y/b_{1/2} = 0.75$		
Taper ratio	**M 0.3**	**M 0.5**	**M 0.7**	**M 0.3**	**M 0.5**	**M 0.7**
0.50	0.81	1.44	3.59	0.99	1.87	4.46
0.75	0.05	0.53	2.39	0.77	1.50	3.76
1.00	0.71	0.33	1.28	0.66	1.27	3.19

TABLE 4.5: Relative error, Δe, of the local lift during the taper ratio variation (2.5D aerodynamic database) in percent

4.2.2 DLR–F4 wing body configuration in steady–state flow

The validation campaign is continued using the DLR–F4 wing/body configuration which contains a swept and twisted nonplanar wing geometry. This geometry contains a fuselage. The purpose of this test case is the demonstration of the capabilities of the novel computational framework to estimate rapidly aerodynamic loads on a, for the civil aerospace industry highly relevant, configuration at transonic flow regimes. The geometry of this configuration is presented in Figure 4.27 which was defined in 1994 by the German aerospace agency, DLR[1][74]. Several experimental wind tunnel measurements of this configuration were conducted by three major European aerospace research agencies[5]. Nowadays, this experimental data obtained from this experiments is widely used to validate numerical CFD frameworks.

This wing/body geometry is inspired by a typical geometry of a modern commercial airliner. The aspect ratio of the DLR–F4 wing is $AR = 9.5$ and the taper ratio is $\gamma = 0.3$. The dihedral of the wing is 4.8° and is constant along the span. The sweep angle at the leading edge of the wing is constant at $\Lambda = 27.1^\circ$. The wing consists of two trapezoidal wing sections. Thus, the quarter chord line of the inner section is swept by $\Lambda_{1/4} = 21.0^\circ$ and the quarter chord line of the outer section is swept by $\Lambda_{1/4} = 25.0^\circ$.

[1]Deutsches Zentrum für Luft– und Raumfahrt

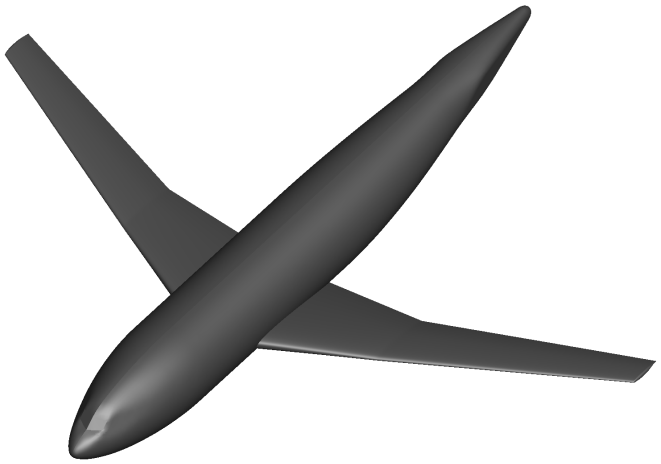

FIGURE 4.27: DLR F-4 configuration

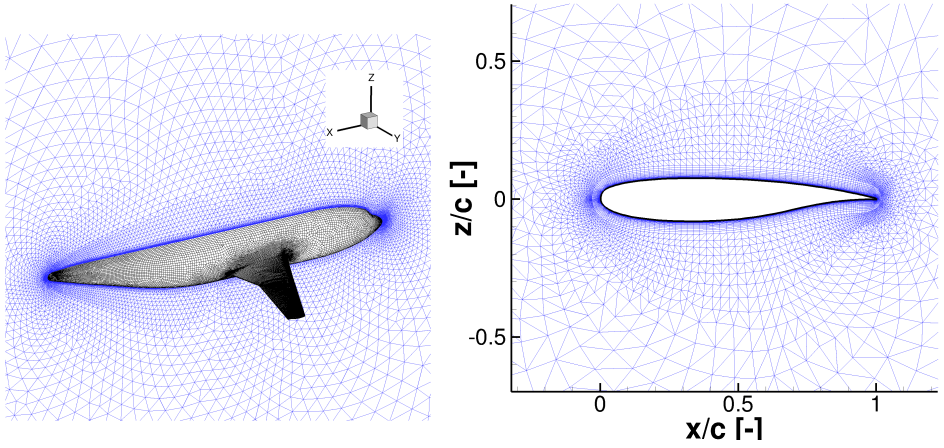

(A) Three–dimensional CFD grid[55] [98] [5]

(B) Two–dimensional CFD grid of the first section at $y/b = 0.185$

FIGURE 4.28: Grids of the three–dimensional DLR F-4 configuration and sectional 2D grid

In Figure 4.28a the employed three–dimensional CFD grid is presented. The three–dimensional mesh is generated by the three–dimensional CFD grid generator SOLAR[32]. Here, only the right half–model of the DLR–F4 configuration is resolved by the 3D CFD mesh, which is a hybrid CFD mesh with 17 layers of regular hexahedral elements in the boundary layer region. The rest of the flow domain is filled up with tetrahedral elements. The farfield has the shape of a half–sphere. This 3D mesh contains nearly 4 Mio. grid points, 2.7 Mio. tetrahedra, 12.9 thousand prism, 79.5 thousand pyramide and 3.5 Mio. hexahedra cells.

The sectional aerodynamic database for FALCon is computed at eight span positions in the local frame of reference at the particular quarter chord sweep, $\Lambda_{1/4}$, for the 2.5D+

aerodynamic database. For the equivalent 2D aerodynamic database the data is computed with respect to the global frame of reference. For the first seven sections (Section 1-7) chordwise experimental aerodynamic data, i.e. non–dimensional pressure coefficient, c_p, is published in the online repository, see Ref. [5]. This data was obtained during the experimental campaigns by using pressure taps on the wing surface of the wind tunnel model at the particular spanwise positions. Therefore, for the hybrid coupling algorithm, the sectional aerodynamic database is precomputed at the same spanwise positions of the wing with the purpose to compare the aerodynamic data between the experimental, 3D CFD and aerodynamic q3D–coupling results. The spanwise position of the first seven sections is shown in Figure 4.33. Section 8 is located directly at the wing tip and is used to cover also the area of the VLM lattice between section 7 and the wing tip to avoid the extrapolation of the aerodynamic database in this area of the lattice. In Table 4.6 the spanwise position, y/b, of the 8 sections is presented.

Section	y/b $[-]$	Chord (proj.) $[m]$	Chord $[m]$	Twist $[^\circ]$	$\Lambda_{1/4}$ $[^\circ]$
1	0.185	0.3145	0.3155	4.58	21.0
2	0.238	0.2874	0.2881	4.23	21.0
3	0.331	0.2398	0.2402	3.43	21.0
4	0.409	0.2028	0.2030	2.55	25.0
5	0.512	0.1855	0.1857	2.20	25.0
6	0.636	0.1647	0.1648	1.73	25.0
7	0.844	0.1298	0.1298	0.85	25.0
8	0.990	0.1052	0.1052	0.01	25.0

TABLE 4.6: Geometrical parameters of the eight sectional airfoils on the DLR-F4 wing

The shape of the aerofoils at those span positions are extracted from the CAD model of the DLR–F4 configuration which is published also in Ref. [5]. For the 2.5D+ sectional database the thickness of all aerofoils is modified using Equation 3.45 in combination with the particular quarter–chord sweep angle, $\Lambda_{1/4}$. For the two–dimensional sectional aerodynamic database the thickness of the aerofoil shapes is not modified as the calculations are performed in the global frame of reference. In total two sets of 8 aerofoil grids were generated. One set concerns 2D sections extracted from the in–flight direction, neglecting the local sweep. The second set relates to sections that were modified to account for the quarter chord sweep. The first set of grids is used to precompute the 2D and the second set of grids is used to obtain the 2.5D+ sectional aerodynamic database, which includes crossflow effects. In Figure 4.28b the 2.5D+ CFD mesh of the first section in the local frame of reference is shown. Here, a hybrid O–mesh is employed, where the first layers are generated by extruding the shape of the aerofoil geometry normally to the initial contour. An initial wall distance of $\Delta y_0 = 1 \cdot 10^{-6}\ m$ is chosen to ensure, that the dimensionless wall distance condition, $y^+ < 1$, is fulfilled for all computations. The rest of the flow field is filled up with an unstructured mesh

consisting of two–dimensional triangles. The 2D meshes for all sections are generated in the same way with the same parameters. In Table 4.6 the geometrical properties for the eight sections are summarised.

In Figure 4.29 the corresponding VLM lattice of the half–wing model is shown. It is a thin lifting–surface created considering the geometrical twist and dihedral of the DLR–F4 wing. The lattice is created between the leading and trailing edge of the three–dimensional wing configuration. The geometrical twist at the root of the wing is 4.584°. The wing tip is not twisted. The fuselage is neglected. Instead, one VLM vortex–ring is placed in this area, where normally the fuselage would be located. Only the half wing is modelled while applying the symmetry condition along the xz–symmetry layer in the linear VLM model.

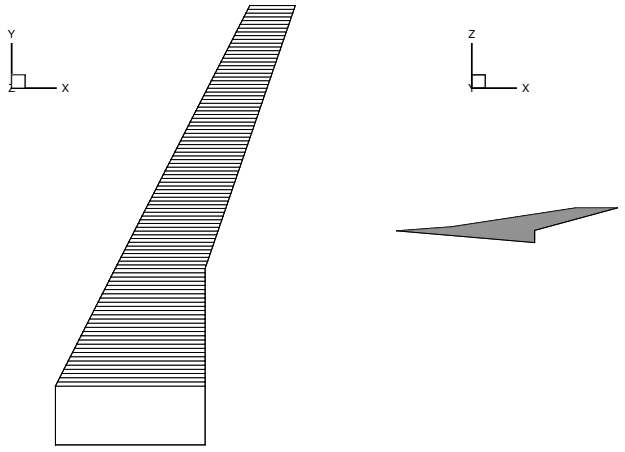

FIGURE 4.29: Vortex–Lattice mesh of the DLR-F4 half–wing configuration

In Figure 4.30 the lift curve over the angle of attack is shown for three different VLM lattices of the DLR-F4 wing at $M = 0.75$, discretised by $N_i = 1$, 3 and 6 VLM vortex–ring elements along the chord. It can be seen that with $N_i = 1$ a grid independent solution is already achieved. Therefore, for the further investigation the lattice is used which is discretised into $N_j = 100$ spanwise and $N_i = 1$ chordwise vortex–ring elements on the half–wing.

This DLR–F4 validation campaign is carried out for high–speed flow regimes only. Here, three Mach–numbers are covered: $M = 0.6$, $M = 0.75$ and $M = 0.8$. In the same way as for the NACA2412 validation campaign the one–equation SA turbulence model in its original formulation is employed[88]. For calculations at $M = 0.6$, the second order central scheme is used to discretise the convective RANS flux. However, due to convergence problems, which were observed at $M = 0.75$ and $M = 0.8$, the convective RANS flux discretisation type is changed to a second–order Upwind AUSMDV scheme[101] for the datasets at $M = 0.75$ and $M = 0.8$. The sectional aerodynamic

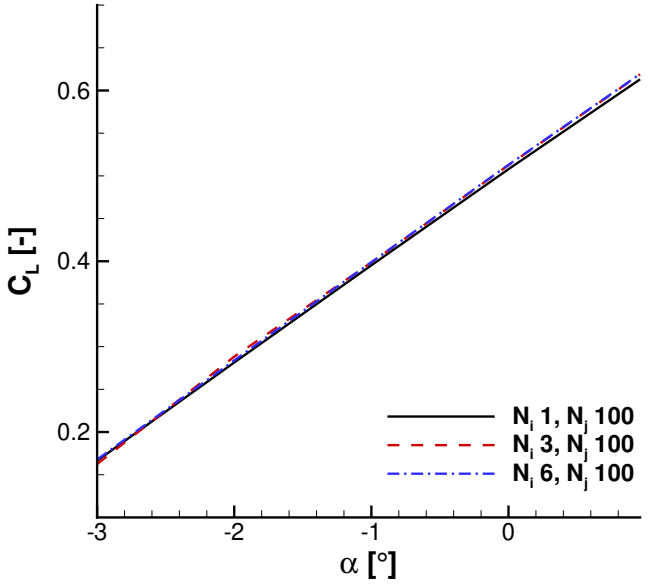

FIGURE 4.30: VLM lattice convergence analysis of the DLR-F4 wing at M 0.75

lift curves of the eight sections are calculated independently from each other for three different Mach–numbers. The parameters of the computations regarding the discretisation schemes and other major settings are kept the same as for the three–dimensional computations. The data points in the aerodynamic 2D/2.5D database which is employed in the 3D solver are resolved with an interval of $\Delta\alpha = 1.0°$.

4.2.2.1 Aerodynamic wing load

The overall aerodynamic forces of the DLR–F4 configuration obtained by the q3D–solver and three–dimensional CFD solver are presented in Figure 4.31. Here, results of the hybrid q3D–solver are presented, where the crossflow is included (2.5D+ aerofoil) and where the crossflow is neglected (2D aerofoil). For the results, where the crossflow is taken into account, the lift curves are estimated in the pre–stall region without any notable discrepancies with respect to three–dimensional numerical reference data. At higher freestream angles of attack notable discrepancies are visible. However, it has to be noted that here due to partly detached flow the 3D RANS–method also does not often predict reliable wing load data. On the other hand, it has to be mentioned that the steady–state aerodynamic q3D–coupling algorithm of `FALCon` is able to predict the impact of the compressibility of the flow onto the stall behaviour of the wing, moving from sharp ($M = 0.6$) to moderate ($M = 0.8$) behaviour. This information is very important during conceptual design stages of an aeroplane sizing study indicating that the data in this region of the freestream angle of attack has to be predicted by a more accurate computational CFD method to obtain more reliable results.

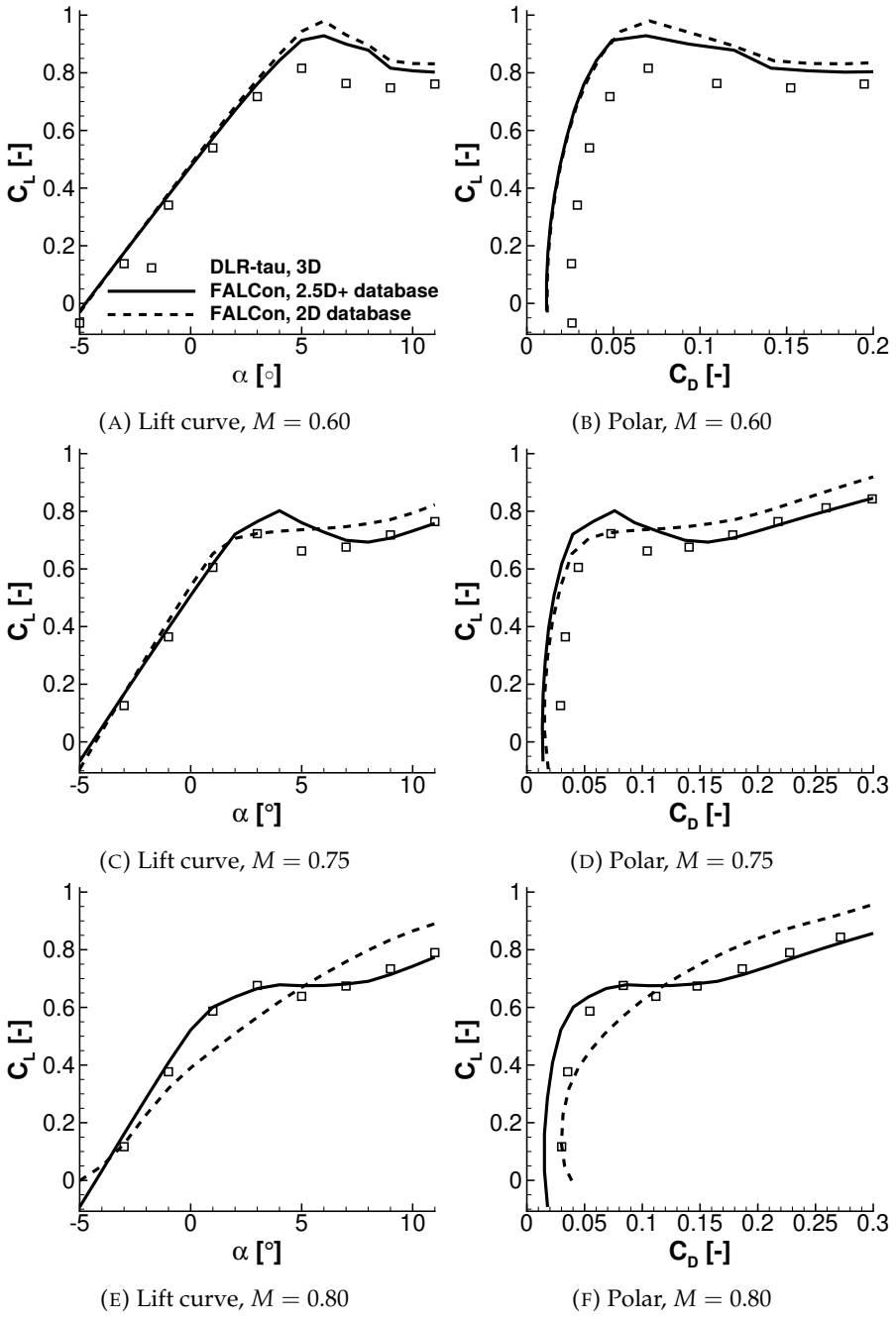

(A) Lift curve, $M = 0.60$ (B) Polar, $M = 0.60$

(C) Lift curve, $M = 0.75$ (D) Polar, $M = 0.75$

(E) Lift curve, $M = 0.80$ (F) Polar, $M = 0.80$

FIGURE 4.31: Overall aerodynamic forces of the DLR-F4 configuration

However, for results, where the crossflow is neglected, discrepancies are present, especially regarding the lift slope, C_L^α. Also, the maximal lift force coefficient, $C_{L,max}$, is overestimated by the hybrid q3D–solver for $M = 0.6$ and $M = 0.75$ for both datasets as here three–dimensional flow effects are present on the surface of the wing which can not be reproduced by the aerodynamic q3D–coupling solver in combination with 2D or 2.5D sectional aerodynamic database of the aerofoils. It has to be noted that in general RANS as a computational fluid dynamic method is not a reliable method when it comes to the predictions of detached flow physics at high angles of attack. However,

under those circumstances it can be still seen that the 3D CFD–RANS solver and FALCon, which incorporates 2D or 2.5D sectional aerodynamic data obtained by a 2D or 2.5D+ RANS CFD solver, are estimating relativly reliable the region where detached flow impacts the solution and stall occurs. Detached flow as a three–dimensional flow phenomena is usually reducing the local aerodynamic loads in these regions of the wing. Thus, in general it can be stated that the aerodynamic q3D–coupling methodology shows promising results, especially before stall–angle, α_{Stall}, and can estimate the region where stall is present, and therefore indicate where a higher–fidelity (and more expensive) CFD method should be used to capture more accurately results including detached flow, if required so.

For the total drag force coefficient, C_D, a constant discrepancy is present with respect to the three–dimensional reference data. The reason for this constant offset of C_D is the missing contribution of the fuselage, which is present in the numerical three–dimensional reference data. According to Ref. [5] the drag force coefficient contribution of the fuselage is $C_{D,body} \approx 9.0 \cdot 10^{-3}$ estimated by wind tunnel experiments.

In Figure 4.32 the spanwise lift distribution of the DLR–F4 is shown for three Mach–numbers at low angles of attack before the stall. For this range, `FALCon` in combination with the 2.5D+ sectional aerodynamic database estimates the lift distributions on this complex wing geometry with great confidence at the same order of accuracy as three–dimensional CFD. However, around the stall angle of attack, α_{stall}, `FALCon` fails to predict partly the spanwise aerodynamic load distribution, as three–dimensional locally not fully developed flow effects appear leading to the violation of the assumption that the flow in the spanwise direction along the quarter–chord line of the wing is locally fully developed and independent along the spanwise direction, see Section 3.3. However, one should consider that during a conceptual stage of a design project, where no high–fidelity 3D solutions of the novel configuration are available, the rapid solution provided by `FALCon` can provide essential information of the nonlinear aerodynamic loading of a wing geometry to the wing designer, and indicate that from a specific high freestream angle of attack, α, another computational methodology with a higher fidelity should be used to capture the detached flow physics more accurately.

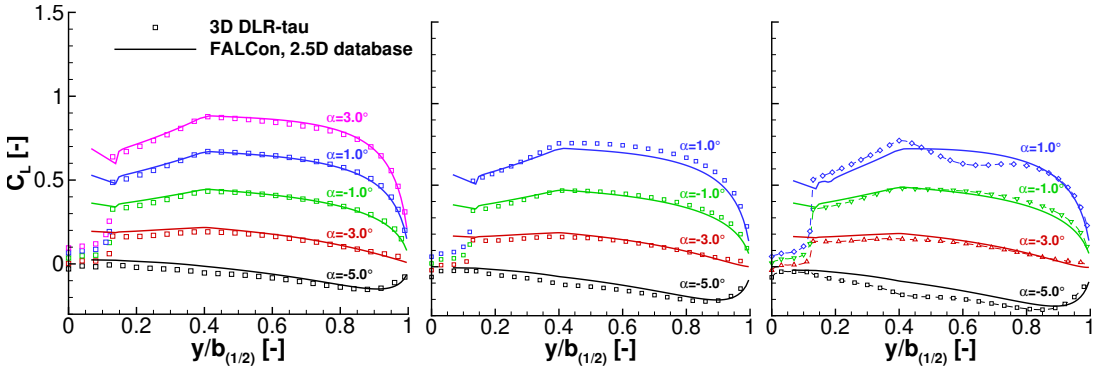

(A) Mach $M = 0.6$ (B) Mach $M = 0.75$ (C) Mach $M = 0.8$

FIGURE 4.32: Lift distribution along wing span of the DLR-F4 configuration

4.2.2.2 Sectional pressure distribution, c_p, at $C_L = 0.5$

The chordwise numerical results of the 7 sections estimated by the hybrid q3D–coupling code including and excluding crossflow effects are compared here with the three–dimensional and experimental reference results at a fixed total lift force coefficient of $C_L = 0.5$. Experimental chordwise data is available and was obtained by using local pressure taps in the DLR-F4 wind tunnel model located at 7 positions of the wing, see Figure 4.33[98][5]. The experimental dataset is obtained from three different wind tunnel measurement campaigns at the Dutch NLR High–Speed Wind Tunnel (HST), the French ONERA Continuous–flow wind tunnel (S2MA) and the British $8ft \times 8ft$ DRA wind tunnel in Bedford. The comparison of the local sectional flow is carried out for three transonic Mach–numbers: $M = 0.6$, $M = 0.75$ and $M = 0.8$.

Mach	α_∞
0.60	0.596°
0.75	0.127°
0.80	-0.048°

TABLE 4.7: Corresponding freestream angle of attack, α_∞, for three–dimensional CFD and q3D aerodynamic load estimations on DLR–F4 configuration corresponding to $C_L = 0.5$

In Table 4.7 the corresponding freestream angle of attack, α_∞, is presented, which corresponds in 3D CFD to an overall aerodynamic load of $C_L = 0.5$ of this DLR–F4 configuration at three different Mach–numbers. These values are estimated for the three–dimensional reference data at $C_L = 0.5$ by interpolation of the total lift curves predicted by the 3D `DLR-tau` CFD solver and presented in Figure 4.31. The numerical results obtained by the hybrid q3D–solver are also calculated at the same freestream angles of attack as three–dimensional reference data. The spanwise local lift of the results estimated by the hybrid q3D–coupling code is overestimated compared to numerical results obtained by three–dimensional `DLR-tau` CFD code as the fuselage is neglected in

hybrid q3D–solver at the symmetry layer. The presented experimental c_p–data is obtained by wind tunnel measurements at $C_L = 0.5$.

Further, in Figure 4.33 the non–dimensional surface pressure distribution, c_p, on the DLR–F4 configuration obtained by three–dimensional DLR-tau CFD code is shown at three different Mach–numbers at $C_L = 0.5$ on the three–dimensional wing geometry. Here, the position of the 7 sections is also marked. It can be seen that at $M = 0.75$ and $M = 0.8$ strong local shocks are present, which are created due to the local compressibility of the fluid. At $M = 0.7$ the shock is present at nearly quarter–chord position of the wing and is moved at $M = 0.8$ towards trailing edge of the geometry, while the shock intensity increases over M.

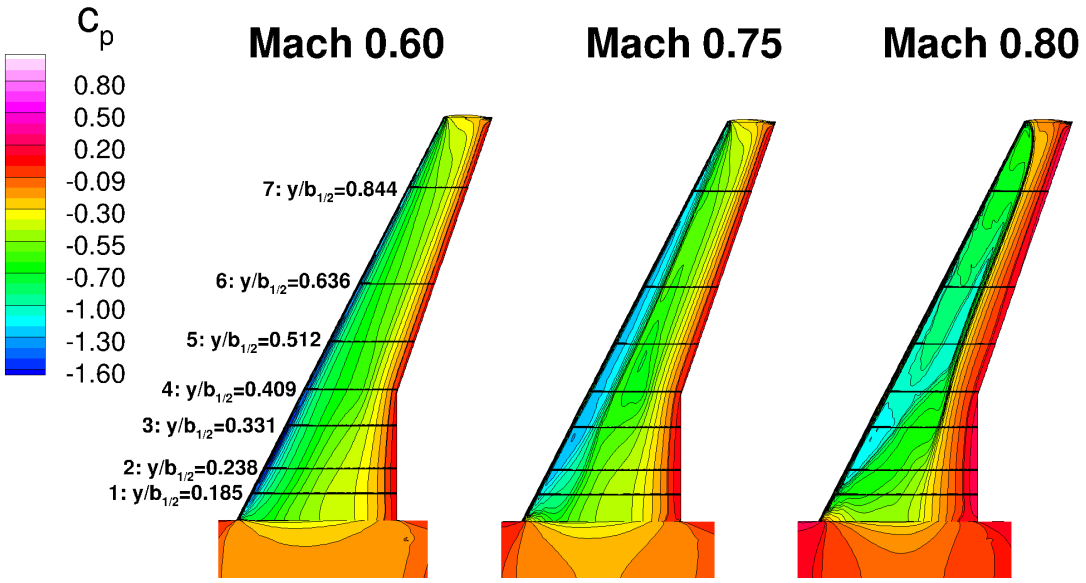

FIGURE 4.33: Surface pressure coefficient, c_p, on the DLR-F4 wing at $C_L = 0.5$, DLR-tau CFD solver

In Figure 4.34, Figure 4.35 and Figure 4.36 the c_p–distributions for the three Mach–numbers at the prescribed seven spanwise sections are shown and compared to three–dimensional reference data and experimental results. For q3D–solver, the c_p–plots are obtained at the particular converged effective angle of attack, α_e, at the spanwise position of the seven sections. For $M = 0.6$ it can be seen that the hybrid q3D–coupling code in combination with the 2.5D+ sectional database estimates the c_p–distribution very well with respect to three–dimensional numerical results and the experimental dataset. However, due to the three–dimensional flow effects on the surface of the wing, the overall results estimated by the hybrid q3D–coupling code are less accurate at those Mach–numbers. For example, it can be seen in Figure 4.33 that the inner wing section between 0% and 30% and the wing tip region between 80% and 100% of the local span, y/b, are highly impacted by three–dimensional flow effects. While the flow around the

wing tip region of the geometry is impacted by the wing tip vortex, the root region of the wing is affected by accelerated flow induced by the fuselage. In the aerodynamic q3D–coupling algorithm the fuselage is not considered, what automatically leads to discrepancies at this inner region of the wing. The reason for this is that here the flow physics violate the ISW hypothesis, which states that the flow along the span direction has to be fully developed and therefore section–wise independent, see Section 3.3. Additionally, at $M = 0.75$ a shock is present at nearly 25% of the local chord, which moves at $M = 0.8$ to 75% of the local chord length. The flow becomes at higher Mach–number more complex and less independent along the local swept span direction due to the dominating local shock leading to less valid results obtained by the hybrid aerodynamic q3D–coupling algorithm.

Moreover, the importance of the local crossflow phenomena in transonic flow regimes is demonstrated here: the solution obtained by the hybrid aerodynamic coupling code in combination with 2D aerofoil is overestimated at some sections due to the neglected crossflow physics. This leads to an incorrect prediction of the sectional shock in transonic flow conditions.

Finally, in Table 4.8 the relative error between the results of the sectional aerodynamic lift, C_L, which are obtained by the quasi–3D steady–state aerodynamic coupling algorithm and 3D `DLR-tau` CFD–solver is presented. This quantity is also estimated by using Equation 4.8. It can be seen that the overall spanwise error is less than 10% for results which are estimated with `FALCon` in combination with the 2.5D+ aerodynamic database. However, for results obtained in combination with the 2D aerodynamic sectional data, the error rises up to nearly 30% at high transonic Mach–numbers.

	2D CFD			**2.5D+ ISW–CFD**		
Section	**M 0.6**	**M 0.75**	**M 0.8**	**M 0.6**	**M 0.75**	**M 0.8**
1	7.72	10.41	26.62	5.44	4.72	2.22%
2	6.10	9.04	25.61	4.01	3.23	0.99%
3	3.21	6.25	25.42	1.13	0.19	1.94%
4	2.78	5.69	25.31	0.00	1.96	3.35%
5	1.74	4.42	24.30	0.50	3.14	2.28%
6	1.67	3.87	23.68	0.60	4.10	2.15%
7	0.24	1.60	27.07	2.02	6.37	7.23%
Average	3.35	5.90	25.43	1.96	3.39	2.88%

TABLE 4.8: Relative error, Δe, of the local lift between aerodynamic q3D–coupling algorithm and 3D `DLR-tau` on the DLR–F4 wing

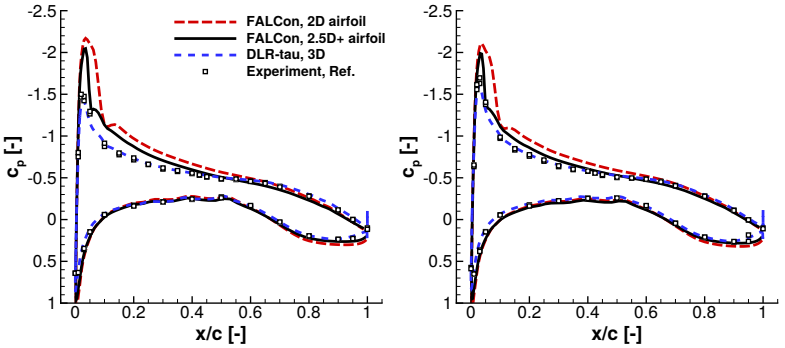

(A) Section 1, $\alpha_{e,2.5D} = 3.09°$

(B) Section 2, $\alpha_{e,2.5D} = 2.96°$

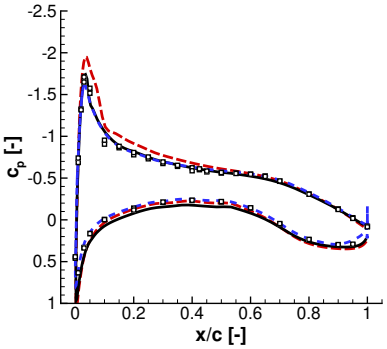

(C) Section 3, $\alpha_{e,2.5D} = 2.61°$

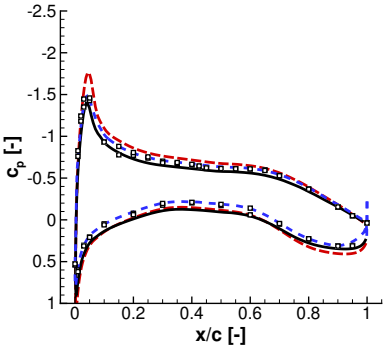

(D) Section 4, $\alpha_{e,2.5D} = 2.28°$

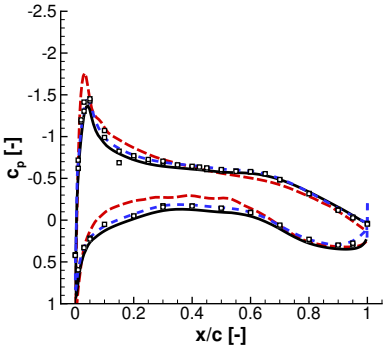

(E) Section 5, $\alpha_{e,2.5D} = 2.20°$

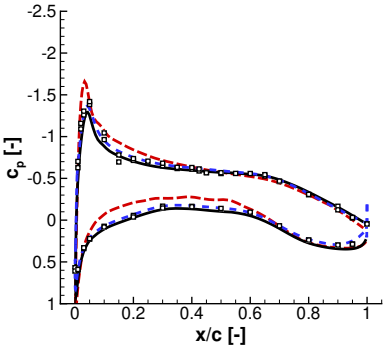

(F) Section 6, $\alpha_{e,2.5D} = 2.01°$

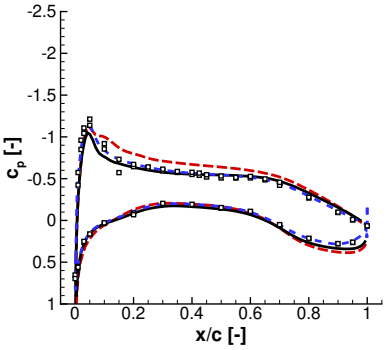

(G) Section 7, $\alpha_{e,2.5D} = 1.32°$

FIGURE 4.34: DLR F-4, sectional c_p-distribution, $C_L = 0.5$, $M = 0.6$, compared to reference experimental data, see Ref. [5]

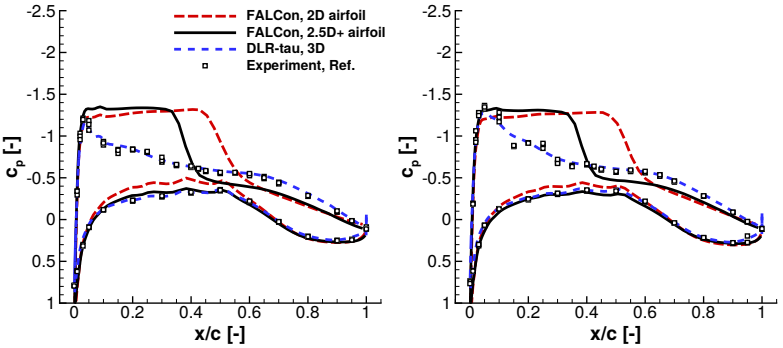

(A) Section 1, $\alpha_{e,2.5D} = 3.09°$

(B) Section 2, $\alpha_{e,2.5D} = 2.96°$

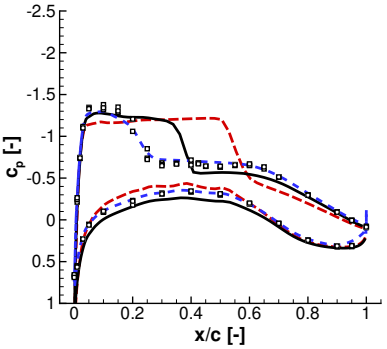

(C) Section 3, $\alpha_{e,2.5D} = 2.61°$

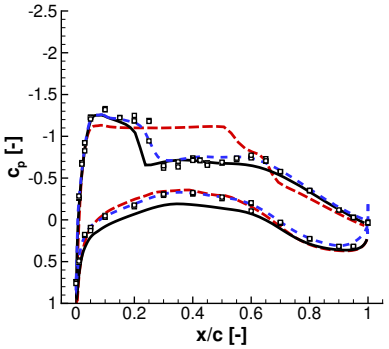

(D) Section 4, $\alpha_{e,2.5D} = 2.28°$

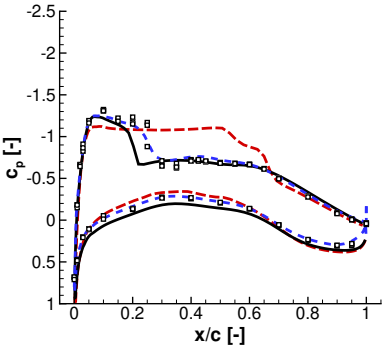

(E) Section 5, $\alpha_{e,2.5D} = 2.20°$

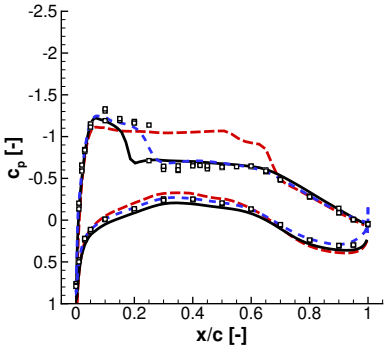

(F) Section 6, $\alpha_{e,2.5D} = 2.01°$

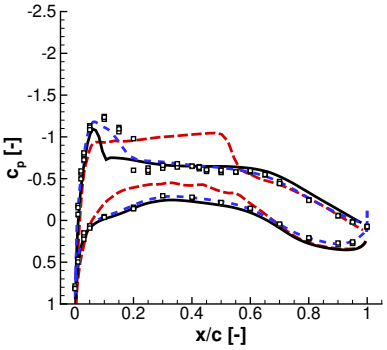

(G) Section 7, $\alpha_{e,2.5D} = 1.32°$

FIGURE 4.35: DLR F-4, sectional c_p-distribution, $C_L = 0.5$, $M = 0.75$, compared to reference experimental data, see Ref. [5]

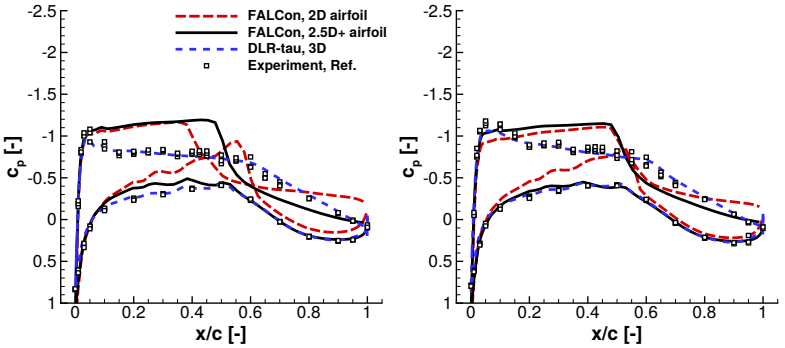

(A) Section 1, $\alpha_{e,2.5D} = 3.09°$

(B) Section 2, $\alpha_{e,2.5D} = 2.96°$

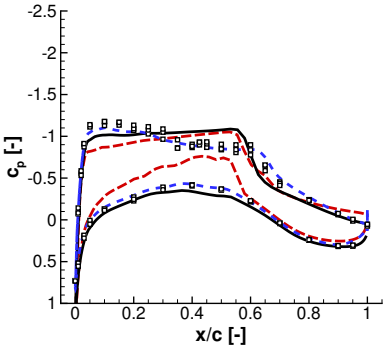

(C) Section 3, $\alpha_{e,2.5D} = 2.61°$

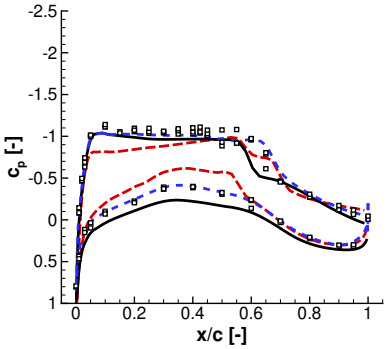

(D) Section 4, $\alpha_{e,2.5D} = 2.28°$

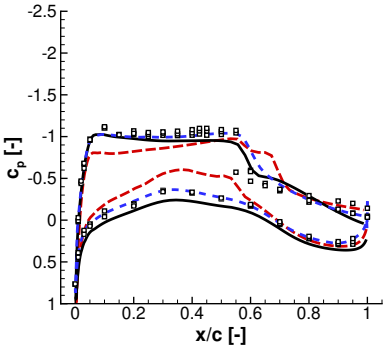

(E) Section 5, $\alpha_{e,2.5D} = 2.20°$

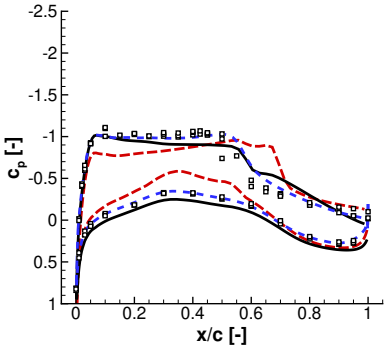

(F) Section 6, $\alpha_{e,2.5D} = 2.01°$

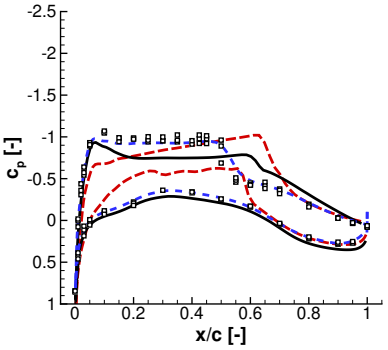

(G) Section 7, $\alpha_{e,2.5D} = 1.32°$

FIGURE 4.36: DLR F-4, sectional c_p-distribution, $C_L = 0.5$, $M = 0.8$, compared to reference experimental data, see Ref. [5]

4.2.3 Computational cost

In this final subsection, the computational cost of this novel solver is discussed for the DLR–F4 test case which is presented here and the speed–up with respect to conventional three–dimensional CFD computations is estimated. For the computation of the viscous 2.5D+ database for all eight sections at three different Mach–numbers and 30 angles of attack (720 steady–state computations in total using the 2.5D+ `DLR-tau` ISW–CFD solver) $3.11 \cdot 10^2$ CPU–hours were required. Similarly, for the estimation of the corresponding 2D database with the same amount of steady–state database $3.23 \cdot 10^2$ CPU–hours were required. In total, 168 single calculations of the steady–state aerodynamic q3D–coupling algorithm at three Mach–numbers and 28 freestream angles of attack were executed for this validation study while employing the 2D and 2.5D sectional aerodynamic database. In total, 634.44 CPU–hours (3.18 CPU–hours per freestream angle of attack of a single `FALCon` calculation including the employed sectional database) were required to obtain data from the hybrid aerodynamic coupling code presented in this thesis.

Task	**Total CPU–hour**
2D sectional database	323.14
2.5D sectional database	310.57
`FALCon` load estimation	0.73
Total	634.44

TABLE 4.9: Total computational CPU–hours necessary to obtain the 2D and 2.5D+ sectional database and the aerodynamic load on the DLR–F4 wing using the hybrid aerodynamic coupling procedure

The total computational cost necessary to compute 42 numerical data points using the conventional three–dimensional full–fidelity `DLR-tau` CFD code can be stated as $3.883 \cdot 10^4$ CPU–hours. Thus, in average for one flow condition, this makes $9.245 \cdot 10^3$ CPU–hours for a `DLR-tau` 3D computation. Therefore, based on the average CPU–hours per one flow condition an average speedup factor of $6.12 \cdot 10^1$ is achieved, which is a significant speed–up achievement compared to conventional three–dimensional CFD methods. Therefore, it can be concluded that a promising trade–off is reached in the computational aerodynamic wing load predictions between numerical accuracy of the q3D–coupling solver (at least until stall occurs) and required computational cost.

4.2.4 Summary

In this section the validation study of the steady–state quasi–3D aerodynamic coupling algorithm was presented and the accuracy and computational cost of this solver was

discussed. Two major test cases were used to demonstrate the capabilities of the novel solver to predict rapidly aerodynamic loads at low– and high–speed flow regimes: The NACA2412–wing and the DLR–F4 configuration. The first study is a systematic study where the accuracy of the aerodynamic q3D–coupling algorithm is evaluated using a swept and unswept NACA2412–wing geometry at low and high freestream angles of attack. Further, the validation campaign is extended by considering wing geometries with various geometrical sweep angles, Λ, and taper ratios, γ. The second test case is the DLR–F4 configuration, which geometry is much more similar to geometries of typical commercial air vehicles, and therefore often used to validated CFD solvers which are applied in aeronautical design and analyses procedures.

This method captures the nonlinear lift slope, C_L^α, at low– and high–speed flow regimes and predicts the flow around the wings at moderate angles of attack, α, with good agreement to equivalent results obtained by a 3D CFD–RANS solver. At moderate freestream angles of attack a typical relative deviation of the total C_L between the q3D–coupling solver and 3D CFD solver ranges between 0.5% and 5.0%. However, when 2D precomputed aerodynamic database is used on a swept wing, the error can reach up to 10%. Thus, it is recommended to use 2.5D sectional aerodynamic databases on swept wing geometries to increase the accuracy of the results by taking crossflow effects into account. Otherwise, by neglecting the crossflow effects the boundary layer and the sectional position of the transonic shock are predicted incorrectly. This 2.5D database has to be precomputed by an ISW–RANS CFD solver model, see Section 3.3.

At high angles of attack in the stall region the q3D–coupling solver is not able to resolve the flow physics with the same accuracy as at low freestream angles of attack as the validity of this solver here is often not given due to three–dimensional locally detached flow areas. However, it gives a rapid indication that at certain aerodynamic flow conditions detached flow is present, which has to be captured by another solver with a higher physical fidelity. However, the rapid indication of the presence of detached flow is very helpful during early aeronautical project stages when high–fidelity three–dimensional numerical results of a novel configuration are not available yet.

4.3 Unsteady aerodynamic model

This section demonstrates the applicability of the complete computational tool `FALCon` to a number of test cases of increasing complexity in unsteady flow regimes. The physics ranges from incompressible to compressible flows in a 2D and 3D setting, driven by unsteady motions at different reduced frequencies. Reference data are obtained from `DLR-Tau` code solving the URANS equations. In all cases the turbulent boundary layer is predicted using the one–equation Spalart–Allmaras turbulence model [88].

4.3.1 Forced harmonic motion in pitch and plunge: aerofoil

The first demonstration test case is for the high subsonic flow around a pitching and plunging NACA 2412 aerofoil. Flow conditions are for $M = 0.7$ and $Re = 5.5 \cdot 10^6$. The harmonic motions are prescribed at low and high values of the reduced frequency, respectively, $k = 0.025$ and 0.750. In pitch, the mean value of the angle of attack and the amplitude are $\alpha_0 = 0°$ and $\alpha_A = 2.51°$, and in plunge, $\xi_0 = 0$ and $\xi_A = 0.1$. The pitching motion is performed around the quarter–chord position of the aerofoil.

Reference data are obtained from time marching the 2D URANS equations. The O–type, structured grid in Figure 4.6 used in all calculations was chosen to guarantee grid independent results. Three levels of grids were generated, from about 25 thousand to 70 thousand grid points. The coarser grid was found adequate to model the unsteady lift coefficient, as reported in Figure 4.37. The convective RANS flux is discretised using the second–order central scheme. Spalart–Almaras turbulence model in its original formulation is employed [88]. For time integration, the dual time–stepping scheme is used. The 2w–cycle multigrid scheme with 50 quasi–steady subiterations per physical time step is chosen at a Courant–Friedrichs–Lewy number of 2.5.

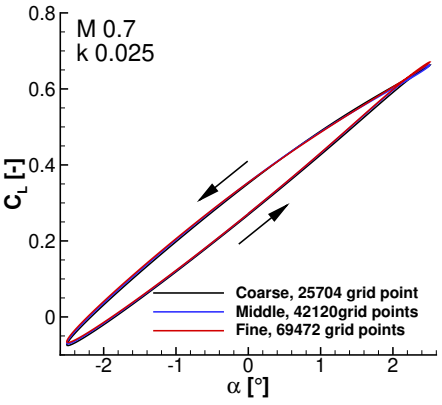

FIGURE 4.37: Grid convergence analysis of the 2D NACA2412 airfoil CFD grid

The analysis setup for FALCon is as follows: the UVLM lattice consists of one single panel ($N_j = 1$ and $N_i = 1$) of high aspect ratio ($AR = 100$) motivated by the 2D aerodynamics of this test case. For the 2D viscous solver around the aerofoil, numerical parameters are identical to those above–mentioned for the reference data. For this 2D case the coupling algorithm initially spawns one URANS analysis at the mean static freestream angle of attack of $\alpha_0 = 0°$. As for the 2D nature of the flow, Equation 3.57 of the unsteady, α–based coupling algorithm simplifies to

$$\alpha_{e,j}^{2D} = \alpha_\infty \tag{4.6}$$

after elimination of the induced angle of attack from the original formulation. As it is known, in 2D flow the induced angle of attack, α_i, is zero as no wing tip and, therefore, no wing tip vortex is present. Thus, in 2D the effective angle of attack becomes the mean static aerodynamic angle of attack of the aerofoil, which is here $\alpha_0 = 0°$. Therefore, only one 2D URANS CFD solver is required at $\alpha_0 = 0°$, which delivers the viscous nonlinear lift force coefficient for the aerodynamic coupling procedure.

For the coupling algorithm, the relaxation factor is set to $\nu = 0.1$, and the convergence criterion at each time step is defined by the parameter $\varepsilon = 1 \cdot 10^{-5}$. This guarantees numerical stability and accuracy during the computations.

Figure 4.38 shows the lift coefficient time responses to forced motions in pitch and plunge in 2D obtained by FALCon. Initial transients were removed and arrows indicate the direction of the loops. A perfect match is observed between the two aerodynamic options for all cases, indicating a correct functioning of the unsteady coupling algorithm in 2D flows.

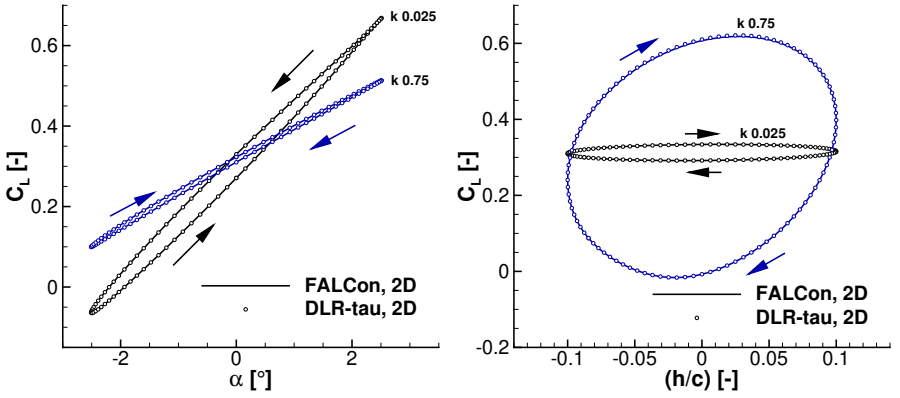

(A) Harmonic pitch oscillation (B) Harmonic plunge oscillation

FIGURE 4.38: NACA2412, 2D airfoil, $M = 0.7$

4.3.2 Forced harmonic motion in pitch and plunge: finite–span wing

The second test case is for a finite–span, unswept and untapered wing. The aspect ratio is 10. The wing cross–section is based on the NACA 2412 aerofoil. The forced harmonic motion in pitch and plunge has the same parameters as described in Section 4.3.1. The test case is run at three values of Mach number ($M = 0.3$, 0.5 and 0.7) keeping the Reynolds number fixed at $5.5 \cdot 10^6$. The pitching motion is performed here around the quarter–chord line of the lattice. This test case allows to investigate predictive performance of the unsteady hybrid aerodynamic q3D–solver taking into account the effect of compressibility and the impact of mild shock waves, which appear and disappear during the forced motion. Also, by using a finite–span wing this chapter investigate the predictive performance of this approach on 3D flow around a wing geometry, where an induced wing tip vortex is present.

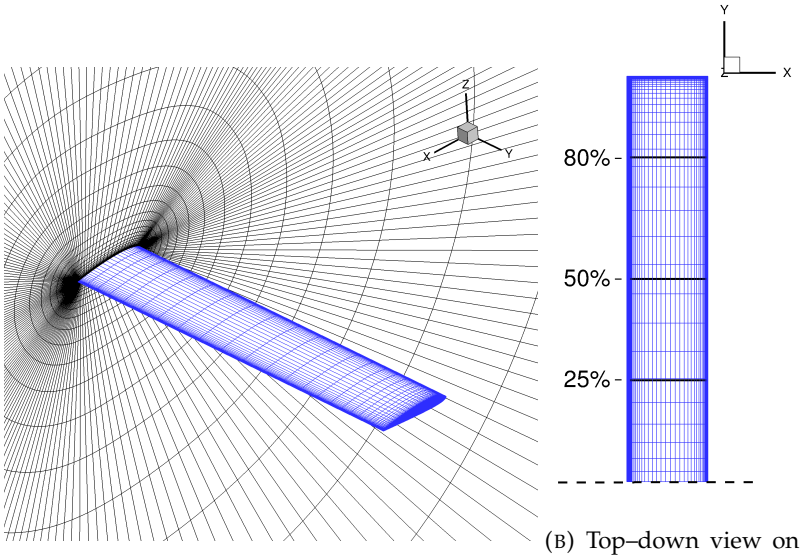

(A) Wall and symmetry boundary

(B) Top–down view on the wall boundary

FIGURE 4.39: NACA2412, 3D grid, unswept, AR10, 2 Mio. grid points

Also here, reference data were obtained solving the 3D URANS equations. Results were calculated for three cycles, using 100 time steps per cycle, to achieve a periodic flow state after the decay of initial transients. The maximum number of pseudo–iterations per time step was set to 600, and the single grid method was used. Other relevant numerical settings were the same as those described in Section 4.3.1 for the 2D NACA2412 aerofoil. Figure 4.39 shows the chosen 3D grid. The grid point distribution at the symmetry plane uses the coarse 2D grid shown in Figure 4.6. This optimal grid for 2D flows was then extruded in the spanwise direction to obtain a 3D grid. It was found that a discretisation with 63 layers of the 2D planes along the span was adequate for grid independent results, as documented in Figure 4.40. The final 3D grid consists of about two million grid points.

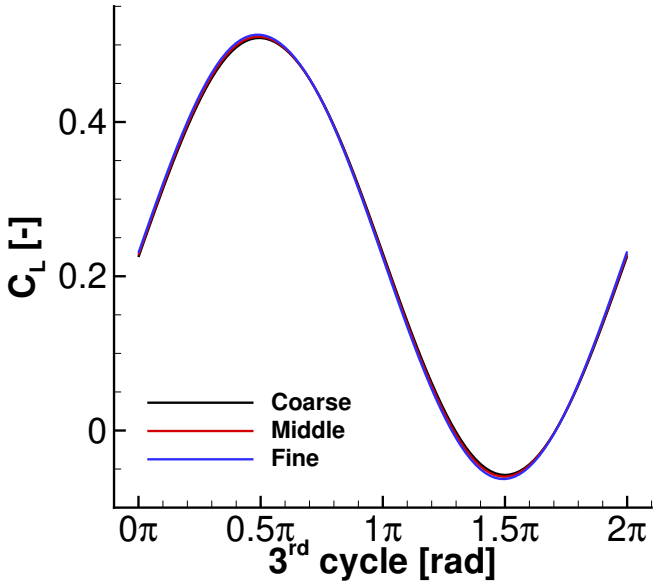

FIGURE 4.40: 3D CFD grid convergence analysis (coarse: 2 Million, middle: 4.2 Million, and fine: 8.97 Million grid points)

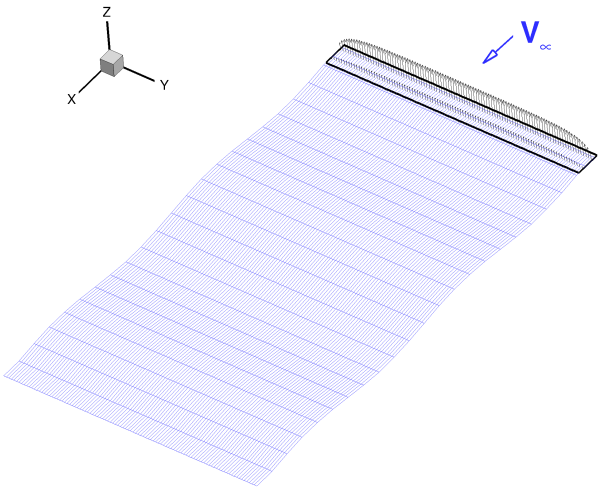

FIGURE 4.41: VLM lattice used for unsteady coupling procedure, AR 10, N_i 2, N_j 100

For the hybrid aerodynamic q3D–solver in `FALCon`, the VLM lattice consists of $N_i = 2$ and $N_j = 100$ panels, as shown in Figure 4.41. Coarser grids revealed a tendency to overestimate the lift coefficient at the lowest and highest values of the angle of attack, as shown in Figure 4.42.

Due to the finite–span of the wing the actual spanwise effective angle of attack, α_e, will not exceed the static freestream angle of attack, α_0, at the symmetry of the wing configuration. However, due to the reduced spanwise lift at the wing tip the actual α_e becomes negative in this region when an unsymmetrical aerofoil geometry is used due to the spanwise lift force converging to no lift directly at the wing wing tip of the

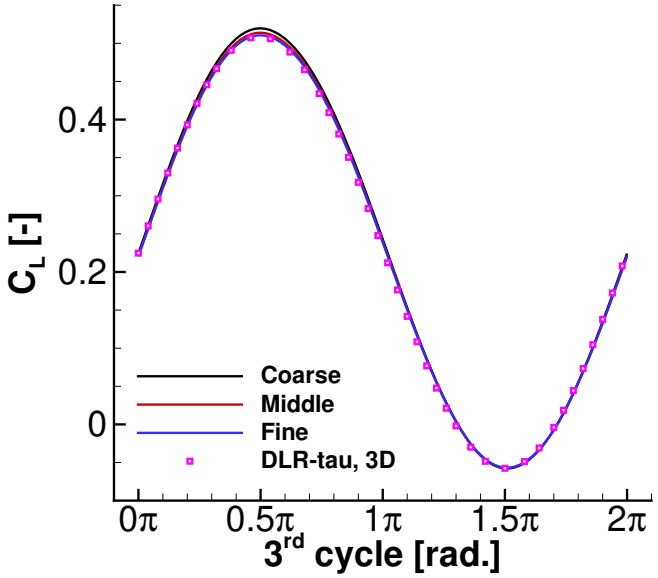

FIGURE 4.42: Grid convergence analysis wing lattice used in the hybrid q3D–solver (coarse: 2×25, middle: 2×50, and fine: 2×100 VLM panels)

geometry. Therefore, the coupling algorithm spawns nine URANS analyses uniformly distributed between -6° and 2° angle of attack. The relaxation factor is $\nu = 0.1$, and the convergence criterion at each time step is based on the tolerance $\varepsilon = 10^{-8}$.

Further, the reproducibility of the flow physics using the hybrid aerodynamic q3D–solver solver is discussed. Reference data are from time marching the 3D URANS equations. Figure 4.43 reports time domain results for the forced motion in pitch, and Figure 4.44 results for the forced motion in plunge. Qualitatively, the fundamental characteristics associated with flow unsteadiness, i.e. reduced frequency and compressibility, are well captured in results obtained by the unsteady q3D solver of `FALCon`. In particular, the hybrid aerodynamic q3D–solver correctly captures the following elements:

- the increase of the hysteresis loops for increasing reduced frequency, and the decrease of this trend for increasing Mach number
- for increasing reduced frequency, loops tilt clockwise and the aerodynamic stiffness, related to the loop mean slope, increases with Mach–number

Qualitatively, the impact of reduced frequency and Mach number on aerodynamic loops are reproduced. Quantitatively, average discrepancies of total lift force coefficient, C_L, over one cycle are observed between 1% for $k = 0.025$ and 11% for $k = 0.75$, as it can be seen in Table 4.10.

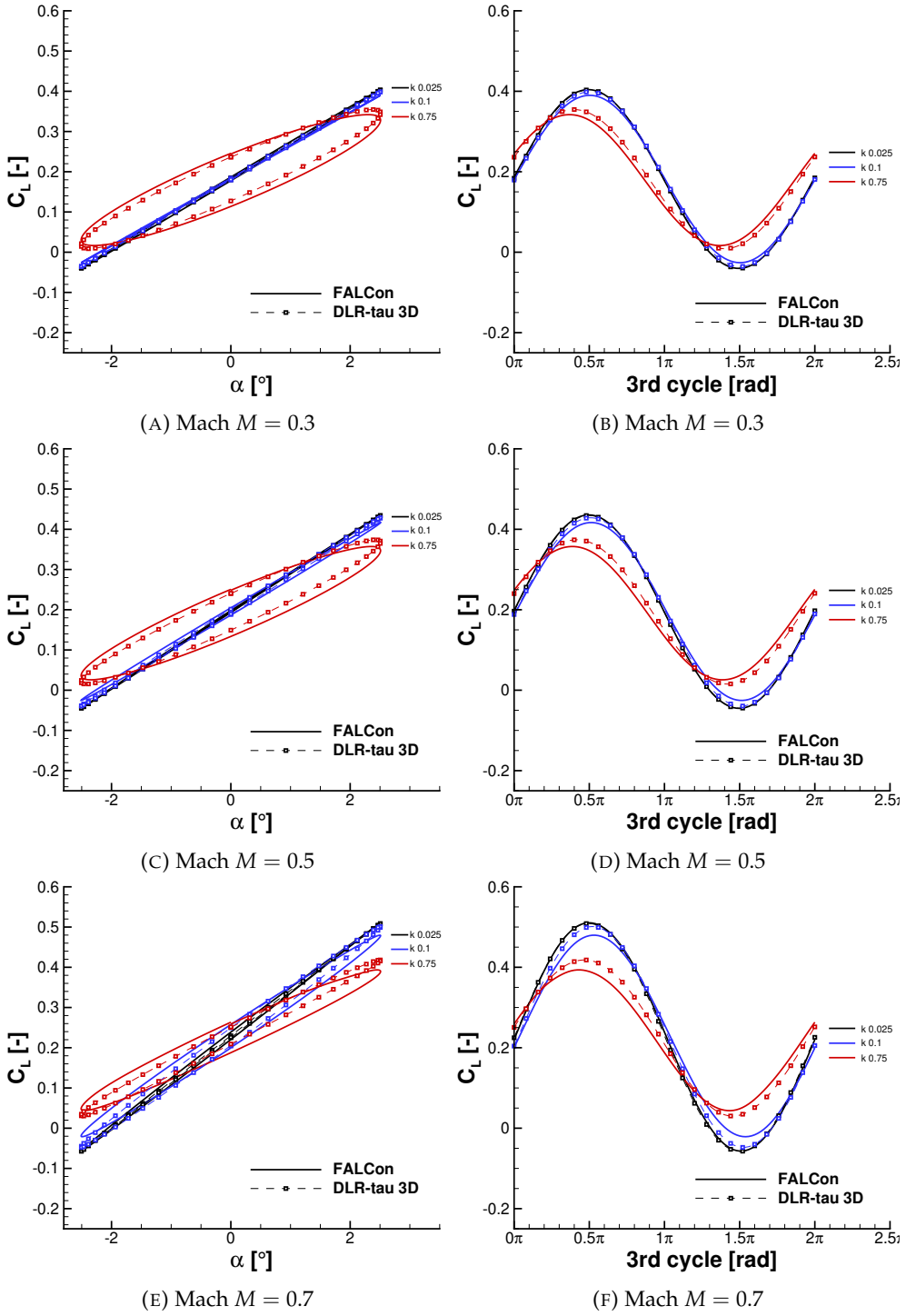

(A) Mach $M = 0.3$ (B) Mach $M = 0.3$

(C) Mach $M = 0.5$ (D) Mach $M = 0.5$

(E) Mach $M = 0.7$ (F) Mach $M = 0.7$

FIGURE 4.43: 3D NACA2412–wing, harmonic pitching oscillation, $Re = 5.5 \times 10^6$, Sweep 0.0°

The relative deviation is obtained by normalising the total deviation of C_L between the two solvers over one (third) cycle with respect to the mean steady–state C_L obtained by 3D `DLR-tau` CFD solver, and finally averaged the time series of the relative deviation over the cycle:

Case	Minimal	Average	Maximal
pitching, $k = 0.025$	0.034	1.798	3.953
pitching, $k = 0.750$	0.163	7.959	14.605
plunging, $k = 0.025$	1.041	1.101	1.219
plunging, $k = 0.750$	0.095	11.544	21.943

TABLE 4.10: Relative deviation of the total C_L between `FALCon` and `DLR-tau` at $M = 0.7$ in percent over the third cycle

$$\Delta\bar{e} = \frac{1}{N}\sum_{k}^{N}\frac{\left|C_{L,k}^{hUVLM} - C_{L,k}^{CFD}\right|}{\bar{C}_L^{CFD}} \tag{4.7}$$

where N is the number of time steps per cycle, $C_{L,k}^{hUVLM}$ is the particular lift force coefficient estimated by the coupling code and $C_{L,k}^{CFD}$ the coefficient obtained from 3D CFD analysis at the k–th time step, $\bar{C}_L^{CFD}$ is the mean coefficient per cycle estimated by 3D CFD analysis. Reproducing these features, in particular point 2 above, guarantees the suitability of the hybrid aerodynamic q3D–solver for future aeroelastic analyses. This solver offers the appealing feature to reconstruct distributed flow features at any spanwise location which does not coincide with the sections used to generate the viscous data. This is done at no extra cost because the existing database is simply interrogated with the effective angle of attack provided by he UVLM solver.

The instantaneous c_p and c_f plots at various flow conditions and all three reduced frequencies are excluded to the appendix of this work. Therefore, in Section A.1.1 (page 164) the instantaneous sectional plots are presented for the pitching motion and in Section A.1.2 (page 208) for the plunging motion. As an example, for $M = 0.7$, the data is summarised in Figures 4.45 and 4.46 for pitching motion and in Figures 4.47 and 4.48 for plunging motion of the wing by overlaying the results obtained at $k = 0.025$ and $k = 0.75$. In every figure the instantaneous c_p and c_f is illustrated separately. To comprehend these articulated figures, rows correspond to four time instants during an oscillatory cycle: maximal position, mean downstroke, minimal position and mean upstroke position of pitch or plunge in third cycle. The columns correspond to three locations along the wing span: 25, 50 and 80% of the half–span, see Figure 4.39b. As an example, the fourth row of the figures reports the instantaneous c_p at stations located at 25, 50 and 80% of the wing span during the upstroke, for $\alpha = 0^\circ$ or $\xi = 0$. In general, the reconstruction of the instantaneous flow features is done well. It is not unexpected that the larger discrepancies in prediction are at the wing tip for all Mach–numbers.

These are due to the presence of a strong wing tip vortex forming around a straight wing. Comparing pitch and plunge, differences seen in the total C_L are attributed to deviations in a) the high speed region of the flow interacting with the wing tip vortex, and b) intensity of the suction peak of the c_p and c_f data between the results of the two solvers at high reduced frequency of $k = 0.75$.

Referring back to Section 4.3.1, where a 2D aerofoil is examined, it can be seen that the discrepancies of the results on this 3D finite–span wing must come from the estimation of the effective angle of attack, α_e, as on a 3D wing geometry it is affected by the non–zero induced angle of attack, α_i, which is neglected for 2D calculation of the aerofoil in the previous section. The induced angle of attack is estimated by UVLM and is of a high importance for the accuracy of the solver. During this work it was figured out that the best overall results are obtained when the induced angle of attack, α_i, is calculated or interpolated at the spanwise quarter–chord position of the VLM lattice. Thus, it can be stated that the accuracy of the coupling code is highly dependent on the accurate estimation of the unsteady spanwise induced angle of attack, α_i. Further work should investigate ways to improve the estimation of the effective angle of attack in unsteady flows and reduce the discrepancies even further also for wing geometries undergoing unsteady motions at high reduced frequencies.

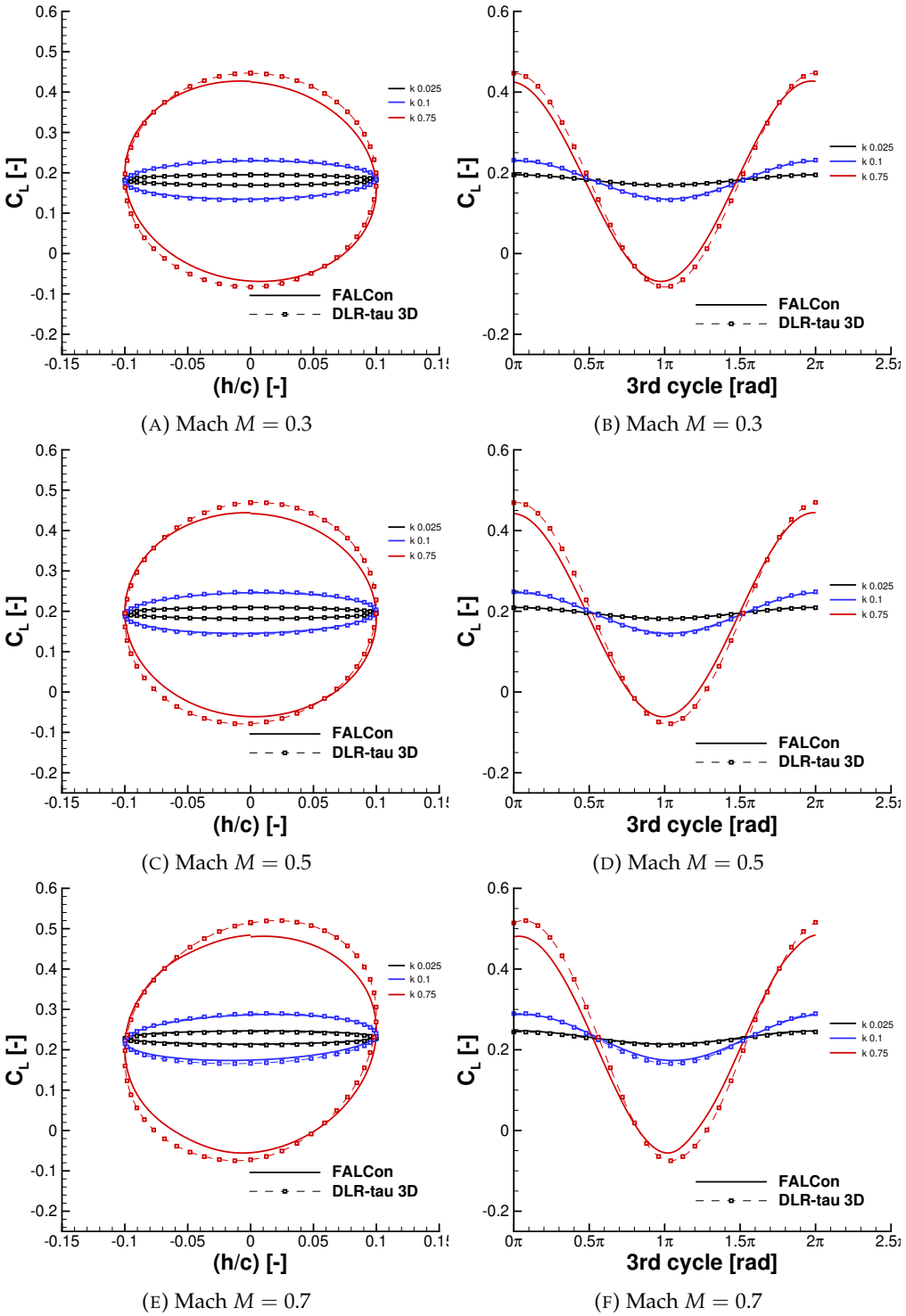

(A) Mach $M = 0.3$

(B) Mach $M = 0.3$

(C) Mach $M = 0.5$

(D) Mach $M = 0.5$

(E) Mach $M = 0.7$

(F) Mach $M = 0.7$

FIGURE 4.44: NACA2412, 3D wing, AR10, harmonic plunging oscillation, $Re = 5.5 \times 10^6$, Sweep 0.0°

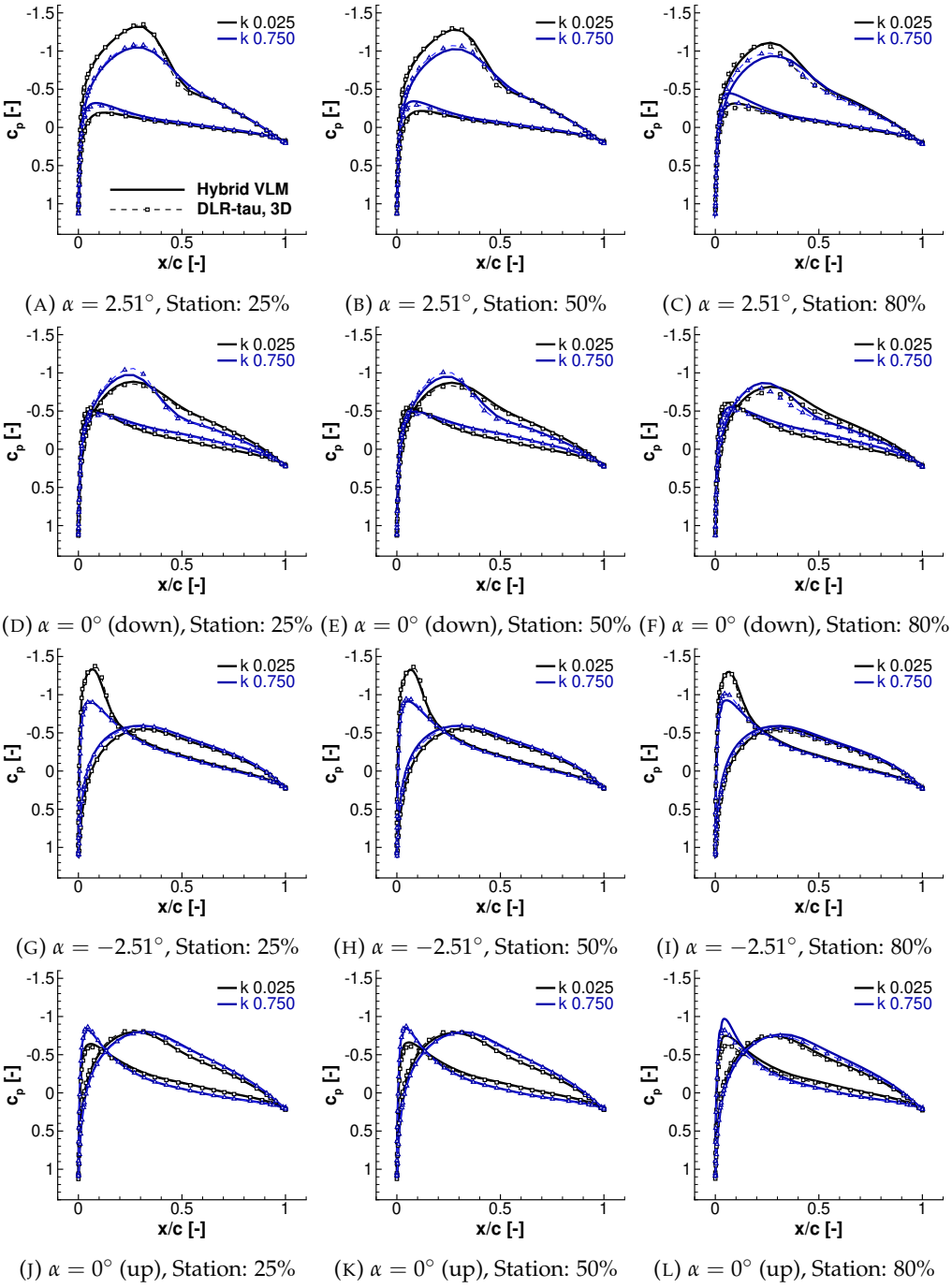

(A) $\alpha = 2.51°$, Station: 25% (B) $\alpha = 2.51°$, Station: 50% (C) $\alpha = 2.51°$, Station: 80%

(D) $\alpha = 0°$ (down), Station: 25% (E) $\alpha = 0°$ (down), Station: 50% (F) $\alpha = 0°$ (down), Station: 80%

(G) $\alpha = -2.51°$, Station: 25% (H) $\alpha = -2.51°$, Station: 50% (I) $\alpha = -2.51°$, Station: 80%

(J) $\alpha = 0°$ (up), Station: 25% (K) $\alpha = 0°$ (up), Station: 50% (L) $\alpha = 0°$ (up), Station: 80%

FIGURE 4.45: Sectional nondimensional pressure coefficient, c_p of a pitching unswept wing at $M = 0.7$ at third cycle

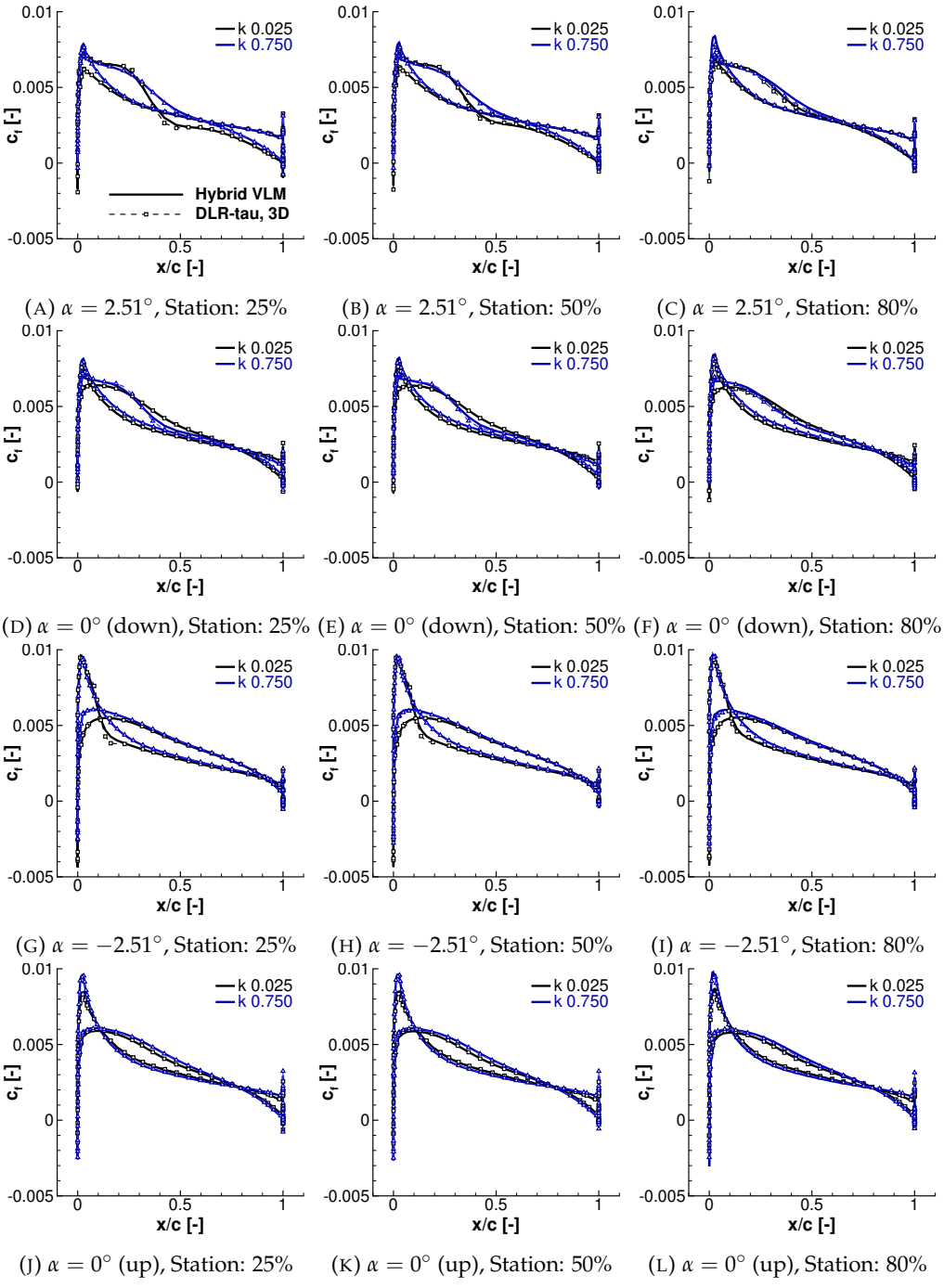

(A) $\alpha = 2.51°$, Station: 25% (B) $\alpha = 2.51°$, Station: 50% (C) $\alpha = 2.51°$, Station: 80%

(D) $\alpha = 0°$ (down), Station: 25% (E) $\alpha = 0°$ (down), Station: 50% (F) $\alpha = 0°$ (down), Station: 80%

(G) $\alpha = -2.51°$, Station: 25% (H) $\alpha = -2.51°$, Station: 50% (I) $\alpha = -2.51°$, Station: 80%

(J) $\alpha = 0°$ (up), Station: 25% (K) $\alpha = 0°$ (up), Station: 50% (L) $\alpha = 0°$ (up), Station: 80%

FIGURE 4.46: Sectional nondimensional friction coefficient, c_f of a pitching unswept wing at $M = 0.7$ at third cycle

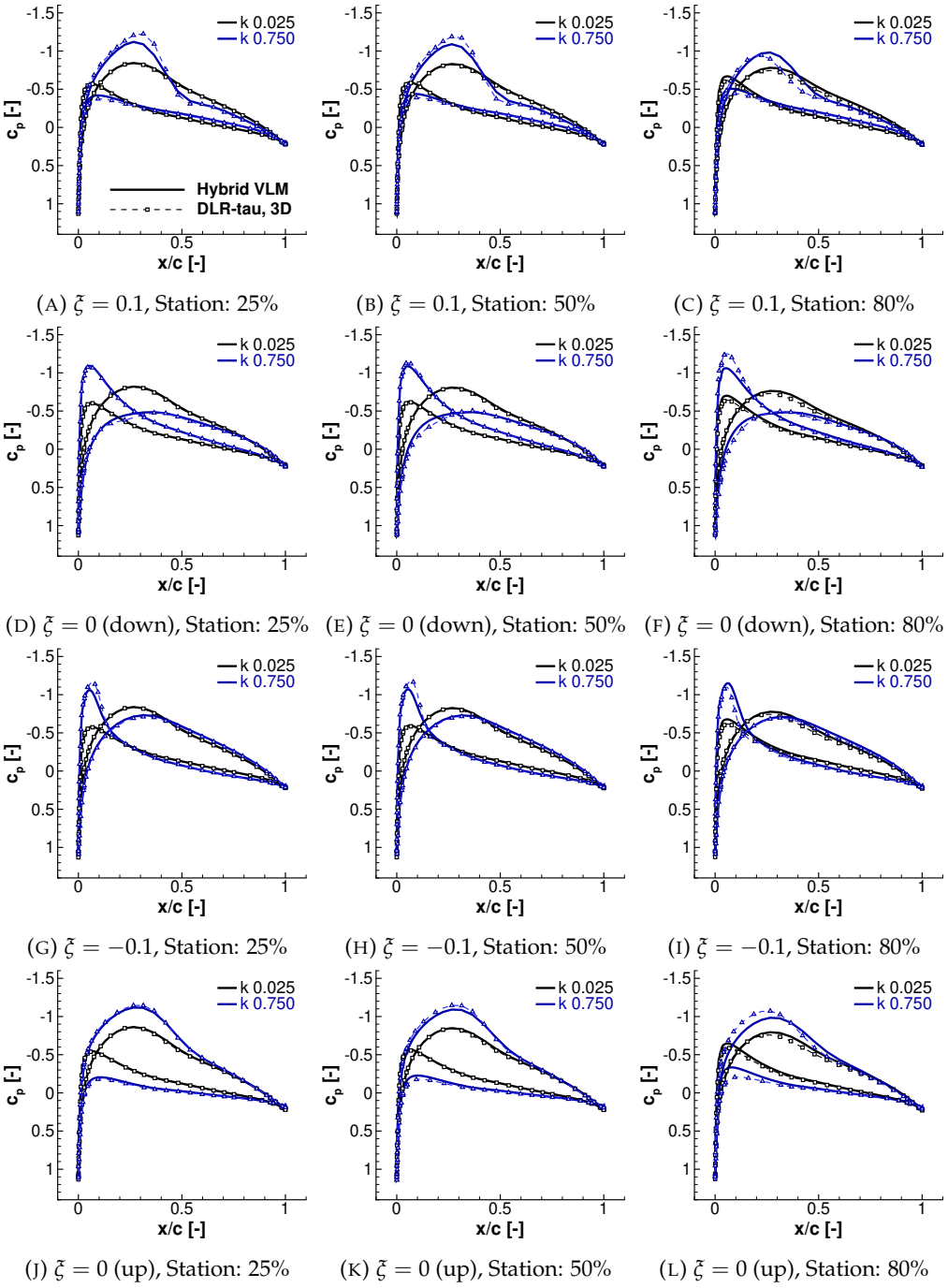

(A) $\xi = 0.1$, Station: 25% (B) $\xi = 0.1$, Station: 50% (C) $\xi = 0.1$, Station: 80%

(D) $\xi = 0$ (down), Station: 25% (E) $\xi = 0$ (down), Station: 50% (F) $\xi = 0$ (down), Station: 80%

(G) $\xi = -0.1$, Station: 25% (H) $\xi = -0.1$, Station: 50% (I) $\xi = -0.1$, Station: 80%

(J) $\xi = 0$ (up), Station: 25% (K) $\xi = 0$ (up), Station: 50% (L) $\xi = 0$ (up), Station: 80%

FIGURE 4.47: Sectional nondimensional pressure coefficient, c_p of a plunging unswept wing at $M = 0.7$ at third cycle

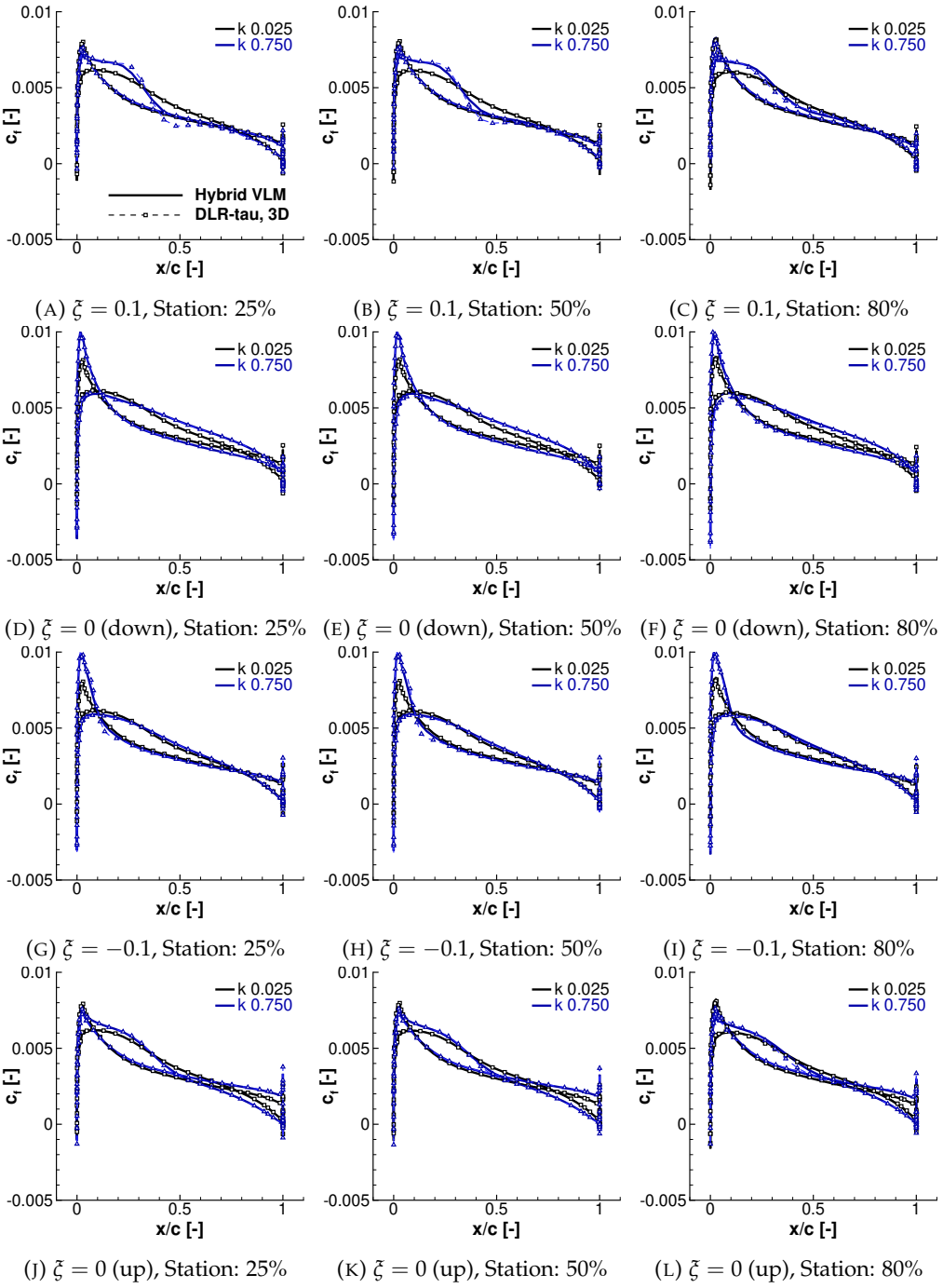

(A) $\xi = 0.1$, Station: 25% (B) $\xi = 0.1$, Station: 50% (C) $\xi = 0.1$, Station: 80%

(D) $\xi = 0$ (down), Station: 25% (E) $\xi = 0$ (down), Station: 50% (F) $\xi = 0$ (down), Station: 80%

(G) $\xi = -0.1$, Station: 25% (H) $\xi = -0.1$, Station: 50% (I) $\xi = -0.1$, Station: 80%

(J) $\xi = 0$ (up), Station: 25% (K) $\xi = 0$ (up), Station: 50% (L) $\xi = 0$ (up), Station: 80%

FIGURE 4.48: Sectional nondimensional friction coefficient, c_f of a plunging unswept wing at $M = 0.7$ at third cycle

4.3.3 Transonic forced harmonic pitch oscillation of the NACA2412–wing at $M = 0.8$

This section presents the unswept NACA2412–wing undergoing forced harmonic pitch oscillation in transonic flow at $M = 0.8$. The amplitude of pitch and reduced frequencies are the same as in the previous subsection. In Figure 4.49 the upper surface of the wing geometry is shown for four stages of the third cycle for two different reduced frequencies: $k = 0.025$ and $k = 0.75$. On the surface the friction coefficient in flow direction, $c_{f,x}$, is plotted and areas of the wing with reversed (i.e. separated) flow are marked.

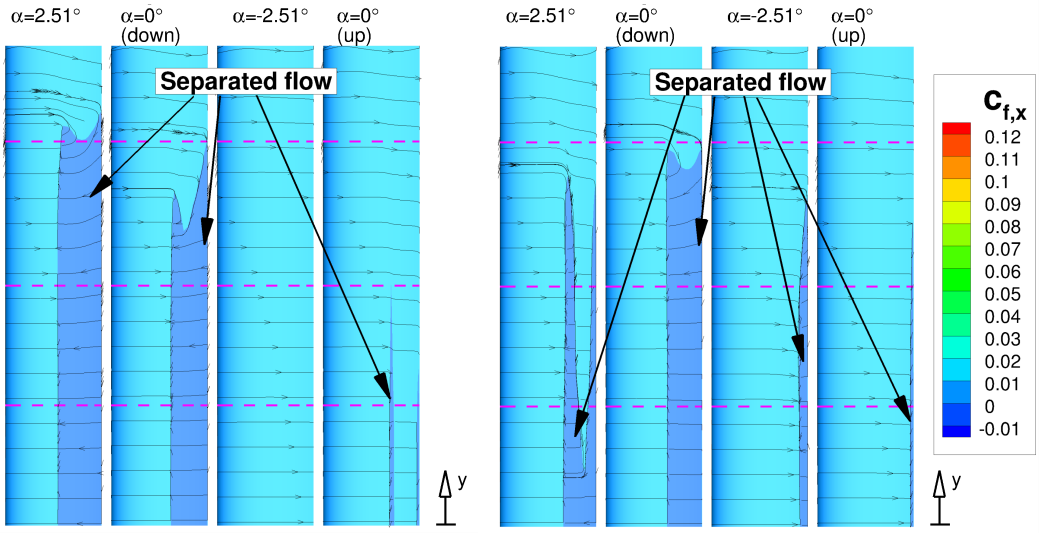

(A) $k = 0.025$ (B) $k = 0.750$

FIGURE 4.49: Areas of reversed flow on the upper surface of the pitching NACA2412 wing at $M = 0.8$; numerical results obtained with 3D `DLR-tau` CFD, symmetry at the bottom of illustration

A comparison of the total aerodynamic lift force coefficient, C_L, of the wing between the two solvers is made in Figure 4.50. Here, it can be seen that the cycle loop is highly nonlinear and is affected by the compressibility of the flow. Also, it can be seen that at $M = 0.8$ `FALCon` is less capable to reconstruct the flow features, as significant discrepancies are present.

The extended sectional flow data at $M = 0.8$ is excluded into the appendix in Section A.1.1.4 on page 197 for pitching and in Section A.1.2.4 on page 241 for plunging. However, a summary of the data for the reduced frequency $k = 0.025$ and 0.75 is presented in Figure 4.51 for the sectional pressure coefficient, c_p, and in Figure 4.52 for the friction coefficient, c_f, at three spanwise stations of the wing during the pitching motion.

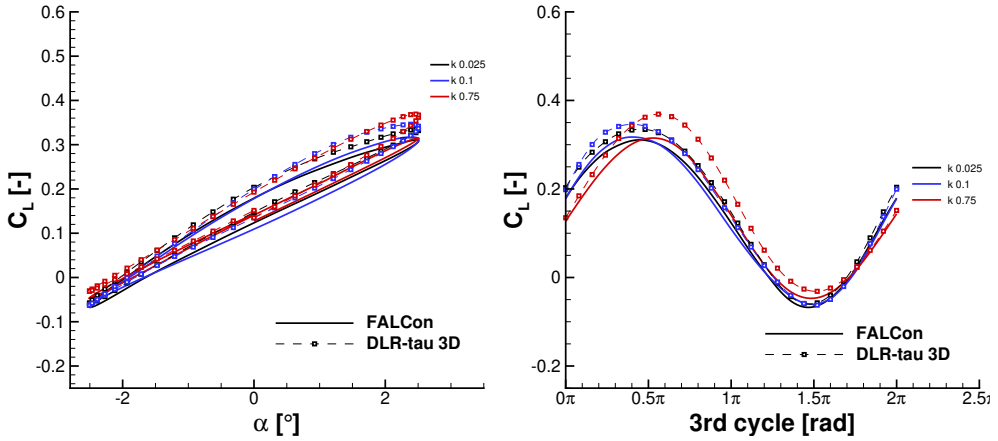

(A) Pitching, third cyle (B) Pitching, time series

FIGURE 4.50: 3D NACA2412–wing in unsteady flow at $M = 0.8$, $Re = 5.5 \times 10^6$, Sweep 0.0°

It can be seen that a local compressible shock is present on the upper surface of the wing which apears and disapears preiodically and extends uniformly in the spanwise direction until it hits a point where it interacts with the vortex emanating at the wing tip. The strong interaction between the shock wave and wing tip vortex, and their complex dynamics, arise from the forced motion. This complex three–dimensional physical phenomenon goes beyond the assumptions underlying the hybrid aerodynamic q3D–solver in `FALCon`, as here the hypothesis of uniform flow is invalid and limitations of the proposed fast methodology start to appear. The flow reconstruction using the hybrid aerodynamic q3D–solver falls short when the flow has a strong three–dimensionality. This can be seen in Figure 4.51 and Figure 4.52 at 50% and, especially, at 80% of the half–wing. In general, one can observe from those two figures that the reconstruction of the flow at lower frequency ($k = 0.025$) outperforms the one at higher frequency ($k = 0.75$). At the higher frequency, the shock position in the outboard sections of the wing may be erroneous.

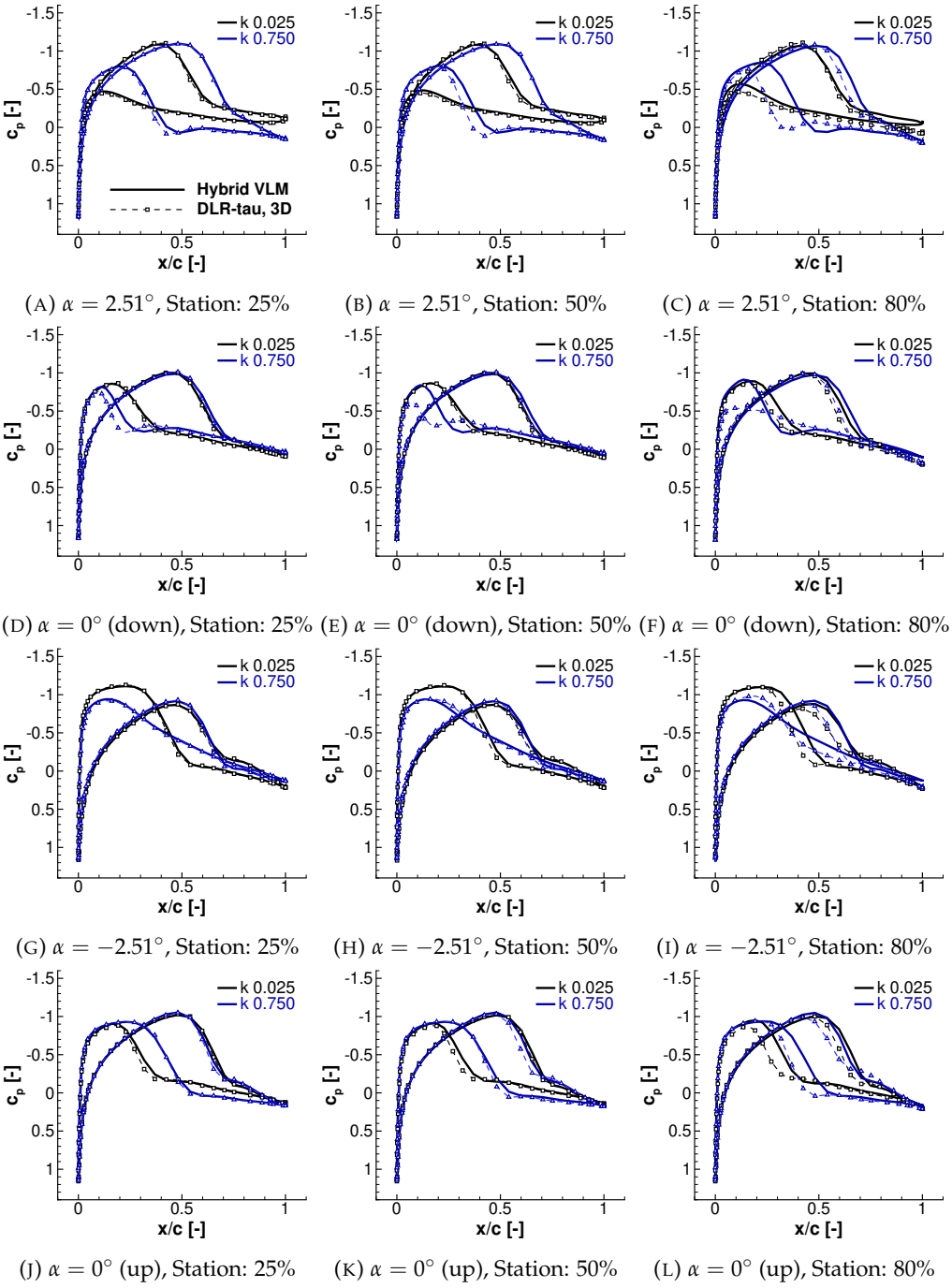

(A) $\alpha = 2.51°$, Station: 25% (B) $\alpha = 2.51°$, Station: 50% (C) $\alpha = 2.51°$, Station: 80%

(D) $\alpha = 0°$ (down), Station: 25% (E) $\alpha = 0°$ (down), Station: 50% (F) $\alpha = 0°$ (down), Station: 80%

(G) $\alpha = -2.51°$, Station: 25% (H) $\alpha = -2.51°$, Station: 50% (I) $\alpha = -2.51°$, Station: 80%

(J) $\alpha = 0°$ (up), Station: 25% (K) $\alpha = 0°$ (up), Station: 50% (L) $\alpha = 0°$ (up), Station: 80%

FIGURE 4.51: Sectional nondimensional pressure coefficient, c_p of a pitching unswept wing at $M = 0.8$ at third cycle

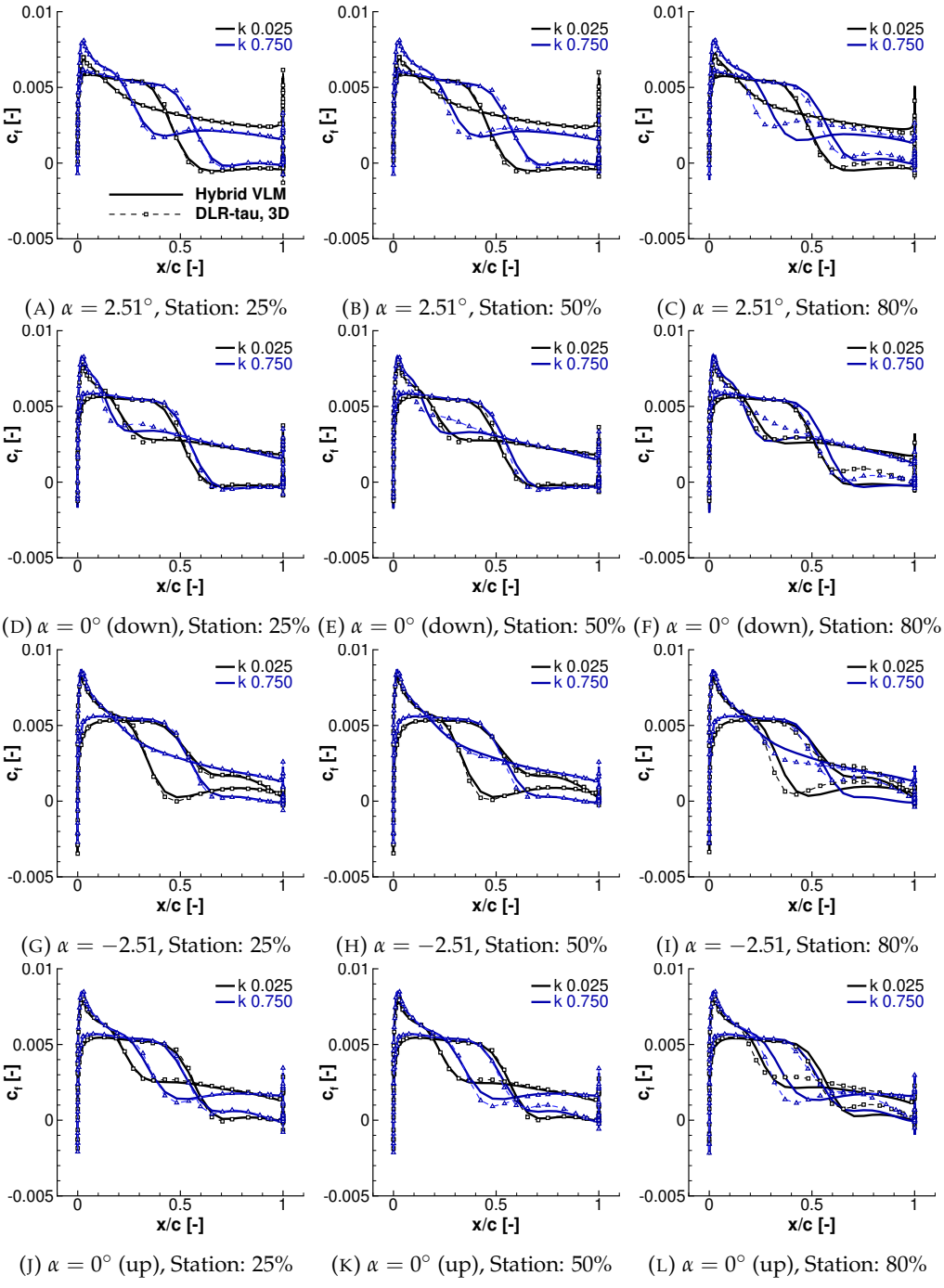

(A) $\alpha = 2.51°$, Station: 25% (B) $\alpha = 2.51°$, Station: 50% (C) $\alpha = 2.51°$, Station: 80%

(D) $\alpha = 0°$ (down), Station: 25% (E) $\alpha = 0°$ (down), Station: 50% (F) $\alpha = 0°$ (down), Station: 80%

(G) $\alpha = -2.51$, Station: 25% (H) $\alpha = -2.51$, Station: 50% (I) $\alpha = -2.51$, Station: 80%

(J) $\alpha = 0°$ (up), Station: 25% (K) $\alpha = 0°$ (up), Station: 50% (L) $\alpha = 0°$ (up), Station: 80%

FIGURE 4.52: Sectional nondimensional friction coefficient, c_f of a pitching unswept wing at $M = 0.8$ at third cycle

4.3.4 Convergence analysis

As an example, the convergence behaviour of the unsteady aerodynamic solver can be seen in Figure 4.53 for the pitching NACA2412–wing at $M = 0.7$ and $k = 0.025$ for the first six initial physical time steps. The solid red line is the average coupling residual over the span and the dashed blue line is the total lift force coefficient, C_L, of the wing. The values are plotted against the total iteration counter, which is incremented throughout the simulation. The beginning and end of a particular time step is marked in the plot. The convergence tolerance is set to $\epsilon < 1 \cdot 10^{-6}$ and the relaxation factor is set to $\nu = 5 \cdot 10^{-2}$, which has been observed as a optimal relaxation factor to provide rapid convergence rate and numerical stability. The estimated freestream angle of attack correction increments, $\Delta\alpha$, from the previous time step are used as initial guess in the next time step to accelerate additionally the convergence of the solution at the following time steps.

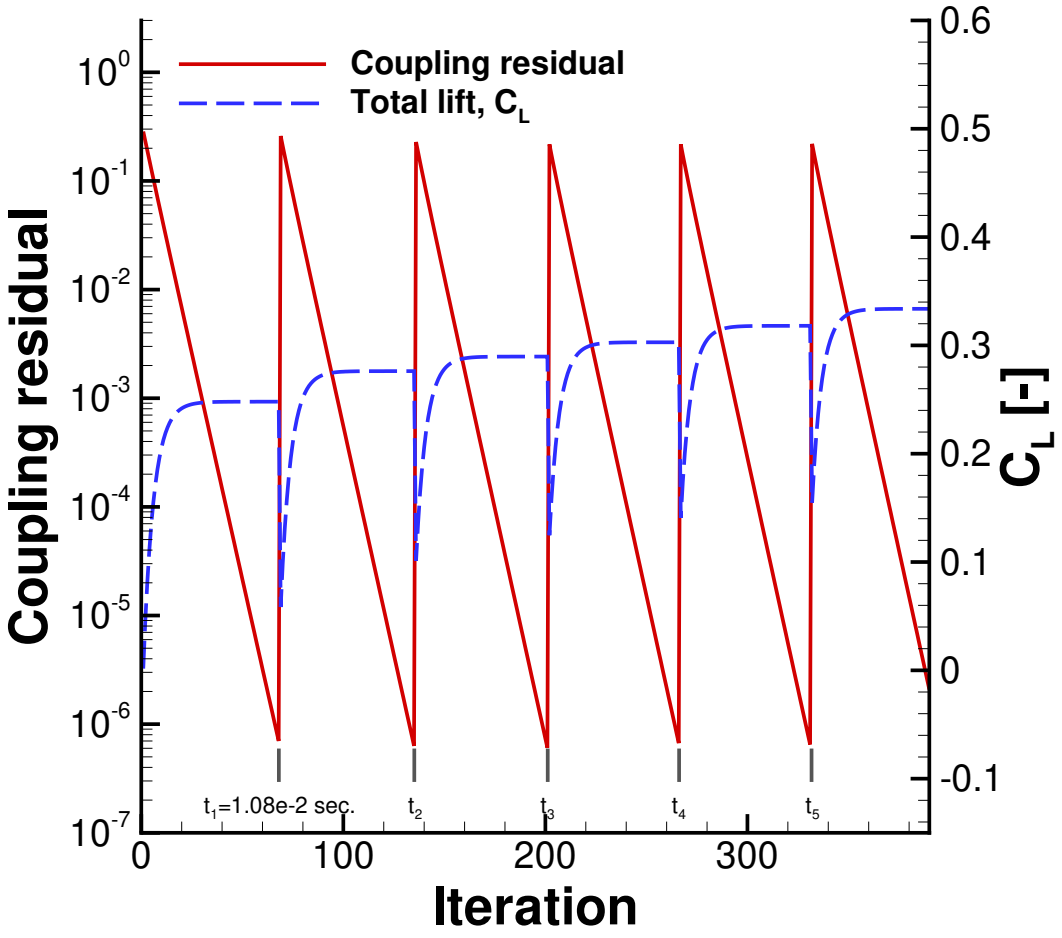

FIGURE 4.53: Convergence behavior of the unsteady aerodynamic coupling code on the pitching NACA2412–wing at $M = 0.7$ and $k = 0.025$

4.3.5 Computational cost

The calculations performed with the unsteady hybrid coupling algorithm in FALCon were running in parallel on 16 processors, where internally the computation of the required aerodynamic database (first part of the algorithm, see Figure 3.9) was performed on 16 cores for every spawned 2D URANS solver in parallel, the UVLM solution was obtained also on 16 cores in parallel and the actual coupling procedure between the UVLM solution and the database was performed on one core (second part of the algorithm). In average, 28 CPU hours (i.e. 1 hour and 45 minutes) were required for a single flow condition to run such a configuration in FALCon for three cycles with 600 dual–time stepping subiterations per physical time step and 100 physical time steps per cycle. From experience, this computational cost can be further decreased by letting the CFD solvers detect quasi–steady flow conditions in 2D sectional flow at a particular time step and exit the dual–time stepping subiterative CFD loop even earlier. However, here a fixed amount of dual–time stepping subiterations in the 2D and 3D CFD solvers are used to create results, which are comparable regarding the computational effort. Thus, the equivalent computations of the 3D CFD reference data using the same CFD settings on the coarsest 3D NACA2412 CFD mesh wing with nearly 2 Mio. grid points required in average 1404.7 CPU–hours for three cycles with 100 physical time steps per cycle (i.e. nearly 22 hours on 64 parallel processors). Therefore, an average speedup factor of 5×10^1 is reached compared to equivalent 3D DLR-tau calculations, which is in between the first and second–order of magnitude.

4.3.6 Summary

This section has presented the results of test cases obtained by the unsteady aerodynamic q3D–solver. The capabilities of the novel aerodynamic solver, which is extended by the author of this work from the steady–state formulation of the aerodynamic q3D–coupling approach, are demonstrated using an unswept NACA2412–wing. The aerodynamic loads are estimated while the wing undergoes a forced harmonic oscillation in pitch or plunge. It is shown that at three different reduced frequencies, $k = 0.025$, $k = 0.1$ and $k = 0.75$, the solver is able to estimate unsteady loads. However, the accuracy of the results at $k = 0.75$ is slightly lower compared to quasi–steady flow at $k = 0.025$. Nevertheless, at all three frequencies the shape of the chordwise c_p and c_f distributions at several span positions is captured in most cases very well and are comparable to equivalent three–dimensional reference data. For the transonic Mach–number, $M = 0.8$, the shock–induced flow separations are captured also in most cases correctly as long as the flow is in spanwise direction locally fully developed.

However, the method fails to capture the aerodynamic load at regions of the wing where not fully developed flow along the span and complex local three–dimensional flow effects are present, i.e. local flow separation spots and interaction between the shock wave and the wing tip vortex.

Moreover, same as for the steady–state formulation the accuracy at the wing tip is slightly decreased for all Mach–numbers as also here a three–dimensional wing tip vortex is present and, therefore, the flow is not fully developed along the span of the wing. Nevertheless, a great trade–off between accuracy and computational cost is achieved by a speedup factor of 5×10^2 compared to full–fidelity three–dimensional computations with 3D URANS `DLR-tau` CFD solver.

4.4 Aeroelasticity

This section concerns a number of aeroelastic test cases in steady–state flow regimes. The results are obtained using the computational FSI–framework `FlexiFALCon`, which is an extension of the `FALCon` framework, validated in previous sections of this chapter, to calculate aerodynamic loads around flexible wing geometries.

4.4.1 Inviscid steady–state NACA0012–wing

In this section a validation test case is presented, in which the linear Vortex–Lattice method (VLM) is coupled with the nonlinear beam model (GEBT) using an isotropic HALE–wing geometry[67][38][87]. In Table 4.11 the structural data of this unswept $AR = 32$ wing is presented. It is an ultra–light wing design with an overall span of 32 m, which has been used in many test cases in the scientific community for validation purposes of computational aeroelasticity frameworks[4]. The freestream flight conditions of these wings are taken from the 1976's Standard Atmosphere model according to a cruise flight level of $H = 20km$. Thus, the freestream density is $\rho_\infty = 0.088\ kg/m^3$ and the freestream velocity is set to $V = 25\ m/s$.

Property	**Unit**	**Value**
Half span	m	16.0
Chord	m	1.0
Mass per unit length of span	kg/m	0.75
Spanwise elastic axis	$-$	50% chord
Center of gravity	$-$	50% chord
Bending rigidity, EI_2	Nm^2	2×10^4
Torsional rigidity, GJ	Nm^2	1×10^4
Bending rigidity (edgewise), EI_3	Nm^2	4×10^6

TABLE 4.11: Patil's isotropic HALE–wing[67]

Here, linear Vortex–Lattice method (VLM) is employed to address the estimation of inviscid aerodynamic loads. The total aerodynamic lift force coefficient, C_L, of a wing obtained by VLM is lower compared to the load estimation obtained using the finite–state aerodynamic model introduced by Peters[70], as the local sectional lift at the wing tips in VLM is reduced due to the wing tip vortex. Thus, the strip–theory is usually overestimating the local spanwise lift at the wing tips leading to a higher deflection and torsion of the wing. Therefore, a direct comparison between VLM and 2D strip–theory on a flexible wing would show a discrepancy in the results. Thus, in this validation study, the results obtained by the linear VLM and nonlinear GEBT model using this wing geometry are also compared with Ref. [87] where Smith et. al. present

numerical data of the same validation test case obtained by a nonlinear beam model in combination with a linear aerodynamic panel–code and inviscid three–dimensional CFD model. Further, Hallissy presented in 2011 also a validation campaign of such an FSI–framework in Ref. [38], where several aerodynamic models were employed to obtain the aerodynamic loads on such a HALE–wing in combination with a nonlinear geometrically exact beam–based FEM–model.

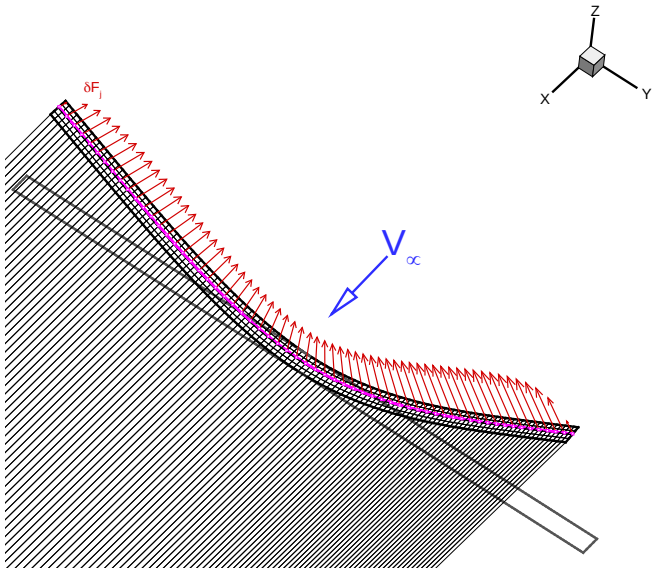

FIGURE 4.54: Patil wing at $\alpha = 4.0°$ and $V = 25\ m/s$, GEBT and linear VLM

In Figure 4.54 the deformed wing geometry is shown at this high–altitude flight condition and the freestream angle of attack of $\alpha = 4°$. This solution is obtained by `FlexiFALCon`. The purple bold line represents the beam geometry and the red arrows the mapped aerodynamic forces on the beam nodes, which are mapped from the VLM lattice mesh.

In Figure 4.55 the deflection and twist of the wing tip of this wing configuration is shown with respect to the freestream velocity and is compared with results presented in Ref. [4]. In this work the authors used the 2D strip theory to estimate the aerodynamic load on the wing, which overestimates the sectional aerodynamic lift force especially close to the wing tips. Therefore, for validation purposes two sets of results are presented obtained by the presented computational framework: In first set the sectional lift is estimated using the 2D strip theory as described in Ref. [4], and in the second set the linear VLM model of `FALCon` is employed. It can be seen, that the wing deflection and twist obtained by the computational framework involving VLM are slightly underestimated due to the lower (and more accurate) lift distribution. However, both data sets are showing good agreement with the reference results.

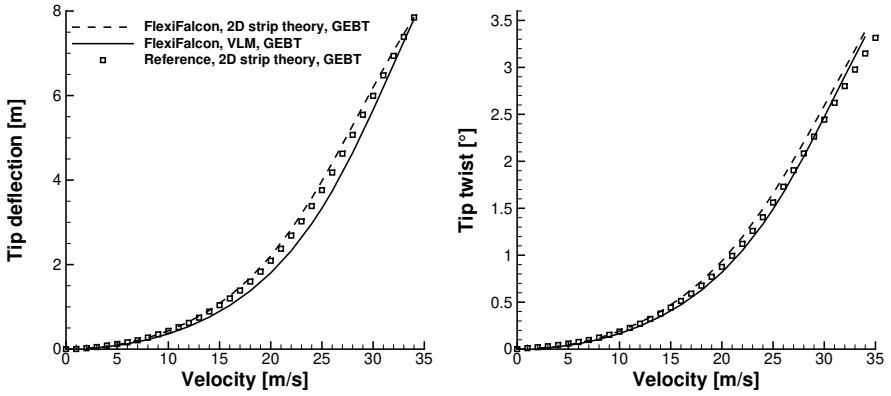

(A) Wing deflection (B) Wing twist

FIGURE 4.55: Patil wing at $\alpha_\infty = 2^\circ$ and cruise altitude of $H = 20000\ m$. Comparison of 2D strip theory and VLM 3D aerodynamic model in combination with linear beam and nonlinear GEBT model, Ref. [4]

The results of this validation study at a single flight condition are presented in Figure 4.56 for two freestream angles of attack, $\alpha_\infty = 2^\circ$ and $\alpha_\infty = 4^\circ$. Here, the results of the nonlinear beam model in combination with linear VLM obtained by `FlexiFALCon` are compared with reference results, where a linear panel code is used in combination with a corresponding nonlinear beam model[87]. In Figure 4.56a the shape of the static wing deflection, in Figure 4.56b the corresponding wing twist along the span and in Figure 4.56c the lift distribution are presented. Two reference data sets are available at $\alpha_\infty = 2^\circ$ and $\alpha_\infty = 4^\circ$. It can be seen, that at $\alpha_\infty = 4^\circ$ the lift distribution, estimated by Smith's panel code, is slightly under–predicted, leading to a small discrepancy of the wing deflection and twist at $\alpha_\infty = 4^\circ$. Finally, in Figure 4.56d the convergence of the maximal structural displacement vector

$$\max \left| [\Delta x^b, \Delta y^b, \Delta z^b, \Delta\theta_x^b, \Delta\theta_y^b, \Delta\theta_z^b]_j^T \right| \rightarrow 0 \quad k \in [1, N_b] \tag{4.8}$$

for all beam nodes and the total linear lift force coefficient, C_L, of the wing are shown for $\alpha_\infty = 2^\circ$ and $\alpha_\infty = 4^\circ$. Here, N_b is the total number of beam nodes.

In Figure 4.57 the corresponding comparison is made, where the hybrid q3D–solver of `FlexiFALCon` is used to estimate the aerodynamic loads at low subsonic speed. The results are compared also at the same flight conditions with results obtained by Smith[87], where inviscid CFD code was used to estimate the aerodynamic loads. It can be clearly seen that the projected wing span of the deformed wing is shortened due to the high vertical deflection, while keeping the total length of the slender structure constant. This can not be modelled with a classical linear beam model due to its linearisation and assumption of small geometrical deformations, which leads to a nonphysical effective

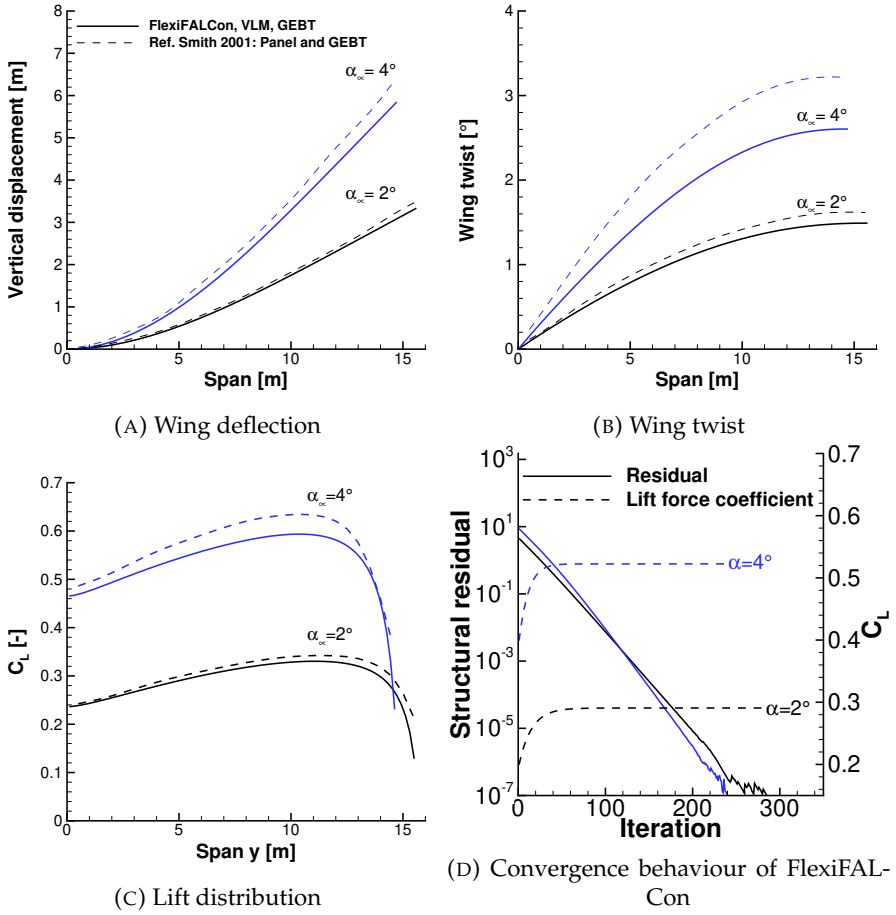

(A) Wing deflection

(B) Wing twist

(C) Lift distribution

(D) Convergence behaviour of FlexiFALCon

FIGURE 4.56: Patil wing at $\alpha_\infty = 2°$ and cruise altitude of $H = 20000\ m$. Comparison of nonlinear GEBT model and linear VLM with[87]

stretching of the wing along its deflected span axis.

In this section it is demonstrated that `FlexiFALCon` is capable of estimating efficiently aeroelastic quantities like wing deflection, twist and aerodynamic load on a highly flexible ultra–light HALE wing when a linear or hybrid q3D–solver is employed in combination with the structural nonlinear GEBT model. The results, obtained by `FlexiFALCon` are in good agreement with reference data sets provided by Smith[87].

4.4.2 Viscous NACA0012–wing in compressible flow

In this section a viscous nonlinear case of a NACA0012–wing is presented, where the estimation of aerodynamic loads is performed over a wide range of the flow velocity including compressible transonic flow regimes (until $M = 0.7$). For this case Palacios was coupling a full–fidelity CFD solver with a geometrically nonlinear beam model[65]. It is also an isotropic wing. The dimensions of this wing are the same as for the wing

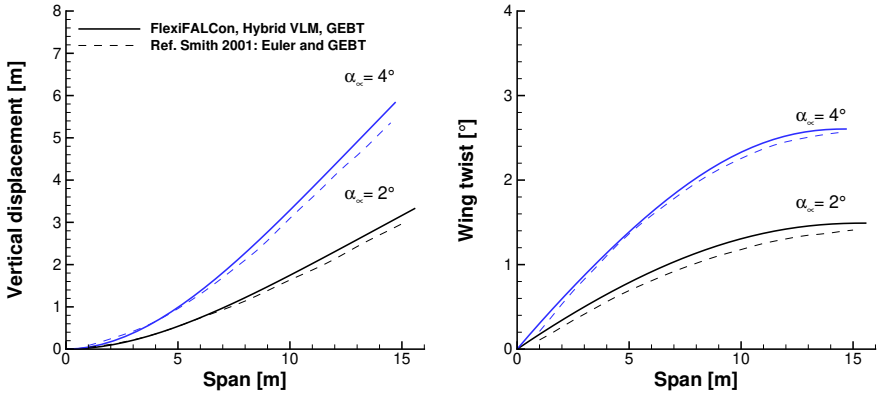

(A) Wing deflection

(B) Wing twist

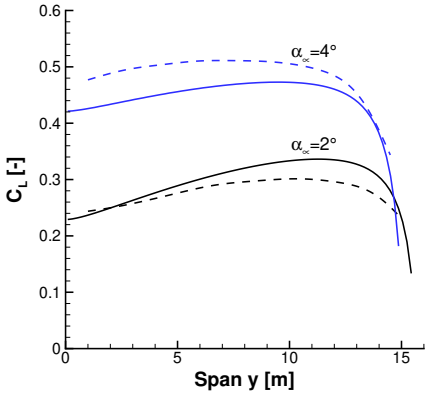

(C) Lift distribution

FIGURE 4.57: Patil wing at $\alpha_\infty = 2^\circ$ and cruise altitude of $H = 20000\ m$. Comparison of nonlinear GEBT model in combination with the hybrid aerodynamic VLM coupling code with Smith[87]

presented in the previous section: The total wingspan is 32 m, and the constant wing chord is $c = 1\ m$. A NACA0012 aerofoil is used along the span of the reference wing geometry, and the stiffness of this wing is increased compared to the classical test case of Patil as it has to withstand higher aerodynamic loads at transonic flow regimes. In Table 4.12 the modified structural and geometrical properties of this NACA0012–wing are presented.

Property	**Unit**	**Value**
Half span	m	16.0
Chord	m	1.0
Spanwise elastic axis	–	25% chord
Bending rigidity, EI_2	Nm^2	8×10^6
Torsional rigidity, GJ	Nm^2	1×10^7
Bending rigidity (edgewise), EI_3	Nm^2	–
Airfoil	–	NACA0012

TABLE 4.12: Palacios' isotropic wing[65]

The freestream flight conditions are kept the same as for Patil's wing in his thesis. The

altitude is $H = 20\ km$ and the freestream density is $\rho_\infty = 0.088\ kg/m^3$. Compared to Patil's wing, here, the aeroelastic axis is moved to 25% of the local chord, leading to a negligible twist of the wing under aerodynamic loads. The employed VLM lattice of the half–wing has $N_j = 100$ spanwise and $N_i = 1$ chordwise vortex–ring elements. The estimation of the aerodynamic loads is performed in this study by the aerodynamic hybrid q3D–coupling algorithm. Therefore, an aerodynamic database of the 2D lift force coefficients along the freestream angle of attack, α, and Mach–number, M, is precomputed by preforming steady–state 2D CFD RANS calculations with the 2D `DLR-tau` CFD solver. The one–equation Spalart–Allmaras turbulence model in its original formulation[88] is employed to model the turbulent boundary layer.

In Figure 4.58 the tip deflection of this NACA0012–wing is shown at different flow velocities. Here, two data sets are obtained using `FlexiFALCon` by employing the hybrid q3D–coupling method and linear VLM. It can be seen that at the higher Mach–number of $M = 0.7$ the wing tip deflects by 28.2% for the linear VLM solver in inviscid flow and by 33.5% for the hybrid q3D–solver in compressible viscous flow with respect to the semi–span of the wing. By employing the hybrid q3D–solver within the FSI–coupling procedure in `FelxiFALCon`, it can be seen that the results are deviating by nearly 5%. The results of the hybrid q3D–solver are in a good agreement with the nonlinear reference data presented by Palacios, who used a three–dimensional CFD RANS solver in combination with a geometrically exact nonlinear beam model[65].

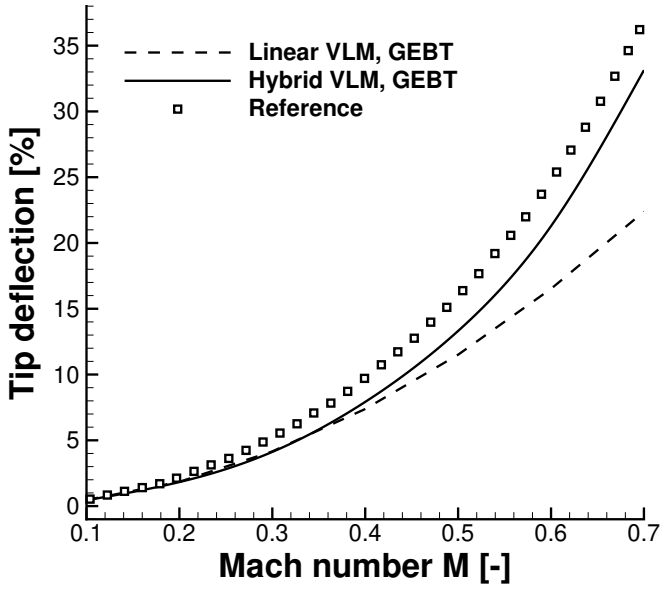

FIGURE 4.58: Normalized wing deflection vs. Mach number at a constant freestream angle of attack $\alpha = 2°$, Ref. [65]

In Figure 4.59a the shape of the wing deflection is shown for this wing at several Mach–numbers ranging from $M = 0.1$ till $M = 0.7$ and in Figure 4.59b the corresponding lift

distribution is shown. At low flow velocities, the shape of the lift distribution is generally similar to an undeformed high–aspect ratio wing. However, at high Mach–number $M = 0.7$ a reduction of the local lift at the outer half of the semi–span is notable.

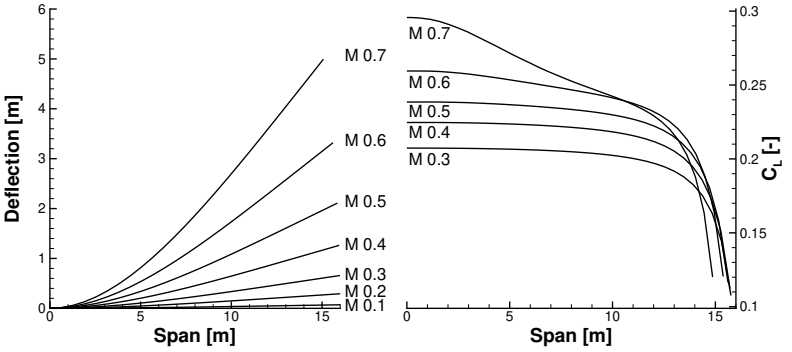

(A) Vertical wing deflection (B) Lift distribution

FIGURE 4.59: Wing deflection and aerodynamic load at $\alpha_\infty = 2°$ using the hybrid aerodynamic coupling algorithm and nonlinear beam model

In Figure 4.60a the sectional pressure coefficient, c_p, of the wing is shown at $M = 0.7$ at three spanwise positions. Further, in Figure 4.60b the corresponding lift distribution which is obtained by the q3D–coupling method in combination with GEBT is compared to linear VLM in combination with GEBT at $M = 0.7$. Here, it can be seen that the compressibility of the fluid needs to be considered as the nonlinear shape and the total lift force coefficient, C_L, differs significantly from results which are obtained in this aeroelasticity analysis employing linear VLM.

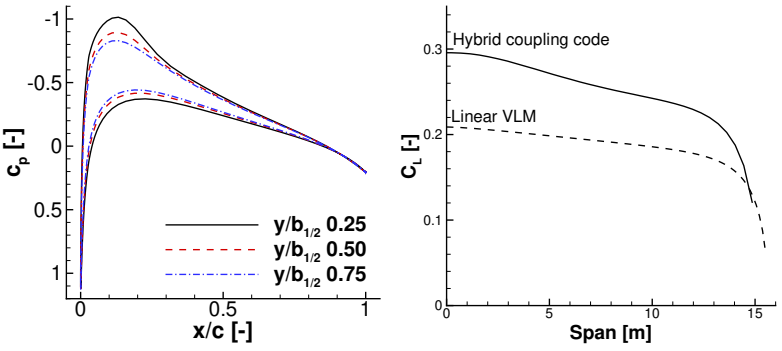

(A) Sectional nondimensional pressure coefficient, c_p, obtained by steady–state q3D solver and GEBT (B) Lift distribution

FIGURE 4.60: Aerodynamic load of statically deformed NACA0012–wing at $M = 0.7$ and $\alpha_\infty = 2°$

The corresponding sectional aerodynamic flow field is presented in Figure 4.61. Here, the Mach–number and c_p–field at three different span positions, 25%, 50% and 75% of the half–span, are shown for results at $M = 0.7$ obtained by the hybrid aerodynamic q3D–coupling code and GEBT. The sectional data is shown according to the effective

angle of attack, $\hat{\alpha}_e$, at the particular span position with respect to the local deformed frame of reference, $< \hat{x}_a, \hat{y}_a, \hat{z}_a >$, see Figure 3.12.

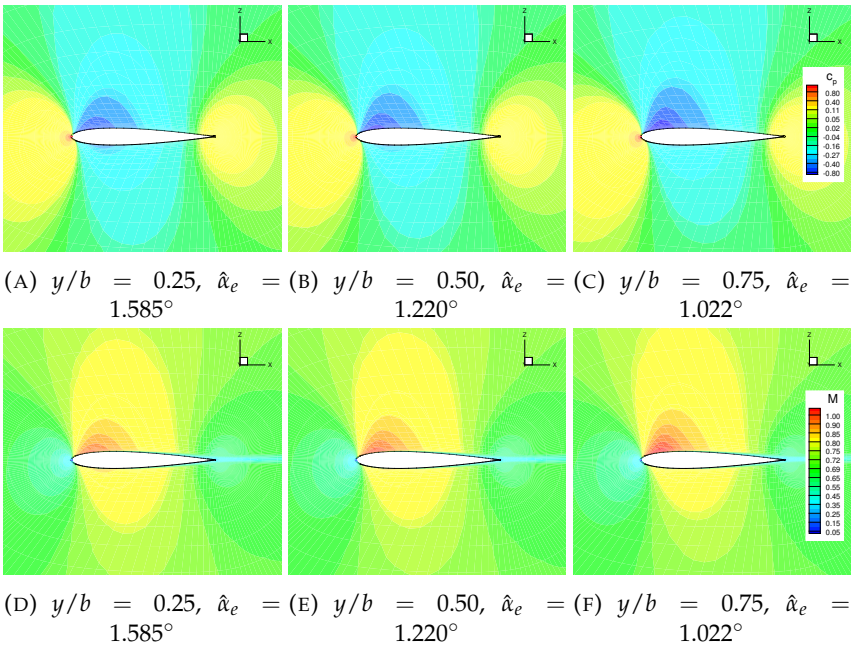

(A) $y/b = 0.25$, $\hat{\alpha}_e = 1.585°$ (B) $y/b = 0.50$, $\hat{\alpha}_e = 1.220°$ (C) $y/b = 0.75$, $\hat{\alpha}_e = 1.022°$

(D) $y/b = 0.25$, $\hat{\alpha}_e = 1.585°$ (E) $y/b = 0.50$, $\hat{\alpha}_e = 1.220°$ (F) $y/b = 0.75$, $\hat{\alpha}_e = 1.022°$

FIGURE 4.61: Sectional flow of the deformed NACA0012–wing at $M = 0.7$ and $\alpha_\infty = 2°$

In Figure 4.62 the inner parameters of the hybrid q3D–solver for the first and last iteration are presented. The spanwise effective angle of attack distribution, $\hat{\alpha}_e$, with respect to the local aerodynamic coupling frame of reference is shown in Figure 4.62a, the correction increment of the freestream angle of attack, $\Delta\alpha$, with respect to the undeformed aerodynamic frame of reference, $< x_a, y_a, z_a >$, is show in Figure 4.62b and, finally, the correction increment of the side–slip angle, $\Delta\beta$, also with respect to the undeformed aerodynamic frame of reference is presented in Figure 4.62c. At the overall freestream angle of attack, $\alpha_\infty = 2°$, the maximal effective angle of attack is $\hat{\alpha}_e = 1.85°$. Due to the wing deflection, $\Delta\beta \approx 0.2°$, is also positive in this case.

The convergence of `FlexiFALCon` for this transonic NACA0012–wing at $M = 0.7$ and $\alpha = 2°$ is presented in Figure 4.63 for the structural and aerodynamic domain, i.e. the hybrid q3D–solver and GEBT solver. Also, the convergence of the total lift force coefficient, C_L, of the flexible wing geometry is shown in the same figure. In this section only one aerodynamic coupling iteration in the aerodynamic q3D–coupling solver is preformed per FSI–coupling step. As `FALCon` saves the aerodynamic correction increments for the angle of attack, $\Delta\alpha$, and side–slip angle, $\Delta\beta$, for the next iteration, the convergence of the structure, see Equation 4.8, and the aerodynamic convergence in the q3D–coupling solver of `FALCon` are performed hand–in–hand in parallel. This saves additional computational cost. For the aerodynamic system and for the FSI–coupling

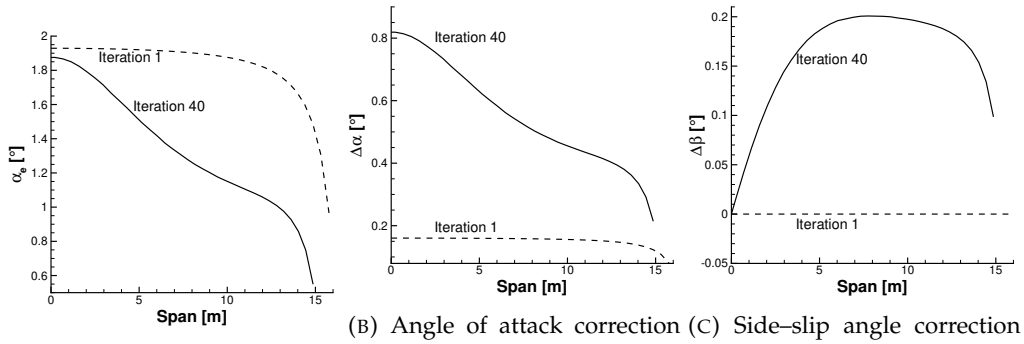

(A) Effective angle of attack, $\hat{\alpha}_e$ (B) Angle of attack correction incriment, $\Delta\alpha$ (C) Side–slip angle correction incriment, $\Delta\beta$

FIGURE 4.62: Spanwise hybrid VLM parameters of the NACA0012–wing at $M = 0.7$ and $\alpha_\infty = 2°$

procedure a constant relaxation factor of $\nu_{q3D} = 0.1$ and $\nu_{FSI} = 0.1$ is used leading to a stable convergence behaviour.

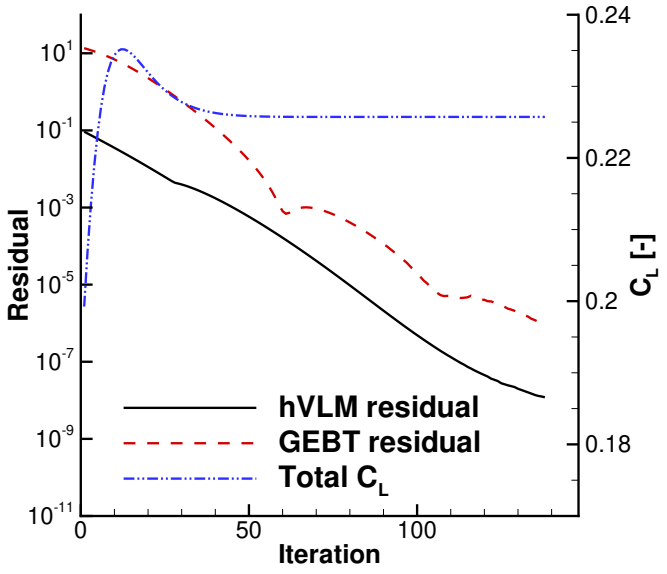

FIGURE 4.63: Convergence behavious of hybrid VLM and GEBT at $M = 0.7$, $\alpha = 2°$

Finally, in Figure 4.64 the total aerodynamic lift force coefficient, C_L, of this wing is shown over the freestream angle of attack, α_∞, separately for $M = 0.3$, $M = 0.5$ and $M = 0.7$. At subsonic flow regimes at $M = 0.3$, due to the low velocity (and therefore lower absolute aerodynamic forces), the influence of the flexibility of the wing on the aerodynamic lift due to the much stiffer structure compared to Patil's original wing is nearly not notable. However, at $M = 0.7$ the reduction of the aerodynamic lift force coefficient, C_L, is clearly notable and can not be neglected during a preliminary sizing study of such future lightweight and flexible aeroplane wing configurations.

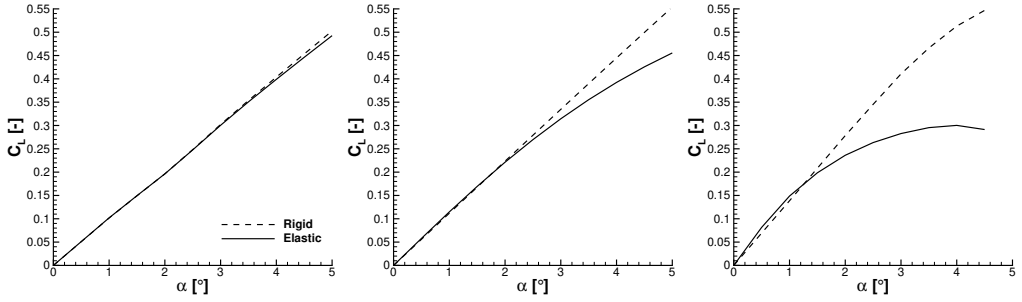

(A) $M0.3$ (B) $M0.5$ (C) $M0.7$

FIGURE 4.64: Rigid and elastic NACA0012 wing, hybrid VLM and GEBT

The computational cost can be expressed as the average and maximal required CPU–time to run one case. For the seven cases of this flexible NACA0012–wing, presented in Figure 4.58, an average CPU–time of 43 seconds and the maximal CPU–time of 45 seconds are required. In average, 137 FSI– and aerodynamic iteration and maximal 149 iterations were required to obtain a numerical solution. The aerodynamic convergence tolerance in all cases is $\varepsilon_{hVLM} < 1 \cdot 10^{-7}$ and the overall aeroelastic equilibrium residual is $\varepsilon_{FSI} < 1 \cdot 10^{-6}$.

4.4.3 Summary

In this section an application of the aerodynamic framework `FALCon` is demonstrated within a steady–state computational FSI–framework `FlexiFALCon`. In the first part of this section this computational aeroelasticity framework is validated using linear VLM and nonlinear structural GEBT solver by using the well–known test case of a ultra–light and ultra–flexible HALE–wing of $AR = 32$ which is defined by Patil. In the second part of this thesis steady–state nonlinear viscous and compressible aerodynamic q3D–coupling method in combination with GEBT is validated at several Mach–numbers by using a much stiffer wing based on Patil's wing geometry. Here, the results are compared to reference data (see Ref. [65]) and show that the numerical solution obtained by `FlexiFALCon` is in good agreement with those reference results. Due to the fact that the computational cost of the hybrid q3D–solver is several orders of magnitude lower than the computational cost of a 3D RANS CFD solver for an equivalent geometry it can be stated that due to the low overall computational cost of `FlexiFALCon` it is possible to use this approach for the prediction of steady–state aerodynamic loads on flexible wing geometries in the industrial environment during conceptual sizing studies of lightweight HAR–wings.

Chapter 5

Conclusion

Over the last decade an effort has been made by the industry to introduce high aspect ratio wings in commercial aviation with the goal of increasing the aerodynamic efficiency, (C_L/C_D), and therefore the overall efficiency of an aeroplane. However, due to the increased flexibility of such a wing additional uncertainties during the conceptual design stage are present, which introduce not negligible overall project risks. The approach in this thesis is to research and construct physics–based models, which can address the additional physical phenomena on such a flexible high aspect ratio wing, which have been previously neglected or estimated using knowledge–based semi–empirical methods. To address efficiently the additional effects coming from the structural flexibility of such a highly loaded lightweight composite wing, the physical modelling of the aeroelastic response is essential and has to be introduced as early as possible during the initial stage of the design project. Therefore, a physics–based engineering tool is required which covers the rapid estimation of steady–state and unsteady aerodynamic load assessments on rigid and flexible wing geometries in subsonic and transonic flow regimes. This engineering tool has to provide accurate results, acceptable for the conceptual and early preliminary design procedures, while requiring low computational cost.

In this thesis, the computational aerodynamic framework `FALCon` and the aeroelastic framework `FlexiFALCon` are presented and validation results are discussed. In both physics–based frameworks semi–empirical corrections of unmodeled flow and structural phenomena are avoided while the computational cost is kept as low as possible. In `FALCon` the complex problem of the flow around a finite–span wing is split into two much simpler problems, where the 3D flow is captured by a computationally cheap 3D linear VLM solver and corrected section–wise by a 2D or 2.5D ISW–CFD solver to take the nonlinear viscous and compressible flow phenomena into account. By incorporating sectional nonlinear data obtained by an ISW–CFD solver the framework is now modelling, as one unified engineering analysis tool, the flow in low subsonic

and high transonic flow conditions, where in the industrial environment a fragmented approach is still employed. The crossflow phenomena on swept wings is modelled in the 2.5D+ ISW–CFD solver by a crosslow momentum equation directly incorporated into the RANS–ISW equations and computed on a truly 2D aerofoil grid. This saves computational cost compared to state–of–the–art ISW–CFD solvers, because this solver performs the computations on a truly 2D airfoil grid. This quasi–3D aerodynamic approach, used for rapid aerodynamic load estimations, is extended in this thesis to unsteady flow regimes allowing unprescribed unsteady motions of the wing geometry to be carried out. This opens up, for example, the possibility to deploy `FALCon` in future studies and assess unsteady aeroelastic responses or perform low–cost nonlinear flight mechanics analyses. The architecture of the framework is build up systematically and is modular with the aim of replacing, extending and improving particular modules of the framework. In `FlexiFALCon`, within an FSI–coupling loop this aerodynamic framework is employed in combination with a geometrically–exact formulated beam model, which models the structural response of the wing. The purpose of this part of the thesis is the demonstration of a seamless integration of `FALCon` in a multi–physics simulation framework, which performs multi–disciplinary analyses of a complex swept or unswept flexible wing geometry.

The presented computational framework is implemented in the programming language Python and follow an object–oriented design. The architecture of the software is highly modular. Computationally intensive routines, for example estimation of the aerodynamic influence matrix in VLM, are moved to a dynamic link library implemented in C, and are loaded into the main Python code. The code is parallelised using the OpenMP library[20][63] and uses well optimised BLAS[9][23] and LAPACK[7][22] libraries to perform linear algebra operations solving the system of linear equations in steady–state and unsteady VLM. Due to the flexible nature of the Python programming language `FALCon` can be easily integrated into other computational frameworks as demonstrated with `FlexiFALCon` or a wing twist optimiser presented in Ref. [108].

5.1 Project summary

During this project a mixed–fidelity low–cost computational aerodynamic framework `FALCon` was implemented, which combines a low–fidelity three–dimensional Vortex–Lattice method (VLM) with nonlinear 2D or 2.5D+ sectional wing aerodynamic data computed by the 2.5D+ ISW–CFD (U)RANS–CFD solver, which resolves flow nonlinearities due to the viscosity and compressibility of the fluid in the particular section. At the beginning of the research the linear VLM was implemented, where the linear steady–state and unsteady VLM builds the foundation of the particular aerodynamic computational framework. The formulation of the steady–state VLM solver

is presented in Section 3.2.1, while the formulation of the unsteady linear VLM is described in Section 3.2.2. The linear VLM code underwent an extensive validation campaign, which results are presented in Section 4.1.1 for the steady–state model and in Section 4.1.2 for the unsteady UVLM. On top of the linear panel code the q3D–coupling algorithm is implemented, which extends the 3D linear aerodynamic panel method by considering flow nonlinearities due to viscosity and compressibility of the fluid. For the steady–state aerodynamic q3D–coupling method the formulation is presented in Section 3.4.1. Here, the linear VLM is coupled on every wing section with precomputed nonlinear lift curves of the particular wing aerofoil. In the unsteady counterpart, presented in Section 3.4.2, the 2D/2.5D+ ISW–URANS `DLR-tau` CFD–solver is directly included into `FALCon` and obtains on–demand the sectional nonlinear viscous aerodynamic data, which is necessary to perform coupling activities also in unsteady flow regimes. The validation results for the steady–state aerodynamic q3D–coupling method of `FALCon` can be found in Section 4.2, and for the unsteady extension of the aerodynamic q3D–coupling method they can be found in Section 4.3. As a last step, the steady–state aerodynamic q3D–coupling method is applied in a computational aeroelasticity framework, where the aerodynamic solver is used to estimate the aerodynamic loads on highly deflected and twisted wing geometries during a numerical fluid–structure–interaction analysis. Therefore, the formulation of the steady–state aerodynamic q3D–coupling algorithm is extended for nonplanar, highly deflected, wing geometries. This nonplanar extension of the aerodynamic q3D–coupling method is discussed in Section 3.5.2. The modified aerodynamic q3D–coupling method and a structural model based on the exact formulation of an anisotropic beam are coupled together in one single FSI–framework, which is discussed in Section 3.5.3. This FSI–framework is called `FlexiFALCon` and is an external wrapper utilising the aerodynamic q3D–coupling approach and the open source structural solver GEBT described in Ref. [110]. The results of the validation of this efficient computational FSI–framework are presented in Section 4.4.

5.1.1 Part I: Steady–state aerodynamic coupling algorithm

The steady–state aerodynamic q3D–coupling algorithm is well known and is deployed already as an engineering analysis tool in the industrial environment. However, the particular research interest here is the analysis of the performance of such an approach in combination with the novel 2.5D+ ISW–RANS CFD formulation implemented in `DLR-tau` solver, see Section 3.3. The novelty of this ISW–CFD solver, which is not part of this work, is the ability to perform flow analysis in low subsonic and high transonic flow regimes using one unified approach. In the current industrial process a fragmented situation is still present. Thus, by applying this novel 2.5D+ ISW–CFD

solver in FALCon on swept and unswept wing geometries a unified aerodynamic q3D–coupling algorithm for low and high speed flow analysis is obtained. This novel solver (and therefore automatically the q3D–solver) resolves essential crossflow phenomena on the ISW–wing sections in the boundary layer and, therefore, estimates the flow separations and locations of the transonic shock waves on swept wing segments accurately. In Section 4.2 aerodynamic flow predictions are presented of two test cases, NACA2412–wing and DLR–F4 wing/body configuration. The NACA2412–wing test case contains a swept and unswept wing geometry. On swept wing geometries two sets of the aerodynamic data is available which is estimated by the aerodynamic q3D–coupling method. For the first set, lift curves are used which were precomputed with conventional 2D CFD solver neglecting automatically crossflow phenomena on swept wings. For the second set of the aerodynamic q3D–coupling results, sectional lift curves are used which were precomputed by the novel ISW solver including physics–based modelling of crossflow effects. Both sets of data were compared to three–dimensional reference results which are obtained by 3D DLR-tau RANS–CFD code on equivalent full–fidelity three–dimensional CFD grids of the configurations. As already mentioned in Section 3.3 the crossflow phenomena has only an influence on the aerodynamic forces at high–speed flow regimes. Therefore, for aerodynamic load analysis of swept wings in low subsonic flow regimes two–dimensional sectional nonlinear aerodynamic database is sufficient. At high–speed flows, however, the consideration of the local crossflow is essential as otherwise the viscous boundary layer and the position of the transonic shock will not be estimated accurately. Also, it is observed that this approach struggles to resolve local flow physics on wing sections where local three–dimensional inhomogeneous flow along the span is present. Such a three–dimensional flow phenomena could be the wing tip vortex, interaction between the transonic shock–wave and the wing tip vortex or local areas on the surface of the wing with detached flow at high freestream angles of attack, α_∞. For example, in Section 4.2 it can be seen that the accuracy of the local aerodynamic flow predictions at 90% of the span near the wing tip of the NACA2412–wing is decreased. The reason for that is the locally not fully developed flow along the span of the wing due to the presence of a wing tip vortex which can not be represented by 2D or 2.5D sectional aerodynamic data of that section. However, in general it can be stated that the developed steady–state aerodynamic q3D–coupling method in combination with the novel 2.5D+ ISW–RANS CFD solver is a highly efficient and unified steady–state aerodynamic analysis approach for swept and unswept wings for low– and high–speed (transonic) flow regime analyses. By including the computational cost of the ISW solver for the pre–computation of the sectional nonlinear aerodynamic data it can be also stated that this aerodynamic solver has a highly reduced computational cost and achieves a speedup factor of $6.12 \cdot 10^1$ compared to equivalent full–fidelity computations using a 3D CFD solver.

5.1.2 Part II: Unsteady aerodynamic coupling algorithm

During this research the steady–state aerodynamic coupling algorithm is extended to unsteady flow regimes. The formulation of this novel unsteady aerodynamic q3D–coupling approach is described in Section 3.4.2. The novelty here is among the first generalised formulation and implementation of an unsteady aerodynamic q3D–coupling algorithm which can estimate unsteady wing loads on the wing geometry as a response to arbitrary kinematic motions. Thus, this aerodynamic solver can be deployed in the analysis of flight physics or in unsteady computational aeroelasticity, where the motion of the VLM lattice over time is a–priory unknown. The novel 2.5D+ ISW–URANS CFD solver, which is part of the `DLR-tau` flow solver, is embedded directly into the unsteady q3D–solver of `FALCon` and the required sectional nonlinear aerodynamic data is estimated here on–demand throughout the simulation. This ensures that the solver is not only restricted to predict unsteady aerodynamic loads as a response of kinematic motions which are prescribed employing a–priori precomputed unsteady sectional aerodynamic database. The on–demand computation of the sectional aerodynamic data throughout the entire simulation at any physical time step allows to predict nonlinear aerodynamic loads on VLM lattices, which are either undergoing as a rigid body kinematic motions in time and space, i.e. flight mechanics, or their geometry is deformed due to the flexibility of the structure, i.e. unsteady aeroelastic analysis. The solver is based on UVLM and is formulated in time–domain. The validation of this solver is performed on the NACA2412–wing geometry and is presented in Section 4.3. The unsteady aerodynamic results are obtained by letting the wing geometries undergo a prescribed forced harmonic oscillation in pitch or plunge. The same as for the steady–state aerodynamic q3D–coupling solver of `FALCon`, the validation is performed by comparing the results obtained by the unsteady aerodynamic q3D–coupling method with results obtained by full–fidelity 3D `DLR-tau` CFD code. The presented unsteady q3D–solver is able to predict accurately the aerodynamics on wing geometries which are undergoing a quasi–steady or highly unsteady motion. However, the unsteady solver inherits the same disadvantages as the steady–state counterpart: The unsteady aerodynamic q3D–coupling method estimates local aerodynamic flow on wings where local three–dimensional flow effects are present with a lower accuracy compared to reference three–dimensional computations. Local detached flow, the wing tip vortex and complex interaction between the transonic shock–wave and the wing tip vortex are not resolved accuratly, as here the flow is not homogeneous along the span and the assumption of quasi–3D flow is not given. On the other side, flow separations are very well resolved as long as they have two–dimensional nature and are independent along the span. By concluding the research of this unsteady aerodynamic q3D–coupling approach it can be stated that the average speedup factor, which is achieved with the unsteady aerodynamic q3D–coupling approach, is $5 \cdot 10^1$ with respect to equivalent

computations using unsteady 3D DLR-tau CFD solver. Therefore, this unsteady aerodynamic q3D–coupling method provides a great trade–off between accuracy and required computational cost.

5.1.3 Part III: Aeroelasticity

The aerodynamic loads on flexible wing geometries can be obtained by deploying a computational aeroelasticity framework where the structural deformation of the wing structure is adjusted as long as no equilibrium is present between the aerodynamic and structural domain of the overall problem. Regarding the computational cost, most fraction of it depends usually on the aerodynamic solver employed in a computational FSI–framework. Therefore, in this research the highly efficient steady–state aerodynamic q3D–coupling method of FALCon is used as a low–cost nonlinear aerodynamic solver. Usually, the existing state–of–the–art aerodynamic q3D–coupling algorithms are formulated "flat" with respect to the span–chord layer and are not assuming a wing with deflected geometry and rotated aerofoil sections along the span. Therefore, in this work the q3D–formulation is extended by a prescribed deflection of the wing along span to make it suitable to be deployed as an aerodynamic solver in a computational aeroelasticity framework, see Section 3.5.2. To the best knowledge of the author this is the first time where an aerodynamic q3D–solver is coupled with a structural solver to obtain a mixed–fidelity aeroelastic framework. The aeroelastic system is described in Section 3.5.3. Especially the mapping procedure of the aerodynamic loads from the aerodynamic q3D–coupling solver onto the FEM–beam and the deformation of the VLM lattice with respect to the deformation of the FEM–beam are discussed here. The mapping procedure is based on linear interpolation. As the structural solver, the GEBT solver developed by Yu and Blair is used in this research[110]. It is important to take geometrical nonlinearities at high wing deflections into account by using a high–fidelity GEBT beam model. This part of the research is kept short as here the overall aim is the demonstration of the possibility of a seamless deployment of the steady–state aerodynamic q3D–coupling solver in an aeroelastic analysis of highly flexible wings. In Section 4.4 the results of the validation study of FlexiFALCon are presented and compared to reference data from literature. Here, FlexiFALCon is validated in steady–state flow regimes only. In this framework the employed aerodynamic model can be switched between the linear steady–state VLM and nonlinear steady–state aerodynamic q3D–coupling method. A great trade–off between the computational cost and accuracy is demonstrated. Such a computational aeroelasticity framework could be deployed within a future sizing study of a HAR–wing for a commercial aeroplane.

As described in Section 1.3 this approach could replace old design methodologies of aeroplane wings in the industrial environment and make a sizing study of an efficient lightweight HAR–wing feasible.

5.2 General results of this thesis

This research has increased the knowledge base in the field of rapid aerodynamic load estimations on rigid and elastic wings in following areas:

- This research helped to understand in detail the impact of the local crossflow phenomena of swept wings onto the overall aerodynamic loads at different flow velocities. By analysing the aerodynamic flow with and without modelling the crossflow phenomena while employing the steady–state aerodynamic q3D–coupling solver a comparison to reference three–dimensional full–fidelity RANS–CFD results is conducted and the impact of the crossflow onto the overall aerodynamic load at different Mach–numbers is identified. It is found that crossflow phenomena is necessary to include at high–speed flow regimes, $M > 0.5$, as a significant impact of this flow phenomena onto the aerodynamic load is notable.
- By employing the 2.5D+ ISW–CFD solver[31] a unified q3D–solver for low subsonic and high transonic flow regimes is created and validated in this thesis. Therefore, a fragmented approach, still present up–to–date in the industrial environment, is not necessary anymore.
- For unsteady flow regimes an aerodynamic q3D–solver is defined which is based on the steady–state aerodynamic q3D–coupling method and is extended with an outer time–marching loop while coupling the linear UVLM and 2D URANS CFD solver. A unified tool for unswept wing geometries is constructed, which can be used for low subsonic and high transonic flow analysis and where the wing geometry can undergo an arbitrary unprescribed motion.
- The coupling of the steady–state aerodynamic q3D–coupling approach with the nonlinear structural beam model leads to the realisation that the steady–state (and unsteady) aerodynamic q3D–coupling procedure needs to be extended by a nonplanar ability to couple the aerodynamic load on highly deflected wings. Thus, the local spanwise aeroelastic deflection angle, $\theta_{x,j}$, of the particular wing section needs to be considered during the aerodynamic q3D coupling procedure on deflected flexible wing geometries.

- The outcome of this research is the aerodynamic framework `FALCon` and aeroelastic FSI–framework `FlexiFALCon`. The two computational frameworks underwent an extensive validation campaign. Both computational frameworks are implemented from scratch by the author of this thesis and are highly extendable.

5.3 Research output

The unsteady q3D–solver of `FALCon` was presented in 2018 at the AIAA Atmospheric Flight Mechanics Conference in Georgia, USA[47] and received *2018 AIAA Atmospheric Flight Mechanics Best Paper Award*[1].

A journal paper which deals with the unsteady aerodynamic q3D–coupling algorithm is revised and accepted for the print[48]. Currently it is under final correction procedure by the authors.

The steady–state q3D–solver was extended by a wing twist variable and was used inside an optimisation framework to optimise the wing twist with the purpose of overall drag minimisation. The results were presented by Gunagda Yang at the *31st Congress of the International Council of the Aeronautical Sciences* in 2018[108].

5.4 Future work

This research shows that the hybrid aerodynamic coupling approach has a great trade–off in steady–state and unsteady flow regimes between accuracy of the numerical results and computational cost when it is compared to 3D CFD methodology. Also, it was demonstrated that such an aerodynamic solver can be easily deployed during a steady–state aeroelastic analysis. However, it is found that the effective angle of attack, α_e, is overestimated when Equation 3.50 is employed in unsteady flow regimes. As stated in Ref. [51] an accurate estimation of α_e is only possible when the involved sectional inviscid lift force coefficient, $C_{L,inv,j}$, contains only circulatory contribution. In unsteady VLM the inviscid lift force coefficient, $C_{L,inv,j}$, contains circulatory and non–circulatory contribution leading to a significantly overestimated value of α_e. Therefore, in the unsteady aerodynamic q3D–coupling method the effective angle of attack is estimated by using Equation 3.57, and is validated in this research using unswept wing geometries.

On swept geometries this approach overestimates the local spanwise lift force coefficient, C_L, at the symmetry of the wing significantly. Therefore, one of the major future effort should be made to extend the unsteady aerodynamic q3D–coupling algorithm also for swept wing geometries.

The presented computational aeroelasticity framework is for now only deployable in combination with the steady–state aerodynamic aerodynamic q3D–coupling solver of `FALCon`. In future, `FlexiFALCon` can be extended also to unsteady flow regimes and could be deployed to perform very efficiently nonlinear unsteady aeroelastic flutter or buffeting analysis on swept and unswept wing geometries. Also here, the computational cost of the overall analysis would be highly reduced due to the cost–efficient aerodynamic q3D–coupling solver approach compared to a conventional 3D unsteady URANS CFD–solver deployed in a computational FSI–framework. Also, it needs to be noted that in future research, it could be stated that a computational aeroelasticity framework where such an unsteady aerodynamic q3D–coupling method is employed is more robust as conventional computational FSI–framework where conventional unsteady 3D CFD solver is used as the aerodynamic model. The reason for this is that during the deformation procedure of the 3D CFD grid so–called "negative volumes" or highly skewed grid cells can be created which would slow down the convergence of the numerical method, decrease the accuracy of the numerical results or simply crash the simulation due to numerical instabilities. On the other side the procedure of the deformation of the thin–wing VLM lattice is highly robust compared to the deformation procedure of a three–dimensional volumetric CFD mesh. During the deformation of the wing geometry it is assumed that the shape of the sectional aerofoils is rigid and can not change its shape. Therefore, the sectional aerofoils placed at several span positions on the VLM mesh are only translated and rotated in space with respect to the current kinematics of the particular wing section. During the nonplanar aerodynamic coupling procedure within the FSI–framework the orientation of the resulting viscous aerodynamic forces coming from the sectional aerodynamic database or the 2D CFD solver instances has to be considered by the actual aeroelastic deflection angle, $\theta_{x,j}$, of the particular wing section.

Appendix A

Appendix

A.1 Sectional flow of the unswept NACA2412–wing in unsteady flow

Detailed results of the validation study of the unsteady q3D–solver by using a pichting and plunging NACA2412–wing are excluded from Section 4.3.2 to the appendix of this thesis. The wing undergoes a forced harmonic oscillation in pitch and plunge at three different reduced frequencies, $k = 0.025$, 0.1 and 0.75, and at four different freestream Mach–numbers, $M = 0.3$, 0.5, 0.7 and 0.8. For the pitch the mean angle of attack and amplitude are $\alpha_0 = 0^\circ$ and $\alpha_A = 2.51^\circ$, and for plunge the mean nondimensional vertical displacement and corresponding amplitude are $\xi_0 = 0$ and $\xi_A = 0.1$. The time history of the pitching angle of attack is described by Equation 4.3 and the nondimensional vertical displacement is described by Equation 4.4.

It has to be mentioned that in the following figures, where the upper wing surface is shown with the particular contour plot, $\varphi = \pi/2$ of the third cycle corresponds to the maximal position, $\varphi = \pi$ correspond to the mean downstroke position, $\varphi = 3\pi/2$ corresponds to the minimal position, and finally $\varphi = 2\pi$ corresponds to the mean upstroke position of the pitching angle of attack or vertical plunging displacement of the wing.

A.1.1 Unsteady force harmonic pitching oscillation

A.1.1.1 Mach $M = 0.3$

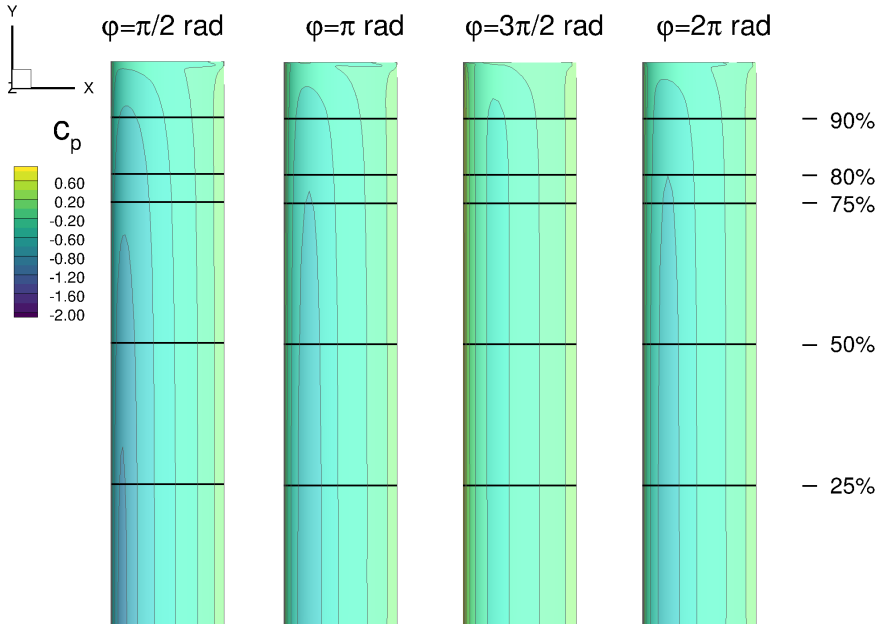

FIGURE A.1: Pressure coefficient, c_p, of the NACA2412–wing at $M = 0.3$ and $k = 0.025$ during forced harmonic pitching oscillation, third cycle

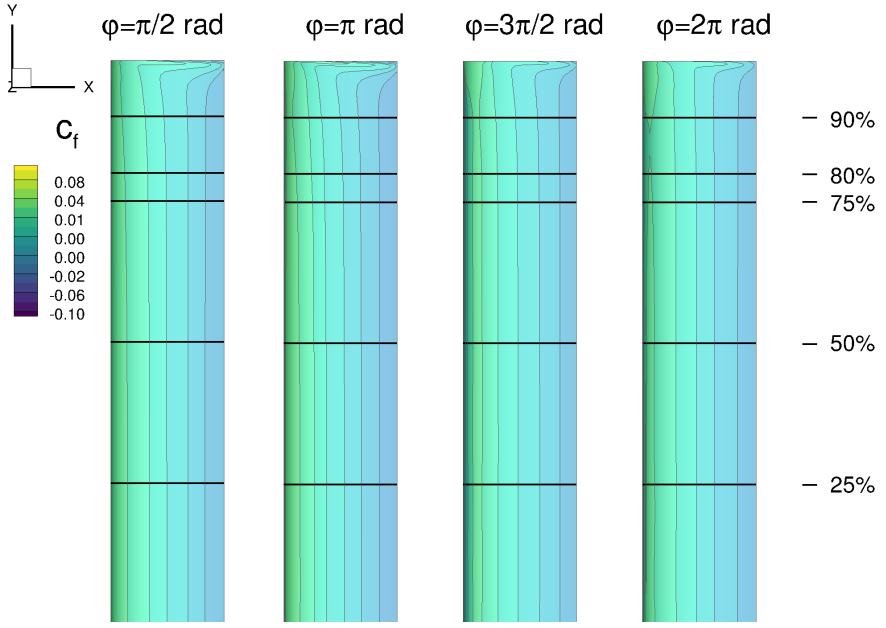

FIGURE A.2: Friction coefficient, c_f, of the NACA2412–wing at $M = 0.3$ and $k = 0.025$ during forced harmonic pitching oscillation, third cycle

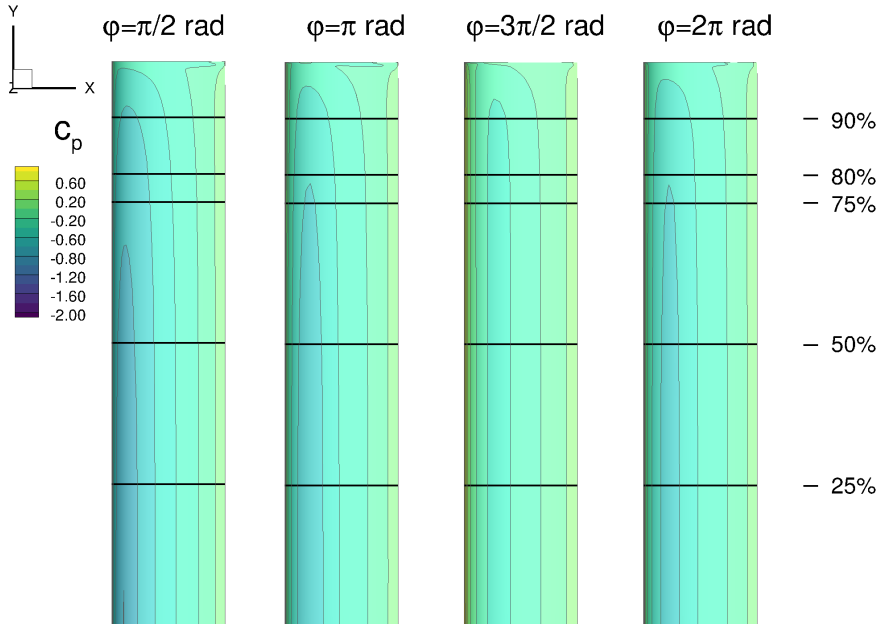

FIGURE A.3: Pressure coefficient, c_p, of the NACA2412–wing at $M = 0.3$ and $k = 0.100$ during forced harmonic pitching oscillation, third cycle

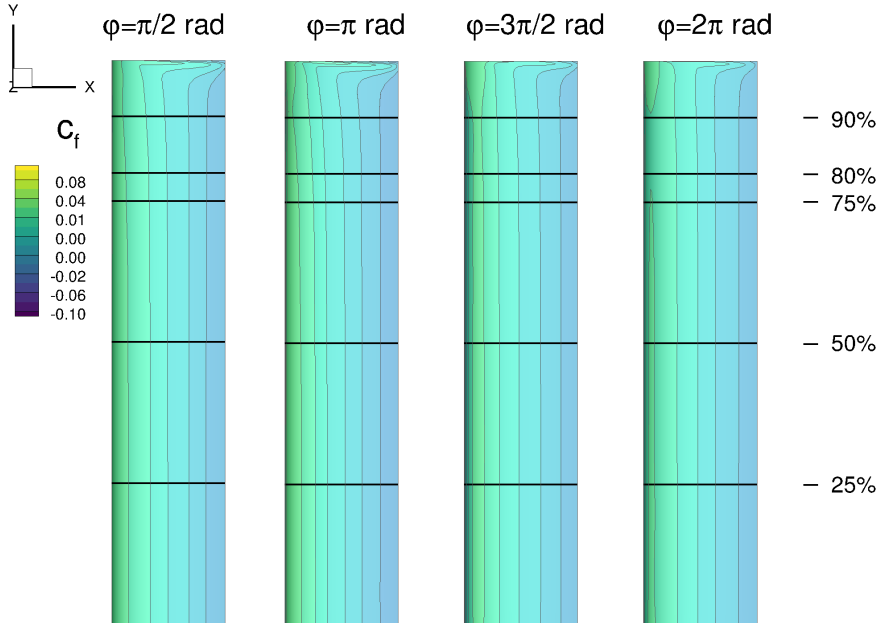

FIGURE A.4: Friction coefficient, c_f, of the NACA2412–wing at $M = 0.3$ and $k = 0.100$ during forced harmonic pitching oscillation, third cycle

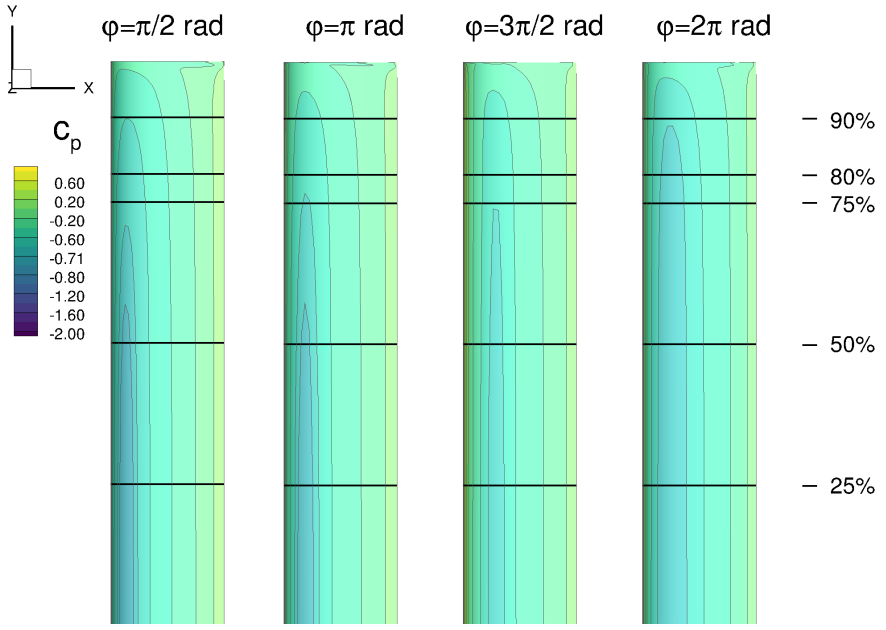

FIGURE A.5: Pressure coefficient, c_p, of the NACA2412–wing at $M = 0.3$ and $k = 0.750$ during forced harmonic pitching oscillation, third cycle

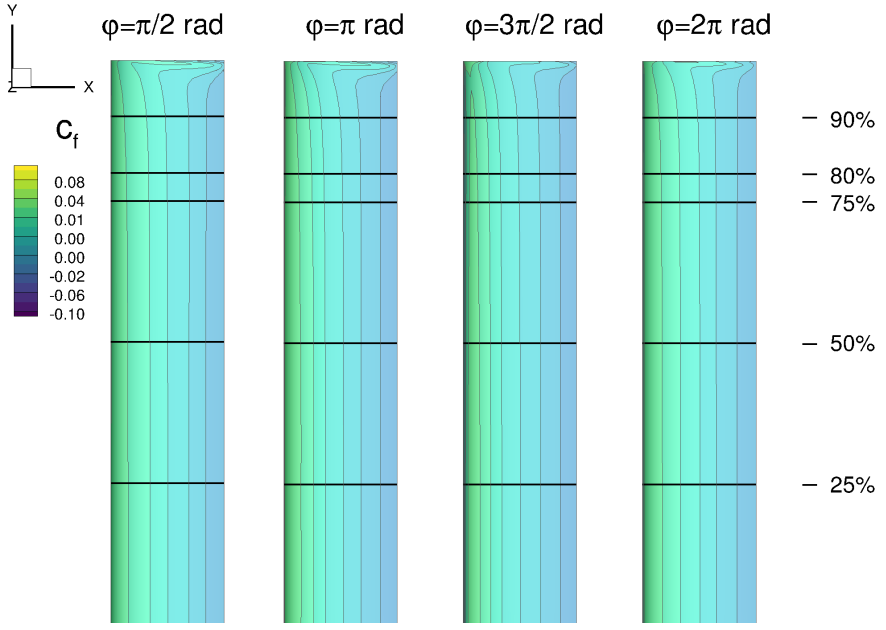

FIGURE A.6: Friction coefficient, c_f, of the NACA2412–wing at $M = 0.3$ and $k = 0.750$ during forced harmonic pitching oscillation, third cycle

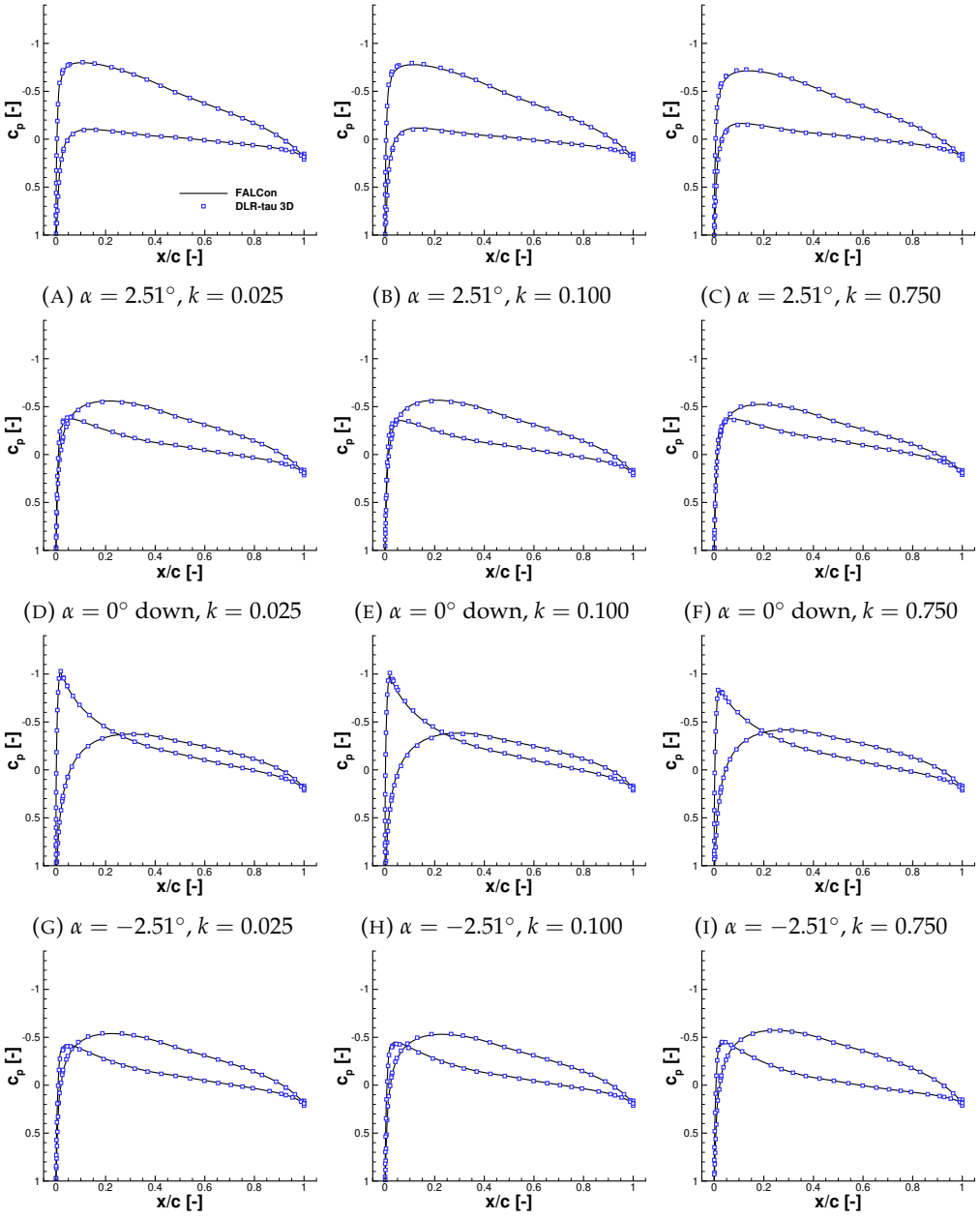

(A) $\alpha = 2.51°$, $k = 0.025$ (B) $\alpha = 2.51°$, $k = 0.100$ (C) $\alpha = 2.51°$, $k = 0.750$

(D) $\alpha = 0°$ down, $k = 0.025$ (E) $\alpha = 0°$ down, $k = 0.100$ (F) $\alpha = 0°$ down, $k = 0.750$

(G) $\alpha = -2.51°$, $k = 0.025$ (H) $\alpha = -2.51°$, $k = 0.100$ (I) $\alpha = -2.51°$, $k = 0.750$

(J) $\alpha = 0°$ up, $k = 0.025$ (K) $\alpha = 0°$ up, $k = 0.100$ (L) $\alpha = 0°$ up, $k = 0.750$

FIGURE A.7: Sectional pressure coefficient, c_p, of the third cycle of the pitching unswept NACA2412 wing at $M = 0.3$ and $\Delta\alpha_A = 2.51°$, at 25% of the half–span

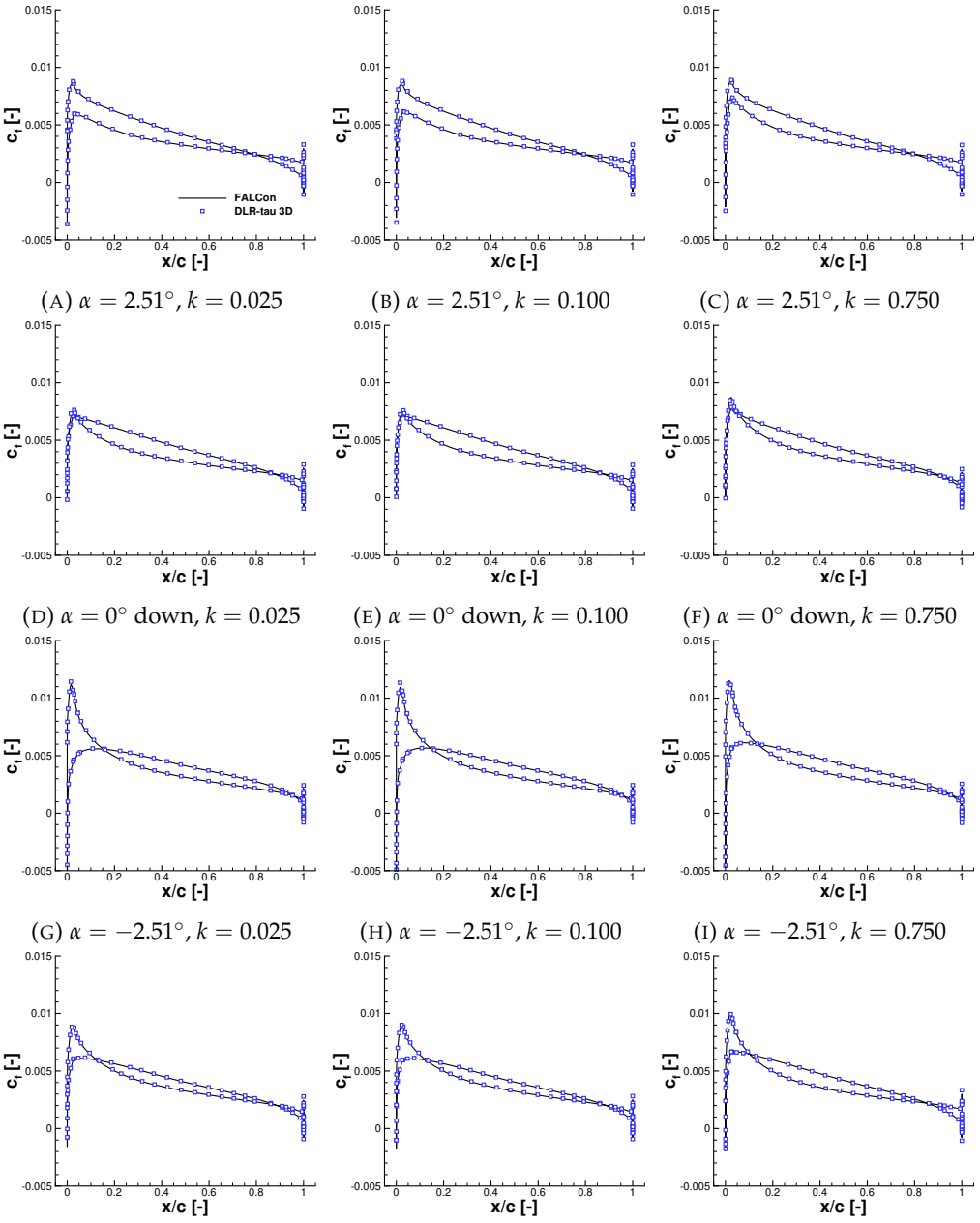

(A) $\alpha = 2.51°$, $k = 0.025$ (B) $\alpha = 2.51°$, $k = 0.100$ (C) $\alpha = 2.51°$, $k = 0.750$

(D) $\alpha = 0°$ down, $k = 0.025$ (E) $\alpha = 0°$ down, $k = 0.100$ (F) $\alpha = 0°$ down, $k = 0.750$

(G) $\alpha = -2.51°$, $k = 0.025$ (H) $\alpha = -2.51°$, $k = 0.100$ (I) $\alpha = -2.51°$, $k = 0.750$

(J) $\alpha = 0°$ up, $k = 0.025$ (K) $\alpha = 0°$ up, $k = 0.100$ (L) $\alpha = 0°$ up, $k = 0.750$

FIGURE A.8: Sectional friction coefficient, c_f, of the third cycle of the pitching unswept NACA2412 wing at $M = 0.3$ and $\Delta\alpha_A = 2.51°$, at 25% of the half–span

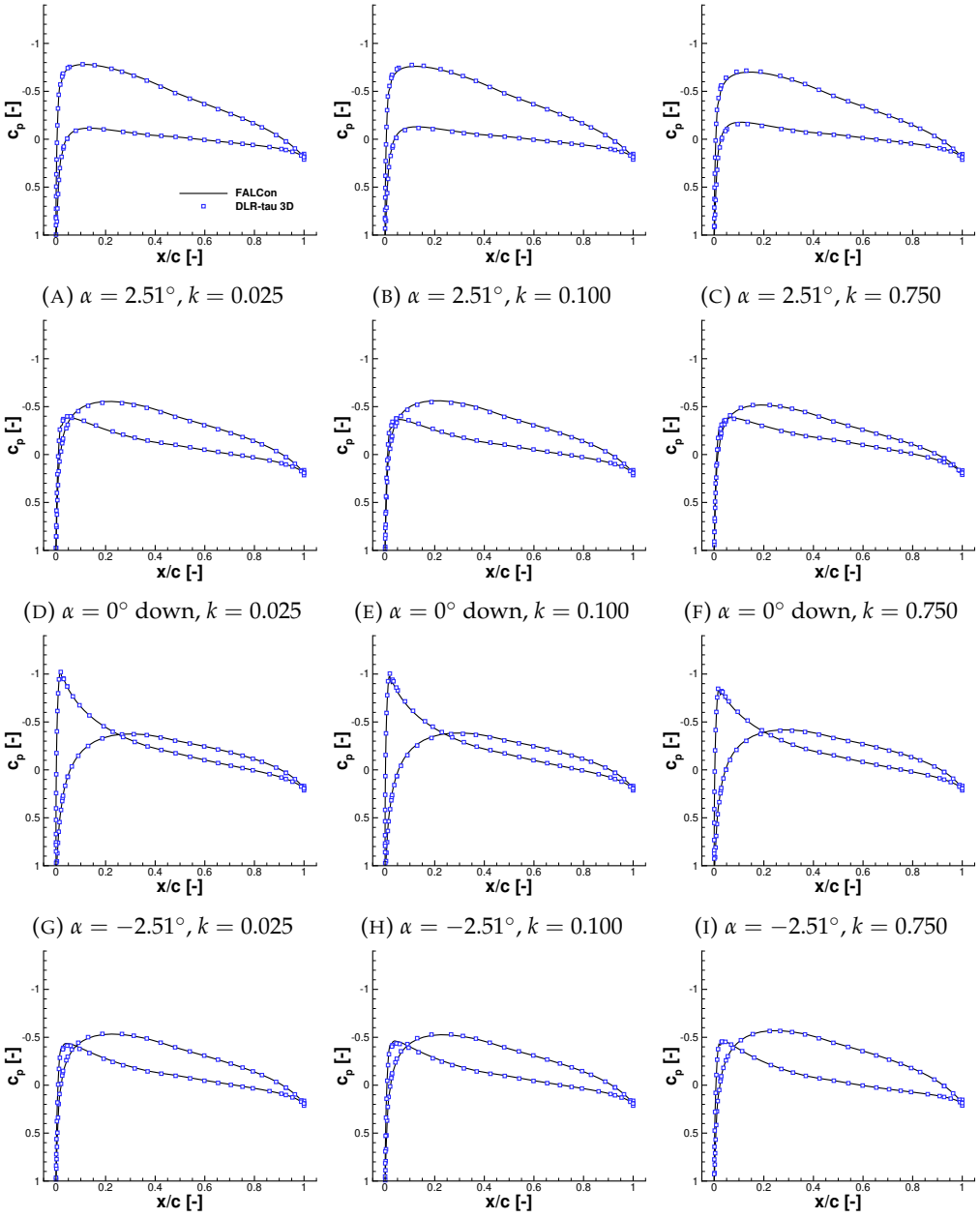

(A) $\alpha = 2.51°$, $k = 0.025$ (B) $\alpha = 2.51°$, $k = 0.100$ (C) $\alpha = 2.51°$, $k = 0.750$

(D) $\alpha = 0°$ down, $k = 0.025$ (E) $\alpha = 0°$ down, $k = 0.100$ (F) $\alpha = 0°$ down, $k = 0.750$

(G) $\alpha = -2.51°$, $k = 0.025$ (H) $\alpha = -2.51°$, $k = 0.100$ (I) $\alpha = -2.51°$, $k = 0.750$

(J) $\alpha = 0°$ up, $k = 0.025$ (K) $\alpha = 0°$ up, $k = 0.100$ (L) $\alpha = 0°$ up, $k = 0.750$

FIGURE A.9: Sectional pressure coefficient, c_p, of the third cycle of the pitching unswept NACA2412 wing at $M = 0.3$ and $\Delta\alpha_A = 2.51°$, at 50% of the half–span

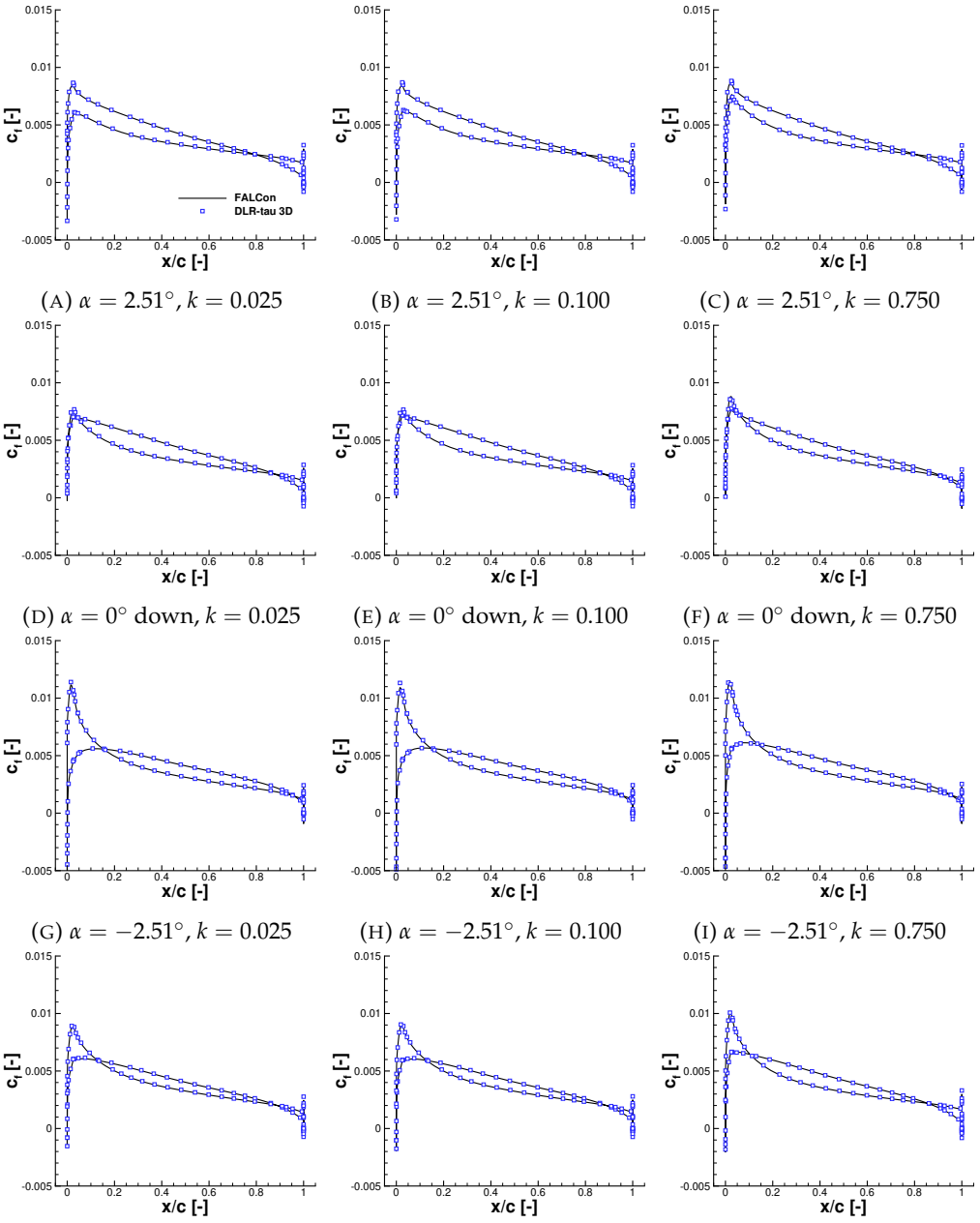

(A) $\alpha = 2.51°$, $k = 0.025$ (B) $\alpha = 2.51°$, $k = 0.100$ (C) $\alpha = 2.51°$, $k = 0.750$

(D) $\alpha = 0°$ down, $k = 0.025$ (E) $\alpha = 0°$ down, $k = 0.100$ (F) $\alpha = 0°$ down, $k = 0.750$

(G) $\alpha = -2.51°$, $k = 0.025$ (H) $\alpha = -2.51°$, $k = 0.100$ (I) $\alpha = -2.51°$, $k = 0.750$

(J) $\alpha = 0°$ up, $k = 0.025$ (K) $\alpha = 0°$ up, $k = 0.100$ (L) $\alpha = 0°$ up, $k = 0.750$

FIGURE A.10: Sectional friction coefficient, c_f, of the third cycle of the pitching unswept NACA2412 wing at $M = 0.3$ and $\Delta\alpha_A = 2.51°$, at 50% of the half–span

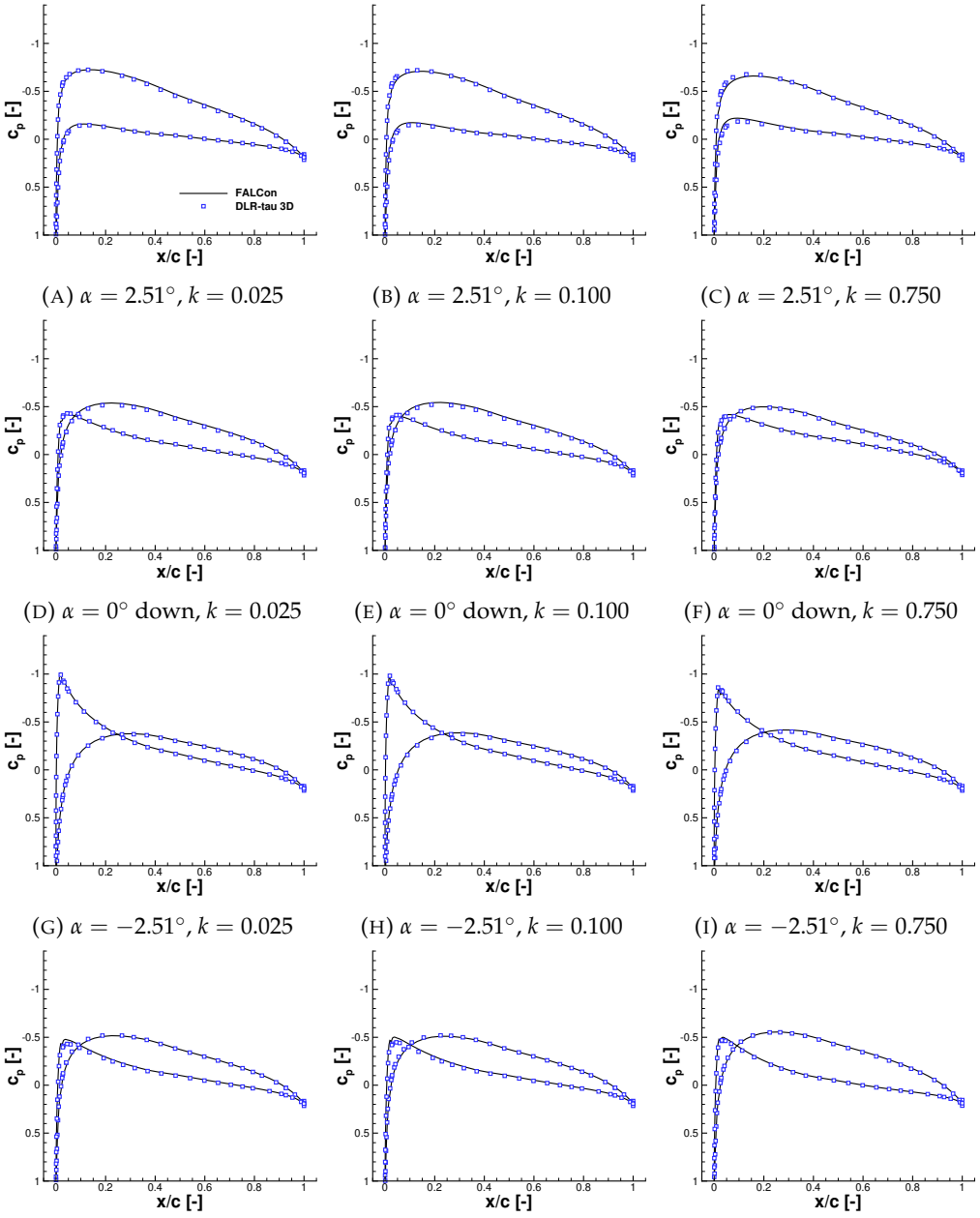

(A) $\alpha = 2.51°$, $k = 0.025$ (B) $\alpha = 2.51°$, $k = 0.100$ (C) $\alpha = 2.51°$, $k = 0.750$

(D) $\alpha = 0°$ down, $k = 0.025$ (E) $\alpha = 0°$ down, $k = 0.100$ (F) $\alpha = 0°$ down, $k = 0.750$

(G) $\alpha = -2.51°$, $k = 0.025$ (H) $\alpha = -2.51°$, $k = 0.100$ (I) $\alpha = -2.51°$, $k = 0.750$

(J) $\alpha = 0°$ up, $k = 0.025$ (K) $\alpha = 0°$ up, $k = 0.100$ (L) $\alpha = 0°$ up, $k = 0.750$

FIGURE A.11: Sectional pressure coefficient, c_p, of the third cycle of the pitching unswept NACA2412 wing at $M = 0.3$ and $\Delta\alpha_A = 2.51°$, at 75% of the half–span

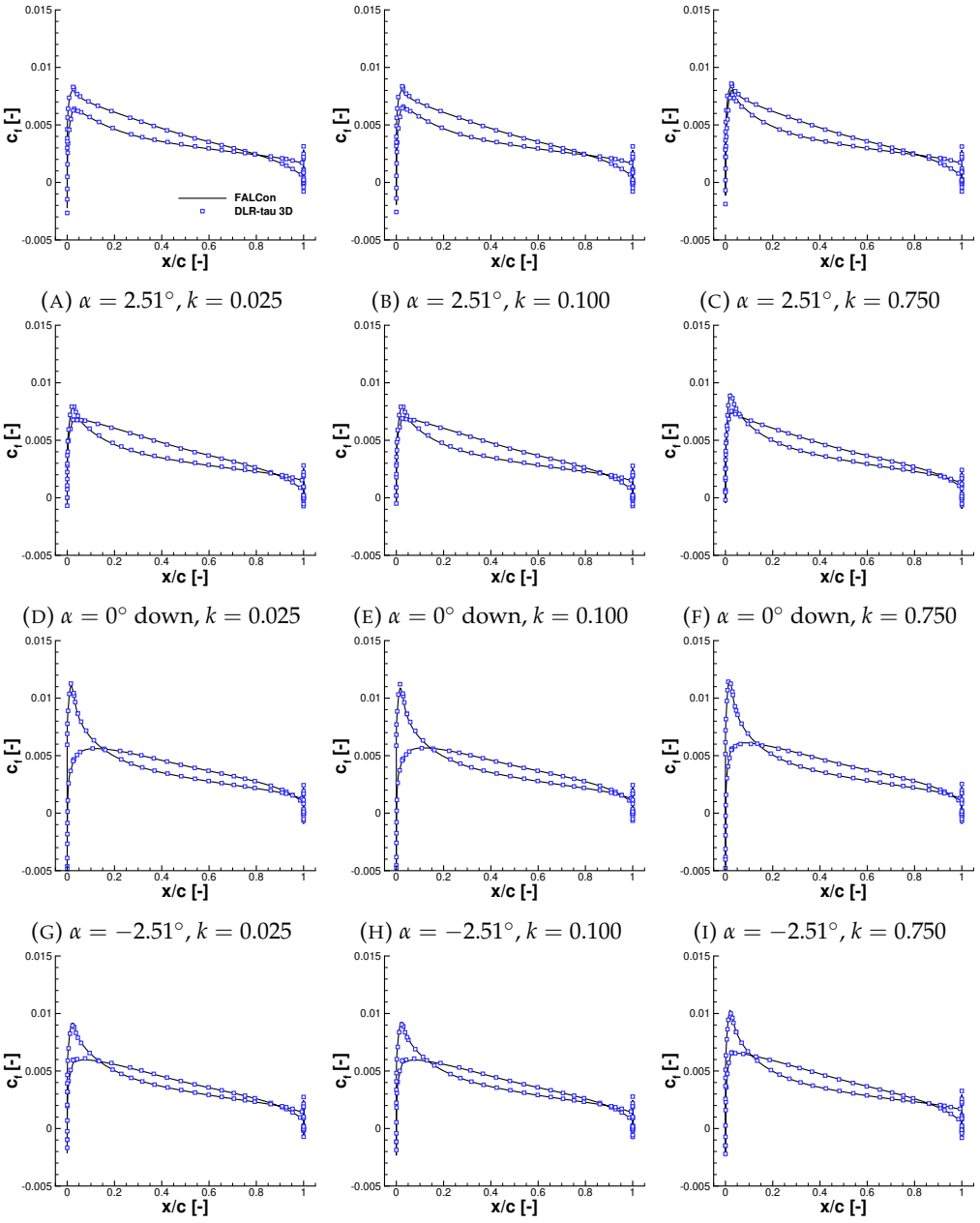

(A) $\alpha = 2.51°$, $k = 0.025$ (B) $\alpha = 2.51°$, $k = 0.100$ (C) $\alpha = 2.51°$, $k = 0.750$

(D) $\alpha = 0°$ down, $k = 0.025$ (E) $\alpha = 0°$ down, $k = 0.100$ (F) $\alpha = 0°$ down, $k = 0.750$

(G) $\alpha = -2.51°$, $k = 0.025$ (H) $\alpha = -2.51°$, $k = 0.100$ (I) $\alpha = -2.51°$, $k = 0.750$

(J) $\alpha = 0°$ up, $k = 0.025$ (K) $\alpha = 0°$ up, $k = 0.100$ (L) $\alpha = 0°$ up, $k = 0.750$

FIGURE A.12: Sectional friction coefficient, c_f, of the third cycle of the pitching unswept NACA2412 wing at $M = 0.3$ and $\Delta\alpha_A = 2.51°$, at 75% of the half–span

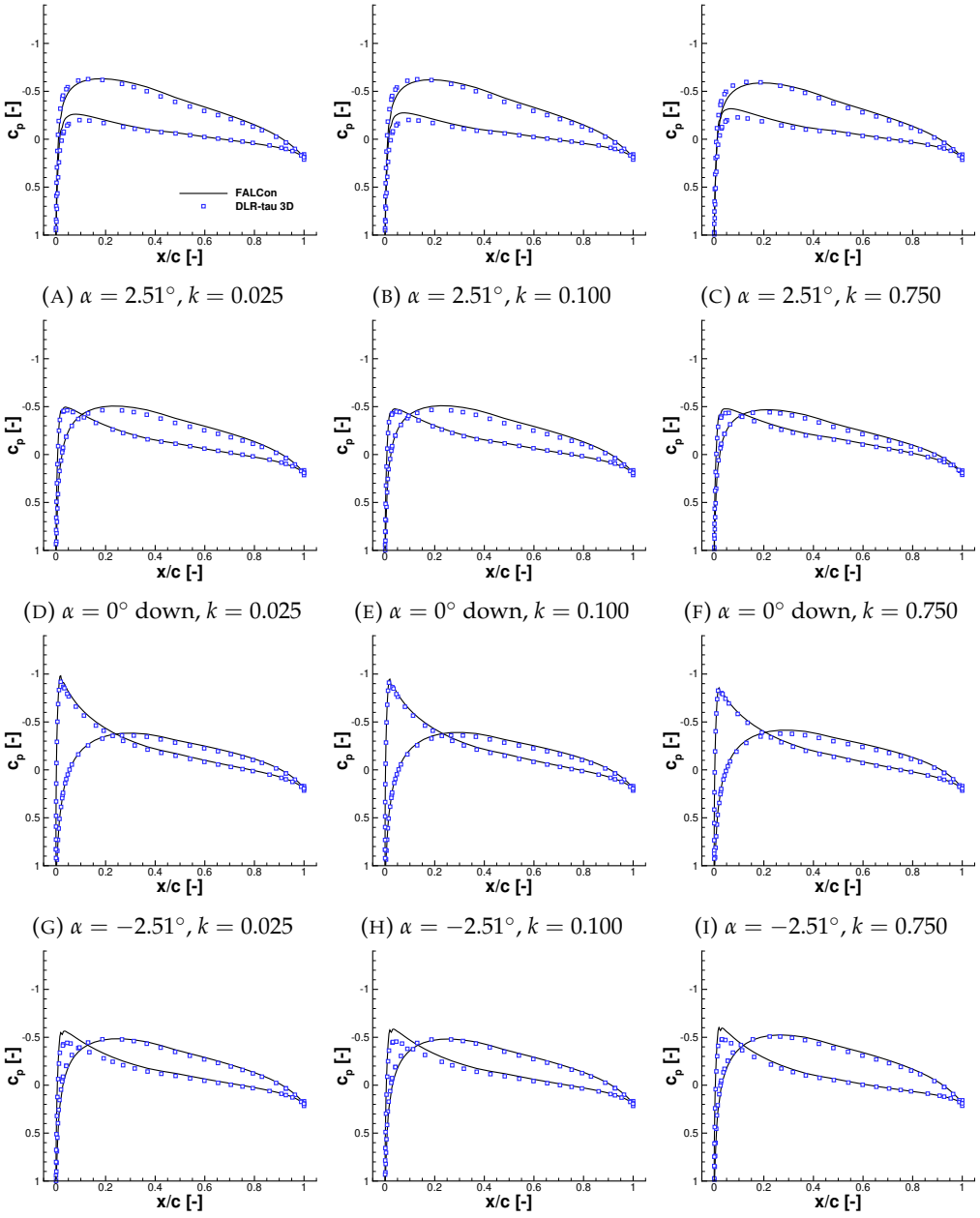

(A) $\alpha = 2.51°$, $k = 0.025$ (B) $\alpha = 2.51°$, $k = 0.100$ (C) $\alpha = 2.51°$, $k = 0.750$

(D) $\alpha = 0°$ down, $k = 0.025$ (E) $\alpha = 0°$ down, $k = 0.100$ (F) $\alpha = 0°$ down, $k = 0.750$

(G) $\alpha = -2.51°$, $k = 0.025$ (H) $\alpha = -2.51°$, $k = 0.100$ (I) $\alpha = -2.51°$, $k = 0.750$

(J) $\alpha = 0°$ up, $k = 0.025$ (K) $\alpha = 0°$ up, $k = 0.100$ (L) $\alpha = 0°$ up, $k = 0.750$

FIGURE A.13: Sectional pressure coefficient, c_p, of the third cycle of the pitching unswept NACA2412 wing at $M = 0.3$ and $\Delta\alpha_A = 2.51°$, at 90% of the half–span

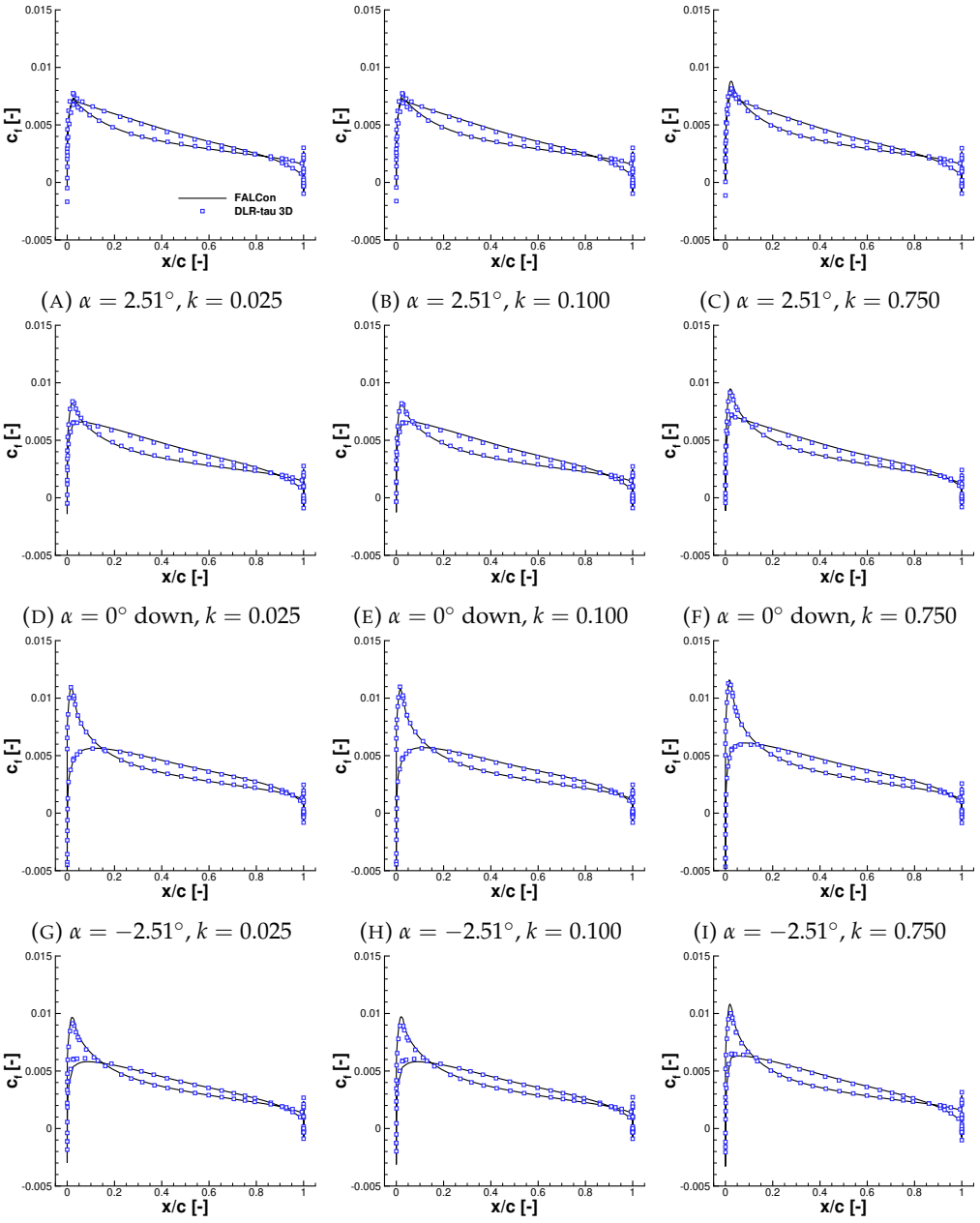

(A) $\alpha = 2.51°$, $k = 0.025$ (B) $\alpha = 2.51°$, $k = 0.100$ (C) $\alpha = 2.51°$, $k = 0.750$

(D) $\alpha = 0°$ down, $k = 0.025$ (E) $\alpha = 0°$ down, $k = 0.100$ (F) $\alpha = 0°$ down, $k = 0.750$

(G) $\alpha = -2.51°$, $k = 0.025$ (H) $\alpha = -2.51°$, $k = 0.100$ (I) $\alpha = -2.51°$, $k = 0.750$

(J) $\alpha = 0°$ up, $k = 0.025$ (K) $\alpha = 0°$ up, $k = 0.100$ (L) $\alpha = 0°$ up, $k = 0.750$

FIGURE A.14: Sectional friction coefficient, c_f, of the third cycle of the pitching unswept NACA2412 wing at $M = 0.3$ and $\Delta\alpha_A = 2.51°$, at 90% of the half–span

A.1.1.2 Mach $M = 0.5$

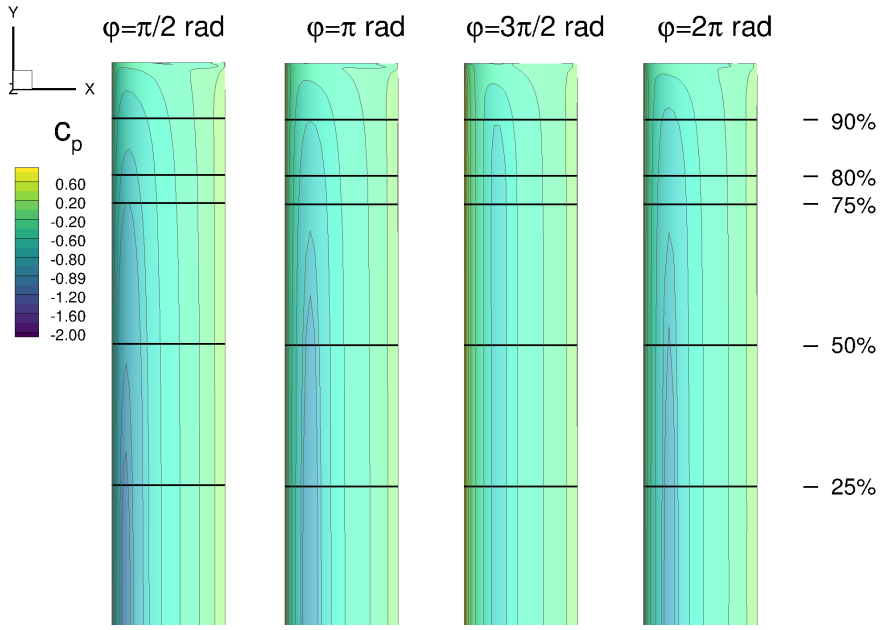

FIGURE A.15: Pressure coefficient, c_p, of the NACA2412–wing at $M = 0.5$ and $k = 0.025$ during forced harmonic pitching oscillation, third cycle

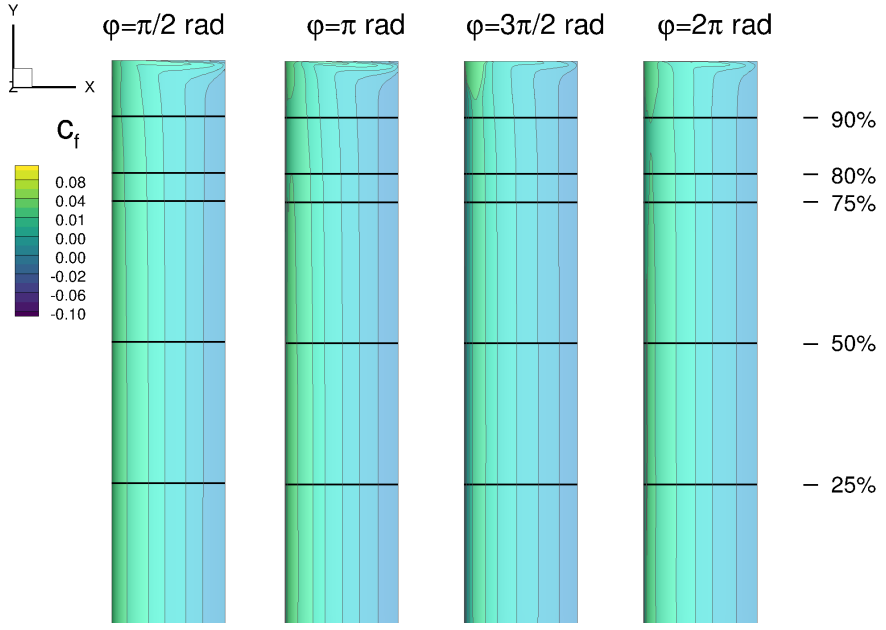

FIGURE A.16: Friction coefficient, c_f, of the NACA2412–wing at $M = 0.5$ and $k = 0.025$ during forced harmonic pitching oscillation, third cycle

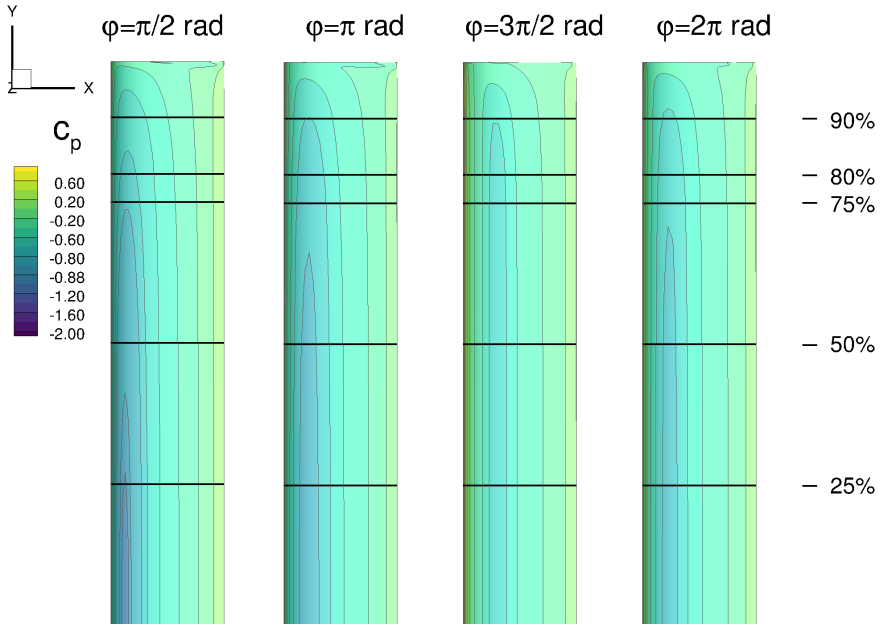

FIGURE A.17: Pressure coefficient, c_p, of the NACA2412–wing at $M = 0.5$ and $k = 0.100$ during forced harmonic pitching oscillation, third cycle

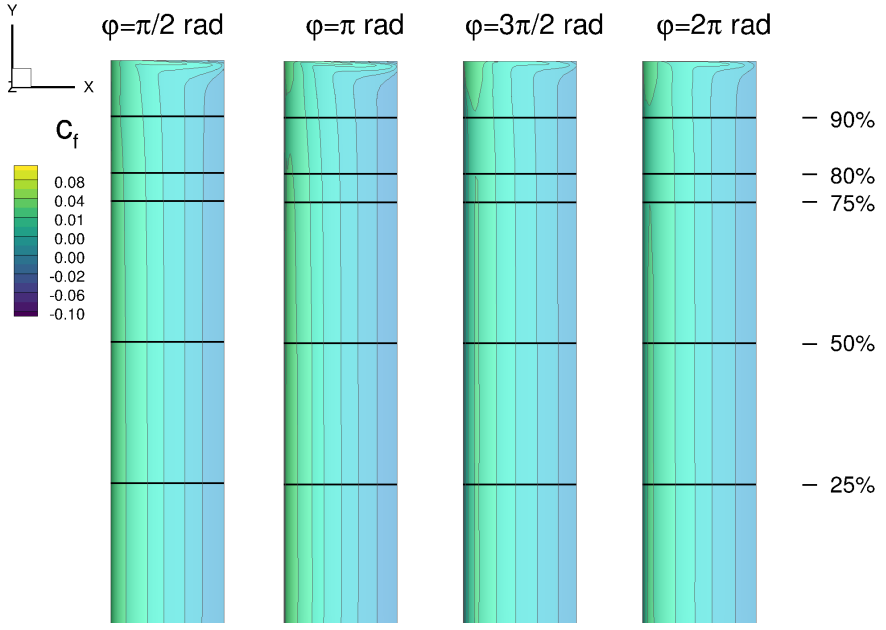

FIGURE A.18: Friction coefficient, c_f, of the NACA2412–wing at $M = 0.5$ and $k = 0.100$ during forced harmonic pitching oscillation, third cycle

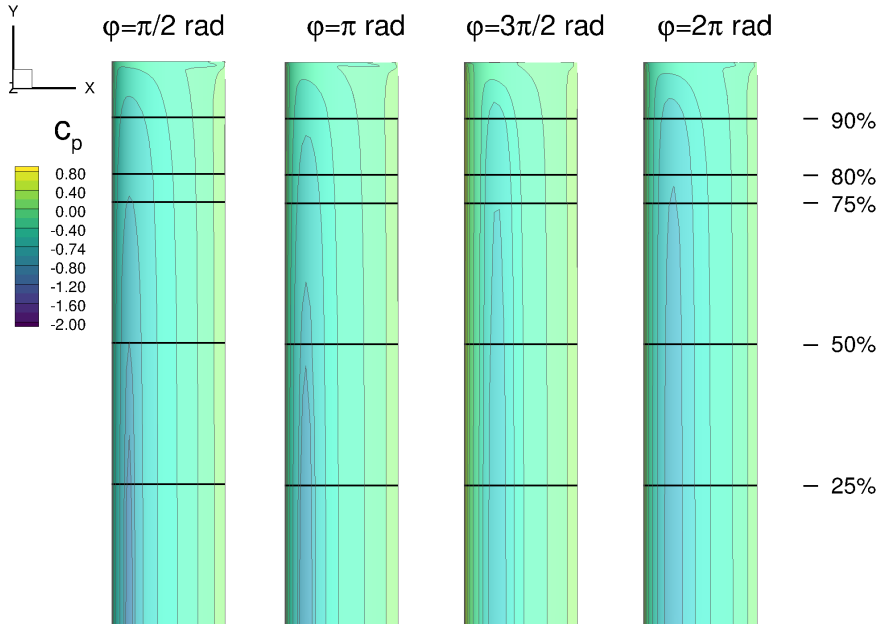

FIGURE A.19: Pressure coefficient, c_p, of the NACA2412–wing at $M = 0.5$ and $k = 0.750$ during forced harmonic pitching oscillation, third cycle

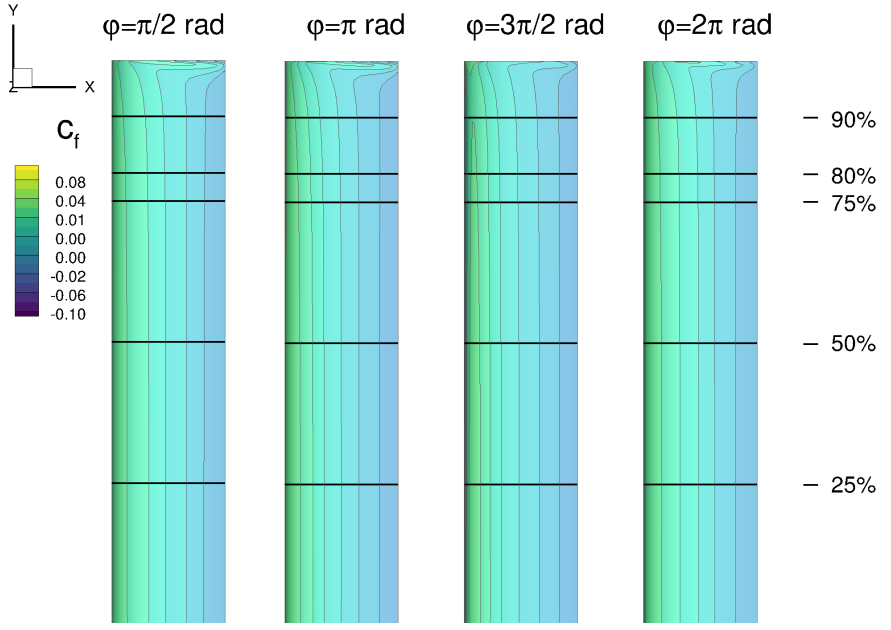

FIGURE A.20: Friction coefficient, c_f, of the NACA2412–wing at $M = 0.5$ and $k = 0.750$ during forced harmonic pitching oscillation, third cycle

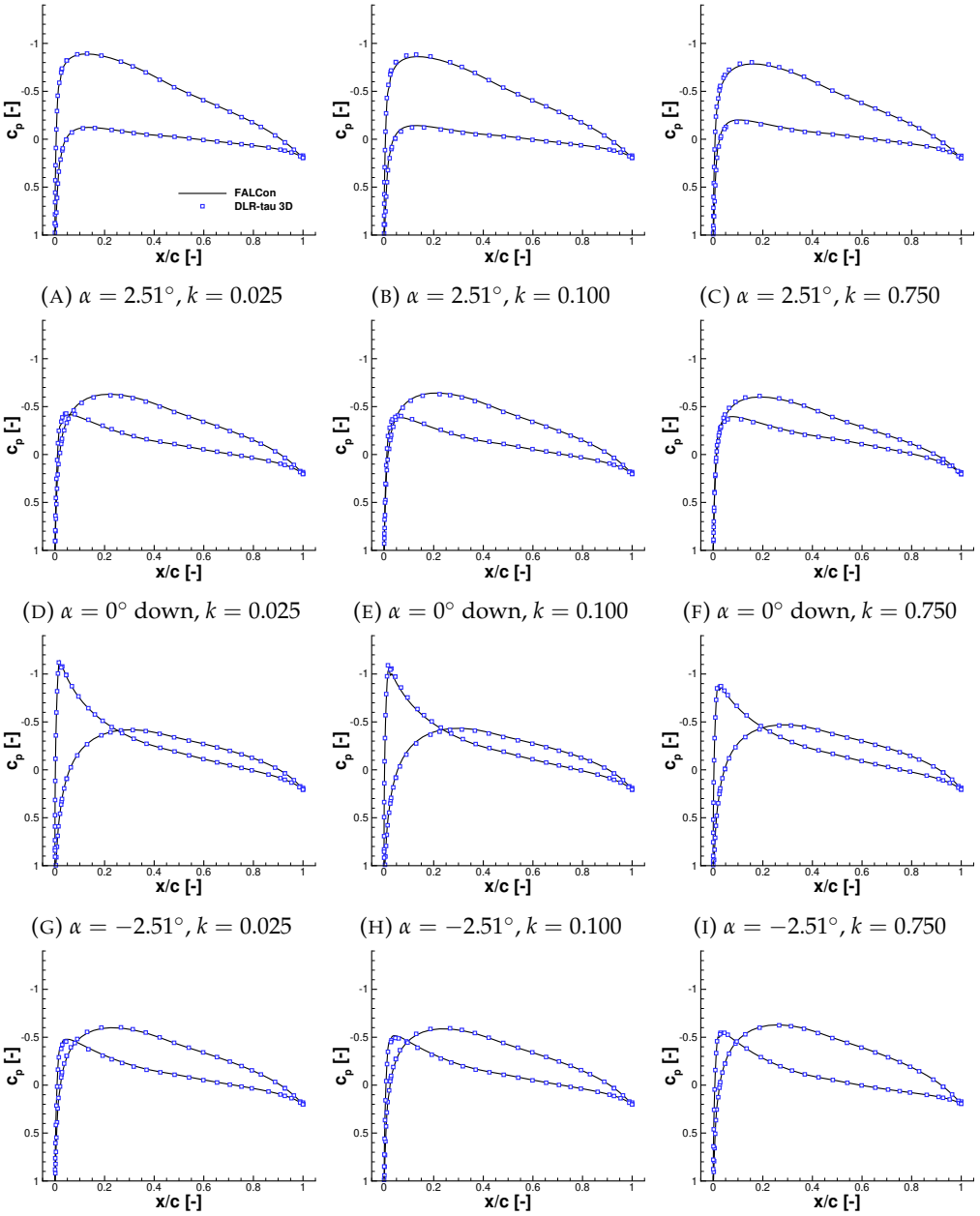

(A) $\alpha = 2.51°$, $k = 0.025$ (B) $\alpha = 2.51°$, $k = 0.100$ (C) $\alpha = 2.51°$, $k = 0.750$

(D) $\alpha = 0°$ down, $k = 0.025$ (E) $\alpha = 0°$ down, $k = 0.100$ (F) $\alpha = 0°$ down, $k = 0.750$

(G) $\alpha = -2.51°$, $k = 0.025$ (H) $\alpha = -2.51°$, $k = 0.100$ (I) $\alpha = -2.51°$, $k = 0.750$

(J) $\alpha = 0°$ up, $k = 0.025$ (K) $\alpha = 0°$ up, $k = 0.100$ (L) $\alpha = 0°$ up, $k = 0.750$

FIGURE A.21: Sectional pressure coefficient, c_p, of the third cycle of the pitching unswept NACA2412 wing at $M = 0.5$ and $\Delta\alpha_A = 2.51°$, at 25% of the half–span

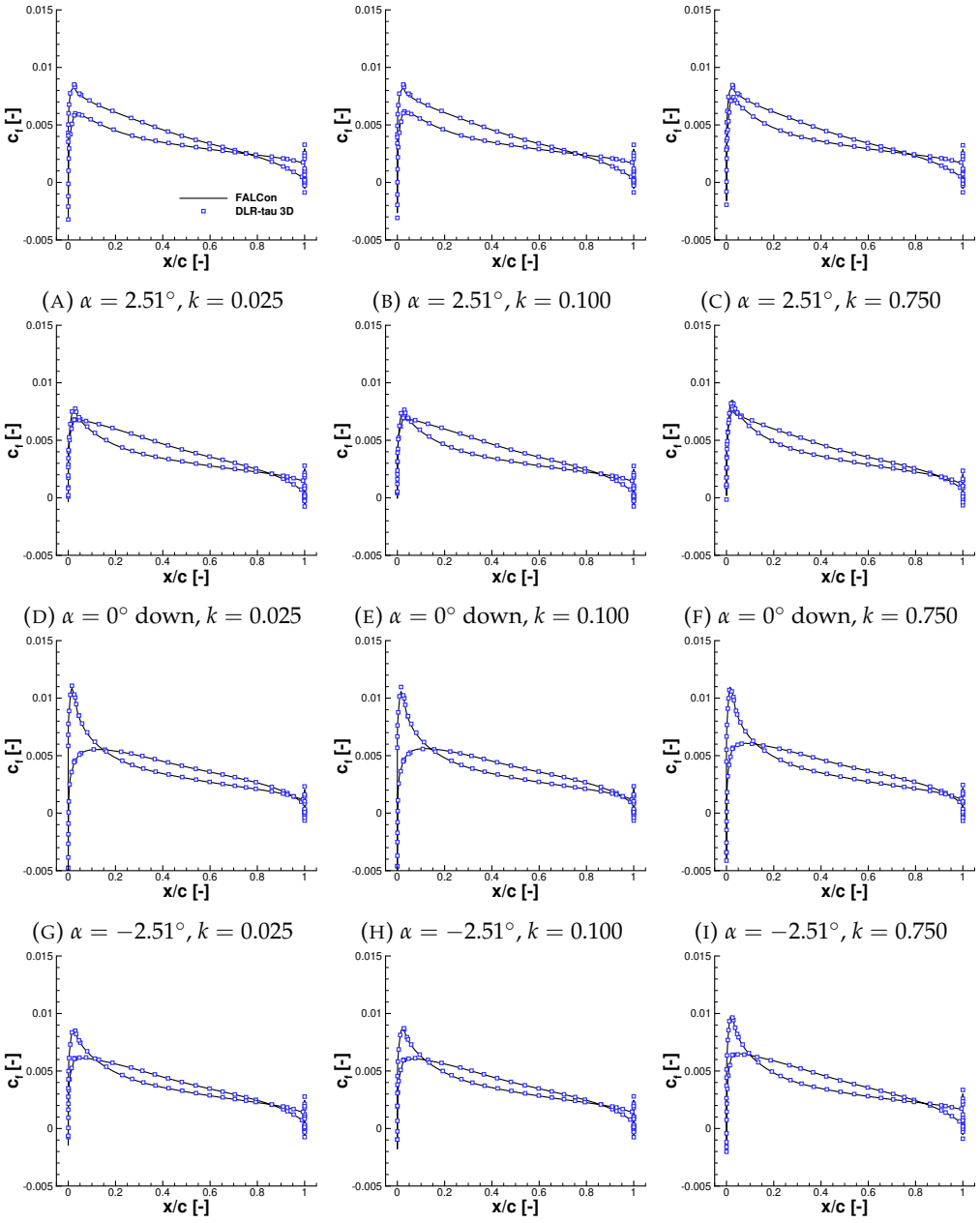

(A) $\alpha = 2.51°$, $k = 0.025$ (B) $\alpha = 2.51°$, $k = 0.100$ (C) $\alpha = 2.51°$, $k = 0.750$

(D) $\alpha = 0°$ down, $k = 0.025$ (E) $\alpha = 0°$ down, $k = 0.100$ (F) $\alpha = 0°$ down, $k = 0.750$

(G) $\alpha = -2.51°$, $k = 0.025$ (H) $\alpha = -2.51°$, $k = 0.100$ (I) $\alpha = -2.51°$, $k = 0.750$

(J) $\alpha = 0°$ up, $k = 0.025$ (K) $\alpha = 0°$ up, $k = 0.100$ (L) $\alpha = 0°$ up, $k = 0.750$

FIGURE A.22: Sectional friction coefficient, c_f, of the third cycle of the pitching unswept NACA2412 wing at $M = 0.5$ and $\Delta\alpha_A = 2.51°$, at 25% of the half–span

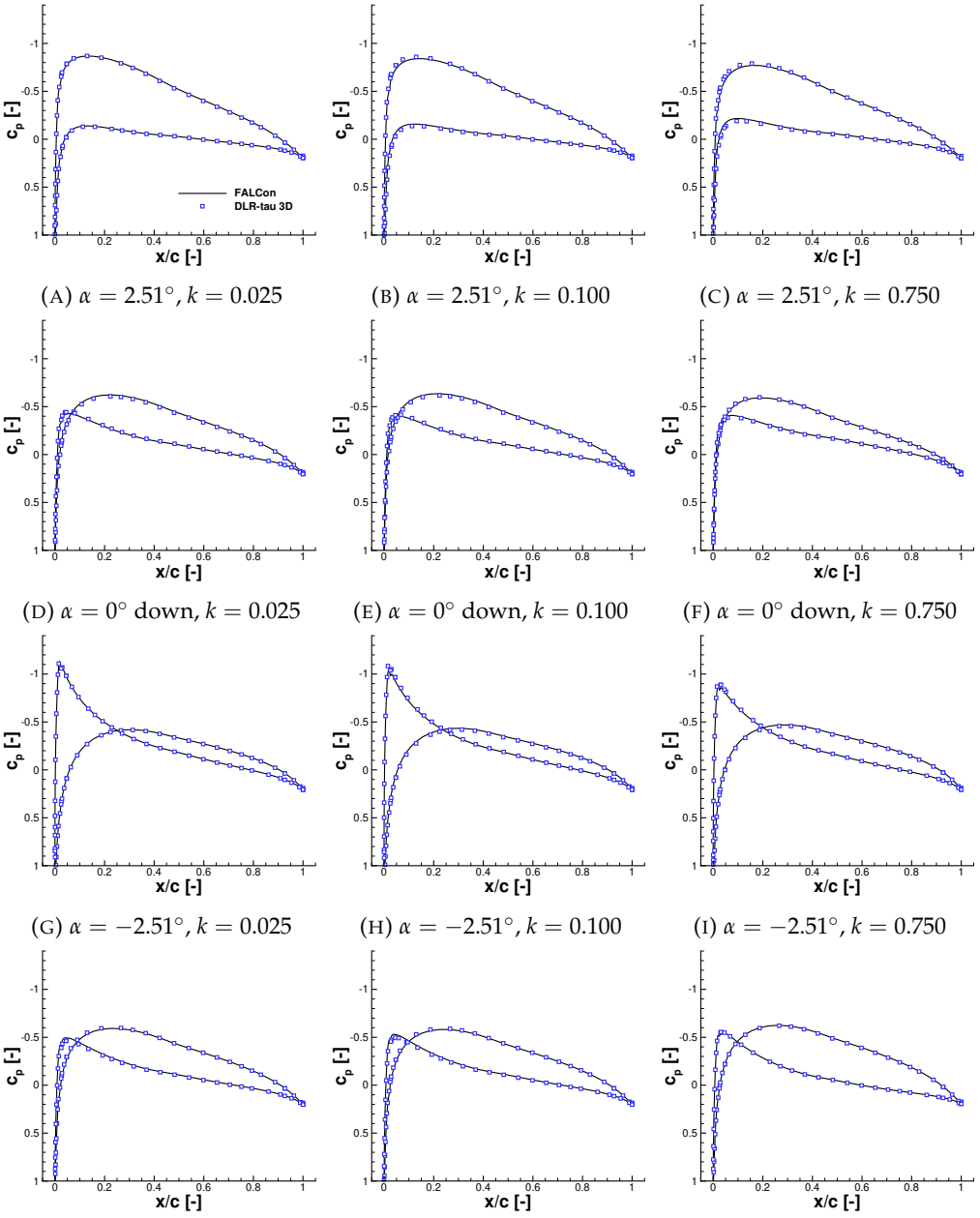

(A) $\alpha = 2.51°$, $k = 0.025$ (B) $\alpha = 2.51°$, $k = 0.100$ (C) $\alpha = 2.51°$, $k = 0.750$

(D) $\alpha = 0°$ down, $k = 0.025$ (E) $\alpha = 0°$ down, $k = 0.100$ (F) $\alpha = 0°$ down, $k = 0.750$

(G) $\alpha = -2.51°$, $k = 0.025$ (H) $\alpha = -2.51°$, $k = 0.100$ (I) $\alpha = -2.51°$, $k = 0.750$

(J) $\alpha = 0°$ up, $k = 0.025$ (K) $\alpha = 0°$ up, $k = 0.100$ (L) $\alpha = 0°$ up, $k = 0.750$

FIGURE A.23: Sectional pressure coefficient, c_p, of the third cycle of the pitching unswept NACA2412 wing at $M = 0.5$ and $\Delta\alpha_A = 2.51°$, at 50% of the half–span

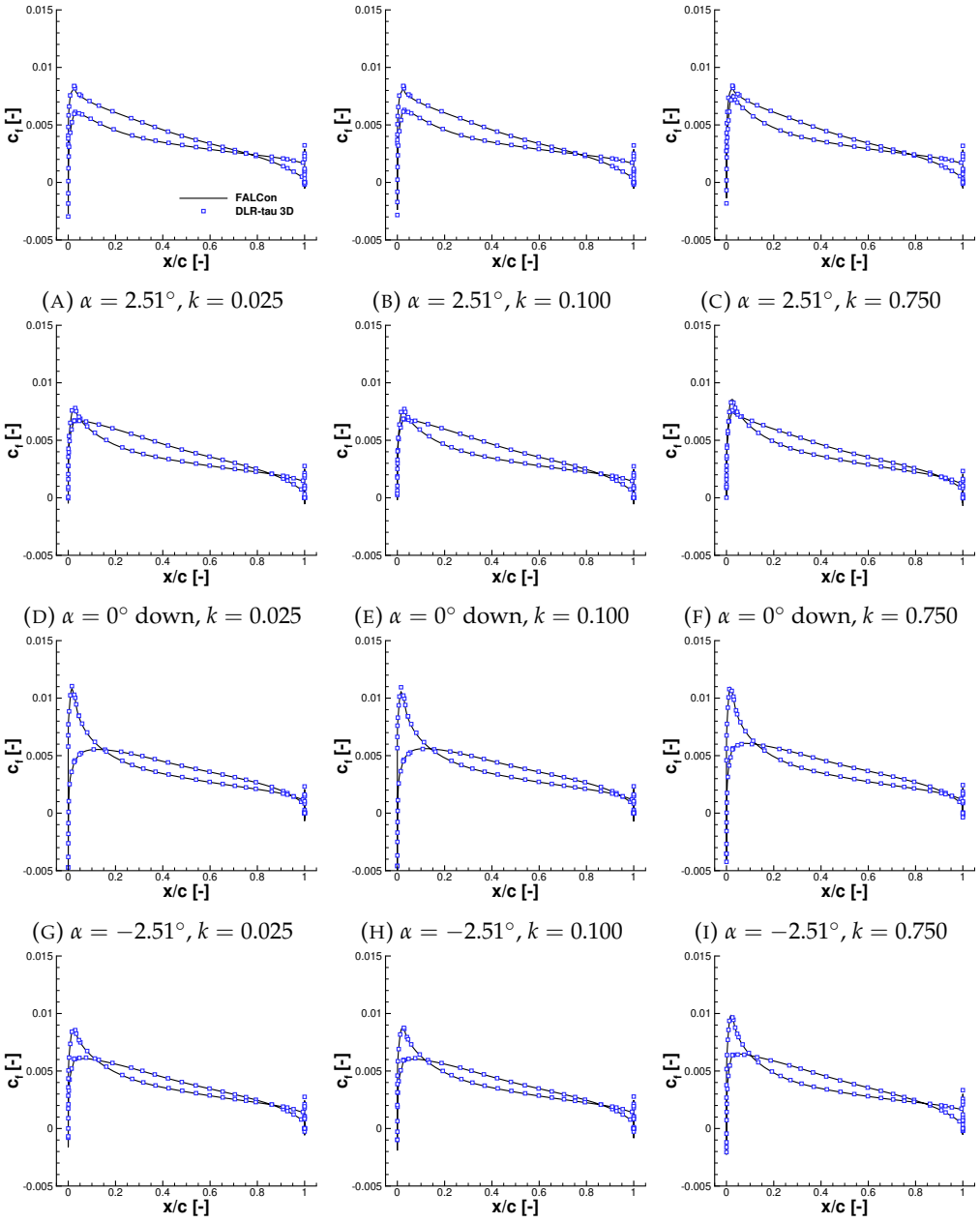

(A) $\alpha = 2.51°$, $k = 0.025$ (B) $\alpha = 2.51°$, $k = 0.100$ (C) $\alpha = 2.51°$, $k = 0.750$

(D) $\alpha = 0°$ down, $k = 0.025$ (E) $\alpha = 0°$ down, $k = 0.100$ (F) $\alpha = 0°$ down, $k = 0.750$

(G) $\alpha = -2.51°$, $k = 0.025$ (H) $\alpha = -2.51°$, $k = 0.100$ (I) $\alpha = -2.51°$, $k = 0.750$

(J) $\alpha = 0°$ up, $k = 0.025$ (K) $\alpha = 0°$ up, $k = 0.100$ (L) $\alpha = 0°$ up, $k = 0.750$

FIGURE A.24: Sectional friction coefficient, c_f, of the third cycle of the pitching unswept NACA2412 wing at $M = 0.5$ and $\Delta\alpha_A = 2.51°$, at 50% of the half–span

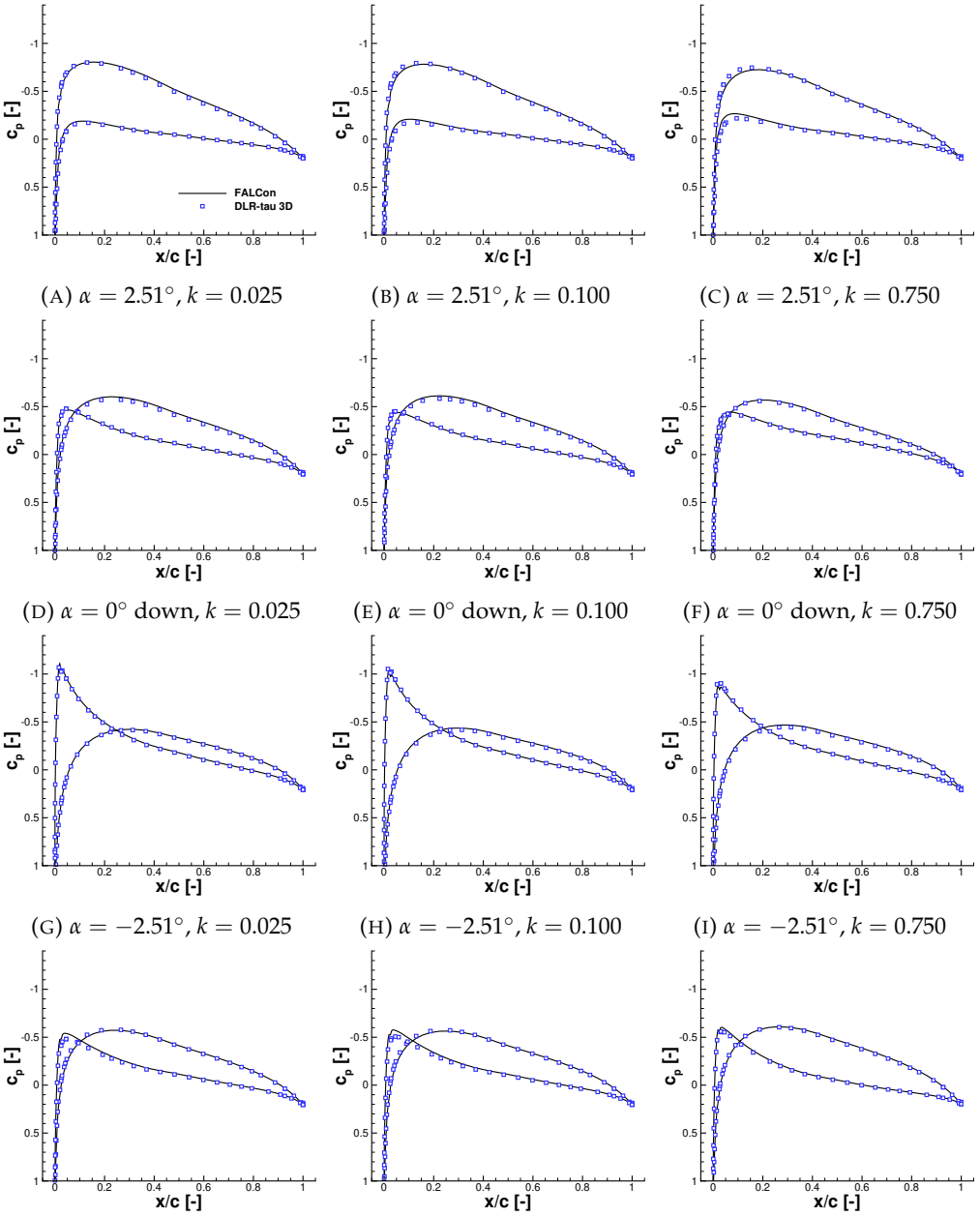

(A) $\alpha = 2.51°$, $k = 0.025$ (B) $\alpha = 2.51°$, $k = 0.100$ (C) $\alpha = 2.51°$, $k = 0.750$

(D) $\alpha = 0°$ down, $k = 0.025$ (E) $\alpha = 0°$ down, $k = 0.100$ (F) $\alpha = 0°$ down, $k = 0.750$

(G) $\alpha = -2.51°$, $k = 0.025$ (H) $\alpha = -2.51°$, $k = 0.100$ (I) $\alpha = -2.51°$, $k = 0.750$

(J) $\alpha = 0°$ up, $k = 0.025$ (K) $\alpha = 0°$ up, $k = 0.100$ (L) $\alpha = 0°$ up, $k = 0.750$

FIGURE A.25: Sectional pressure coefficient, c_p, of the third cycle of the pitching unswept NACA2412 wing at $M = 0.5$ and $\Delta\alpha_A = 2.51°$, at 75% of the half–span

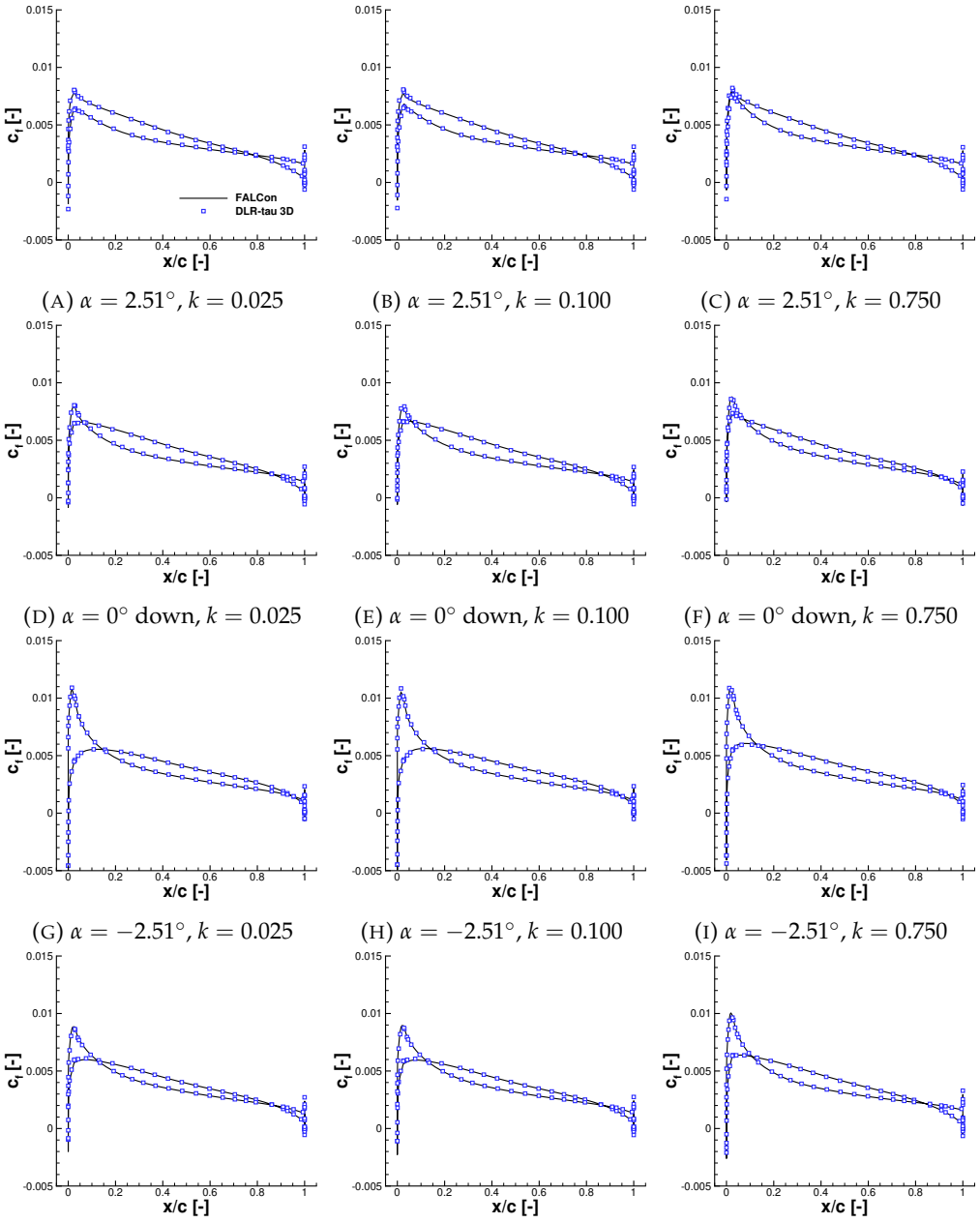

(A) $\alpha = 2.51°$, $k = 0.025$ (B) $\alpha = 2.51°$, $k = 0.100$ (C) $\alpha = 2.51°$, $k = 0.750$

(D) $\alpha = 0°$ down, $k = 0.025$ (E) $\alpha = 0°$ down, $k = 0.100$ (F) $\alpha = 0°$ down, $k = 0.750$

(G) $\alpha = -2.51°$, $k = 0.025$ (H) $\alpha = -2.51°$, $k = 0.100$ (I) $\alpha = -2.51°$, $k = 0.750$

(J) $\alpha = 0°$ up, $k = 0.025$ (K) $\alpha = 0°$ up, $k = 0.100$ (L) $\alpha = 0°$ up, $k = 0.750$

FIGURE A.26: Sectional friction coefficient, c_f, of the third cycle of the pitching unswept NACA2412 wing at $M = 0.5$ and $\Delta\alpha_A = 2.51°$, at 75% of the half–span

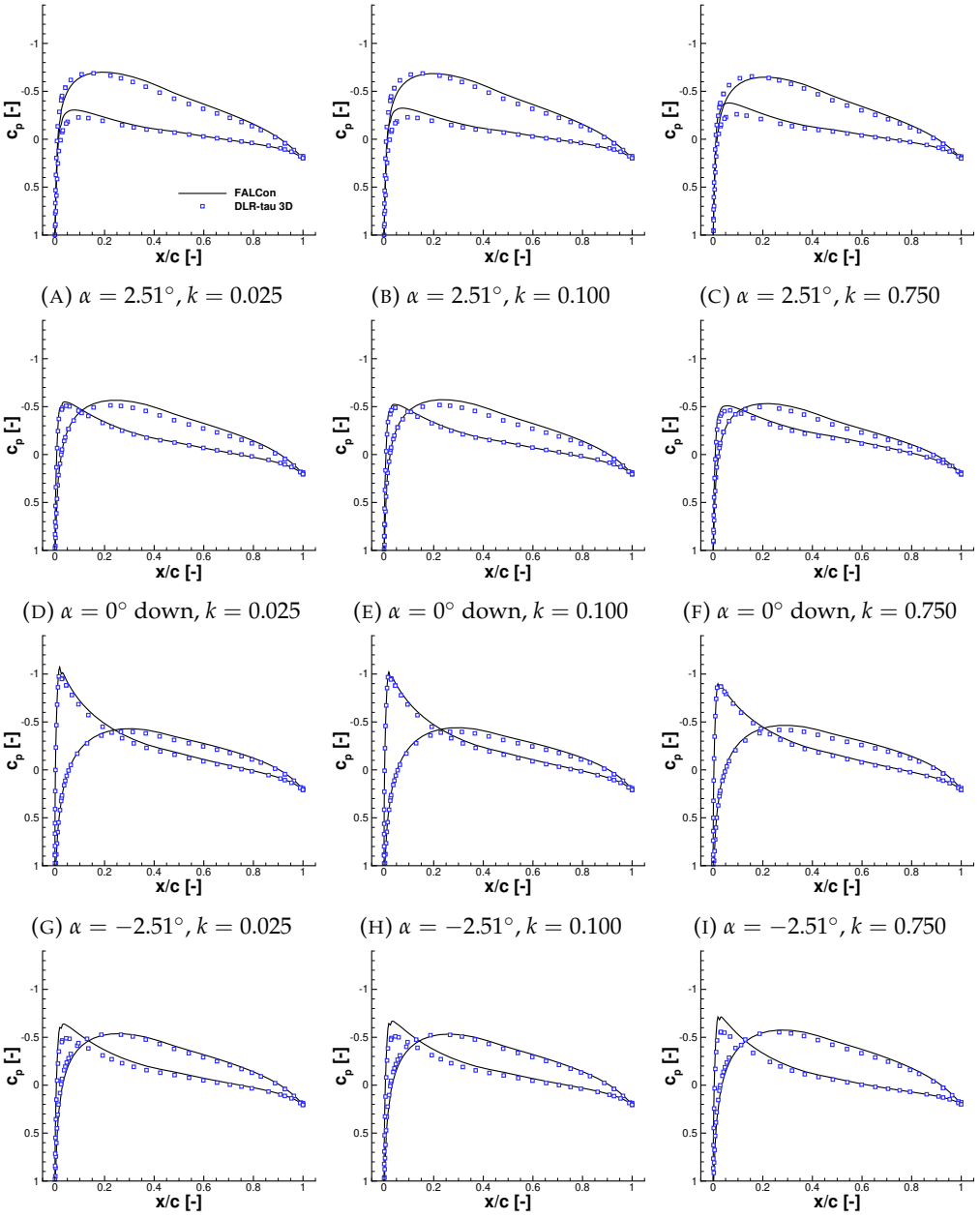

(A) $\alpha = 2.51°$, $k = 0.025$ (B) $\alpha = 2.51°$, $k = 0.100$ (C) $\alpha = 2.51°$, $k = 0.750$

(D) $\alpha = 0°$ down, $k = 0.025$ (E) $\alpha = 0°$ down, $k = 0.100$ (F) $\alpha = 0°$ down, $k = 0.750$

(G) $\alpha = -2.51°$, $k = 0.025$ (H) $\alpha = -2.51°$, $k = 0.100$ (I) $\alpha = -2.51°$, $k = 0.750$

(J) $\alpha = 0°$ up, $k = 0.025$ (K) $\alpha = 0°$ up, $k = 0.100$ (L) $\alpha = 0°$ up, $k = 0.750$

FIGURE A.27: Sectional pressure coefficient, c_p, of the third cycle of the pitching unswept NACA2412 wing at $M = 0.5$ and $\Delta\alpha_A = 2.51°$, at 90% of the half–span

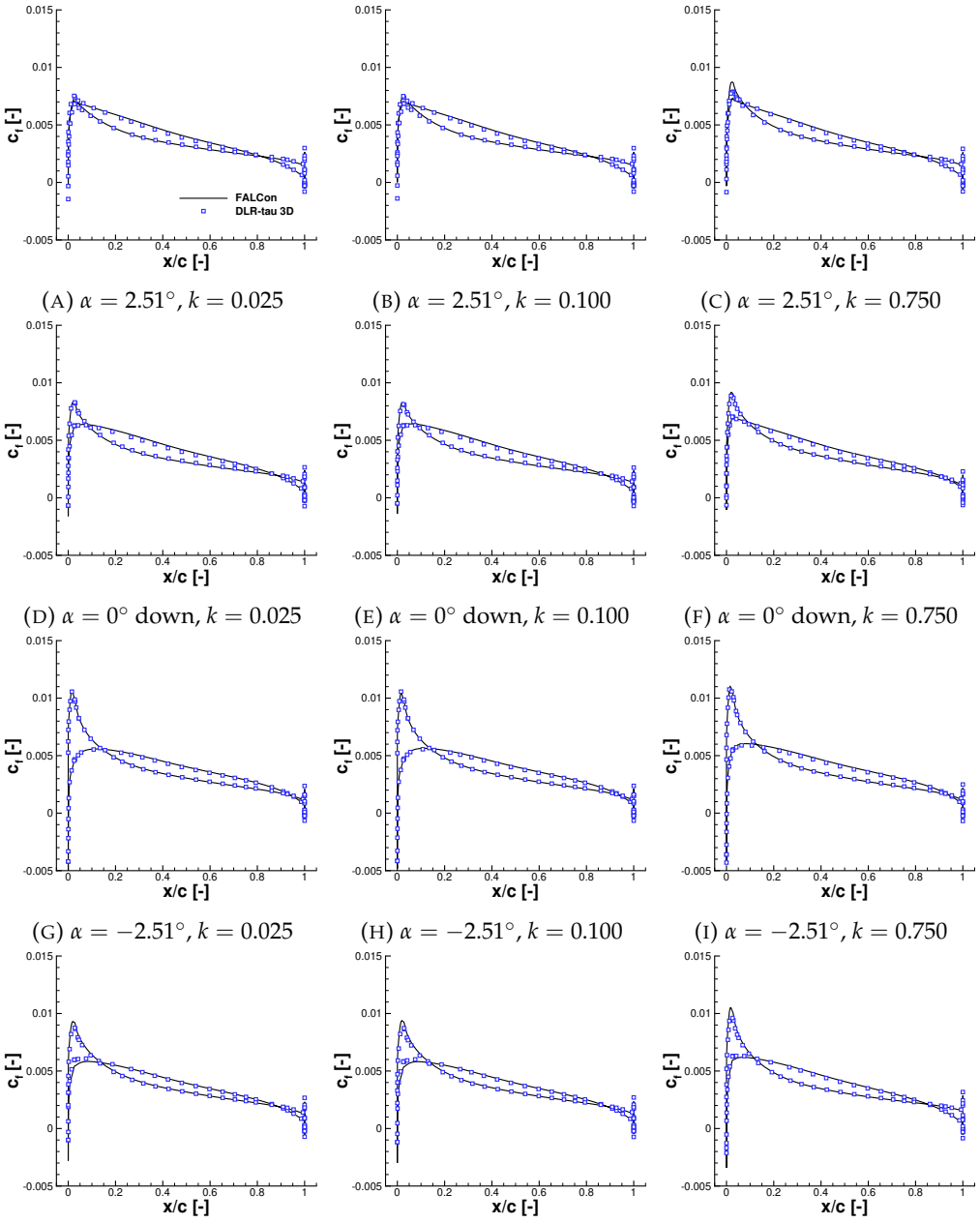

(A) $\alpha = 2.51°$, $k = 0.025$ (B) $\alpha = 2.51°$, $k = 0.100$ (C) $\alpha = 2.51°$, $k = 0.750$

(D) $\alpha = 0°$ down, $k = 0.025$ (E) $\alpha = 0°$ down, $k = 0.100$ (F) $\alpha = 0°$ down, $k = 0.750$

(G) $\alpha = -2.51°$, $k = 0.025$ (H) $\alpha = -2.51°$, $k = 0.100$ (I) $\alpha = -2.51°$, $k = 0.750$

(J) $\alpha = 0°$ up, $k = 0.025$ (K) $\alpha = 0°$ up, $k = 0.100$ (L) $\alpha = 0°$ up, $k = 0.750$

FIGURE A.28: Sectional friction coefficient, c_f, of the third cycle of the pitching unswept NACA2412 wing at $M = 0.5$ and $\Delta\alpha_A = 2.51°$, at 90% of the half–span

A.1.1.3 Mach $M = 0.7$

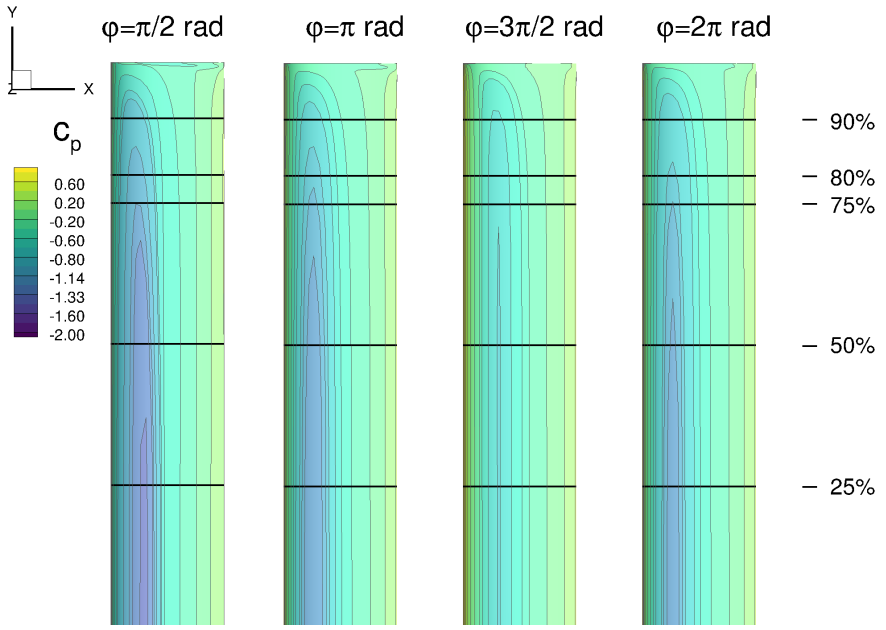

FIGURE A.29: Pressure coefficient, c_p, of the NACA2412–wing at $M = 0.7$ and $k = 0.025$ during forced harmonic pitching oscillation, third cycle

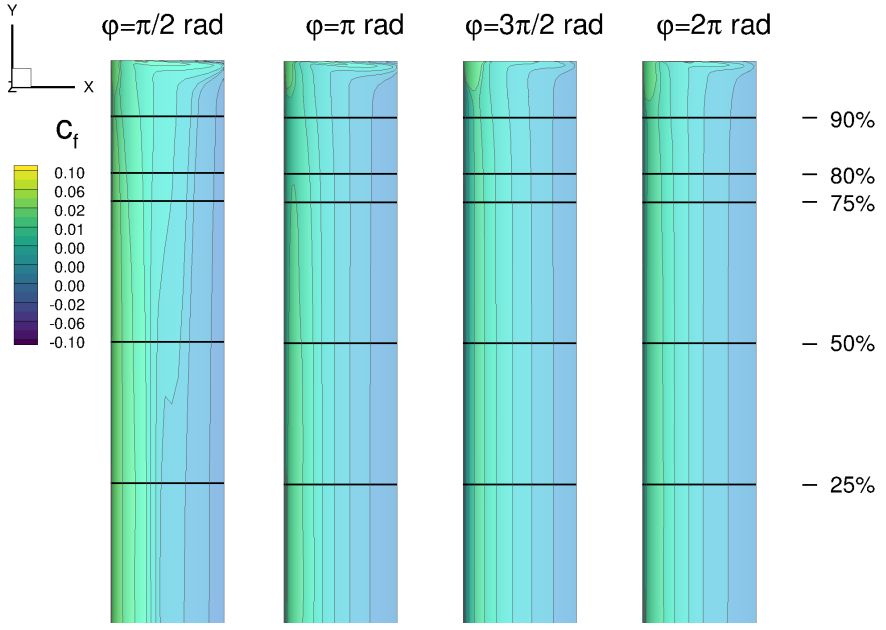

FIGURE A.30: Friction coefficient, c_f, of the NACA2412–wing at $M = 0.7$ and $k = 0.025$ during forced harmonic pitching oscillation, third cycle

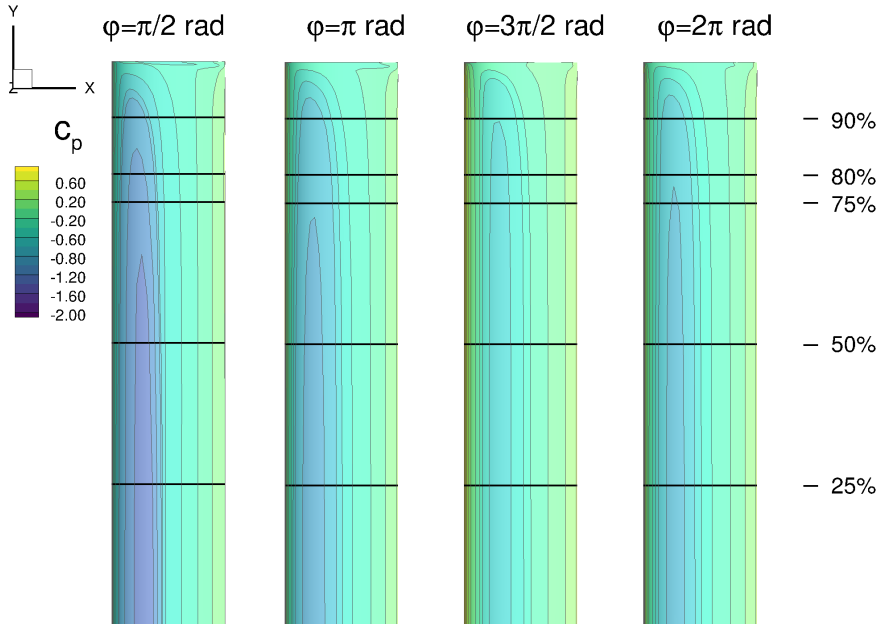

FIGURE A.31: Pressure coefficient, c_p, of the NACA2412–wing at $M = 0.7$ and $k = 0.100$ during forced harmonic pitching oscillation, third cycle

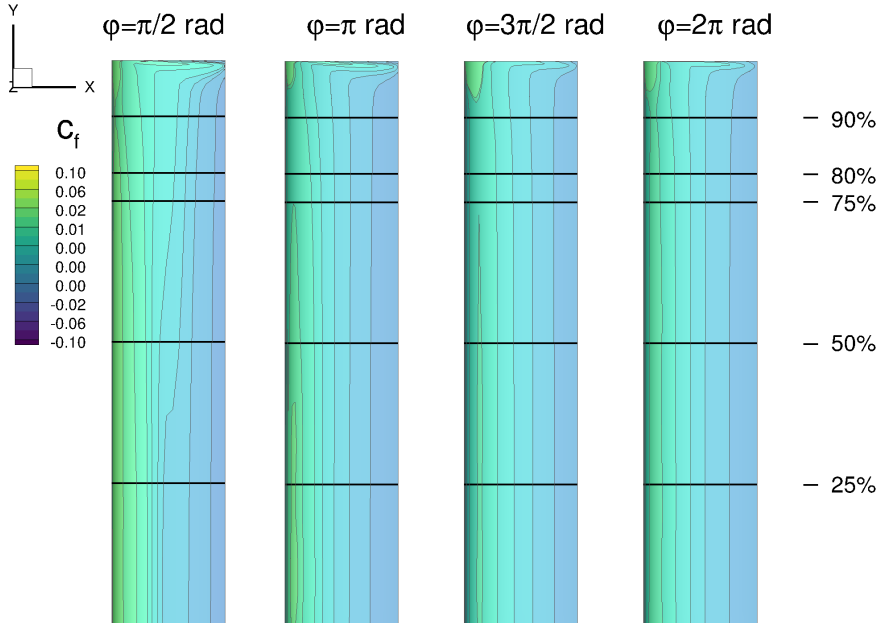

FIGURE A.32: Friction coefficient, c_f, of the NACA2412–wing at $M = 0.7$ and $k = 0.100$ during forced harmonic pitching oscillation, third cycle

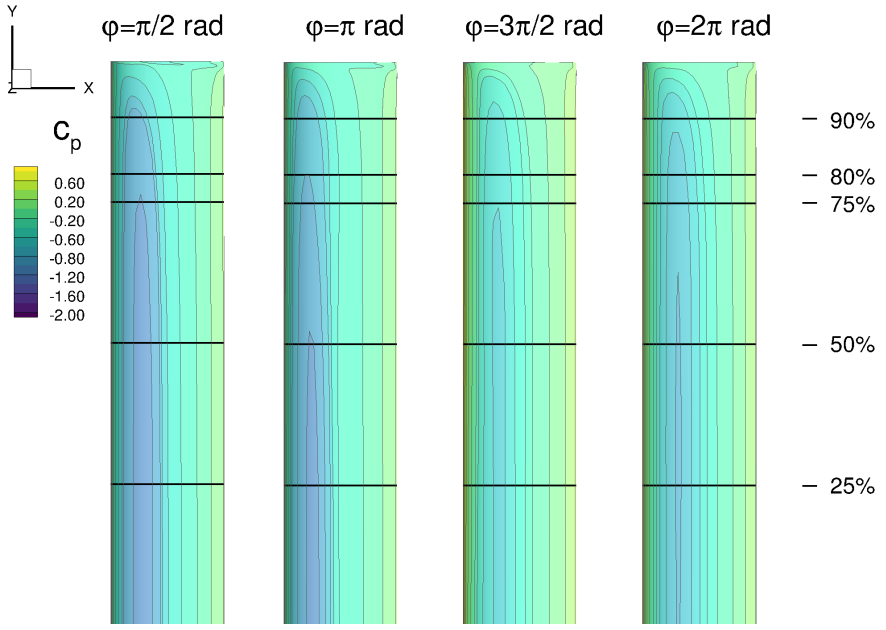

FIGURE A.33: Pressure coefficient, c_p, of the NACA2412–wing at $M = 0.7$ and $k = 0.750$ during forced harmonic pitching oscillation, third cycle

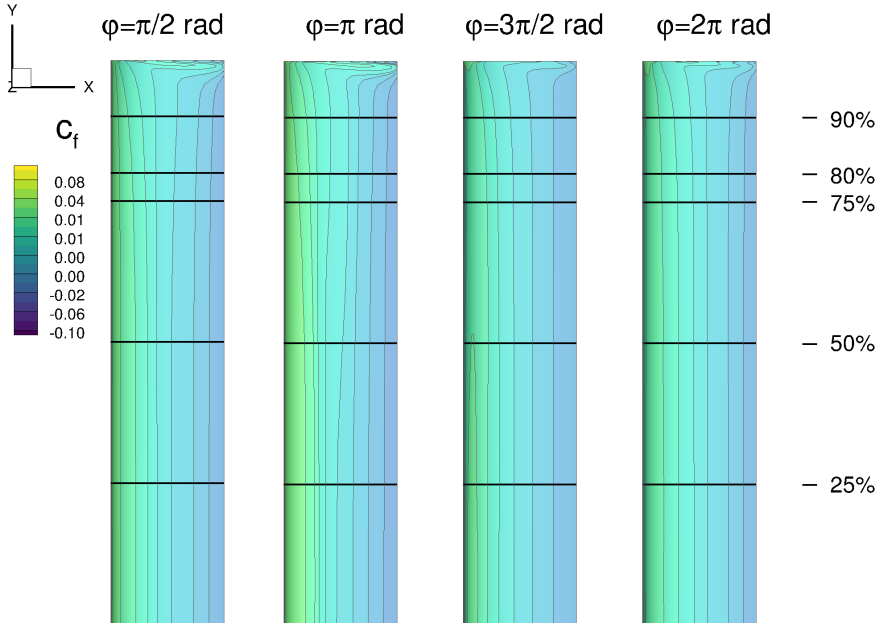

FIGURE A.34: Friction coefficient, c_f, of the NACA2412–wing at $M = 0.7$ and $k = 0.750$ during forced harmonic pitching oscillation, third cycle

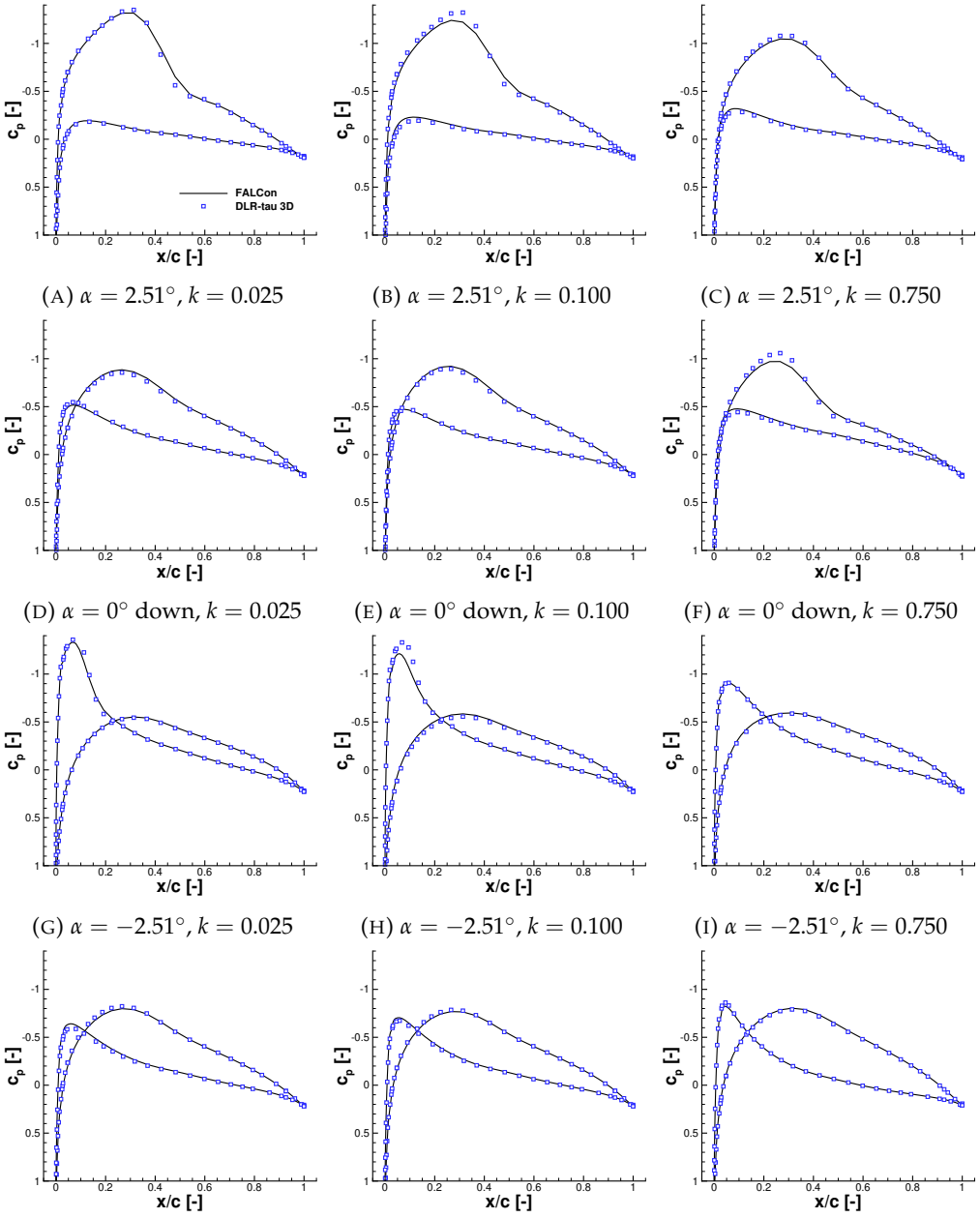

(A) $\alpha = 2.51°$, $k = 0.025$ (B) $\alpha = 2.51°$, $k = 0.100$ (C) $\alpha = 2.51°$, $k = 0.750$

(D) $\alpha = 0°$ down, $k = 0.025$ (E) $\alpha = 0°$ down, $k = 0.100$ (F) $\alpha = 0°$ down, $k = 0.750$

(G) $\alpha = -2.51°$, $k = 0.025$ (H) $\alpha = -2.51°$, $k = 0.100$ (I) $\alpha = -2.51°$, $k = 0.750$

(J) $\alpha = 0°$ up, $k = 0.025$ (K) $\alpha = 0°$ up, $k = 0.100$ (L) $\alpha = 0°$ up, $k = 0.750$

FIGURE A.35: Sectional pressure coefficient, c_p, of the third cycle of the pitching unswept NACA2412 wing at $M = 0.7$ and $\Delta\alpha_A = 2.51°$, at 25% of the half–span

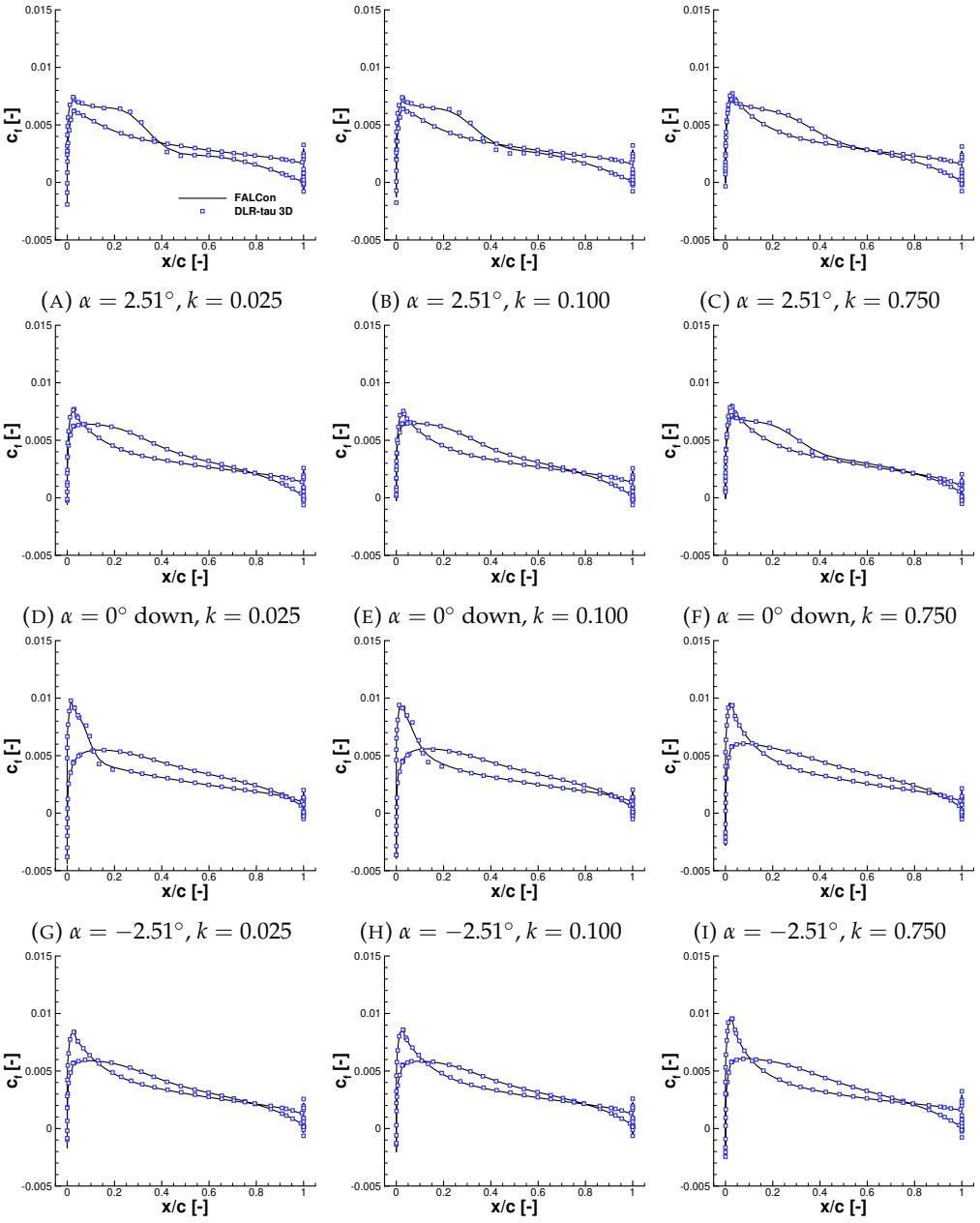

(A) $\alpha = 2.51°$, $k = 0.025$ (B) $\alpha = 2.51°$, $k = 0.100$ (C) $\alpha = 2.51°$, $k = 0.750$

(D) $\alpha = 0°$ down, $k = 0.025$ (E) $\alpha = 0°$ down, $k = 0.100$ (F) $\alpha = 0°$ down, $k = 0.750$

(G) $\alpha = -2.51°$, $k = 0.025$ (H) $\alpha = -2.51°$, $k = 0.100$ (I) $\alpha = -2.51°$, $k = 0.750$

(J) $\alpha = 0°$ up, $k = 0.025$ (K) $\alpha = 0°$ up, $k = 0.100$ (L) $\alpha = 0°$ up, $k = 0.750$

FIGURE A.36: Sectional friction coefficient, c_f, of the third cycle of the pitching unswept NACA2412 wing at $M = 0.7$ and $\Delta\alpha_A = 2.51°$, at 25% of the half–span

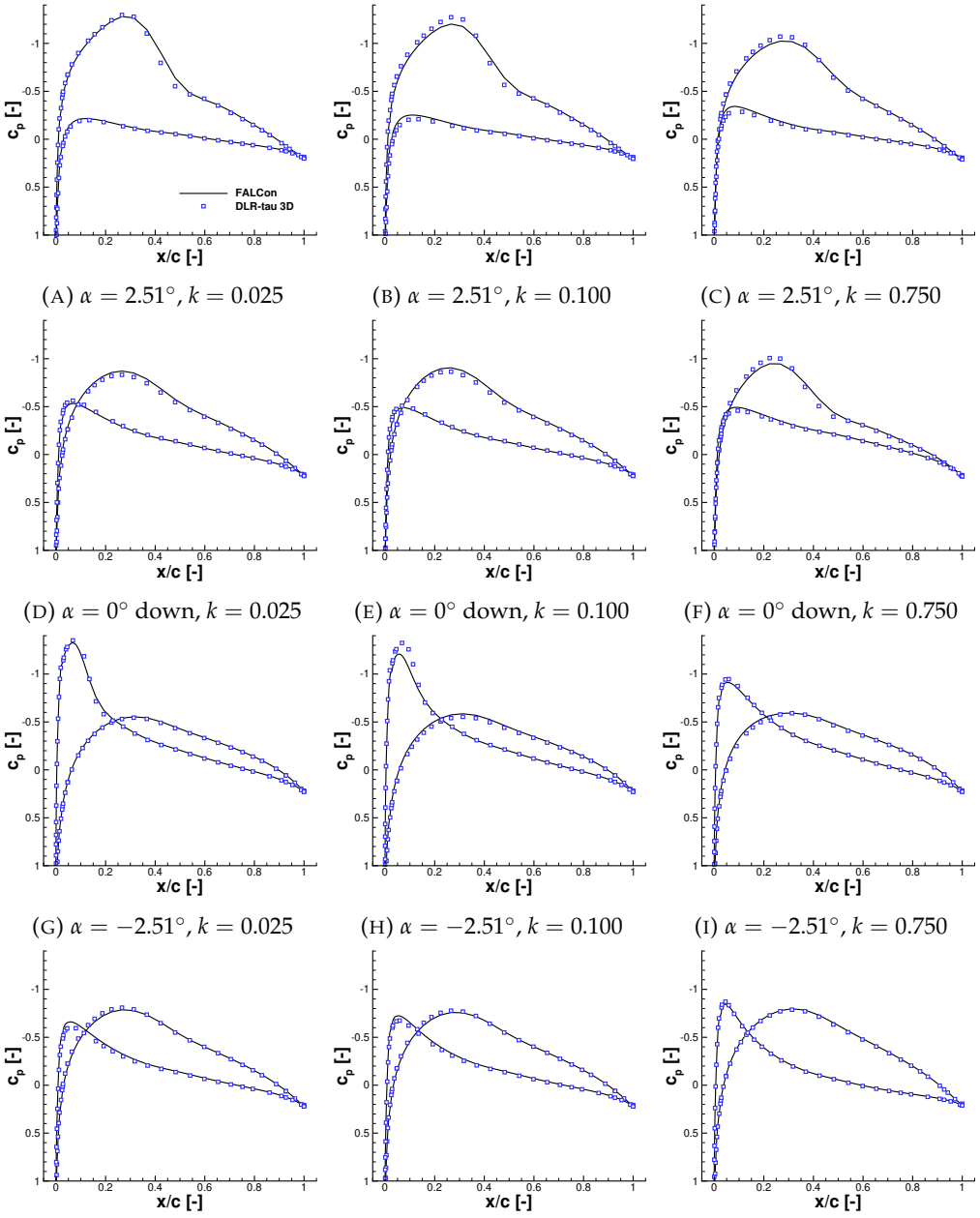

(A) $\alpha = 2.51°$, $k = 0.025$ (B) $\alpha = 2.51°$, $k = 0.100$ (C) $\alpha = 2.51°$, $k = 0.750$

(D) $\alpha = 0°$ down, $k = 0.025$ (E) $\alpha = 0°$ down, $k = 0.100$ (F) $\alpha = 0°$ down, $k = 0.750$

(G) $\alpha = -2.51°$, $k = 0.025$ (H) $\alpha = -2.51°$, $k = 0.100$ (I) $\alpha = -2.51°$, $k = 0.750$

(J) $\alpha = 0°$ up, $k = 0.025$ (K) $\alpha = 0°$ up, $k = 0.100$ (L) $\alpha = 0°$ up, $k = 0.750$

FIGURE A.37: Sectional pressure coefficient, c_p, of the third cycle of the pitching unswept NACA2412 wing at $M = 0.7$ and $\Delta\alpha_A = 2.51°$, at 50% of the half–span

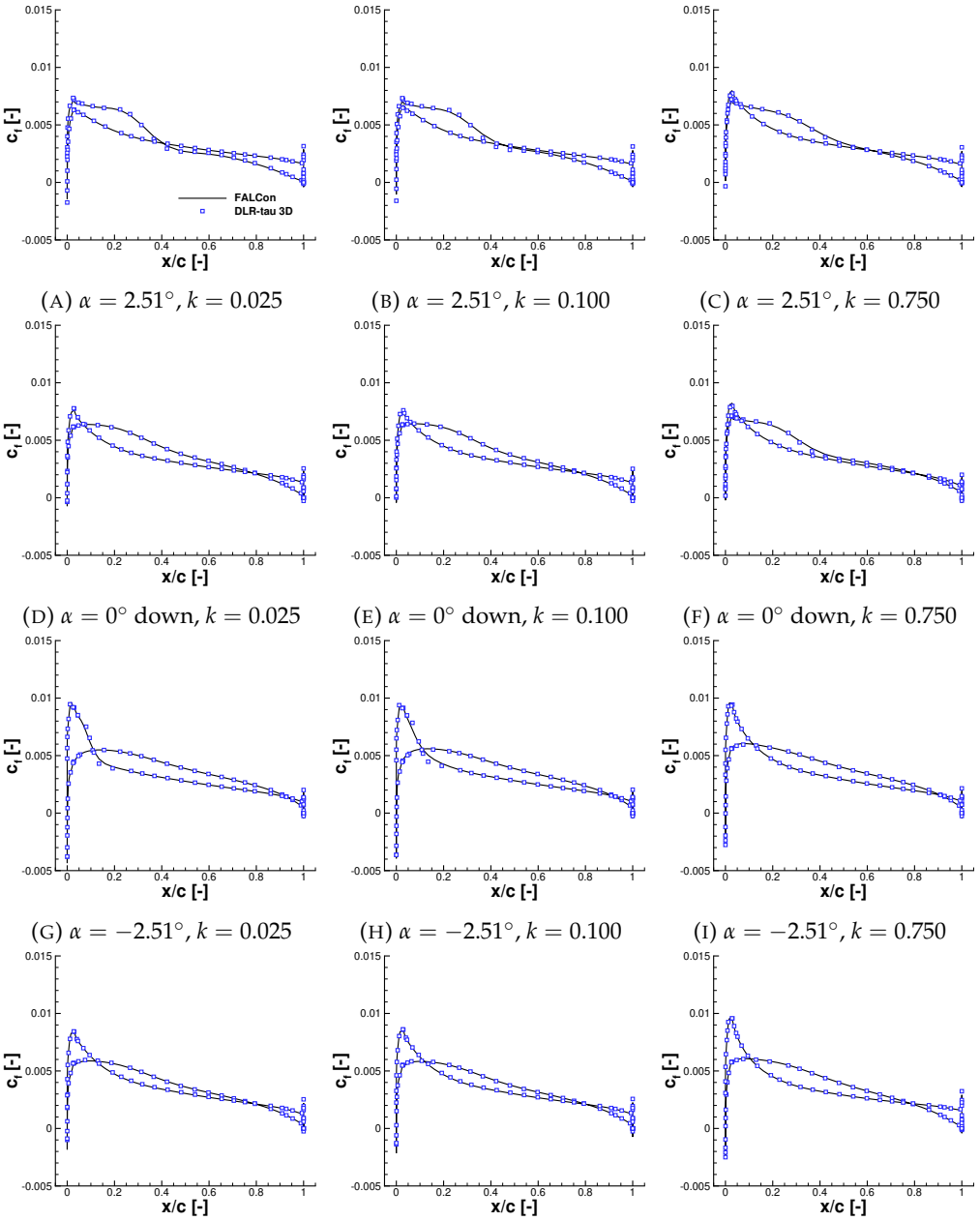

(A) $\alpha = 2.51°$, $k = 0.025$ (B) $\alpha = 2.51°$, $k = 0.100$ (C) $\alpha = 2.51°$, $k = 0.750$

(D) $\alpha = 0°$ down, $k = 0.025$ (E) $\alpha = 0°$ down, $k = 0.100$ (F) $\alpha = 0°$ down, $k = 0.750$

(G) $\alpha = -2.51°$, $k = 0.025$ (H) $\alpha = -2.51°$, $k = 0.100$ (I) $\alpha = -2.51°$, $k = 0.750$

(J) $\alpha = 0°$ up, $k = 0.025$ (K) $\alpha = 0°$ up, $k = 0.100$ (L) $\alpha = 0°$ up, $k = 0.750$

FIGURE A.38: Sectional friction coefficient, c_f, of the third cycle of the pitching unswept NACA2412 wing at $M = 0.7$ and $\Delta\alpha_A = 2.51°$, at 50% of the half–span

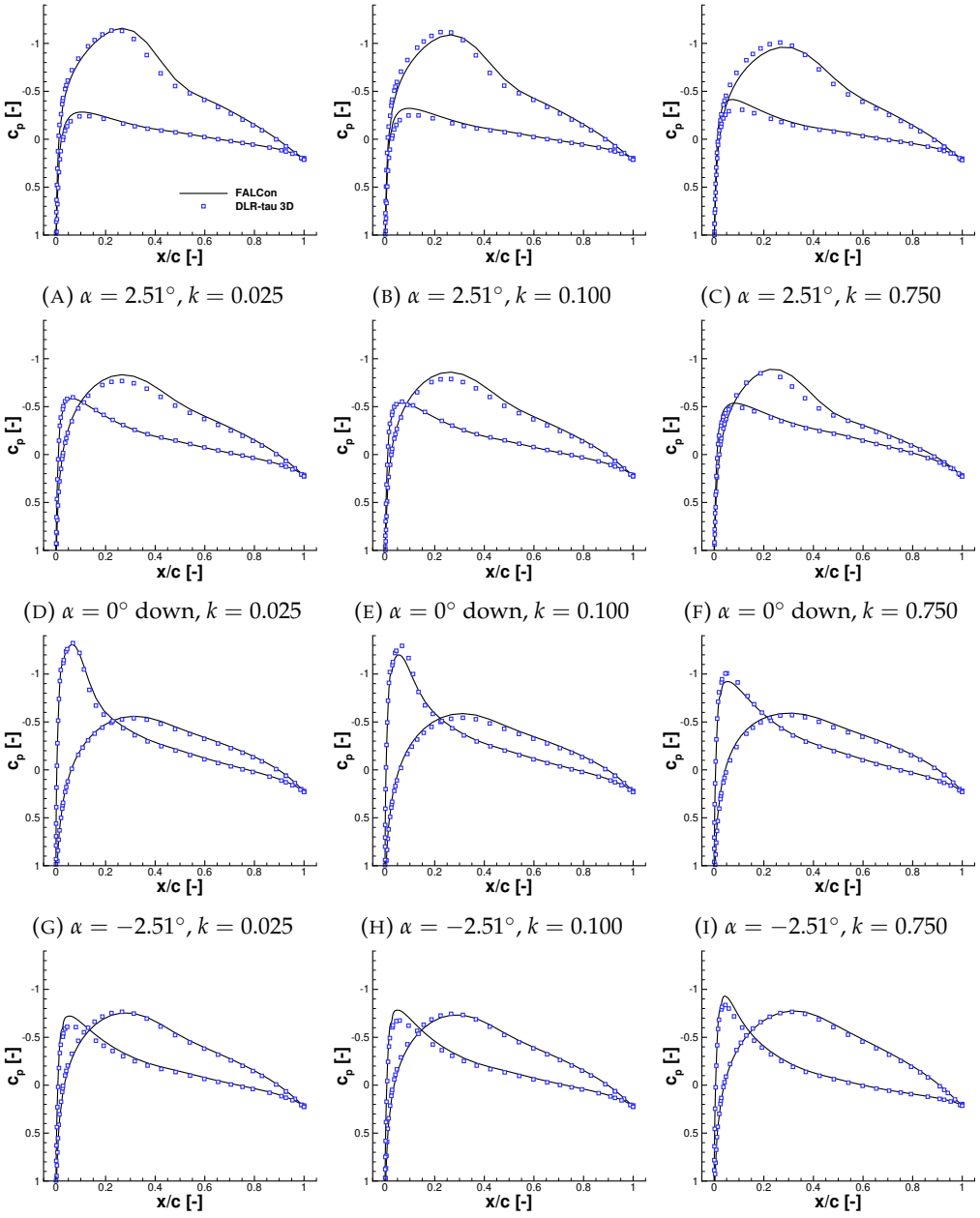

(A) $\alpha = 2.51°$, $k = 0.025$ (B) $\alpha = 2.51°$, $k = 0.100$ (C) $\alpha = 2.51°$, $k = 0.750$

(D) $\alpha = 0°$ down, $k = 0.025$ (E) $\alpha = 0°$ down, $k = 0.100$ (F) $\alpha = 0°$ down, $k = 0.750$

(G) $\alpha = -2.51°$, $k = 0.025$ (H) $\alpha = -2.51°$, $k = 0.100$ (I) $\alpha = -2.51°$, $k = 0.750$

(J) $\alpha = 0°$ up, $k = 0.025$ (K) $\alpha = 0°$ up, $k = 0.100$ (L) $\alpha = 0°$ up, $k = 0.750$

FIGURE A.39: Sectional pressure coefficient, c_p, of the third cycle of the pitching unswept NACA2412 wing at $M = 0.7$ and $\Delta\alpha_A = 2.51°$, at 75% of the half–span

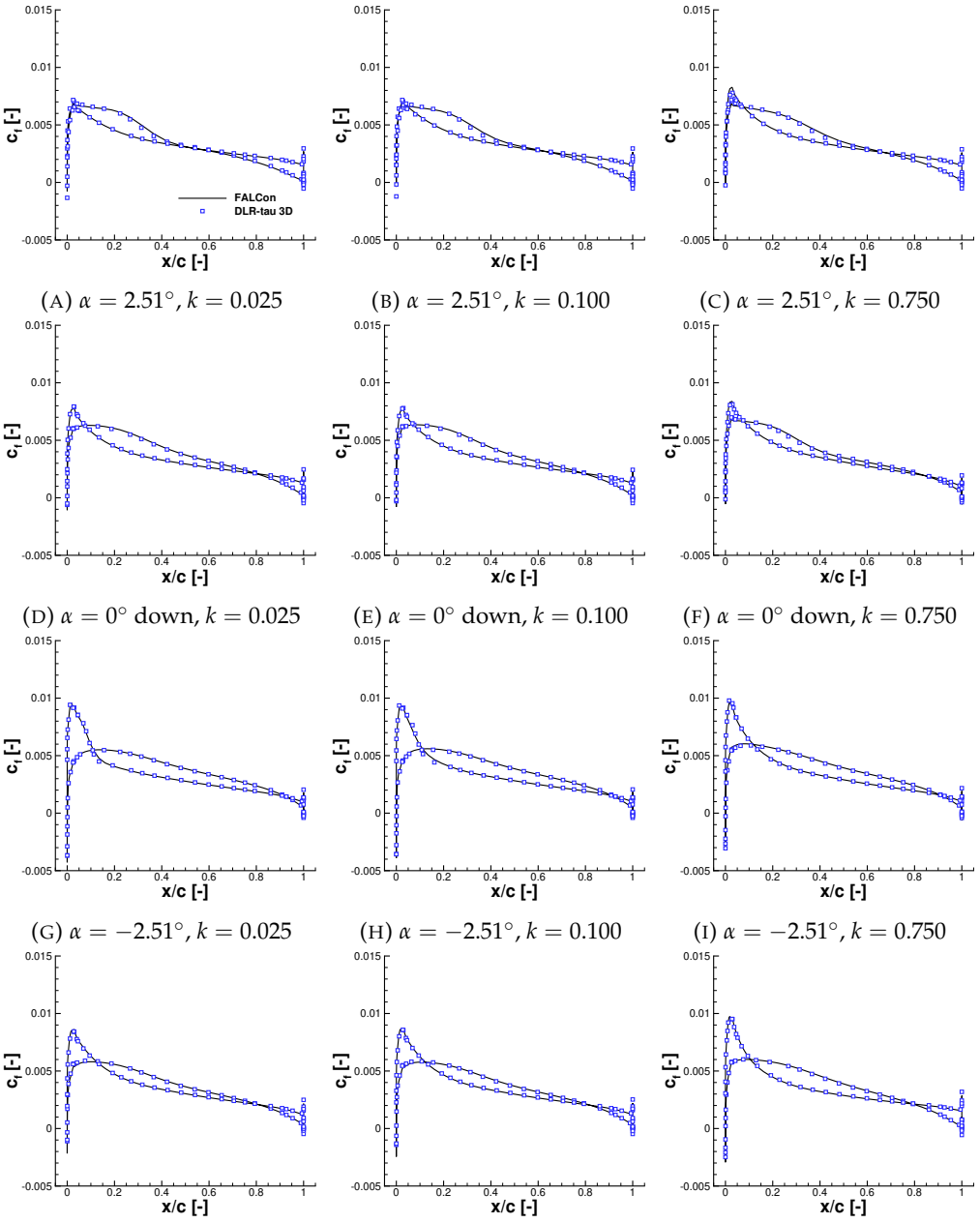

(A) $\alpha = 2.51°$, $k = 0.025$ (B) $\alpha = 2.51°$, $k = 0.100$ (C) $\alpha = 2.51°$, $k = 0.750$

(D) $\alpha = 0°$ down, $k = 0.025$ (E) $\alpha = 0°$ down, $k = 0.100$ (F) $\alpha = 0°$ down, $k = 0.750$

(G) $\alpha = -2.51°$, $k = 0.025$ (H) $\alpha = -2.51°$, $k = 0.100$ (I) $\alpha = -2.51°$, $k = 0.750$

(J) $\alpha = 0°$ up, $k = 0.025$ (K) $\alpha = 0°$ up, $k = 0.100$ (L) $\alpha = 0°$ up, $k = 0.750$

FIGURE A.40: Sectional friction coefficient, c_f, of the third cycle of the pitching unswept NACA2412 wing at $M = 0.7$ and $\Delta\alpha_A = 2.51°$, at 75% of the half–span

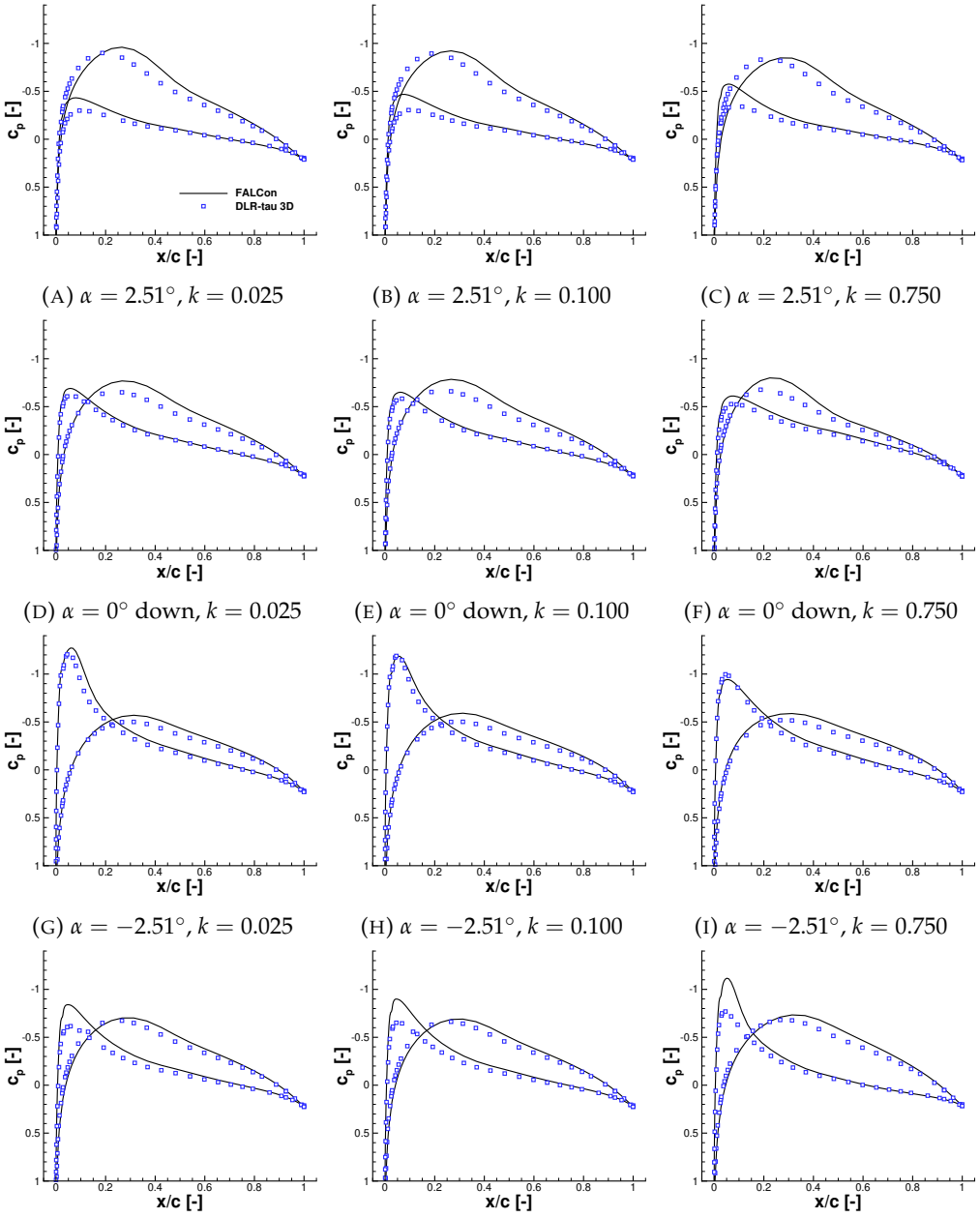

(A) $\alpha = 2.51°$, $k = 0.025$ (B) $\alpha = 2.51°$, $k = 0.100$ (C) $\alpha = 2.51°$, $k = 0.750$

(D) $\alpha = 0°$ down, $k = 0.025$ (E) $\alpha = 0°$ down, $k = 0.100$ (F) $\alpha = 0°$ down, $k = 0.750$

(G) $\alpha = -2.51°$, $k = 0.025$ (H) $\alpha = -2.51°$, $k = 0.100$ (I) $\alpha = -2.51°$, $k = 0.750$

(J) $\alpha = 0°$ up, $k = 0.025$ (K) $\alpha = 0°$ up, $k = 0.100$ (L) $\alpha = 0°$ up, $k = 0.750$

FIGURE A.41: Sectional pressure coefficient, c_p, of the third cycle of the pitching unswept NACA2412 wing at $M = 0.7$ and $\Delta\alpha_A = 2.51°$, at 90% of the half–span

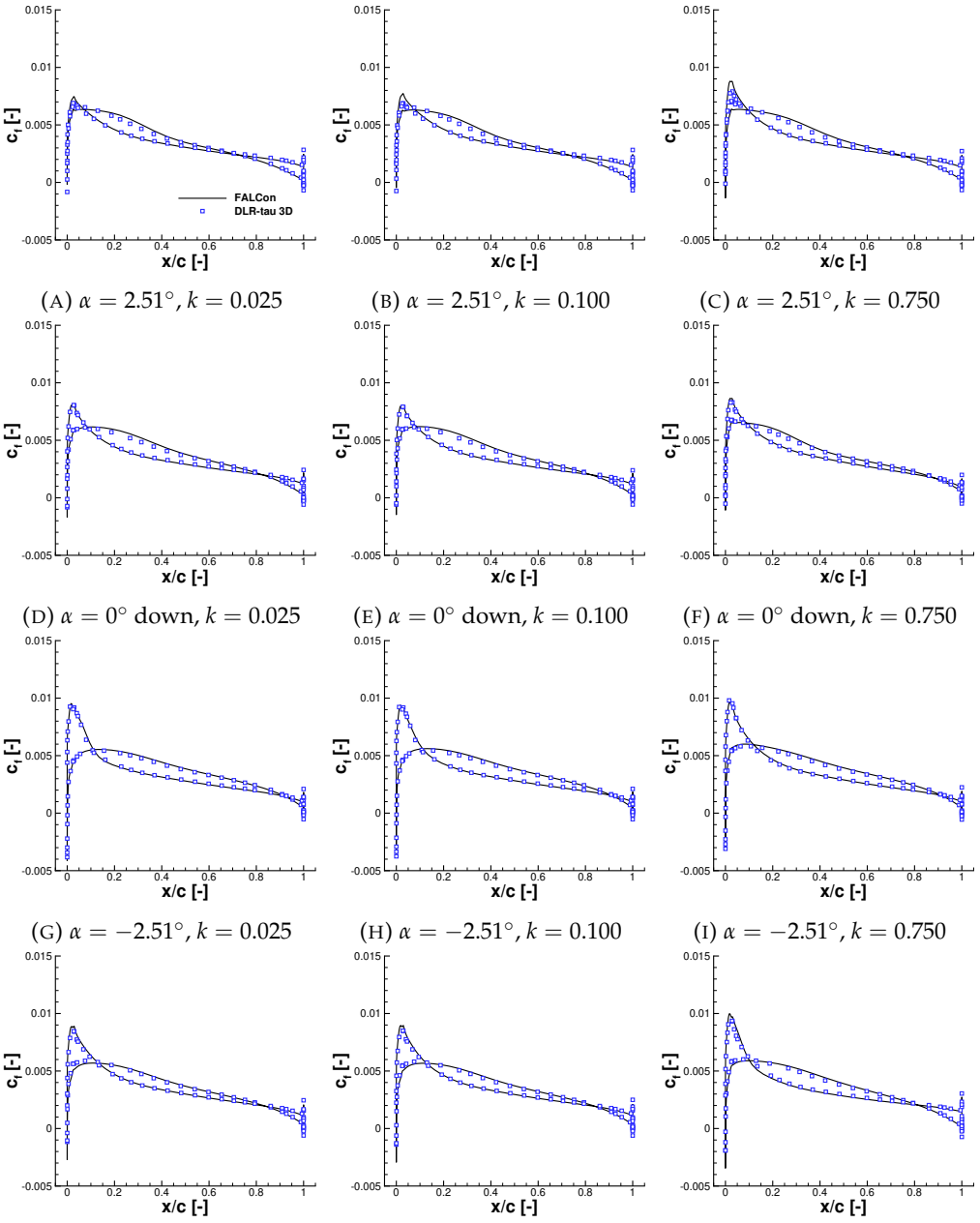

(A) $\alpha = 2.51°$, $k = 0.025$ (B) $\alpha = 2.51°$, $k = 0.100$ (C) $\alpha = 2.51°$, $k = 0.750$

(D) $\alpha = 0°$ down, $k = 0.025$ (E) $\alpha = 0°$ down, $k = 0.100$ (F) $\alpha = 0°$ down, $k = 0.750$

(G) $\alpha = -2.51°$, $k = 0.025$ (H) $\alpha = -2.51°$, $k = 0.100$ (I) $\alpha = -2.51°$, $k = 0.750$

(J) $\alpha = 0°$ up, $k = 0.025$ (K) $\alpha = 0°$ up, $k = 0.100$ (L) $\alpha = 0°$ up, $k = 0.750$

FIGURE A.42: Sectional friction coefficient, c_f, of the third cycle of the pitching unswept NACA2412 wing at $M = 0.7$ and $\Delta\alpha_A = 2.51°$, at 90% of the half–span

A.1.1.4 Mach $M = 0.8$

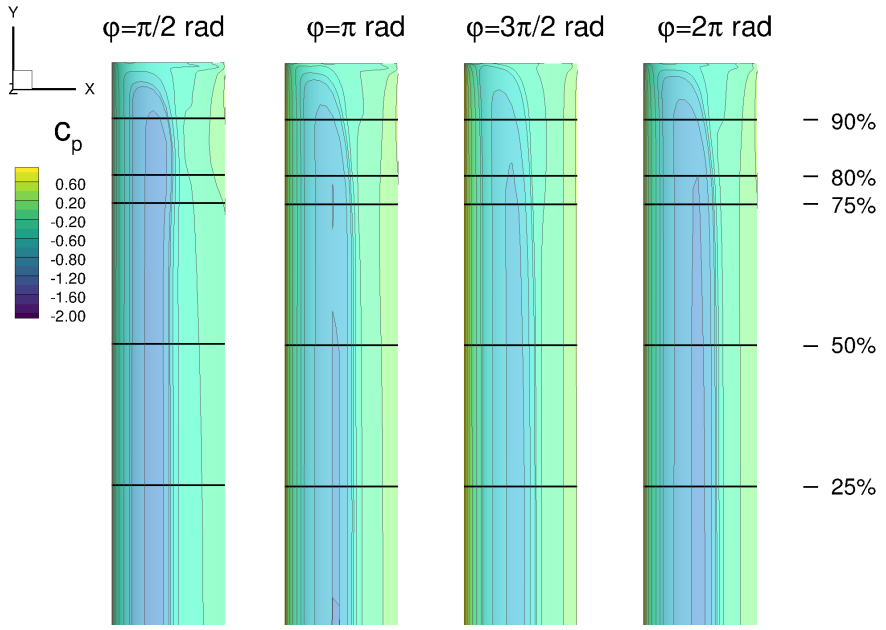

FIGURE A.43: Pressure coefficient, c_p, of the NACA2412–wing at $M = 0.8$ and $k = 0.025$ during forced harmonic pitching oscillation, third cycle

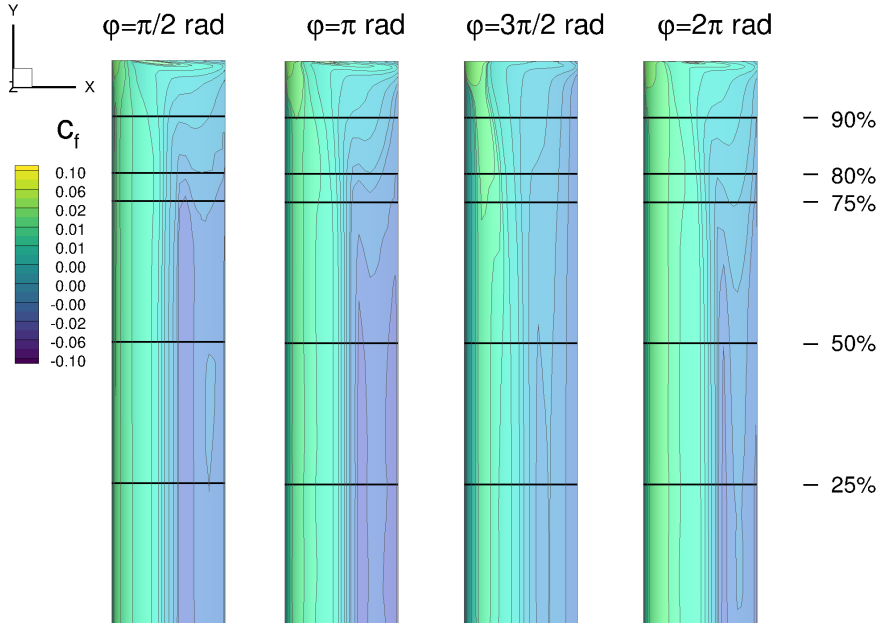

FIGURE A.44: Friction coefficient, c_f, of the NACA2412–wing at $M = 0.8$ and $k = 0.025$ during forced harmonic pitching oscillation, third cycle

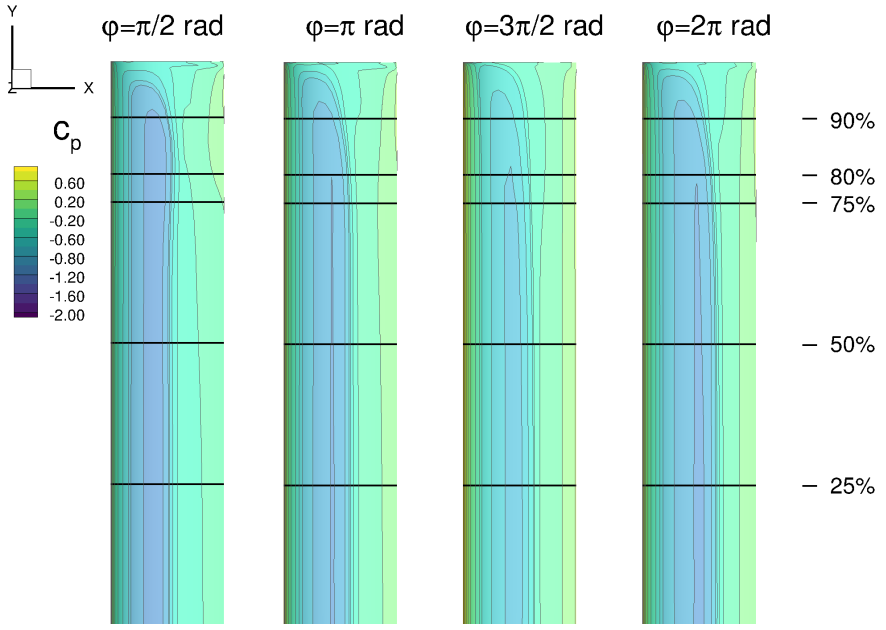

FIGURE A.45: Pressure coefficient, c_p, of the NACA2412–wing at $M = 0.8$ and $k = 0.100$ during forced harmonic pitching oscillation, third cycle

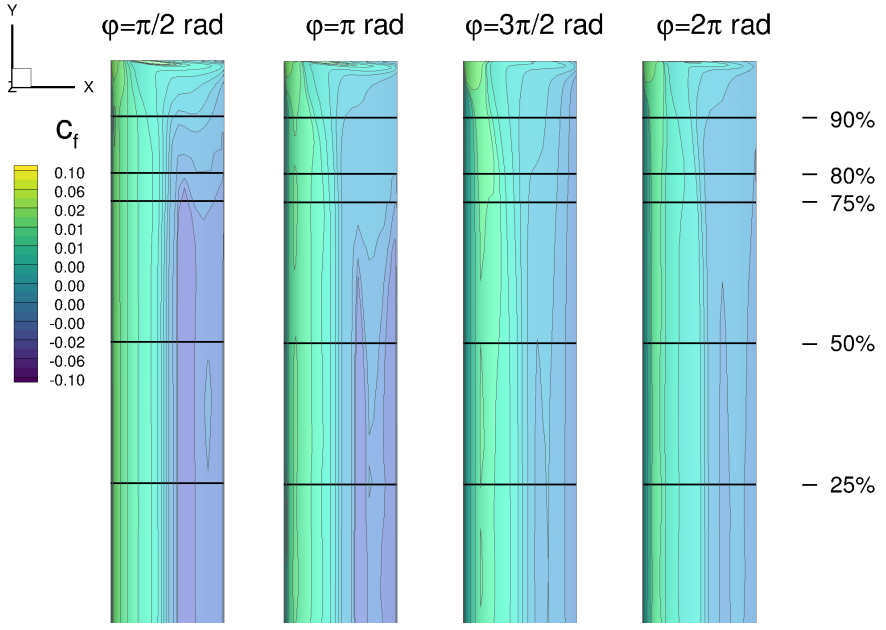

FIGURE A.46: Friction coefficient, c_f, of the NACA2412–wing at $M = 0.8$ and $k = 0.100$ during forced harmonic pitching oscillation, third cycle

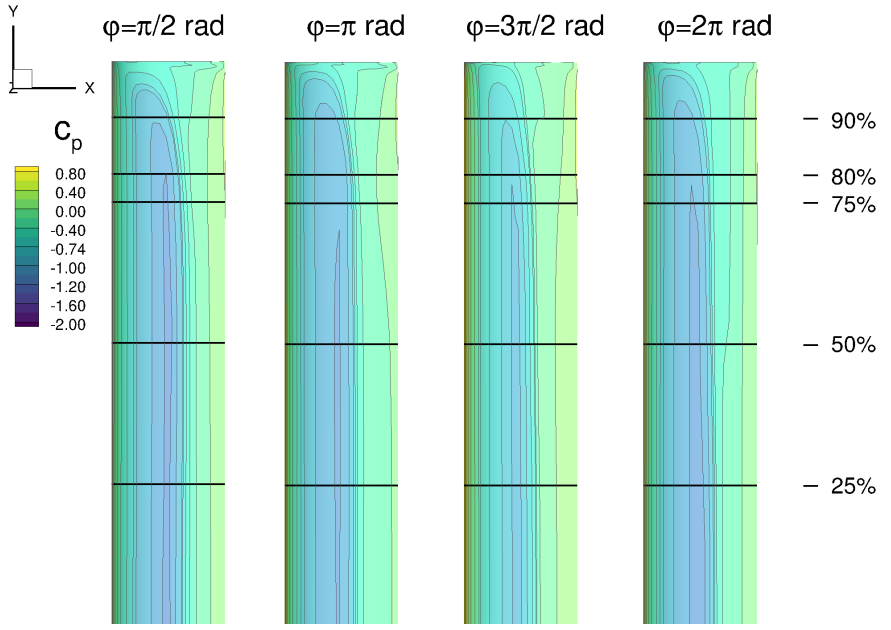

FIGURE A.47: Pressure coefficient, c_p, of the NACA2412–wing at $M = 0.8$ and $k = 0.750$ during forced harmonic pitching oscillation, third cycle

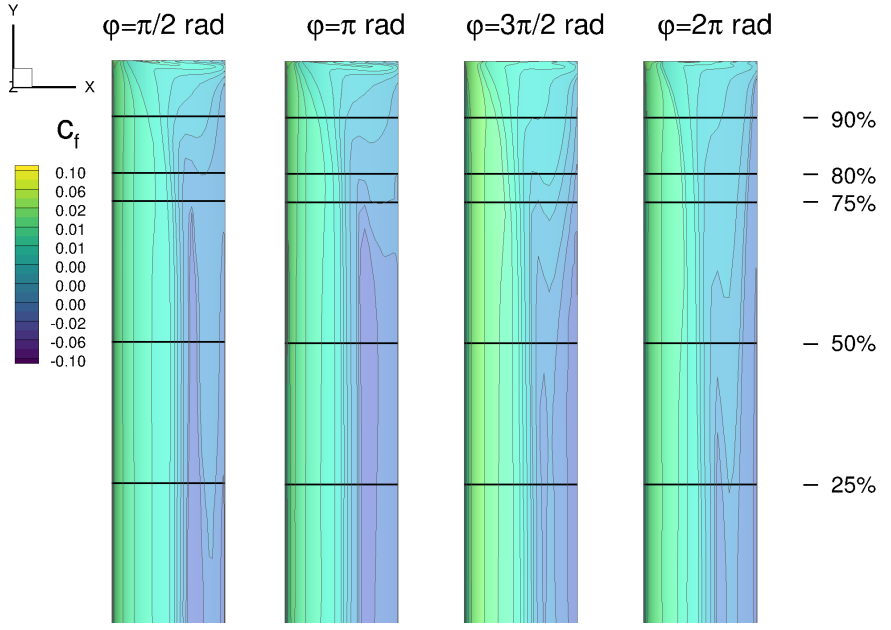

FIGURE A.48: Friction coefficient, c_f, of the NACA2412–wing at $M = 0.8$ and $k = 0.750$ during forced harmonic pitching oscillation, third cycle

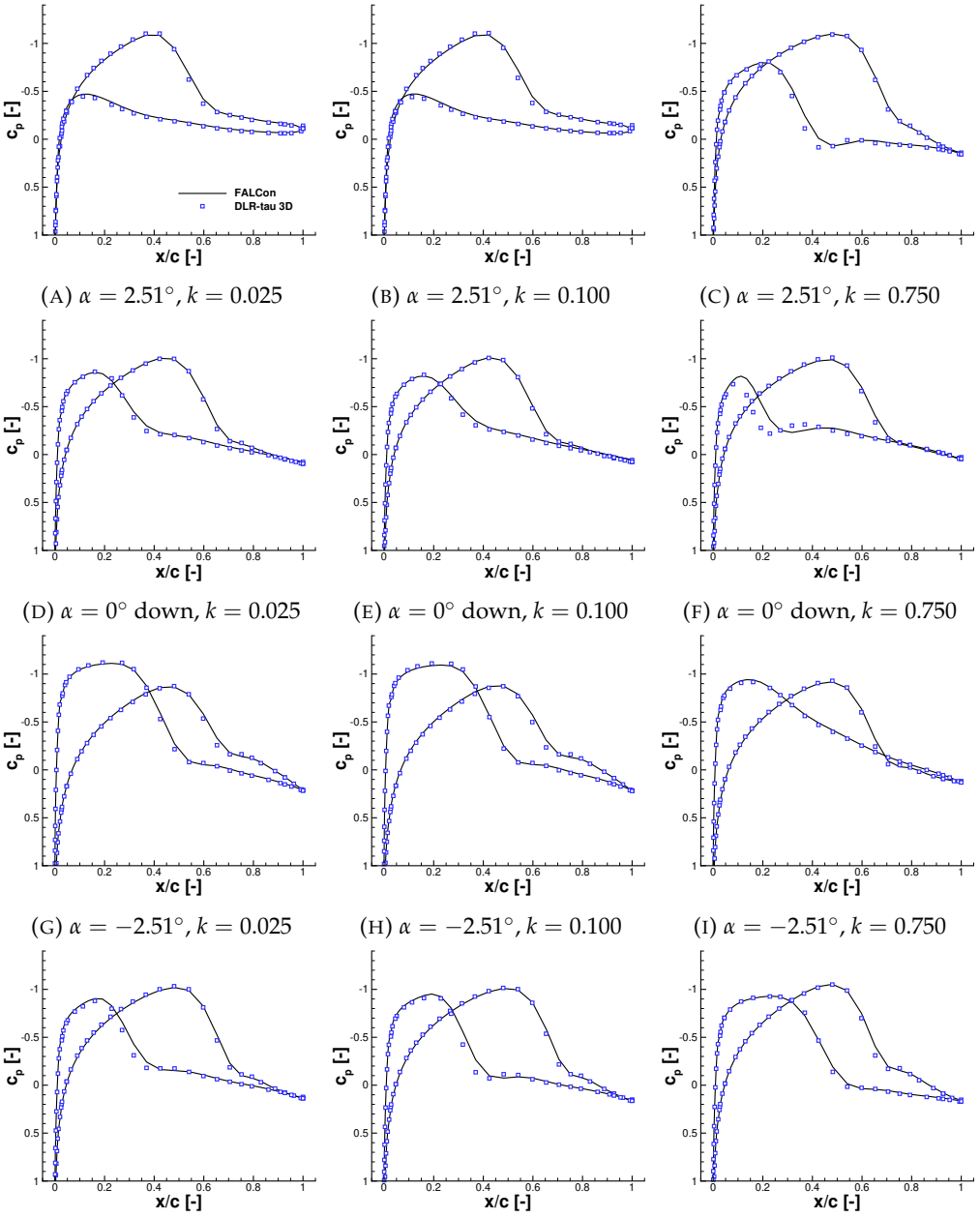

(A) $\alpha = 2.51°$, $k = 0.025$ (B) $\alpha = 2.51°$, $k = 0.100$ (C) $\alpha = 2.51°$, $k = 0.750$

(D) $\alpha = 0°$ down, $k = 0.025$ (E) $\alpha = 0°$ down, $k = 0.100$ (F) $\alpha = 0°$ down, $k = 0.750$

(G) $\alpha = -2.51°$, $k = 0.025$ (H) $\alpha = -2.51°$, $k = 0.100$ (I) $\alpha = -2.51°$, $k = 0.750$

(J) $\alpha = 0°$ up, $k = 0.025$ (K) $\alpha = 0°$ up, $k = 0.100$ (L) $\alpha = 0°$ up, $k = 0.750$

FIGURE A.49: Sectional pressure coefficient, c_p, of the third cycle of the pitching unswept NACA2412 wing at $M = 0.8$ and $\Delta\alpha_A = 2.51°$, at 25% of the half–span

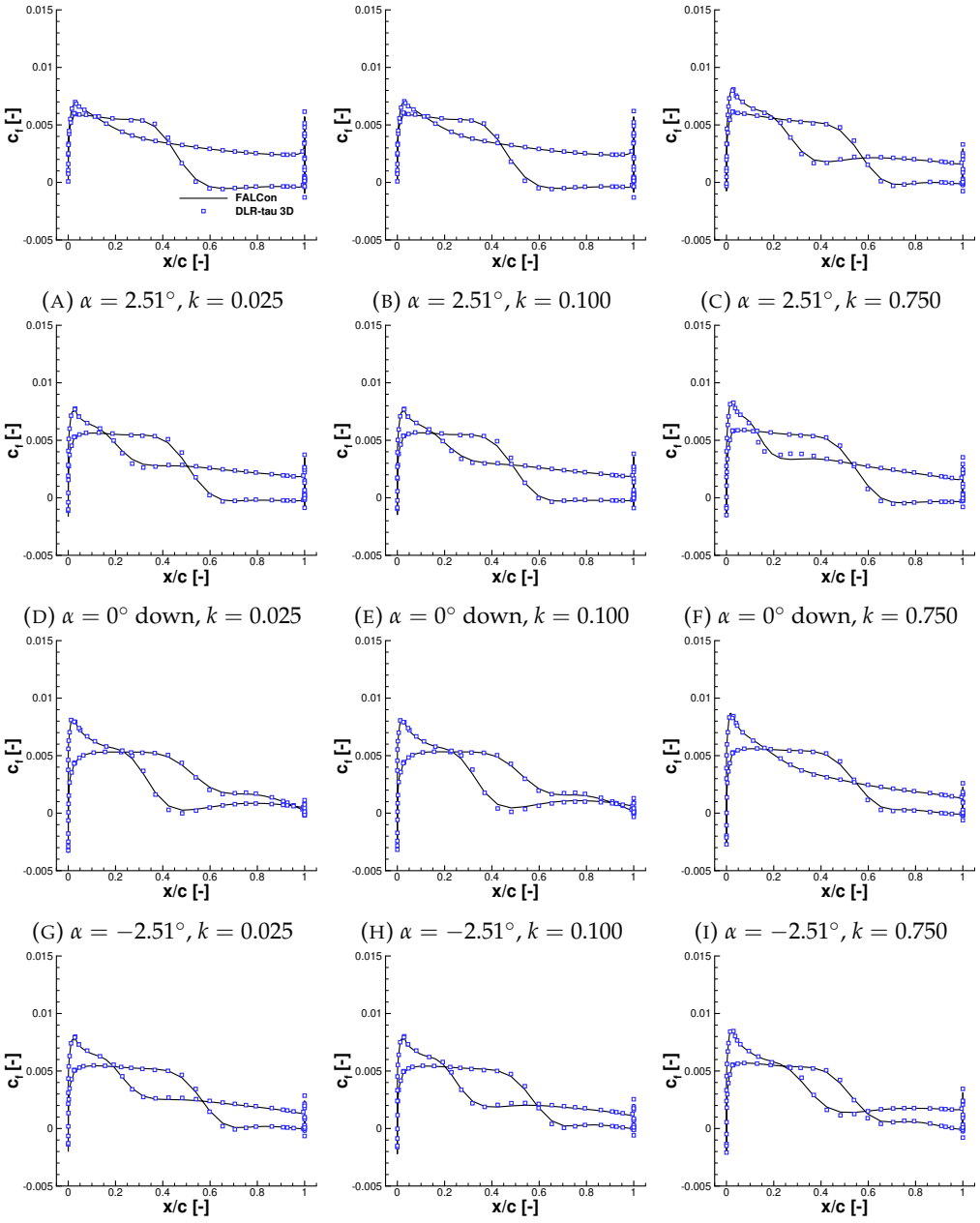

(A) $\alpha = 2.51°$, $k = 0.025$ (B) $\alpha = 2.51°$, $k = 0.100$ (C) $\alpha = 2.51°$, $k = 0.750$

(D) $\alpha = 0°$ down, $k = 0.025$ (E) $\alpha = 0°$ down, $k = 0.100$ (F) $\alpha = 0°$ down, $k = 0.750$

(G) $\alpha = -2.51°$, $k = 0.025$ (H) $\alpha = -2.51°$, $k = 0.100$ (I) $\alpha = -2.51°$, $k = 0.750$

(J) $\alpha = 0°$ up, $k = 0.025$ (K) $\alpha = 0°$ up, $k = 0.100$ (L) $\alpha = 0°$ up, $k = 0.750$

FIGURE A.50: Sectional friction coefficient, c_f, of the third cycle of the pitching unswept NACA2412 wing at $M = 0.8$ and $\Delta\alpha_A = 2.51°$, at 25% of the half–span

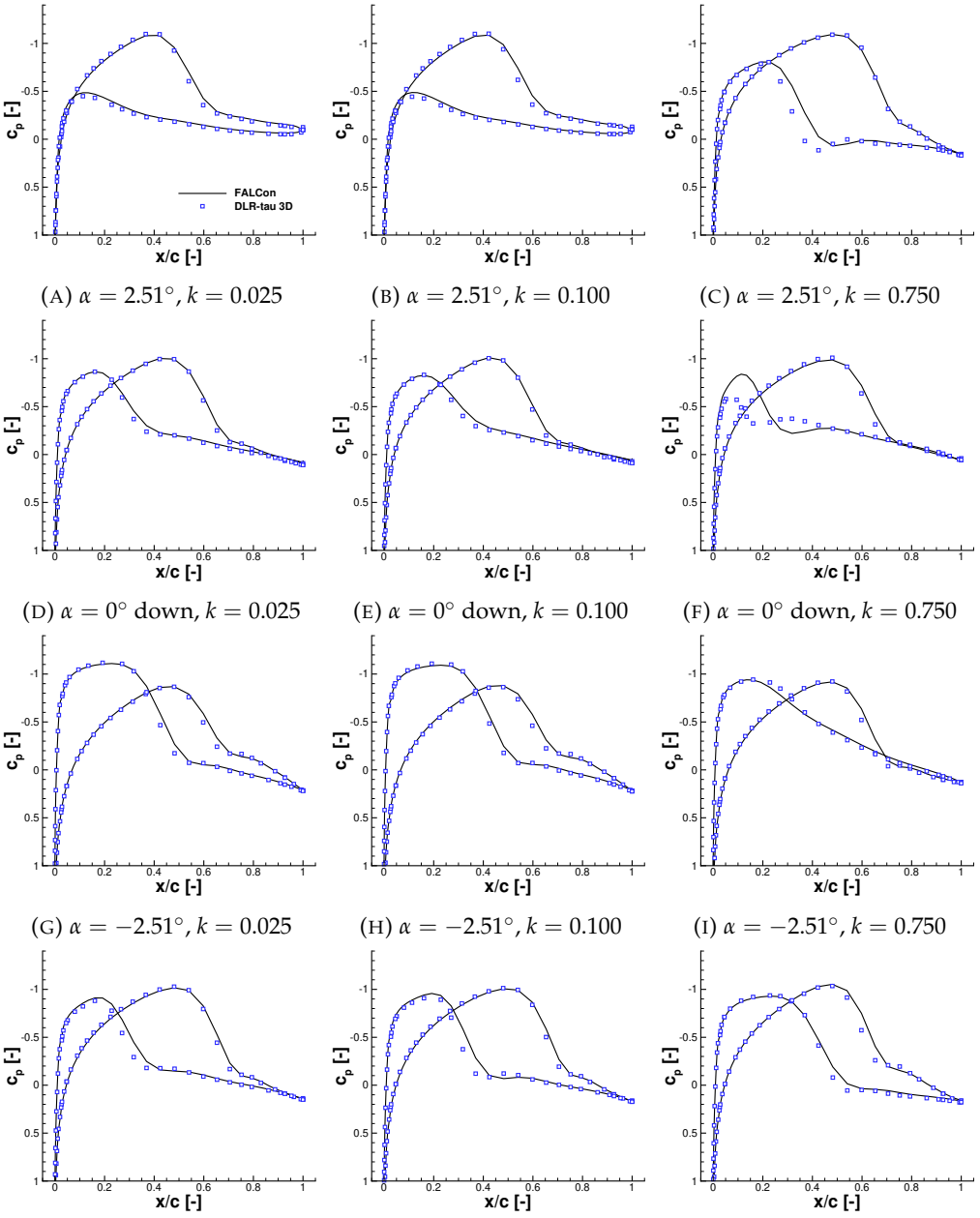

(A) $\alpha = 2.51°$, $k = 0.025$ (B) $\alpha = 2.51°$, $k = 0.100$ (C) $\alpha = 2.51°$, $k = 0.750$

(D) $\alpha = 0°$ down, $k = 0.025$ (E) $\alpha = 0°$ down, $k = 0.100$ (F) $\alpha = 0°$ down, $k = 0.750$

(G) $\alpha = -2.51°$, $k = 0.025$ (H) $\alpha = -2.51°$, $k = 0.100$ (I) $\alpha = -2.51°$, $k = 0.750$

(J) $\alpha = 0°$ up, $k = 0.025$ (K) $\alpha = 0°$ up, $k = 0.100$ (L) $\alpha = 0°$ up, $k = 0.750$

FIGURE A.51: Sectional pressure coefficient, c_p, of the third cycle of the pitching unswept NACA2412 wing at $M = 0.8$ and $\Delta\alpha_A = 2.51°$, at 50% of the half–span

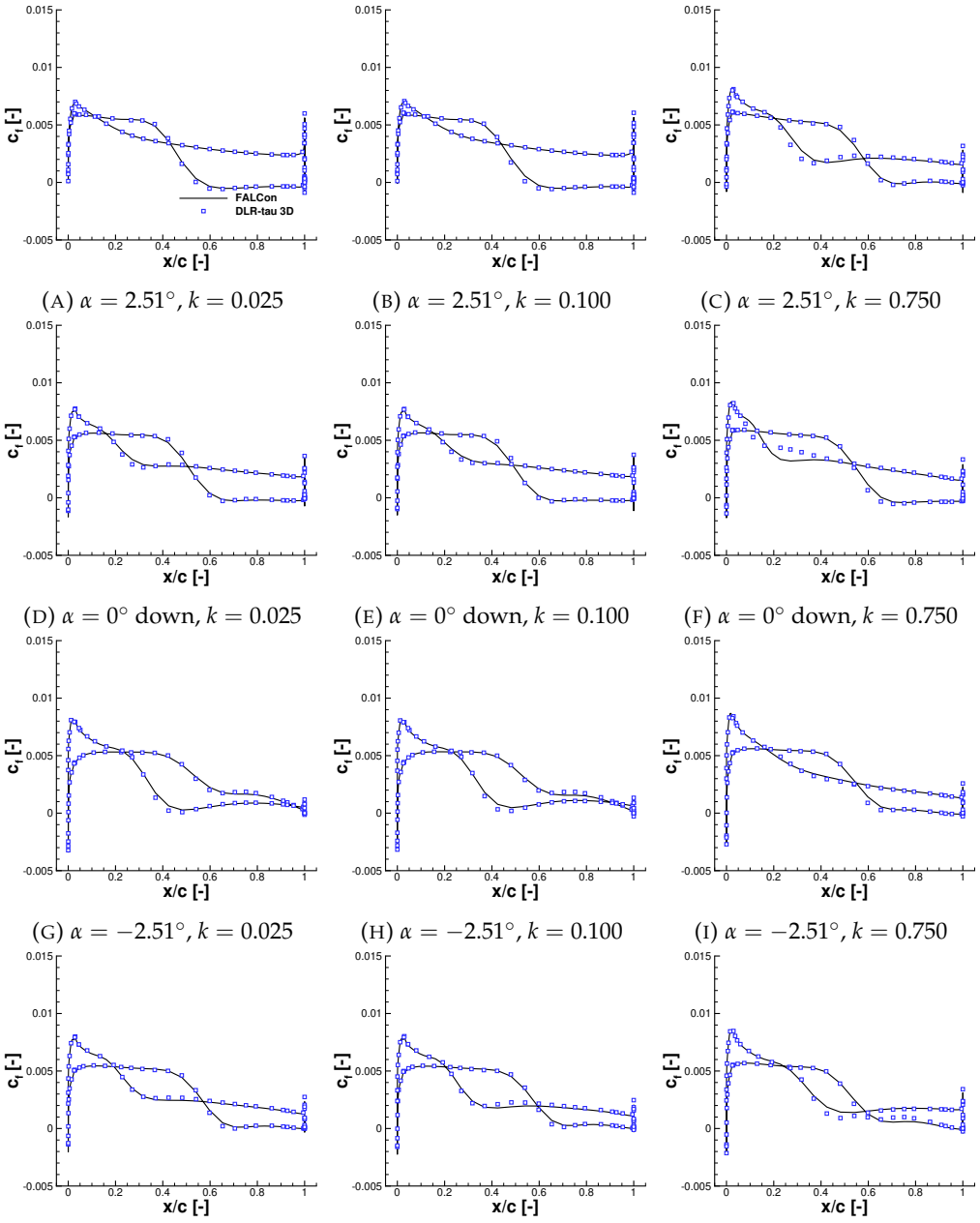

(A) $\alpha = 2.51°$, $k = 0.025$ (B) $\alpha = 2.51°$, $k = 0.100$ (C) $\alpha = 2.51°$, $k = 0.750$

(D) $\alpha = 0°$ down, $k = 0.025$ (E) $\alpha = 0°$ down, $k = 0.100$ (F) $\alpha = 0°$ down, $k = 0.750$

(G) $\alpha = -2.51°$, $k = 0.025$ (H) $\alpha = -2.51°$, $k = 0.100$ (I) $\alpha = -2.51°$, $k = 0.750$

(J) $\alpha = 0°$ up, $k = 0.025$ (K) $\alpha = 0°$ up, $k = 0.100$ (L) $\alpha = 0°$ up, $k = 0.750$

FIGURE A.52: Sectional friction coefficient, c_f, of the third cycle of the pitching unswept NACA2412 wing at $M = 0.8$ and $\Delta\alpha_A = 2.51°$, at 50% of the half–span

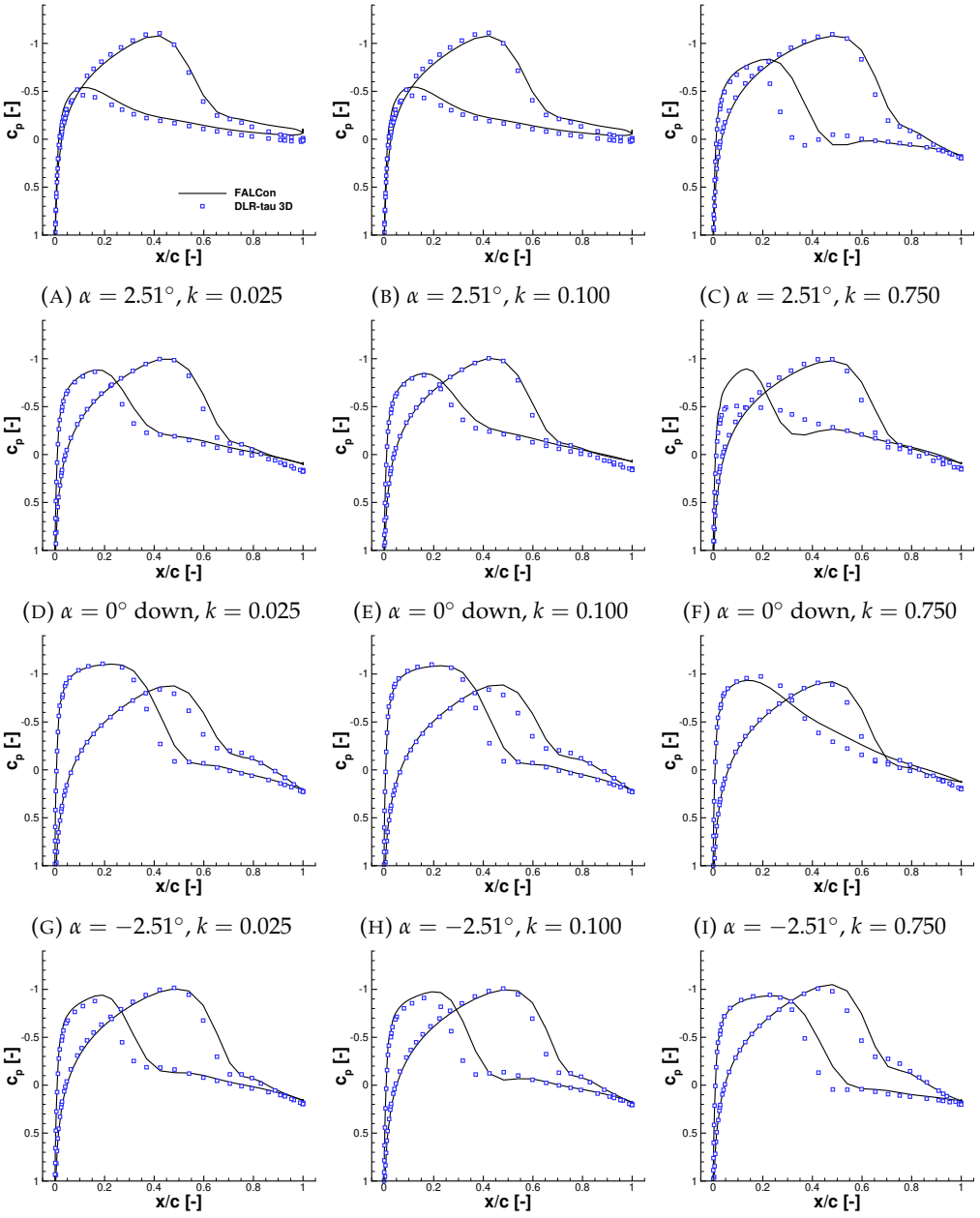

(A) $\alpha = 2.51°$, $k = 0.025$ (B) $\alpha = 2.51°$, $k = 0.100$ (C) $\alpha = 2.51°$, $k = 0.750$

(D) $\alpha = 0°$ down, $k = 0.025$ (E) $\alpha = 0°$ down, $k = 0.100$ (F) $\alpha = 0°$ down, $k = 0.750$

(G) $\alpha = -2.51°$, $k = 0.025$ (H) $\alpha = -2.51°$, $k = 0.100$ (I) $\alpha = -2.51°$, $k = 0.750$

(J) $\alpha = 0°$ up, $k = 0.025$ (K) $\alpha = 0°$ up, $k = 0.100$ (L) $\alpha = 0°$ up, $k = 0.750$

FIGURE A.53: Sectional pressure coefficient, c_p, of the third cycle of the pitching unswept NACA2412 wing at $M = 0.8$ and $\Delta\alpha_A = 2.51°$, at 75% of the half–span

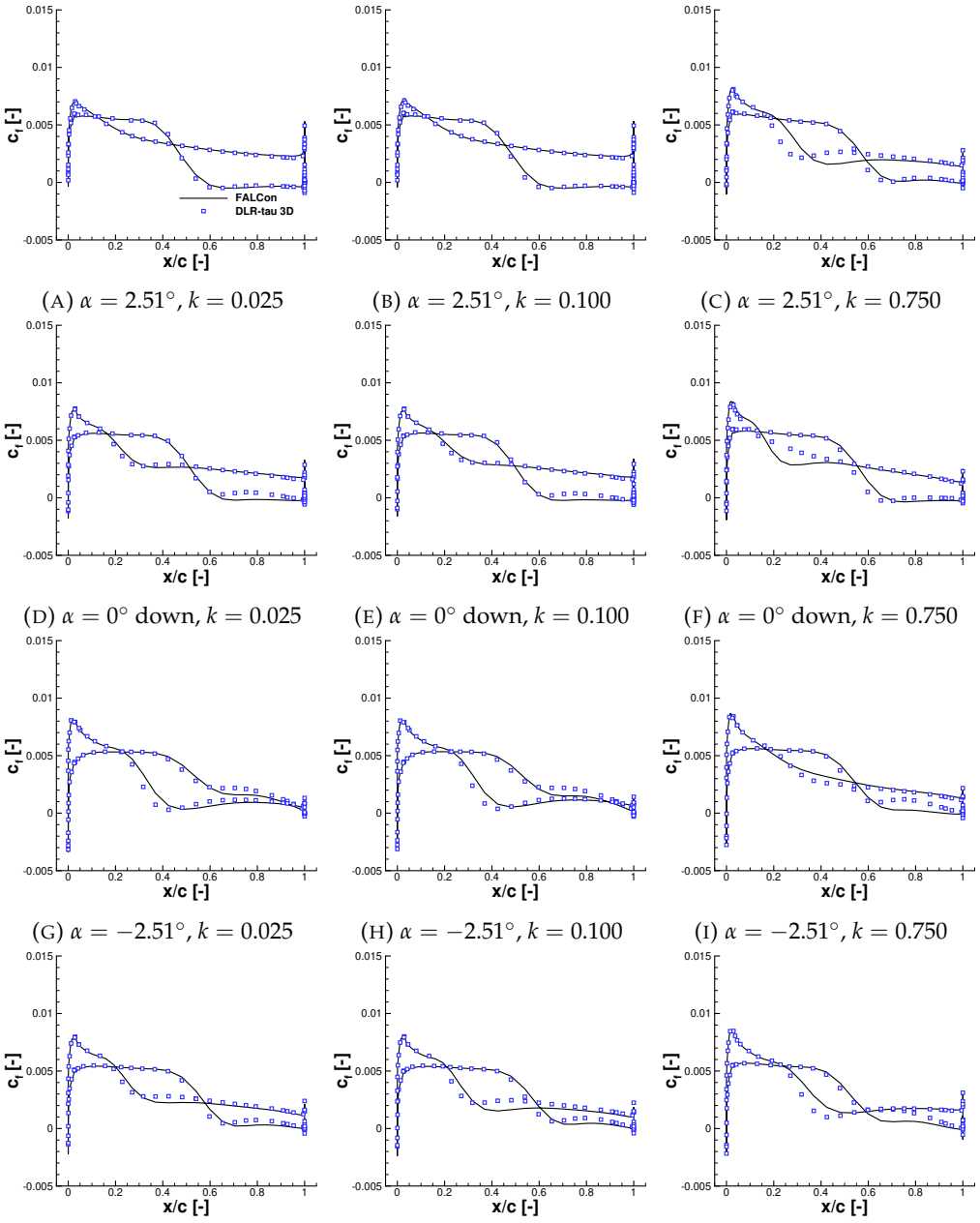

(A) $\alpha = 2.51°$, $k = 0.025$ (B) $\alpha = 2.51°$, $k = 0.100$ (C) $\alpha = 2.51°$, $k = 0.750$

(D) $\alpha = 0°$ down, $k = 0.025$ (E) $\alpha = 0°$ down, $k = 0.100$ (F) $\alpha = 0°$ down, $k = 0.750$

(G) $\alpha = -2.51°$, $k = 0.025$ (H) $\alpha = -2.51°$, $k = 0.100$ (I) $\alpha = -2.51°$, $k = 0.750$

(J) $\alpha = 0°$ up, $k = 0.025$ (K) $\alpha = 0°$ up, $k = 0.100$ (L) $\alpha = 0°$ up, $k = 0.750$

FIGURE A.54: Sectional friction coefficient, c_f, of the third cycle of the pitching unswept NACA2412 wing at $M = 0.8$ and $\Delta\alpha_A = 2.51°$, at 75% of the half–span

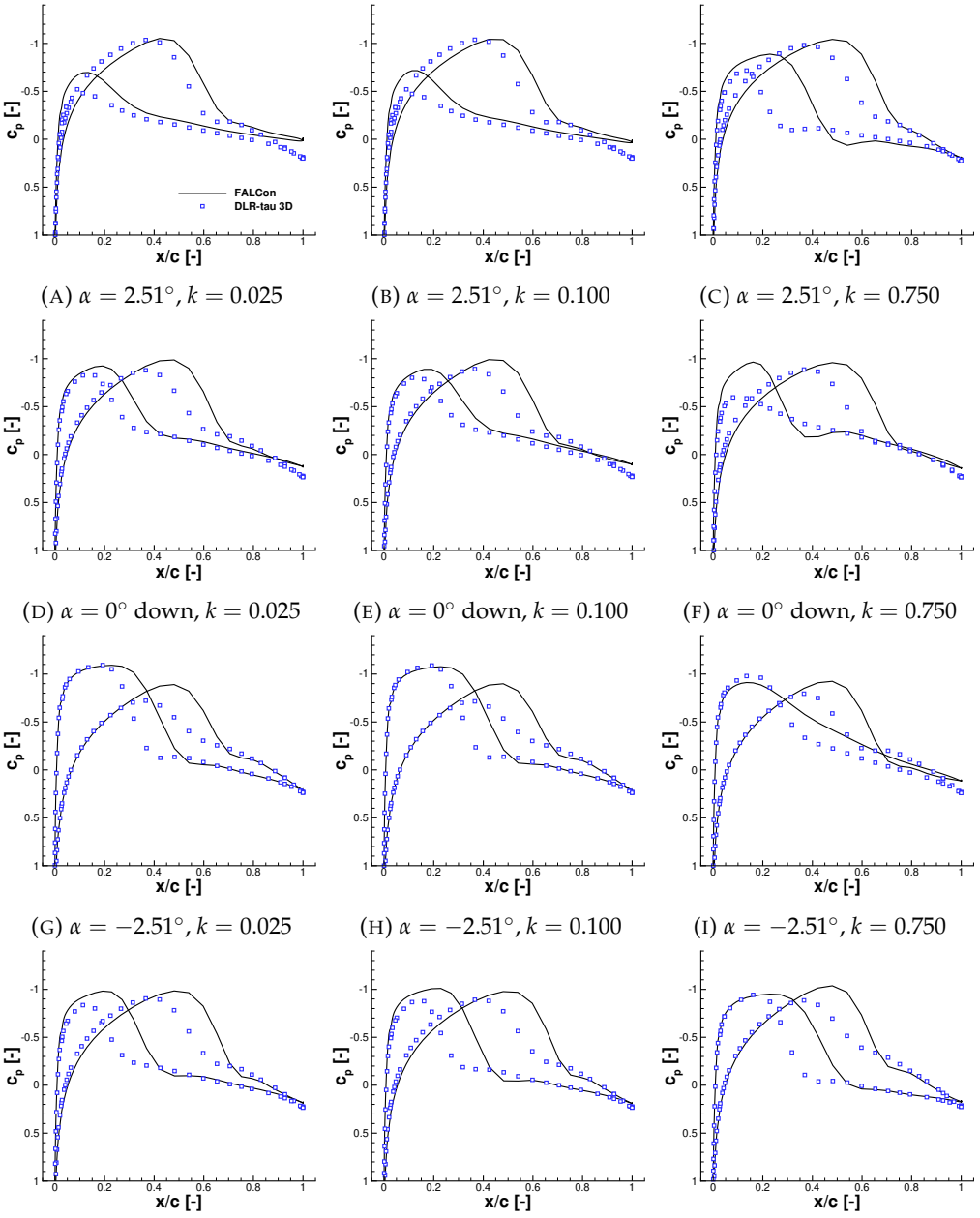

(A) $\alpha = 2.51°$, $k = 0.025$ (B) $\alpha = 2.51°$, $k = 0.100$ (C) $\alpha = 2.51°$, $k = 0.750$

(D) $\alpha = 0°$ down, $k = 0.025$ (E) $\alpha = 0°$ down, $k = 0.100$ (F) $\alpha = 0°$ down, $k = 0.750$

(G) $\alpha = -2.51°$, $k = 0.025$ (H) $\alpha = -2.51°$, $k = 0.100$ (I) $\alpha = -2.51°$, $k = 0.750$

(J) $\alpha = 0°$ up, $k = 0.025$ (K) $\alpha = 0°$ up, $k = 0.100$ (L) $\alpha = 0°$ up, $k = 0.750$

FIGURE A.55: Sectional pressure coefficient, c_p, of the third cycle of the pitching unswept NACA2412 wing at $M = 0.8$ and $\Delta\alpha_A = 2.51°$, at 90% of the half–span

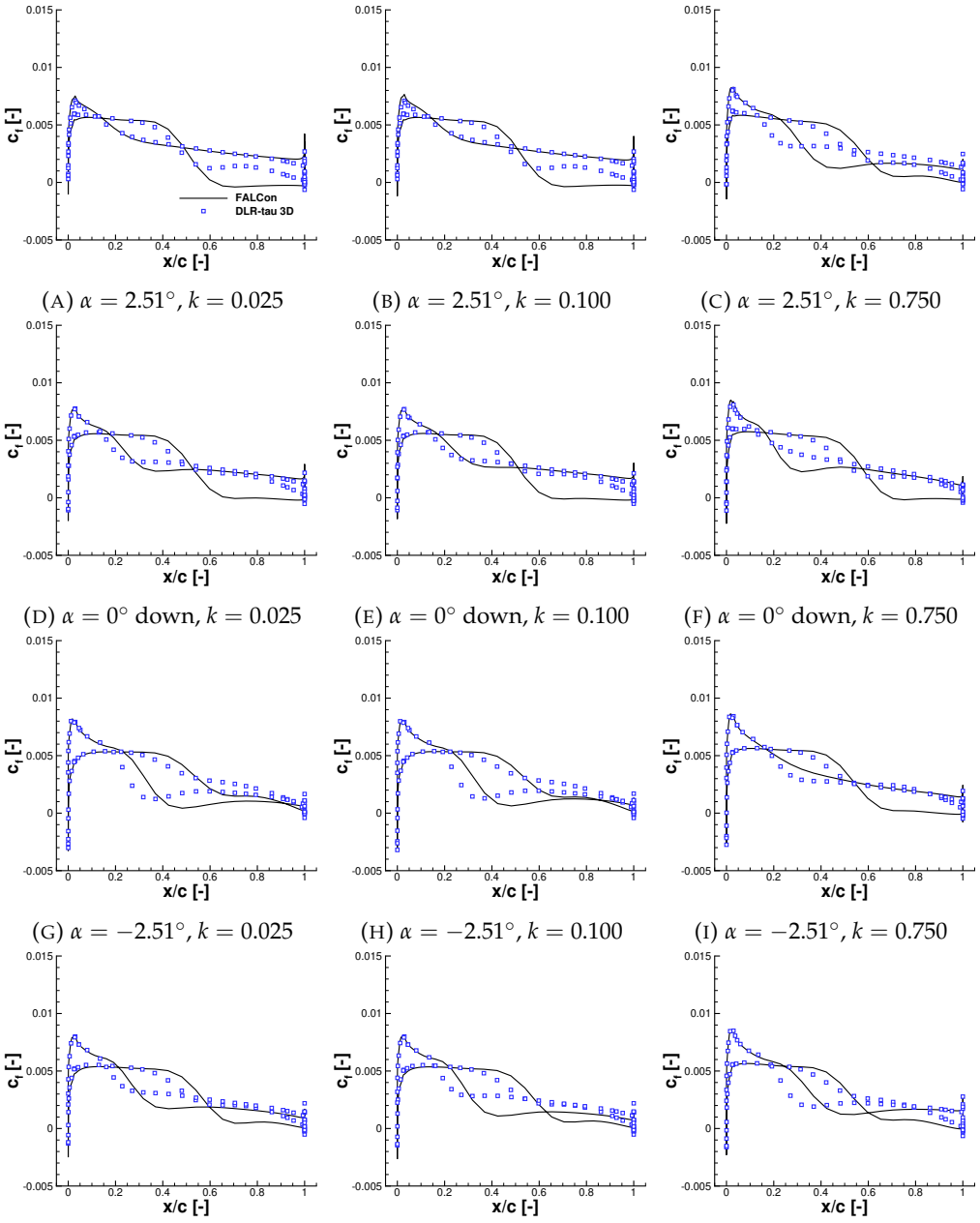

(A) $\alpha = 2.51°$, $k = 0.025$ (B) $\alpha = 2.51°$, $k = 0.100$ (C) $\alpha = 2.51°$, $k = 0.750$

(D) $\alpha = 0°$ down, $k = 0.025$ (E) $\alpha = 0°$ down, $k = 0.100$ (F) $\alpha = 0°$ down, $k = 0.750$

(G) $\alpha = -2.51°$, $k = 0.025$ (H) $\alpha = -2.51°$, $k = 0.100$ (I) $\alpha = -2.51°$, $k = 0.750$

(J) $\alpha = 0°$ up, $k = 0.025$ (K) $\alpha = 0°$ up, $k = 0.100$ (L) $\alpha = 0°$ up, $k = 0.750$

FIGURE A.56: Sectional friction coefficient, c_f, of the third cycle of the pitching unswept NACA2412 wing at $M = 0.8$ and $\Delta\alpha_A = 2.51°$, at 90% of the half–span

A.1.2 Unsteady force harmonic plunging oscillation

A.1.2.1 Mach $M = 0.3$

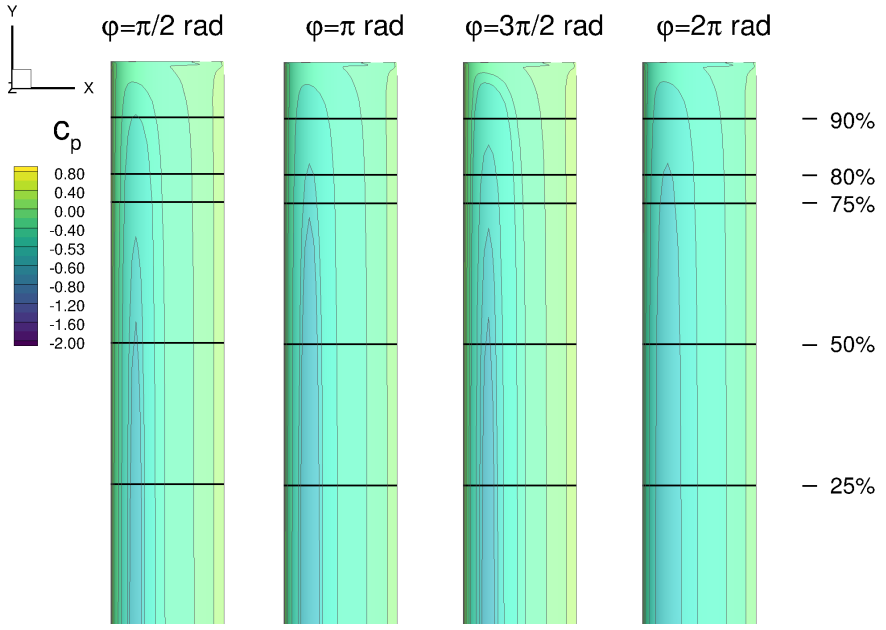

FIGURE A.57: Pressure coefficient, c_p, of the NACA2412–wing at $M = 0.3$ and $k = 0.025$ during forced harmonic plunging oscillation, third cycle

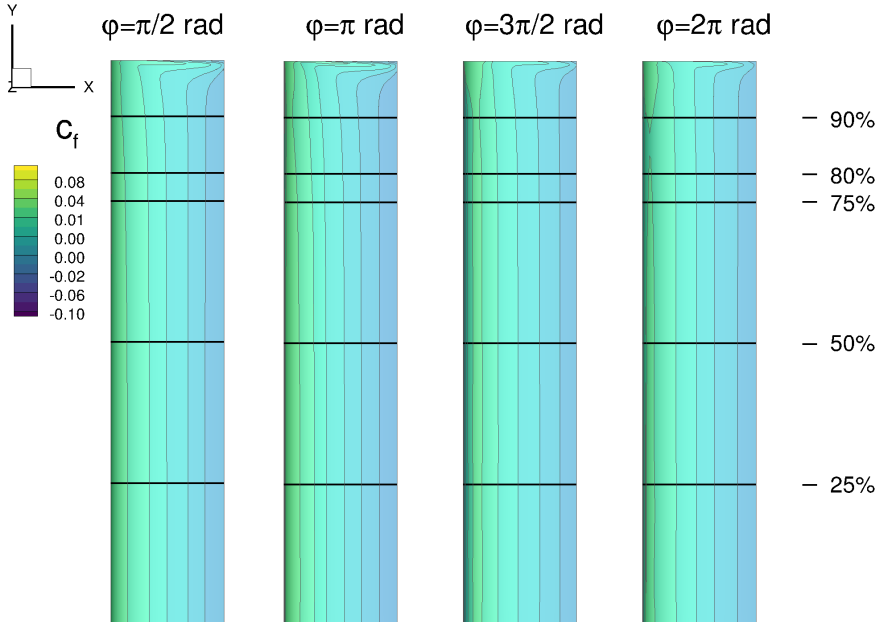

FIGURE A.58: Friction coefficient, c_f, of the NACA2412–wing at $M = 0.3$ and $k = 0.025$ during forced harmonic plunging oscillation, third cycle

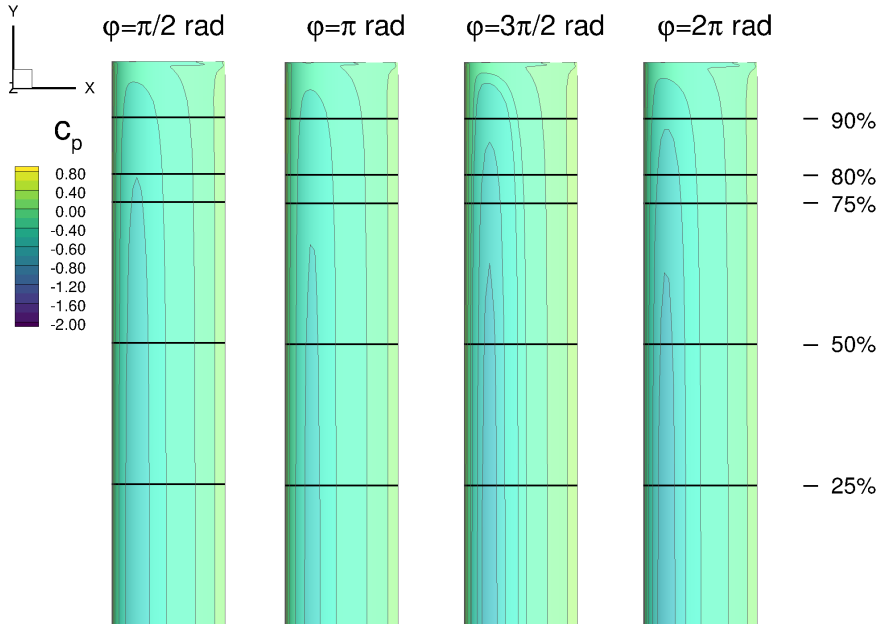

FIGURE A.59: Pressure coefficient, c_p, of the NACA2412–wing at $M = 0.3$ and $k = 0.100$ during forced harmonic plunging oscillation, third cycle

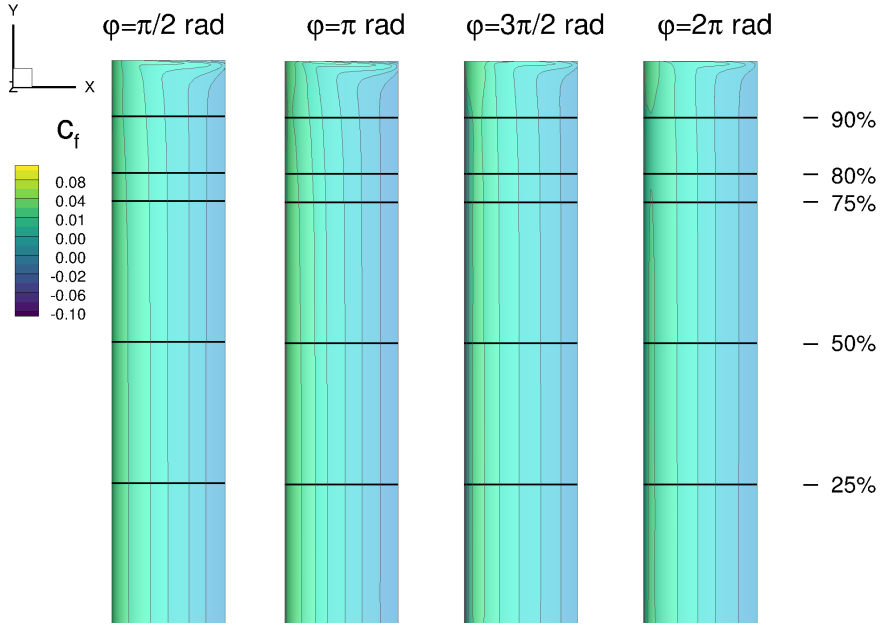

FIGURE A.60: Friction coefficient, c_f, of the NACA2412–wing at $M = 0.3$ and $k = 0.100$ during forced harmonic plunging oscillation, third cycle

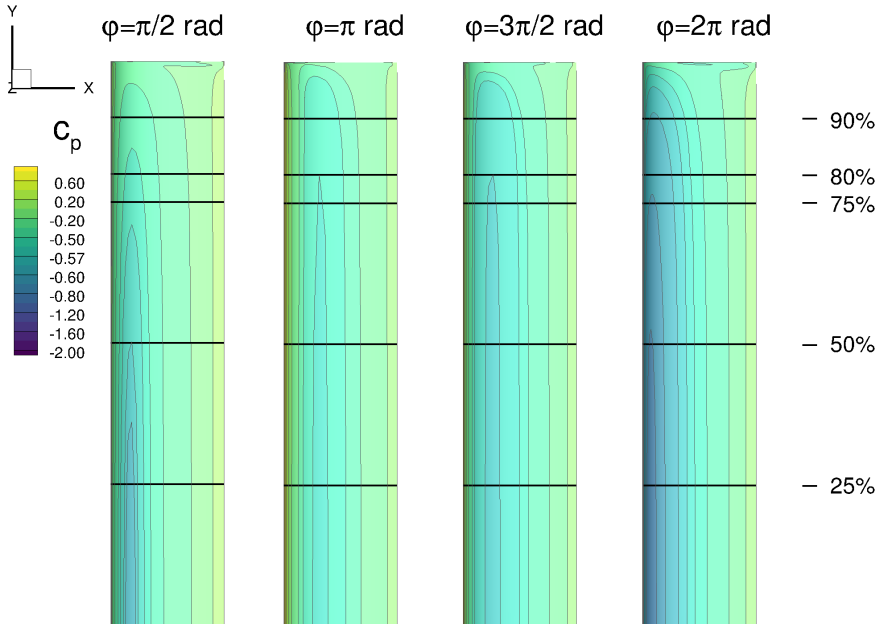

FIGURE A.61: Pressure coefficient, c_p, of the NACA2412–wing at $M = 0.3$ and $k = 0.750$ during forced harmonic plunging oscillation, third cycle

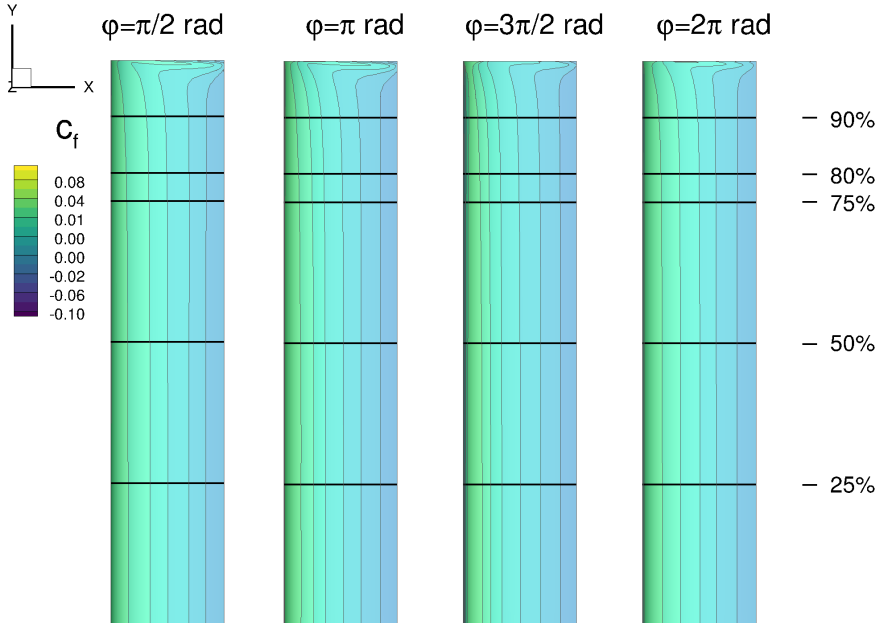

FIGURE A.62: Friction coefficient, c_f, of the NACA2412–wing at $M = 0.3$ and $k = 0.750$ during forced harmonic plunging oscillation, third cycle

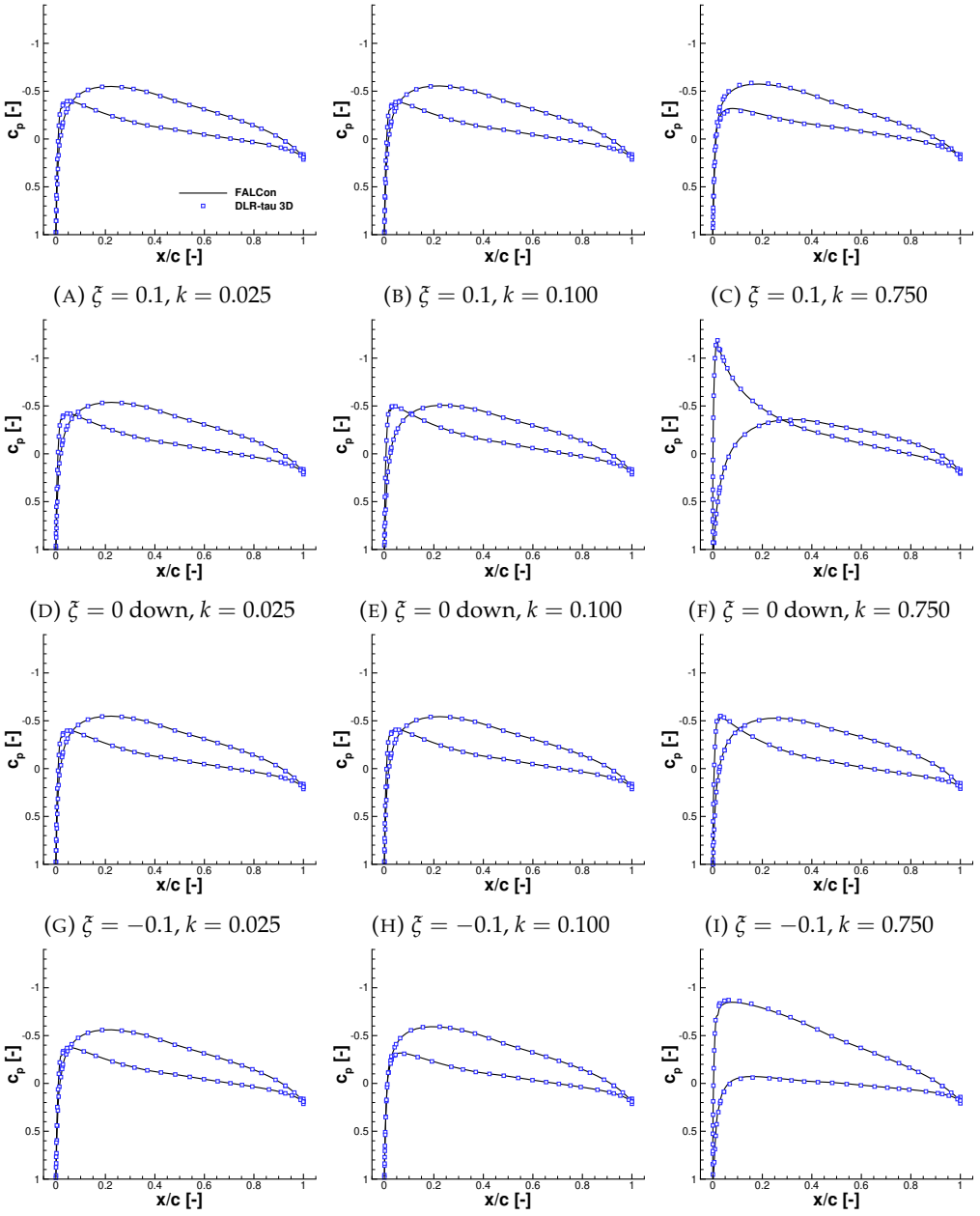

(A) $\xi = 0.1$, $k = 0.025$ (B) $\xi = 0.1$, $k = 0.100$ (C) $\xi = 0.1$, $k = 0.750$

(D) $\xi = 0$ down, $k = 0.025$ (E) $\xi = 0$ down, $k = 0.100$ (F) $\xi = 0$ down, $k = 0.750$

(G) $\xi = -0.1$, $k = 0.025$ (H) $\xi = -0.1$, $k = 0.100$ (I) $\xi = -0.1$, $k = 0.750$

(J) $\xi = 0$ up, $k = 0.025$ (K) $\xi = 0$ up, $k = 0.100$ (L) $\xi = 0$ up, $k = 0.750$

FIGURE A.63: Sectional pressure coefficient, c_p, of the third cycle of the plunging unswept NACA2412 wing at $M = 0.3$ and $\xi_A = 0.1$, at 25% of the half–span

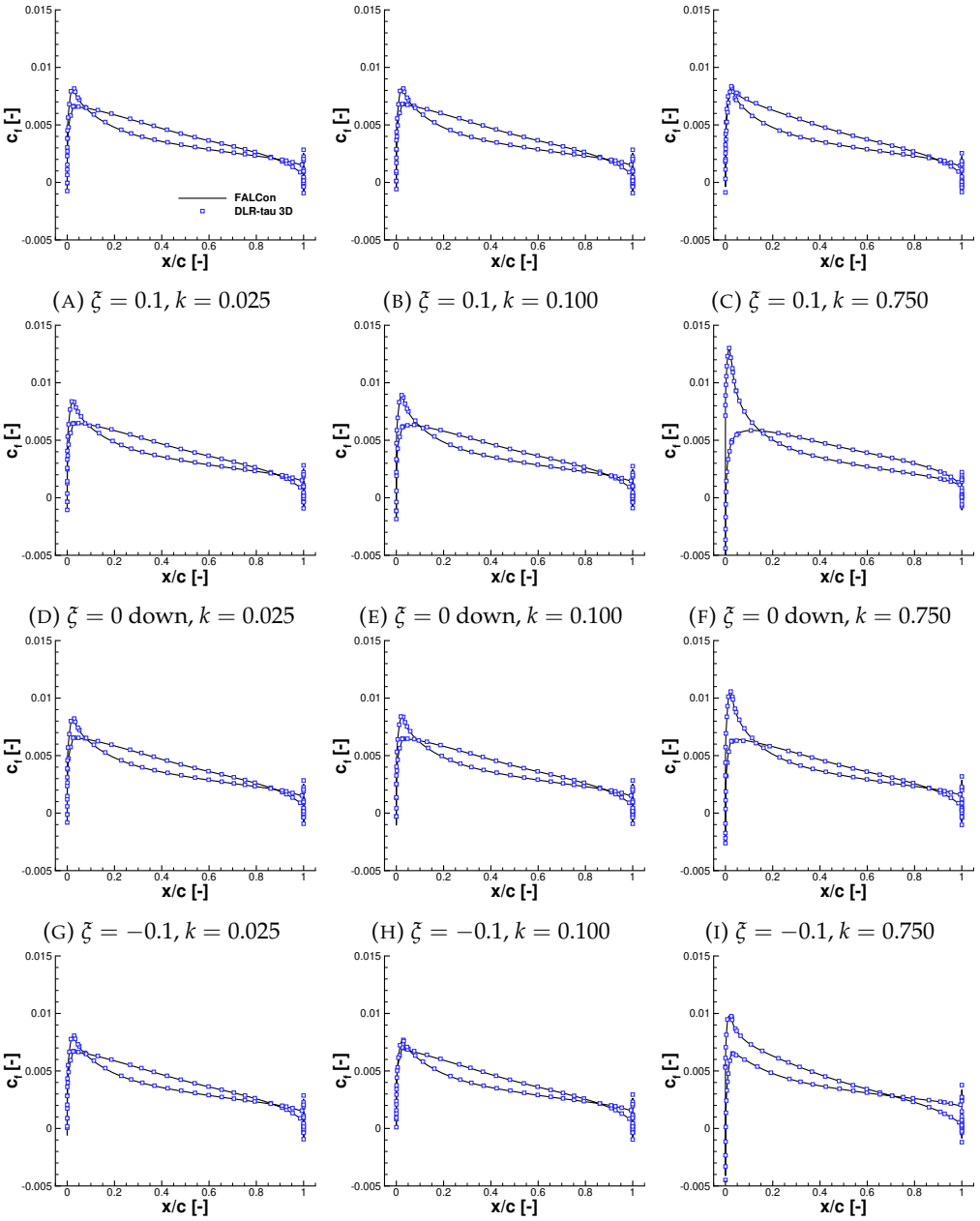

(A) $\xi = 0.1$, $k = 0.025$ (B) $\xi = 0.1$, $k = 0.100$ (C) $\xi = 0.1$, $k = 0.750$

(D) $\xi = 0$ down, $k = 0.025$ (E) $\xi = 0$ down, $k = 0.100$ (F) $\xi = 0$ down, $k = 0.750$

(G) $\xi = -0.1$, $k = 0.025$ (H) $\xi = -0.1$, $k = 0.100$ (I) $\xi = -0.1$, $k = 0.750$

(J) $\xi = 0$ up, $k = 0.025$ (K) $\xi = 0$ up, $k = 0.100$ (L) $\xi = 0$ up, $k = 0.750$

FIGURE A.64: Sectional friction coefficient, c_f, of the third cycle of the plunging unswept NACA2412 wing at $M = 0.3$ and $\xi_A = 0.1$, at 25% of the half–span

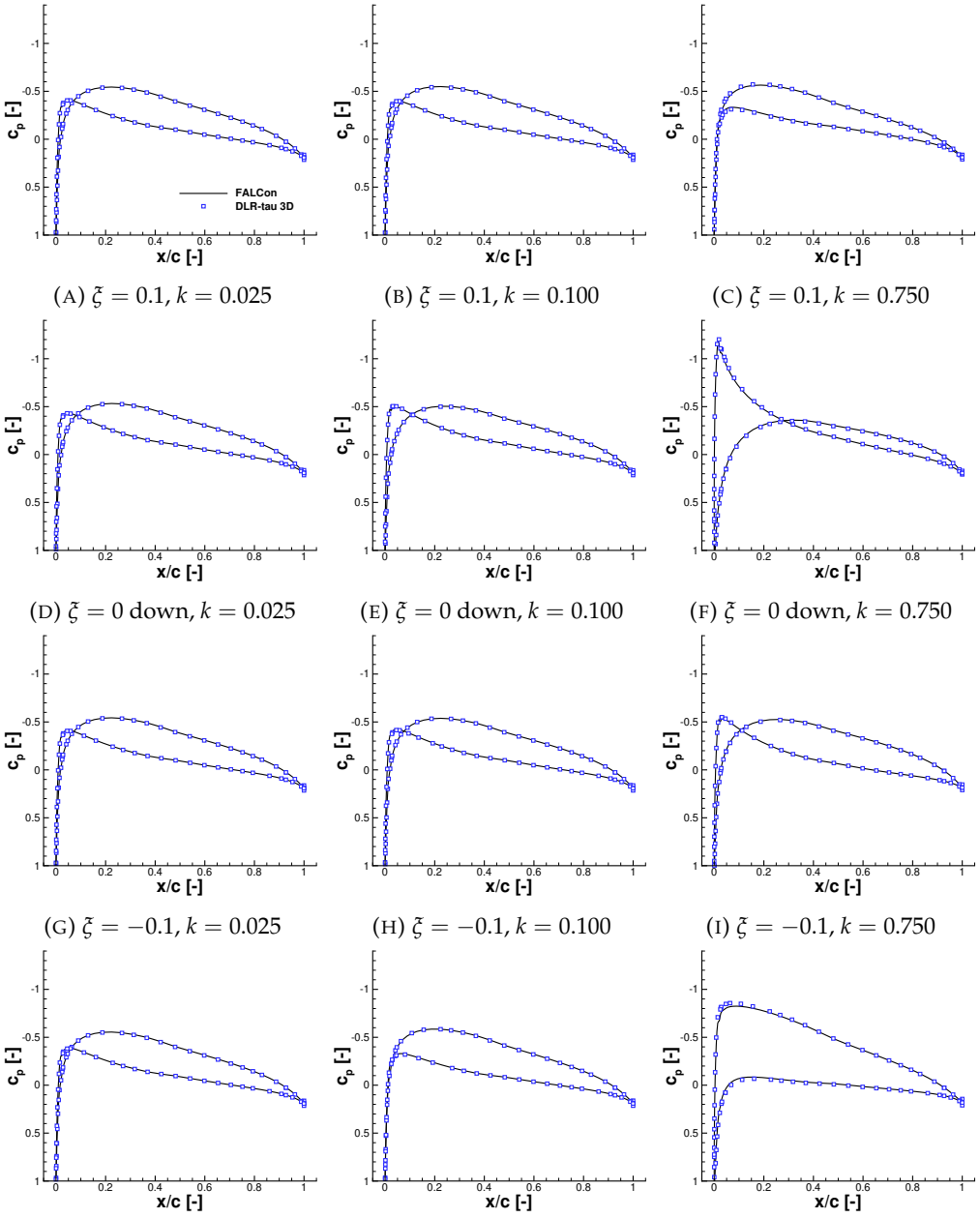

(A) $\xi = 0.1$, $k = 0.025$ (B) $\xi = 0.1$, $k = 0.100$ (C) $\xi = 0.1$, $k = 0.750$

(D) $\xi = 0$ down, $k = 0.025$ (E) $\xi = 0$ down, $k = 0.100$ (F) $\xi = 0$ down, $k = 0.750$

(G) $\xi = -0.1$, $k = 0.025$ (H) $\xi = -0.1$, $k = 0.100$ (I) $\xi = -0.1$, $k = 0.750$

(J) $\xi = 0$ up, $k = 0.025$ (K) $\xi = 0$ up, $k = 0.100$ (L) $\xi = 0$ up, $k = 0.750$

FIGURE A.65: Sectional pressure coefficient, c_p, of the third cycle of the plunging unswept NACA2412 wing at $M = 0.3$ and $\xi_A = 0.1$, at 50% of the half–span

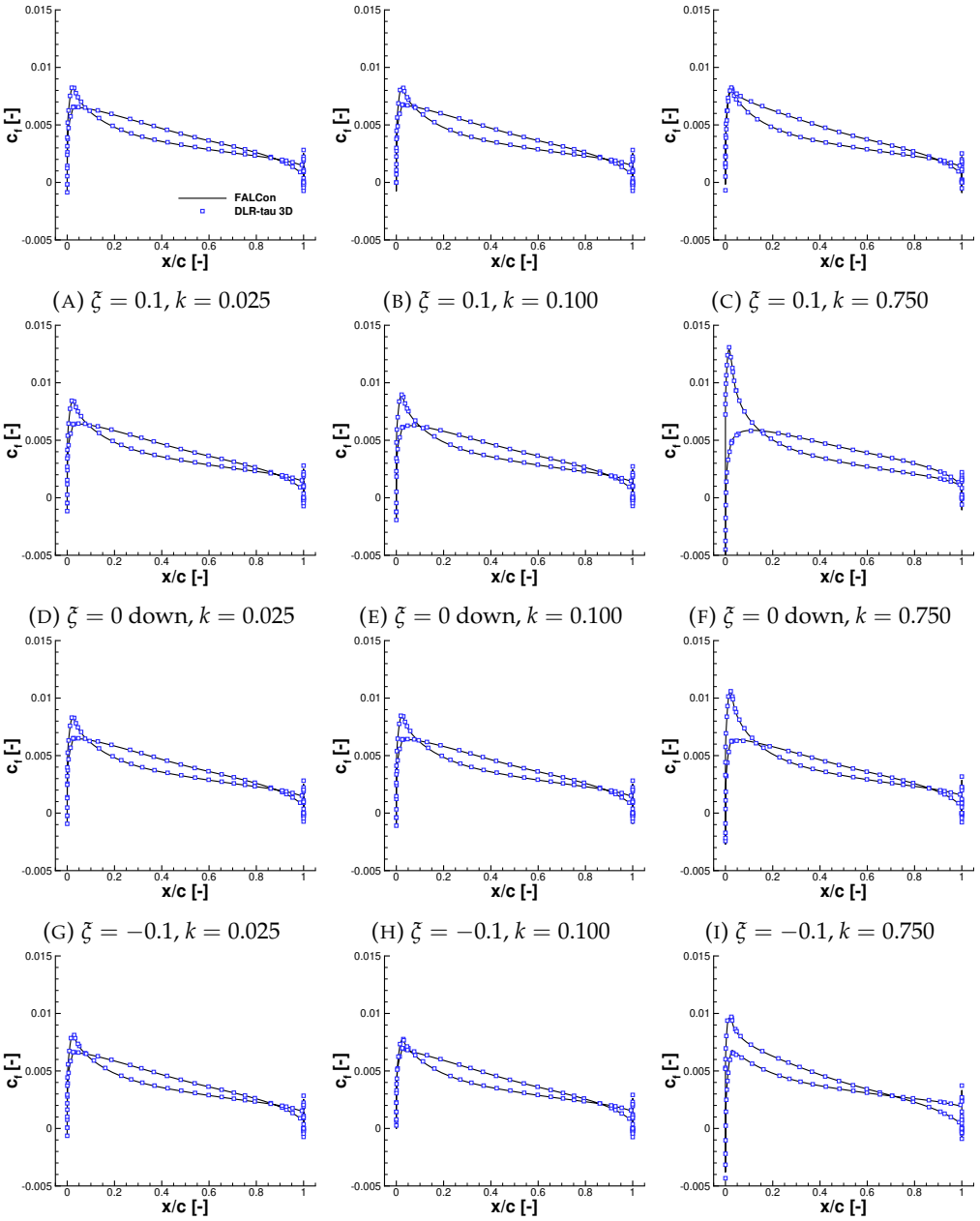

(A) $\xi = 0.1$, $k = 0.025$ (B) $\xi = 0.1$, $k = 0.100$ (C) $\xi = 0.1$, $k = 0.750$

(D) $\xi = 0$ down, $k = 0.025$ (E) $\xi = 0$ down, $k = 0.100$ (F) $\xi = 0$ down, $k = 0.750$

(G) $\xi = -0.1$, $k = 0.025$ (H) $\xi = -0.1$, $k = 0.100$ (I) $\xi = -0.1$, $k = 0.750$

(J) $\xi = 0$ up, $k = 0.025$ (K) $\xi = 0$ up, $k = 0.100$ (L) $\xi = 0$ up, $k = 0.750$

FIGURE A.66: Sectional friction coefficient, c_f, of the third cycle of the plunging unswept NACA2412 wing at $M = 0.3$ and $\xi_A = 0.1$, at 50% of the half–span

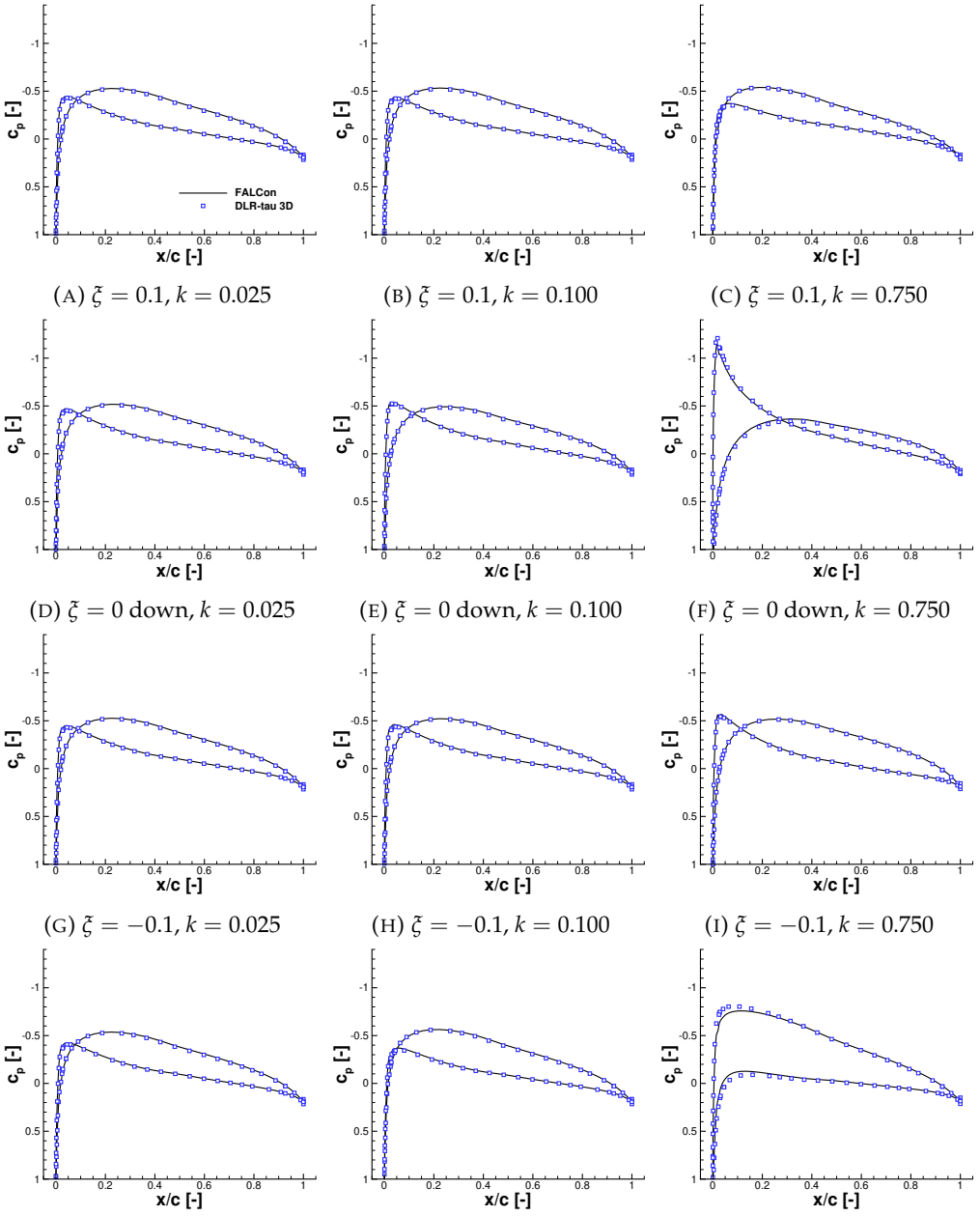

(A) $\xi = 0.1$, $k = 0.025$ (B) $\xi = 0.1$, $k = 0.100$ (C) $\xi = 0.1$, $k = 0.750$

(D) $\xi = 0$ down, $k = 0.025$ (E) $\xi = 0$ down, $k = 0.100$ (F) $\xi = 0$ down, $k = 0.750$

(G) $\xi = -0.1$, $k = 0.025$ (H) $\xi = -0.1$, $k = 0.100$ (I) $\xi = -0.1$, $k = 0.750$

(J) $\xi = 0$ up, $k = 0.025$ (K) $\xi = 0$ up, $k = 0.100$ (L) $\xi = 0$ up, $k = 0.750$

FIGURE A.67: Sectional pressure coefficient, c_p, of the third cycle of the plunging unswept NACA2412 wing at $M = 0.3$ and $\xi_A = 0.1$, at 75% of the half–span

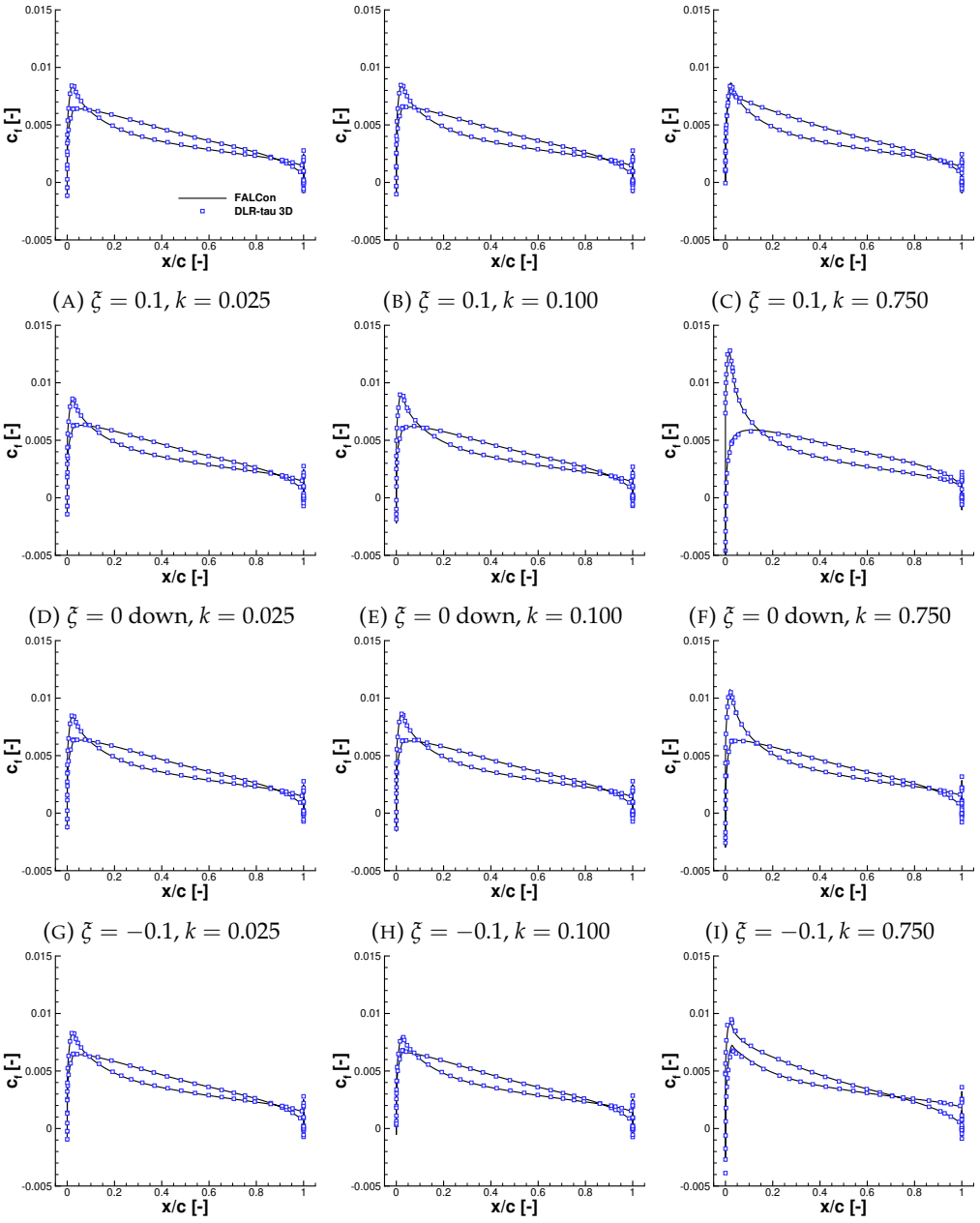

(A) $\xi = 0.1$, $k = 0.025$ (B) $\xi = 0.1$, $k = 0.100$ (C) $\xi = 0.1$, $k = 0.750$

(D) $\xi = 0$ down, $k = 0.025$ (E) $\xi = 0$ down, $k = 0.100$ (F) $\xi = 0$ down, $k = 0.750$

(G) $\xi = -0.1$, $k = 0.025$ (H) $\xi = -0.1$, $k = 0.100$ (I) $\xi = -0.1$, $k = 0.750$

(J) $\xi = 0$ up, $k = 0.025$ (K) $\xi = 0$ up, $k = 0.100$ (L) $\xi = 0$ up, $k = 0.750$

FIGURE A.68: Sectional friction coefficient, c_f, of the third cycle of the plunging unswept NACA2412 wing at $M = 0.3$ and $\xi_A = 0.1$, at 75% of the half–span

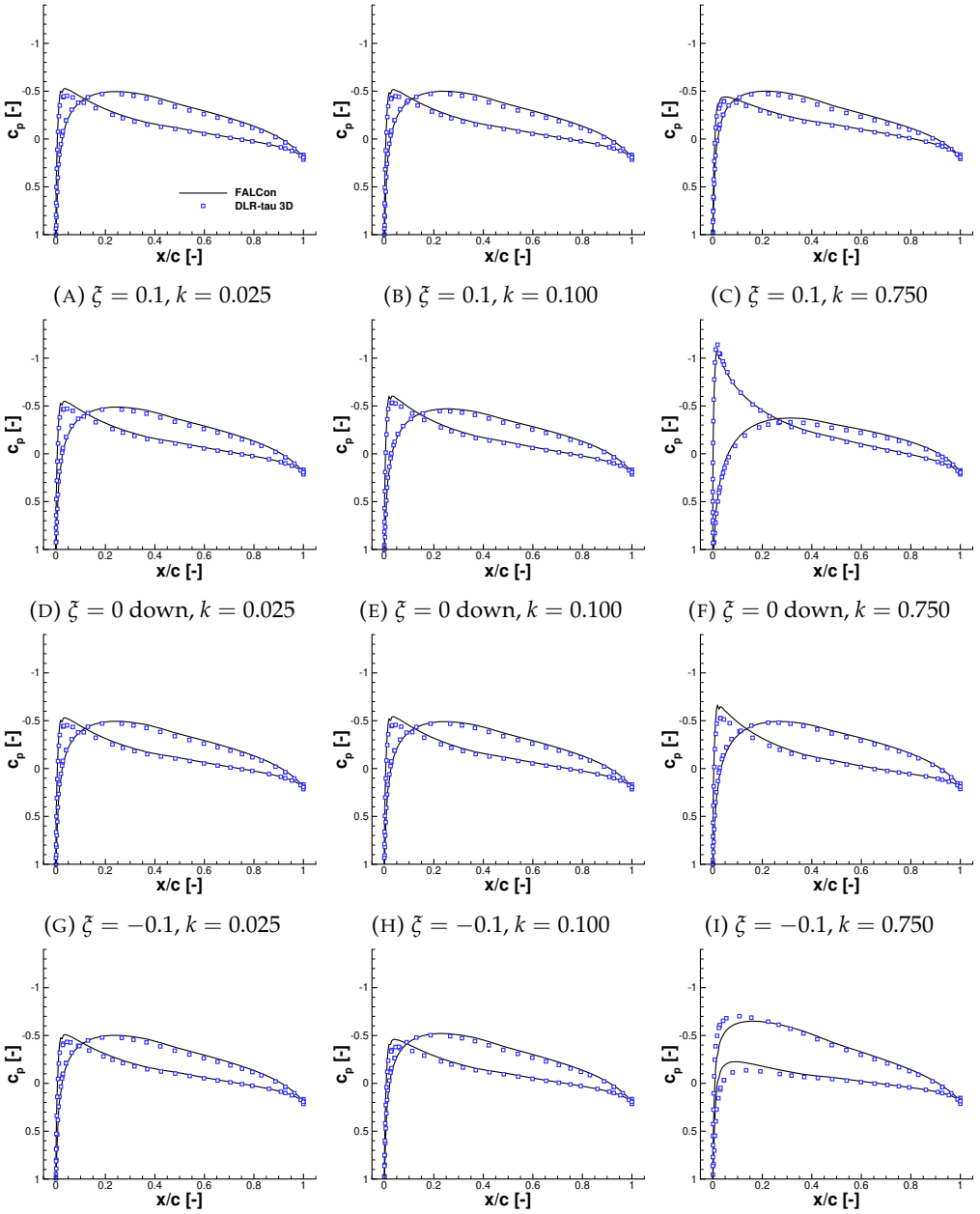

(A) $\xi = 0.1$, $k = 0.025$ (B) $\xi = 0.1$, $k = 0.100$ (C) $\xi = 0.1$, $k = 0.750$

(D) $\xi = 0$ down, $k = 0.025$ (E) $\xi = 0$ down, $k = 0.100$ (F) $\xi = 0$ down, $k = 0.750$

(G) $\xi = -0.1$, $k = 0.025$ (H) $\xi = -0.1$, $k = 0.100$ (I) $\xi = -0.1$, $k = 0.750$

(J) $\xi = 0$ up, $k = 0.025$ (K) $\xi = 0$ up, $k = 0.100$ (L) $\xi = 0$ up, $k = 0.750$

FIGURE A.69: Sectional pressure coefficient, c_p, of the third cycle of the plunging unswept NACA2412 wing at $M = 0.3$ and $\xi_A = 0.1$, at 90% of the half–span

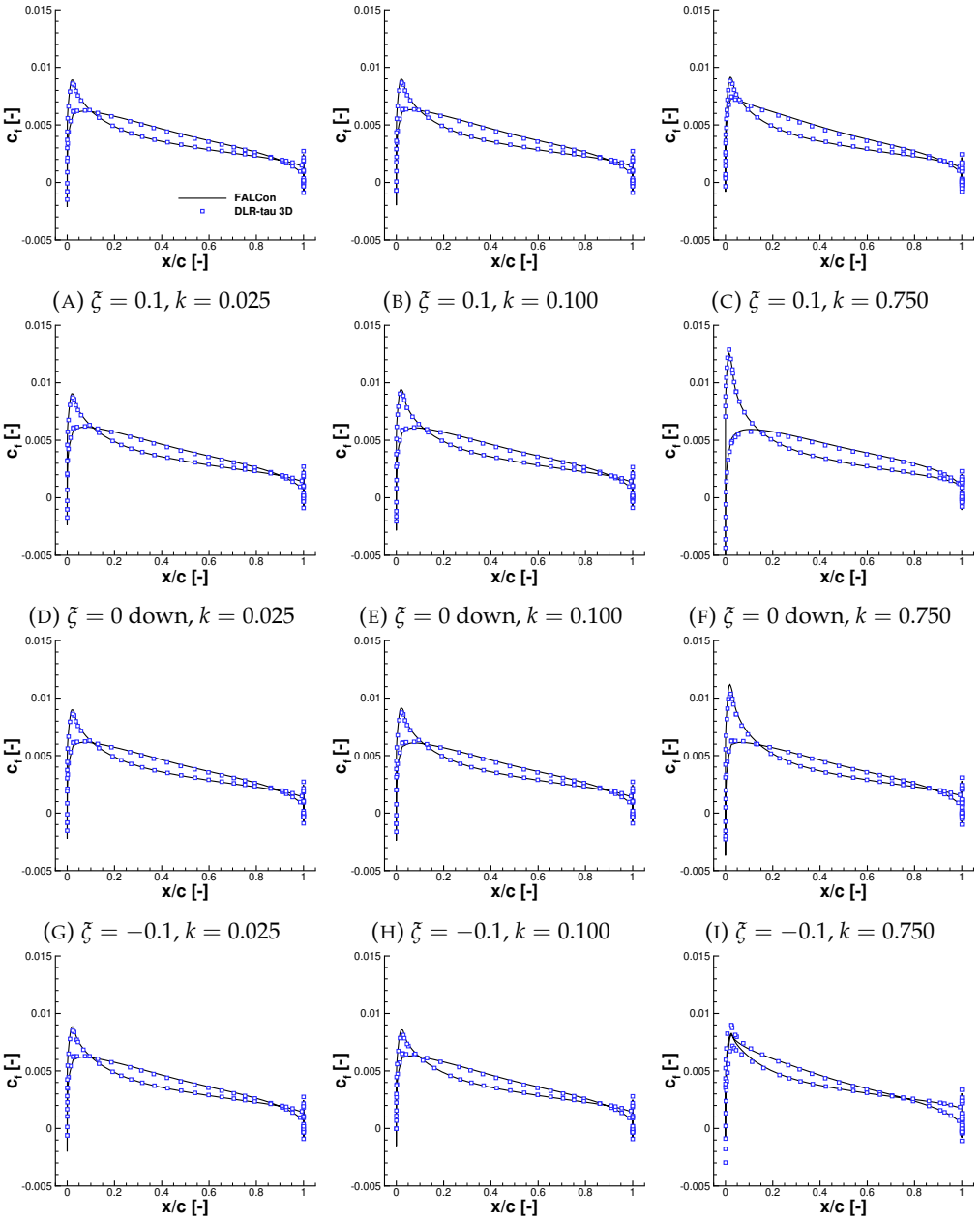

(A) $\xi = 0.1$, $k = 0.025$ (B) $\xi = 0.1$, $k = 0.100$ (C) $\xi = 0.1$, $k = 0.750$

(D) $\xi = 0$ down, $k = 0.025$ (E) $\xi = 0$ down, $k = 0.100$ (F) $\xi = 0$ down, $k = 0.750$

(G) $\xi = -0.1$, $k = 0.025$ (H) $\xi = -0.1$, $k = 0.100$ (I) $\xi = -0.1$, $k = 0.750$

(J) $\xi = 0$ up, $k = 0.025$ (K) $\xi = 0$ up, $k = 0.100$ (L) $\xi = 0$ up, $k = 0.750$

FIGURE A.70: Sectional friction coefficient, c_f, of the third cycle of the plunging unswept NACA2412 wing at $M = 0.3$ and $\xi_A = 0.1$, at 90% of the half–span

A.1.2.2 Mach $M = 0.5$

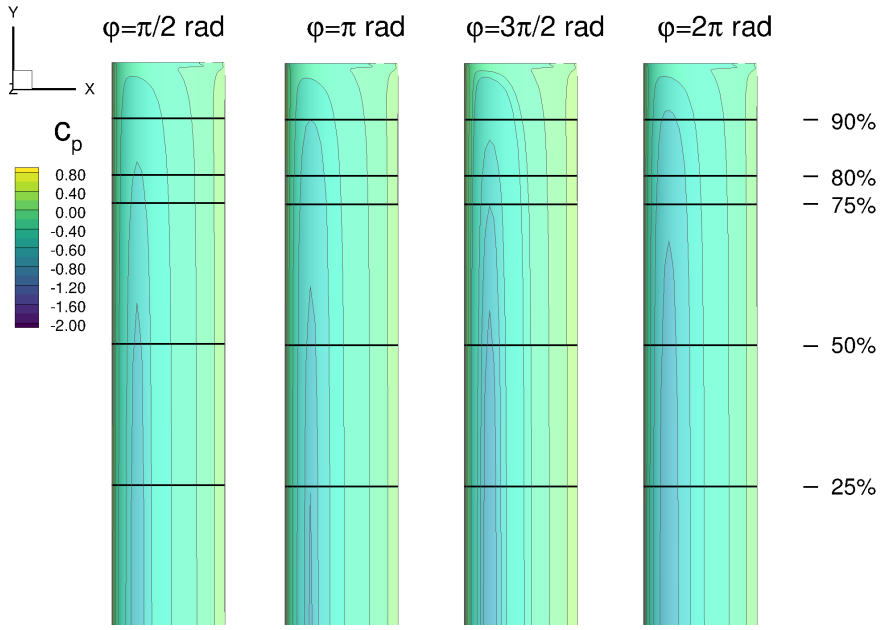

FIGURE A.71: Pressure coefficient, c_p, of the NACA2412–wing at $M = 0.5$ and $k = 0.025$ during forced harmonic plunging oscillation, third cycle

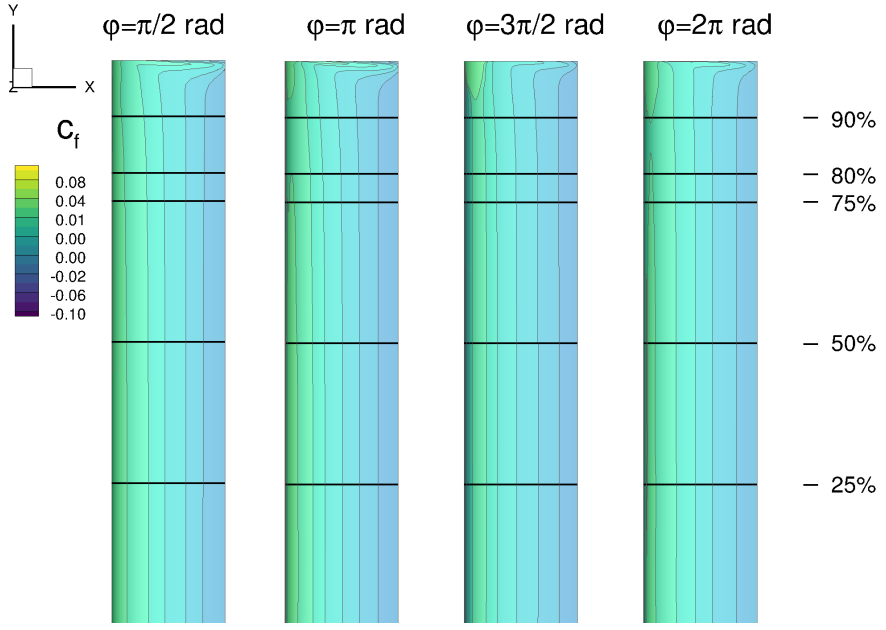

FIGURE A.72: Friction coefficient, c_f, of the NACA2412–wing at $M = 0.5$ and $k = 0.025$ during forced harmonic plunging oscillation, third cycle

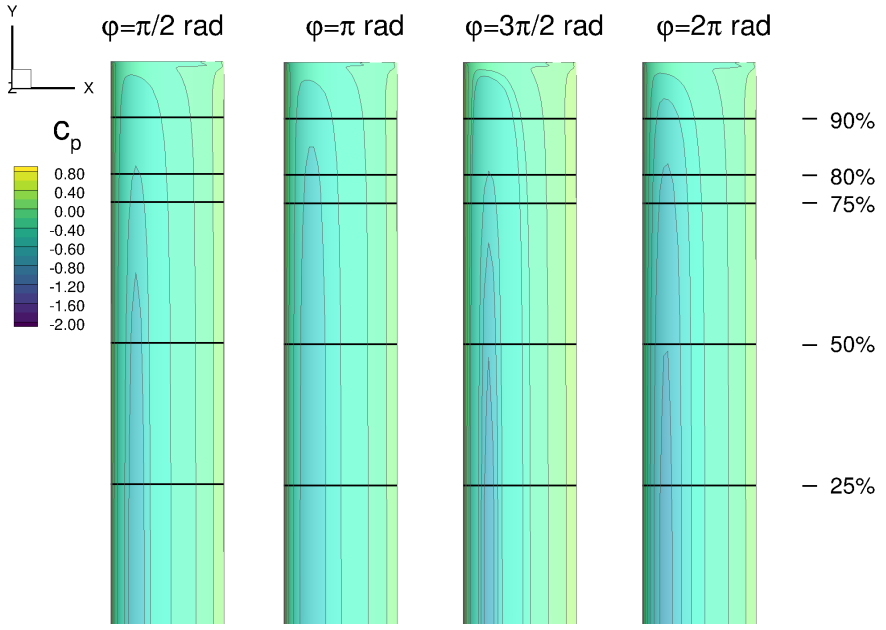

FIGURE A.73: Pressure coefficient, c_p, of the NACA2412–wing at $M = 0.5$ and $k = 0.100$ during forced harmonic plunging oscillation, third cycle

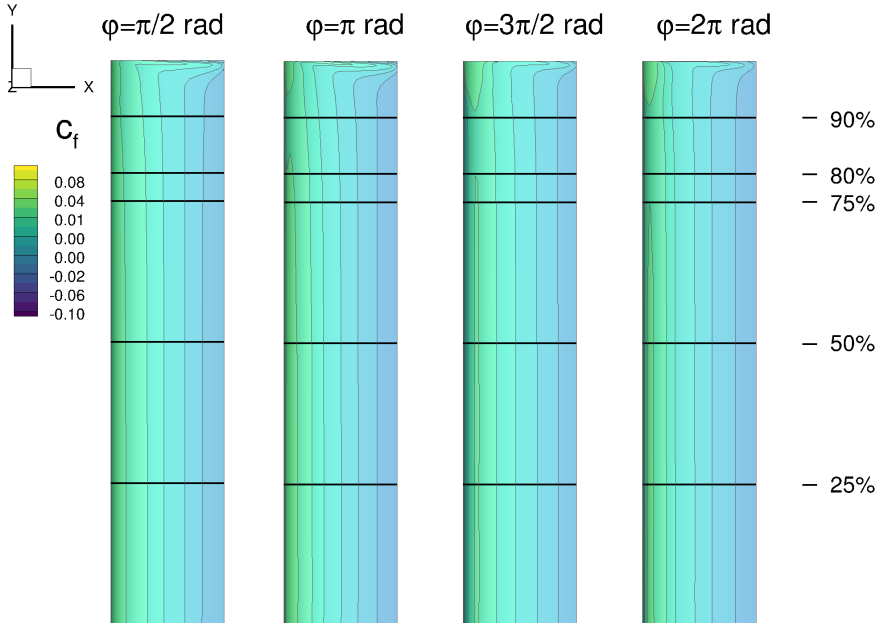

FIGURE A.74: Friction coefficient, c_f, of the NACA2412–wing at $M = 0.5$ and $k = 0.100$ during forced harmonic plunging oscillation, third cycle

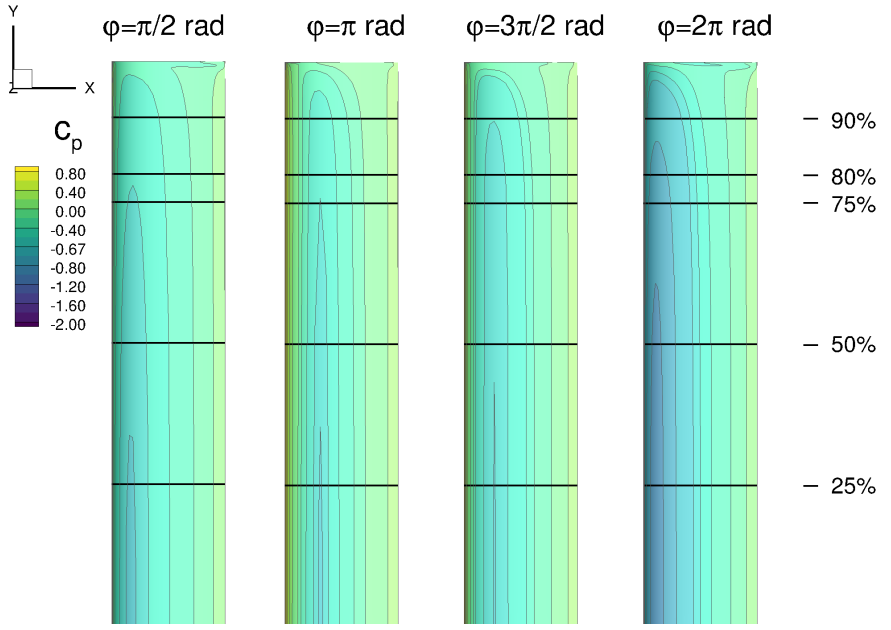

FIGURE A.75: Pressure coefficient, c_p, of the NACA2412–wing at $M = 0.5$ and $k = 0.750$ during forced harmonic plunging oscillation, third cycle

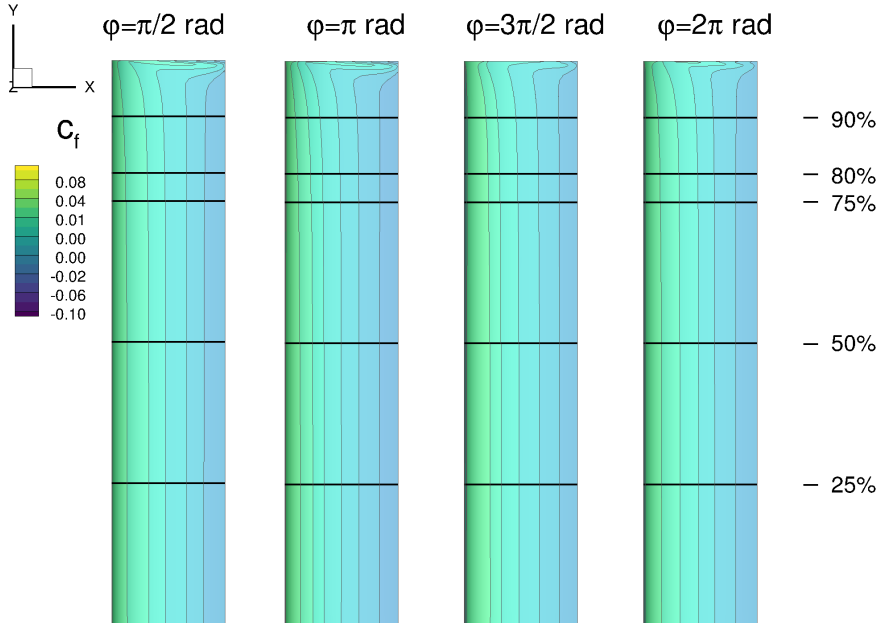

FIGURE A.76: Friction coefficient, c_f, of the NACA2412–wing at $M = 0.5$ and $k = 0.750$ during forced harmonic plunging oscillation, third cycle

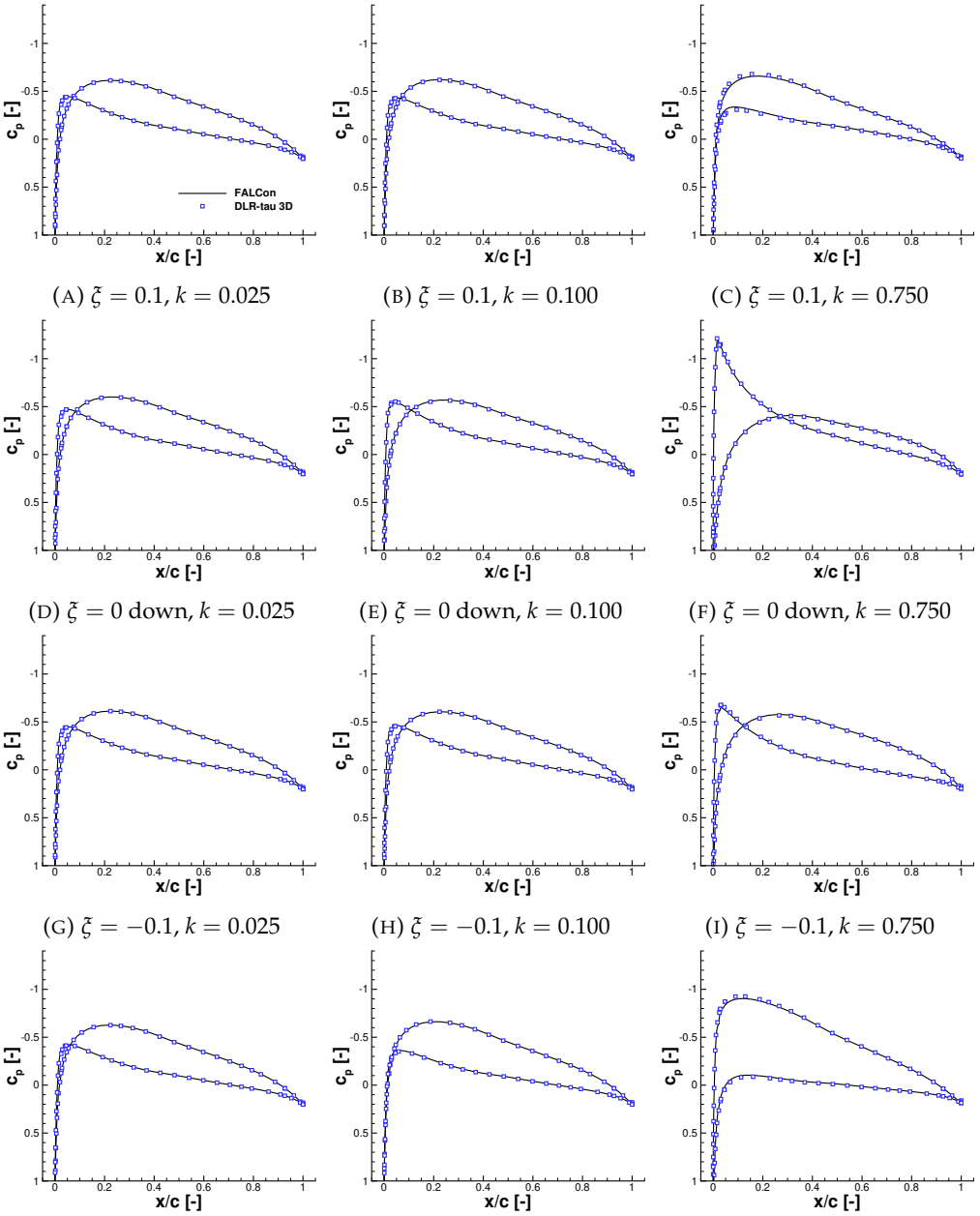

(A) $\xi = 0.1$, $k = 0.025$ (B) $\xi = 0.1$, $k = 0.100$ (C) $\xi = 0.1$, $k = 0.750$

(D) $\xi = 0$ down, $k = 0.025$ (E) $\xi = 0$ down, $k = 0.100$ (F) $\xi = 0$ down, $k = 0.750$

(G) $\xi = -0.1$, $k = 0.025$ (H) $\xi = -0.1$, $k = 0.100$ (I) $\xi = -0.1$, $k = 0.750$

(J) $\xi = 0$ up, $k = 0.025$ (K) $\xi = 0$ up, $k = 0.100$ (L) $\xi = 0$ up, $k = 0.750$

FIGURE A.77: Sectional pressure coefficient, c_p, of the third cycle of the plunging unswept NACA2412 wing at $M = 0.5$ and $\xi_A = 0.1$, at 25% of the half–span

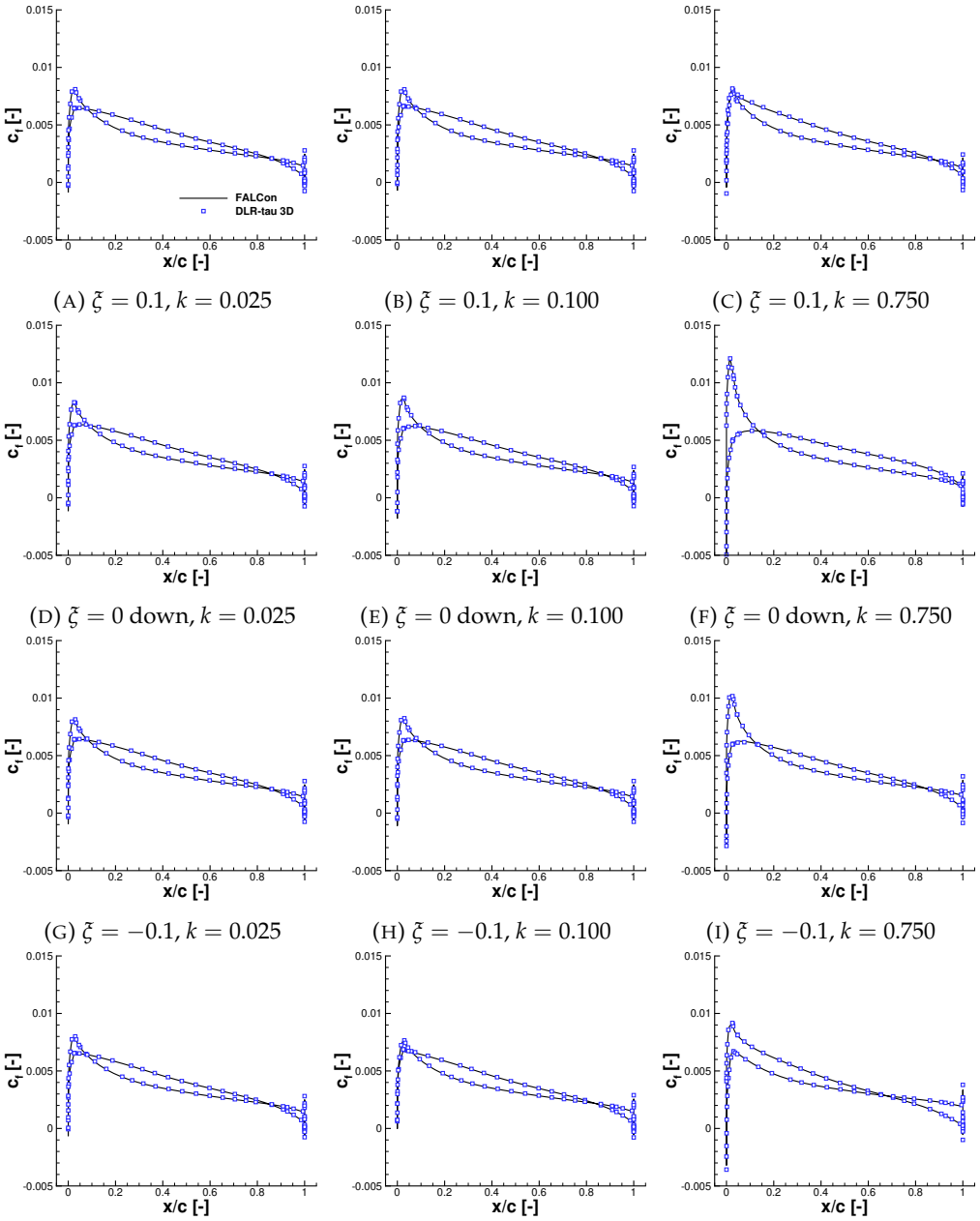

(A) $\xi = 0.1$, $k = 0.025$ (B) $\xi = 0.1$, $k = 0.100$ (C) $\xi = 0.1$, $k = 0.750$

(D) $\xi = 0$ down, $k = 0.025$ (E) $\xi = 0$ down, $k = 0.100$ (F) $\xi = 0$ down, $k = 0.750$

(G) $\xi = -0.1$, $k = 0.025$ (H) $\xi = -0.1$, $k = 0.100$ (I) $\xi = -0.1$, $k = 0.750$

(J) $\xi = 0$ up, $k = 0.025$ (K) $\xi = 0$ up, $k = 0.100$ (L) $\xi = 0$ up, $k = 0.750$

FIGURE A.78: Sectional friction coefficient, c_f, of the third cycle of the plunging unswept NACA2412 wing at $M = 0.5$ and $\xi_A = 0.1$, at 25% of the half–span

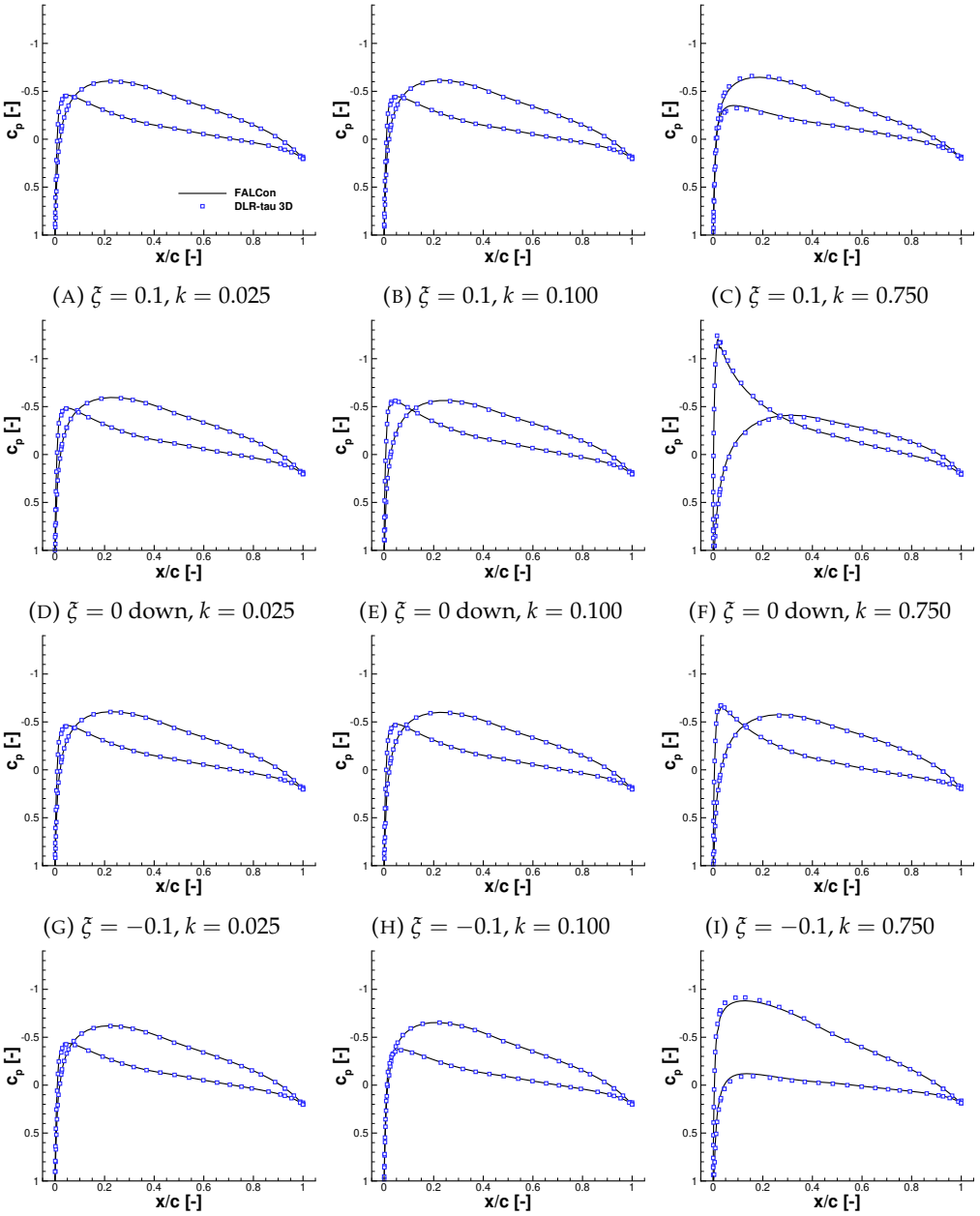

(A) $\xi = 0.1$, $k = 0.025$ (B) $\xi = 0.1$, $k = 0.100$ (C) $\xi = 0.1$, $k = 0.750$

(D) $\xi = 0$ down, $k = 0.025$ (E) $\xi = 0$ down, $k = 0.100$ (F) $\xi = 0$ down, $k = 0.750$

(G) $\xi = -0.1$, $k = 0.025$ (H) $\xi = -0.1$, $k = 0.100$ (I) $\xi = -0.1$, $k = 0.750$

(J) $\xi = 0$ up, $k = 0.025$ (K) $\xi = 0$ up, $k = 0.100$ (L) $\xi = 0$ up, $k = 0.750$

FIGURE A.79: Sectional pressure coefficient, c_p, of the third cycle of the plunging unswept NACA2412 wing at $M = 0.5$ and $\xi_A = 0.1$, at 50% of the half–span

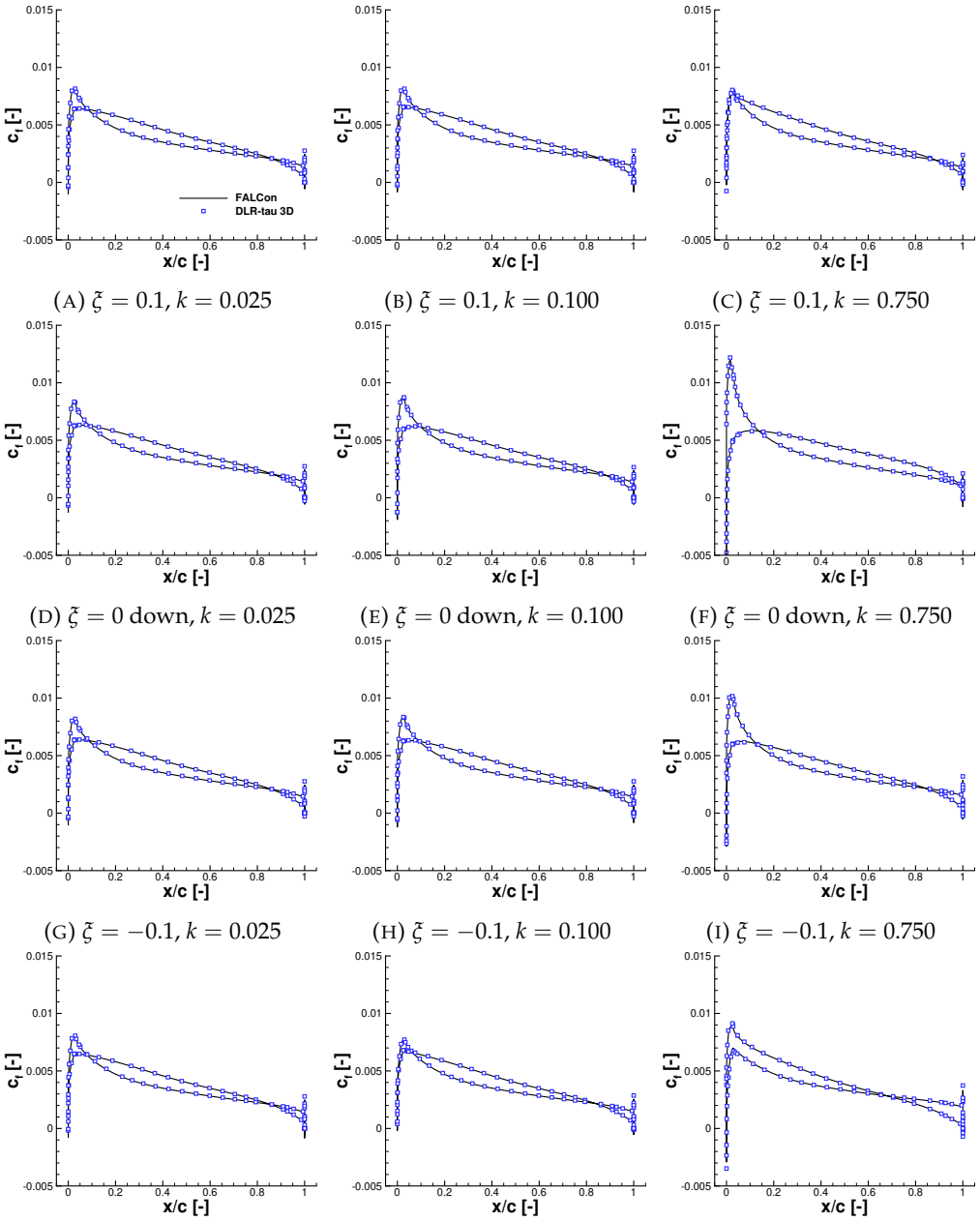

(A) $\xi = 0.1$, $k = 0.025$ (B) $\xi = 0.1$, $k = 0.100$ (C) $\xi = 0.1$, $k = 0.750$

(D) $\xi = 0$ down, $k = 0.025$ (E) $\xi = 0$ down, $k = 0.100$ (F) $\xi = 0$ down, $k = 0.750$

(G) $\xi = -0.1$, $k = 0.025$ (H) $\xi = -0.1$, $k = 0.100$ (I) $\xi = -0.1$, $k = 0.750$

(J) $\xi = 0$ up, $k = 0.025$ (K) $\xi = 0$ up, $k = 0.100$ (L) $\xi = 0$ up, $k = 0.750$

FIGURE A.80: Sectional friction coefficient, c_f, of the third cycle of the plunging unswept NACA2412 wing at $M = 0.5$ and $\xi_A = 0.1$, at 50% of the half–span

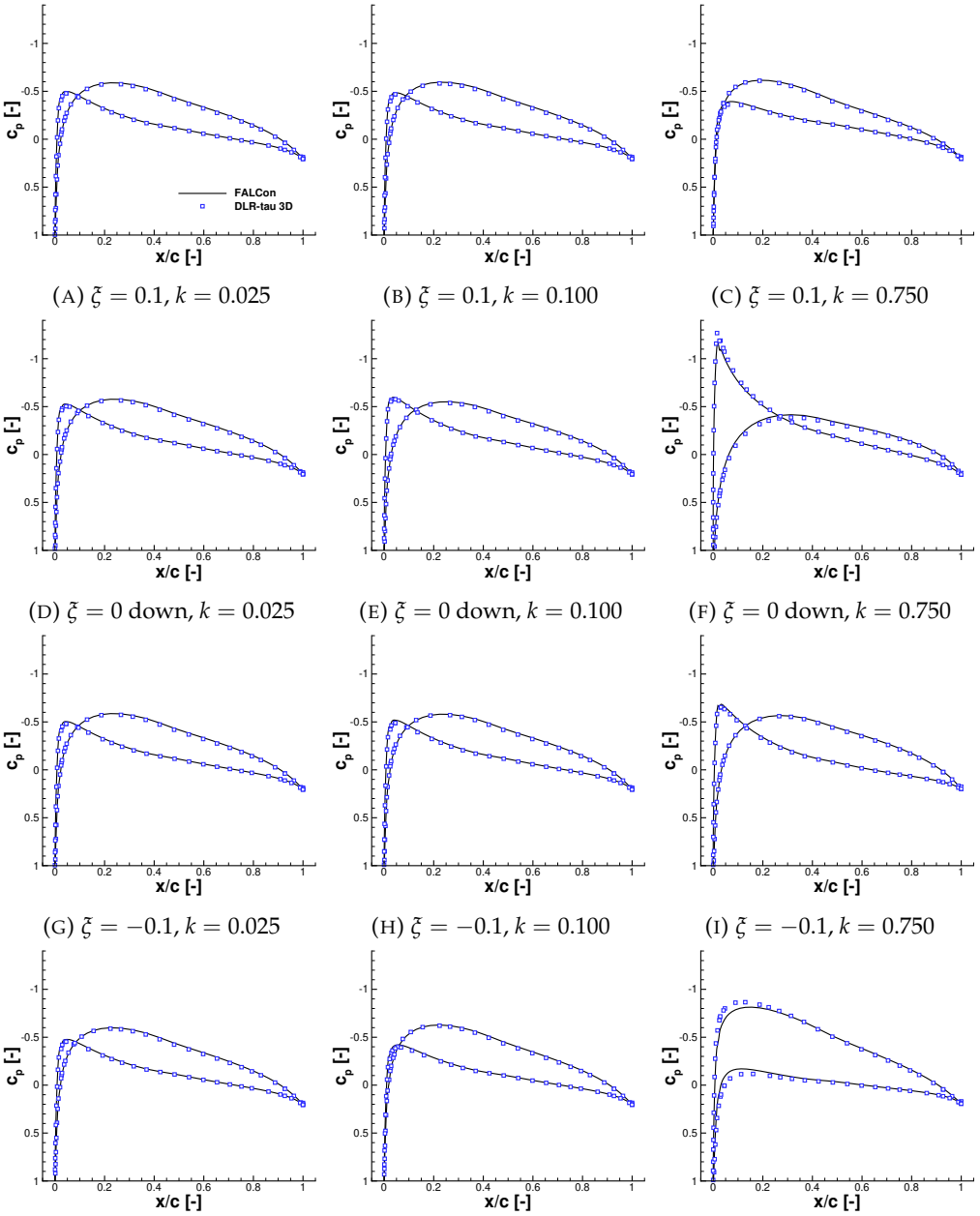

(A) $\xi = 0.1$, $k = 0.025$ (B) $\xi = 0.1$, $k = 0.100$ (C) $\xi = 0.1$, $k = 0.750$

(D) $\xi = 0$ down, $k = 0.025$ (E) $\xi = 0$ down, $k = 0.100$ (F) $\xi = 0$ down, $k = 0.750$

(G) $\xi = -0.1$, $k = 0.025$ (H) $\xi = -0.1$, $k = 0.100$ (I) $\xi = -0.1$, $k = 0.750$

(J) $\xi = 0$ up, $k = 0.025$ (K) $\xi = 0$ up, $k = 0.100$ (L) $\xi = 0$ up, $k = 0.750$

FIGURE A.81: Sectional pressure coefficient, c_p, of the third cycle of the plunging unswept NACA2412 wing at $M = 0.5$ and $\xi_A = 0.1$, at 75% of the half–span

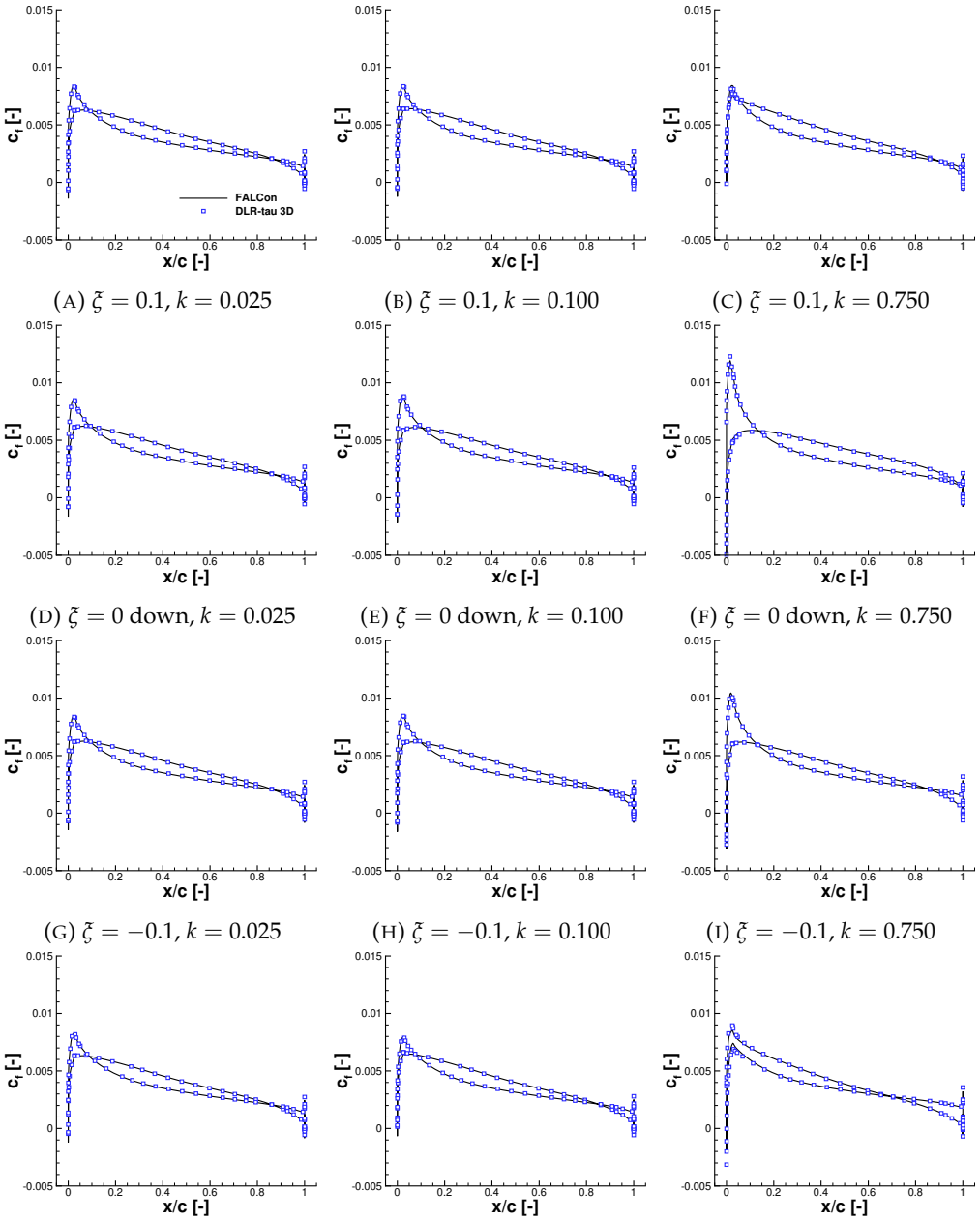

(A) $\xi = 0.1$, $k = 0.025$ (B) $\xi = 0.1$, $k = 0.100$ (C) $\xi = 0.1$, $k = 0.750$

(D) $\xi = 0$ down, $k = 0.025$ (E) $\xi = 0$ down, $k = 0.100$ (F) $\xi = 0$ down, $k = 0.750$

(G) $\xi = -0.1$, $k = 0.025$ (H) $\xi = -0.1$, $k = 0.100$ (I) $\xi = -0.1$, $k = 0.750$

(J) $\xi = 0$ up, $k = 0.025$ (K) $\xi = 0$ up, $k = 0.100$ (L) $\xi = 0$ up, $k = 0.750$

FIGURE A.82: Sectional friction coefficient, c_f, of the third cycle of the plunging unswept NACA2412 wing at $M = 0.5$ and $\xi_A = 0.1$, at 75% of the half–span

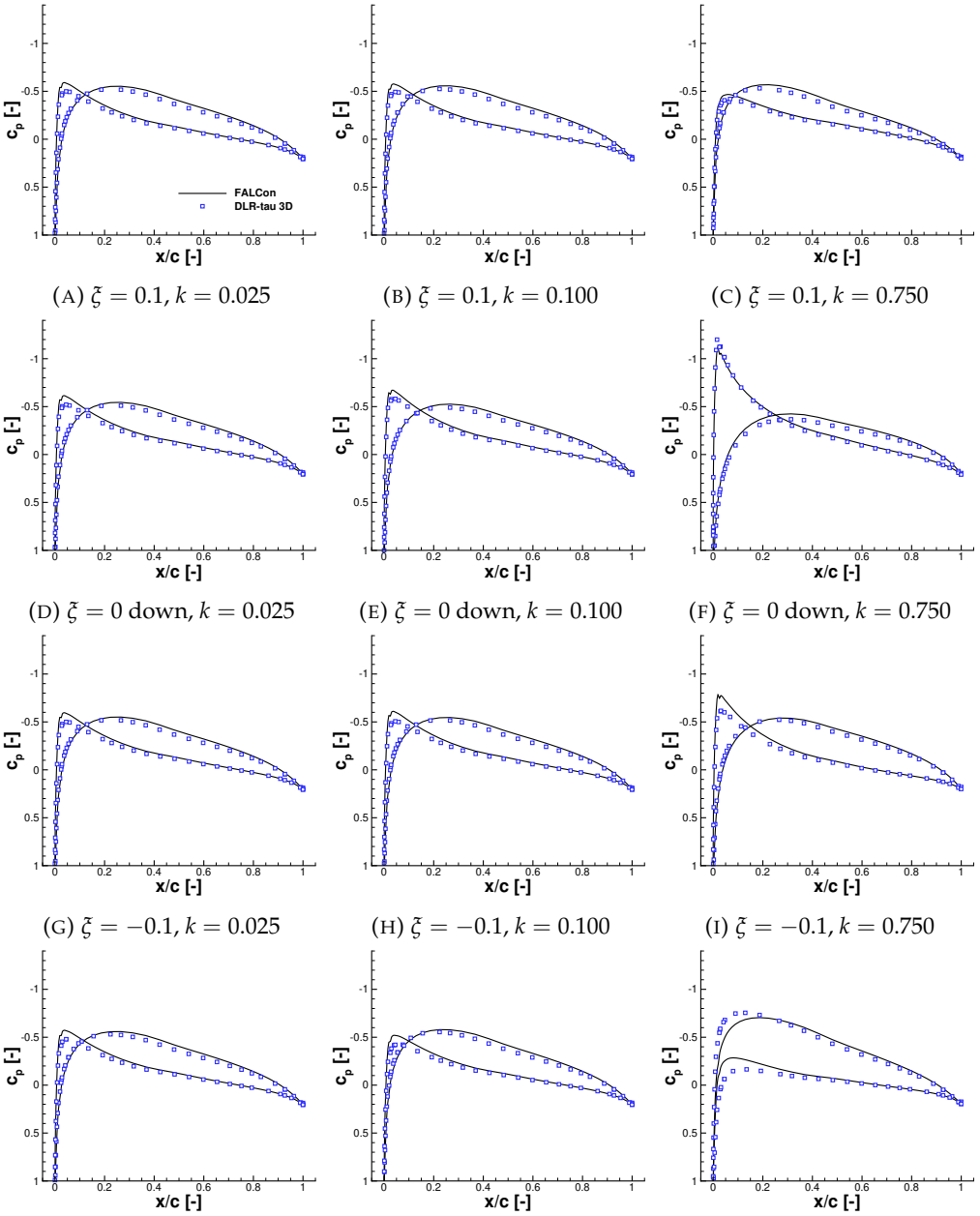

(A) $\xi = 0.1$, $k = 0.025$ (B) $\xi = 0.1$, $k = 0.100$ (C) $\xi = 0.1$, $k = 0.750$

(D) $\xi = 0$ down, $k = 0.025$ (E) $\xi = 0$ down, $k = 0.100$ (F) $\xi = 0$ down, $k = 0.750$

(G) $\xi = -0.1$, $k = 0.025$ (H) $\xi = -0.1$, $k = 0.100$ (I) $\xi = -0.1$, $k = 0.750$

(J) $\xi = 0$ up, $k = 0.025$ (K) $\xi = 0$ up, $k = 0.100$ (L) $\xi = 0$ up, $k = 0.750$

FIGURE A.83: Sectional pressure coefficient, c_p, of the third cycle of the plunging unswept NACA2412 wing at $M = 0.5$ and $\xi_A = 0.1$, at 90% of the half–span

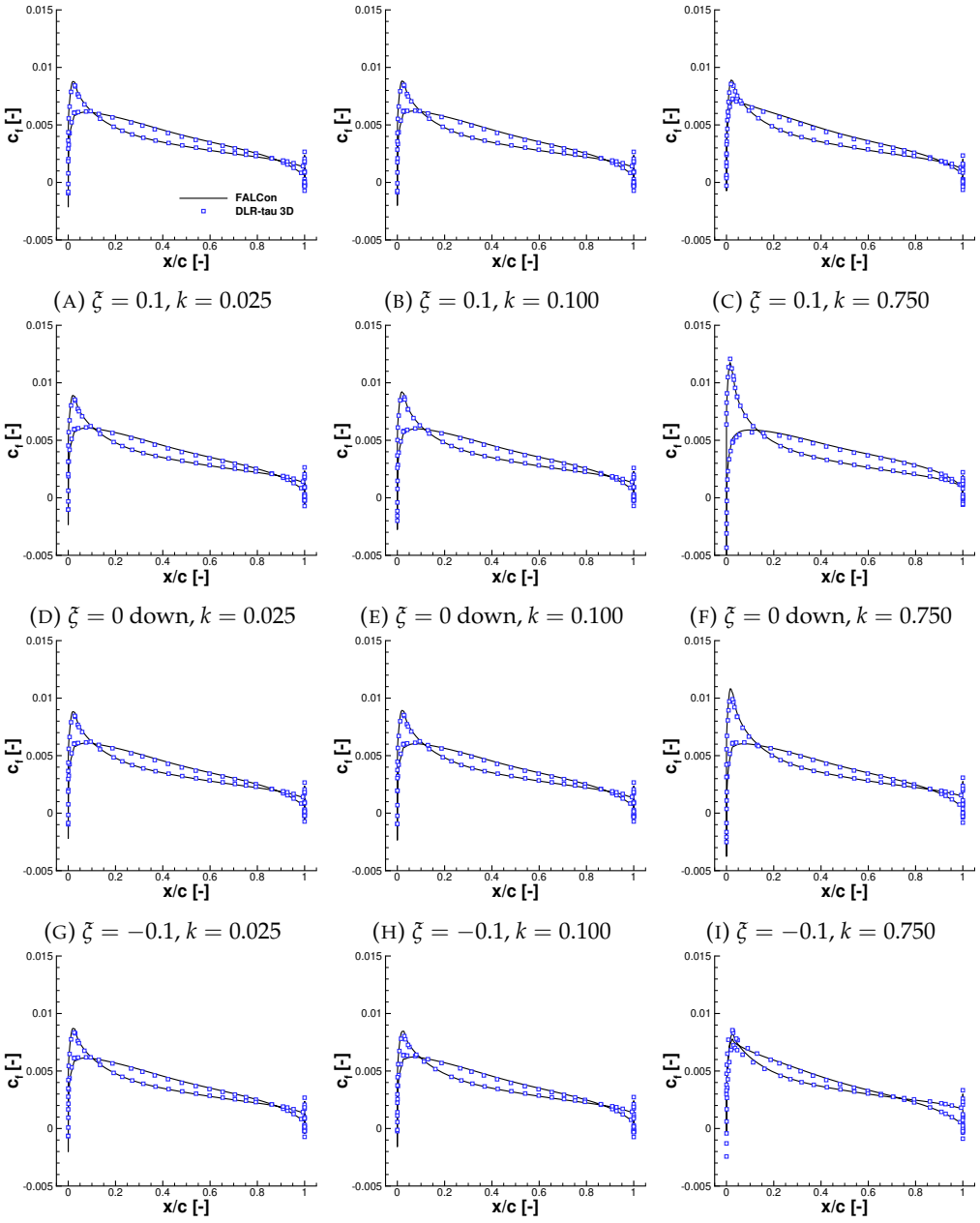

(A) $\xi = 0.1$, $k = 0.025$ (B) $\xi = 0.1$, $k = 0.100$ (C) $\xi = 0.1$, $k = 0.750$

(D) $\xi = 0$ down, $k = 0.025$ (E) $\xi = 0$ down, $k = 0.100$ (F) $\xi = 0$ down, $k = 0.750$

(G) $\xi = -0.1$, $k = 0.025$ (H) $\xi = -0.1$, $k = 0.100$ (I) $\xi = -0.1$, $k = 0.750$

(J) $\xi = 0$ up, $k = 0.025$ (K) $\xi = 0$ up, $k = 0.100$ (L) $\xi = 0$ up, $k = 0.750$

FIGURE A.84: Sectional friction coefficient, c_f, of the third cycle of the plunging unswept NACA2412 wing at $M = 0.5$ and $\xi_A = 0.1$, at 90% of the half–span

A.1.2.3 Mach $M = 0.7$

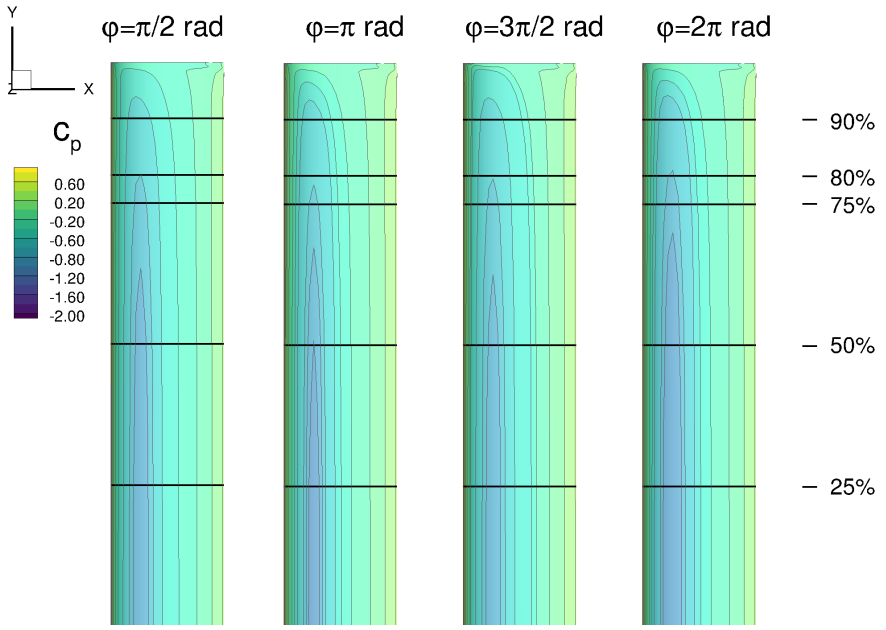

FIGURE A.85: Pressure coefficient, c_p, of the NACA2412–wing at $M = 0.7$ and $k = 0.025$ during forced harmonic plunging oscillation, third cycle

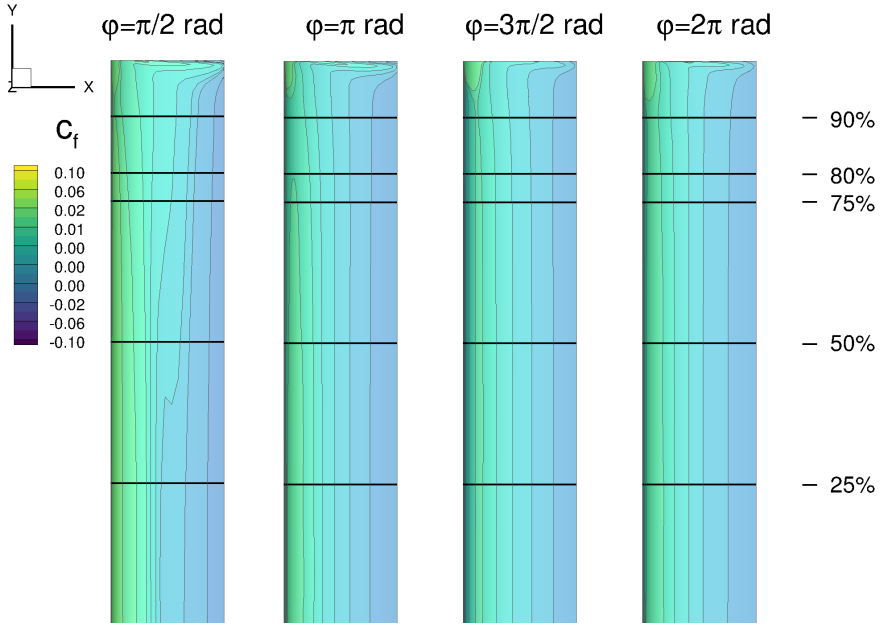

FIGURE A.86: Friction coefficient, c_f, of the NACA2412–wing at $M = 0.7$ and $k = 0.025$ during forced harmonic plunging oscillation, third cycle

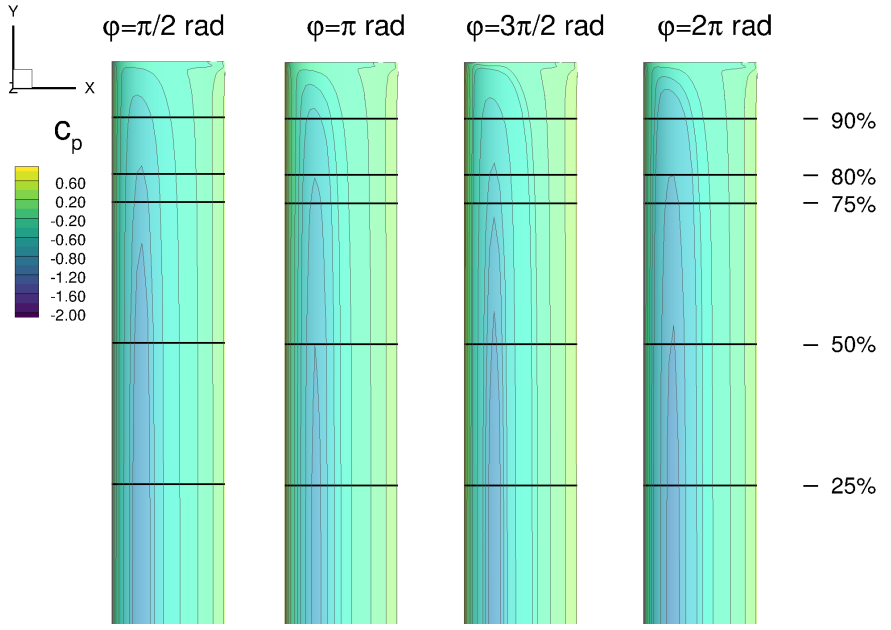

FIGURE A.87: Pressure coefficient, c_p, of the NACA2412–wing at $M = 0.7$ and $k = 0.100$ during forced harmonic plunging oscillation, third cycle

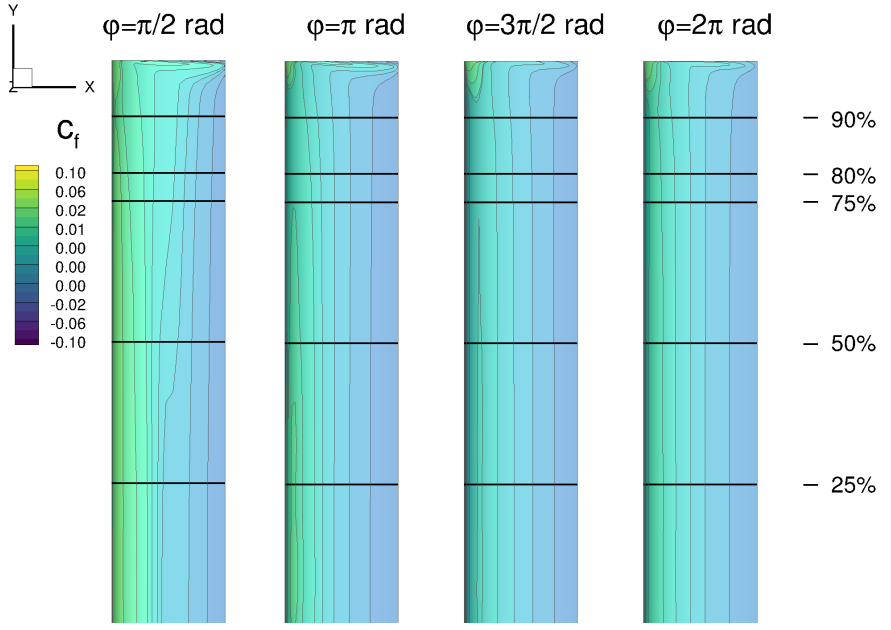

FIGURE A.88: Friction coefficient, c_f, of the NACA2412–wing at $M = 0.7$ and $k = 0.100$ during forced harmonic plunging oscillation, third cycle

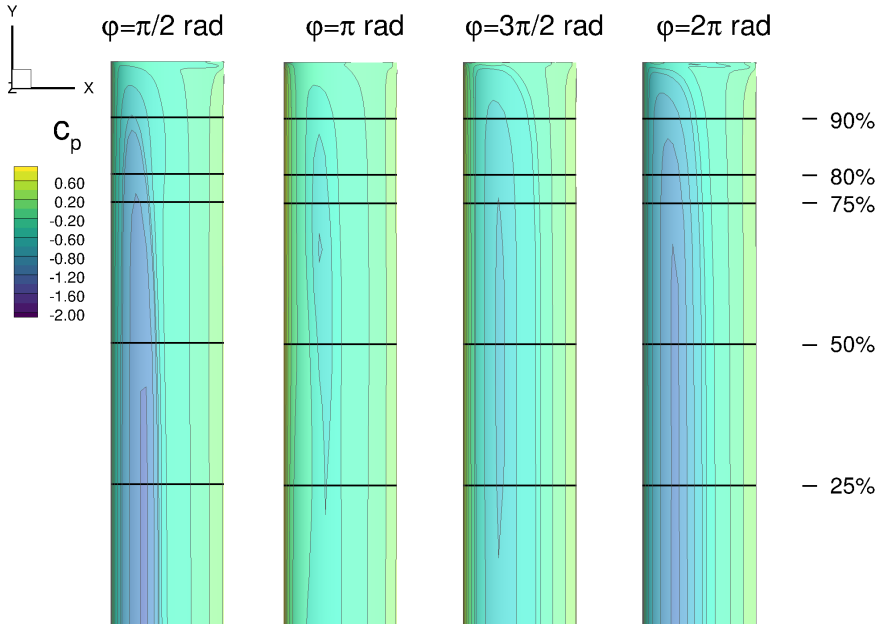

FIGURE A.89: Pressure coefficient, c_p, of the NACA2412–wing at $M = 0.7$ and $k = 0.750$ during forced harmonic plunging oscillation, third cycle

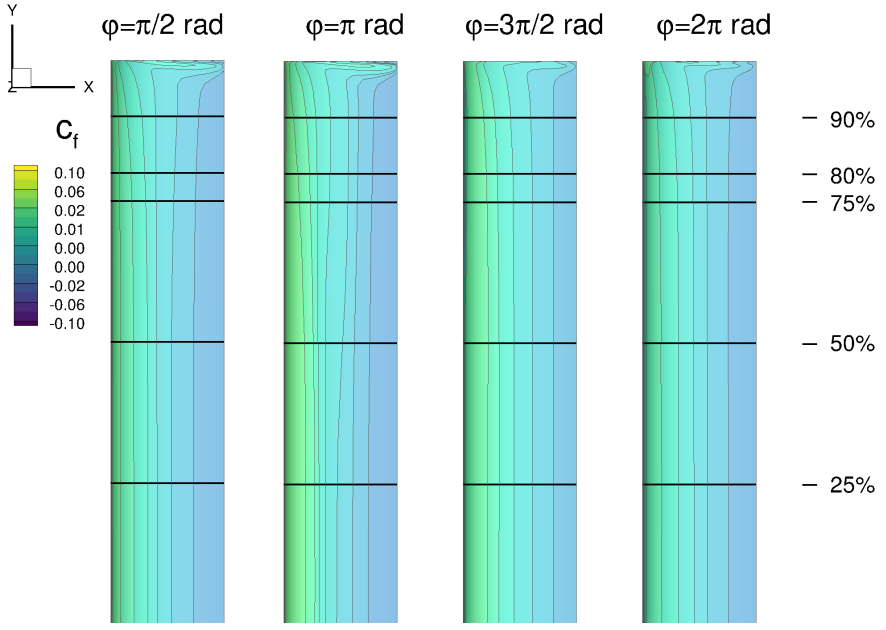

FIGURE A.90: Friction coefficient, c_f, of the NACA2412–wing at $M = 0.7$ and $k = 0.750$ during forced harmonic plunging oscillation, third cycle

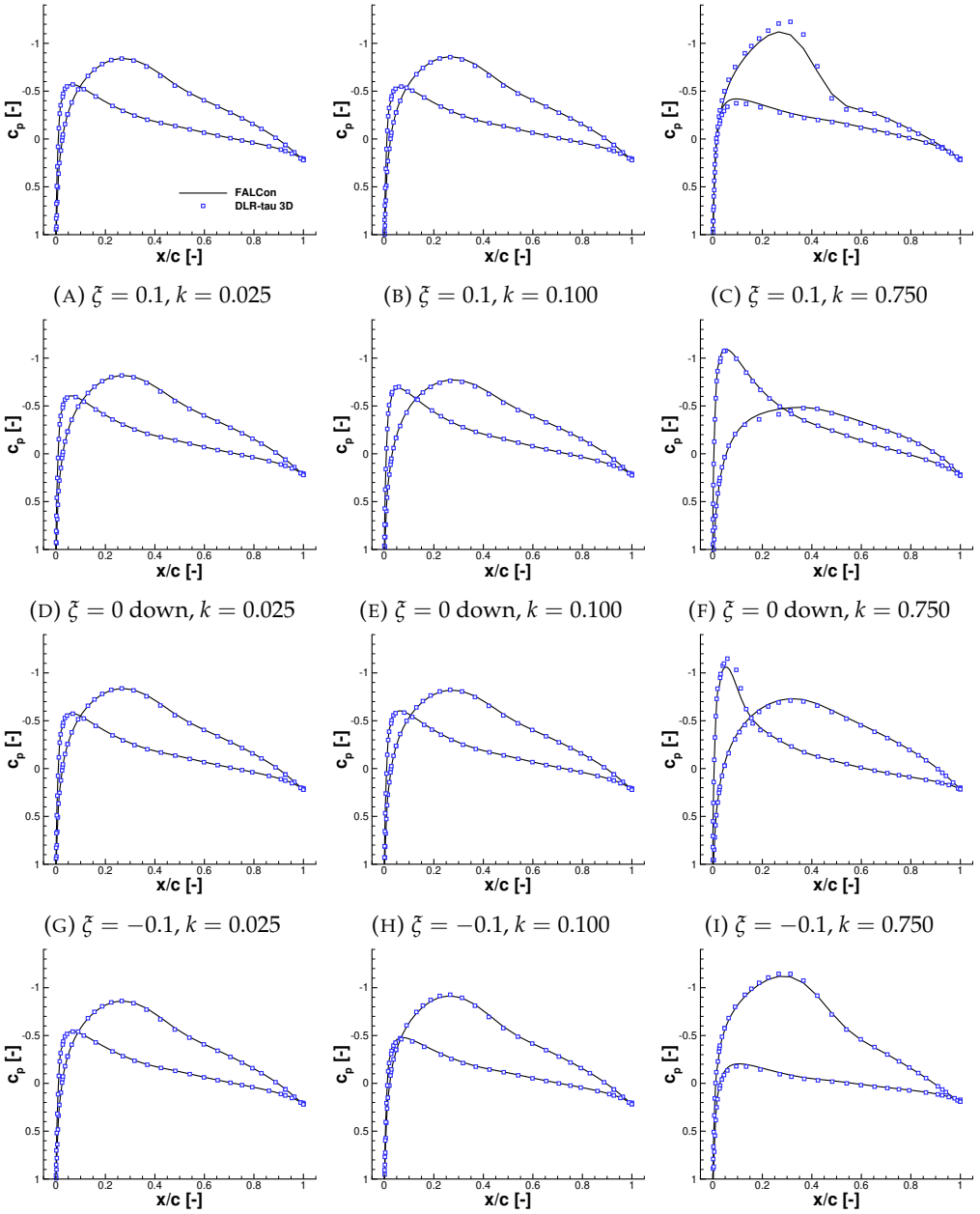

(A) $\xi = 0.1$, $k = 0.025$ (B) $\xi = 0.1$, $k = 0.100$ (C) $\xi = 0.1$, $k = 0.750$

(D) $\xi = 0$ down, $k = 0.025$ (E) $\xi = 0$ down, $k = 0.100$ (F) $\xi = 0$ down, $k = 0.750$

(G) $\xi = -0.1$, $k = 0.025$ (H) $\xi = -0.1$, $k = 0.100$ (I) $\xi = -0.1$, $k = 0.750$

(J) $\xi = 0$ up, $k = 0.025$ (K) $\xi = 0$ up, $k = 0.100$ (L) $\xi = 0$ up, $k = 0.750$

FIGURE A.91: Sectional pressure coefficient, c_p, of the third cycle of the plunging unswept NACA2412 wing at $M = 0.7$ and $\xi_A = 0.1$, at 25% of the half–span

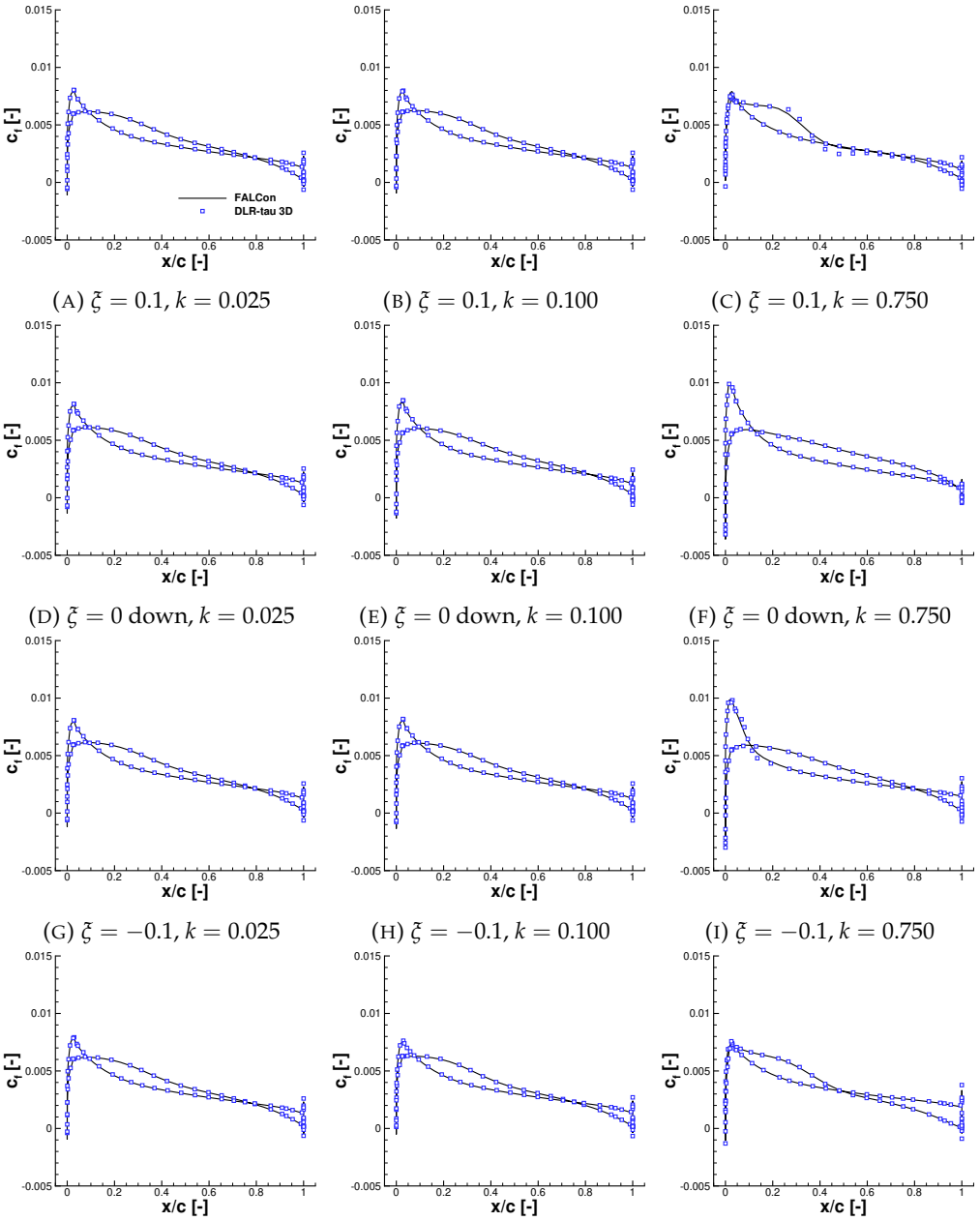

(A) $\xi = 0.1$, $k = 0.025$ (B) $\xi = 0.1$, $k = 0.100$ (C) $\xi = 0.1$, $k = 0.750$

(D) $\xi = 0$ down, $k = 0.025$ (E) $\xi = 0$ down, $k = 0.100$ (F) $\xi = 0$ down, $k = 0.750$

(G) $\xi = -0.1$, $k = 0.025$ (H) $\xi = -0.1$, $k = 0.100$ (I) $\xi = -0.1$, $k = 0.750$

(J) $\xi = 0$ up, $k = 0.025$ (K) $\xi = 0$ up, $k = 0.100$ (L) $\xi = 0$ up, $k = 0.750$

FIGURE A.92: Sectional friction coefficient, c_f, of the third cycle of the plunging unswept NACA2412 wing at $M = 0.7$ and $\xi_A = 0.1$, at 25% of the half–span

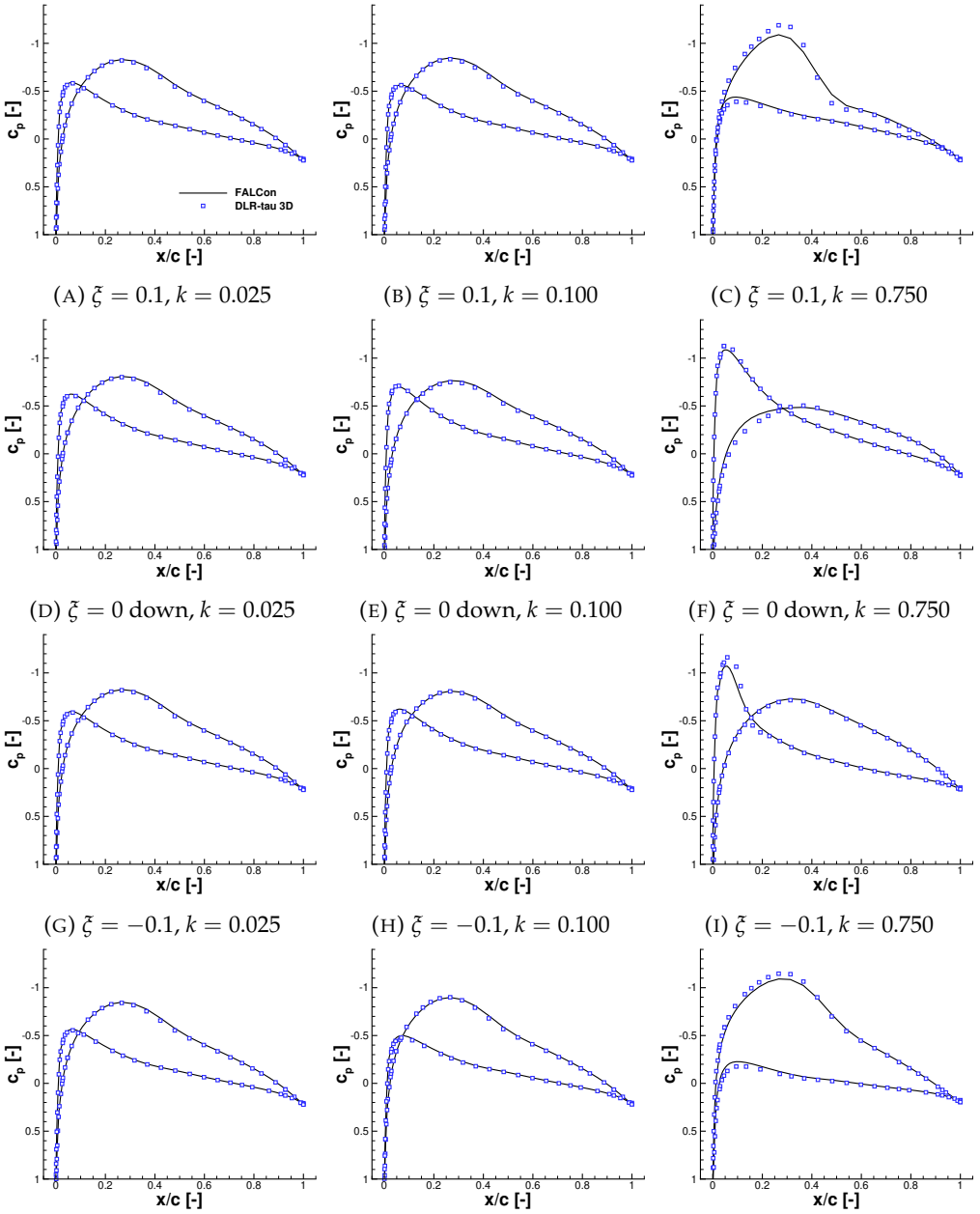

(A) $\xi = 0.1$, $k = 0.025$ (B) $\xi = 0.1$, $k = 0.100$ (C) $\xi = 0.1$, $k = 0.750$

(D) $\xi = 0$ down, $k = 0.025$ (E) $\xi = 0$ down, $k = 0.100$ (F) $\xi = 0$ down, $k = 0.750$

(G) $\xi = -0.1$, $k = 0.025$ (H) $\xi = -0.1$, $k = 0.100$ (I) $\xi = -0.1$, $k = 0.750$

(J) $\xi = 0$ up, $k = 0.025$ (K) $\xi = 0$ up, $k = 0.100$ (L) $\xi = 0$ up, $k = 0.750$

FIGURE A.93: Sectional pressure coefficient, c_p, of the third cycle of the plunging unswept NACA2412 wing at $M = 0.7$ and $\xi_A = 0.1$, at 50% of the half–span

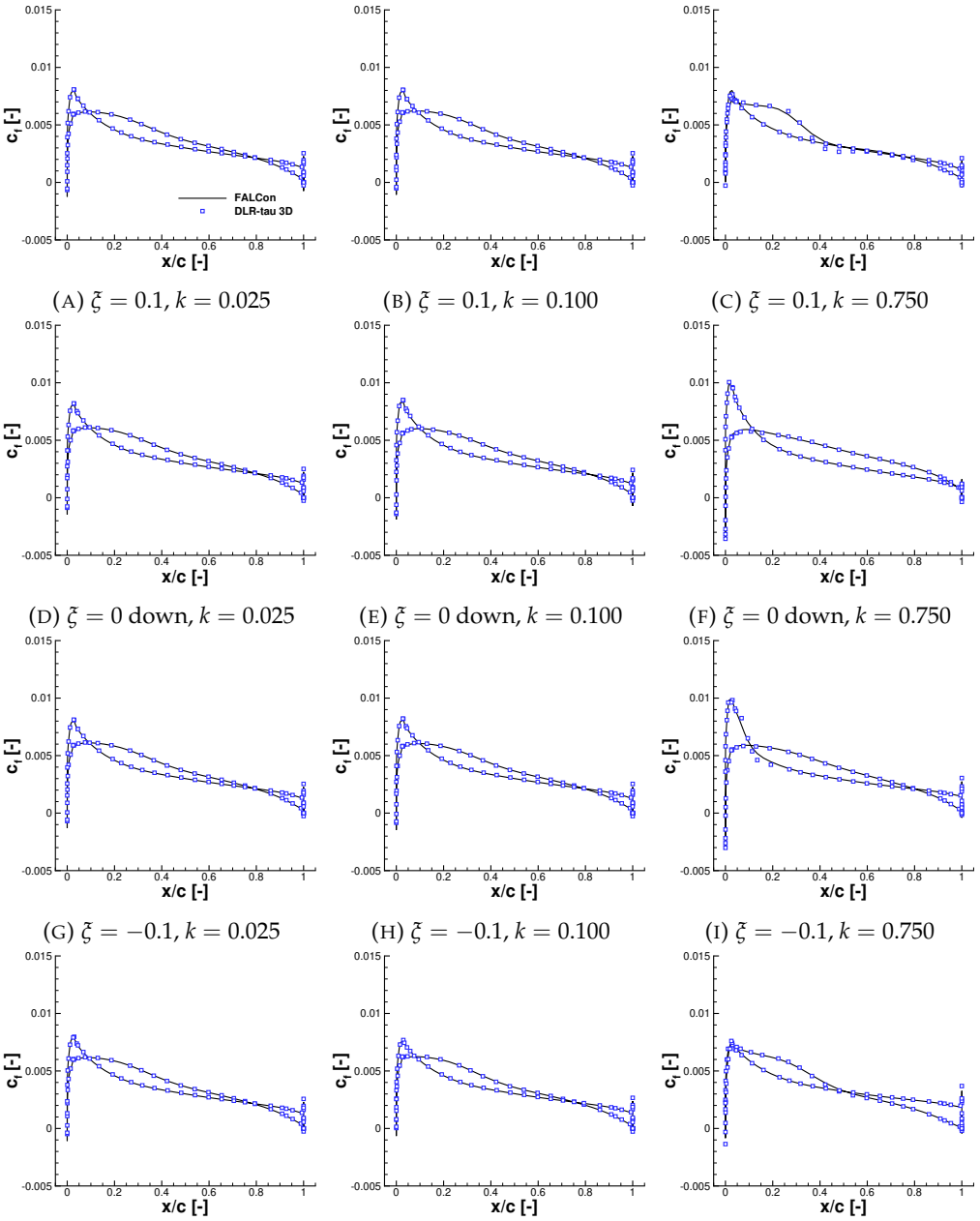

(A) $\xi = 0.1$, $k = 0.025$ (B) $\xi = 0.1$, $k = 0.100$ (C) $\xi = 0.1$, $k = 0.750$

(D) $\xi = 0$ down, $k = 0.025$ (E) $\xi = 0$ down, $k = 0.100$ (F) $\xi = 0$ down, $k = 0.750$

(G) $\xi = -0.1$, $k = 0.025$ (H) $\xi = -0.1$, $k = 0.100$ (I) $\xi = -0.1$, $k = 0.750$

(J) $\xi = 0$ up, $k = 0.025$ (K) $\xi = 0$ up, $k = 0.100$ (L) $\xi = 0$ up, $k = 0.750$

FIGURE A.94: Sectional friction coefficient, c_f, of the third cycle of the plunging unswept NACA2412 wing at $M = 0.7$ and $\xi_A = 0.1$, at 50% of the half–span

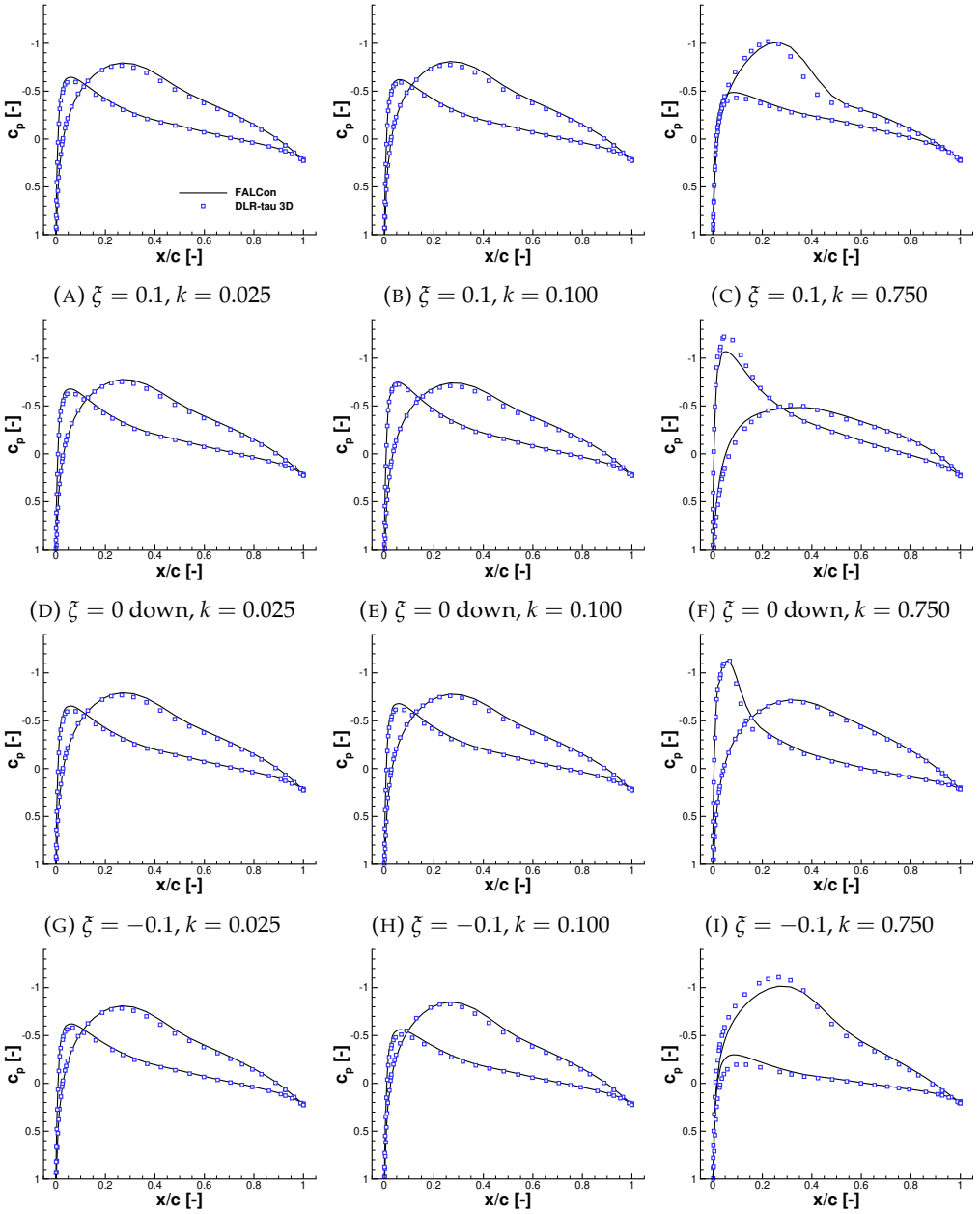

(A) $\xi = 0.1$, $k = 0.025$ (B) $\xi = 0.1$, $k = 0.100$ (C) $\xi = 0.1$, $k = 0.750$

(D) $\xi = 0$ down, $k = 0.025$ (E) $\xi = 0$ down, $k = 0.100$ (F) $\xi = 0$ down, $k = 0.750$

(G) $\xi = -0.1$, $k = 0.025$ (H) $\xi = -0.1$, $k = 0.100$ (I) $\xi = -0.1$, $k = 0.750$

(J) $\xi = 0$ up, $k = 0.025$ (K) $\xi = 0$ up, $k = 0.100$ (L) $\xi = 0$ up, $k = 0.750$

FIGURE A.95: Sectional pressure coefficient, c_p, of the third cycle of the plunging unswept NACA2412 wing at $M = 0.7$ and $\xi_A = 0.1$, at 75% of the half–span

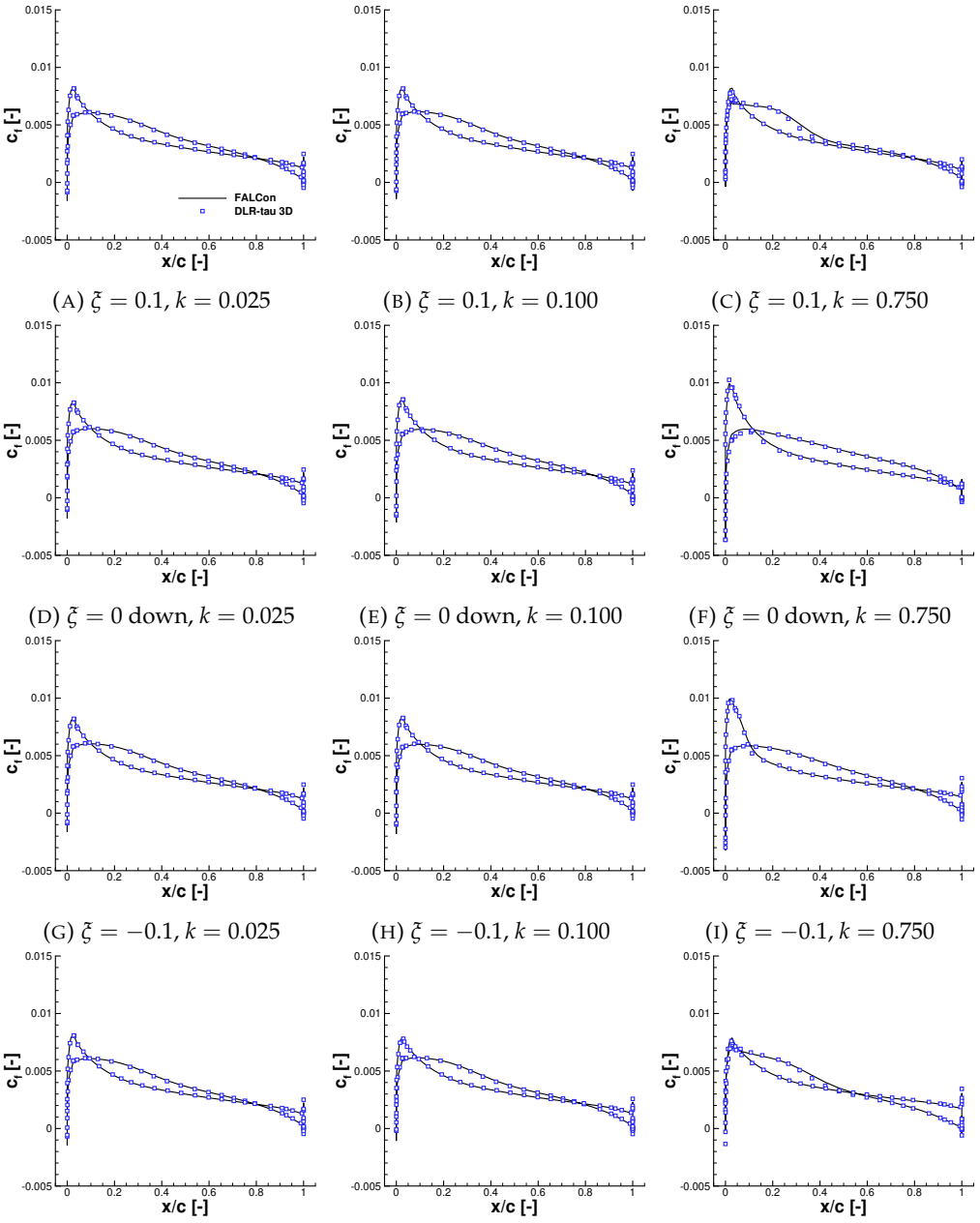

(A) $\xi = 0.1$, $k = 0.025$ (B) $\xi = 0.1$, $k = 0.100$ (C) $\xi = 0.1$, $k = 0.750$

(D) $\xi = 0$ down, $k = 0.025$ (E) $\xi = 0$ down, $k = 0.100$ (F) $\xi = 0$ down, $k = 0.750$

(G) $\xi = -0.1$, $k = 0.025$ (H) $\xi = -0.1$, $k = 0.100$ (I) $\xi = -0.1$, $k = 0.750$

(J) $\xi = 0$ up, $k = 0.025$ (K) $\xi = 0$ up, $k = 0.100$ (L) $\xi = 0$ up, $k = 0.750$

FIGURE A.96: Sectional friction coefficient, c_f, of the third cycle of the plunging unswept NACA2412 wing at $M = 0.7$ and $\xi_A = 0.1$, at 75% of the half–span

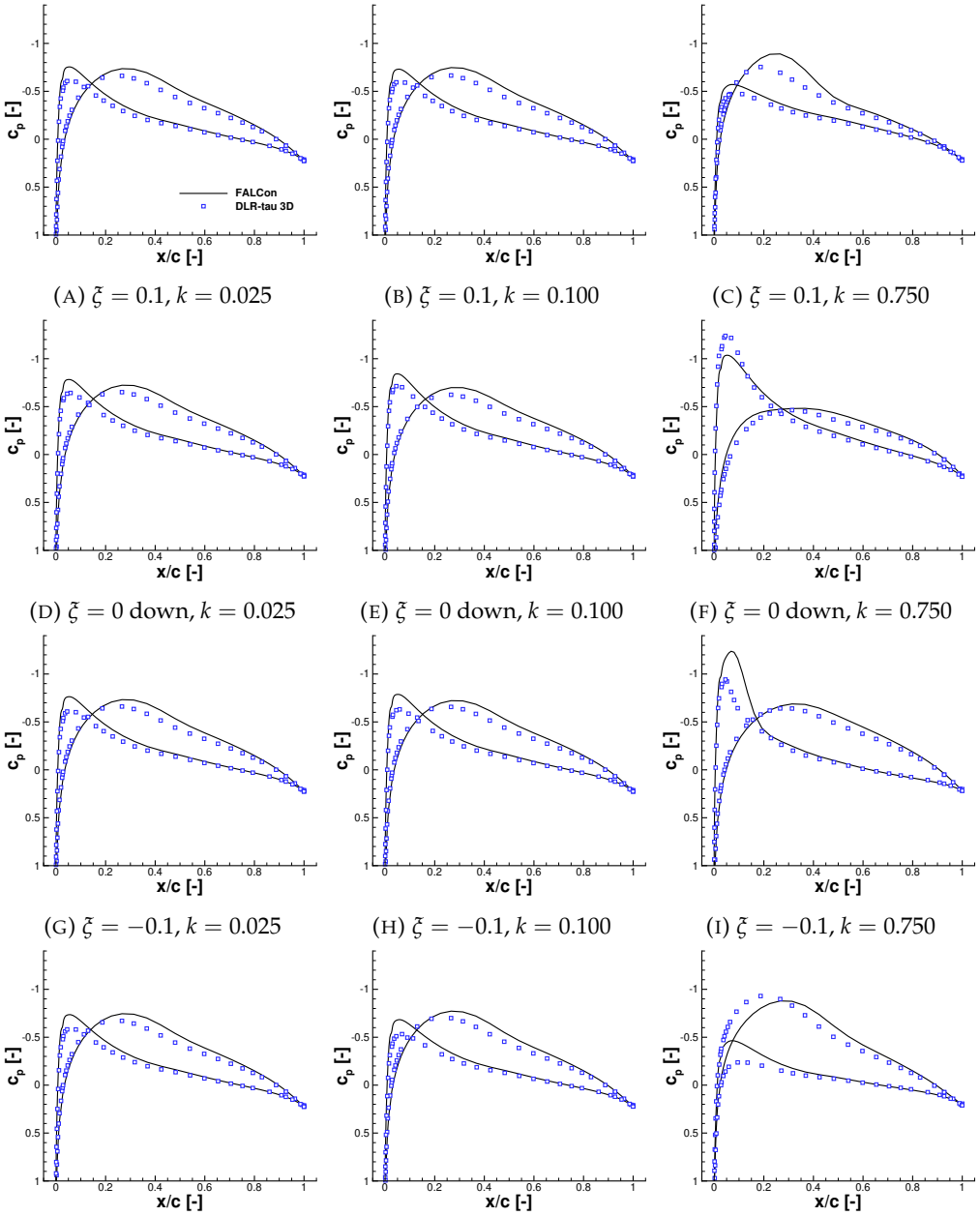

(A) $\xi = 0.1$, $k = 0.025$ (B) $\xi = 0.1$, $k = 0.100$ (C) $\xi = 0.1$, $k = 0.750$

(D) $\xi = 0$ down, $k = 0.025$ (E) $\xi = 0$ down, $k = 0.100$ (F) $\xi = 0$ down, $k = 0.750$

(G) $\xi = -0.1$, $k = 0.025$ (H) $\xi = -0.1$, $k = 0.100$ (I) $\xi = -0.1$, $k = 0.750$

(J) $\xi = 0$ up, $k = 0.025$ (K) $\xi = 0$ up, $k = 0.100$ (L) $\xi = 0$ up, $k = 0.750$

FIGURE A.97: Sectional pressure coefficient, c_p, of the third cycle of the plunging unswept NACA2412 wing at $M = 0.7$ and $\xi_A = 0.1$, at 90% of the half–span

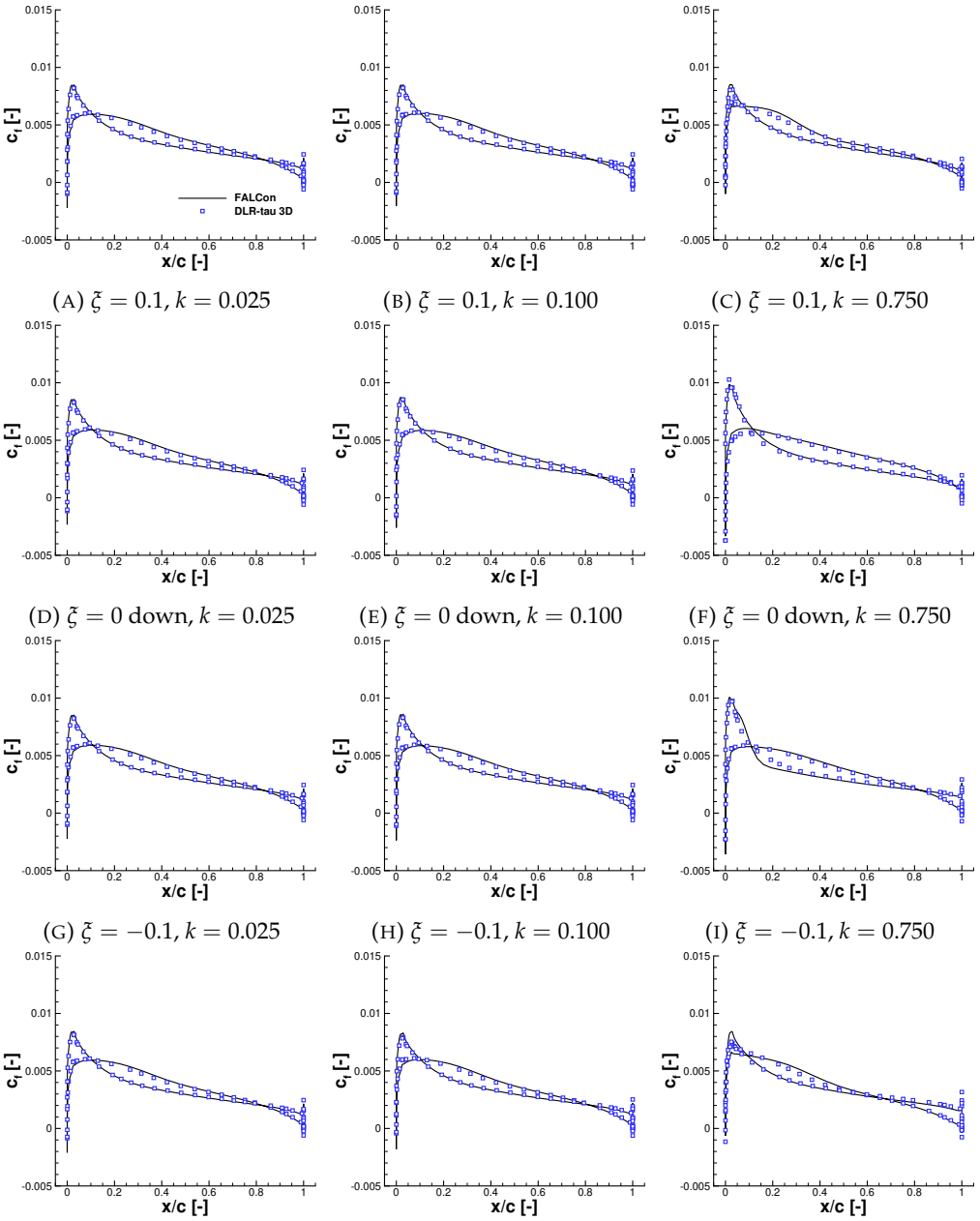

(A) $\xi = 0.1$, $k = 0.025$ (B) $\xi = 0.1$, $k = 0.100$ (C) $\xi = 0.1$, $k = 0.750$

(D) $\xi = 0$ down, $k = 0.025$ (E) $\xi = 0$ down, $k = 0.100$ (F) $\xi = 0$ down, $k = 0.750$

(G) $\xi = -0.1$, $k = 0.025$ (H) $\xi = -0.1$, $k = 0.100$ (I) $\xi = -0.1$, $k = 0.750$

(J) $\xi = 0$ up, $k = 0.025$ (K) $\xi = 0$ up, $k = 0.100$ (L) $\xi = 0$ up, $k = 0.750$

FIGURE A.98: Sectional friction coefficient, c_f, of the third cycle of the plunging unswept NACA2412 wing at $M = 0.7$ and $\xi_A = 0.1$, at 90% of the half–span

A.1.2.4 Mach $M = 0.8$

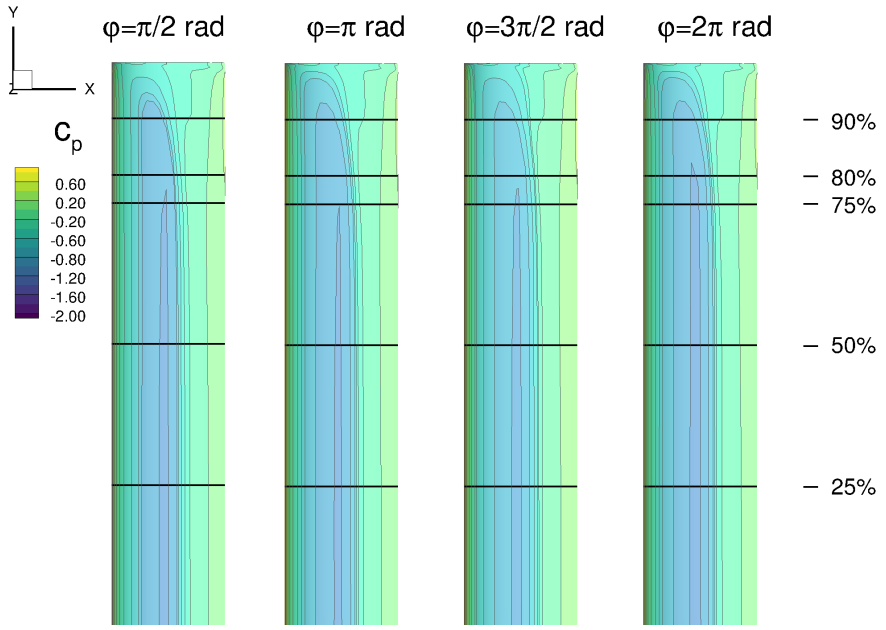

FIGURE A.99: Pressure coefficient, c_p, of the NACA2412–wing at $M = 0.8$ and $k = 0.025$ during forced harmonic plunging oscillation, third cycle

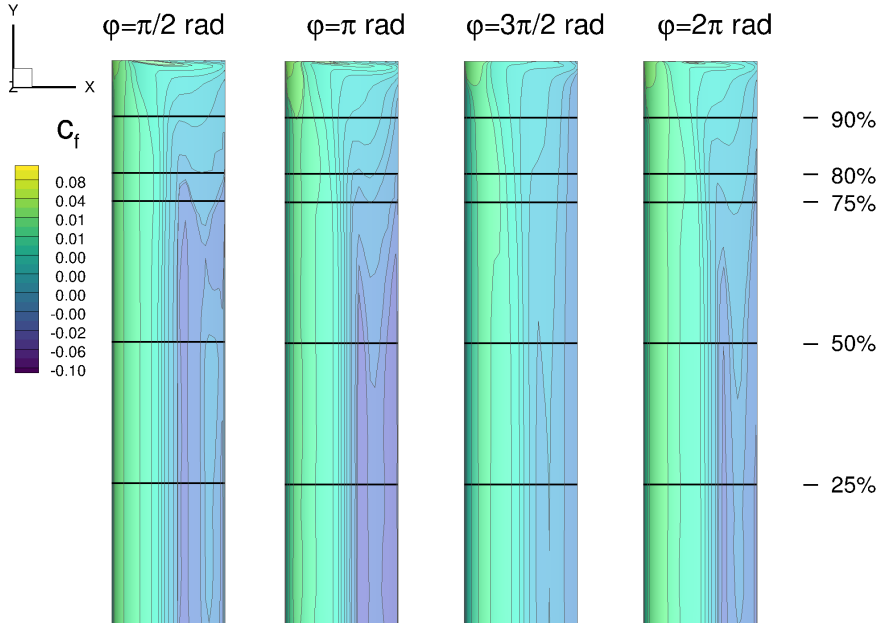

FIGURE A.100: Friction coefficient, c_f, of the NACA2412–wing at $M = 0.8$ and $k = 0.025$ during forced harmonic plunging oscillation, third cycle

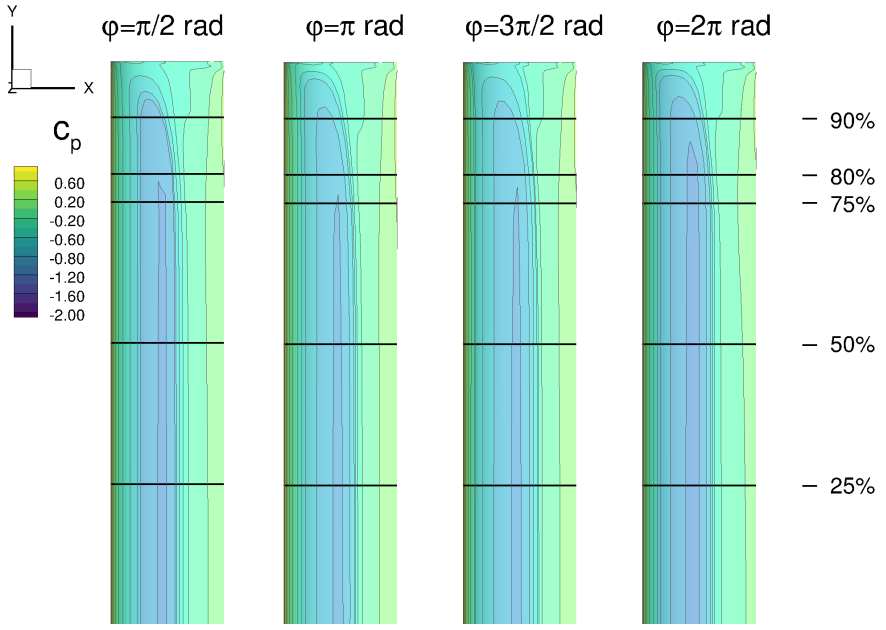

FIGURE A.101: Pressure coefficient, c_p, of the NACA2412–wing at $M = 0.8$ and $k = 0.100$ during forced harmonic plunging oscillation, third cycle

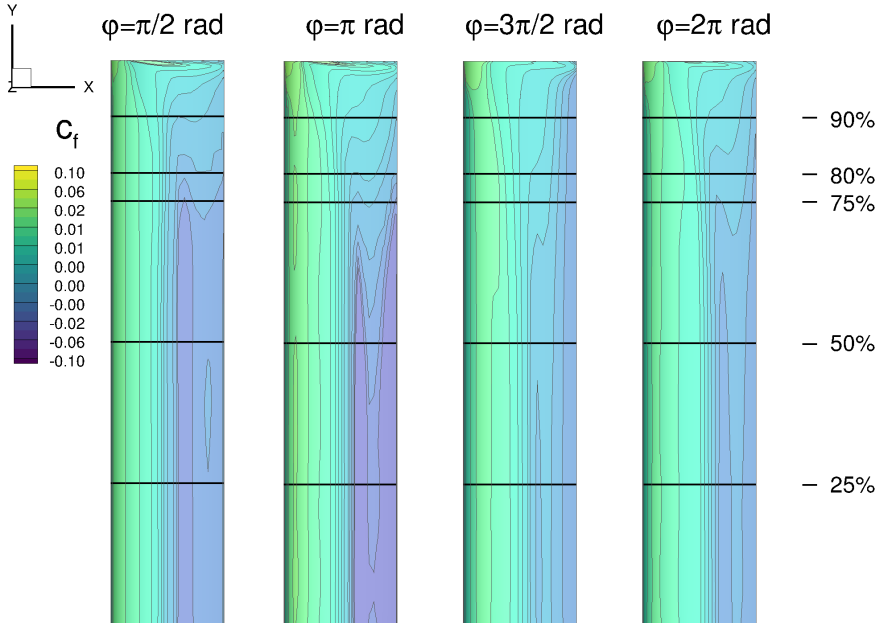

FIGURE A.102: Friction coefficient, c_f, of the NACA2412–wing at $M = 0.8$ and $k = 0.100$ during forced harmonic plunging oscillation, third cycle

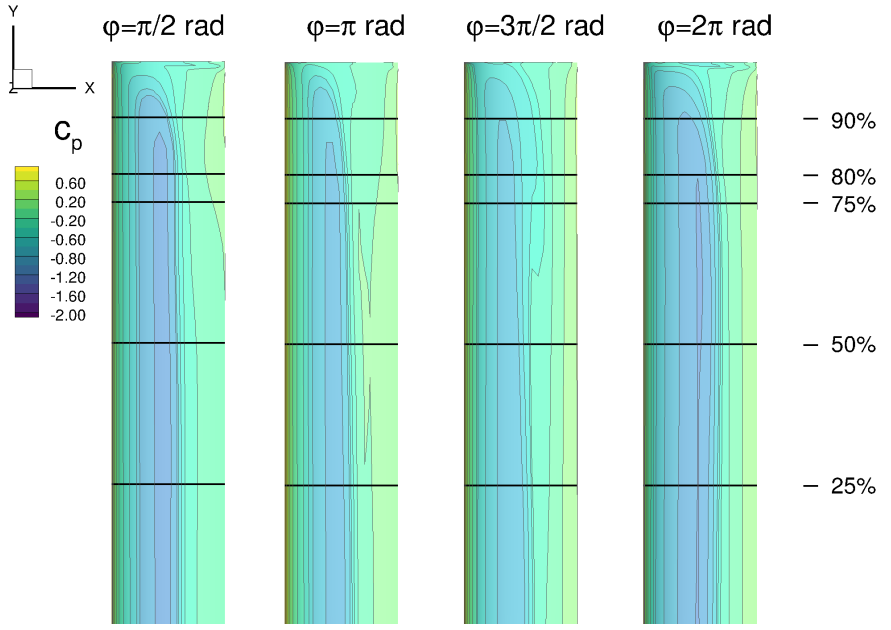

FIGURE A.103: Pressure coefficient, c_p, of the NACA2412–wing at $M = 0.8$ and $k = 0.750$ during forced harmonic plunging oscillation, third cycle

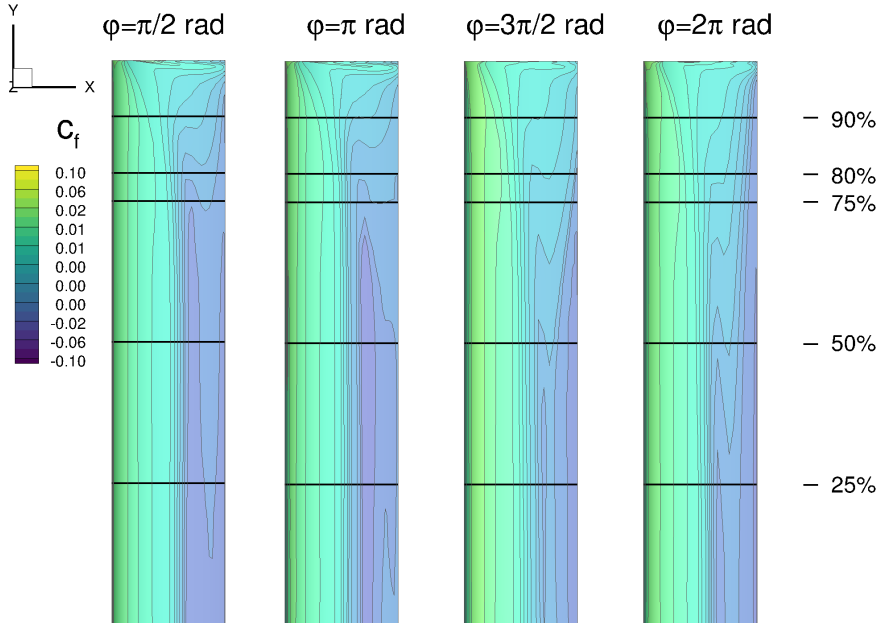

FIGURE A.104: Friction coefficient, c_f, of the NACA2412–wing at $M = 0.8$ and $k = 0.750$ during forced harmonic plunging oscillation, third cycle

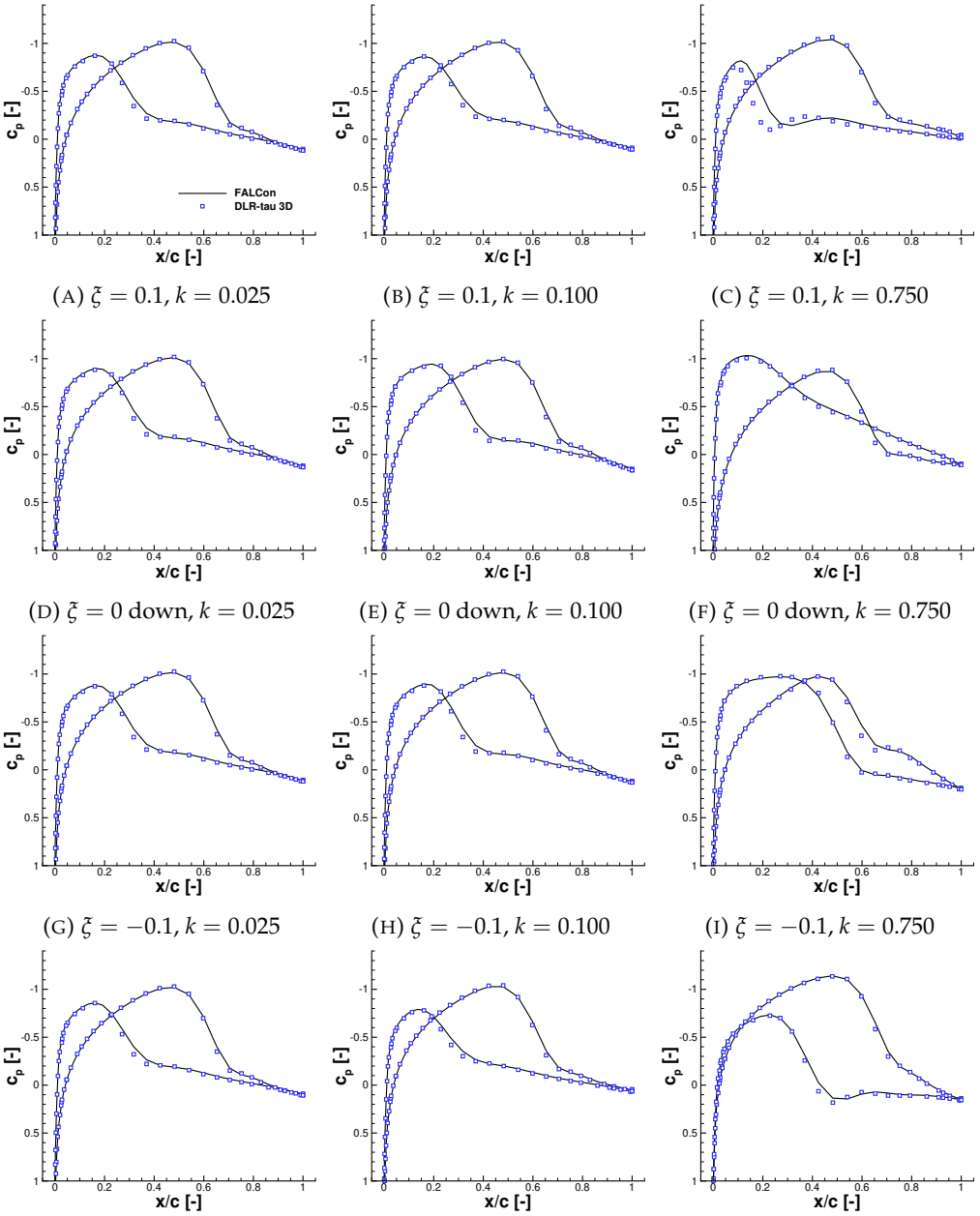

(A) $\xi = 0.1$, $k = 0.025$ (B) $\xi = 0.1$, $k = 0.100$ (C) $\xi = 0.1$, $k = 0.750$

(D) $\xi = 0$ down, $k = 0.025$ (E) $\xi = 0$ down, $k = 0.100$ (F) $\xi = 0$ down, $k = 0.750$

(G) $\xi = -0.1$, $k = 0.025$ (H) $\xi = -0.1$, $k = 0.100$ (I) $\xi = -0.1$, $k = 0.750$

(J) $\xi = 0$ up, $k = 0.025$ (K) $\xi = 0$ up, $k = 0.100$ (L) $\xi = 0$ up, $k = 0.750$

FIGURE A.105: Sectional pressure coefficient, c_p, of the third cycle of the plunging unswept NACA2412 wing at $M = 0.8$ and $\xi_A = 0.1$, at 25% of the half–span

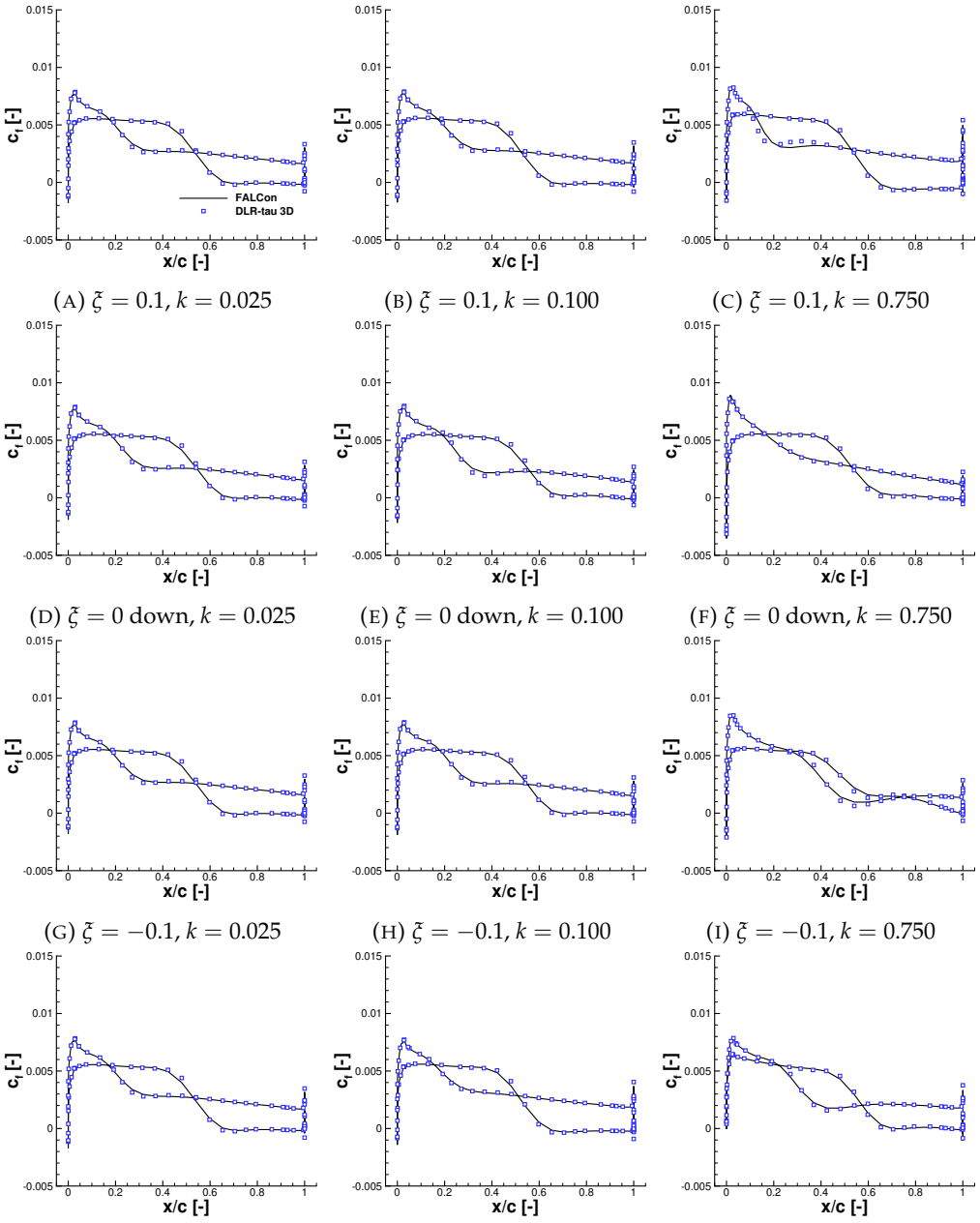

(A) $\xi = 0.1$, $k = 0.025$ (B) $\xi = 0.1$, $k = 0.100$ (C) $\xi = 0.1$, $k = 0.750$

(D) $\xi = 0$ down, $k = 0.025$ (E) $\xi = 0$ down, $k = 0.100$ (F) $\xi = 0$ down, $k = 0.750$

(G) $\xi = -0.1$, $k = 0.025$ (H) $\xi = -0.1$, $k = 0.100$ (I) $\xi = -0.1$, $k = 0.750$

(J) $\xi = 0$ up, $k = 0.025$ (K) $\xi = 0$ up, $k = 0.100$ (L) $\xi = 0$ up, $k = 0.750$

FIGURE A.106: Sectional friction coefficient, c_f, of the third cycle of the plunging unswept NACA2412 wing at $M = 0.8$ and $\xi_A = 0.1$, at 25% of the half–span

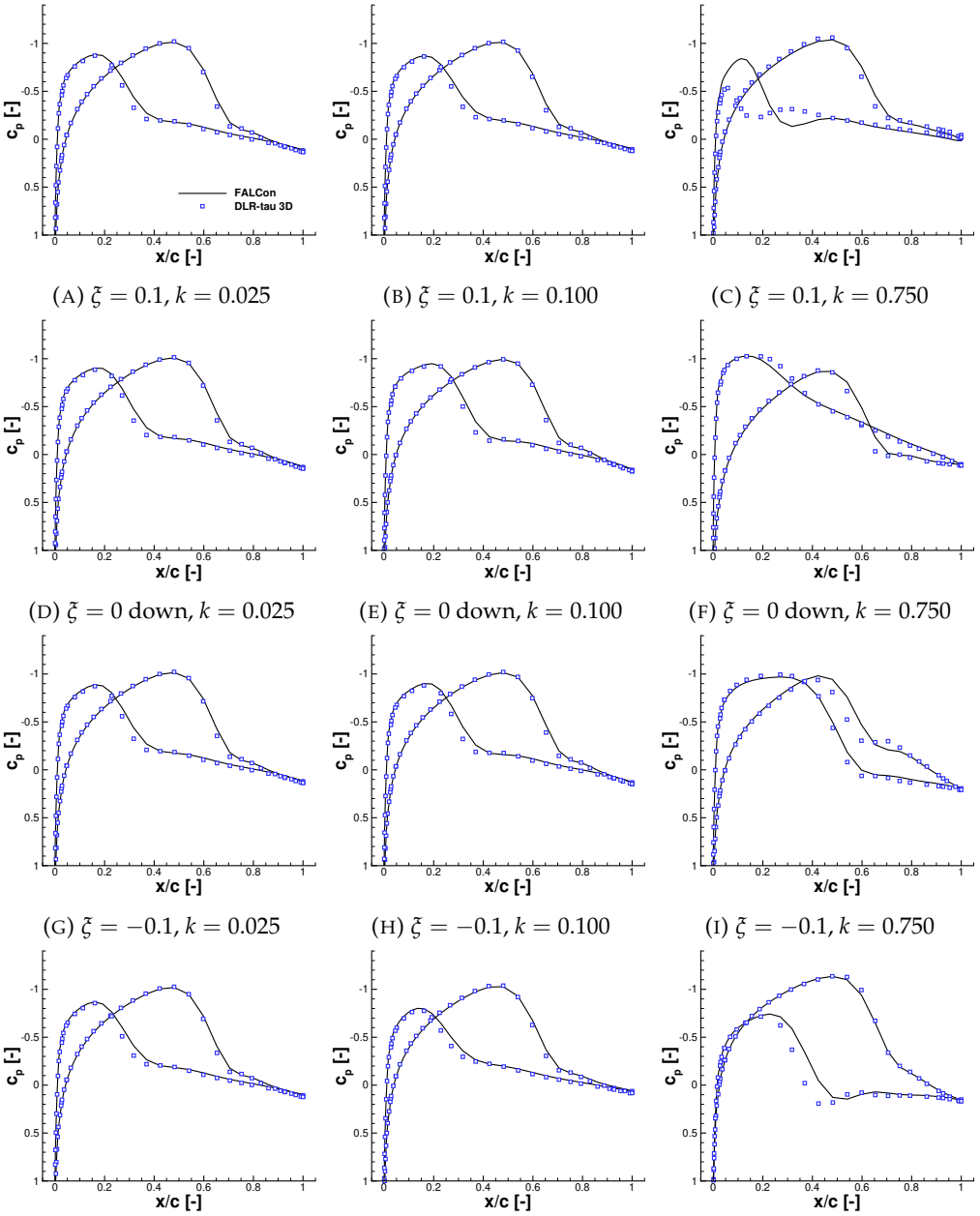

(A) $\xi = 0.1$, $k = 0.025$ (B) $\xi = 0.1$, $k = 0.100$ (C) $\xi = 0.1$, $k = 0.750$

(D) $\xi = 0$ down, $k = 0.025$ (E) $\xi = 0$ down, $k = 0.100$ (F) $\xi = 0$ down, $k = 0.750$

(G) $\xi = -0.1$, $k = 0.025$ (H) $\xi = -0.1$, $k = 0.100$ (I) $\xi = -0.1$, $k = 0.750$

(J) $\xi = 0$ up, $k = 0.025$ (K) $\xi = 0$ up, $k = 0.100$ (L) $\xi = 0$ up, $k = 0.750$

FIGURE A.107: Sectional pressure coefficient, c_p, of the third cycle of the plunging unswept NACA2412 wing at $M = 0.8$ and $\xi_A = 0.1$, at 50% of the half–span

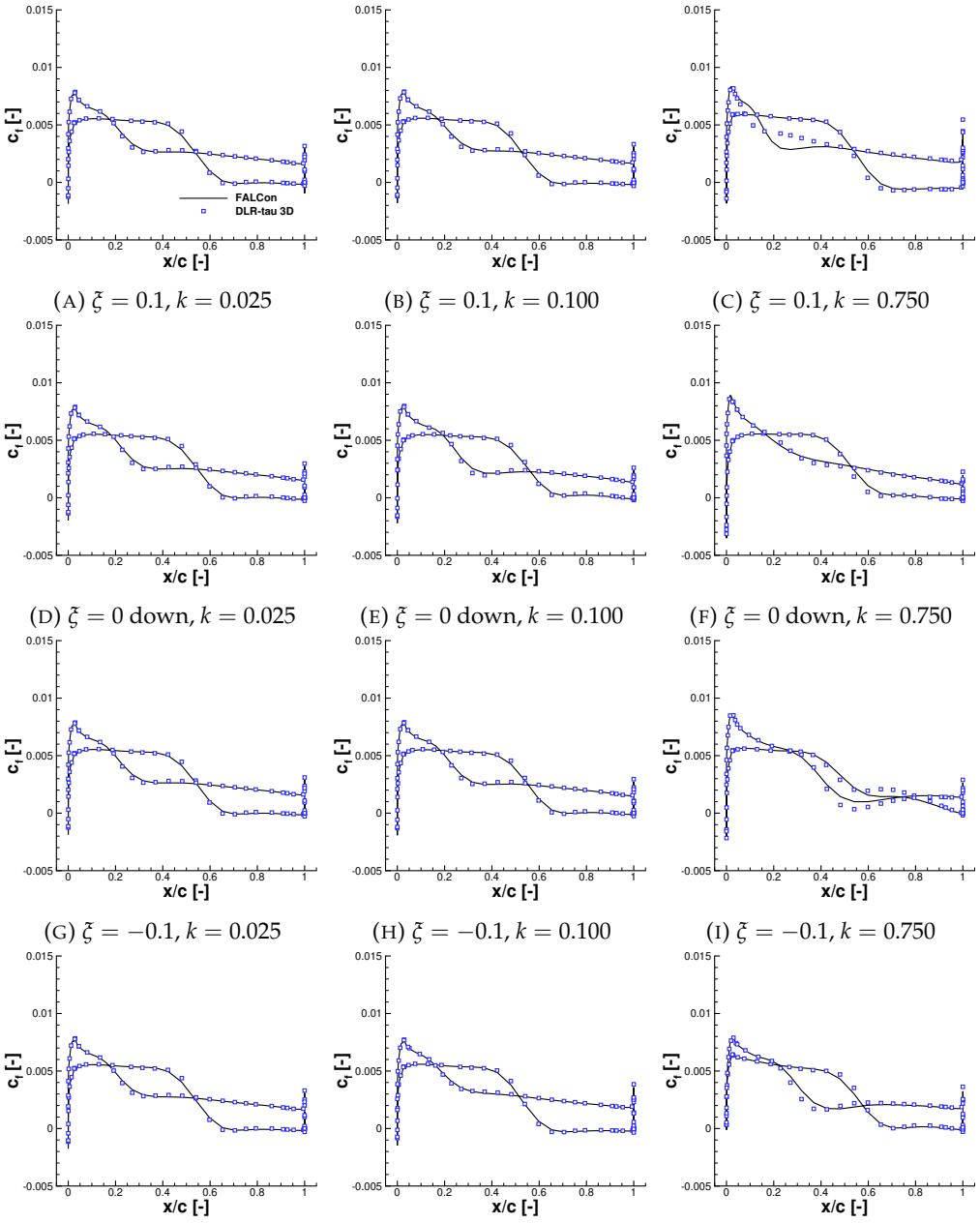

(A) $\xi = 0.1$, $k = 0.025$ (B) $\xi = 0.1$, $k = 0.100$ (C) $\xi = 0.1$, $k = 0.750$

(D) $\xi = 0$ down, $k = 0.025$ (E) $\xi = 0$ down, $k = 0.100$ (F) $\xi = 0$ down, $k = 0.750$

(G) $\xi = -0.1$, $k = 0.025$ (H) $\xi = -0.1$, $k = 0.100$ (I) $\xi = -0.1$, $k = 0.750$

(J) $\xi = 0$ up, $k = 0.025$ (K) $\xi = 0$ up, $k = 0.100$ (L) $\xi = 0$ up, $k = 0.750$

FIGURE A.108: Sectional friction coefficient, c_f, of the third cycle of the plunging unswept NACA2412 wing at $M = 0.8$ and $\xi_A = 0.1$, at 50% of the half–span

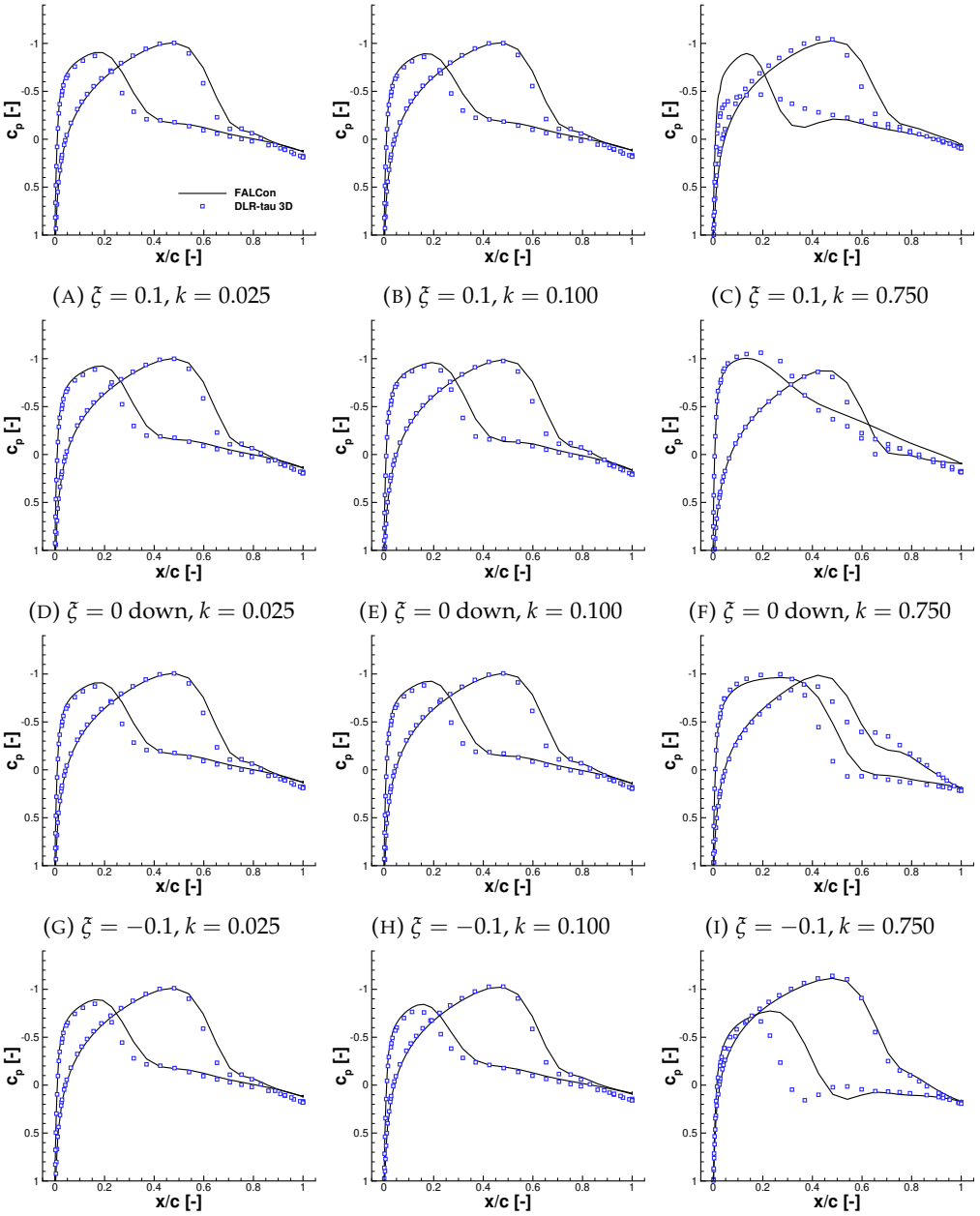

(A) $\xi = 0.1$, $k = 0.025$ (B) $\xi = 0.1$, $k = 0.100$ (C) $\xi = 0.1$, $k = 0.750$

(D) $\xi = 0$ down, $k = 0.025$ (E) $\xi = 0$ down, $k = 0.100$ (F) $\xi = 0$ down, $k = 0.750$

(G) $\xi = -0.1$, $k = 0.025$ (H) $\xi = -0.1$, $k = 0.100$ (I) $\xi = -0.1$, $k = 0.750$

(J) $\xi = 0$ up, $k = 0.025$ (K) $\xi = 0$ up, $k = 0.100$ (L) $\xi = 0$ up, $k = 0.750$

FIGURE A.109: Sectional pressure coefficient, c_p, of the third cycle of the plunging unswept NACA2412 wing at $M = 0.8$ and $\xi_A = 0.1$, at 75% of the half–span

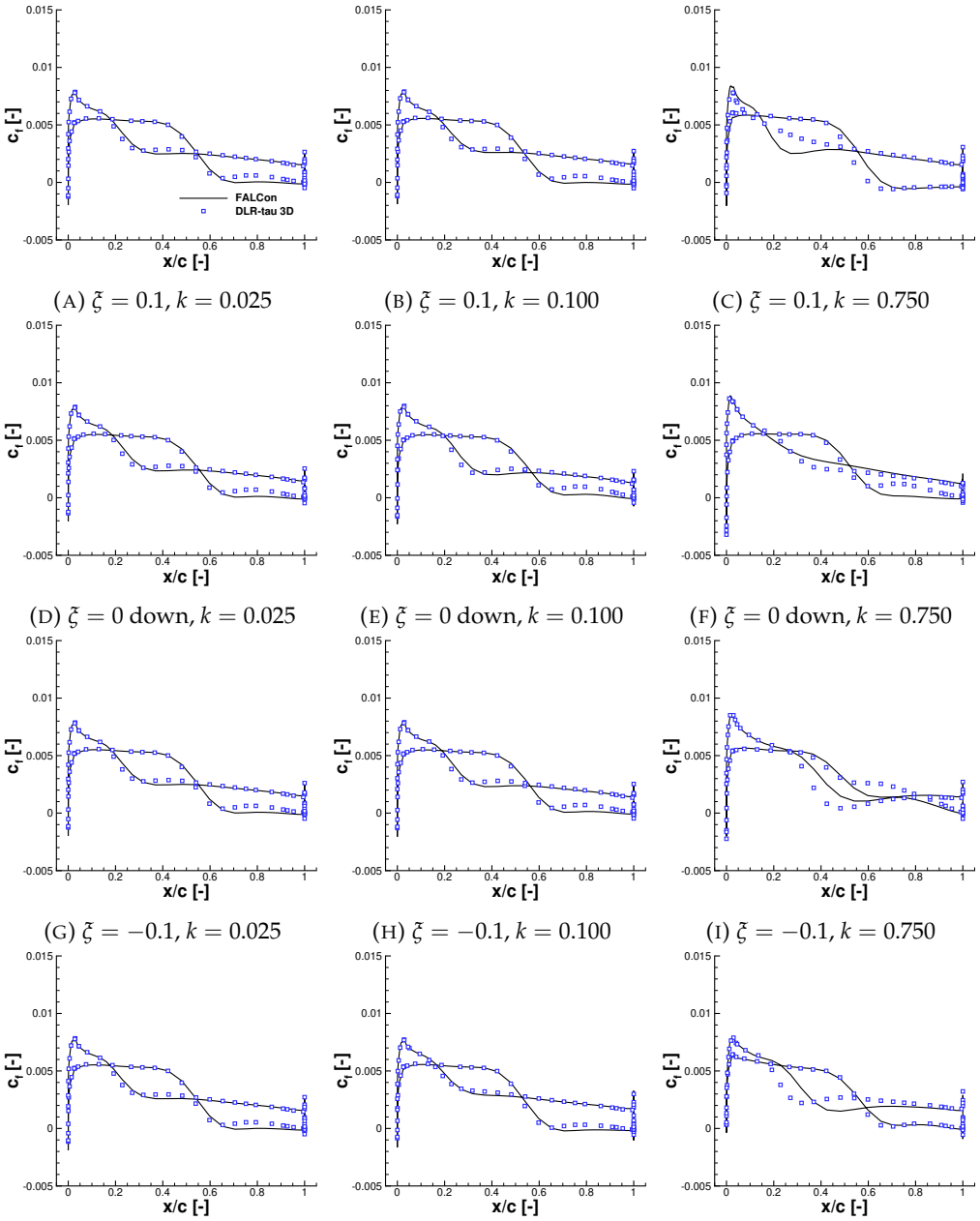

(A) $\xi = 0.1$, $k = 0.025$ (B) $\xi = 0.1$, $k = 0.100$ (C) $\xi = 0.1$, $k = 0.750$

(D) $\xi = 0$ down, $k = 0.025$ (E) $\xi = 0$ down, $k = 0.100$ (F) $\xi = 0$ down, $k = 0.750$

(G) $\xi = -0.1$, $k = 0.025$ (H) $\xi = -0.1$, $k = 0.100$ (I) $\xi = -0.1$, $k = 0.750$

(J) $\xi = 0$ up, $k = 0.025$ (K) $\xi = 0$ up, $k = 0.100$ (L) $\xi = 0$ up, $k = 0.750$

FIGURE A.110: Sectional friction coefficient, c_f, of the third cycle of the plunging unswept NACA2412 wing at $M = 0.8$ and $\xi_A = 0.1$, at 75% of the half–span

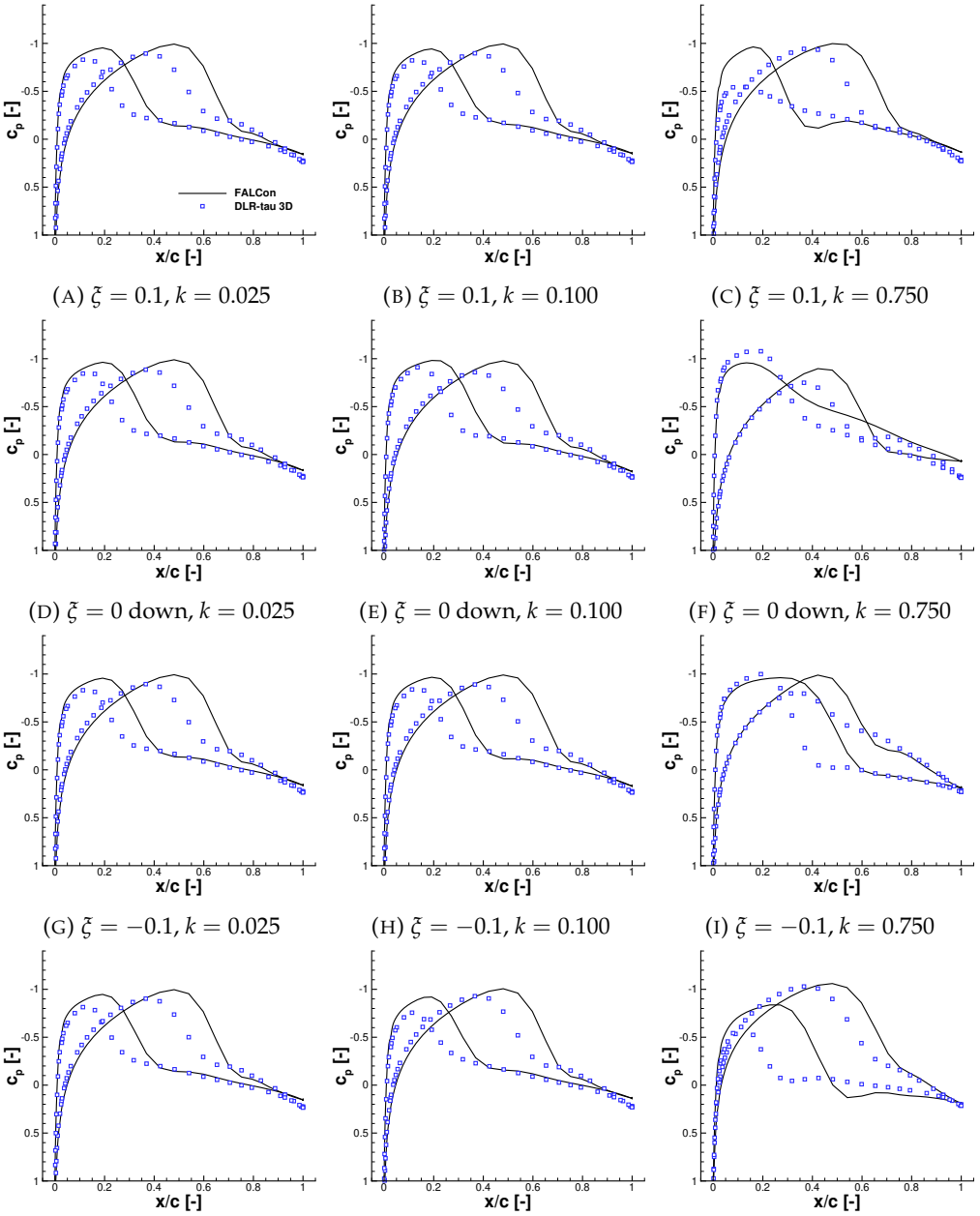

(A) $\xi = 0.1$, $k = 0.025$ (B) $\xi = 0.1$, $k = 0.100$ (C) $\xi = 0.1$, $k = 0.750$

(D) $\xi = 0$ down, $k = 0.025$ (E) $\xi = 0$ down, $k = 0.100$ (F) $\xi = 0$ down, $k = 0.750$

(G) $\xi = -0.1$, $k = 0.025$ (H) $\xi = -0.1$, $k = 0.100$ (I) $\xi = -0.1$, $k = 0.750$

(J) $\xi = 0$ up, $k = 0.025$ (K) $\xi = 0$ up, $k = 0.100$ (L) $\xi = 0$ up, $k = 0.750$

FIGURE A.111: Sectional pressure coefficient, c_p, of the third cycle of the plunging unswept NACA2412 wing at $M = 0.8$ and $\xi_A = 0.1$, at 90% of the half–span

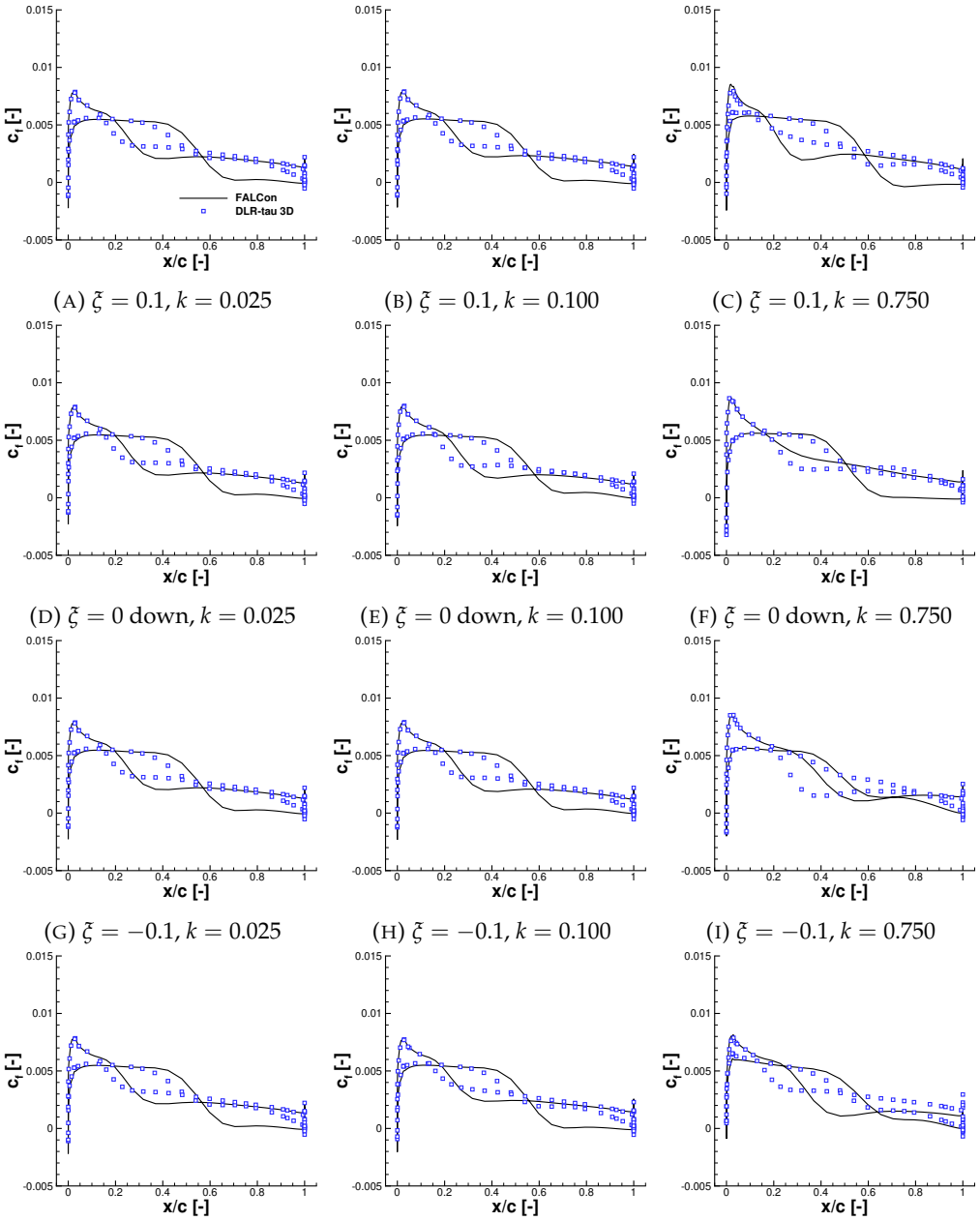

(A) $\xi = 0.1$, $k = 0.025$ (B) $\xi = 0.1$, $k = 0.100$ (C) $\xi = 0.1$, $k = 0.750$

(D) $\xi = 0$ down, $k = 0.025$ (E) $\xi = 0$ down, $k = 0.100$ (F) $\xi = 0$ down, $k = 0.750$

(G) $\xi = -0.1$, $k = 0.025$ (H) $\xi = -0.1$, $k = 0.100$ (I) $\xi = -0.1$, $k = 0.750$

(J) $\xi = 0$ up, $k = 0.025$ (K) $\xi = 0$ up, $k = 0.100$ (L) $\xi = 0$ up, $k = 0.750$

FIGURE A.112: Sectional friction coefficient, c_f, of the third cycle of the plunging unswept NACA2412 wing at $M = 0.8$ and $\xi_A = 0.1$, at 90% of the half–span

References

[1] Aviation 2019 best papers. https://staging-iac2019.rd.net/aviation/program/recognition. Accessed: 2019-09-08.

[2] ACARE. Strategic research agenda. Vol. 2(September):12–19, 10 2002.

[3] Frederico Afonso, José Vale, Éder Oliveira, Fernando Lau, and Afzal Suleman. A review on non-linear aeroelasticity of high aspect-ratio wings, 2017. ISSN 03760421.

[4] Kamran Ahmad, Hammad Rahman, and Hassan Junaid Hasham. Nonlinear static aeroelastic analysis of high aspect ratio wing. In *Proceedings of 2014 11th International Bhurban Conference on Applied Sciences & Technology (IBCAST) Islamabad, Pakistan, 14th-18th January, 2014*, pages 349–353. IEEE, 2014.

[5] AIAA. 1st aiaa cfd drag prediction workshop. https://aiaa-dpw.larc.nasa.gov/Workshop1/workshop1.html, 2001. URL https://aiaa-dpw.larc.nasa.gov/Workshop1/workshop1.html. Accessed: 2019-01-04.

[6] Airbus. Airbus. Global market forecast 2007–2026. *2007*, 2007.

[7] E. Angerson, Z. Bai, J. Dongarra, A. Greenbaum, A. McKenney, J. Du Croz, S. Hammarling, J. Demmel, C. Bischof, and D. Sorensen. Lapack: A portable linear algebra library for high-performance computers. In *Supercomputing '90:Proceedings of the 1990 ACM/IEEE Conference on Supercomputing*, pages 2–11, 1990.

[8] K. J. Badcock, S. Timme, S. Marques, H. Khodaparast, M. Prandina, J. E. Mottershead, A. Swift, A. Da Ronch, and M. A. Woodgate. Transonic aeroelastic simulation for instability searches and uncertainty analysis. *Progress in Aerospace Sciences*, 47(5):392–423, 2011. ISSN 0376-0421. .

[9] L Susan Blackford, Antoine Petitet, Roldan Pozo, Karin Remington, R Clint Whaley, James Demmel, Jack Dongarra, Iain Duff, Sven Hammarling, Greg Henry, et al. An updated set of basic linear algebra subprograms (blas). *ACM Transactions on Mathematical Software*, 28(2):135–151, 2002.

[10] Max Blair. A compilation of the mathematics leading to the doublet-lattice method. *USAF WL-TR-95-3022*, 1994.

[11] Boeing Commercial Airplanes. *Boeing. Current market outlook 2008–2027*. Number September. Boeing, 2008.

[12] Benjamin J. Brelje and Joaquim R.R.A. Martins. Electric, hybrid, and turboelectric fixed-wing aircraft: A review of concepts, models, and design approaches. *Progress in Aerospace Sciences*, (June):1–19, 2018. ISSN 03760421. .

[13] O. C. de Resende. The evolution of the aerodynamic design tools and transport aircraft wings at embraer. *Journal of The Brazilian Society of Mechanical Sciences and Engineering - J BRAZ SOC MECH SCI ENG*, 26, 12 2004. .

[14] Luca Cavagna, Sergio Ricci, and Lorenzo Travaglini. Neocass: An integrated tool for structural sizing, aeroelastic analysis and mdo at conceptual design level. *Progress in Aerospace Sciences*, 47(8):621 – 635, 2011. ISSN 0376-0421. . Special Issue - Modeling and Simulating Aircraft Stability and Control.

[15] Luca Cavagna, Sergio Ricci, and Lorenzo Travaglini. NeoCASS: An integrated tool for structural sizing, aeroelastic analysis and MDO at conceptual design level. *Progress in Aerospace Sciences*, 47(8):621–635, 2011. ISSN 03760421. . URL http://dx.doi.org/10.1016/j.paerosci.2011.08.006.

[16] Rauno Cavallaro and Luciano Demasi. Challenges, Ideas, and Innovations of Joined-Wing Configurations: A Concept from the Past, an Opportunity for the Future. *Progress in Aerospace Sciences*, 87:1–93, 2016. ISSN 03760421. .

[17] Carlos ES Cesnik and Dewey H Hodges. Vabs: a new concept for composite rotor blade cross-sectional modeling. *Journal of the American helicopter society*, 42 (1):27–38, 1997.

[18] C-S Chang, Dewey H Hodges, and Mayuresh J Patil. Flight dynamics of highly flexible aircraft. *Journal of Aircraft*, 45(2):538–545, 2008.

[19] Andrea Da Ronch, Marco Panzeri, Anas Abd Bari, Roberto d'Ippolito, and Matteo Franciolini. Adaptive design of experiments for efficient and accurate estimation of aerodynamic loads. *Aircraft Engineering and Aerospace Technology*, 89(4): 558–569, 2017.

[20] Leonardo Dagum and Ramesh Menon. Openmp: an industry standard api for shared-memory programming. *Computational Science & Engineering, IEEE*, 5(1): 46–55, 1998.

[21] M.J. de C. Henshaw, K.J. Badcock, G.A. Vio, C.B. Allen, J. Chamberlain, I. Kaynes, G. Dimitriadis, J.E. Cooper, M.A. Woodgate, A.M. Rampurawala, D. Jones, C. Fenwick, A.L. Gaitonde, N.V. Taylor, D.S. Amor, T.A. Eccles, and C.J. Denley.

Non-linear aeroelastic prediction for aircraft applications. *Progress in Aerospace Sciences*, 43(4):65 – 137, 2007. ISSN 0376-0421. .

[22] LAPACK documentation, 2016. Available at http://www.netlib.org/lapack/.

[23] OpenBLAS documentation, 2016. Available at http://www.openblas.net/.

[24] Mark Drela. Integrated simulation model for preliminary aerodynamic, structural, and control-law design of aircraft. In *40th Structures, Structural Dynamics, and Materials Conference and Exhibit*, page 1394, 1999.

[25] Mark Drela and Michael B. Giles. Viscous-inviscid analysis of transonic and low reynolds number airfoils. *AIAA Journal*, 25(10):1347–1355, 1987. . URL https://doi.org/10.2514/3.9789.

[26] Mark Drela and Harold Youngren. Athena vortex lattice. *http://web.mit.edu/drela/Public/web/avl/*, 2020.

[27] J. Drofelnik, A. Da Ronch, M. Franciolini, and A. Crivellini. Fast identification of transonic buffet envelope using computational fluid dynamics. *Aircraft Engineering and Aerospace Technology*, 91(2):309–316, 2019. .

[28] J. Droflenik and A. Da Ronch. 2.5d+ user guide. Technical report, Documentation for DLR-Tau flow solver, 2017.

[29] Ali Elham and Michel J. L. van Tooren. Coupled adjoint aerostructural wing optimization using quasi-three-dimensional aerodynamic analysis. *Structural and Multidisciplinary Optimization*, 54(4):889–906, Oct 2016. ISSN 1615-1488. . URL https://doi.org/10.1007/s00158-016-1447-9.

[30] V.M. Falkner. The accuracy of calculations based on vortex lattice theory. *Rep. No. 9621, British A.R.C.*, 1946.

[31] M. Franciolini, A. Da Ronch, J. Drofelnik, D. Raveh, and A. Crivellini. Efficient infinite-swept wing solver for steady and unsteady compressible flows. *Aerospace Science and Technology*, 72:217 – 229, 2018. ISSN 1270-9638. .

[32] Michele Gaffuri and Joël Brezillon. Unstructured mesh capabilities for supersonic wing design at low speed conditions. In *CFD & OPTIMIZATION 2011 - 048, ECCOMAS Thematic Conference CFD & OPTIMIZATION*, 01 2011.

[33] S. Gallay and E. Laurendeau. Nonlinear generalized lifting-line coupling algorithms for pre/poststall flows. *AIAA Journal*, 53(7):1784–1792, Apr 2015. ISSN 0001-1452. . URL http://dx.doi.org/10.2514/1.J053530.

[34] S Gallay and E Laurendeau. Preliminary-design aerodynamic model for complex configurations using lifting-line coupling algorithm. *Journal of Aircraft*, 53 (4):1145–1159, 2016.

[35] Joseph Garcia and Guru Guruswamy. Aeroelastic analysis of transonic wings using navier-stokes equations and a nonlinear beam finite element model. In *40th Structures, Structural Dynamics, and Materials Conference and Exhibit*, page 1215, 1999.

[36] W. R. Graham, C. A. Hall, and M. Vera Morales. The potential of future aircraft technology for noise and pollutant emissions reduction. *Transport Policy*, 34:36–51, 2014. ISSN 0967070X. .

[37] Justin S. Gray, John T. Hwang, Joaquim R. R. A. Martins, Kenneth T. Moore, and Bret A. Naylor. Openmdao: an open-source framework for multidisciplinary design, analysis, and optimization. *Structural and Multidisciplinary Optimization*, 59(4):1075–1104, Apr 2019. ISSN 1615-1488. .

[38] Ben Hallissy and Carlos Cesnik. High-fidelity aeroelastic analysis of very flexible aircraft. In *52nd AIAA/ASME/ASCE/AHS/ASC Structures, Structural Dynamics and Materials Conference 19th AIAA/ASME/AHS Adaptive Structures Conference 13t*, page 1914, 2011.

[39] Ping He, Charles A. Mader, Joaquim R. R. A. Martins, and Kevin J. Maki. Dafoam: An open-source adjoint framework for multidisciplinary design optimization with openfoam. *AIAA Journal*, 58(3):1304–1319, 2020. .

[40] Dewey H Hodges. A mixed variational formulation based on exact intrinsic equations for dynamics of moving beams. *International journal of solids and structures*, 26(11):1253–1273, 1990.

[41] Dewey H Hodges. *Nonlinear composite beam theory*. American Institute of Aeronautics and Astronautics, 2006.

[42] Dagenhart J Ray and William S Saric. Crossflow stability and transition experiments in swept-wing flow. Technical report, NASA Langley Research Center; Hampton, VA United States, 1999.

[43] A. Jameson, W. Schmidt, and E. Turkel. Numerical solutions of the euler equations by finite volume methods using runge–kutta time–stepping schemes. In *14th Fluid and Plasma Dynamics Conference, Fluid Dynamics and Co–located Conferences, Palo Alto, CA*, 1981. .

[44] Thushara Kandaramath Hari, Zahira Yaakob, and Narayanan N. Binitha. Aviation biofuel from renewable resources: Routes, opportunities and challenges. *Renewable and Sustainable Energy Reviews*, 42:1234–1244, 2015. ISSN 13640321. .

[45] Joseph Katz and Allen Plotkin. *Low-speed aerodynamics*, volume 13. Cambridge University Press, 2001.

[46] Bhupendra Khandelwal, Adam Karakurt, Paulas R. Sekaran, Vishal Sethi, and Riti Singh. Hydrogen powered aircraft: The future of air transport. *Progress in Aerospace Sciences*, 60:45–59, 2013. ISSN 03760421. .

[47] Daniel Kharlamov, Jernjej Drofelnik, Andrea Da Ronch, and Scott Walker. Rapid load calculations using an efficient unsteady aerodynamic solver. In *2018 Atmospheric Flight Mechanics Conference*, page 3621, 2018. . URL https://arc.aiaa.org/doi/abs/10.2514/6.2018-3621.

[48] Daniel Kharlamov, Andrea Da Ronch, Jernej Drofelnik, , and Scott Walker. Fast load calculations based on a generalised unsteady coupling algorithm. *AIAA Journal*, 2020. Under review.

[49] Bertrand Kirsch, Olivier Montagnier, Emmanuel Benard, and Thierry Faure. Dynamic aeroelastic simulation of composite wing for hale uav application. In *European Conference for AeroSpace Sciences, Milan*, 07 2017. .

[50] Bertrand Kirsch, Olivier Montagnier, Emmanuel Bénard, and Thierry Faure. Assessment of aeroelastic tailoring effect on high-aspect-ratio composite wing flutter speed using an open source reduced order model solver. In *18 th European Conference on Composite Materials*, pages 24–28, 2018.

[51] Thomas Lambert, Norizham Abdul Razak, and Grigorios Dimitriadis. Vortex lattice simulations of attached and separated flows around flapping wings. *Aerospace*, 4(2), 2017. ISSN 2226-4310. . URL http://www.mdpi.com/2226-4310/4/2/22.

[52] J. G. Leishman and T. S. Beddoes. A Semi-Empirical Model for Dynamic Stall. *Journal of the American Helicopter Society*, 1989. ISSN 21616027. .

[53] J. G. Leishman and K. Q. Nguyen. State-space representation of unsteady airfoil behavior. *AIAA Journal*, 28(5):836–844, 1990. . URL https://doi.org/10.2514/3.25127.

[54] J Gordon Leishman and TS Beddoes. A semi-empirical model for dynamic stall. *Journal of the American Helicopter society*, 34(3):3–17, 1989.

[55] David W. Levy, Thomas Zickuhr, John Vassberg, Shreekant Agrawal, Richard A. Wahls, Shahyar Pirzadeh, and Michael J. Hemsch. Data summary from the first aiaa computational fluid dynamics drag prediction workshop. *Journal of Aircraft*, 40(5):875–882, Sep 2003. ISSN 0021-8669. . URL http://dx.doi.org/10.2514/2.6877.

[56] Dongfeng Li, Chunlin Gong, Andrea Da Ronch, Gang Chen, and Yueming Li. An efficient implementation of aeroelastic tailoring based on efficient computational fluid dynamics-based reduced order model. *Journal of Fluids and Structures*, 84: 182 – 198, 2019. ISSN 0889-9746. .

[57] Joaquim R. R. A. Martins and Andrew B. Lambe. Multidisciplinary design optimization: A survey of architectures. *AIAA Journal*, 51(9):2049–2075, 2013. .

[58] H Multhopp and M Schwabe. *Die Berechnung der Auftriebsverteilung von Tragflügeln*. 1938.

[59] Joseba Murua. *Flexible Aircraft Dynamics with a Geometrically-Nonlinear Description of the Unsteady Aerodynamics*. PhD thesis, Imperial College London, United Kingdom, 2012.

[60] Joseba Murua, Rafael Palacios, and J. Michael R. Graham. Applications of the unsteady vortex-lattice method in aircraft aeroelasticity and flight dynamics. *Progress in Aerospace Sciences*, 55(Supplement C):46 – 72, 2012. ISSN 0376-0421. .

[61] Joseba Murua, Rafael Palacios, and J Michael R. Graham. Assessment of wake-tail interference effects on the dynamics of flexible aircraft. *AIAA journal*, 50(7): 1575–1585, 2012.

[62] Joseba Murua, Pablo Martínez, Héctor Climent, Louw van Zyl, and Rafael Palacios. T-tail flutter: Potential-flow modelling, experimental validation and flight tests. *Progress in Aerospace Sciences*, 71:54 – 84, 2014. ISSN 0376-0421.

[63] OpenMP Architecture Review Board. OpenMP application program interface version 3.0, May 2008. URL `http://www.openmp.org/mp-documents/spec30.pdf`.

[64] Muhammad F. Othman, Gustavo H.C. Silva, Pedro H. Cabral, Alex P. Prado, Alberto Pirrera, and Jonathan E. Cooper. A robust and reliability-based aeroelastic tailoring framework for composite aircraft wings. *Composite Structures*, 208:101 – 113, 2019. ISSN 0263-8223. .

[65] Rafael Palacios and Carlos Cesnik. Static nonlinear aeroelasticity of flexible slender wings in compressible flow. In *46th AIAA/ASME/ASCE/AHS/ASC Structures, Structural Dynamics and Materials Conference*, page 1945, 2005.

[66] Matthieu Parenteau, Frederic Plante, Eric Laurendeau, and Michel Costes. Unsteady coupling algorithm for lifting-line methods. In *55th AIAA Aerospace Sciences Meeting*, page 0951, 2017.

[67] Mayuresh J Patil. *Nonlinear aeroelastic analysis, flight dynamics, and control of a complete aircraft*. PhD thesis, School of Aerospace Engineering, Georgia Institute of Technology, 1999.

[68] Mayuresh J. Patil, Dewey H. Hodges, and Carlos E. S. Cesnik. Nonlinear Aeroelasticity and Flight Dynamics of High-Altitude Long-Endurance Aircraft. *Journal*

of Aircraft, 38(1):88–94, 2001. ISSN 0021-8669. . URL http://arc.aiaa.org/doi/10.2514/2.2738.

[69] M.J. Patil and D.H. Hodges. On the importance of aerodynamic and structural geometrical nonlinearities in aeroelastic behavior of high-aspect-ratio wings. *Journal of Fluids and Structures*, 19(7):905 – 915, 2004. ISSN 0889-9746. .

[70] David A Peters, Swaminathan Karunamoorthy, and Wen-Ming Cao. Finite state induced flow models. i-two-dimensional thin airfoil. *Journal of Aircraft*, 32(2): 313–322, 1995.

[71] P. Piperni, A. DeBlois, and R. Henderson. Development of a multilevel multidisciplinary-optimization capability for an industrial environment. *AIAA Journal*, 51(10):2335–2352, Aug 2013. ISSN 0001-1452. . URL http://dx.doi.org/10.2514/1.J052180.

[72] C. Pornet and A. T. Isikveren. Conceptual design of hybrid-electric transport aircraft. *Progress in Aerospace Sciences*, 79:114–135, 2015. ISSN 03760421. .

[73] Daniel Raymer. *Aircraft design: a conceptual approach*. American Institute of Aeronautics and Astronautics, Inc., 2018.

[74] G. Redeker, R. Müller, D. Isaacs, and R. Hirdes. A selection of experimental test cases for the validation of cfd codes. Technical Report 303, Advisory group for aerospace research and development, 7 Rue ancelle, 92200 Neuilly-Sur-Seine, France, aug 1994.

[75] Carlo E.D. Riboldi. An optimal approach to the preliminary design of small hybrid-electric aircraft. *Aerospace Science and Technology*, 81:14–31, 2018. ISSN 12709638. . URL https://doi.org/10.1016/j.ast.2018.07.042.

[76] Arthur Rizzi. Modeling and simulating aircraft stability and control—the simsac project. *Progress in Aerospace Sciences*, 47(8):573 – 588, 2011. ISSN 0376-0421. . Special Issue - Modeling and Simulating Aircraft Stability and Control.

[77] A. Da Ronch, M. Ghoreyshi, and K. J. Badcock. On the generation of flight dynamics aerodynamic tables by computational fluid dynamics. *Progress in Aerospace Sciences*, 47(8):597–620, November 2011.

[78] DAVID M. SCHUSTER, JOSEPH VADYAK, and ESSAM ATTA. Static aeroelastic analysis of fighter aircraft using a three-dimensional navier-stokes algorithm. *Journal of Aircraft*, 27(9):820–825, 1990. .

[79] Dieter Schwamborn, Thomas Gerhold, and Ralf Heinrich. The DLR TAU–code: recent applications in research and industry. In *Proceedings of the European Conference on Computational Fluid Dynamics (ECCOMAS)*, September 2006.

[80] WR Sears. Some recent developments in airfoil theory. *Journal of the Aeronautical Sciences*, 23(5):490–499, 1956.

[81] Alessandro Sgueglia, Peter Schmollgruber, Nathalie Bartoli, Emmanuel Benard, Joseph Morlier, John Jasa, Joaquim R. R. A. Martins, John T. Hwang, and Justin S. Gray. Multidisciplinary design optimization framework with coupled derivative computation for hybrid aircraft. *Journal of Aircraft*, 57(4):715–729, 2020. .

[82] Christopher M. Shearer and Carlos E.S. Cesnik. Nonlinear Flight Dynamics of Very Flexible Aircraft. *Journal of Aircraft*, 44(5):1528–1545, 2007. ISSN 0021-8669. . URL http://arc.aiaa.org/doi/10.2514/1.27606.

[83] Christopher M Shearer and Carlos ES Cesnik. Nonlinear flight dynamics of very flexible aircraft. *Journal of Aircraft*, 44(5):1528–1545, 2007.

[84] Robert J. S. Simpson, Rafael Palacios, and Joseba Murua. Induced-drag calculations in the unsteady vortex lattice method. *AIAA Journal*, 51(7):1775–1779, May 2013. ISSN 0001-1452. . URL https://doi.org/10.2514/1.J052136.

[85] James C Sivells and Robert H Neely. Method for calculating wing characteristics by lifting-line theory using nonlinear section lift data. Technical report, DTIC Document, 1947.

[86] J.C. Sivells and G.C. Westrick. *Method for Calculating Lift Distributions for Unswept Wings with Flaps Or Ailerons by Use of Nonlinear Section Lift Data*. National Advisory Committee for Aeronautics, NACA R-1090. U.S. Government Printing Office, 1952.

[87] M Smith, M Patil, and D Hodges. Cfd-based analysis of nonlinear aeroelastic behavior of high-aspect ratio wings. In *19th AIAA Applied Aerodynamics Conference*, page 1582, 2001.

[88] Philippe Spalart and Steven Allmaras. A one-equation turbulence model for aerodynamic flows. *AIAA*, 439, 01 1992. .

[89] Weihua Su and Carlos E. S. Cesnik. Nonlinear Aeroelasticity of a Very Flexible Blended-Wing-Body Aircraft. *Journal of Aircraft*, 47(5):1539–1553, 2010. ISSN 0021-8669. . URL http://arc.aiaa.org/doi/10.2514/1.47317.

[90] Itiro Tani. *A simple method of calculating the induced velocity of a monoplane wing*. Aeronautical Research Institute, Tokyo Imperial University, 1934.

[91] Theodore Theodorsen and WH Mutchler. General theory of aerodynamic instability and the mechanism of flutter. *National Advisory Committee for Aeronautics Washington, DC, USA*, 1935.

[92] Walter Tollmien, Hermann Schlichting, Henry Görtler, and FW Riegels. Applications of modern hydrodynamics to aeronautics. In *Ludwig Prandtl Gesammelte Abhandlungen*, pages 433–515. Springer, 1961.

[93] Giuseppe Trapani, A Mark Savill, T. Kipouros, Christian Agostinelli, and Abdul Rampurawala. A rapid approach to the aerodynamic design of a flexible high-lift wing, 2014. URL https://arc.aiaa.org/doi/abs/10.2514/6.2014-2011.

[94] Jing-Biau Tseng and C. Edward Lan. *Calculation of aerodynamic characteristics of airplane configurations at high angles of attack*, volume 4182. National Aeronautics and Space Administration, Scientific and Technical . . . , 1988.

[95] C.P. van Dam. The aerodynamic design of multi-element high-lift systems for transport airplanes. *Progress in Aerospace Sciences*, 38(2):101 – 144, 2002. ISSN 0376-0421. .

[96] C.P. Van Dam, J.C. Vander Kam, and J.K. Paris. Design-oriented high-lift methodology for general aviation and civil transport aircraft. *Journal of aircraft*, 38(6): 1076–1084, 2001.

[97] Louw H. Van Zyl and Edward H. Mathews. Aeroelastic analysis of t-tails using an enhanced doublet lattice method. *Journal of Aircraft*, 48(3):823–831, 2011. .

[98] John Vassberg, Pieter Buning, and C Rumsey. Drag prediction for the dlr-f4 wing/body using overflow and cfl3d on an overset mesh. In *40th AIAA Aerospace Sciences Meeting & Exhibit*, page 840, 2002.

[99] Cipolla Vittorio, Frediani Aldo, Abu Salem Karim, Binante Vincenzo, Rizzo Emanuele, and Maganzi Marco. Preliminary transonic CFD analyses of a PrandtlPlane transport aircraft. *Transportation Research Procedia*, 29:82–91, 2018. ISSN 23521465. .

[100] Patrick C. Vratny and Mirko Hornung. Sizing Considerations of an Electric Ducted Fan for Hybrid Energy Aircraft. *Transportation Research Procedia*, 29(2017): 410–426, 2018. ISSN 23521465. .

[101] Yasuhiro Wada and Meng-Sing Liou. A flux splitting scheme with high-resolution and robustness for discontinuities. In *32nd Aerospace Sciences Meeting and Exhibit*, page 83, 1994.

[102] Qi Wang and Wenbin Yu. Geometrically nonlinear analysis of composite beams using wiener-milenković parameters. *Journal of Renewable and Sustainable Energy*, 9(3):033306, 2017. .

[103] Qi Wang, Wenbin Yu, and Michael Sprague. Geometric nonlinear analysis of composite beams using wiener-milenković parameters. In *54th AIAA/ASME/ASCE/AHS/ASC Structures, Structural Dynamics, and Materials Conference*, page 1697, 2013.

[104] Zhicun Wang, Ping C Chen, Danny D Liu, and Dean T Mook. Nonlinear-aerodynamics/nonlinear-structure interaction methodology for a high-altitude long-endurance wing. *Journal of aircraft*, 47(2):556–566, 2010.

[105] A Westenberger. Liquid hydrogen fuelled aircraft–system analysis. Technical report, European Commission Final Technical Report No. GRD1-1999-10014, 2003.

[106] Ludovic Wiart, Olivier Atinault, Richard Grenon, Bernard Paluch, and David Hue. Development of NOVA Aircraft Configurations for Large Engine Integration Studies. *33rd AIAA Applied Aerodynamics Conference*, (June):1–30, 2015. .

[107] Changchuan Xie, Libo Wang, Chao Yang, and Yi Liu. Static aeroelastic analysis of very flexible wings based on non-planar vortex lattice method. *Chinese Journal of Aeronautics*, 26(3):514 – 521, 2013. ISSN 1000-9361. .

[108] Guangda Yang, Andrea Da Ronch, Daniel Kharlamov, and Jernej Drofelnik. Wing twist optimisation using aerodynamic solvers of different fidelity. In *31st Congress of the International Council of the Aeronautical Sciences (ICAS 2018)*, 2018. URL https://eprints.soton.ac.uk/423722/.

[109] Wenbin Yu. *Variational asymptotic modeling of composite dimensionally reducible structures*. PhD thesis, Aerospace Engineering, Georgia Institute of Technology, 2002.

[110] Wenbin Yu and Maxwell Blair. Gebt: A general-purpose nonlinear analysis tool for composite beams. *Composite Structures*, 94(9):2677–2689, 2012.

[111] Wenbin Yu and Qi Wang. Geometrically Exact Beam Theory. https://cdmhub.org/resources/gebt, 2014. [Online; accessed 19-July-2019].